



---

**Forschungszentrum Karlsruhe**  
in der Helmholtz-Gemeinschaft

---

**Wissenschaftliche Berichte**  
FZKA 7383

**Nuclear Fusion Programme  
Annual Report of the  
Association Forschungszentrum  
Karlsruhe/EURATOM  
January 2007 – December 2007**

**Programm Kernfusion**

**Juni 2008**



# **Forschungszentrum Karlsruhe**

in der Helmholtz-Gemeinschaft

Wissenschaftliche Berichte

FZKA 7383

Nuclear Fusion Programme  
Annual Report of the  
Association Forschungszentrum Karlsruhe/  
EURATOM  
January 2007 – December 2007

compiled by I. Pleli  
Programm Kernfusion

This work, supported by the European Communities under the contract of Association between EURATOM and Forschungszentrum Karlsruhe, was carried out within the framework of the European Fusion Development Agreement. The views and opinions expressed herein do not necessarily reflect those of the European Commission.

Für diesen Bericht behalten wir uns alle Rechte vor

Forschungszentrum Karlsruhe GmbH  
Postfach 3640, 76021 Karlsruhe

Mitglied der Hermann von Helmholtz-Gemeinschaft  
Deutscher Forschungszentren (HGF)

ISSN 0947-8620

urn:nbn:de:0005-073833

## Introduction

The worldwide energy consumption is mainly covered by fossil energy sources. Their environmental impact, to a certain extent already visible, requires in the long term new ways of energy supply. In addition the worldwide energy demand will substantially increase in the course of this century in particular in populous countries such as China and India. Nuclear fusion offers an option of an environmental benign energy source with favourable safety features and almost unlimited fuel resources.

Nuclear fusion research is aiming to generate the physical and technical basis of a fusion power station which, similar to the sun, gains energy from the fusion of light atoms. In order to attain ignition of the plasma, the fuel, a mixture of deuterium/tritium (isotopes of hydrogen), must be confined by strong magnetic fields and heated up to more than 100 million degrees.

The construction of the experimental reactor ITER which will start in Cadarache/France in the framework of a worldwide project by 2008 marks the next big step on the way to a fusion power station. For the first time a fusion power of 500 Mega Watt will be generated by a long burning plasma and applied technologies will undergo extended tests. The construction costs including personnel are about 5 billion EURO.

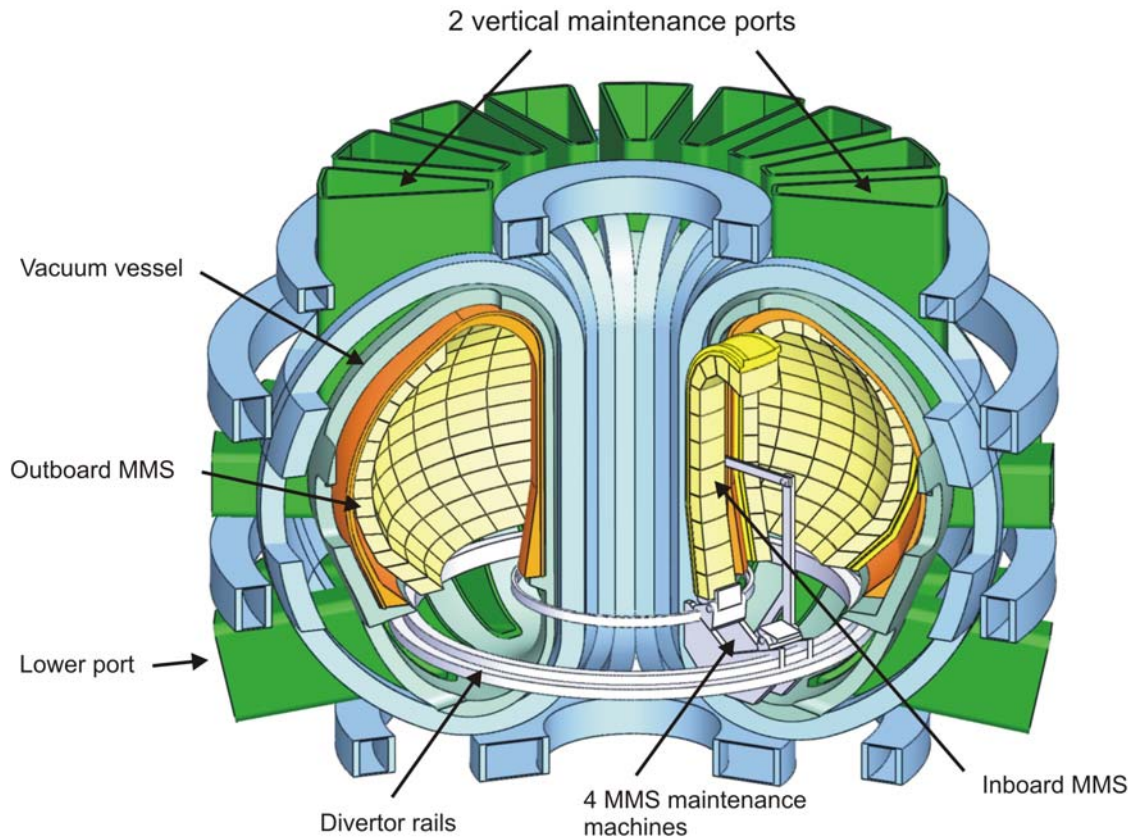
In the framework of the European Fusion Programme the Association FZK-EURATOM is developing key technologies in the areas of superconducting magnets, microwave heating systems (Electron-Cyclotron-Resonance-Heating, ECRH), the deuterium-tritium fuel cycle, He-cooled breeding blankets, a He-cooled divertor and structural materials as well as refractory metals for high heat flux applications including a major participation in the international IFMIF project. Furthermore investigations on plasma wall interactions and core and divertor modelling are carried out and a global plasma model is being developed.

The results from experimental activities such as the tests of high temperature superconducting current leads in the test facility TOSKA, the quasi-stationary gyrotron operation and the operation of fuel cycle subsystems and components with deuterium-tritium have already been utilised for the design work for ITER. In addition large progress has been made in the engineering design of test blanket modules for ITER.

With the construction of ITER new challenges have to be mastered by the EURATOM-Associations. While up to now concepts for components and systems have been developed and their functionality has been tested in laboratory scale or semi-technical scale, now plant components have to be constructed for fabrication and their integration into the plant has to be supported. In order to effectively deploy personal and financial resources consortia of European Association Laboratories are being formed which will bear the responsibility for the realisation of components and systems in accordance with the procurement packages of ITER. This concerns systems in the range of ten up to one hundred millions EURO which require the specific know-how of fusion laboratories. The Association FZK-EURATOM is going to lead a consortium for the construction of the European test blanket module (TBM) systems and a consortium for the construction of the upper port plug ECRH microwave launcher. The negotiations to form these consortia are near to be finalized. In addition the Association FZK-EURATOM is also involved in other consortia such as the fuel cycle and the development and procurement of gyrotrons providing microwaves of 170 GHz and 2 MW output power for ITER. Furthermore the already existing co-operation with industrial companies is being intensified.

The detailed design and construction of ITER components and subsystems needs to be supported by experiments such as prototype testing, validation of scale up factors and additional R&D. For this purpose a helium loop HELOKA is being constructed which not only serves for experimental investigations of the TBM, but also as a pilot loop in view of the loops to be installed in ITER for the cooling of test blanket modules.

The demonstration power station DEMO constitutes the next step beyond ITER which is supposed to be planned after some years of ITER operation. In the framework of a European DEMO study the Association FZK-EURATOM is developing the so-called multi-module blanket concept which promises reduced plant shutdown times during remotely controlled exchange of blankets and thus contributes to an increased plant availability.



Remotely controlled exchange of blanket modules according to the MMS concept.

Furthermore a helium cooled divertor for DEMO is under development. First thermomechanical and thermohydraulic simulations supplemented by experimental investigations have demonstrated that the reference multi-jet concept for the He cooled divertor is able to withstand the heat load in a fusion power reactor.

About 230 professionals and technicians are involved in the fusion programme of the Association FZK-EURATOM with additional support of technical departments.

Progress from January 2007 to December 2007 is reported here. More information is available from the programme management and from the responsible scientists. The website [www.fzk.de/fusion](http://www.fzk.de/fusion) offers further access to the fusion activities of FZK.

# Contents

Page

## Introduction

<b>Plasma Edge</b> .....	1
EFDA/05-1305 (TW5-TPP-BEDAM)      Modelling of Material Damage to Be-clad and Be-coated ITER Plasma Facing Components under Type I ELMs, Disruptions and Mitigated Disruptions, and Scoping Studies for First Experimental Validations .....	3
TW5-TPP-ITERTRAN      Modelling of ITER Divertor Target Damage and Plasma Contamination following ELMs and Disruptions .....	7
TW6-TPP-DAMTRAN      Modelling of ITER Plasma Components Damage and Consequences for Plasma Evolution following ELMs and Disruptions .....	10
TW6-TPP-DUSTGEN      Evaluation of Dust Generation Rates for the Plasma Edge/Divertor Conditions Expected during ELMs and Disruptions for the ITER QDT = 10 Reference Scenario with CFC/W and W Divertor Target by Models Validated with Plasma Gun Experiments .....	15
Divertor and Core Plasma Modelling for ITER .....	18
<b>Heating and Current Drive - Physics</b> .....	25
TW6-TPHE-ECHULA      Upper Launcher Structural Integration and Launcher Handling Test Facility .....	27
<b>Heating and Current Drive – Diagnostics</b> .....	33
EFDA/06-1417 (TW6-TPDS-WINCOD2)      ITER Practice for Non-Metallic Replaceable Window Assemblies .....	35
EFDA/06-1446 (TW6-TPDS-DIADES9)      Diagnostic Design for ITER: Bolometry (Engineering Analysis for Bolometer Cameras) .....	40
<b>Vessel/In-Vessel</b> .....	41
EFDA/07-1704-1624 (TW6-TVV-LEAKD2)      Leak Localisation for In-vessel Components .....	43
<b>Magnet Structure and Integration</b> .....	47
EFDA/03-1105 (TW3-TMSC-CRYLAB)      Cryogenic Laboratory Tests for V-I Characterisation of Subcable Samples .....	49
EFDA/05-1274 (TW5-TMSM-CRYTES)      Cryogenic Testing of Materials, Welds and ITER Mock-ups for Magnet Structures .....	54
EFDA/06-1400 (TW6-TMSP-PFWDES2)      Review of PF2-PF5 Winding Design (ITA 11-88).....	60
EFDA/06-1522 (TW6-TMSC-COILMO)      Definition of Procedures for Coil Electrical Testing and Preparation for PF Transient Analysis.....	62
TW5-TMSF-HTSMAG      Scoping Study of HTS Fusion Magnets .....	65
<b>Breeding Blanket</b> .....	67
TW5-TTB-001      Construction of the High Pressure Helium Loop (HELOKA-HP/TB) for Testing of TBMs .....	69
EFDA/06-1393 (TW6-TTB-RFMON1)      Technical Monitoring Assessment of the EU/RF Collaborative Task on the Development of Diagnostic Systems for Electromagnetic TBMs.....	72
EFDA/06-1394 (TW6-TTBB-RFMON2)      Technical Monitoring and Assessment of the EU/RF Collaborative Task on the Fabrication of Beryllium Pebbles for Fusion Application and Beryllium Recycling .....	73

<b>Breeding Blanket – HCPB Blanket Concept</b> .....		77
TTBB-001	Helium Cooled: TBM Design, Integration and Analysis .....	79
	TW5-TTBB-001 D 2 Detailed Design of Sub-components and Prototypical Mock-ups for the HCPB TBM Qualification .....	79
	TW5-TTBB-001 D 8 Detailed HCPB TBM Development Work Plan and First Technical Specification Document .....	83
	TW5-TTBB-001 D 10 Manufacturing and Testing of a FW Channel Mock-up for Experimental Investigation of Heat Transfer with He at 80 bars and Reference Cooling Conditions. Comparison with Numerical Modeling.....	85
	TW5-TTBB-001 D 11 Analyses for the HELICA and HEXCALIBER Experiments using the ABAQUS Drucker-Prager Model.....	89
	TW6-TTBB-001 D 3 HCPB TBM Design and Integration Analysis .....	91
TTBB-003	Helium Cooled: Out of Pile Testing.....	93
	TW5-TTBB-003 D 1 Manufacturing and Testing of Mock-ups for Investigation of Coolant Flow in the Manifold System of HCPB TBM (GRICAMAN Experiments).....	93
TTBB-005b	Helium Cooled: Modelling of Swelling and Tritium Release in Beryllium under Irradiation .....	99
	TW2-TTBB-005b D 1 Effect of Radiation Damage and Gas Diffusion in Irradiated Beryllium: Results of High Resolution Micro- Tomography .....	99
TTBB-006	Helium Cooled: Breeder and Neutron Multiplier Materials.....	103
	TW6-TTBB-006 D 1 Development of Beryllium and Beryllium Alloy Pebble Beds with Improved Tritium Release Characteristics .....	103
	TW6-TTBB-006 D 2 Procurement and Quality Control of 7 kg of $\text{Li}_4\text{SiO}_4$ Pebbles for Planned Testing of Breeder Unit Mock-ups.....	108
<b>Breeding Blanket – HCLL Blanket Concept</b> .....		111
TTBC-005	Helium Cooled lithium Lead: Process and Auxiliary Components .....	113
	TW6-TTBC-005 D 4 Preparation of Coated Specimens for a Dedicated Pb-Li Compatibility Test: Specimen with Al Coating Produced by an Electrochemical Deposition Process .....	113
TTBC-006	Helium-Cooled Lithium Lead: Magneto-Hydrodynamics and Liquid Metal Materials.....	120
	TW5-TTBC-006 D 1 MHD Experiments on a 3D Relevant Mock-up of the HCLL TBM.....	120
<b>Materials Development – Structural Materials</b> .....		125
EFDA/06-1520 (TW6-TTB-EUROFER)	Support and Follow-up of the EFDA/06-1903 Art. 7 Contract for Procurement of EUROFER for the TBM Fabrication Technology Trials and Mock-ups .....	127
TTMS-001	Irradiation Performance .....	129
	TW2-TTMS-001b D 5 Tensile, Charpy and Fatigue Specimen Testing after Neutron Irradiation up to 15 dpa in the Range of 250°C – 450°C, Completion of the Irradiation and Post-Irradiation Examination .....	129
	TW2-TTMS-001b D 9 Fast Reactor Irradiation up to 30 dpa, at 340°C of Tensile, Charpy and LCF RAF/M Specimens, Completion of the PIE .....	134
	TW4-TTMS-001 D 1 Fabrication and Irradiation of Fe-54 enriched Samples to Study the Influence of He/dpa Ratio on Materials Degradation up to Medium Dose Level.....	138
	TW5-TTMS-001 D 2	
	TW5-TTMS-001 D 10 Mechanical Post Irradiation Examinations of FZK-Specimens Irradiated in the ARBOR-2 Experiment in the BOR 60 Reactor .....	140

	<b>Page</b>
TW5-TTMS-001 D 11	Historical Development of EUROFER and a Critical Assessment of its Chemical Composition ..... 144
TW5-TTMS-001 D 11	Assessment of Impact Test Experiments on Irradiated EUROFER 97 and other RAFM Steels..... 149
TTMS-003	Compatibility with Hydrogen and Liquids ..... 151
TW6-TTMS-003 D 3	Corrosion Testing of EUROFER in Liquid PbLi ..... 151
TTMS-004	Qualification Fabrication Processes..... 157
TW6-TTMS-004 D 1-3	Improve Design Limits of Welded Components through Improved Post Weld Heat Treatments, Qualification and Improvement of Welded and Diffusion Bonded Joints ..... 157
TTMS-005	Rules for Design, Fabrication and Inspection ..... 161
TW2-TTMS-005b D 4	Creep-fatigue Lifetime Prediction Rules for Irradiated EUROFER ..... 161
TW5-TTMS-005 D 3	SSTT: Model the Ductile Region – Development of Models for Transferability of Small Size Specimens to Standard Size and FW Applications
and	
TW6-TTMS-005 D 12	SSTT: Continuation of the Modelling the Ductile Region – Development of Models for Transferability of Small Size Specimens to Standard Size and FW Applications ..... 163
TW5-TTMS-005 D 5	High Temperature Fracture Mechanical (creep-fatigue) Rules: Formulation and Implementation ..... 167
TW5-TTMS-005 D 6	Define and Perform Accompanying Experiments to D 5 (e.g. creep crack growth at 550°C)..... 168
TW6-TTMS-005 D 3	Formulation and Implementation of Design Rules for Joints (TIG, EB, Laser Diffusion Welds)..... 170
TW6-TTMS-005 D 4	Experimental Verification and Validation of Newly Implemented HT Creep-fatigue Rules ..... 172
TW6-TTMS-005 D 5	Qualification of NDT (non-destructive detection techniques) for Evaluation of Limits of Detectable Cracks..... 175
TTMS-006	High Performance Steels ..... 178
TW6-TTMS-006 D 5	Nano Composites Ferritic Steels for HT Application: Identification of Promising Candidate Alloy Compositions and Respective Fabrication Routes According to the Outcome of the 2004 Study. Production of Different Laboratory Batches (14%Cr) ..... 178
TW6-TTMS-006 D 6	Investigate Joining Technologies for ODS/ODS and ODS/ conventional EUROFER..... 182
TW5-TTMS-006 D 10	Characterisation of Reference EU-ODS-EUROFER Batch: Optimisation of Heat Treatment, Ageing Behaviour and Microstructural Characterisation..... 184
TTMS-007	Modelling of Irradiation Effects ..... 189
TW5-TTMS-007 D 5	Defect Microstructure Evolution..... 189
TW5-TTMS-007 D 10	
TW5-TTMS-007 D 7	Production and Characterization of Single Fe-Cr Crystals and Elaboration of a Critical Review of the Physical Metallurgy of EUROFER Alloying Elements and Impurities, Heat-treatment/Phases/Microstructure, Phase Stability, and Segregation ..... 194
TW6-TTMS-007 D 10	
EFDA/06-1469 (TW6-TTMS-MODINI2)	Parametrization of Dislocation Dynamics Code for Non-irradiated and Irradiated Fe ..... 197

		<b>Page</b>
<b>Materials Development – Advanced Materials</b> .....		203
TTMA-002	Divertor and Plasma Facing Materials .....	205
	TW3-TTMA-002 D 3 Mechanical Testing of Improved W Alloys: Tensile and Fracture Toughness Testing .....	205
	TW3-TTMA-002 D 7 TW6-TTMA-002 D 6 Fundamental Studies on Mechanical Properties of W-alloys .....	208
	TW6-TTMA-002 D 8 Production of Small Laboratory Scale Batches of Improved Materials for Characterization.....	211
<b>Materials Development – IFMIF</b> .....		215
TTMI-003	IFMIF – Test Facility .....	217
	TW6-TTMI-003 D 1 Manufacturing and Procurement of a Complete HFTM Compartment Including the Whole Set of Test Samples and the Qualification of Brazing Procurement for the Heating Systems .....	217
	TW6-TTMI-003 D 5 Structural Materials Selection Guideline for In-Test-Cell Components .....	222
EFDA/05-1291 (TW5-TTMI-003a)	Preliminary Design Description Document for the IFMIF Test Facility.....	225
<b>Fuel Cycle – Vacuum Pumping</b> .....		227
TW5-TTFF-VP 51	Mechanical Tests and Post-operational Examination of TIMO .....	229
TW5-TTFF-VP 58	Upgrade of TIMO .....	232
EFDA/06-1468 (TW6-TTFF-VP 54)	Support to EFDA CSU Garching in Monitoring of Contract for ITER 1:1 Prototype Torus Exhaust Cryopump (PTC) Fabrication and Associated Fatigue Test (under Task TW6-TTFF-VP 55) .....	235
EFDA/07-1704-1566 (TW6-TTFF-VP 78)	ITER Torus Cryopump Mechanical and Thermal EM Load Study .....	238
TW5-TTFF-VP 57	ITERVAC Validation Test .....	241
EFDA/06-1498 (TW6-TTFF-VP 68)	Conductance Modelling of ITER Divertor Torus Pumping Duct.....	245
TW6-TTFF-VP 53	Tritium Test of Ferrofluidic Cartridge Seals for Roots Roughing Pump .....	248
<b>Fuel Cycle – Tritium Plant</b> .....		251
TW3-TTFD-TR 31 and TW4-TTFD-TR 41 and TW4-TTFD-TR 43	Improvements to the Mechanical Design of the PERMCAT Component..... Experimental Investigation of Undesired Side-reactions in PERMCAT Comparison of Batch and Continuous Operation Modes for the Impurity Processing Stage of the Tokamak Exhaust Processing System	253
TW1-TTF/TEP 13A and TW3-TTFD-TR 33	Self-assay, Fast Delivery Tritium Storage Bed Development .....	261
TW4-TTFD-TR 44	Determination of Isotopic Effect during Rapid Delivery from Storage Beds	265
TW4-TTFD-TR 47	Inactive Tests of Selected Composition Control Loop Performance under Typical ITER Operating Conditions.....	265
TW4-TTFD-TR 47	Upgrading of LPCE (Liquid Phase Catalytic Exchange) Column for Trade-off Studies between WDS and ISS .....	266
TW6-TTFD-TR 64	Endurance Tests of Water Detritiation System .....	268
TW6-TTFD-TR 56	Isotope Separation Tests for Evaluation of Column Packing Options .....	270
TW6-TTFD-TR 63	Testing of Isotope Separation System (ISS) with the WDS .....	271

	<b>Page</b>
EFDA/06-1510 (TW6-TTFD-TPI 55)	Update of ITER ISS-WDS Process Design – 1..... 273
EFDA/06-1451 (TW6-TTFD-TPI 57)	Dynamic Modelling of ITER Tritium Inventories (TRIMO)..... 275
EFDA/05-1251 (TW5-TTFD-TPI 54)	Development of a Tritium Manual for ITER..... 276
<b>Safety Analysis and Environmental Impact</b>	..... 277
TW6-TSS-SEA 2.1	Occupational Radiation Exposure – ALARA in ITER: Further Refinement..... 279
TW5-TSS-SEA 3.5C	In-vessel Safety: Small and Medium Scale Experiments on Combined Hydrogen/ Dust Explosions and Mitigation for Model Development..... 281
EFDA/06-1517 (TW6-TSS-SEA 4.5)	Feasibility Study of Possible Prevention of Hydrogen and Dust Explosion in ITER by Injection of Neutral Gas..... 284
TW6-TSS-SEP 1	Uncertainty Assessment and Analysis of ITER In-VV Tritium Inventory Determination..... 286
EFDA/06-1489 (TW6-TSS-SEP 2)	Doses to the Public due to ITER Accidental Releases ..... 287
EFDA/06-1415 (TW6-TSL-002)	Safety Assessment for EU-Test Blanket Modules to support ITER Licensing Process – 4 ..... 288
<b>DEMO Conceptual Studies</b>	..... 293
TRP-001	PPCS He-cooled Divertor Concepts ..... 295
	TW6-TRP-001 D 1+2 He-cooled Divertor Development: Conceptual Design, Analysis, and Tests ..... 295
TRP-002	DEMO Physics Studies ..... 308
	TW6-TRP-002 D 3 Development of an Improved Treatment of Plasma Radiation for Medium- and High-Z Impurities ..... 308
TRP-005	Neutronic Analysis ..... 310
	TW6-TRP-005 D 1 TBR and Shielding Analyses for the HCPB DEMO Reactor ..... 310
EFDA/06-1454 (TW6-TRP-007)	DEMO Conceptual Design – FZK Contribution..... 312
TRP-012	Optimisation of a Fusion Power Plants for the Production of Hydrogen ..... 316
	TW6-TRP-012 D 1b Optimisation of a ‘Start-up’ Scenario where the Power is less than 100 MW ..... 316
	TW6-TRP-012 D 2 Assessment of the Impact of a Fusion Power Plant for H <sub>2</sub> Production on Internal Components ..... 318
<b>Design Support and Procurement</b>	..... 323
EFDA/05-1331 (TW5-TDS-CLDES)	Final Design of HTS Current Leads for ITER..... 325
<b>JET Technology</b>	..... 329
JW2-FT-2.4	Tritium Inventories of Spent Cryopanel and Waste conditioning ..... 331
JW4-FT-3.18	Assessment of in-situ Detritiation in JET ..... 333
JW5-FT-5.20	Shutdown Dose Rate at JET Tokamak – Code Benchmark ..... 338

<b>Heating Systems Technology Project</b>	341
EC Coaxial Cavity Gyrotrons and Test Facility:	
TW6-THHE-CCGDS4 D 1b	343
Design, Support to the Industrial Development and Preparation of Technical Specifications	
and	
TW6-THHE-CCGT1 D 1	343
Scientific Execution and Co-ordination of the Tests	
EFDA/05-1352	348
(TW5-THHN-MONRF)	
Monitoring the EU/RF Collaborative Tasks on the First ITER NB Injector and the ITER NB Test Facility	
EFDA/06-1502	352
(TW6-THHN-NBD1)	
Design Activities for the First ITER HNB Injector	
<b>Physics</b>	355
ECR Heating and Current Drive – Step-Tunable Gyrotron Development	357
Microwave Heating for Wendelstein 7-X	362
<b>Underlying Technology</b>	371
Operation of the Fusion Materials Laboratory	373
Appendix I	375
FZK Departments Contributing to the Fusion Programme	
Appendix II	377
Fusion Programme Management Staff	
Appendix III	379
Glossary	

## **Plasma Edge**



## EFDA/05-1305 (TW5-TPP-BEDAM)

# Modelling of Material Damage to Be-clad and Be-coated ITER Plasma Facing Components under Type I ELMs, Disruptions and Mitigated Disruptions, and Scoping Studies for First Experimental Validations

## 1. Introduction

The ITER candidate material beryllium will be located at the main chamber wall in form of Be-clad blanket modules. In addition, Be-coated plasma facing components are likely to appear in both divertor legs, where Be eroded from the main chamber wall may form deposits covering in a large proportion the CFC and W armour. In this report, the main results of systematic computer simulations for Be surface damage under high heat loads anticipated in ITER, carried out in 2007 in FZK-IHM, are reported. In the computer modelling the newly upgraded code MEMOS is applied. The Be armour damages are expected to be evaporation, melt motion and melt splashing. For all ITER transient events, in particular the ELMs and mitigated disruptions, the formation of metallic droplets and the splashing of the melt layer can play a major role, thus determining the lifetime of the plasma facing metallic armour.

The melt pool depth and the evaporation thickness at target heat depositions of  $Q = 0.2$  to  $2 \text{ MJ/m}^2$  and pulse durations  $\tau = 0.2$  to  $0.6 \text{ ms}$  are estimated accounting for the vapour shielding, a model of which is implemented in MEMOS. The influence of the Lorentz force on the Be bulk and macrobrush armour damage is investigated and compared with that of tangential friction forces for the cross-currents up to  $2 \text{ kA/cm}^2$ . The dependence of the maximum surface temperature at the upper Be-wall on the ELM heat flux for different ELM durations  $\tau$  is calculated. The melt motion damage to the Be macrobrush armours caused by the tangential friction force is analyzed for different sizes of Be-brushes. The simulations demonstrate that for brush sizes below  $2 \text{ cm}$ , the melt motion velocity becomes significantly smaller than that for the bulk Be, and thus the surface is damaged much less. Increasing the brush size up to  $4 \text{ cm}$  leads to elimination of this favourable effect.

## 2. The bulk Be melt pool depth and evaporation thickness

The following main improvements have been implemented in MEMOS: the thermophysical properties of bulk Be and Be coatings on bulk W and CFC as well as a vapour shield model. The vapour shield model allowed taking into account the decrease of the heat load at the target surface due to ion stopping in the evaporated material. This model is appropriate in the case of weak and moderate ELMs where radiation processes in the vapour shield can be neglected. The implementation of a rather simple Be macrobrush geometry with different brush sizes has also been done. Only the most characteristic features of the macrobrush geometry are taken into account.

Then systematic simulations of the erosion of the bulk Be target caused by surface evaporation and surface melt motion were performed for the given parameters. It was assumed that the target is heated by either a plasma stream with an ion energy of  $100 \text{ eV}$  or electromagnetic radiation with a power density  $Q$  having a Gaussian profile with a half-width of  $4 \text{ cm}$  and peak values of up to  $2 \text{ MJ/m}^2$ . The inclined plasma stream was dumped at the Be armour, aiming at the estimation of the first wall erosion after ITER ELMs and the erosion at future plasma gun experiments on Be. Several scenarios for the reference heat load duration  $\tau = 0.5 \text{ ms}$ , different heat loads with peak values up to  $1.0 \text{ MJ/m}^2$ , and a tangential pressure  $p_{\parallel} = 0, 10^{-2}$

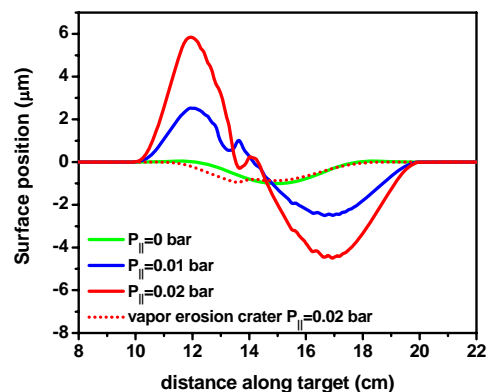


Fig. 1: The final crater profile for scenarios with different tangential friction force;  $Q = 1 \text{ MJ/m}^2$ ,  $\tau = 0.5 \text{ ms}$

and 0.02 bar with a rectangular pulse shape were simulated. The calculations demonstrated that for  $Q > 0.6 \text{ MJ/m}^2$  the tangential pressure generates a violent melt motion with the velocities exceeding 3 m/s for  $p_{\parallel} = 10^{-2} \text{ bar}$  and 7 m/s for  $p_{\parallel} = 0.02 \text{ bar}$ , which causes the formation of a mountain at the left side of the heated region of  $h \approx 3 \text{ }\mu\text{m}$  ( $p_{\parallel} = 10^{-2} \text{ bar}$ ) and  $h \approx 6 \text{ }\mu\text{m}$  ( $p_{\parallel} = 0.02 \text{ bar}$ ) height. Correspondingly, a deep crater with  $d \approx 2.5 \text{ }\mu\text{m}$  ( $p_{\parallel} = 10^{-2} \text{ bar}$ ) and  $d \approx 5 \text{ }\mu\text{m}$  ( $p_{\parallel} = 0.02 \text{ bar}$ ) depth appears. As an example, Fig. 1 demonstrates the calculated damage to the bulk Be.

The influence of the Lorentz force on the Be armour damage is investigated and compared with the influence of  $p_{\parallel}$  for a wide range of the current density  $j$  crossing the Be armour ( $0\text{-}2 \text{ kA/cm}^2$ ) in a strong magnetic field. The Lorentz force generates also a violent melt motion with the velocities exceeding 1.5 m/s for  $j = 0.5 \text{ kA/cm}^2$ , 3.5 m/s for  $j = 1 \text{ kA/cm}^2$  and 7.5 m/s for  $j = 2 \text{ kA/cm}^2$ . Such melt motion causes the formation of a roughness of about  $10 \text{ }\mu\text{m}/\text{shot}$ . Fig. 2 demonstrates the calculated damage to the bulk Be. The influence of the tangential friction force and of the Lorentz force on the melt motion damage to the Be target has been investigated and compared. The simulation demonstrates that both forces in combination may compensate each other if they are applied in the opposite directions. For instance, the melt velocity may drop below 1 m/s and thus the erosion crater depth below  $1 \text{ }\mu\text{m}$ , which becomes comparable with the evaporation thickness.

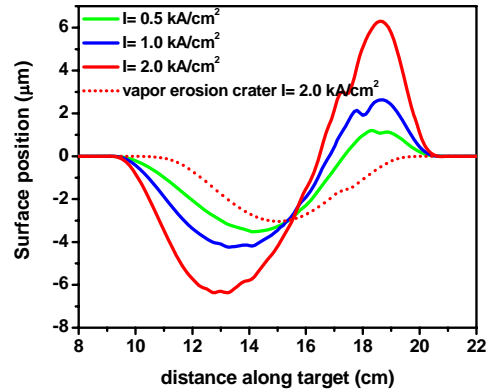


Fig. 2: Final crater profile for scenarios with different current densities.  $Q = 1.25 \text{ MJ/m}^2$ ,  $\tau = 0.5 \text{ ms}$ .

The upgraded code MEMOS was also applied for the estimation of the melt erosion of Be-coatings on W and CFC bulk materials, i.e., for the calculation of the melt pool depth and the evaporation erosion of the Be coating as functions of the melt layer thickness for the moderate heat loads expected at ITER ELMs:  $Q = 0.8 - 1 \text{ MJ/m}^2$  with  $\tau = 0.5 \text{ ms}$ . The numerical simulations demonstrated that the calculated thickness of the melt layer is always below  $50 \text{ }\mu\text{m}$  and depends on the thickness of the Be-layer that covers the bulk material with higher thermal conductivity.

Further, MEMOS simulations were carried out in order to estimate the dependence of the threshold of the ITER Upper Wall melting and the corresponding thickness of the melt layer, and the respective dependence on the ELM heat load shape in the range of  $\tau = 0.2\text{-}0.5 \text{ ms}$ . These simulations demonstrated that large ELMs with a peak power density larger than  $1.2 \text{ GW/m}^2$  heat the Upper Wall so that significant melting occurs. The surface temperature of the Upper Wall is shown in Fig. 3.

For the evaluation of the radiation heat load at the First Wall, the code FOREV was applied. The special FOREV simulations for ITER disruption consequences aimed at some important peculiarities of the energy loss from the hot core during the thermal quench phase. The matter is that a considerable amount of carbon is vaporized from the divertor targets after a disruption penetrates into the core. The radiation losses of the contaminated plasma are distributed over the entire First Wall, which reduces the divertor heat load. The simulations demonstrated that the Upper and Outer Walls are the mostly irradiated regions. The disruption scenarios where carbon penetration into the pedestal is negligible are shown to be not dangerous for the first wall. The maximum of the surface temperature remains below  $1100 \text{ K}$ .

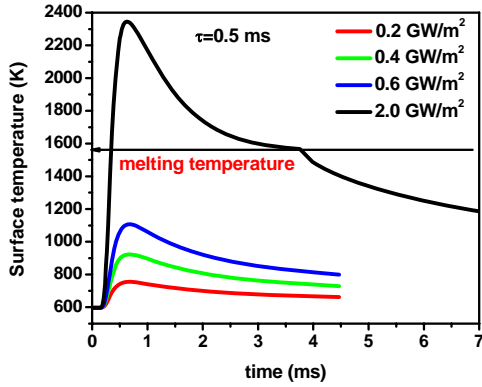


Fig. 3: Surface temperatures of the ITER Upper Be Wall as functions of time for different heat fluxes.

It has to be noted that FOREV uses the penetration depth of carbon as a phenomenological fitting parameter, so its results should be still validated against available experiments. However, to benchmark MEMOS simulations against radiation heat loads, the current FOREV results were used. In cases with a high power release (e.g. 130 GW), the First Wall radiation loads can produce an essential damage to the Be armour in spite of the relatively small evaporation depth of several  $\mu\text{m}$ , because a melt pool of up to 100  $\mu\text{m}$  depth was obtained. The melt pool and the erosion rate of the Be bulk First Wall along the poloidal coordinate from the Inner Divertor ( $x = 0 \text{ m}$ ) to the Outer Divertor ( $x = 18 \text{ m}$ ) are demonstrated in Fig. 4 and 5 for the scenario with 130 GW during 3 ms.

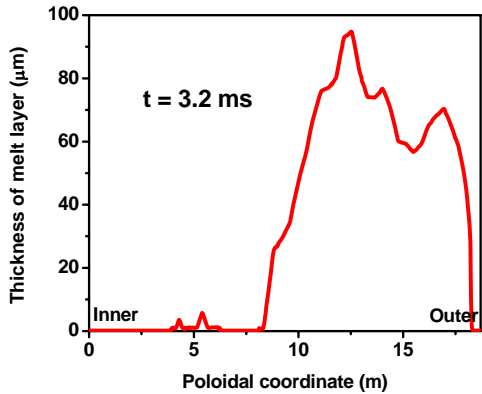


Fig. 4: Distribution of melt pool depth along the First Wall surface.

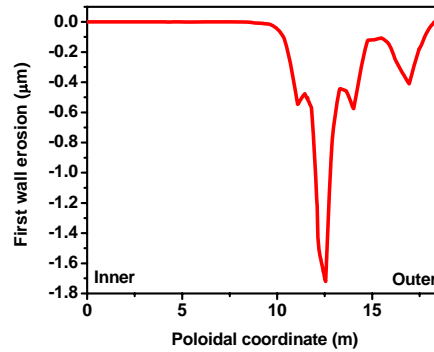


Fig. 5: Distribution of the final erosion profile due to evaporation along the First Wall surface.

### 3. MEMOS calculations for the beryllium macro brushes

The Be-brush geometry with different brush sizes  $D$  is also implemented in the code MEMOS, as it was earlier done for tungsten macro brushes. The melt motion damage to the Be macrobrush armour caused by the tangential friction force has been analyzed for different sizes:  $D = 1, 2, 4$  and  $8 \text{ cm}$ , and compared with that for the bulk target. As it has been mentioned, at the bulk target surface the tangential pressure  $p_{||} = 0.02 \text{ bar}$  generates a violent melt motion with the maximum velocity exceeding  $7 \text{ m/s}$ . In the case of the macro brush target, the melt velocity can be reduced significantly: down to  $1.2 \text{ m/s}$  at  $D=1 \text{ cm}$  and  $5.5 \text{ m/s}$  at  $D=4 \text{ cm}$ , however about  $7 \text{ m/s}$  for  $D=8 \text{ cm}$  (Fig. 6).

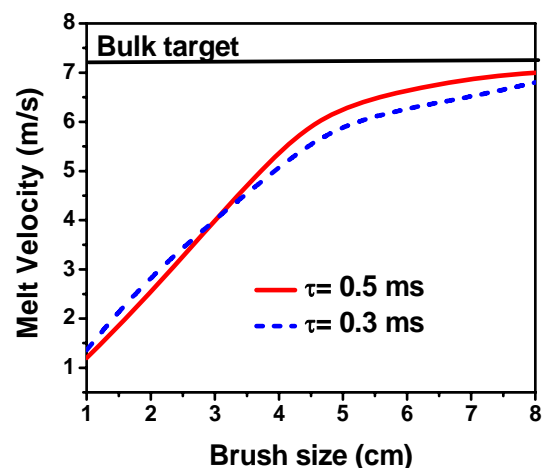


Fig. 6:  $V_{\text{max}}$  vs. brush sizes.  $Q = 1 \text{ MJ/m}^2$ ,  $p_{||}=0.02 \text{ bar}$ . ( $2 \text{ GW/m}^2$ ), ELM duration  $\tau = 0.5 \text{ ms}$ .

### 4. Conclusions

The further development of the code MEMOS aiming at the modelling of the damage under the transient heat loads to the ITER Be-clad PFCs is characterized. The upgraded MEMOS is applied for the estimation of the melt pool depth and the evaporation erosion. The simula-

tions demonstrated that the melt pool thickness is below 50  $\mu\text{m}$ , and evaporation occurs for heat loads exceeding 1  $\text{MJ}/\text{m}^2$ .

For the bulk Be, the dependences of the melting pool depth and the evaporation thickness on the heat load duration have been obtained. The influence of the Lorentz force on the Be-armour damage is calculated in a strong magnetic field and compared with that of the tangential friction force for electric cross-current densities up to 2  $\text{kA}/\text{cm}^2$ . Both forces are comparable and, in particular, they may compensate each other if being applied in the opposite directions.

For the Be-brush armour, the melt motion damage caused by the tangential friction force is analyzed for different brush sizes up to 4 cm. It is shown that increasing the size up to of 4 cm leads to a significant increase of the melt velocity. Therefore, for ITER design, a the brush size of 1 cm is recommended. Simulations have also been carried out in order to estimate the ITER Upper Wall melting. The simulations demonstrated that large ELMs with a peak power density larger than 1.2  $\text{GW}/\text{m}^2$  heat the Upper Wall so that significant melting occurs.

The next steps of the work on the melt motion Be damage are a further improvement of the vapour shield modelling, obtaining actual cross-currents for adequate calculations of Lorentz forces using the code TOKES, and the validation of the code MEMOS against experimental data to be obtained with the upgraded facility QSPA-T now suitable for beryllium experiments.

#### Staff:

B.N. Bazylev  
I.S. Landman  
S.E. Pestchanyi

#### Literature:

- [1] B.N. Bazylev, G. Janeschitz, I.S. Landman, S.E. Pestchanyi, A. Loarte, Melt layer damage simulation of first wall beryllium armour under heat loads caused by ITER transient events, 34<sup>th</sup> European Physical Society Conference (EPS) on Plasma Physics, Warsaw, Poland, 2-6 July 2007, paper P4.038, to be issued on CD.

## **TW5-TPP-ITERTRAN**

### **Modelling of ITER Divertor Target Damage and Plasma Contamination following ELMs and Disruptions**

#### **1. Introduction**

The ELMy H-mode is an operation scenario foreseen for the future tokamak ITER. However, this regime is associated with ELM caused heat fluxes 2 to 3 orders of magnitude higher than the background value of a few MW/m<sup>2</sup> at the divertor armour to be made of carbon fibre composite (CFC). The ITER type I ELMs would release up to 20 MJ during 0.3-0.6 ms, dumping a power density of up to 10 GW/m<sup>2</sup> onto the divertor armour. The current tokamaks do not produce such ELMs, powerful enough to cause vaporization at the divertor surface. Therefore numerical predictive simulations using the two-dimensional RMHD code FOREV have been carried out with respect to the high wall loads. FOREV is now able to calculate the whole process lasting a few ms. For simulation of later consequences of ITER ELMs, the two-dimensional multi-fluid integrated tokamak code TOKES is being developed.

The whole scenario to be calculated is as follows. The vaporized and ionised carbon fills the scrape-off layer (SOL) with a density varying between 10<sup>20</sup> and 10<sup>21</sup> m<sup>-3</sup>. Carbon ions penetrate further into the core, re-radiating electron thermal energy from the whole plasma volume. In total the plasma impact and the radiation load cause damage to both the divertor plates and the entire first wall surface to be made of the metals beryllium and tungsten. To calculate the brittle destruction (BD) erosion of CFC and the melt motion erosion of metallic surfaces, the codes PEGASUS and MEMOS are applied.

The work done in the frame of the ITERTRAN task on plasma relevant issues (plasma and radiation impact, contamination of confinement region) and on the damage to the metallic wall components was almost finished earlier and was described in the previous annual report. Here, the remaining work done on the BD damage is described.

#### **2. Simulations for the CFC NB31 with PEGASUS and a validation against plasma gun experiments**

The CFC materials have a complex structure consisting of a carbon fibre framework immersed into a carbon matrix. Main component of the framework are the pitch fibres perpendicular to the armour surface, they provide a high thermal conductivity of the CFC. The pitch fibres are woven and needled by so called PAN fibres arranged parallel to the heated surface. It was recently announced that a reference material for the future tokamak ITER developed for the divertor armour is going to be the CFC NB41, which is the improved CFC NB31 with the same fibre structure of 28% of pitch fibres, 6% of woven PAN fibres and 2% of needling PAN fibres. The improvements of NB41 compared to NB31 concern only the technology of the graphitisation process. Only the physical investigations for the NB31 are done so far. Earlier comprehensive experimental investigations of NB31 with the plasma gun facilities MK-200UG and QSPA (TRINITI, Troitsk Russia) demonstrated high BD erosion rates at the conditions expected for the ITER H-mode operation.

The latest FZK activity on modelling CFC involved experimental validation of the vaporization threshold of NB31 obtained by the code PEGASUS. For this reason, special measurements of the CFC surface temperature under pulsed heat loads simulating ITER Type I ELMs have been performed experimentally at the plasma gun MK-200UG where the CFC samples were exposed to hot hydrogen plasma streams. The time dependence of the surface temperature under various heat loads has been registered and used for estimations of CFC thermal conductivity.

The corresponding CFC simulations with PEGASUS have initially resulted in a large disagreement between the measured surface temperatures and the numerical results. In these

simulations the thermal conductivity of CFC known as a function of temperature in the range up to  $1.5 \times 10^3$  K and its inversely proportional extrapolation up to 4500 K was used. To identify the reason for the disagreement, a morphological and post mortem analysis of the CFC was performed. It revealed that in a thin surface layer of 50-100 $\mu$ m the pitch fibres are partially damaged and a thin layer of redeposited carbon of  $\sim 5\mu$ m thickness covers the CFC surface.

The analysis allowed drawing a conclusion about a significant degradation of the thermal conductivity near the CFC surface in the whole temperature range from room temperature up to 4500 K, attributed to the observed cracking of the CFC pre-surface bulk after multiple plasma gun shots. Estimations have also shown that the redeposited layer of carbon with a thickness of a few microns cannot influence the measured surface temperatures substantially, because for that its thermal conductivity would have to be unrealistically large.

Therefore, for validation of the code, the function of the thermal conductivity dependence on temperature was multiplied by a factor 0.45 in the pre-surface layer. With this factor, the measured time dependences of the CFC surface temperature are reproduced in the simulations at different power densities in the most appropriate way,, as it is demonstrated in Figs. 1 and 2.

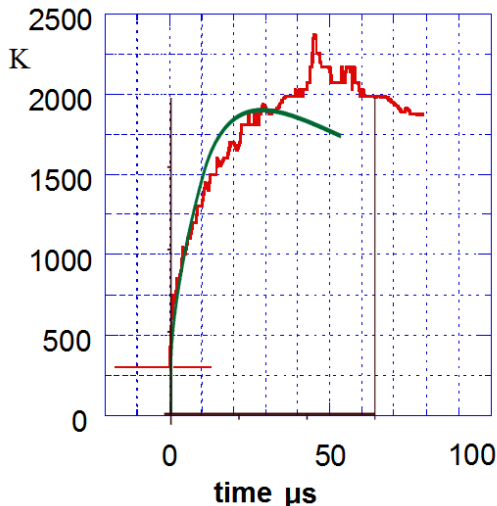


Fig. 1: The CFC surface temperature measured (red) in a shot with an energy deposition of  $0.09 \text{ MJ/m}^2$  and simulated (green) using the thermal conductivity reduced by a factor 0.45.

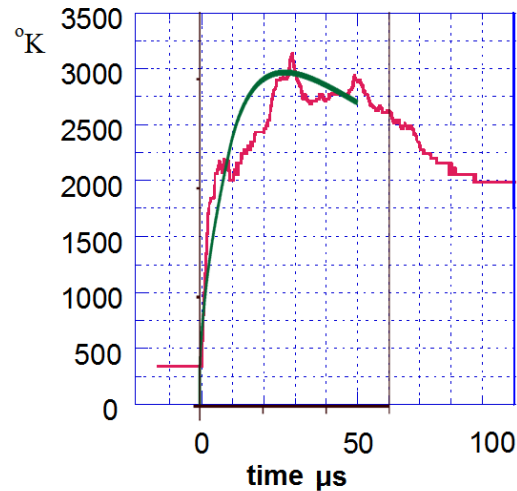


Fig. 2: The CFC surface temperature measured (red) in a shot with an energy deposition of  $0.145 \text{ MJ/m}^2$  and simulated (green) using the thermal conductivity reduced by a factor 0.45.

Additional confirmation for the pre-surface cracking of CFC under multiple pulse loads has been obtained from measurements of the plasma shield density performed in the same time at the MK-200UG in front of the CFC target. The enhanced vaporisation at the heated CFC surface really starts at the rather low heat load of  $\sim 0.1 \text{ MJ/m}^2$ , which is impossible to reproduce in the simulations if assuming the reference thermal conductivity. The simulation that results in the measured low vaporization threshold should assume that the overheated surface spots are thermally isolated from the bulk due to the cracks.

### 3. Conclusions

The results of the surface temperature measurement of a CFC target in the MK-200UG facility have been analysed. Numerical simulation of the time dependence of the surface temperature of the sample has revealed that the reference temperature dependence for the thermal conductivity of the CFC NB31 is incompatible with the experimental measurements. The most probable reason for this degradation is a brittle destruction of CFC during several hundred severe thermal shocks, which will be met in ITER. The results of the numeric simulations with decreased thermal conductivity proved that the pre-surface thermal conductivity

degradation occurs not only at high temperatures, but also at any temperature of the target. The effect of thermal conductivity degradation is important for the ITER operation and needs further investigation.

Staff:

B.N. Bazylev  
I.S. Landman  
S.E. Pestchanyi

Literature:

- [1] A. Zhitlukhin, N. Klimov, I. Landman, J. Linke, A. Loarte, M. Merola, V. Podkovyrov, G. Federici, B. Bazylev, S. Pestchanyi, V. Safronov, T. Hirai, V. Maynashev, V. Levashov, A. Muzichenko, Effects of ELMs on ITER divertor armour materials, *J. Nucl. Mater.* 363 (2007) 301-307.
- [2] B.N. Bazylev, G. Janeschitz, I.S. Landman, A. Loarte, S.E. Pestchanyi, Melt damage simulation of W- macro-brush and divertor gaps after multiple transient events in ITER. *J. Nucl. Mater.* 363 (2007) 1011-1015
- [3] I.E. Garcusha, B.N. Bazylev, A.N. Bandura, O.V. Burka, V.V. Chebotarev, I.S. Landman, N.V. Kulik, V.A. Makhraj, Yu.V. Petrov, D.G. Solyakov, V.I. Tereshin, Tungsten melt layer erosion due to JxB force under conditions relevant to ITER ELMs. *J. Nucl. Mater.* 363 (2007) 1021-1025
- [4] I.S. Landman, G. Janeschitz, Numerical simulations of plasma wall interactions for ITER, *J. Nucl. Mater.* 363 (2007) 1061-1065.
- [5] S. Pestchanyi, I. Landman, ELM induced carbon contamination of ITER core, *J. Nucl. Mater.* 363 (2007) 1081-1086.
- [6] V.I. Tereshin, A.N. Bandura, O.V. Byrka, V.V. Chebotarev, I.E. Garkusha, I. Landman, V.A. Makhraj, I.M. Neklyudov, D.G. Solyakov, A.V. Tsarenko, Application of powerful quasi-steady-state plasma accelerators for simulation of ITER transient heat loads on divertor surfaces, *Plasma Phys. Contr. Fus.* 49 (2007) A231-A239.
- [7] A. Loarte, G. Saibene, R. Sartori, V. Riccardo, P. Andrew, J. Paley, W. Fundamenski, T. Eich, A. Herrmann, G. Pautasso, A. Kirk, G. Counsell, G. Federici, G. Strohmayer, D. Whyte, A. Leonard, R.A. Pitts, I. Landman, B. Bazylev, S. Pestchanyi, Transient heat loads in current fusion experiments, extrapolation to next step devices and consequences for their operation, *Physica scripta T128* (2007) p. 222-238.
- [8] B.N. Bazylev, G. Janeschitz, I. Landman, S. Pestchanyi, A. Loarte, G. Federici, M. Merola, J. Linke, A. Zhitlukhin, V. Podkovyrov, N. Klimov, V. Safronov, ITER transient consequence for material damage: modelling versus experiments. *Physica Scripta.* T128 (2007) 229-233.
- [9] V.A. Makhraj, A.N. Bandura, O.V. Burka, I.E. Garcusha, V.V. Chebotarev, V.I. Tereshin, I. Landman, Effect of preheating on the damage to tungsten targets after repetitive ITER ELM-like heat loads, *Physica Scripta.* T128 (2007) 239-241.
- [10] G. Sergienko, B. Bazylev, A. Huber et al., Erosion of tungsten limiter under high heat flux in TEXTOR. *J. Nucl. Mater.* 363-365 (2007) 96-100t.
- [11] G. Sergienko, B. Bazylev, T. Hirai et al., Experience with bulk tungsten test-limiters under high heat loads: melting and melt layer propagation, *Physica Scripta.* T128 (2007) 81-86.
- [12] I.S. Landman, G. Janeschitz, Contamination of ITER core by impurities of tungsten and carbon, 8th Intern. Symp. on Fus. Nucl. Technology, ISFNT-8, Heidelberg, Germany, Sep. 30 – Oct. 5 (2007) paper #179.
- [13] B.N. Bazylev, G. Janeschitz, I. Landman, S. Pestchanyi, A. Loarte, G. Federici, M. Merola, J. Linke, T. Hiraia, A. Zhitlukhin, V. Podkovyrov, N. Klimov, Damage to tungsten macro-brush targets under multiple ELM-like heat loads. Experiments vs. numerical simulations and extrapolation to ITER, 8th Intern. Symp. on Fus. Nucl. Technology, ISFNT-8, Heidelberg, Germany, Sep. 30 – Oct. 5 (2007) paper PS1-2104.

## **TW6-TPP-DAMTRAN**

### **Modelling of ITER Plasma Component Damage and Consequences for Plasma Evolution following ELMs and Disruptions**

#### **1. Introduction**

In the future tokamak ITER the plasma edge localized modes (ELMs) may produce vaporization erosion at the divertor surfaces. In the periods between ELMs the main erosion mechanism is sputtering. The eroded species such as carbon, tungsten and beryllium contaminate the scrape-off layer (SOL) and then the confined core plasma. The contamination deteriorates the reactor performance, decreasing the fusion energy gain, or can even lead to disruptions of confinement.

The FZK computer modelling is aimed at identifying the tolerable ELM frequency in the H-mode of ITER operation is carried out using the two-dimensional (2D) MHD codes FOREV and TOKES that describe the core and SOL plasmas. In these codes the surface processes such as the sputtering and the vaporization at the wall surfaces and the back propagation of eroded species into the core is simulated. Below, the latest applications of FOREV, that simulated disruption caused contamination, and of TOKES, that performed first benchmark simulations with Be-C-W wall, is described.

Another kind of ITER wall erosion is surface melting of metallic targets (Be and W) caused by disruption- or ELM pulse loads. For modelling the melt motion damage, the incompressible fluid dynamics code MEMOS was applied. The new development of MEMOS, namely the implementation of 3D heat transport in the wall bulk and an algorithm for 2D melt motion along the wall surface, is described.

#### **2. FOREV modelling of plasma contamination after ITER disruption**

During a disruption, that can be caused by previous contamination of core plasma after multiple ELMs, the heat load on the target surface increases drastically compared to that of ELMs. However, the surface impact is limited due to a vapour shield that forms from eroded and ionized material close to the separatrix strike position (SSP). A large fraction of impacting deuterium-tritium (DT) plasma is reradiated by the vapour shield carbon plasma being widely distributed over surrounding structures of the divertor and first wall. The carbon expands into the SOL and penetrates inside the tokamak separatrix. By this way the thermal energy of the confined DT plasma is also reradiated directly from the pedestal onto the entire first wall surface. In the FOREV scenario simulating this complex process (Fig. 1), deterioration of the plasma confinement is assumed due to a drastic increase of the DT cross-diffusion coefficient  $D_{\perp}$ , fitting its magnitude to the impact fluxes from  $q = 30$  to  $q = 130$  GW anticipated for ITER disruptions. At the disruption onset  $D_{\perp}$  grows linearly during 0.2 ms and then it remains constant for 3 ms.

Target vaporization starts at the time from 0.06 ms ( $q = 130$ ) to 0.2 ms ( $q = 30$ ). The carbon expanding in the SOL has varying temperatures of a few eV and densities of  $10^{21}$ - $10^{22}$  m<sup>-3</sup> that depend on  $q$ . The heat flux of the DT plasma dumped from the pedestal into the SOL is not sufficient for increasing the temperature of the dense carbon plasma, because the energy is immediately converted into the radiation. As result, the power at the divertor target is reduced to about  $10^{-2}q$ , but a small vaporization rate is maintained.

Then the SOL carbon plasma diffuses inside the separatrix and also to the first wall, which takes place in vicinity of the x-point. In the pedestal the carbon acquires the high temperature of the DT plasma, and thus it expands there along the magnetic surfaces faster than in the SOL, which causes fast significant radiation cooling of the confined plasma. The dependence of the radiation power from the divertor region on time in comparison with that from the ped-

estal is shown in Fig. 2 for  $q = 63$  GW. The disruptions with smaller  $q$  produce radiation mainly from the divertor region, and increasing  $q$  leads to larger radiation loads from the pedestal, the fraction of which reaches 85% at  $q = 130$  GW. In the latter case the pedestal plasma is eventually cooled down to a few eV, what means the complete loss of confinement within 3 ms.

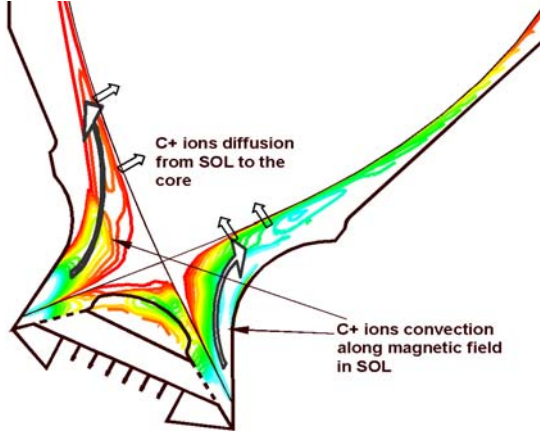


Fig. 1: Transport of C-ions in the ITER vessel: red colour corresponds to a minimum ion density  $n_{\min}$ , cyan – to the maximum  $n_{\max}$  that can reach  $3 \times 10^{22} \text{ m}^{-3}$ .

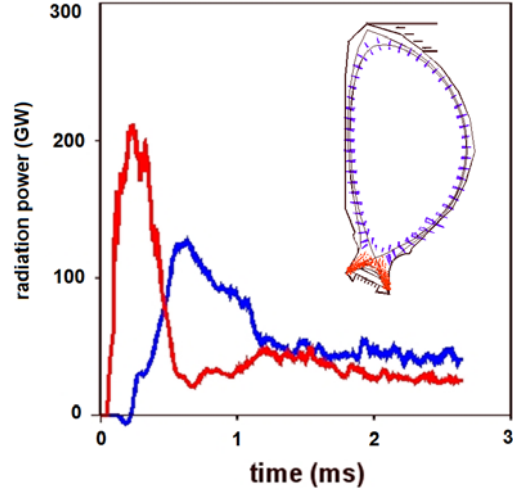


Fig. 2: Simulated radiation power from the divertor region (in red) and the core (blue) for a disruption with  $q = 63$  GW.

### 3. TOKES development for integrated simulations of ITER ELMy H-mode

The code TOKES was designed for an integrated simulation of tokamak plasma equilibrium and surface processes, initially with the wall materials Be and carbon fibre composite (CFC) aiming in particular at the plasma contamination following transient events such as ELMs on time intervals much larger than those achievable with the FOREV. The W species is now also implemented in TOKES and the code is applied for simulations with C-W-Be-wall. Earlier the Pfirsch-Schlüter plasma diffusion model, the influx of neutrals from the walls, and fuelling including pellets and heating by neutral beams have been implemented. The wall and the contours of the poloidal magnetic flux  $w(r,z)$  obey toroidal symmetry and can have arbitrary poloidal shapes (Fig. 3). The triangular grid coupled with the contours allows uniform calculations.

The new TOKES features include 1) the gyro-Bohm plasma transport model that takes account of the neo-classical effect, which allowed controlled fusion power and feedback on the beam heating, and 2) the improved plasma impact model based on the guiding centre approximation for the ions lost through the separatrix and then guided to the vicinity of SSP (marked with “ $s_1$ ” and “ $s_2$ ” at Fig. 3). Either the W-divertor or that with the replacements of W by two C-armour fragments at  $X = (2.8-3.4)$  and  $(5.3-5.9)$  m (see Fig. 3) is simulated. For the first wall ( $X < 2$  and  $X > 7$  m), a Be-armour is set.

Without the ELMs, the surface temperature remains below the vaporization point. In this case the physical sputtering erosion and the backscattering of impacting ions are taken into account. The atoms scattered from the SSP have significant chances to strike secondarily the dome

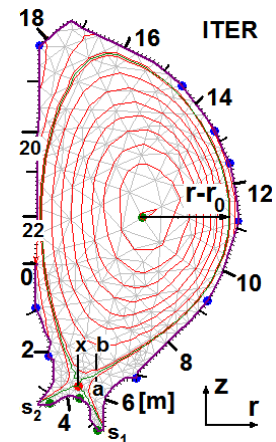


Fig. 3: The ITER layout and the wall coordinate  $X$ , with the circles marking the extremes of the magnetic flux  $w$ .

and thus produce sputtered W-atoms even with the C-wall at the SSP. The secondary sputtering is obtained to be so significant that tolerable contaminations could be obtained only with wide gaps in the dome surface, occupying up to 90% at  $X = (3.5-4.0)$  and  $(4.7-5.2)$  m; through the gaps effective pumping-out is assumed. In the vessel, the atoms propagate either freely until the last contour of the confinement region ("b" on Fig. 3) or it is assumed that they are fully stopped in the SOL.

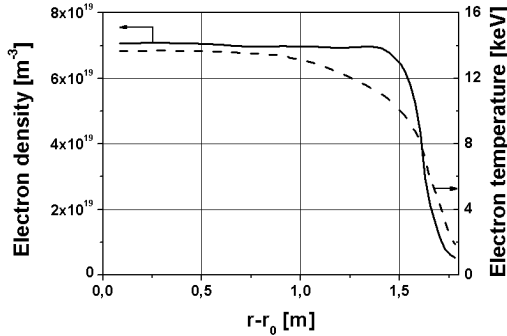


Fig. 4: Dependencies of electron density and electron temperature on the coordinate  $r - r_0$  shown in Fig. 1.

For the Be-C-W wall at the discharge time  $t = 200$  s, Fig. 4 shows completely saturated density and temperature of electrons. There is no unlimited contamination: the impurity densities remain limited as  $n_W < 5 \times 10^{15} \text{ m}^{-3}$ ,  $n_C < 3 \times 10^{16} \text{ m}^{-3}$  and  $n_{Be} < 2 \times 10^{15} \text{ m}^{-3}$ , which is attributed to the entrainment of impurities by the outflow of D- and T-ions fuelled (by equal amounts) into the confinement region. The heat outflow from the plasma reaches 82 MW and the radiation losses 5 MW. These losses are balanced by the fusion power of 57 MW of  $\alpha$ -particles and the beam power of 30 MW. The maximum temperature of the wall surface (at the SSP of the outer divertor) reached 3254 K. At  $t = 400$  s a fusion gain 9.5 is obtained.

SSP of the outer divertor) reached 3254 K. At  $t = 400$  s a fusion gain 9.5 is obtained.

The ELMs as simulated with TOKES can cause untimely discharge interruption. To estimate the range of tolerable ELMs, the ELM energy  $W_{ELM}$  [MJ] was varied in a wide range keeping for distinctness the ELM duration  $\tau_{ELM} = 0.3$  ms. At  $4 < W_{ELM} < 15$  the termination time is calculated as  $t_{max}[s] \approx 3 \times (15 - W_{ELM})^2 / (W_{ELM} - 4)^2$ . At  $W_{ELM} < 4$ ,  $t_{max} = \infty$  is obtained, and at  $W_{ELM} > 15$  the discharge termination occurs immediately after reaching the excessive vaporization temperature 4100 K of C-fragments during the first ELM. Thus the tolerable ELMs correspond to  $W_{ELM} < 4$  MJ.

An attempt to solely replace the C-fragments by the W-wall resulted in immediate termination even of an ELM-free discharge within one second caused by a drastic increase of the tungsten density in the confinement region. Thus at the current development state of TOKES the implemented design of the tungsten divertor seems not feasible.

#### 4. Upgrading of MEMOS for 2D melt motion and 3D wall heating

The melt erosion experiments performed earlier with the plasma gun facilities QSPA and MK-200UG (TRINITI, Troitsk, Russia) clearly indicated the importance of 2D effects such as melting of tungsten macrobrush edges in the lateral direction and transversal melt layer displacement with respect to the impacting plasma stream. Those damages would be equivalent to edge melting of the ITER poloidal divertor plates and the corresponding melt layer displacement. Near the molten edges the wall temperature needs to be described with a 3D algorithm. In order to predict those details of melt damage in ITER, the generalization of the 1D code MEMOS (with the already available 2D bulk temperature algorithm) to the additional dimensions has been done.

A 3D thermal transport solver to the Stefan problem has been developed and implemented, which allows accounting of melting- and resolidification fronts of the melt layer. The 1D melt motion model of MEMOS that is based on the shallow water approximation taking into account the surface tension and viscosity of molten metal has been generalized for 2D calculations. Plasma pressure and surface tension gradient, tangential pressure of inclined impact and the Lorentz force caused by the current crossing the target surface in a strong magnetic field, which are the driving forces, are also adjusted to the 2D algorithm, as well as the macrobrush peculiarities of the edge heating by the plasma stream. The appropriate 2D bound-

ary conditions at the diverse surfaces involved (including the rare surface, the melt surface and the water cooled surface) are implemented.

Then test simulations for the bulk tungsten target for evaporation and melt motion damage have been performed. It was assumed that the target is heated by an axially symmetrical plasma stream having a Gaussian profile with a radial half-width of 10 cm and a rectangular peak load of  $2 \text{ MJ/m}^2$ . Several 2D scenarios were simulated: with a load duration of  $\tau = 0.5 \text{ ms}$  and a tangential pressure of  $p_{||} = 0$  and  $0.02 \text{ bar}$  and compared with earlier validated 1D simulations. Figs. 5 and 6 demonstrate the obtained resolidification profiles after loading the target. Comparison with the results of 1D simulations using the previous version of the code MEMOS-1.5D demonstrated qualitative and quantitative agreements between 1D and 2D simulations.

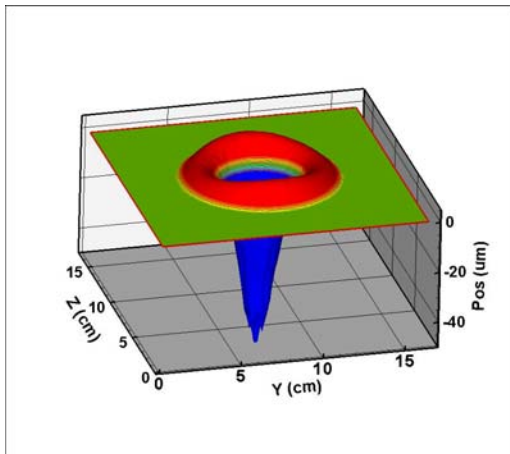


Fig. 5: The final crater profile for the scenarios with  $Q = 2 \text{ MJ/m}^2$ ,  $\tau = 0.5 \text{ ms}$ ,  $p_{||} = 0 \text{ bar}$ .

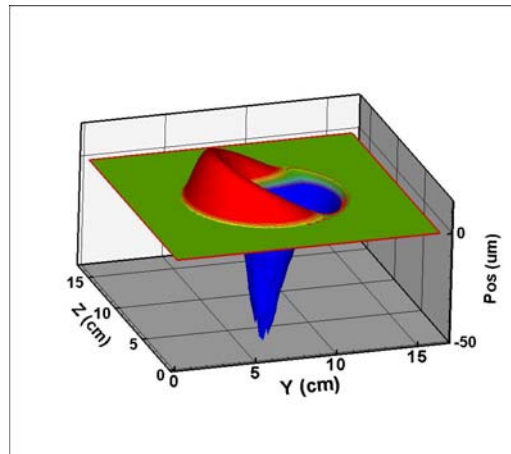


Fig. 6: The final crater profile for the scenarios with  $Q = 2 \text{ MJ/m}^2$ ,  $\tau = 0.5 \text{ ms}$ ,  $p_{||} = 0.02 \text{ bar}$ .

The case with  $p_{||} = 0 \text{ bar}$  corresponds to the perpendicular impact of the plasma stream at the target surface. The case with  $p_{||} = 0.02 \text{ bar}$  corresponds to the inclined impact of the plasma stream. In Fig. 5, radially symmetric melt motion and in Fig. 6, a melt layer shift in the direction of the plasma stream and formation of a “mountain” are clearly seen.

## 5. Conclusions

During the simulations of the consequences of ITER disruptions with the code FOREV, an important peculiarity of the energy loss during the thermal quench has been revealed: in the course of disruption a considerable amount of carbon plasma vaporized from the divertor targets can penetrate into the core. This plasma can irradiate up to 85% of the energy of the confined plasma, which reduces drastically the divertor heat load.

The plasma contamination by wall impurities obtained with the integrated code TOKES showed the well-known, large difference between a carbon-based armour and a tungsten armour in the vicinity of the separatrix strike points. These calculations demonstrate the achieved abilities of TOKES and can provide some useful insight into important aspects of tokamak physics, although they are of benchmark character and need further validation. The most urgent next step of TOKES development is concerning the search for an operation regime with a significantly decreased separatrix temperature  $T_S$  ( $T_S \ll 1.5 \text{ keV}$ ) which would suppress sputtering thus making tungsten attractive also at the SSP.

The code MEMOS was further developed implementing arbitrary 2D surface geometry of a W-macrobrush, which allowed improved simulations aiming at optimization of different details of the ITER design for a metallic armour. In the 1D tests with the 2D algorithm the calculated melt motion reproduced the previous 1D results of MEMOS.

Staff:

B.N. Bazylev  
I.S. Landman  
S.E. Pestchanyi

Literature:

- [1] Pestchanyi, Simulation of ITER first wall radiation heat load during the disruption, 34<sup>th</sup> European Physical Society Conference (EPS) on Plasma Physics, Warsaw, Poland, 2-6 July 2007, paper D2.007, to be issued on CD.
- [2] I.S. Landman, G. Janeschitz, Plasma convection in ITER integrated modelling with the code TOKES, 34<sup>th</sup> European Physical Society Conference (EPS) on Plasma Physics, Warsaw, Poland, 2-6 July 2007, paper P4.116, to be issued on CD.
- [3] I.S. Landman, G. Janeschitz, Contamination of ITER Core by Impurities of Tungsten and Carbon, 8<sup>th</sup> Intern. Symp. on Fus. Nucl. Technology, ISFNT-8, Heidelberg, Germany, Sep. 30 – Oct. 5 (2007) paper PS2-2008.

## TW6-TPP-DUSTGEN

### Evaluation of Dust Generation Rates for the Plasma Edge/Divertor Conditions Expected during ELMs and Disruptions for the ITER QDT = 10 Reference Scenario with CFC/W and W Divertor Target by Models Validated with Plasma Gun Experiments

#### 1. Introduction

The tritium retention problem is a critical issue for the tokamak ITER. In particular, tritium is trapped in carbon dust, where it is retained in form of various hydrocarbons. The dust appears inside the vacuum vessel mainly as a result of brittle destruction (BD) damage to the divertor armour. The ITER reference armour material is a carbon fibre composite (CFC) with 28% of pitch fibres (the fibres perpendicular to the heated surface), 6% of woven PAN fibres and 2% of needling fibres (they are parallel to the surface). This CFC has a high thermal conductivity and a low erosion rate appropriate for the tokamak stationary regimes with target surface temperatures up to 1500 K. However, plasma gun simulations of ITER H-mode transient events such as ELMs and disruptions demonstrated high BD erosion rates of CFC. At temperatures approaching 4000 K, the CFC armour can also be significantly eroded by surface vaporization, which can additionally contribute to the dust generation. The activity reported here assumes only BD mechanism of dust production after ELMs.

Earlier, a theoretical analysis of the CFC BD mechanism had been developed and implemented in the three-dimensional thermomechanic code PEGASUS. The CFC BD occurs due to cracks caused by a strong localized thermostress at the surface irradiated with the pulsed loads. In particular, this model can describe the generation of dust with various sizes and shapes. Therefore, a special PEGASUS upgrade has been done aiming at the dust particles area available for tritium accumulation, namely by collecting statistical data on the distribution of the sizes of the dust particles taking off the surface. After the upgrade, the code is applied for simulations of carbon dust production after ITER ELMs.

#### 2. Validation simulations on dust generation

A PEGASUS numerical sample is composed of very small cubical cells connected by bonds of predefined mean strength and failure stress values specific for the CFC grain structure. When in the course of calculation the local thermostress exceeds the failure stress, the inter-cellular bonds get broken, which results sometimes in separation of CFC fragments (the dust particles) from the bulk. The particle size is defined as the diagonal of the minimal parallelepiped enclosing the particle, and the size distribution function is calculated. It is also to mention that apart of the numerical upgrade for discrimination of separated fragments, a significant additional effort was undertaken for an appropriate visualization of the fibre debris.

To validate the code, the most important numerical parameters such as the grain size have been fitted to available data obtained in earlier plasma gun experiments at the facility MK-200UG with the graphite MPG-8 under the loads relevant to ITER disruptions. Special PEGASUS simulations for these experiments have been performed, using the known mean strength for the grain boundaries  $\sigma_b = 3 \cdot 10^{-3} E_{||}$  and three mean grain sizes:  $\lambda = 3, 5$  and  $8 \mu\text{m}$  ( $E_{||}$  is the Young's modulus in the layer direction of the carbon crystal). The graphite grain distribution for  $\lambda = 3 \mu\text{m}$  is shown in Fig. 1. The number of dust particles decreases exponentially with the particle size.

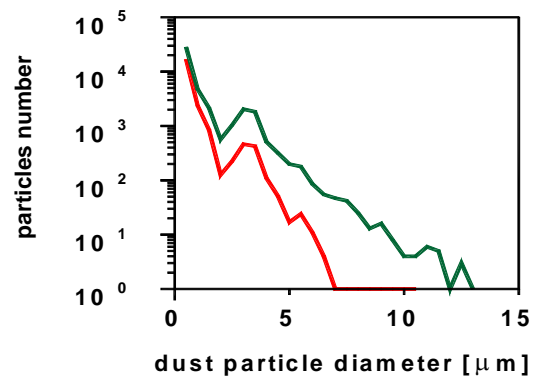


Fig. 1: Dust particles distribution function for simulated graphite with  $\lambda = 3 \mu\text{m}$ . Upper curve:  $\sigma_b = 3 \cdot 10^{-3} E_{||}$ ; Lower curve:  $\sigma_b = 4 \cdot 10^{-3} E_{||}$ .

The PEGASUS parameter  $\lambda = 3 \mu\text{m}$  fits the experiments in the best way, and microscopic measurements revealed grain sizes from 2 to 3  $\mu\text{m}$ .

A parametric study for the size distribution function carried out varying  $\lambda$  and  $\sigma_b$  has suggested a rather strong dependence on both parameters (see Fig. 2). Increase of  $\sigma_b$  drastically decreases the number of dust particles with large sizes, which is not confirmed by the experiments. Increase of  $\lambda$  leads to BD erosion of small intergranular particles only, and the grains with small sizes remain being attached to the sample, which is also far from the experiments. The comparison with the experiments allowed eventually to draw a conclusion that  $\sigma_b = 3 \cdot 10^{-3} E_{\parallel}$  and  $\lambda = 3 \mu\text{m}$  ought to be kept in all further simulations in order to ensure realistic results. The dependence of the calculated erosion on time is shown in Fig. 3. The erosion rate fits well the value 0.4  $\mu\text{m}$  per shot measured at the MK-200UG.

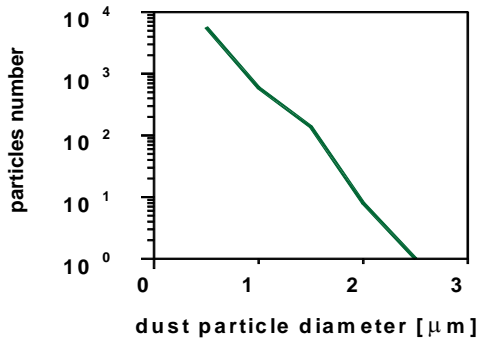


Fig. 2: Dust particles distribution function for  $\lambda = 5 \mu\text{m}$  and  $\sigma_b = 5 \cdot 10^{-3} E_{\parallel}$ .

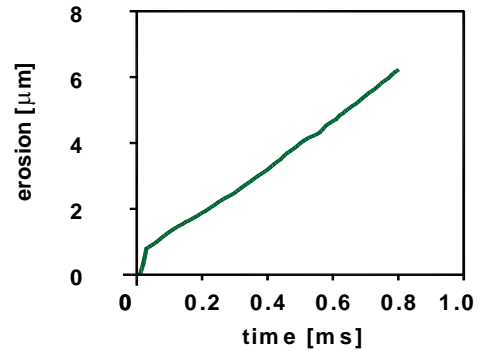


Fig. 3: Erosion rate dependence on time calculated for graphite at  $\sigma_b = 3 \cdot 10^{-3} E_{\parallel}$  and  $\lambda = 3 \mu\text{m}$ .

### 3. PEGASUS simulations for the dust production from CFC

Simulations of dust production from the MPG-8 graphite target under disruption-like surface heat loads at the MK-200UG facility allowed the validation of PEGASUS' fitting parameters. As it was concluded from comparisons with experiments on the plasma gun MK-200UG and QSPA with CFC targets, a noticeable difference between the MPG-8 graphite and the CFC is that the debris of the CFC contains much larger particles of  $\sim 100 \mu\text{m}$  size than that of graphite. Therefore, simulations for the CFC structure using PEGASUS have been performed assuming that the matrix parameters, mean grain size and the mean failure stress for the matrix grain boundaries are the same as the values used for the MPG-8 graphite:  $\lambda = 3 \mu\text{m}$  and  $\sigma_b = 3 \cdot 10^{-3} E_{\parallel}$ . The  $\sigma_b$  of the PAN fibres has been chosen 12 times larger than that of the matrix.

Fig. 4 illustrates the results of simulations of CFC brittle destruction and carbon dust production under disruption-like surface heat loads. The distribution function for the dust particles produced in the simulation after the time corresponding to 3 shots of the MK-200UG facility is shown. It is seen that it has an exponentially decreasing part (sizes less than 15  $\mu\text{m}$ ) similar for the dust distribution function of MPG-8 graphite. Besides, several larger particles of sizes from 20  $\mu\text{m}$  to 50  $\mu\text{m}$  appeared at that time. With ongoing time, the number of large particles and their maximal sizes are increased. The eroded surface morphology can be described as follows. The main erosion results from the CFC matrix, but the PAN fibres are also significantly eroded. The simulated eroded CFC surface is morphologically similar to the eroded CFC surface obtained in the experiments.

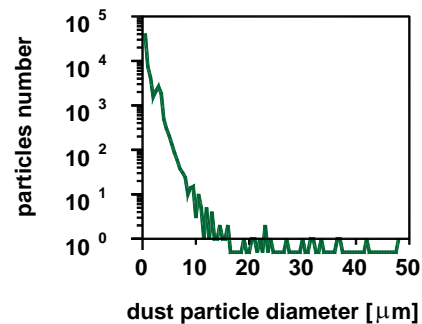


Fig. 4: Dust particles distribution function for simulated CFC with  $\lambda = 3 \mu\text{m}$  and  $\sigma_b = 3 \cdot 10^{-3} E_{\parallel}$ .

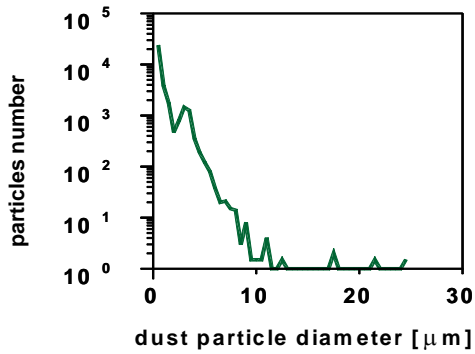


Fig. 5: Dust particles distribution function for CFC after an ELM-like surface heat load of 2 GW/m<sup>2</sup> at 0.5 ms.

The simulations for ELM-like heat loads to the CFC have been performed using also the parameters obtained from the comparison of the experimental data with the results of PEGASUS simulations. The simulation corresponds to a total ELM energy load of 1 MJ/m<sup>2</sup> and an ELM duration of 0.5 ms. Results obtained are qualitatively the same as that for the disruption-like heat loads. The size distribution 0.5 ms after the start of heating is shown in Fig.5. Initially, dust particles with small sizes of less than 10 μm and with rather continuous size distribution appeared. Then, at the end of the ELM, separate debris of larger sizes up to 25 μm were produced. The total erosion rate obtained

for the simulated sample is about 1 μm during the shot duration of 0.5 ms.

#### 4. Conclusions

Simulation of the production of carbon dust has been performed using the PEGASUS code. The experimental data on the MPG-8 graphite and CFC erosion rates, dust particles distribution functions and net dust production measured at the MK-200UG and MK-200CUSP facilities have been used for calibration of the code. From these experiments one can conclude that the CFC fibres erode as fibre debris of 100-200 μm length and with the diameter of 15-20 μm that fits the PAN fibre diameter. After the validation the PEGASUS simulations reproduced the main morphology features of eroded surfaces of graphite and the sizes of debris, as well as the measured erosion rate. The results of the simulations were obtained without taking into account carbon vaporization. Vaporization of the dust particles can change the distribution function, so this process should be investigated separately.

According to the calculations, noticeable brittle destruction erosion of CFC starts when the surface temperature reaches a threshold value of approximately 4000 K. The time delay of the brittle destruction from the start of heating is determined by an approximate formula linking the surface temperature, heat flux to the surface and heating time:

$$T(0, t)[K] = 10^2 Q \left[ \frac{GW}{m^2} \right] \sqrt{t[\mu s]}$$

With a heat load of 0.5 ms duration, this corresponds to the erosion onset at a total absorbed energy of 0.75 MJ/m<sup>2</sup>. According to the simulations, after reaching the threshold temperature the CFC erosion rate becomes approximately constant, and the distribution function for the dust particles evolves similarly, independent of the heat load. Initially, dust particles of small sizes (less than 10-12 μm) and with approximately exponential distribution on the particle size appear and later the particle sizes increase. The formation time for the exponential particle distribution and the time for larger debris appearance are inversely proportional to the heat load, but even for the lowest heat flux in the simulations the large particles have finally appeared, albeit in this case at times that are much larger than the ELM duration.

#### Staff:

S.E. Pestchanyi

#### Literature:

- [1] S.E. Pestchanyi, Simulation of dust production in ITER transient events, 8<sup>th</sup> Intern. Symp. on Fus. Nucl. Technology, ISFNT-8, Heidelberg, Germany, Sep. 30 – Oct. 5 (2007) paper PS1-1308.

## Divertor and Core Plasma Modelling for ITER

### 1. Introduction

The goal of the core and divertor plasma modelling program is the development, improvement, and application to ITER of a set of modelling codes which describe the ITER plasma from the core to the divertor plates in a coherent way so as to permit a consistent prediction of ITER plasma operating modes, operating windows, performance, and scenarios. Two codes are used for this purpose: the 2D coupled fluid-Monte Carlo code B2-EIRENE for two-dimensional modelling of the ITER divertor and scrape-off layer, and the ICPS model incorporated into the 1D ASTRA transport code for one-dimensional modelling of the ITER core and pedestal. The two codes communicate via scaling laws derived for the separatrix parameters from stand-alone runs of the codes. A variant of the model, which uses a simpler two-point SOL/divertor model, is used to fit results from the experiments. Quantitative predictive modelling of ITER is done with the more complete model.

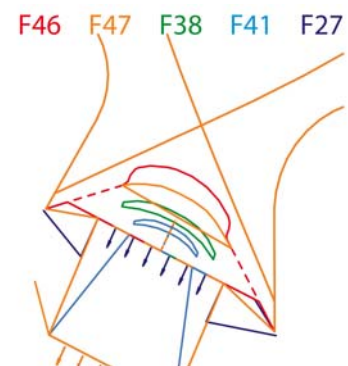
ITER performance modelling, crucial to establish the expected performance of ITER and to define the operating scenarios to obtain this performance, can be carried out only with such an integrated plasma model which describes in a coherent way the entire plasma from the centre via the pedestal and the scrape-off layer to the divertor plate. Our model has been developed in the framework of a quadripartite collaboration (FZ Karlsruhe, ITER International Team, Hydro-Québec, Varennes, Québec, Canada, and INRS-EMT, Varennes, Québec, Canada), as described in previous Annual Reports.

The previous version of the model and the results obtained were described in the previous Annual Reports and references therein, as well as in [1] through [7]. Results obtained in this calendar year have been reported at the EPS conference, Warsaw 2007, and are detailed in [8] through [12].

### 2. Divertor Plasma Modelling

Studies with a view to optimising the ITER divertor design had been carried out, notably to re-assess with the full nonlinear model the role of the divertor “dome” and the effect of variations of its shape on divertor performance. The results of these studies, relative to presence or absence of dome, the effect of gaps between the divertor cassettes, and the sensitivity to target shape are detailed in the previous Annual report. In addition, the effect of movement of the separatrix strike-points on the targets (20 cm displacement was found to be tolerable) and of upper versus midplane gas puffs was assessed.

In order to optimise further the divertor geometry, a systematic reduction in dome size was studied during the present year and reported at the EPS conference. The various geometries investigated are shown on the right. As in previous studies, the operational window is compared for physically similar operation, i.e. at the same divertor neutral pressure relative to that leading to full detachment of the inner divertor (the edge-based density limit). The results and the required normalisation factor (between 0.69 and 1) are shown in Fig. 1a. With this normalisation, the neutral influx to the core, which can affect the core confinement, is matched well for all the geometries in the comparison.



F47 has higher neutral pressure below the X-point and higher  $n_{DT}$  (not shown) at the separatrix but is otherwise similar to F46 where the dome is closer to the X-point. At first glance, therefore, the comparison between F46 and F47 shows that increasing the distance from the

X-point to the dome while maintaining the dome width and the pumping channel under the dome appears to have little if any deleterious effect.

Subsequently there is a clear trend: the peak power loading becomes progressively lower, and the helium density at the separatrix progressively higher, as the dome is reduced in size and eventually removed, e.g. the smallest dome, F41, gives 30% reduction of the power load for a factor 3 increase of the helium concentration at the separatrix, and complete removal of the dome would have twice this effect.

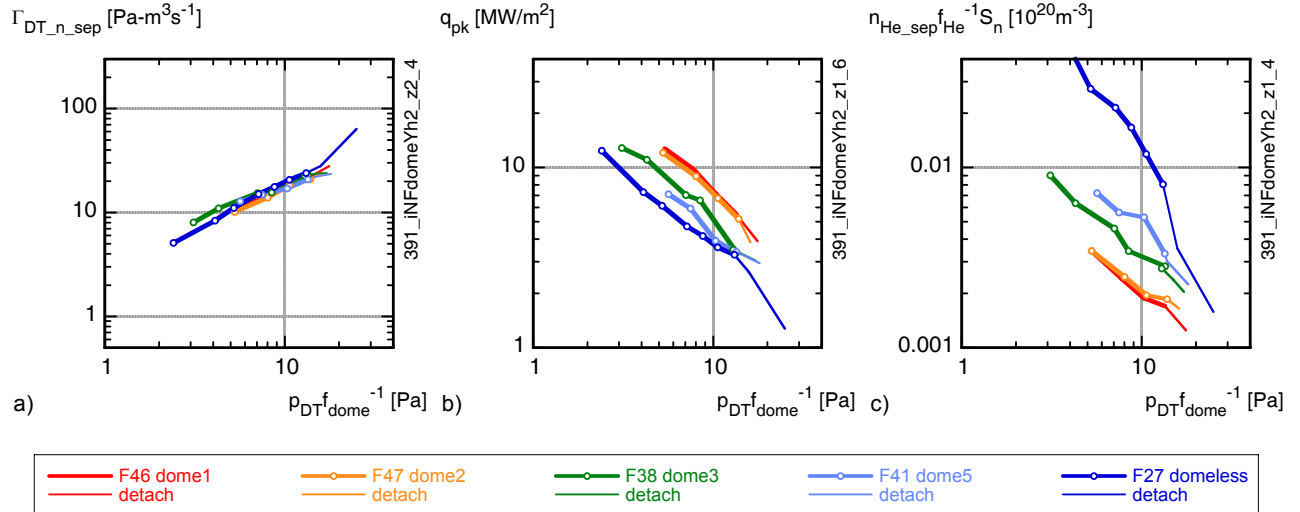
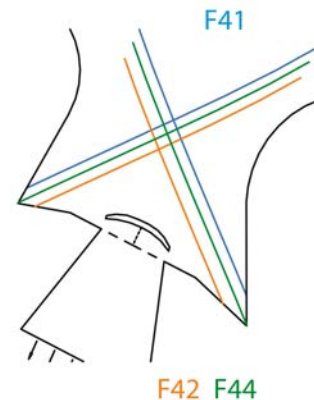


Fig. 1: Neutral DT influx to the core (a), peak power loading of the target (b), and helium density at the separatrix (c) vs. the normalised neutral pressure in the PFR for different dome configurations. The helium density is scaled with the fusion power and pumping speed.  $f_{dome}$  is 1 (F46), 0.84 (F47), 0.74 (F38), 0.68 (F41) and 0.69 (F27).

In conclusion, whereas the complete removal of the dome would require up to an order of magnitude higher pumping speed to keep the helium low, a strongly reduced dome would offset a 30% improvement in  $q_{pk}$  against a factor 2 to 3 degradation in helium pumping. Engineering considerations (neutron shielding, diagnostic access, etc.) are also important.

A further study investigated the influence of moving the strike point from the vertical target to the divertor floor (this would require a redesign for power handling) which would in principle allow a wide excursion of the separatrix strike-points over the divertor floor if the dome height is reduced. The configurations examined are shown at the right with the divertor shape of F41 but with the strike-points either in the corners between the vertical target and the divertor floor (F44), or definitely on the floor (F42).



Shifting the strike-points to the divertor corners (F44) results in no qualitative change in the performance, although the peak power is somewhat lower and the helium density somewhat higher, as for the case of the dome size variation. vertical targets, and thus larger domes are equally good for this.

However, when the strike-points are on the divertor floor (F42), the divertor operation is completely different. Full plasma detachment with maximum temperature well below 1 eV occurs in the inner divertor at all pressures studied, and in the outer divertor for the higher pressures. The neutral influx to the core is a factor 2 to 5 higher than for the strike-point on the vertical target or at the corners. For the bottom strike, the inner divertor is strongly detached (Fig. 2). The outer divertor also becomes detached with a violent transition (second to

third point on yellow curve in Fig. 2) and this at much lower pressure than the vertical strike case. For the bottom strike case, the plasma is hottest at the strike point and cold outboard of this, whereas for the vertical target case in partial detachment, the plasma is hotter outboard of the (partially detached) strike point, leading to much more gradual changes. Therefore, since no operational window for partial detachment exists for the operation with a strike point on the divertor floor, the operational flexibility of the divertor at burn resulting from a reduction in dome height is only slightly increased since the strike point must remain on the vertical target, but start-up flexibility may be better.

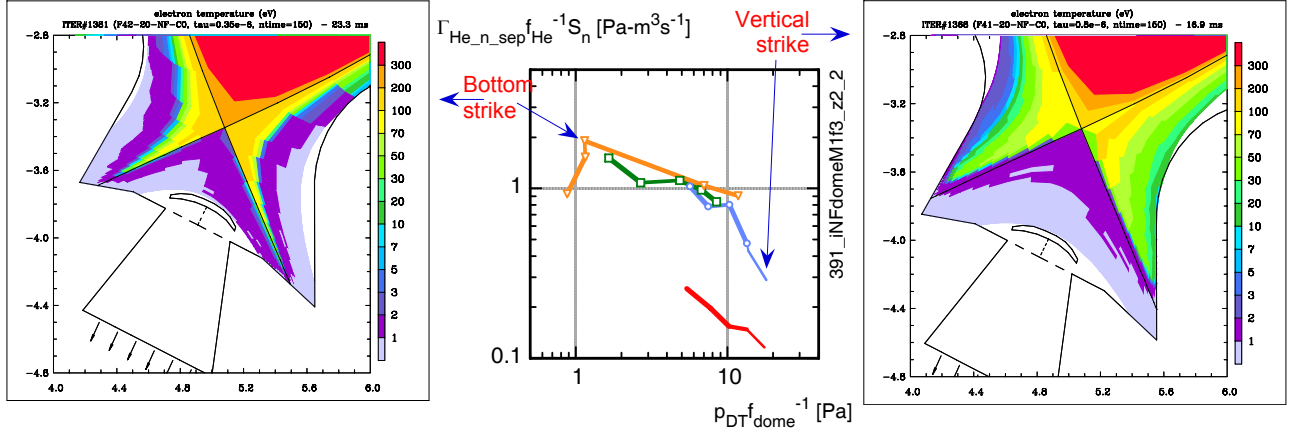


Fig. 2: Neutral He influx to the core (middle), 2D plot of electron temperature for bottom strike (left) and vertical target strike position (right). Cases plotted are indicated on the graph.

As a further flexibility study, and to prepare a study of ITER carbon-less operation at a later stage, seed impurities (neon) were added to the edge plasma. Even with carbon-covered walls, these seeded impurities can affect the divertor performance. A first series of runs with the SOL input power  $P_{\text{SOL}}$  of 100 MW and the Ne puffing rate adjusted to keep the total radiation from Ne at 14 MW (concentration from 0.7 to 1.3%) is presented in Fig. 3, where one can see that the presence of neon reduces the carbon concentration by a similar amount, 0.5 to 1%.

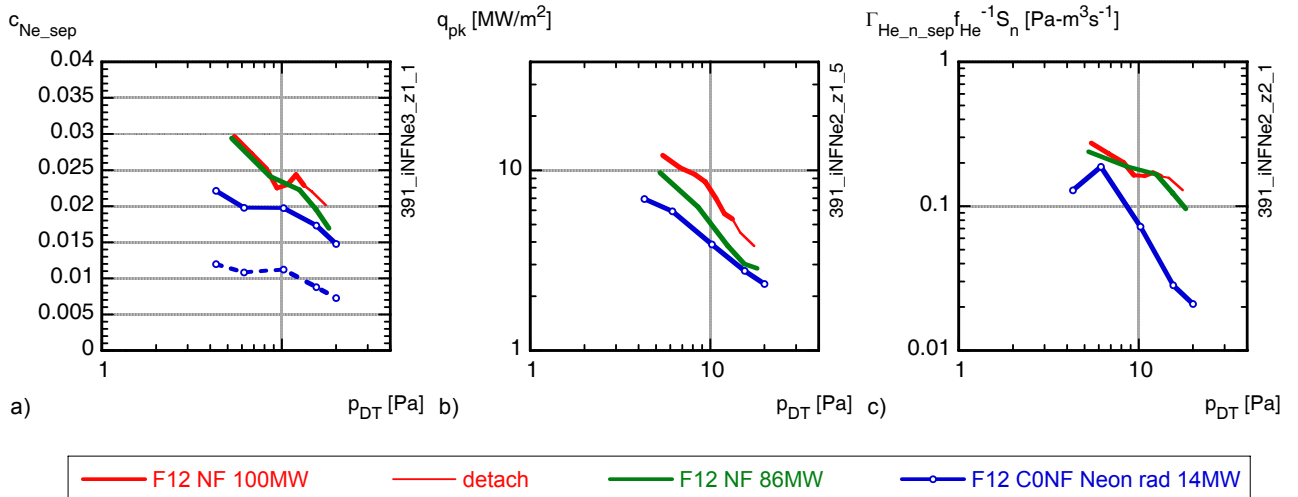


Fig. 3: Impurity concentration (solid: C, dashed: Ne) (a), peak power loading of the target (b), and helium atom flux across the separatrix (c) vs. the neutral pressure in the PFR without neon at 100 and 86 MW, and with 14 MW neon radiation at 100 MW input power to the SOL

This leads to a reduction of carbon radiation by 5 MW, i.e. an increase of the total radiation including neon by 9 MW. The seeded neon radiates more effectively than carbon, and the radiation peaks further from the divertor plate, so that the peak power load on the divertor

plates is lower. Seeding by neon affects the helium density little, and reduces the helium neutral flux .

In addition to these results with carbon-covered walls, initial simulations with full neon seeding and carbon-free machine have been started and will be reported in the next Annual Report.

### 3. Core Plasma Modelling

Core plasma modelling was focussed on issues demanded in the frame of the ITER design review. In particular, a description of the ITER operating window was developed and applied to the study of the consequences of reduced confinement (because of small rotation) and additional reduction of either the main magnetic field (if the design superconductor margin were not attainable) or the plasma elongation (if the vertical stability had to be improved). The study [8], reported in [11], quantified the reduction of the operating window, and provided initial device parameters designed to counter this reduction. Fig. 4 illustrates the generation of the operating window for the ITER-relevant case of low toroidal momentum input. The plasma density and auxiliary heating power are systematically varied so that all plasma parameters are then known as a function of the input parameters. The relevant limits are low Q (e.g.  $Q=5$  –yellow line), maximum available heating power (=73 MW, green), edge density limit (throughput limit for partial detachment =90% of edge density limit, dashed blue curve), maximum alpha power at given beam power (low temperature limit at high density – middle figure, dark blue line), and the LH transition at low power (red line).

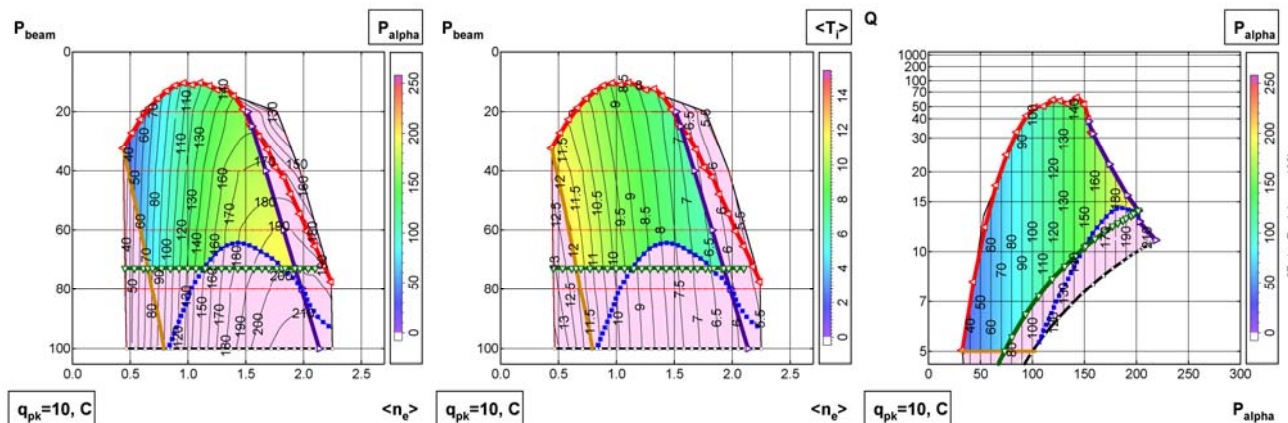


Fig. 4: Generation of the operating diagram by variation of beam power and plasma density. Plotted against these values are contour plots of alpha particle power (left) and average ion temperature (middle). The right plot shows the same data for  $\alpha$  power but plotted in the Q-P $\alpha$  plane. Relevant limits are indicated.

The operating window is the coloured region inside all these limits. From the right-hand figure, it is seen that the width and height of the operating window can be characterized by the maximum  $P_\alpha$  attained and by the Q which corresponds to this power. These quantities are plotted in fig. 5 for the different variations investigated.

The top line of fig. 5 indicates the effect of hypothetical variations inside the present ITER coil set. The left-hand panel shows that the reduction of the  $\alpha$  enhancement factor from 2 (appropriate for toroidal momentum input) to 1 (appropriate for ITER) does not reduce the maximum power but does reduce the window in Q so that, while Q remains high, ignition is no longer attained.

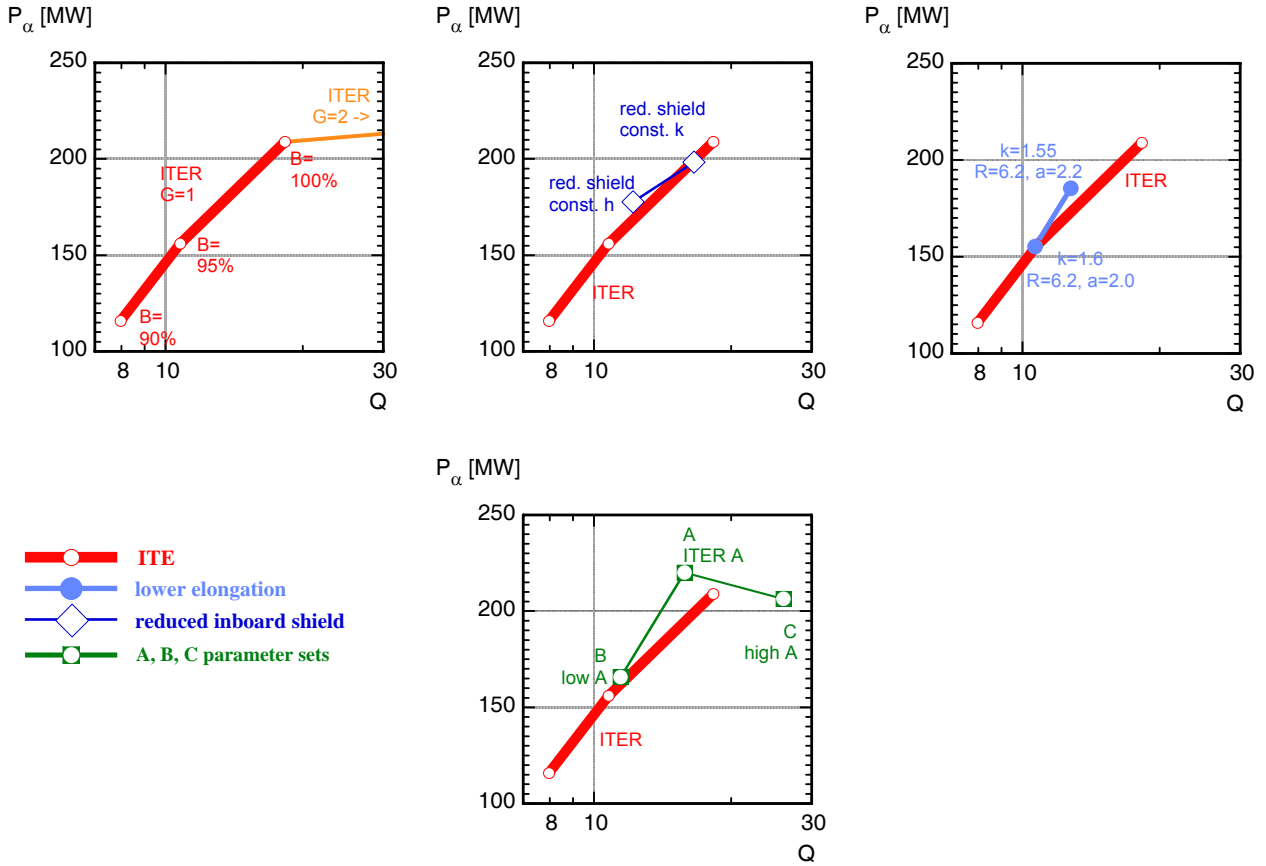


Fig. 5: Indicators for height and width of operating space in  $Q$ - $P_\alpha$  plane (max.  $P_\alpha$  and corresponding  $Q$ ) for (top row) ITER a) as field is reduced and with b) reduced shield thickness and c) lower elongation. d) Superposition of cases A,B,C in bottom row. All for  $\alpha$  enhancement factor  $G = 1$  except as indicated.

A subsequent decrease of the superconductor current-field product ( $jxB$ ) by 10% (95%  $B$ ) reduces the operating window significantly, and, with a further decrease of 10%, the minimal values for the ITER mission are jeopardized. The consequences of an increased vertical stability requirement at full field have been similarly examined. If the elongation of the plasma were reduced from  $\kappa = 1.7$  to  $\kappa = 1.6$ , the operating diagram is almost exactly that shown here for 95% field.

A possible avenue to recover the operational space lost due to reduced superconductor  $jxB$  could be a reduction of the inboard shielding thickness (incorporation e.g. of tungsten) thereby providing additional space for the plasma inside the same coils. The middle panel shows the effect for a) a 10 cm reduction inboard at constant elongation (8.5 cm reduction top and bottom) and b) at constant plasma height (no reduction top and bottom).

A possible avenue to recover the operational space lost due to larger vertical stability margin could be a larger major and minor radius plasma if steps can be taken to reduce the field ripple. The right-hand panel shows the effect for a 20 cm increase in major and minor radius at full superconductor  $jxB$  product.

Finally, parameter sets of somewhat larger machines are determined which have the same 0-D performance, and roughly the same burn flux and compressive vault stress as the full field ITER, but at  $\sim 10\%$  reduced superconductor  $jxB$ . A very simple cost function based on a combination of TF energy and surface area and fitted to systems code runs would place these devices (A,B, and C of the middle panel of fig. 5) at 1.07 of the cost of ITER.

From integrated modelling, we have thus developed a description of the ITER operating window. We have shown that the loss in operating space resulting from a hypothetical 5% re-

duction in field or 6% reduction in elongation could be largely recovered if some design changes were feasible or by a modest increase of machine size by 20-25 cm.

#### 4. Perspectives

Work on divertor and core modelling for ITER is continuing, with particular emphasis on:

- In two-dimensional modelling of the ITER scrape-off and divertor plasma with walls having realistic carbon erosion-deposition, extension of the model to include temperature- and flux-dependent variation of the carbon erosion at the target, continuation of the study of variations of ITER geometry with the nonlinear neutral model, further application of the code with both linear and nonlinear neutral models to a highly radiating prototypical DEMO plasma, and initial studies including seeded impurities in the edge plasma.
- In one-dimensional modelling of the plasma core, the work will concentrate on integration of scaling advances from the two-dimensional modelling, variation of the impurity model for present experiments once validated data on impurity transport become available, extension of the modelling of ITER and a highly radiating prototypical DEMO to operational modes with longer pulses and initial development of the model toward hybrid operation.

#### Staff:

H. D. Pacher (INRS-EMT, Varennes, Québec, Canada),  
G. W. Pacher (Hydro-Québec, Varennes, Québec, Canada)  
A. S. Kukushkin (ITER Organization)  
G. Janeschitz  
I. Landman  
S. Pestchanyi - with the collaboration of G. Pereverzev (IPP Garching)

#### Literature:

- [1] Pacher, G.W., Pacher, H.D., Janeschitz, G., Kukushkin, A.S., Pereverzev, G., Plasma Phys. Control. Fusion **46** (2004) A257
- [2] Kukushkin, A.S., Pacher, H.D., et al., Nucl. Fusion **45** (2005) 608
- [3] Pacher, H.D., Kukushkin, A.S., Pacher, G.W., Janeschitz, G., Coster, D.P., Kotov, V., Reiter, D., J. Nucl. Mat. **363–365**(2007) 400–406
- [4] Kukushkin, A.S., Pacher, H.D., Kotov, V., Reiter, D., Coster, D.P., Pacher, G.W., J. Nucl. Mat. **363–365**(2007) 308–313
- [5] Janeschitz, G., Pacher, G.W., Pacher, H.D., Kukushkin, A.S., Proc. 33rd EPS Conf. on Plasma Physics, Rome, Italy (2006).
- [6] Kukushkin, A. S., Pacher, H. D., Kotov, V., Reiter, D., Coster, D., Pacher, G. W., Nucl. Fusion **47**(2007) 698–705,
- [7] Pacher, G.W., Pacher, H.D., Janeschitz, G., Kukushkin, A.S., Kotov, V., Reiter, D., Nucl. Fusion **47**(2007) 469-478
- [8] Kukushkin A.S., Pacher H.D., "On Carbon Deposition in First Wall Gaps", presented to ITPA Topical Group on Divertor and SOL Physics, Garching 2007
- [9] Pacher G.W., Pacher H.D., Kukushkin, A.S., "Sensitivity of the ITER operating window to variation of transport and magnetic field", INRS-EMT Report INRS-EMT-037-0607, 2007
- [10] Kukushkin, A.S., Pacher, H.D., Kotov, V., Reiter, D., Coster, D., Pacher, G.W., Proc. 34th EPS Conf. on Plasma Physics, Warsaw, Poland 2007
- [11] Pacher G.W., Pacher H.D., Kukushkin A.S., Janeschitz G., Proc. 34th EPS Conf. on Plasma Physics, Warsaw, Poland 2007
- [12] Pacher H.D., Pacher G.W., in collaboration with ITER IT Garching, FZ Karlsruhe, Max-Planck-Institut für Plasmaphysik Garching, EFDA CSU Garching, "Divertor and core plasma modelling for ITER - Final Report June 2007", INRS-EMT Report, INRS-EMT-038-0607, June, 2007



## **Heating and Current Drive – Physics**



## **TW6-TPHE-ECHULA**

### **Upper Launcher Structural Integration and Launcher Handling Test Facility**

#### **Introduction**

The Electron Cyclotron Heating and Current Drive (ECH&CD) system in ITER is aimed to support the plasma heating as well as to control plasma instabilities by a mm-wave power of up to 20 MW at 170GHz through the Upper Launcher.

The development of the Upper Launcher is organized by the "ECHULA group" of EURATOM associations (ENEA/CNR Milano, CRPP Lausanne, FZK Karlsruhe, FOM Rijnhuizen, IPP Garching / IPF Stuttgart) within EFDA. The development covers the mm-wave system, structural components and maintenance issues.

The main objective of the ECH Upper Launcher is to stabilise the Neoclassical Tearing Modes (NTM) which is achieved by steering the mm-wave beams over a range of plasma areas (typically  $\rho_p$  of 0.64 - 0.9) with a CD efficiency sufficient to stabilise 3/2 and 2/1 NTMs for the reference scenario 2, but also for the hybrid scenario (#3) and for the low-q operation (scenario #5). It is further desirable that the ECH Upper Launchers can be used to access the  $q=1$  region of plasmas with positive shear to provide control of the sawtooth period and amplitude. The current reference design achieves this functionality with 4 "Extended Performance front steering Launchers" or EPLs which cover  $\rho_p$  of 0.4 - 0.9.

During ITER operation the launcher structure has to withstand neutron heating as well as extreme forces and torque moments during plasma disruptions. The former quite simple launcher structure in smaller toruses has to evolve to a very rigid and efficiently cooled system. This structural system of each launcher integrates the mm-wave beam lines and their components. It consists of two separate units, namely the blanket shield module (BSM) forming the plasma-facing component and the launcher main structure, which includes the internal shield. The main structure is bolted at the launcher back-end as a cantilever to the port extension of the vacuum vessel. The BSM and the main structure are formed as welded assemblies. The capability of the structural design to provide communality with diagnostics launchers as well as fabrication and cost considerations have led to the currently pursued "slim wall" design. This structure is characterised by a single wall central section of the main frame, whereas the front section has double walls, where meandering paths are formed for main launcher cooling system fed by the blanket water primary heat transfer system ("blanket water"). Apart from very efficient and homogeneous heat removal which is particularly advantageous for removing the nuclear heat load generated at the front sections, the double wall sections serve together with the actively cooled internals as heater elements during bake-out with blanket water at 240°C and 4.4 MPa.

Along with the thermo-hydraulic verifications based on the actual design, basic studies of remote handling are to accompany the structural design development given the need to insure the feasibility of dedicated RH processes. For this purpose, a launcher handling test facility (LHT) is being set up to provide a full scale experimental site with a cooling water loop providing ITER blanket water parameters (operation/bake out conditions), a remote handling area, observation units and a control/data acquisition unit. In the post-TW6 period, the remote handling technologies and processes will assume a novel focus on quality assurance aspects and form the basis of a future assembly and testing facility for the various structural and mm-wave components to be manufactured at industry during the procurement phase.

#### **Upper Launcher Structural Integration**

For the structural integration of the mm-wave system into the Upper Port Plug, a detailed design was developed. It is composed of a detachable blanket shield module (BSM) on the main structure setting the frame. The current reference design is the mm-wave model UL06a

which is characterised by a mitre bend section in the central part of the internal shield and waveguides running from the launcher back-end (housing the isolation valves and the torus windows) up to almost the front section of the internal shield (cf. Fig. 1). MM-wave design updates issued in 2007 provided precisions for the mm-wave system such as the interfacing components to the torus windows (model UL07a) and to refinements in the mm-wave steering and alignment (model UL07b), but were not calling in revisions of the design of the internals of the structural system.

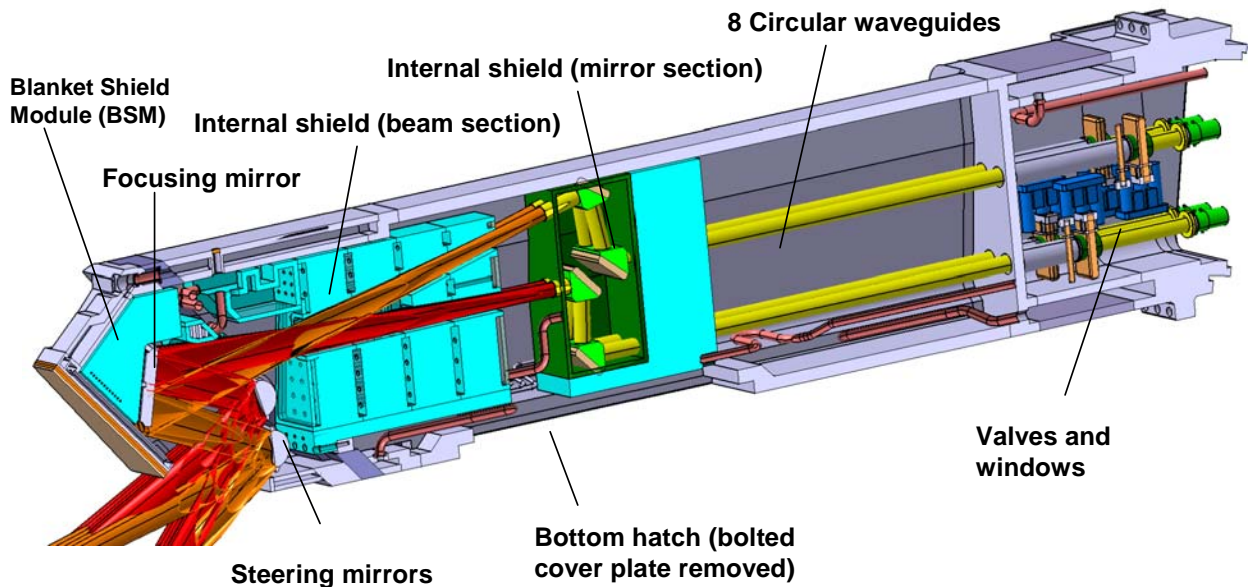


Fig. 1: Structural components as of the current model for the Extended Performance (EP) Launcher based on the UL06a model for the mm-wave design

However, the transition to a quasi-optical beam line design, which has just started, will replace most of the waveguides and the mitre bends by Gaussian optics (including mirrors in central internal shield area), and thus modify significantly the (internal) shield configuration. Thus the current detailed design of the shield blocks and of the internal shield is seen to provide the basis for the forthcoming revision and further detailing of the cooling routing and maintenance access.

### Design Cycle and numerical analysis

In the design cycle of the Upper Launcher the structural components are analysed in numerical simulations. The results form the input for further design optimization considering normal and off-normal (e.g. plasma disruptions) tokamak operation. The numerical simulations can be divided in neutron flux, thermal, structural and thermo-structural analyses.

In the neutron flux analyses different variants of the shielding configuration for the Extended Performance front steering Launcher (EPL) were compared in terms of nuclear response functions in the critical positions. Neutron damage (dpa), nuclear heating, helium production rate, neutron, and gamma fluxes have been calculated under the conditions of ITER operation. It was shown that the radiation shielding criteria are satisfied and the supposed shutdown dose rates are below the ITER nuclear design limits.

For the first wall panel is a component with critical design requirements, normal operational loads have so far been taken into account in the thermal-mechanical analysis using the following terms for volumetric and heat loads.

- The volumetric thermal load the front panel is subject to is caused by neutron and gamma heating. In the present design, a heat load of 3.4/5.1/5.1 W/cm<sup>3</sup> has been as-

sumed in Be/Cu-alloy/SS layers with uniform distribution over the volume of each material.

- The maximum heat flux perpendicular to the surface of the beryllium layer is  $0.5 \text{ MW/m}^2$ . It is assumed to be uniform over the surface. Possible extremely short surface heat loads incident parallel to the surface of the Be layer have recently been noted as an additional issue producing peak loads higher by one order of magnitude, occurring during disruptions and Vertical Displacement Events (VDEs). Given their strong dependence on the actual geometrical configuration of the Be layer and thus on potential shading effects, the proper analysis has to await the design progress for the neighbouring regular blankets.

The specifications of cut-outs in the BSM below the launcher are still based on the initial beam lines for the front steering launcher. The specifications which are also documented to the ITER-IO are seen as a conservative estimate for the requirements for the EPL reference designs and thus require only final up-dating at the last stage of the design development, when the final design of the mm-wave beam lines will be available.

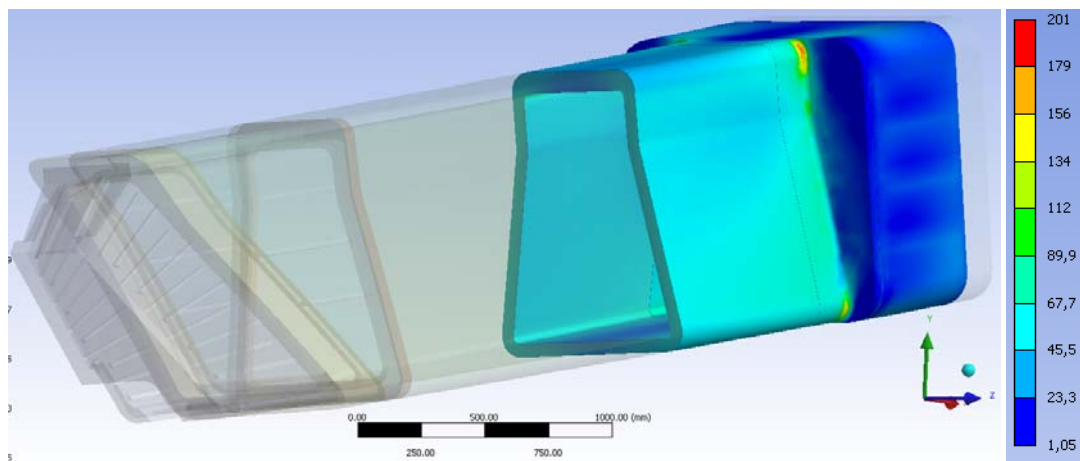


Fig. 2: Von Mises stresses at the launcher back end during a VDE-III with fast linear decay (15 MA current breakdown in 40 ms).

During plasma disruptions, the fast poloidal field change induces eddy currents on the Upper Launcher which interact with the strong static magnetic field. As a result, high mechanical loads act on the structure (Fig. 2) which has to remain within the spacing to the neighbouring components. The numerical electro-magnetic analysis was combined with a structural analysis of the Upper Launcher structure to examine the maximum deflection. The structural design turned out to be capable to withstand the high loads.

### The Launcher Handling Test Facility and Remote Handling

The structural design has to be proven and realized using appropriate manufacturing techniques. Especially the complex double wall structure of the Blanket Shield Module with its integrated cooling loops requires leading edge technologies and new manufacturing processes. Prototypes of the parts close to the plasma are under construction and will be tested in a recently constructed Launcher Handling Test Facility (Fig. 3) under conditions close to ITER operation. This includes normal operation with cooling water flowing through the prototype at  $150^\circ\text{C}$  and 30 bars as well as bake out at  $240^\circ\text{C}$  and 44 bars or thermal shock.

The prototype tests will allow the definition of acceptance tests for the subsequent manufacturing phase of the launchers. Besides for prototype testing, the facility will be used also to develop and validate tools and processes of remote handling for hot cell operation like assembly and mm-wave component alignment.



Fig. 3: The Launcher Handling Test Facility (left) with a manipulator arm (middle) and a manufacturing study of the double wall structure (right).

## Conclusions

The design of the Upper Launcher was updated to the recent progresses in the mm-wave design. The numerical analyses were extended to improve the design of the structural components and adapted to the new mm-wave design, e.g. the front steering mirror unit. Some details like the cut out in the Blanket Shield Module will be updated with the expected new mm-wave beam line design. Prototype manufacturing is in progress and will allow testing in the recently built up Launcher Handling Test Facility. Maintenance tools and remote handling processes are planned to be developed and tested at this facility.

### Staff:

U. Fischer  
G. Gantenbein  
G. Hailfinger  
R. Heidinger  
K. Kleefeldt  
W. Leonhardt  
M. Lux  
A. Meier  
D. Mellin  
T. Scherer  
A. Serikov  
P. Severloh  
P. Späh  
D. Strauß  
H. Tsige-Tamirat  
A. Vaccaro  
J. Weggen

### Literature:

- [1] I. Danilov, R. Heidinger, A. Meier, B. Piosczyk, M. Schmid, P. Späh, W. Bongers, M. Graswinckel, B. Lamers, A.G.A. Verhoeven; High-power short-pulse, mechanical, and thermohydraulic tests of the window prototype for remote steering launcher; *Fusion Science and Technology*, 52(2007) pp250-55
- [2] R. Heidinger, I. Danilov, A. Meier, B. Piosczyk, P. Späh, M. Thumm, W. Bongers, M. Henderson, F. Leuterer, A.G.A. Verhoeven, D. Wagner; Development of high-power window prototypes for ECH&CD launchers; *Fusion Engineering and Design*, 82(2007) pp693-99
- [3] P. Späh, R. Heidinger, G. Hailfinger, M. Henderson, K. Kleefeldt, A. Serikov, E. Ciattaglia, G. Saibene; Design and analysis of the structural components in the ITER ECH upper port plug; *Fusion Engineering and Design*, 82(2007) pp700-08
- [4] M.A. Henderson, S. Alberti, P. Benin, T. Bonicelli, R. Chavan, D. Campbell, S. Cirant, G. Dammertz, O. Domicchi, O. Dumbrajs, D. Fasel, T.P. Goodman, R. Heidinger, J.P. Hogge, W. Kasperek, C. Lievin, B. Piosczyk, E. Poli, G. Ramponi, G. Saibene, O. Sauter, A. Serikov, G. Taddia, M. Thumm, M.Q. Tran, A.G.A.

- Verhoeven, H. Zohm; EU developments of the ITER ECRH system; Fusion Engineering and Design, 82(2007) pp454-62
- [5] M.A. Henderson, R. Heidinger, D. Strauss; Overview of the ITER EC Upper Launcher; accepted for publication in Nuclear Fusion
- [6] M. Thumm, S. Alberti, A. Arnold, P. Brand, H. Braune, G. Dammertz, V. Erckmann, G. Gantenbein, E. Giguet, R. Heidinger, J.P. Hogge, S. Illy, W. Kasperek, H.P. Laqua, F. Legrand, W. Leonhardt, C. Lievin, G. Michel, G. Neffe, B. Piosczyk, M. Schmid, K. Schwörer, M.Q. Tran; EU megawatt-class 140-GHz CW gyrotron; IEEE Transactions on Plasma Science, 35(2007) pp143-53
- [7] D. Wagner, F. Leuterer, A. Manini, F. Monaco, M. Münich, F. Ryter, H. Schütz, J. Stober, H. Zohm, T. Franke, I. Danilov, R. Heidinger, M. Thumm, G. Gantenbein, W. Kasperek, C. Lechte, A. Litvak, G. Denisov, E. Tai, L. Popov, V. Nichiporenko, V. Myasnikov, E. Solyanova, S. Malygin, F. Meo, P. Woskov; The new multifrequency electron cyclotron resonance heating system for ASDEX upgrade; Fusion Science and Technology, 52(2007) pp. 313-20
- [8] R. Heidinger, I. Danilov, A. Meier, A. Arnold, J. Flamm, M. Thumm, F. Leuterer, J. Stober, D. Wagner; Low power mm-wave transmission characteristics of a frequency tuneable double disk CVD-diamond window; Joint 32nd Internat. Conf. on Infrared and Millimetre Waves, and 15th Internat. Conf. on Terahertz Electronics, Cardiff, GB, September 2-7, 2007, **Invited Keynote** + CD + Book of Abstracts
- [9] R. Heidinger; 6th Int. Kharkov Symposium on Physics and Engineering of Microwaves, Millimeter and Submillimeter waves (MSMW'07), 2007 Kharkov (UA), June 25-30, 2007, **Invited Paper** + Paper in MSMW'07 Symposium Proceedings, IEEE Catalog Number: 07EX1786, ISBN 1-4244-1237-4
- [10] P. Spaeh, R. Heidinger, K. Kleefeldt, A. Serikov, D. Strauss, M. Henderson; Shield components adopted to the ITER ECRH Upper Launcher; Joint 32nd Internat. Conf. on Infrared and mm Waves, and 15th Internat. Conf. on TeraHertz Electronics, Cardiff, GB, September 2-7, 2007, Poster + CD + Book of Abstracts
- [11] R. Heidinger, K. Kleefeldt, A. Meier, T. Scherer, P. Spaeh, D. Strauss, Design and Analysis of the Shielding Structure in the ECH Upper Port Plug at ITER; Workshop on RF Heating of Fusion Plasmas, September 10-12, 2007, Heidelberg, Presentation + CD-ROM + Book of Abstracts
- [12] T.A. Scherer, R. Heidinger, D. Strauss, A. Meier; Design Aspects for ITER RF Windows; Workshop on RF Heating of Fusion Plasmas, September 10-12, 2007, Heidelberg, Presentation + CD-ROM + Book of Abstracts
- [13] A. Serikov, U. Fischer, R. Heidinger, P. Spaeh, S. Stickel, H. Tsige-Tamirat; Overview on the neutronics for the ITER ECRH Launcher; Workshop on RF Heating of Fusion Plasmas, September 10-12, 2007, Heidelberg, Presentation + CD-ROM + Book of Abstracts
- [14] D. Strauß, R. Heidinger, G. Hailfinger, K. Kleefeldt, A. Serikov, P. Späh; Structural and Electromagnetic Loads on THE ECRH Upper Launcher at ITER; Workshop on RF Heating of Fusion Plasmas, September 10-12, 2007, Heidelberg, Presentation + CD-ROM + Book of Abstracts



## **Heating and Current Drive – Diagnostics**



## EFDA/06-1417 (TW6-TPDS-WINCOD2) ITER Practice for Non-Metallic Replaceable Window Assemblies

### Objectives

ITER diagnostics and heating systems require the use of window components with parts made of non-metallic materials (i.e. flange mounted windows). Each window assembly represents a combination of metallic and non-metallic parts. Some of these components, being part of the primary vacuum boundary, have the function of confining the products of the nuclear reactions. The ITER site will be licensed and therefore will have to comply with the French statutory requirements [1,2,3].

The primary confinement component (the ITER vacuum vessel VV) is designed and fabricated based on existing industrial pressure vessel codes with special amendments to take into account the requirements of the ITER VV (SDC-IC [4]).

Requirements for window assemblies generally are not covered by traditional pressure vessel codes. Additionally, existing national or international industrial standards that specify the criteria for the design, the manufacturing, testing and the inspection of these parts and components are generally not directly applicable to ITER. Nevertheless, if a non-harmonized standard fits the application better than harmonized ones, engineering justification is provided in this document, under the condition that an equivalent safety level is assured.

Window assemblies are located on the ITER vacuum vessel port plugs, inaccessible during machine operation and during moving of the main in-vessel components during a shutdown. The assemblies must be operational continuously for the operating life of ITER. Thus the window assemblies are made readily and simply maintainable, by the provision of remote handling features compatible with planned remote handling (RH) tools.

Window assemblies for a variety of diagnostic systems [5,6] have much in common in their design and manufacture. There are strict quality assurance procedures required for materials and processes used in their manufacture. Their manufacture and testing is essentially the same irrespective of the diagnostic that they apply to. Fig.1 shows typical window designs for ECRH and diagnostic windows.

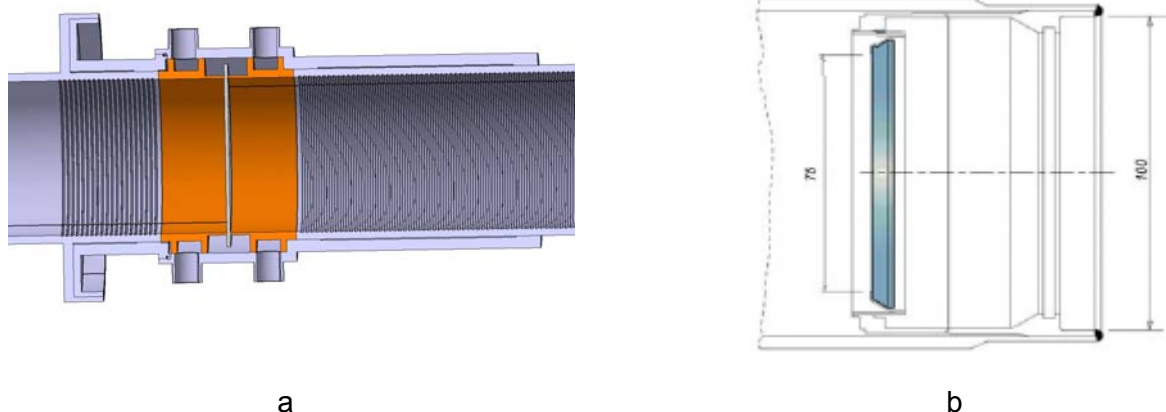


Fig. 1: Typical window design:  
a) CVD diamond window for ECRH (75mm, brazed in a corrugated waveguide), b) Diagnostic window.

Window assemblies for the plasma heating (ECRH) consist of torus and gyrotron windows. Torus window assemblies form a primary tritium confinement in ITER electron cyclotron heating and current drive (ECH&CD) system. They have to provide adequate transmission for the

high power mm-wave beam lines integrated into the launcher. These windows are welded to the closure plate by a stainless steel socket, with an intermediate isolation valve to provide vacuum-tight isolation from the torus, for in-line testing and during in-situ replacement. Gyrotron windows brazed to the output flange of the gyrotrons have no tritium barrier functionality. All designs of the window assemblies for the plasma heating are rated for 2MW/CW operation.

It is therefore necessary to recommend additional codes and standards with guidelines regarding the design, manufacturing and testing for window assemblies. For this purpose, a set of two documents has been prepared in 2007:

- a) „Engineering Justification Document“
- b) „Supporting R&D and Qualification Document“

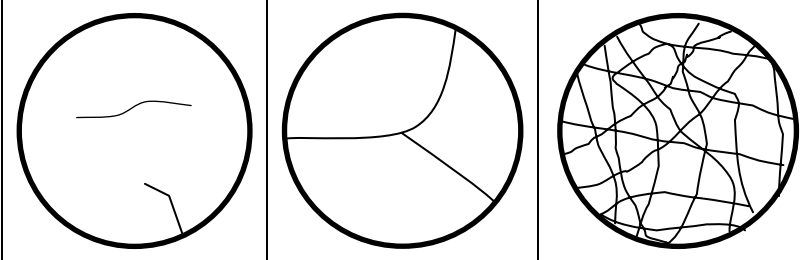
Document a) contains a detailed support of the soundness of the criteria contained in the technical specifications. Document b) defines all the R&D required to validate the defined criteria. The elaboration of these two documents has been performed in a collaboration with C. Waldon (JET, Culham) with respect to the JET documents c) „Existing Practice Document“ und d) „Technical Specification Document“.

**Project activities: Document preparation**

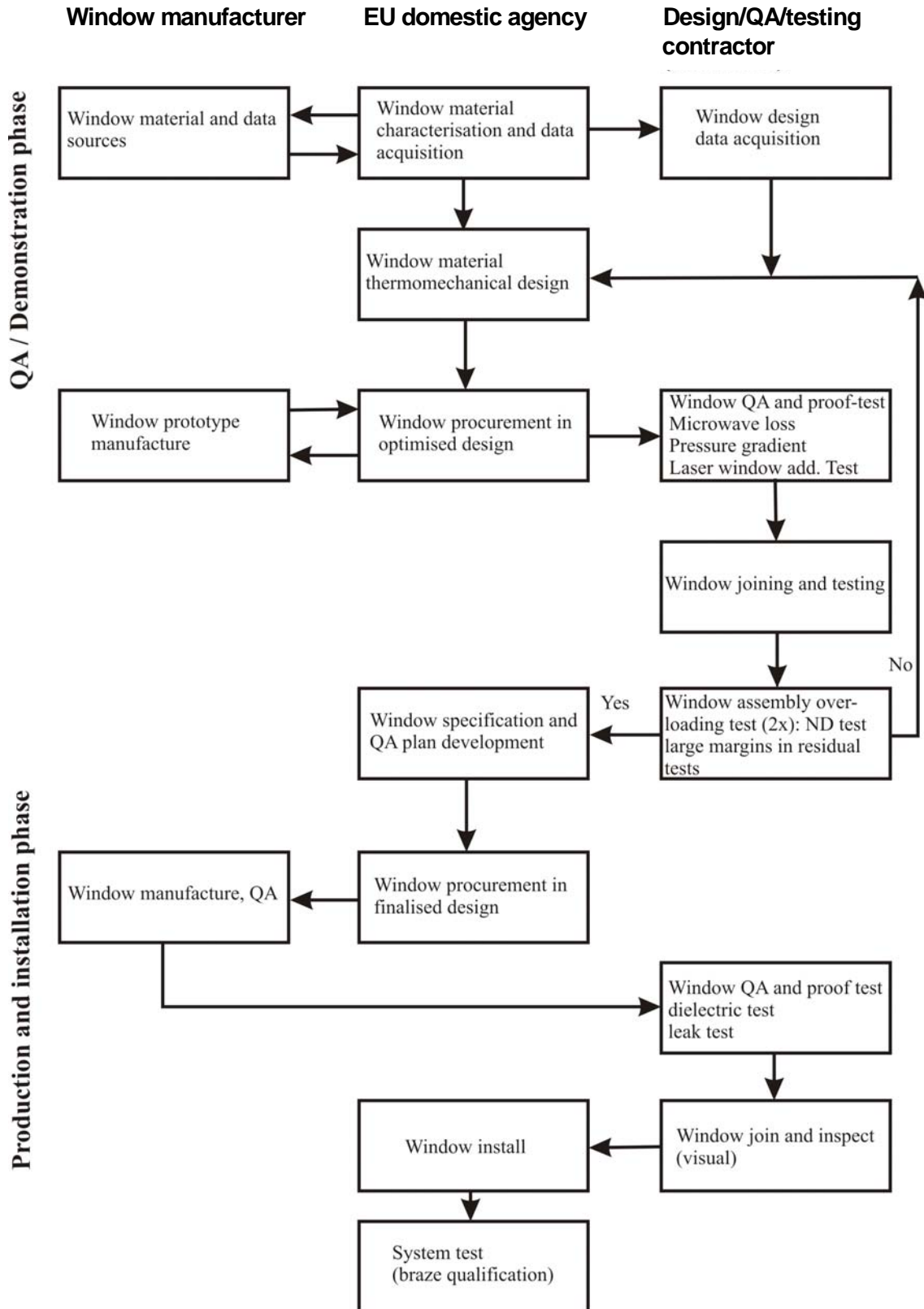
*Engineering Justification Document (EJD)*

This document is applicable for ITER windows with non-metallic components and allocates a compilation of materials and arguments for the codes and standards rules with the goal to formulate conclusive window design criteria. The purpose of the report is to provide the Engineering Justification for the “ITER Practice for Non-Metallic Replaceable Windows Assemblies” document.

The document contains a detailed description of actual diagnostic and ECRH window configurations. A classification by materials, sizes, bonding and joining, applications and design is given. An important part of this document is a literature study about the radiation resistance of the allowed window materials where radiation damages are quantified. Considerable operation loads (OL) and failure modes (FM) are discussed in detail:

1) Operation loads	2) Failure modes		
Thermal and vacuum cycling	<b>Mechanical failure</b> Induced by monotonic (M) or cyclic (C) loads  <b>Physical consequences</b> M/C: loss of integrity in metallic parts and in joining zones M: crack formation in brittle window disk		
Neutron loading			
Microwave heating load			
Water pressure			
Port deflection (seismic, VDE, etc...)			
Overpressure			
Water strike			
Manufacturing loads			
Transportation loads	<b>Electro-chemical failure</b> Corrosion Erosion		
Installation loads			

For the justification of the above-mentioned operation loads and failure modes, a list of failure events in existing fusion machines has been compiled. Well-recognized industrial codes of practice („Industrial Codes“, e.g.: ISO, EN, MIL, ASTM, ISPEL) provide specifications and classifications for ceramic (brittle) materials for ITER window assemblies. A summary plan for window procurement and testing is given in the following scheme:



The RDQ document is applicable for ITER windows with non-metallic components and indicates the test methods that have already been performed (reference to R&D tasks and related documents) and those that are still required. The purpose of the report is to provide the qualification and to support R&D activities for the "ITER Practice for Non-Metallic Replaceable Window Assemblies" document.

The goal of the "Qualification and Supporting R&D Document" is to guarantee an enhanced reliability of the window materials and the design and to support the quality assurance (QA) for the window assemblies. Corresponding to the existing R&D methods for diagnostic and heating window assemblies, described in detail, the potential need of additional tests that are required to provide engineering evidence of soundness of selected criteria are described.

A survey of existing and newly proposed window types and assemblies should be conducted on the basis of the expected operation loads and conditions and failure modes. Structural details, e.g.: ceramic windows, joints, coatings and other structural discontinuities will be part of this survey.

The design optimization is possible by prevention of M- and C-type damages according to the following strategies:

1. Design by rule
2. Design by analysis

Rules for the techniques of joining ceramic disks to the metallic components should include important material properties like:

- Design strength
- Failure strength (as a function of test time)
- Physical properties (Young's modulus (stress-strain behaviour))
- Thermal Expansion Coefficient (CTE)
- Thermal conductivity
- Density
- Toughness (if a fracture approach is to be developed)
- Resistance to cyclic loading (C-type), fatigue strength with size and numbers of cycles)
- Resistance to creep behaviour (strength versus temperature and time)
- Low and high temperature behaviour of the joining

## **Outlook**

The EFDA-Task: EFDA/06-1417 / FU06-CT-2006-00072 / TW6-TPDS-WINCOD2 „ITER Practice for non-Metallic Replaceable Window Assemblies – 2“ is completed with the preparation of the both documents: "Engineering Justification Document" and "Qualification and Supporting R&D Document".

### Staff:

I. Danilov  
R. Heidinger  
A. Meier  
T.A. Scherer

## Literature:

- [1] Le décret no 63-1228 du 11 décembre 1963 modifié relative aux installations nucléaires.
- [2] L'arrêté du 10 août 1984 relatif à la qualité de la conception, de la construction et de l'exploitation des installations nucléaires de base.
- [3] L'arrêté du 12 décembre 2005 relatif aux équipements sous pression nucléaires.
- [4] In-vessel Components, SDC-IC (ITER\_D\_222RHC v2.0).
- [5] C. I. Walker, "Diagnostic Windows for ITER Practice for Non-Metallic Window Assemblies", ITER\_D\_22JP2H.
- [6] Technical Specifications - ITER Practice for NON-Metallic Replaceable Window Assemblies (ITER\_D\_24H5FR v1.0).
- [7] T. A. Scherer, I. Danilov, "Engineering Justification Document for ITER Practice for Non-Metallic Replaceable Window Assemblies", TW6-TPDS-WINCOD, EFDA/06-1417.
- [8] T. A. Scherer, I. Danilov, "Qualification and Supporting R&D Document for ITER Practice for Non-Metallic Replaceable Window Assemblies", TW6-TPDS-WINCOD, EFDA/06-1417.
- [9] C. Waldon, "Existing Practice Document for ITER Practice for Non-Metallic Replaceable Window Assemblies", TW6-TPDS-WINCOD, CD/E&CG/T/080.
- [10] C. Waldon, "Technical Specification Document for ITER Practice for Non-Metallic Replaceable Window Assemblies", TW6-TPDS-WINCOD.
- [11] R. Heidinger, M. Thumm, H. Budig, J. Burbach, I. Danilov, G. Dammerz, S. Illy, A. Meier, B. Piosczyk, M. Rhode, R. Schneider, P. Severloh, J. Szczesny, P. Willing, "ITER ECRF Window Development", Final Report, EFDA Task TW2-TPHE-ECRWIN, 2005.
- [12] R. Heidinger, J. Burbach, I. Danilov, A. Meier, „Torus and gyrotron window design and development“, Final Report, Subtask C, EFDA Task TW3-TPHE-ECHULA, 2005.
- [13] R. Heidinger, I. Danilov, A. Meier, „Updating of torus window design to modifications in mm-wave design“, report, EFDA Task TW5-TPHE-ECHULA, 2005

## EFDA/06-1446 (TW6-TPDS-DIADES9) Diagnostic Design for ITER: Bolometry (Engineering Analysis for Bolometer Cameras)

The objective of Task Deliverable 5.3 is to contribute to the development of the Project Plan for the procurement package related to the bolometer and pressure-gauge diagnostics and the advancement of the design in critical areas.

The main objective of the work performed by FZK under Task Deliverable 5.3 was to contribute to the conceptual engineering analysis and feasibility study of the bolometer camera integration in the divertor and behind the blanket by evaluating nuclear heat loads and materials using existing information on the nuclear environment in ITER.

Engineering CAD models of the bolometer mini cameras were provided by the Max Planck Institute for Plasma Physics (IPP) Garching. For illustration purposes, Fig. 1 shows the CAD model of the divertor with integrated bolometer camera. The models were converted at FZK into a geometry representation suitable for Monte Carlo neutron/photon transport calculations with the MCNP code by making use of the interface programme McCad. The converted models were integrated into the global MCNP model of a 40° ITER torus sector. Monte Carlo calculations simulating the neutron and photon transport were performed to assess the nuclear heating in the bolometer camera. The resulting nuclear heating was calculated on the basis of the nominal ITER fusion power of 500 MW. Detailed tables of the nuclear power density ( $W/cm^3$ ) were prepared for the divertor bolometer and two different camera types (T301 and T302) integrated behind the outboard shielding blanket in the torus mid-plane.

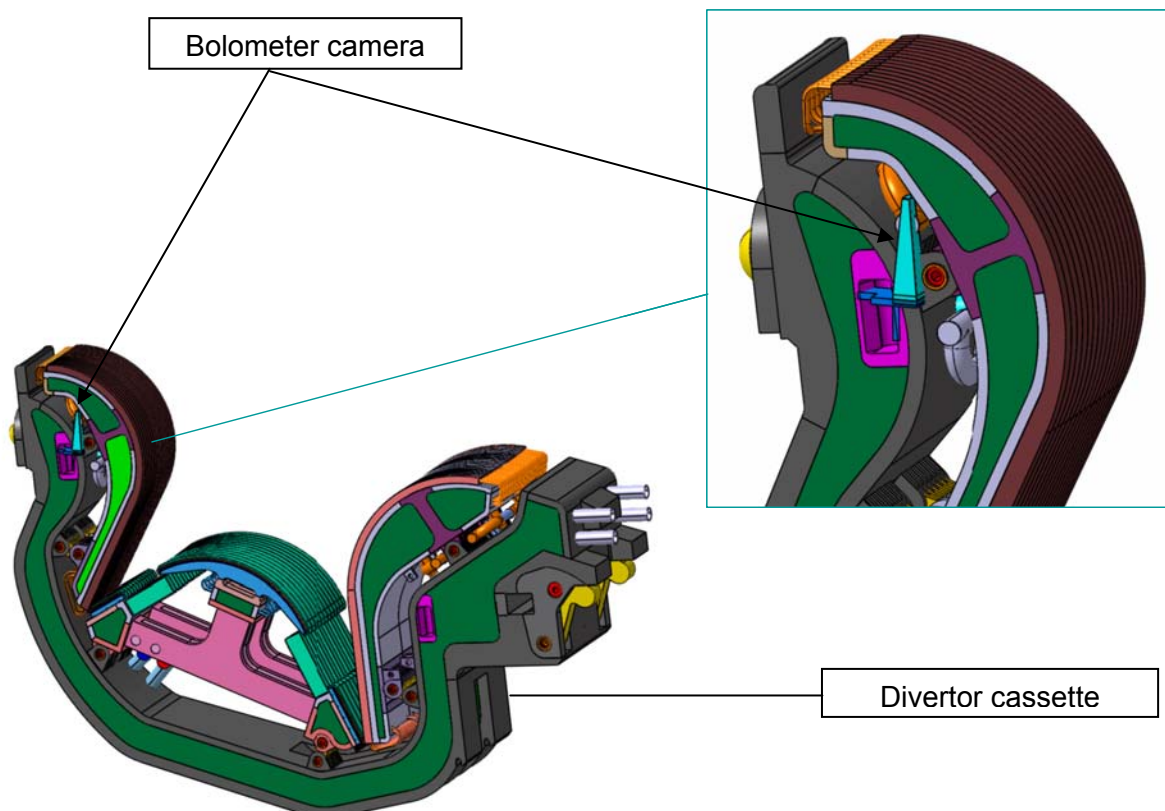


Fig. 1: ITER divertor with integrated bolometer mini camera (CAD model).

### Staff:

U. Fischer  
A. Serikov

S. Stickel  
H. Tsige-Tamirat

## **Vessel/In-Vessel**



## **EFDA/07-1704-1624 (TW6-TVV-LEAKD2) Leak Localisation for In-vessel Components**

### **Background and objectives**

Experience from systems with water cooled components in fusion devices shows that components can be expected to develop leaks during operation, often in unexpected places. The demands on leak localisation are unique in ITER because of the level of leak detection required combined with the environment in which the detection has to be performed. Where space and practicality allow for it, vulnerable components will be provided with monitored interspaces like bellows or windows, but for in-vessel components this is not the case.

In the current configuration for the water circuits it is possible to isolate leaks to 8 blanket modules, 3 divertor segments, an individual limiter, or an individual port plug. Increased ex-vessel segregation is being considered to bring this down to 2, 3 or 4 blanket modules, 1 divertor segment, 1 limiter, and 1 port plug. The techniques which can be used to isolate to this level over the leak range  $10^{-7}$  Pa m<sup>3</sup>s<sup>-1</sup> to  $10^2$  Pa m<sup>3</sup>s<sup>-1</sup> (equivalent He) are essentially conventional and do not require any in-vessel access. There is not yet a proven method, however, within the current scope of equipment to be supplied to ITER, to allow for leaks to be further localised in-vessel, or to distinguish between a leak on the PFC or its in-vessel feeding manifold or piping.

### **Plan and share with CEA**

To achieve the goal of the task several sub-tasks have to be performed, which is done in a shared collaboration with CEA, which has gained wide expertise in localisation of water leaks during operation of the actively cooled components in TORE SUPRA:

- Subtask 1: the collection and analysis of the ITER requirements and geometrical constraints (FZK).
- Subtask 2: critical analysis of the present ITER water circuits and proposal for improvements; review of experience of water leaks and leak detection in the present devices (CEA).
- Subtask 3: review of techniques and classification of their viability for ITER (FZK).
- Subtask 4: proposal for a test programme (FZK).
- Subtask 5: proposal for a possible leak detection scheme for ITER pending the results from proof-of-principle tests at the point before (CEA).

### **ITER requirements and geometrical constraints**

The ITER plasma chamber (torus) is a vacuum vessel, the shield (blanket) modules are attached to the inside walls and protect the superconducting coils from the neutron radiation and reject the heat coming from the plasma (Fig. 1). At the bottom there are 54 divertor cassettes which transmit the ash from the fusion reaction together with unburned fuel and impurities to the pumping ports and absorb the heat coming with this gas from the plasma. All components are cooled by water. There are thousands of weld joints, kilometers of pipework, and many thermally and mechanically loaded components. The plasma is very sensitive to the impurities, the maximum water leak could be  $10^{-7}$  Pa·m<sup>3</sup>/s. The access into the plasma chamber cannot be hands-on, the remote access still requires several months for reduction of the induced radioactivity and opening of double sealed ports. The goal of the leak localisation is firstly to define a single leaky component as fast as possible, secondly to define the details of the leak location (front wall/back manifold), and thirdly to assess the size of the leak in order to take a decision of the urgency for component replacement or in-situ repair.

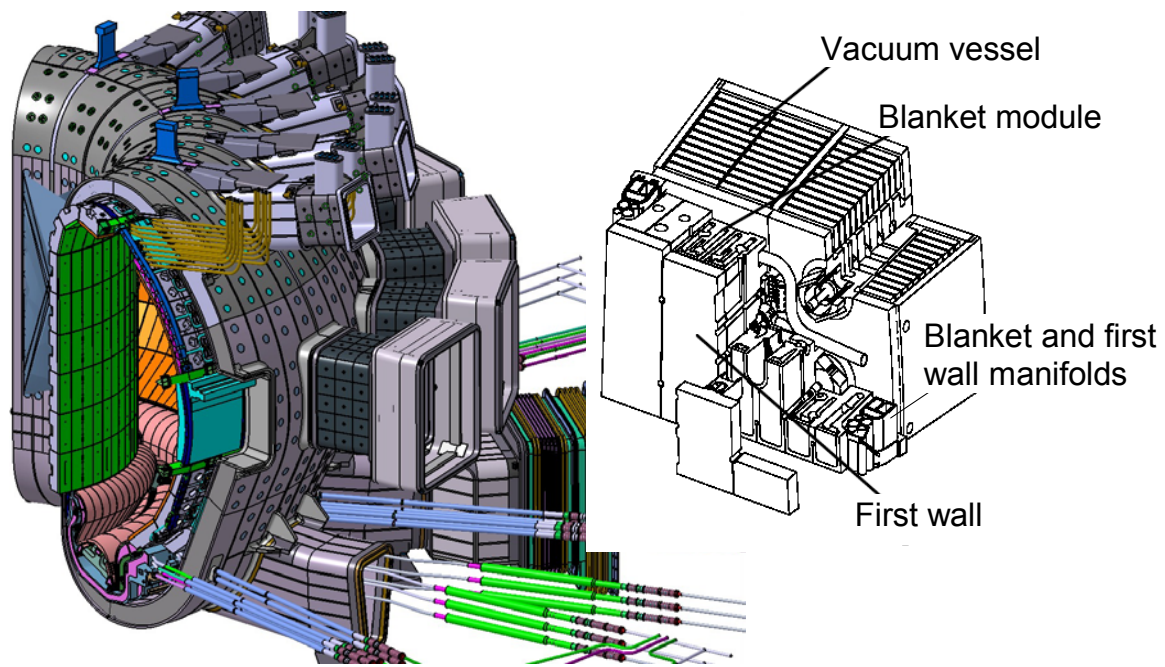


Fig. 1: ITER torus cross-section and one blanket module.

## Review of techniques and classification of their viability for ITER

The following leak localisation methods have been looked at:

1. Segregation of a cooling circuit of a leaky component: This method shall be the main one. The number of cooling loops does not allow relying on a segregation of less than 8 blanket modules or 3 divertor cassettes. This method does not allow specifying the location of the leak (front/back). Draining and drying is being investigated by CEA in frame of this task.
2. The segregation method could be enhanced with the addition of a tracer into a cooling circuit. Use of organic tracers and different inert gases has been investigated. This method cannot be applied for ITER, because the cooling system is the primary circuit with containment and radioactive stability function, the water chemistry cannot cope with any further impurities.
3. Remote manipulator with a RGA head or sniffer: Such a manipulator is under development ("snake arm") and will likely be used at the hydrogen stage of ITER operation. However it is considered to be difficult to rely on it after the start of tritium campaigns.
4. Laser induced fluorescence: Cannot be used, because it requires an addition of Kr or another agent into the water.
5. Laser spectroscopy: Differential laser adsorption or tunable laser with the wave length close to the resonance length of the H<sub>2</sub>O vapour scan the chamber along the first wall and the reflected signal is analysed. Can be applied, but is limited to a sensitivity not better than 10<sup>-7</sup> Pa·m<sup>3</sup>/s.
6. Spectroscopic method: Scan the first wall by the wide angle viewing system during a plasma or glow discharge and look in the spectrum for OH\* band coming from the water vapour excitation. The key issue is that the viewing system for ITER has to be

made radiation hard, which significantly reduces the efficiency in UV light. This issue remains to be clarified. Use of spectroscopic leak localisation is only possible if the plasma discharge is on or if the glow discharge can be started (toroidal magnetic field must be turned off). The spectroscopic methods can be considered as a complimentary to other ones. The overall strategy of the leak localisation based on spectroscopy is considered to be most promising.

### Spectroscopic method

The water vapour penetrating to the vacuum vessel and excited by either working plasma discharge or by glow discharge illuminates the light with multiple spectrum bands, of which the band OH\* 306-309 nm was analytically selected to be most suitable for detection, as it can easily be distinguished on the background of the bands of other species expected in the ITER plasma. The sensitivity of this system for the ITER geometry from  $10 \times 10 \text{ cm}^2$  first wall area is illustrated in the diagram Fig. 2, for an UV spectrometer with 0.4 transmission probability, as well as the presence of the water background in the plasma and the diffused light from other bands, and the typical value for the fast electron density in the negative glow near the first wall. Theoretically a leak less than  $10^{-8} \text{ Pa} \cdot \text{m}^3/\text{s}$  can be detected.

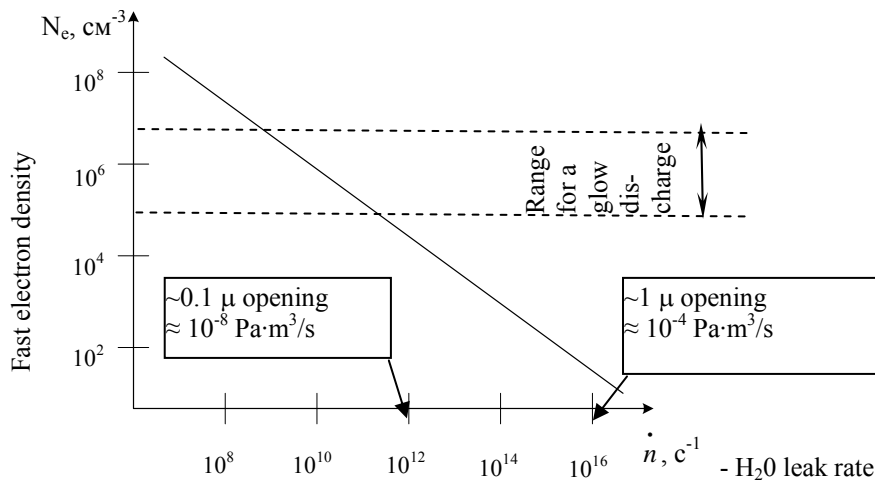


Fig. 2: Detectable leak rate vs. fast electron density.

Experiments with water dosing into a plasma discharge have been performed in Moscow Engineering Physics University together with Lebedev Physical Institute (Moscow) on an adiabatic trap [1]. The tests were performed in air, argon and deuterium and could successfully confirm that the spectroscopic method based on the glow discharge excitation of a hydroxyl can be used for sub-micron leaks localisation in ITER.

### Staff:

A. Antipenkov  
Chr. Day

### Literature:

- [1] A. Antipenkov, O. Afonin, I. Vizgalov, V. Kurnaev, V. Kolesnikov, Water micro-leaks detection in ITER torus, Questions of Atomic Science and Engineering, Moscow, 2006, issue 3, 46-55 (in Russian)



## **Magnet Structure and Integration**



## EFDA/03-1105 (TW3-TMSC-CRYLAB) Cryogenic Laboratory Tests for V-I Characterisation of Subcable Samples

The objective of this work is to perform measurements of the V-I characteristics of Nb<sub>3</sub>Sn sub-size (>30 strands) cable-in-conduit-conductors (CICC) under applied longitudinal strain in liquid He (T=4.2K) and high magnetic fields (up to B=14 T).

Emphasis shall be put on the measurement of the thermal pre-strain of the strands. To this end the experimental set-up shall be capable of performing accurate measurements of specimens having – in particular – different conduit materials, thickness, cables sizes and void fractions [1, 2]. The strain applied to the strand shall be – typically – up to ≈ 1.5%. The instrumentation sensitivity is planned to allow measurements of critical electric fields as low as E=10 μV/m with a sensitivity better than 1 μV/m.

After the experimental set-up has been completed, instrumented and accurately calibrated, specimen testing shall be started. All specimens (not heat treated) will be made available by EFDA. In total, during the contract period, about 25 specimens shall be tested.

Therefore, in the late 1985's the *FBI*-facility was established at the Forschungszentrum Karlsruhe to investigate the influence of applied longitudinal strain (*F*) and magnetic field (*B*) on the critical current (*I<sub>c</sub>*) at liquid helium temperature. The facility contains two separate experimental setups to cover tests on single superconducting strands and also on CICC [3, 4]. Within this work the facility was upgraded and is now under use for performance tests of advanced single strands and sub-stage CICC developed for ITER [5].

### Cable-in-conduit sub-stage samples

In a first stage of this program a systematic characterization of the influence on the critical current *I<sub>c</sub>* of the main cable parameters, like cable pattern, void fraction and twist pitch was performed. For this purpose several samples were manufactured under the supervision of CEA, France. The details of the used strand, CICC and further details of the measurement are already given in [6].

#### A. *I<sub>c</sub>(B)* dependence

In Figure 1 the magnetic field dependence on *I<sub>c</sub>* of the two different strand types is plotted, normalized to the number of superconducting strands. The data of the measured samples collapses to two main *I<sub>c</sub>(B)* lines: one for OST Type 1 and one for OST Type 2 which is shifted about 10% to lower values. Here no significant influence of the cable parameters can be seen except the strand origin. This effect is understandable when looking at the different critical current density values which is higher for OST Type 1 than Type 2.

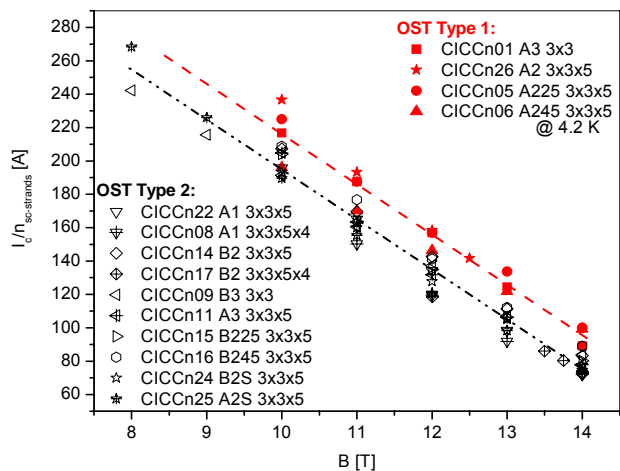


Fig. 1: Summary of the *I<sub>c</sub>(B)* measurements normalized to the number of superconducting strands of all sub-stage CICC made from OST Type 1 and OST Type 2 strands. The measurements were performed at 4.2 K.

#### B. *I<sub>c</sub>(ε)* dependence

In the previous report [7] the strain effect on *I<sub>c</sub>* at 12 T is already summarized. The curves show a clear dependence regarding the cable layout of the sample. For the OST Type 1 samples the highest *I<sub>c</sub>* is reached as already seen in *I<sub>c</sub>(B)*. However, increasing the void fraction seems to decrease *I<sub>c</sub>*.

Within Figure 2, 3 and 4 the data is shown for OST Type 1 and OST Type 2 separately, illustrating the influence of the void fraction and also for the twist pitch. Examining the results from the samples, it is obvious that the VAMAS strand properties can not be recovered (OST ~310 A  $I_c$  at 12 T obtained within the single strand test program [6]). The experiments about  $I_c(\epsilon)$  show a clear influence of the cable layout. There is not such a difference before stretching in the  $I_c(B)$  data. This can be understood, because the Lorentz force on the conductor level is not significant. However, the increase of Lorentz force per strand, due to the increasing  $I_c$  during stretching, reveals a sensitivity and degradation of some of the samples.

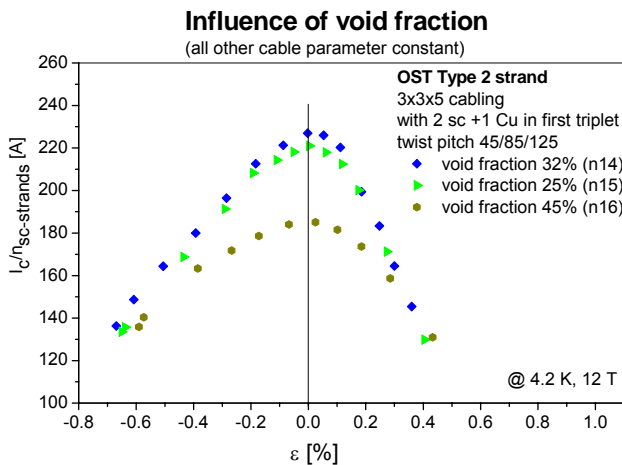


Fig. 2: Data for OST Type 1

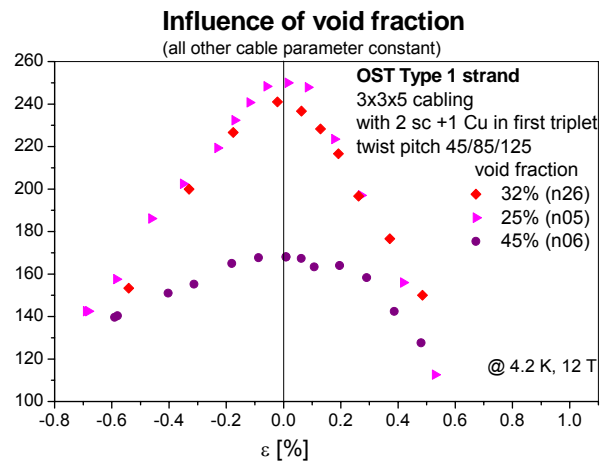


Fig. 3: Data for OST Type 2

In these two graphs the influence of the void fraction is shown, while keeping the other cabling parameters constant. Clearly the effect of a reduced maximum  $I_c$  with higher void fraction can be seen.

As a tendency:

- OST Type 1 behave better than OST Type 2
- 32% and 25% void fraction samples are the best of OST Type 2
- 45% void fraction samples, small twist pitches samples, B3 and A3 (all s.c. strands sample) are the worst
- no clear influence of the cable pattern (size) of the sample is seen

With the data obtained it is possible to look at the  $I_c(12\text{ T})$  performance loss beginning with the single strand going through the different sub-cable stages. In Figure 5 the different normalized single strand values are shown without applied strain.

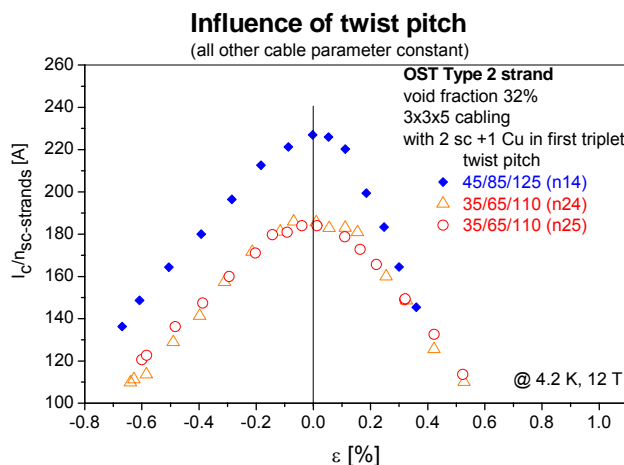


Fig. 4: Here for OST Type 2 the influence of the twist pitch is shown, while keeping the other cabling parameters constant. The shorter twist pitch results in a reduced maximum  $I_c$ .

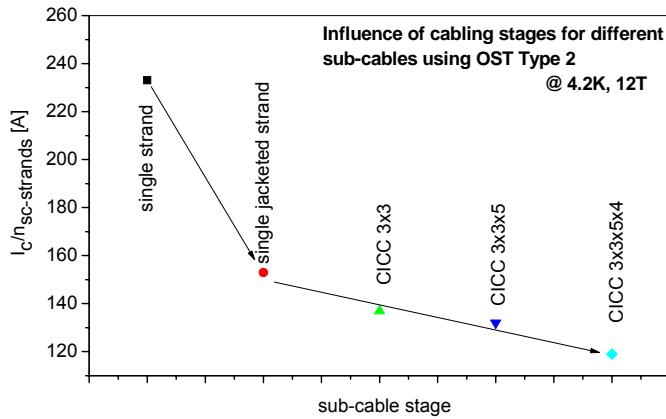


Fig. 5: The performance drop for OST Type 2 strand through different sub-cable stages.

In the next stage the sensitivity to strand origin (companies) was examined. Therefore, samples with strand material from five different manufacturers were prepared. In Table 1 details of the used ITER relevant strands coming from different suppliers are summarized. Strands coming from ALSTOM and SMI (B203, 492 filaments) are due to their layout not ITER relevant. ALSTOM provided strands with a diameter of 1.33 mm upon request to investigate the impact of transversal load on thicker strands. The diameter of

1.33 mm was chosen to replace the first triplet with the same non-Cu area. SMI uses powder in tube technique. However, the results are summarized also in Figure 6 and Figure 7. Figure 6 below gives an overview of the critical current versus magnetic field normalized to the number of superconducting strands within the CICC. The two lines indicates the  $I_c(B)$  behaviour of OST Type 1 and Type 2 as given in Figure 1.

Table 1			
EAS	OST	OCSI	PORI
<ul style="list-style-type: none"> <li>■ <math>J_c \sim 780 \text{ A/mm}^2</math></li> <li>■ Non-Cu losses <math>200 \text{ kJ/m}^3</math></li> <li>■ Cu:non-Cu ratio 0.92</li> <li>■ NSTT8305-HK002-A2</li> </ul>	<ul style="list-style-type: none"> <li>■ <math>J_c \sim 1150 \text{ A/mm}^2</math></li> <li>■ Non-Cu losses <math>900 \text{ kJ/m}^3</math></li> <li>■ Cu:non-Cu ratio 1</li> <li>■ 7730-1 / 7878-1</li> </ul>	<ul style="list-style-type: none"> <li>■ <math>J_c \sim 950 \text{ A/mm}^2</math></li> <li>■ Non-Cu losses <math>1000 \text{ kJ/m}^3</math></li> <li>■ Cu:non-Cu ratio 1.45</li> <li>■ NS026001</li> </ul>	<ul style="list-style-type: none"> <li>■ <math>J_c \sim 900 \text{ A/mm}^2</math></li> <li>■ Non-Cu losses <math>650 \text{ kJ/m}^3</math></li> <li>■ Cu:non-Cu ratio 1</li> <li>■ NT8301-1</li> </ul>

The  $I_c(B)$  dependence of the different conductors varies in a wide range, which can be seen also in  $I_c(\epsilon)$  of Figure 7, due to the different types and layouts of the strand itself. All cable parameters were kept constant as void fraction and twist pitch.

Concentrating at 12 T the difference in  $I_c$  is still not that large as at 9 T, giving a critical current around 100 A. While under applied strain the reached maximum critical current for one strand differs remarkably. However, for ALSTOM the significant larger strand diameter of 1.33 mm compared to 0.81 mm of the other strands must be considered, reducing the current by a factor of 2.7. The SMI strand is a binary compound which has a stronger critical current strain dependence as ternary or quaternary compound. EAS is a quaternary the others are ternary.

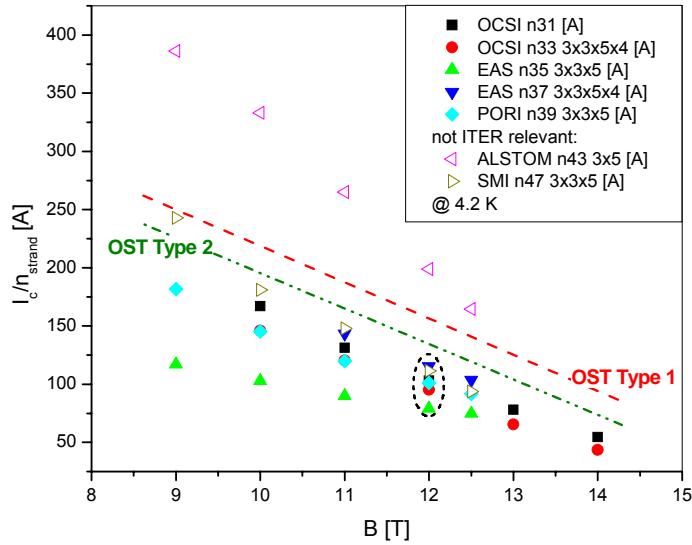


Fig. 6:  $I_c(B)$  of CICC using different strand suppliers.

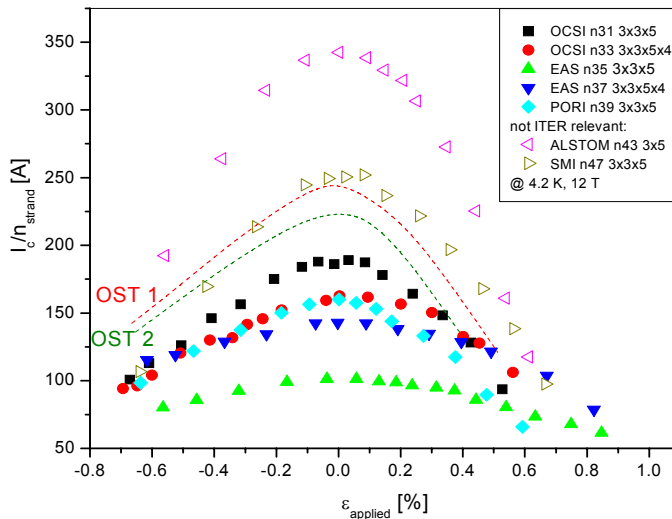


Fig. 7:  $I_c(\epsilon)$  of CICC using different strand suppliers.

The results obtained with the first stage of the test programme gives indications for an optimization of an ITER cable layout. A more in-depth analysis of the samples test results is being done by CEA under EFDA contract 04-1127.

**Staff:**

K.-P. Weiss  
H.Kiesel

**Literature:**

- [1] J.W. Ekin, "Filamentary A15 Superconductors", M. Suenaga, A.F. Clark, Eds. New York and London: Plenum Press, 187 (1980).
- [2] W. Specking, J.L. Duchateau, "Improvement of  $I_c$  in  $Nb_3Sn$  conductors by reduction of the axial prestrain", Transactions on Applied Superconductivity 5 (2), 845 (1995).

- [3] W. Specking and R. Flükiger, "A compact 5 kN test facility for superconducting conductors carrying up to 1.5 kA in magnetic fields up to 14T", *Journal de Physique* 45, C1-79 (1984).
- [4] W. Specking, A. Nyilas, M. Klemm, A. Kling, and R. Flükiger, "The effect of axial stresses on  $I_c$  of sub-size NET  $Nb_3Sn$  conductors", *Proceedings of the 11<sup>th</sup> International Conference on Magnet Technology (MT-11)*, 1009 (1989).
- [5] A. Vostner, E. Salpietro, K.P. Weiss, W.H. Fietz, A. della Corte, L. Muzzi, "The FBI facility – a test rig for critical current measurements on CICC as a function of strain", *IEEE Transactions on Applied Superconductivity* 15 (2): 1387, (2005).
- [6] A. Vostner and E. Salpietro, "The European  $Nb_3Sn$  advanced strand development programme", *Fusion Engineering and Design* 75-9: 169 (2005).
- [7] Nuclear Fusion Programme, *Annual Report of the Association Forschungszentrum Karlsruhe / EURATOM*, FZKA 7291 / EUR 22705 ISSN 0947-8620, 55 (2007).

## EFDA/05-1274 (TW5-TMSM-CRYTES) Cryogenic Testing of Materials, Welds and ITER Mock-ups for Magnet Structures

Besides of the cryogenic material testing for the magnet windings and structures [1] of the experimental reactor ITER, experiments within the development of the European-Dipole were performed. This facility is a second full-size cable in conduit conductor test rig to be operated at the same institution at CRPP, Switzerland as SULTAN. Within this programme conduit material and structural material had to be mechanically investigated as described below.

The static material and component tests are conducted according to the existing standards. For tensile tests the applicable document ISO/CD 19819 "Metallic materials – Tensile testing in Liquid Helium" are the basis of those investigations. Fracture toughness tests are conducted using the ASTM standards E 813-89 and the newly developed JETT (J-Evaluation on Tensile Test) technique and fatigue life tests according to ASTM standards. Hourglass specimens were prepared for the fatigue life investigations of the base material and butt welds of the candidate CS jacket materials.

### Test facilities

The following test facilities are used in the frame of this Contract:

- Cryogenic tensile/compression material cyclic investigation facility, system MTS (+/-25 kN) working between 295 K and 7 K
- Cryogenic tensile/compression material cyclic investigation facility, system MTS (+/-50 kN) working at 295 K and at 77 K (LN<sub>2</sub>);
- Cryogenic tensile material cyclic investigation facility, system Schenck (630 kN) working at 4.2 K (LHe).

### Tensile test of Aluminum material at 4.2 K

Standard tensile tests were performed on aluminium specimen as given in Figure 1 summarizing the results in Table 1. Further notched specimen (see Figure 2) made from the same material were used to investigate fracture mechanics. With the results from Table 2 the  $J$ -Integral, which is the areal integral of the load-displacement curve, the critical  $K_{Ic}$  could be calculated (Table 3) using a Youngs Modulus of 72 GPa and the expression  $K_{Ic} = (E * J)^{0.5}$ .

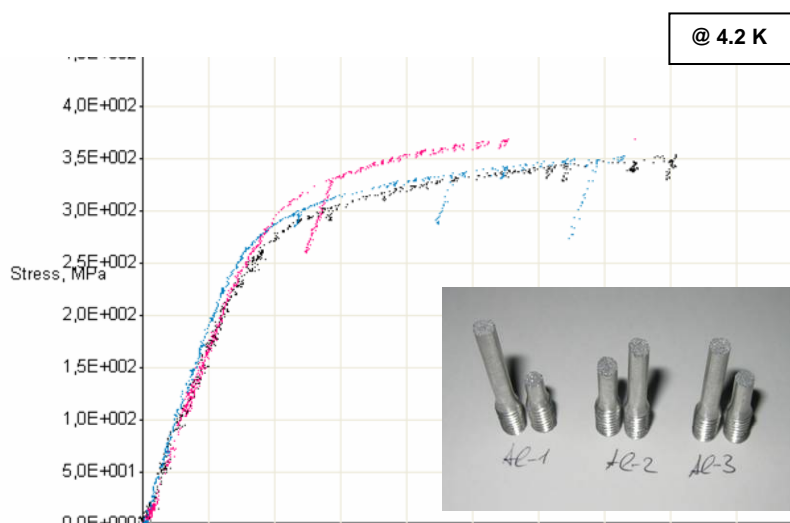


Fig. 1: Stress-strain curve and specimen after tensile testing at 4.2 K.

Table 1: Tensile properties of aluminium material at 4.2 K.

Specimen	T [K]	Young Modulus [GPa]	Yield Strength [MPa]	Ultimate Tensile Strength [MPa]	Uniform El. [%]	Total El. [%]
T-AI-1	4.2	69.6	293	353	2	2
T-AI-2	4.2	71	322	369	1.4	1.4
T-AI-3	4.2	76.3	296	352	1.8	1.8

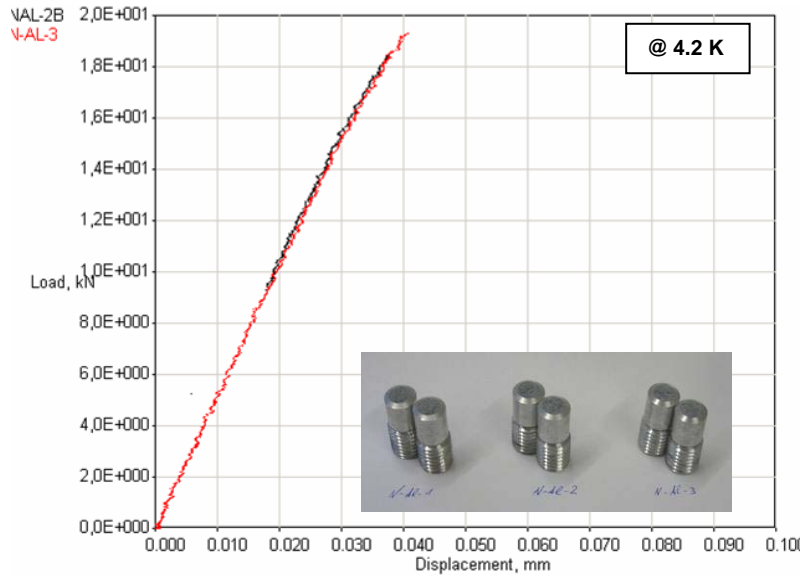


Fig. 2: Stress-strain curve and notched specimen after testing at 4.2 K.

Table 2: Results from notched aluminium specimen at 4.2 K.

Specimen	T [K]	Test section length, l [mm]	Major diameter, D [mm]	Notch diameter, d [mm]	Maximum load, P [kN]	Sharp notch strength, $\sigma_s$ [MPa]
N-AI-1	4.2	28	12.7	8.96	-*	-*
N-AI-2	4.2	28	12.7	8.96	18.47	293
N-AI-3	4.2	28	12.7	8.96	19.29	306

\* Due to a failure in machine control sample N-AI-1 was loaded and destroyed before the data acquisition started.

Table 3: Calculated critical J and K.

Specimen	T [K]	Critical J [N/mm]	Critical K [MPa m <sup>0.5</sup> ]
N-AI-1	4.2	-	-
N-AI-2	4.2	2,7	13,9
N-AI-3	4.2	2,5	13,4

Tensile test of welded Dipole Conduit (316LN AOD) 7 K

Several cable-in-conduit-conductor (CICC) types were considered for the European-Dipole. One conduit type was 316LN AOD (argon–oxygen decarburization). Here two welded samples provided by EFDA, the first sample with an OD 16,5 mm and ID 13 mm and a second sample having an OD of 17,7 mm and ID 14,3 mm.

To perform measurements flat tensile and JETT specimen were machined by EDM method. In Figure 3 the specimen are shown prepared for testing. Figure 4 gives the stress strain curve of the tested tensile specimen, while Table 4 lists the mechanical data obtained. Using the *J*-Integral method on the JETT specimen again the critical  $K_I$  can be obtained (Table 5) using a Youngs Modulus of 220 GPa.



Fig. 3: Welded Dipole conduit material, the obtained specimen made by EDM and installed in the test facility.

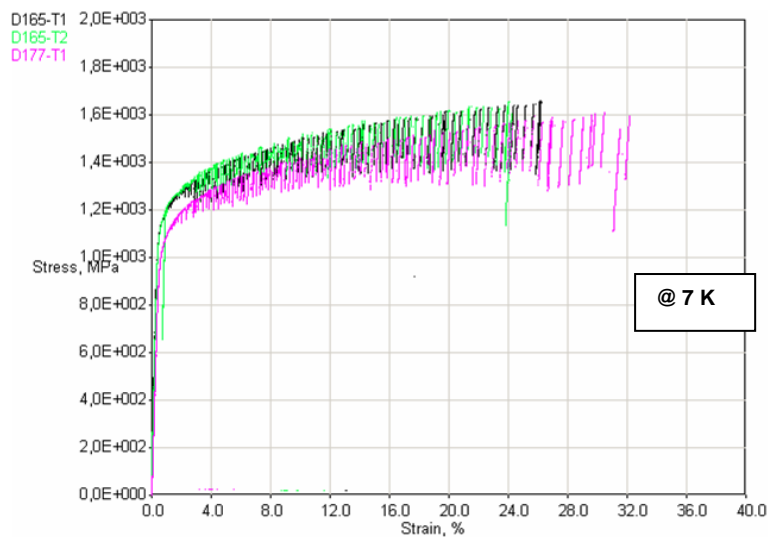


Fig. 4: Stress-strain curves as measured from welded Dipole conduit material at 7 K.

Table 4: Results under tensile load of welded Dipole Conduit.

Specimen	T [K]	Young Modulus [GPa]	Yield Strength [MPa]	Ultimate Tensile Strength [MPa]	Uniform El. [%]	Total El. [%]
D177-T1	7	218	1023	1609	30,5	32,2
D165-T1	7	235	1138	1659	26,1	26,2
D165-T2	7	224	1137	1653	24,1	24,2

Table 5: J-Integral Results obtained from JETT specimen.

Specimen	T [K]	Critical J [N/mm]	Critical K [MPa m <sup>0.5</sup> ]
D177-J1	7	196	208
D165-J1	7	183	200

### Mechanical Test of Solder Filled Dipole Conductor at 4.2 K

Another CICC type was a rectangular shaped conductor filled with solder to provide additional mechanical stabilization for the Nb<sub>3</sub>Sn strand inside. These results are basis for a computational modelling of the mechanical properties of the conductor done by EFDA. The geometry of the sample was 15.9 mm x 13.25 mm / A overall ~ 200.15 mm<sup>2</sup>. The used conduit material was 316LN with a thickness of about 1.65 mm / A ~ 86.25 mm<sup>2</sup>. The cable inside follows the pattern of (3x3)x4x4 strands with a diameter of ~0.815 mm. In Figure 5 the CICC is seen prepared for tensile testing. Figure 6 shows the stress strain curve giving a Youngs Modulus of 128 GPa and a yield strength of 282 MPa.

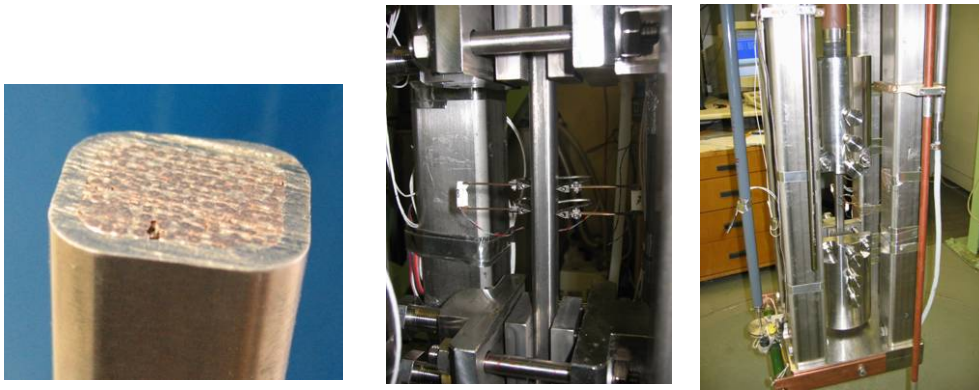


Fig. 5: CICC Dipole conduit filled with solder to be tensile tested at 4.2K.

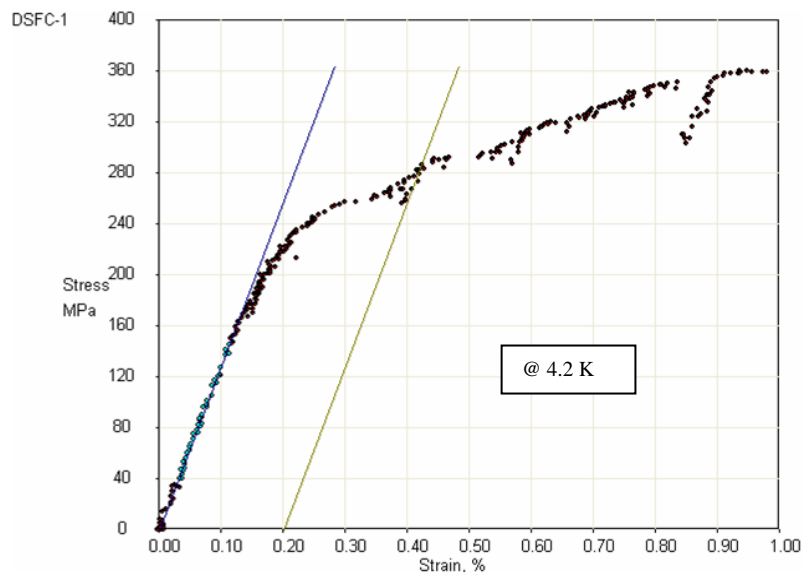


Fig. 6: Mechanical results for axial tensile test ( $A_{\text{overall}}$  used).

Beside the tensile test also compression tests were conducted with an applied load on the long and on the short side of the conductor. In Figure 7 the compression test with load applied on the long side of the CICC is shown resulting in a stiffness of about 657 kN/mm at 4.2 K. The short side test is displayed in Figure 8 giving a stiffness of approximately 393 kN/mm at 4.2 K.

To complete this testing program the solder material itself was also tested as shown in Figure 9. The tensile test results are given in Table 6. With this all material properties of the CICC is given (Nb<sub>3</sub>Sn from other tests) so far and can be used for modelling.

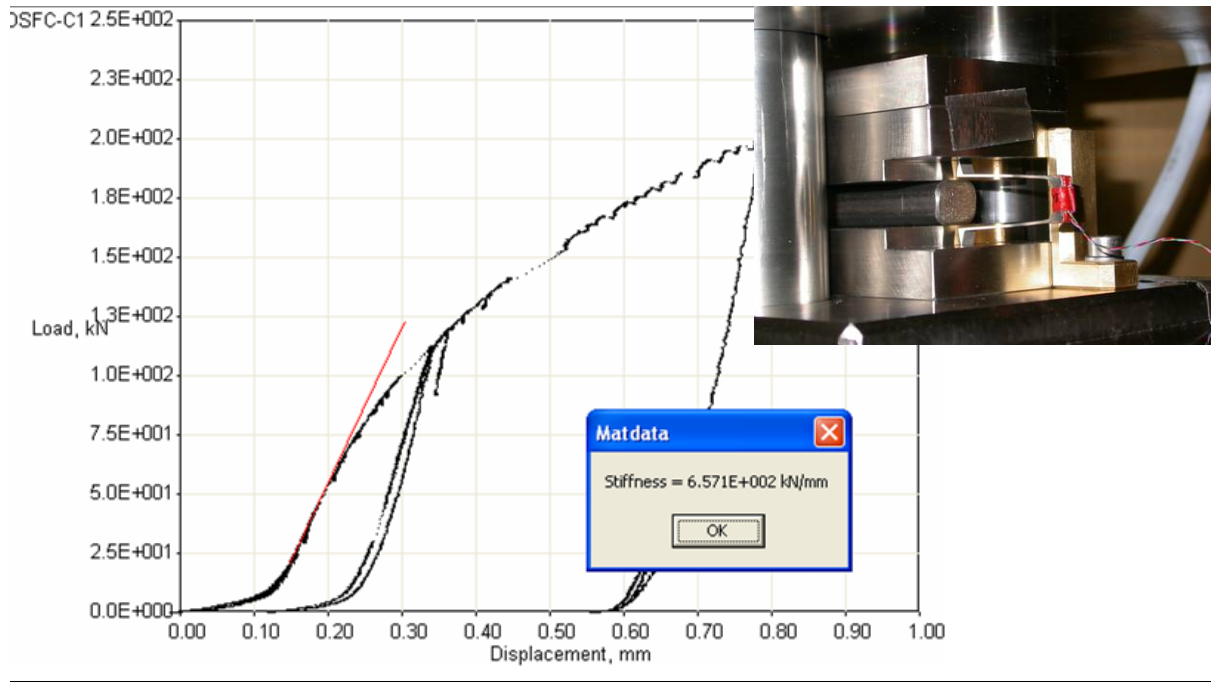


Fig. 7: Compression test with load applied on the long side of the CICC.

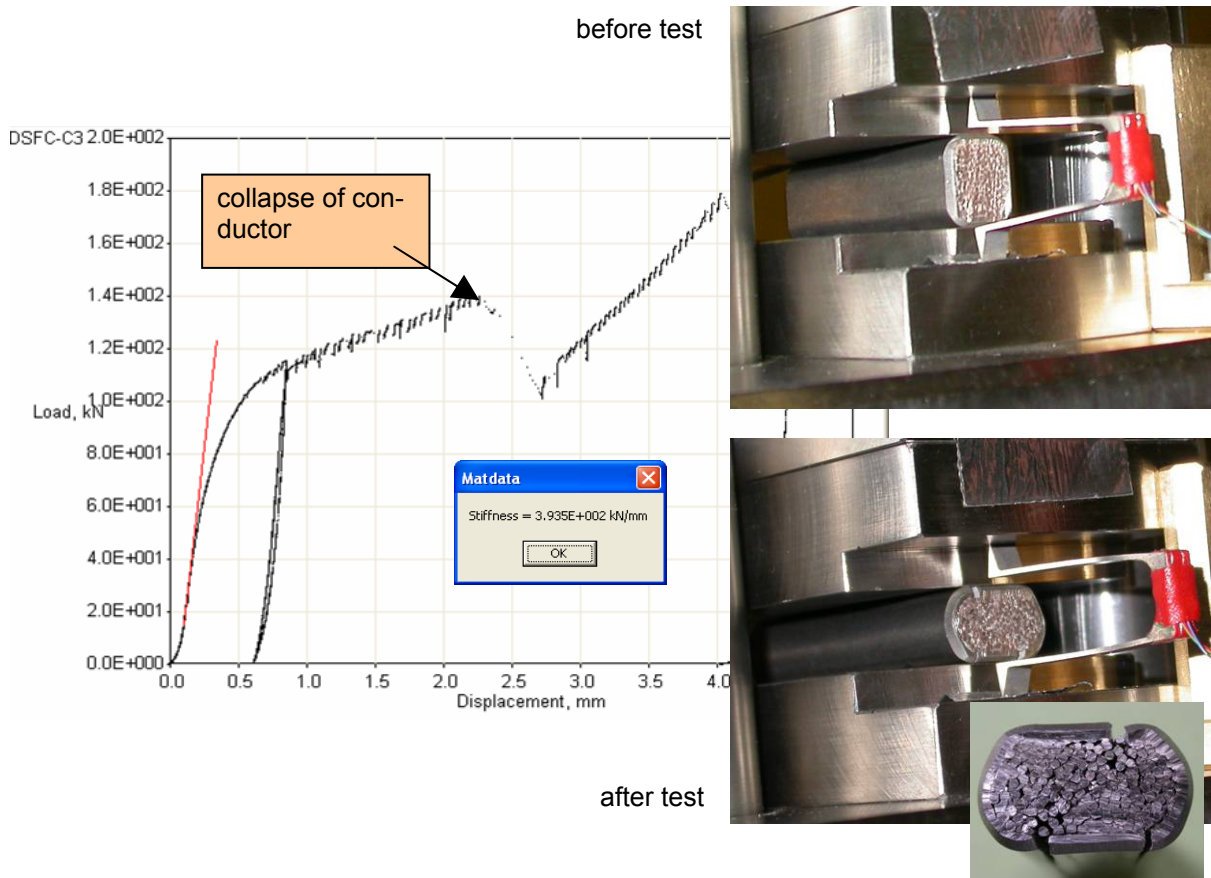


Fig. 8: Compression test with load applied on the short side of the CICC.

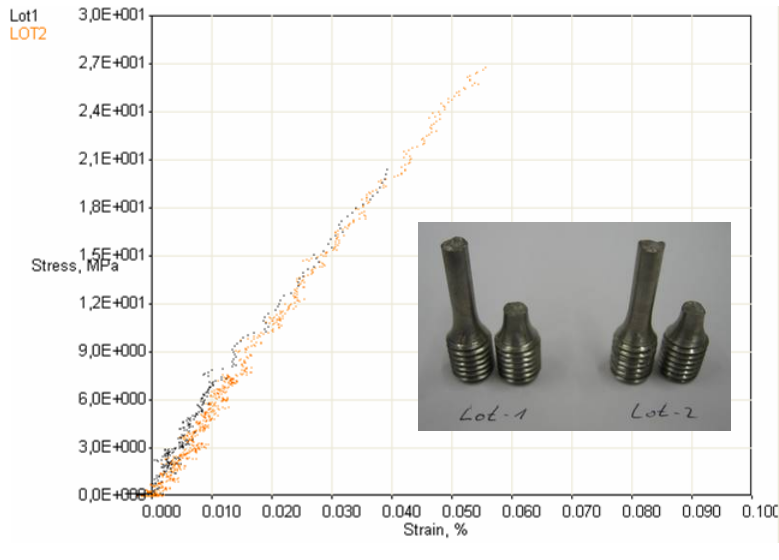


Fig. 9: Tensile test of solder material at 7 K.

Table 6: Tensile test results for solder material.

Specimen	T [K]	Young Modulus [GPa]	Ultimate Tensile Strength [MPa]	Total El. [%]
Lot-1	7	63,2	20,5	0,04
Lot-2	7	55,6	26,8	0,05

Tensile behaviour of soft magnetic iron material provided by Cern between 295 K and 7 K

Table 7 shows the determined mechanical properties of the provided ferritic material by CERN, Geneva. This material was selected as the main structure of the dipole magnet and is a so called low carbon ferritic steel. As obvious the total elongation at fracture of this material is around 0.5 % strain at 7 K, which indicates the brittleness of this material. The same material was tested also with respect to the fracture toughness in two orientations at 7 K. The determined values according to ASTM E 399 standard are  $\sim 30 \text{ MPa}\sqrt{\text{m}}$  at 7 K, which indicates its brittle characteristics. This behaviour must be assessed into design consideration using the fundamentals of fracture mechanics philosophy.

Table 7: Tensile properties of soft magnetic iron at different temperatures and at two different orientations.

Specimen	T [K]	Young's Modulus [GPa]	Yield Strength [MPa]	Ultimate Tensile strength [MPa]	Uniform El. [%]	Total El. [%]
Cernx-1	295	205	115	249	32	52
Cernx-2	7	200	-	723	0,5	0,5
Cernx-3	233	196	151	260	$\sim 25$	$\sim 50$
Cerny-1	295	200	123	282	26	44
Cerny-2	7	211	-	926	0,5	0,5
Cerny-3	90	210	642	653	5,9	20

Staff:

K.-P. Weiss  
H. Kiesel

Literature:

[1] Nuclear Fusion Programme, Annual Report of the Association Forschungszentrum Karlsruhe / EURATOM, FZKA 7291 / EUR 22705 ISSN 0947-8620, 55 (2007).

## **EFDA/06-1400 (TW6-TMSP-PFWDES2) Review of PF2-PF5 Winding Design (ITA 11-88)**

### **Objectives**

Since 2001, two manufacturing studies on the ITER PF coils 2 till 5 have been completed by EUPT, but there has been no overall review of the winding design itself. Several features of the present design for ITER PF are investigated by CRPP. ITP supports CRPP concerning the high voltage related issues.

### **Maximum electrical field stress and intermediate screen for turn insulation**

A special feature of the present PF coil design is the use of steel wraps embedded in the insulation layer that are intended to act as screens for the detection of impending shorts. Electrostatic field calculations were performed assuming a maximum terminal to terminal voltage of 25.7 kV and symmetrical grounding. Results for local internal overvoltages during transient excitation of the PF coil system are not available at this time. Hence a linear voltage distribution was assumed for the calculation. With these assumptions the electric field stress in the PF turn insulation stays well within the ITER design value of 3 kV / mm. Peak electric fields are higher in the design with metallic screen than in the one without screen.

It is unclear if the detection system for insulation failure – necessitating the metallic screen in the turn insulation, complex instrumentation and dedicated monitoring electronics – increases the overall reliability of the PF coils. The detection of small leakage currents which do not require double pancake bypassing has very little practical use. It seems much more likely that the complexity of the detection system for insulation failure risks introducing additional design weaknesses and manufacturing faults. In addition, a fault will be limited within a double pancake at least in PF 3 or 4. Hence it will be difficult to take the decision for a repair interval if a fault in the insulation is detected by the intermediate screen system.

It is therefore recommended by the PF coil winding design review group not to implement this system and to remove the metallic screen from the turn insulation. A strict insulation withstand test just before the sealing of a double pancake with epoxy resin is advisable.

### **Functionality of separation plates**

An other important feature is the implementation of separation plates between the double pancakes of the PF coils 3 and 4. These plates should protect a double pancake from damage from a short/arc in an adjacent one. The heat generated by an arc between turns and the subsequent ohmic heating during current decay in the jacket are substantial. Because heat conduction along the conductor is slow at high temperatures, it is essential that double pancakes are thermally well insulated from each other. The separation plates should thus be made of a material with high temperature resistance and low thermal conductivity.

### **Joint technique for PF coils**

It may be possible to re-arrange the joint locations between double pancakes to reduce the number of access ports and bypass cables and provide an option to bypass also the uppermost and lowermost double pancakes in a winding pack. A change would require a more in-depth design study. The PF winding design review group proposes a joint technology for the double-pancake joints similar to the one realised in TF Model Coil. A clean and practical joint insulation technique is available as well.

## **Conclusion**

The performed calculations deliver no electrical field stress above the ITER design criteria. A change of the ITER design is recommended because the intermediate screen should not be used. Further verification of the winding design is necessary as soon as data of the transient electrical behaviour of the PF coils are available.

### Staff:

S. Fink

## EFDA/06-1522 (TW6-TMSC-COILMO)

### Definition of Procedures for Coil Electrical Testing and Preparation for PF Transient Analysis

#### 1. Introduction

In the case of a quench, a fast discharge of the coils will be necessary to avoid damage of the coils. During such fast discharges high voltages can occur on the coils. Due to the large dimensions of the coils and the large number of turns in them, a low resonance frequency is expected, which causes non-linear voltage distributions inside the coils. To make sure that the different kinds of insulation can withstand the voltage stress, calculations on this topic were started in 2007.

The process of calculation consists of two main parts:

1. calculations with the finite element method programme (FEM) and
2. calculations with the network programme.

In the first step a model of the CS PF coils system will be built up in the FEM programme Maxwell. The programme will calculate the impedance and the capacitance matrix. In the next step a network model with lumped elements will be built up in the network programme. In the last step the voltage stress of each winding can be calculated and analysed in the network programme.

#### 2. Influence of the Cooling Tube on the Inductance of the PF Cable

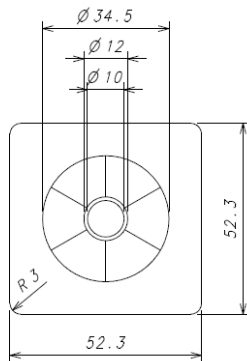


Fig. 1: Dimensions of the PF 3 coil conductor.

Before a model of the CS PF coil system could be initialized preparative calculations were made to see the influence of the particular parts of the cable (Fig. 1) on the inductance of it. To check the influence of the central hole for the inductance, a calculation model with 2 pairs of conductors was made. Each pair consists in one conductor shape with central hole and one without central hole (Fig. 2). One pair of conductors has a main radius of 80mm and the other pair has main radius of 350mm.

The results from these model calculations showed that the changes by introducing the central hole in the conductor are only in the range of approx. 2.3% over the whole frequency range.

As a consequence of these calculations it will be possible in further calculations of the CS PF coil system to replace models of the cables with cooling tubes by models without cooling tubes which will reduce the necessary calculation time. However, by such a replacement it should be taken into account that the inductance should be reduced by 2.3% because of the difference in the inductance between ring and circle conductors.

#### 3. Influence of the Stainless Steel Jacket on the Inductance of the CS Conductor at Different Frequencies

The CS and PF conductors are cable-in-conduit type conductors, with a stainless steel jacket. Fig. 2 shows the model of PF 3 cable with stainless steel jacket used for the calculation of skin or proximity effects in the cable (cable diameter 34.5 mm, square jacket 52.3 mm). The cable of the CS and PF coils consist of thin filaments (strands) with diameter of 0.83 mm. Additionally the filaments are transposed, thus there is no skin or proximity effect in the cable. For the stainless steel



Fig. 2: Model of one PF 3 conductor (red) including stainless steel jacket (blue) without central hole.

jacket skin and proximity effect has to be considered. Fig. 3 shows 2 D plots of the calculated current density and magnetic field strength at 1 Hz and 4 kHz.

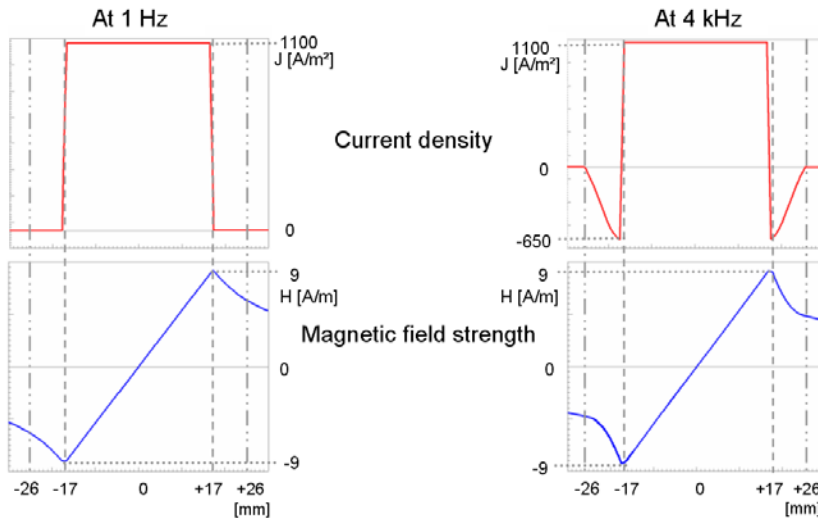


Fig. 3: Current density and magnetic field strength at 1 Hz and 4 kHz.

At 1 Hz the current density distribution is constant inside of the cable and 0 in the jacket. The magnetic field strength increases linear from the centre of the cable and decreases with  $1/r$  outside of the cable. At frequency of 4 kHz again the current density distribution inside of the cable is constant but induced current in the stainless steel jacket that flows in the opposite direction is visible. The induced current causes a stronger

reduction of the magnetic field strength outside of the cable in comparison with magnetic field strength at 1 Hz. This means that due to induced currents in the stainless steel jacket there is a reduction of the inductance of the whole conductor.

In the next step the self and mutual inductance between two conductors with stainless steel jacket was calculated at different frequencies. Fig. 4 shows the behaviour of the self and mutual inductance at different frequencies. The self inductance of cable 1 and cable 2 has the same value over the whole frequency range. Beyond 1 Hz there is a strong decrease of the self and mutual inductance until at frequencies higher than 100 Hz they come back to a constant value. This means that at frequencies higher than 100 Hz the coupling between two conductors with stainless steel jacket is very low and can be neglected.

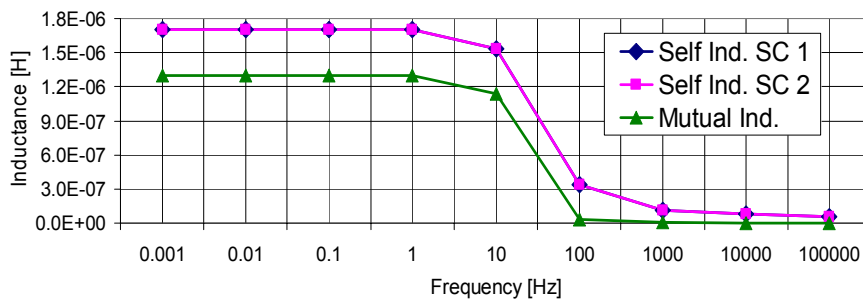


Fig. 4: Frequency dependence of the self and mutual inductance of a cable-in-conduit conductor.

In further calculations the coupling in the frequency range between 1 Hz and 100 Hz will be analysed in detail, especially the magnitude of the induced current on mutual conductor.

#### 4. High voltage calculations for ITER TF

The transient electrical behaviour of the ITER TF coil system was investigated for perfectly synchronised safety discharge and 2 special fault cases [1]. Jitter of the commutation process in the resistor paths and other effects are presently examined to complete a reliable basis for the determination of the maximum high voltage stress within the ITER TF system.

Staff:

A. Winkler

S. Fink

W. H. Fietz

Literature:

- [1] S. Fink, W. H. Fietz, A. M. Miri, X. Quan, A. Ulbricht; Study of the transient behaviour of the present ITER TF coil design for determination of the test voltages and procedures, FZKA 7053, Forschungszentrum Karlsruhe, 2004

## **TW5-TMSF-HTSMAG Scoping Study of HTS Fusion Magnets**

### **Objectives**

High temperature superconductors have successfully demonstrated their considerable advantages over conventional materials and entered the market. Therefore, an R&D programme was launched in Japan and EU in order to design and construct high temperature superconducting (HTS) components for ITER. As a result of this program a 60 kA HTS current lead was successfully manufactured and tested in Japan in 2002. The EU 70 kA ITER prototype current lead using HTS was tested in 2004 and 2005 in various cooling modes. The introduction of HTS current leads between the NbTi bus bar and the resistive heat exchanger significantly reduces the heat load at the 4.5 K level, thereby considerable saving costs of the cryogenic system.

After the Forschungszentrum Karlsruhe and CRPP have shown with the 70 kA HTS current lead that high temperature superconducting materials can be used for ITER, these materials should be introduced in other components, primarily in fusion magnets. First a scoping study of HTS fusion magnets shall be performed to check the benefits of using high temperature superconducting materials in fusion magnets including the identification of potential problems.

In collaboration with other associations the Forschungszentrum Karlsruhe assesses different operating scenarios which are:

3. "High field option": Operating temperature at 5 K and high toroidal magnetic fields in the range of 15 to 20 T. In this case a comparison LTS vs. HTS shall be included.
4. "Intermediate temperature": Operating temperatures in the range of 20 to 30 K and ITER-like magnetic fields, i.e., 10 to 15 T.
5. "High temperature": Operating temperatures in the range of 65 K and ITER-like magnetic fields, i.e., 10 to 15 T.

In collaboration with the other associations the work is divided in manageable parts for each association. The work performed at the Forschungszentrum Karlsruhe focuses on the third operating scenario, i.e., the high temperature option.

### **Main results of the investigations for a HTS Fusion Conductor**

Considering the material properties, there are a lot of data available in literature but with a large spread depending on the specific wire preparation. So a careful characterization of the material with respect to superconducting, electrical, thermal, mechanical and AC loss properties is absolutely necessary. This was done in the frame of the EFDA task HTSPER.

A layout of at least a 20 kA class conductor is necessary for a DEMO type fusion reactor otherwise the coil performance may not be fulfilled. This is a big challenge for a conductor with the present current densities of existing HTS tapes @ 50 K. An increase of the critical current density by a factor of 10 would be helpful because then an operation temperature of 65 K could be used.

The operation current of a conductor made of YBCO<sub>CC</sub> is limited by number of tapes which can be used for cabling. There are a lot of innovative ideas discussed in the community how to come to a low AC loss high current conductor.

A first analysis of hot spot temperature and AC losses was performed but of course detailed investigations of hot spot as well as detailed quench analyses have to be done for the final

conductor and coil layout. Due to the high current density in the YBCO layer, the copper stabilizer needs to be large to count for hot spot. For this a good contact to the superconductor is required, therefore current transfer and current distribution are issues.

Quench propagation is a critical issue and the mechanism present in YBCO\_CC is up to now not really understood. More investigations (modeling and experimental) are required and novel quench protection techniques may be needed in superconductors made of YBCO\_CC. A stability analysis should be done to confirm that this will be not a problem.

Since the AC losses seem to be the challenging design issue (e.g. plasma disruption and plasma formation), a detailed analysis of the magnetic field changes during a plasma cycle has to be performed. In contradiction to ITER, the transverse field changes have to be split up in the components parallel and perpendicular to the ab-plane of the YBCO coated conductor because the losses are quite different. A very rough estimate has been done but all this has to be demonstrated by AC loss experiments relevant for DEMO.

Related to AC losses is the cooling issue because the deposited power has to be removed from the conductor. It has to be clarified if indirect cooling is possible or direct cooling can be used.

To solve manufacturing issues with respect to structure reinforcement, react&wind technology may be used because of the very high temperature required during heat treatment of the HTS wires.

Due to the limited refrigerator power saving for the magnet system, other reduction options are to be considered, for example the drop of the radiation shield.

The design of a high current fusion cable is directly coupled to progresses in the available critical current density. However, even if industry will be able to deliver improved HTS material, the optimization with respect to AC losses, quench propagation, and electrical stabilization is extremely challenging. Therefore basic research is necessary which is directly focused on the development of such a high current fusion cable. Only with additional ideas and progresses a high current HTS fusion cable can be realized that gives the performance of today's existing LTS fusion cables at a temperature level well beyond 50 K.

Staff:

W.H. Fietz  
R. Heller

## **Breeding Blanket**



## **TW5-TTB-001**

### **Construction of the High Pressure Helium Loop (HELOKA-HP/TBM) for Testing of TBMs**

The objective of this task is to construct the HELOKA-HP/TBM loop as presented and agreed in the "EFDA HELOKA Assessment Report" in a renovated building of FZK comprising the purchase of loop components and supply systems, acceptance tests at the manufacturer's site, installation, commissioning and acceptance tests.

#### **Status at the beginning of the reviewed period**

After identifying a proper experimental hall for HELOKA-HP (June 2005) the already existing auxiliary systems have been analysed and tested. Based on the results of these tests it has been decided to upgrade the control of the water cooling system to meet HELOKA requirements. This upgrade was included in the Stage 1 of the HELOKA Data Acquisition and Control System (DACS) together with the control and monitoring of the existing power supply system.

In parallel with these activities, the official construction authorisation for the supporting structure of the HELOKA facility was obtained in May 2006 and a contract to manufacture it has been awarded.

Concerning the fabrication of the main components, the Helium-Helium heat exchanger has been manufactured and the on-shop tests have been performed.

#### **Establishment of infrastructures**

The contract for the Stage 1 of the DACS was awarded to Siemens by the end of 2006. The contract negotiation, which began in January 2007, comprised also the phase of the detailed design. The final design document, namely version 4.1 of the "Technical Specification for DACS for the HELOKA General Services Subsystem", which is part of the Siemens contract, was issued in April 2007. The contract with Siemens was signed in May 2007.

A major design modification was considered necessary, namely the introduction of a large bypass in addition to the small "Dummy Load" bypass foreseen for load simulation during the DACS Stage 1 commissioning. This bypass is going to be used for the hydrodynamic commissioning of the loop and, also, for the future operation of the water cooling system with multiple consumers (thermal loads). The document comprising the design of the main bypass and a few other minor changes, namely "DACS Stage 1 design review", was issued in June 2007.

During the contract development, the following components were selected and ordered: the control valves for the main bypass and the DL bypass (FLOWSERVE), the Water Management System (NALCO), the thyristor unit for the DL heater (AEG), the flow meters (MECON).

Both the Water Cooling System (WCS) hall and the control room were prepared by dismantling the old motors and old cabinets and construction and mounting of a frame for the new cabinets.

In the first half of 2007 the supporting structure for HELOKA was manufactured and delivered to the experimental hall. In order to facilitate the construction of the loop, only the main frame of the structure has been assembled. The minor structure elements are going to be installed as the construction of the loop requires.

## **Fabrication of main components**

The procurement of the main components for HELOKA was started within 2006 and is presently in various stages of completion, as follows:

### 1. Helium-Helium heat exchanger (economizer):

- the unit has been delivered at FZK on 22<sup>nd</sup> of January 2007;
- on 16<sup>th</sup> of February the acceptance tests have been performed; the leakage of the unit has been measured and was found to be better than 10e-6 mbar.l/s;

### 2. Helium-water heat exchanger (cooler):

- The component has been ordered on 6<sup>th</sup> of March 2007 from Wilhelm Deller GmbH;
- The unit is a classical tube-and-shell heat exchanger with helium flowing in the tubes and water on the shell side;
- The manufacturing process is presently finished and the unit is prepared for the pressure test in the factory. This pressure test is going to be performed with air for the tubes (Helium) side and water for the shell side.
- The delivery of the cooler is scheduled for the week 50 (2007).
- Following the delivery the leak test is going to be performed as part of the acceptance procedure. This test is scheduled for January 2008.

### 3. Helium heater:

- The manufacturing of this component has been assigned to Klöpper-Therm GmbH (contract signed on 10<sup>th</sup> of October 2007);
- The unit is presently in design phase; the delivery is scheduled for July 2008 (week 30).

### 4. Pipes for HELOKA: the tendering procedure for buying the pipes for HELOKA has been closed on 5<sup>th</sup> of October 2007 and the contract should be awarded by the end of this year;

### 5. Valves for HELOKA: the technical specifications for the control and isolation valves to be installed in HELOKA have been finalized on 30<sup>th</sup> of October 2007; the tendering action has been effectively started on 26<sup>th</sup> of November and is going to be closed on 17<sup>th</sup> of December 2007.

### 6. Dust filter for HELOKA: the technical specifications are finalized;

### 7. Vacuum system: the technical specifications have been done and a tendering action has been launched in September 2007;

### 8. Data Acquisition and Control System (DACS) stage 1:

- For the DACS stage 1 contract has been awarded;
- Implementation of the design phase finalized by version 4.1 of the "Technical Specification (April 2007), which is part of the Siemens contract
- Order for the Siemens contract (May 2007)
- Enlarging the purpose of the DACS Stage 1 by introducing the Bypass finalized through "DACS Stage 1 design review" (June 2007)
- Analysis of the Design Report submitted by Siemens for DACS Stage 1 (November-December 2007)

9. DACS stage 2: the technical specifications are going to be finalized by the end of the year.

Staff:

T. Ili  
B. Ghidersa  
V. Marchese  
G. Messemer  
A. Jianu  
E. Magnani  
A. Brecht  
N. Prothmann

**EFDA/06-1393 (TW6-TTB-RFMON1)**  
**Technical Monitoring Assessment of the EU/RF Collaborative Task on the Development of Diagnostic Systems for Electromagnetic TBMs**

Scope of this task is to support the EU/RF collaborative task on "Development of diagnostic systems for HCPB and HCLL EM-TBMs" (TASK 1 - EFDA/05-994 contract with EFREMOV). In particular, to prepare and check all input technical data necessary for the performing of the task, to perform the technical monitoring and to assess the technical reports.

The following topics are included in the collaboration and will be summarized in dedicated reports:

Report part 1: Development and conceptual design of EMMS

Report part 2: Development and conceptual design of MMS

Report part 3: EM-analysis of HCPB-TBM

Report part 4: Stress analysis of HCPB-TBM

Report part 5: EM-analysis of HCLL-TBM

Report part 6: Stress analysis of HCLL-TBM

During the kick-off phase of the task in 2006 the technical specifications for the HCPB- and the HCLL TBM (designed by CEA) were collected by FZK and issued to Efremov in the frame of deliverable stage I. In addition to the technical specifications this report also includes the minutes of the kick-off meetings.

In March 2007 the intermediate meeting took place at Efremov institute (St. Petersburg) and the first results on the task were presented by Efremov. The draft version of deliverable stage II (Technical monitoring and assessment of the EU/RF collaborative task) was issued by FZK in July 2007. The final meeting took place at Barcelona in November 2007 where the final draft reports on the task were presented by Efremov.

The results were discussed and possible fields for future collaboration were pointed out (detailed discussion will follow in January 2008).

Staff:

H. Neuberger

R. Roccella

## **EFDA/06-1394 (TW6-TTB-RFMON2)**

# **Technical Monitoring and Assessment of the EU/RF Collaborative Task on the Fabrication of Beryllium Pebbles for Fusion Application and Beryllium Recycling**

## **1. Introduction**

Within the frame of the EFDA/05-994 contract with EFREMOV Institute (Saint Petersburg, Russian Federation), technical monitoring and assessment of the EU/RF collaborative Task on "Fabrication of Beryllium pebbles for fusion application and Beryllium recycling" was performed. The objective of this activity is the exploration of the possibilities to identify the properties of Be pebbles defined as a base material for application in Solid Breeder Blanket. The different aspects of the fabrication and utilization of Be pebbles with different morphology should be investigated. The implementation of this task will enable to qualify initial beryllium materials for further application in Solid Breeder Blanket. In addition, the particular features of beryllium recycling after operation will be considered and analyzed.

## **2. Scope of the work**

FZK compiled needed input technical information, which may be defined as necessary for the realization of the collaborative Task, transmitted this information to EFREMOV Institute and provided sufficient explanation. Also FZK is responsible for the technical supervision and assessment of this Task.

EFREMOV Institute is responsible for the following activities:

- Fabrication of three batches of pebbles with different average grain sizes (10-30; 30-60; >100  $\mu\text{m}$ ) in amount of 200  $\text{cm}^3$  each.
- Characterisation of produced three batches of pebbles (optical and scanning microscopy, microstructure analysis, chemical analysis, packing density measurements).
- Experimental modelling of pebble bed with produced Be pebbles will be performed. The model pebble bed will have approximate diameter of 10 mm and height of 100 mm.
- The specialized facility with Be analyser of flowing gas through pebble bed will be adjusted for the experiments on the influence of temperature (up to 500  $^{\circ}\text{C}$ ) and vibration on the model pebble beds. The content of Be in the flowing inert gas will be determined.
- Preparation of the analytical review on the beryllium recycling.

## **3. Technical monitoring and assessment in the Year 2007**

### **3.1 Meetings**

#### *3.1.1 Kick-off Meeting at FZK*

In the frame of the Contract, a Kick-off meeting has been organized on February 15, 2007 at FZK with attendees from Russian Federation, EFDA and FZK. Subject of the Kick-off meeting was the start of the collaborative tasks on "fabrication of Be pebbles for fusion application and Be recycling". The following objectives have been discussed during the Kick-off meeting:

- Scope of Work,
- Work plan,
- Deliverables,
- Time schedule,
- Organizational matters.

The technical tasks of the collaboration have been discussed in detail and they were agreed upon the kick-off meeting.

One should also note that, within the Russian Federation, the EFREMOV subcontractor is the Bochvar Institute which has long-term and in-depth experience in R&D of Beryllium products. Also the status of Be R&D program in EU, FZK and Bochvar Institute were discussed.

Participants of the Kick-off meeting:

A. Möslang (chairman)	FZK Karlsruhe, Germany
M. Zmitko	EFDA Garching, Germany
P. Kurinskiy	FZK Karlsruhe, Germany
I. Kupriyanov	Bochvar Institute, Russian Federation

### 3.1.2 Progress Meeting at Bochvar Institute

The next meeting was held on November 28, 2007 at Bochvar Institute (Moscow, Russian Federation) with attendees from Russian Federation, EFDA and FZK. The main objective of this meeting was the monitoring of the current status of fabrication and characterisation of beryllium pebbles.

Participants of the progress meeting:

V. Pantsyrny (chairman)	Bochvar Institute, Russian Federation
M. Zmitko	EFDA Garching, Germany
P. Kurinskiy	FZK Karlsruhe, Germany
I. Kupriyanov	Bochvar Institute, Russian Federation

## 3.2 Deliverables

### 3.2.1 Kick-off Report

The kick-off report on Task TW6-TTB-RFMON2 issued in April, 2007 contains, besides the agenda and the minutes of the meeting, a copy of presentations and a draft version of the "end user liabilities" [1].

### 3.2.2 Intermediate report from Bochvar Institute (Deliverable 1)

In the frame of the Task, the technical report "Analysis of Capabilities and Features of Beryllium Reprocessing/Recycling after Neutron Irradiation" containing a comprehensive analytical review on the beryllium recycling has been sent from Bochvar Institute [2].

## 4. Current Status of the Works on TW6-TTB-RFMON2 Task

According to information obtained on Progress Meeting at Bochvar Institute, the fabrication of Be pebbles is still in the process.

Fabrication of Be pebbles is based on the ball milling of Be billets or ingots having three different grain sizes (10-30, 30-60, >100  $\mu\text{m}$ , according to the Task requirements). This operation is followed, consequently, by the sieving (+0,8 -1,2 mm) and cleaning of Be pebbles.

Fabrication of Be pebbles with the average grain size more than 100  $\mu\text{m}$  is already finished (Fig. 1). One should also note that chemical composition, size distribution and maximum/minimum dimensions of these pebbles have been already evaluated. Some analysis of microstructure of Be pebbles was performed as well.

Fabrication of Be pebbles with two other grains sizes (30-60 and >100  $\mu\text{m}$ ) is in the process and expected to be completed in the beginning of Year 2008.



Fig. 1: Be pebbles having average grain size >100  $\mu\text{m}$ .

In the frame of the Task, experimental modelling of pebble bed with produced Be pebbles has to be performed at Bochvar Institute. The content of Be in the flowing inert gas through pebble bed has to be determined by the special analyser. This work has been started at Bochvar Institute but some adjustment of conditions of experimental modelling concerning:

- temperature,
- frequency of vibration of the model pebble beds

is still required.

## 5. Forecast Progress for the next months

Following actions has to be performed in FZK:

- To determine whether uranium content in Be pebbles has to be evaluated;
- Adjustment of the parameters of the experimental modelling of Be pebble beds;
- To clarify the requirements to the transport container for Be pebbles;
- Preparation of the documentation needed to provide the transport of Be pebbles from Russian Federation to Germany (e.g., Material Safety Data Sheet).

### Staff:

A. Möslang  
P. Kurinskiy

Literature:

- [1] A. Möslang "Technical Monitoring and Assessment of the EU/RF Collaboration on Fabrication of Be pebbles for Fusion Application and Be Recycling", Kick-off report on Task TW6-TTB-RFMON2;
- [2] I.B. Kupriyanov, A.A. Borisov, N.M. Meshcheryakov, G.N. Nikolayev, I.V. Mukhin, O.A. Ustinov, V.I. Pant-syrny "Analysis of Capabilities and Features of Beryllium Reprocessing/Recycling after Neutron Irradiation", Report on EFDA Contract No. 05/994, Agreement No.460/400--59-2006.

# **Breeding Blanket HCPB Blanket Concept**



## TTBB-001 Helium Cooled: TBM Design, Integration and Analysis

### TW5-TTBB-001 D 2 Detailed Design of Sub-components and Prototypical Mock-ups for the HCPB TBM Qualification

#### a) Design report for GRICAMAN mock-ups

The objective of this task is to contribute to the out-of-pile testing of Helium-Cooled-Pebble-Bed Test Blanket Module (hereafter TBM). The envisaged activity focuses on out-of-pile testing of a look-alike mock-up of the TBM manifold system, in particular to the optimization of the coolant flow. The Gricaman flow domain involves the upper toroidal-poloidal half of TBM bound at the outlets of FW channels, at the outlets of by-pass pipes and at the inlets of BU's. As working fluid air at absolute pressure of 3bar and ambient temperature will be used in the experiment. The Gricaman facility is designed keeping real geometry of manifold 2 and manifold 3 and replacing complicated grid and cap cooling channels with simple pipes having the same flow resistance as the real channels. The flow distribution in manifold 2 will be determined measuring flow rates through each equivalent grid/cap channel. The measurements will be done by flow meters with floating body. For experimental determination of the flow distribution in manifold 3 the flow rate will be measured in each equivalent BU pipe using flow meters operating on calorimetric basis. A number of pressure measurements are foreseen along manifold 2 in order to provide data for experimental verification of numerically found strong pressure gradients. Pressure measurements in manifold 3 are also foreseen in order to determine pressure distribution at inlets of BU pipes. The flow resistance as well as internal flow distribution within both vertical and horizontal stiffening grids will be investigated in Gricaman pre-experiments. The cap channels will be experimentally investigated after Gricaman tests are completed because the geometry of these channels will probably have to be redefined in order to reach required flow distribution in manifold 2. A draft version of the report has been prepared and sent to EFDA in August 2007. The Figures 1 - 4 are taken from the report.

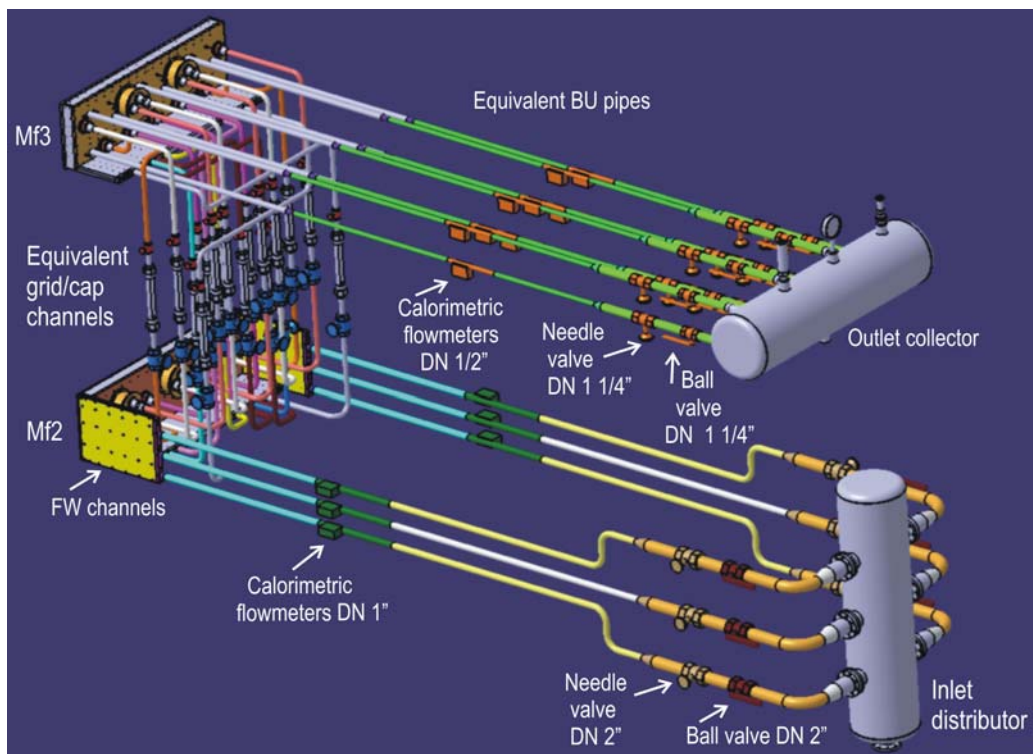


Fig. 1: Design of Gricaman experimental facility

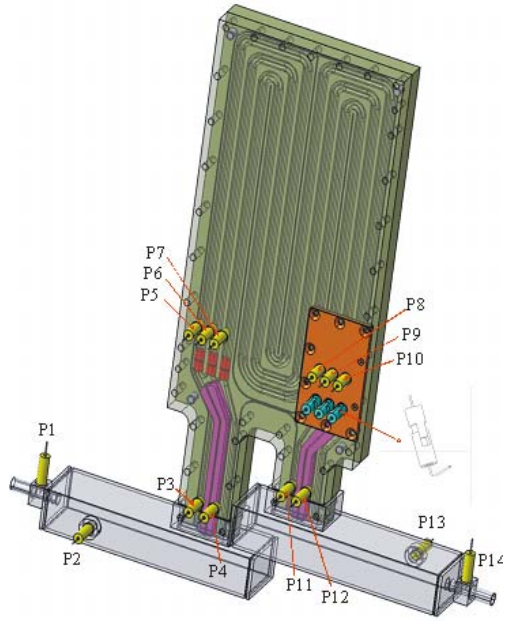


Fig. 2: Mock up for investigation of fluid flow in cooling channels of horizontal stiffening grid.

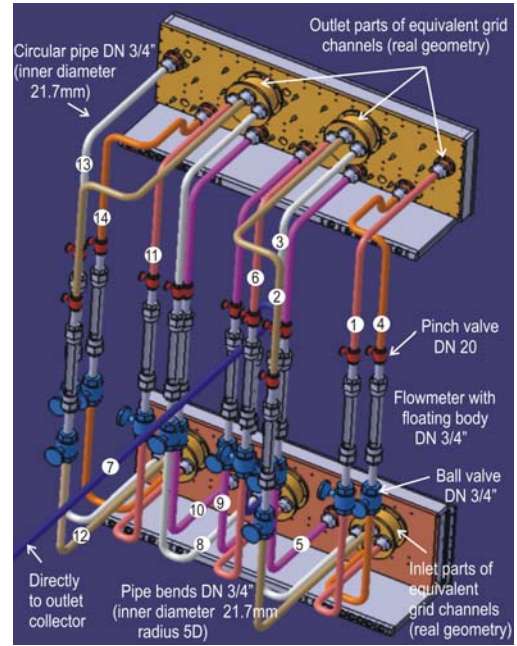


Fig. 3: Design of equivalent grid channels in Gricaman facility.

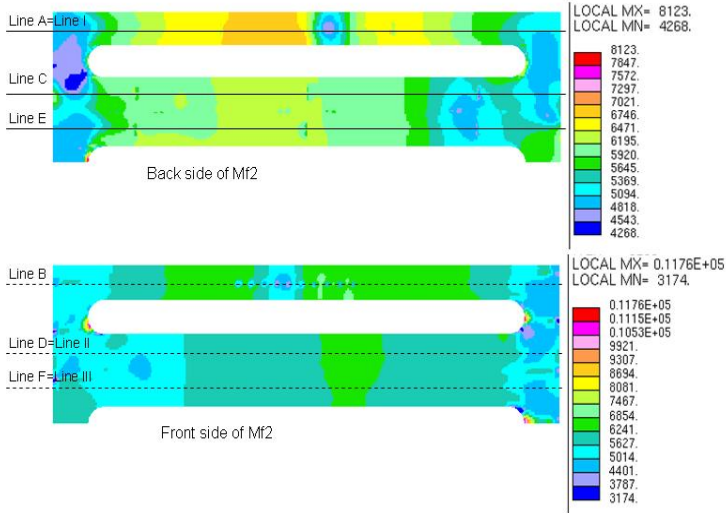
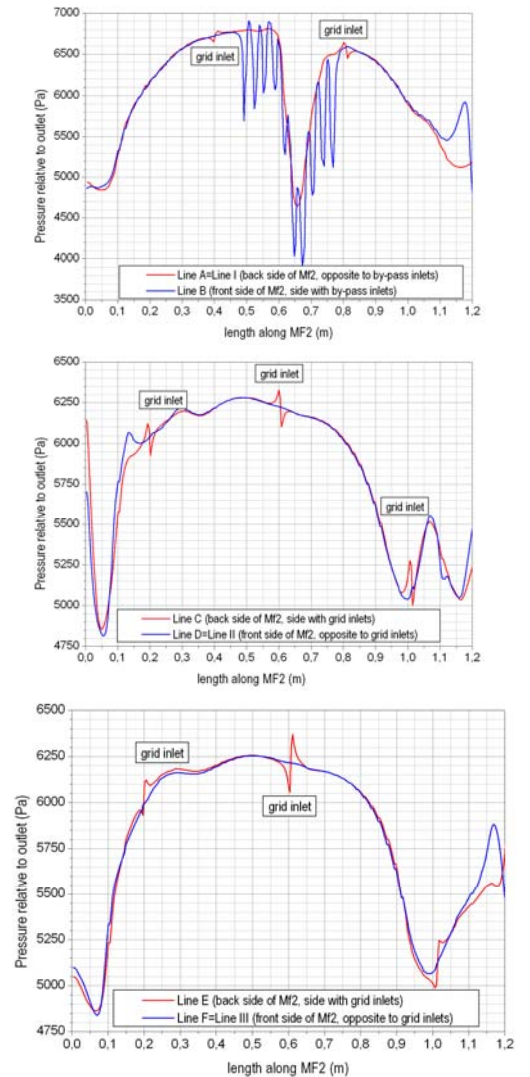


Fig. 4: Computed pressure profiles used for definition of pressure measuring positions in manifold 2. Pressure taps are positioned along line A, Line D and Line F.



Staff:

M. Ilic

**b) Design report for HETRA mock-up**

The design of the first wall (FW) of the TBM is important for the safe operation of TBM because the first wall is one of the most loaded components of the TBM. The maximal heat load is  $500\text{kW/m}^2$  and the nominal heat flux is  $270\text{kW/m}^2$  during the operation in ITER. Structural material of the FW is the Reduced Activation ferritic-martensitic steel EUROFER. The preliminary computations show, that the temperatures are close to the limits allowed for the structural material ( $\sim 550^\circ\text{C}$ ). In order to prove the validity of numerical computations, the HETRA experimental facility is designed for the investigation of the temperatures and the heat transfer coefficients in the first wall. A revised draft version of the report has been sent to EFDA in July 2007. The Figures 5 - 8 are taken from the dedicated report.

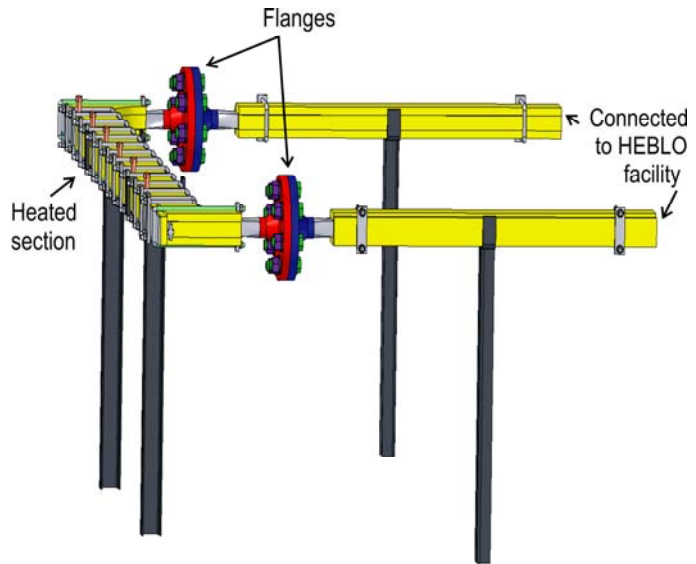


Fig. 5: Design of HETRA experimental facility.

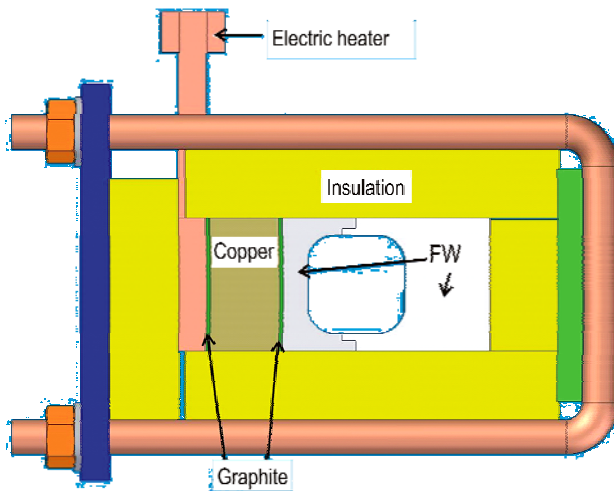


Fig. 6: Arrangement of heated test section.

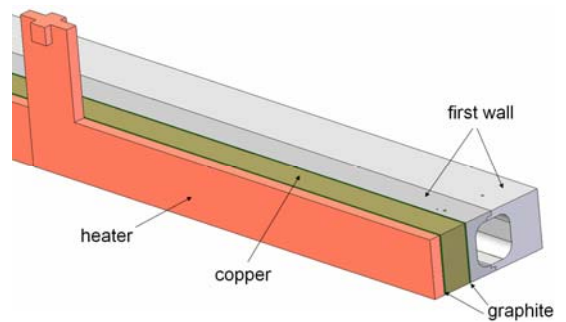


Fig. 7: Arrangement of electrical heaters which provides uniform heat flux at heated channel wall.

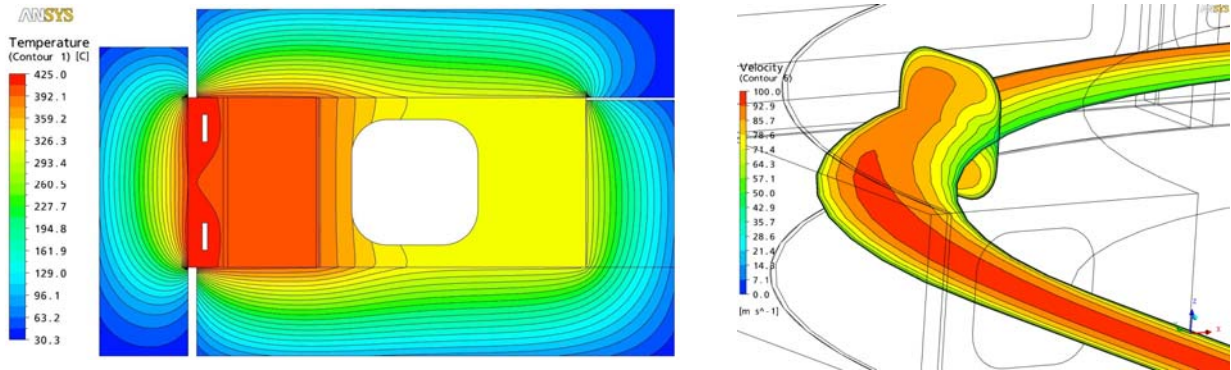


Fig. 8: Preliminary computational results for temperature distribution in cross-section of heated section (left) and velocity distribution in channel (right).

The current status of HETRA is as follows (status 07/2007):

- The first wall channel has been ordered in FZK. The material (Eurofer 97) under investigation from the point of view of welding and manufacturing possibilities. The test welding is done, the welding probe are under metallurgical analysis.
- Call for final offers from Bach Resistor Ceramics GmbH (heaters), Microtherm (insulation), SGL Technologies GmbH (graphite). Delivery time of the components is about 1 month.
- Preliminary CFD calculations of heat transfer in HETRA test section are done and on that basis temperature measuring positions are defined.

Staff:

M. Ilic  
G. Messemer  
B. Kiss (KFKI, Hungary)

## TW5-TTBB-001 D 8 Detailed HCPB TBM Development Work Plan and First Technical Specification Document

### Objective

The objective of this task is to contribute together with the EFDA management to the preparation of the task breakdown, the work plan and the technical specification document for the HCPB TBM. The work plan should define the milestones that are foreseen in the next years, identify all tasks that are necessary to achieve them and define the dependencies among the different tasks and milestones. In addition to the TBM development, the plan will consider the development of the necessary ancillary systems (helium coolant, tritium extraction, coolant purification), and the related measurement systems (e.g. Neutronic and Tritium) and diagnostic.

### Results in 2007

In Table 1, the main R&D activities necessary for the realisation of the HCPB blanket are summarised. The different activities have been classified according to the specificity for this blanket concept: in red we find R&D that are related to the materials, technology and processes that are related only to the solid breeder blanket, in green R&D with potential synergism with other blanket concepts and in blue R&D that can be shared almost completely with other blanket concepts.

Table 1: R&D for the development of the solid breeder blanket and its tests in ITER.

Task	Title:	Short description:
1	Ceramic Breeder Development	Production and characterisation of ceramics for DEMO/FPP and TBM
2	Beryllium as Neutron Multiplier Development	Production and characterisation of Beryllium for DEMO/FPP and TBM
3	Thermo-mechanics of the Pebble Bed (temperature control in pebble beds).	Modelling tools development for design calculations
4	Tritium extraction and recovery in the purge flow	Design of the purge flow loop for DEMO/FPP and test in ITER
5	Be/steam, Be/air reaction in safety analyses	Production on data on Be-steam, Be-air reaction and modelling
6	Neutronic performances (tritium breeding ratio)	Neutronic design and design calculations for blankets and tests in ITER
7	Tritium control: coolant purification & permeation barriers.	Control of T in the coolant loop. Permeation study and development of permeation barriers, design of the purification systems for the coolant
8	Tritium inventory in materials (i.e. T retention in Be)	Tritium retention in Be
9	Diagnostics	Development of diagnostic systems and sensors
10	Steel development and Fabrication technologies	EUROFER development and fabrication technologies for plates.
11	Helium cooling technology for fusion reactors	Enhancement of cooling performances and development of Helium cooling systems
12	Reactor Integration	For DEMO/FPP and ITER

For each of these groups of activities, a detailed R&D programme has been provided, differentiating activities necessary for the test in ITER (with high priority in the development programme) and long term activities for the development of the DEMO Blanket.

### **Status of the work**

Starting from this analysis a Work Breakdown Structure for the Project has been derived. The technical specification document will be completed in 2008.

#### Staff:

L.V. Boccaccini

## TW5-TTBB-001 D 10

# Manufacturing and Testing of a FW Channel Mock-up for Experimental Investigation of Heat Transfer with He at 80 bars and Reference Cooling Conditions. Comparison with Numerical Modeling

## 1. Introduction

The thermo-hydraulic design of the first wall with helium cooling is a critical issue for the fusion blanket and also for the test in ITER. Requirements for its design are: U shape with geometrically similar cooling channels in toroidal-radial plane; EUROFER as material with maximum allowable temperature of 823K; heat flux on plasma facing side of  $270\text{kW/m}^2$  in nominal regime that in an excess case can reach  $500\text{kW/m}^2$  on  $\sim 20\%$  of plasma facing surface; heat flux of 60 and  $35\text{ kW/m}^2$  from breeding units in the middle and side parts, respectively, and helium with inlet pressure of 8MPa and inlet temperature of 573K as the coolant. Under these conditions the design margins are narrow and a good confidence in the results of the computational tools used in the design is requested. In the relation to this HETRA (HEat TRAnsfer) experiment has been proposed in the framework of development activities for the first wall cooling.

The HETRA experiment has been motivated by corresponding three-dimensional (3D) numerical analyses which revealed significant effects of the asymmetrical heat loads on the cooling of the first wall. These analyses have shown that the heat transfer coefficient in the first wall is  $\sim 15\%$  lower than predicted by one-dimensional heat transfer evaluations based on Dittus-Boelter-like correlations and that satisfactory cooling of the first wall can be achieved only with hydraulically rough channels. Additionally, due to strong temperature gradients in the cross-section of the first wall, the procedure for heat transfer evaluations applied in codes for stress analyses had to be modified in order to obtain reliable predictions of thermal stresses. The verification of the methods developed will be done on the basis of the results of the HETRA experimental campaign. A single first wall channel will be tested in a Helium cycle at 8MPa, while the surface heat load will be represented by a set of electrical heaters. The goal of the experiment is to verify results of 3D computational analysis through: (i) detailed temperature measurements in the structure of the first wall and (ii) measurements of pressure losses in the first wall channel.

## 2. Design of HETRA experimental facility

The main components of HETRA experimental facility are presented in Figure 1. The facility involves only one U sweep of the first wall channel with belonging steel structure because the corresponding computational results show similar behaviour of the mean heat transfer coefficient along all three channel sections. The cooling channel in HETRA test section will be fabricated from EUROFER by milling channel halves. The channel will be divided into the following parts for the fabrication: inlet side part, outlet side part, two bends and the straight heated section (this section will also be divided into two parts). The channel parts will

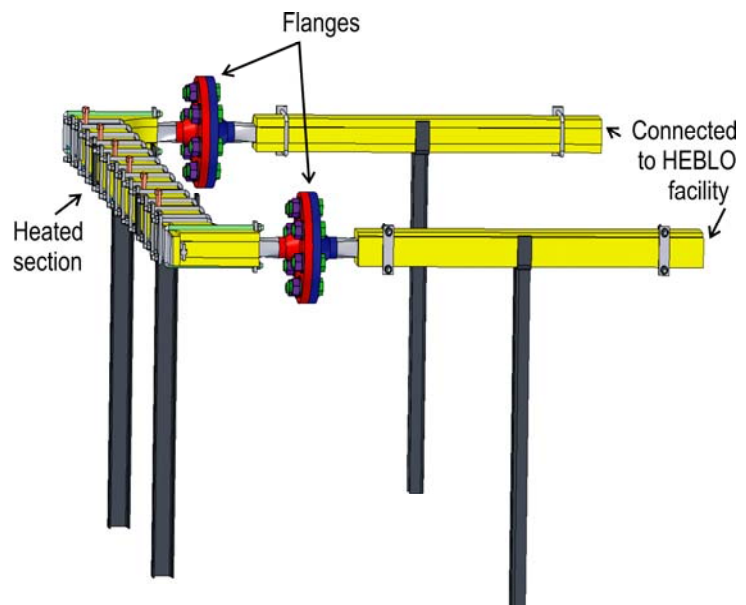


Fig 1. Layout of HETRA experimental facility.

be connected by Electron beam welding (EB) in longitudinal direction and by Tungsten inert gas welding (TIG) in the lateral direction. The probe with electron beam welding has been performed and satisfactory weld properties are obtained: welding seam does not penetrate the channel, measured hardness values are below the allowed values and fine grained structure is obtained. The tests with welding in the lateral direction have shown that the applied TIG welding procedure has to be improved.

The long straight section representing plasma facing part of the first wall will be connected by flanges to the two channel bends to enable tests with different roughness of the channel surface. The first tests will be done with the absolute roughness of the channel wall of  $20\mu\text{m}$  as the numerical results have shown that this magnitude provides reliable cooling of the first wall.

The test section will be heated only on the side representing plasma facing side of the first wall. The heating of the back side of the first wall which in TBM comes from breeding units is in HETRA experiments neglected due to its multiple lower magnitude. The heat flux of  $270\text{kW/m}^2$  at the plasma facing side of the first wall is in HETRA experiments simulated by a set of 8 flat ceramic heaters. Figure 3 shows heater arrangement at HETRA heated section. To ensure uniform heat flux and to diminish effects of imperfect thermal contact, surface of both, the heaters and the first wall, will be covered by thin graphite layers (thickness of  $0.5\text{mm}$ ) between which a  $10\text{mm}$  layer of copper is placed (see Figure 2). The whole facility is covered with  $10\text{mm}$  thick insulation.

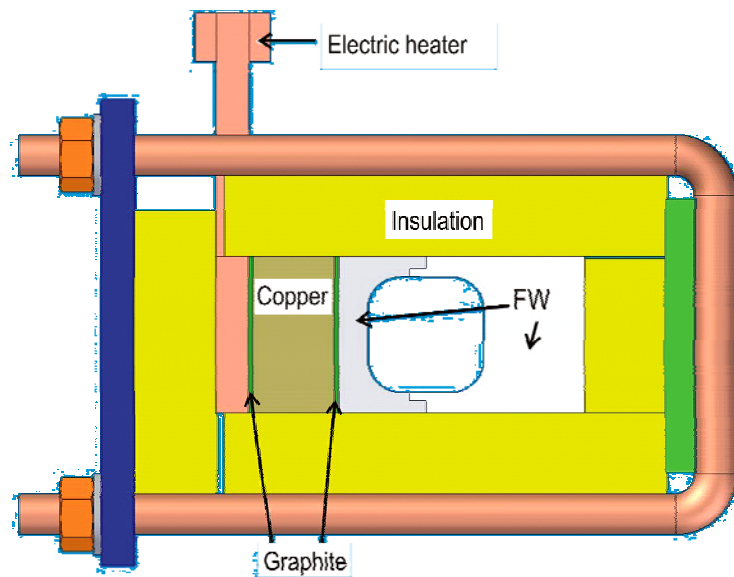


Fig. 2: Arrangement of heated HETRA section.

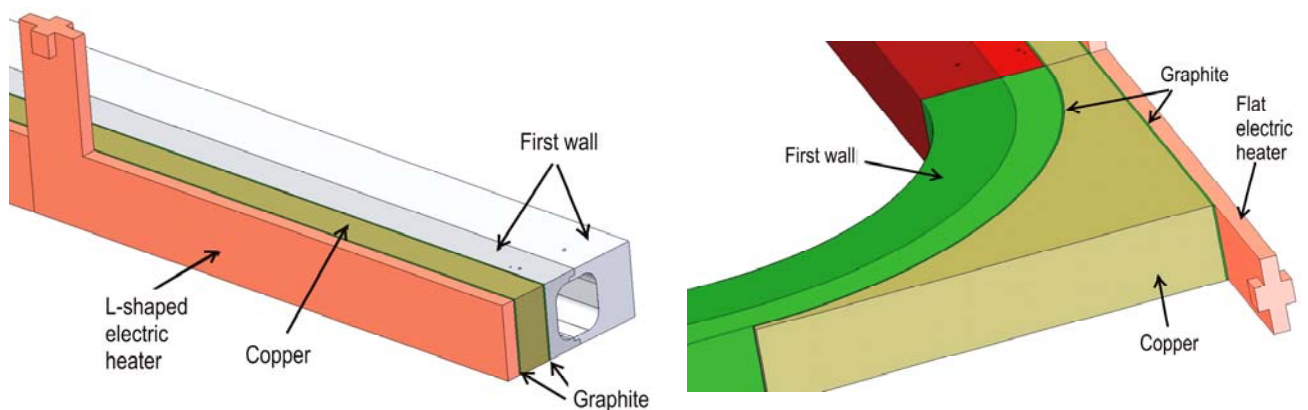


Fig. 3: Arrangement of heaters at HETRA heated section.

### 3. Definition of measuring positions in HETRA experimental facility

The tests will be done in a Helium cycle at  $8\text{MPa}$  for mass flow rate of  $0.1\text{kg/s}$  and inlet temperature of  $573\text{K}$ . Pressure losses will be determined through differential pressure measurements between several relevant locations along the channel.

As the temperature measurements within the flow domain would disturb the fluid stream significantly due to high coolant velocities, the computational results will be verified only via experimentally determined steel temperatures. For that purpose 8 sets of temperature measurements will be performed along the heated section (see Figure 4). The measuring planes will be positioned in the middle of the heating elements to avoid the effects of the discrete heaters. Within each set the temperature of the steel will be measured at 12 positions. The measurements will be done applying thermocouples with diameter of 0.5mm. The thermocouples will be inserted orthogonally to the heat flux (from bottom/top side of heated section) in order to minimize temperature gradients along the thermocouple cable.

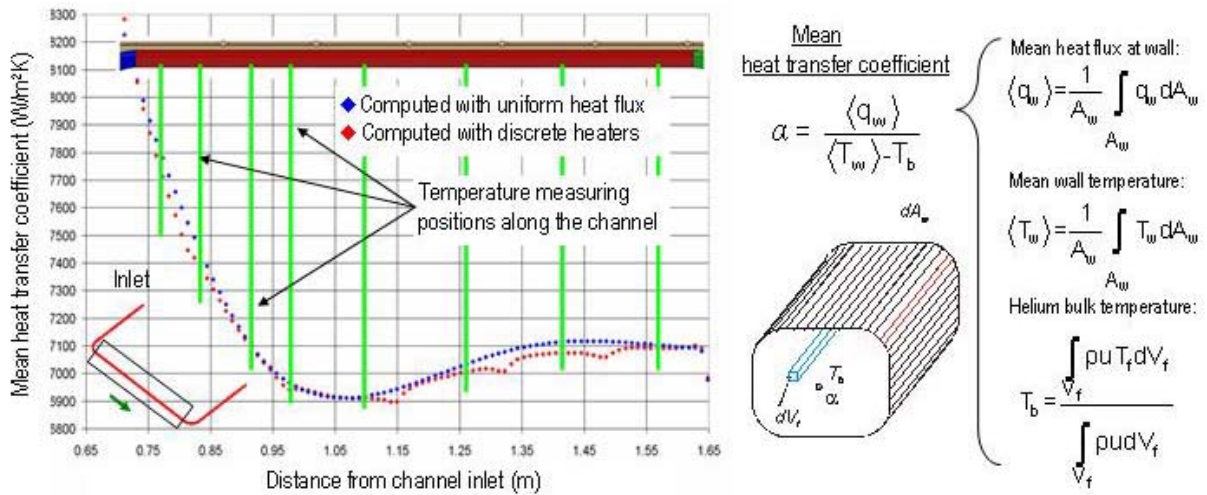


Fig. 4: Definition of measuring planes (green lines) in HETRA heated section.

The thermocouples are so placed in the cross-section of the first wall to obtain temperature data along three constant z coordinate, i.e. corresponding temperature gradients along four lines (see Figure 5). It is noted that the measuring positions are slightly staggered in longitudinal direction in order to avoid the disturbance of the heat flow.

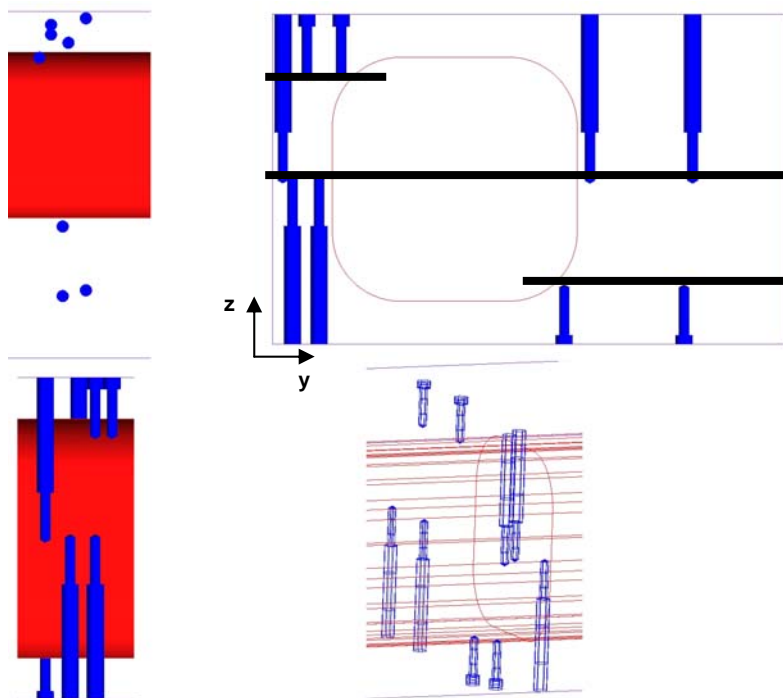


Fig. 5: Measuring positions within one measuring plane at HETRA heated section.

#### **4. Conclusions**

HETRA facility has been designed for verification of numerically found effects of asymmetrical heating on the cooling of the first wall. The investigations will be performed for a portion of the first wall containing one U sweep of the cooling channel. The tests will be done in a Helium cycle at 80 bars. The heat load of  $270\text{kW/m}^2$  on the surface representing plasma facing side of the first wall will be achieved by a set of electrical heaters. The numerical results will be verified through comparison with detailed temperature measurements in the steel structure.

#### **Staff:**

T. Ihli

M. Ilic

B. Kiss

G. Messemer

E. Stratmanns

## TW5-TTBB-001 D 11

### Analyses for the HELICA and HEXCALIBER Experiments using the ABAQUS Drucker-Prager Model

Two out-of-pile mock up experiments, HELICA and HEXCALIBER launched in HE-FUS 3 in ENEA Brasimone [1], have been analyzed in this task. The constitutive model of pebble beds, developed in Forschungszentrum Karlsruhe [2, 3], has been implemented in the commercial finite element package ABAQUS. This constitutive model is mainly based on the modified Drucker-Prager-Cap model. The validation of lithium orthosilicate and beryllium pebble beds used in experiments was first made based on the material database [4].

Fully coupled thermo-mechanical analyses of these mock up experiments have been performed. The finite element models are simplified using generalized plane strain elements. The calculated results are reported, including temperature, displacement, stress-strain field and the effective thermal conductivity of pebble beds. The temperature and displacement in HELICA are compared with the available experimental data, measured by thermo-couples (TCs) and LVDTs.

In HELICA, one layer of lithium orthosilicate has been heated by two electric heaters, ramping from 0 to  $42 \text{ kW/m}^2$  in 6 one-hour steps. Two loading cycles have been simulated using the finite element method. Figure 1 shows the comparison between the measurements and the FE prediction of temperature in the positions of TCs. The mechanical fields, such as stresses and strains, have also been obtained. The cyclic effects on the temperature field in HELICA are moderate, due to the fact that the thermal conductivity of ceramic pebble beds is less sensitive to the changing of strains.

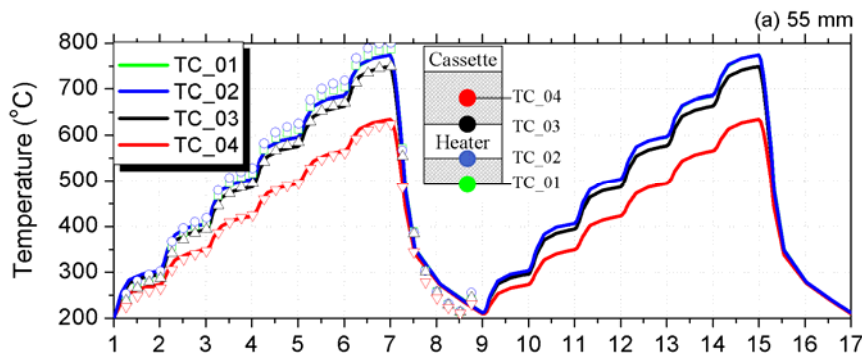


Fig. 1: Temperature changes over time during two loading cycles at 55 mm; to the first wall. Dots, experimental data; solid lines, F.E. calculation (unit: °C).

The HEXCALIBER mock-up experiment includes two lithium orthosilicate pebble layers and two beryllium pebble layers, and in each layer two electric heaters are placed to provide the designed surface heat flux. Figure 2 shows the temperature distribution at the maximum heat flux ( $42 \text{ kW/m}^2$ ) with the deformed configuration, and the coolant temperature is set to be  $450^\circ\text{C}$  according to the information from ENEA Brasimone. Meanwhile, the stress-strain fields and the inelastic strain dependent thermal conductivity have been obtained.

The final report on this task has been finalized and submitted in September, 2007.

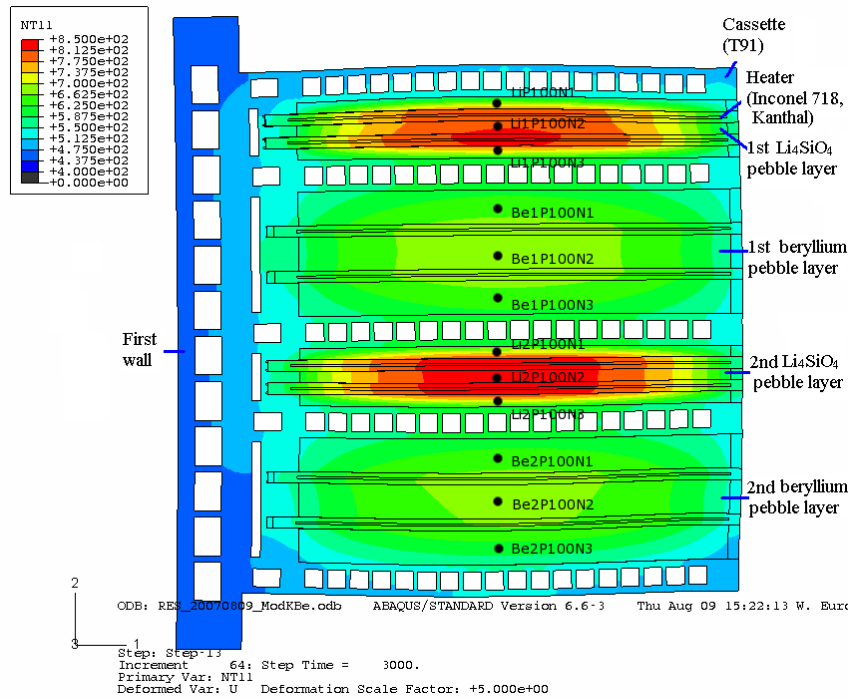


Fig. 2: Temperature profile of HEXCALIBER at the maximum electrical load (unit: °C), with deformations at a scale factor of 5.

Staff:

Y. Gan  
M. Kamlah

Literature:

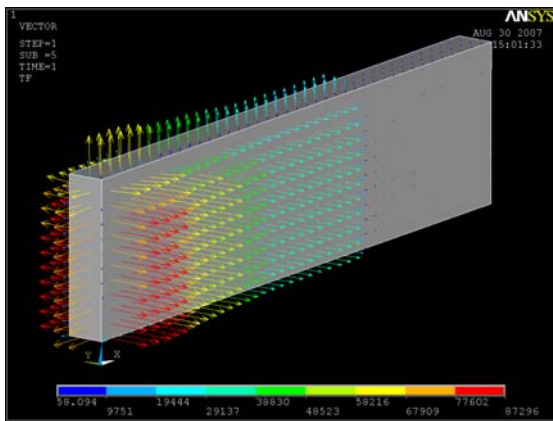
- [1] G. Dell'Orco, P. A. Di Maio, R. Giammusso, A. Malavasi, L. Sansone, A. Tincani and G. Vella, Progress in the benchmark exercise for analyzing the lithiate breeder pebble bed thermo-mechanical behaviour, Fusion Engineering and Design 81 (2006) 169-174.
- [2] Y. Gan and M. Kamlah, Identification of material parameters of a thermo-mechanical model for pebble beds in fusion blankets, Fusion Engineering and Design 82 (2007) 189-206.
- [3] D. Hofer and M. Kamlah, Drucker-Prager-Cap creep modelling of pebble beds in fusion blankets, Fusion Engineering and Design 73 (2005) 105-117.
- [4] J. Reimann, R. Knitter, A. Moeslang, B. Alm, P. Kurinskiy, R. Rolli, C. Adelhelm, H. Harsch and G. Raeke, Production and characterization of breeder and multiplier materials in support of the HELICA and HEXCALIBER experiments, Final Report on TW5-TTBB-006 D1+D2, 2006.

## TW6-TTBB-001 D 3 HCPB TBM Design and Integration Analysis

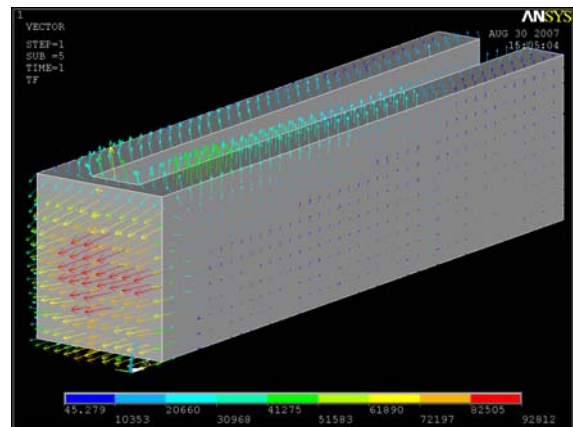
The objective of the task is the continuation of the engineering design work on the HCPB TBM System. In particular the updating of the TBM design, the production of detailed drawing of the TBM, the mechanical integration of the instrumentation, the definition of maintenance sequences, and design and integration of the Helium Cooling System (HCS).

### TBM update according to frame design

The outer dimensions of the TBM have been updated due to the changed requirements of the port plug frame geometry. A set of CAD drawings is available. Additionally the first wall analysis has been updated and an analysis concerning the heat flow from the pebble beds towards the steel structure has been started.



Heat flow from ceramic pebble bed



Heat flow from Beryllium pebble bed

Due to changed boundary conditions the arrangement of the TBM will be changed from horizontal to vertical due to the requirement of introduction of a correction coil to compensate the ripple effect due to ferromagnetic influence of the TBM. Additionally the attachment system proposed (shear keys and flexible cartridges) is currently re-designed.

The report on the TBM design update will be issued in 06/2008.

### Staff:

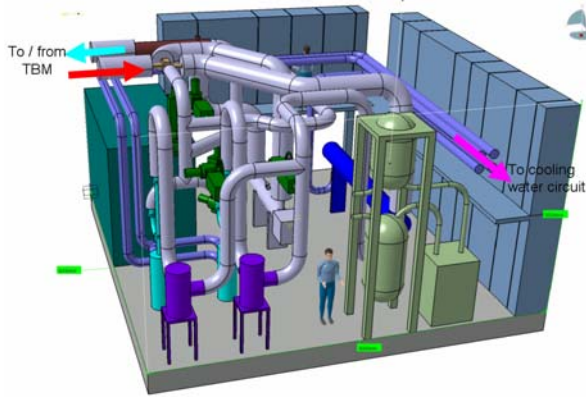
H. Neuberger  
R. Roccella  
B. Dolensky

### TBM HCS integration and analysis

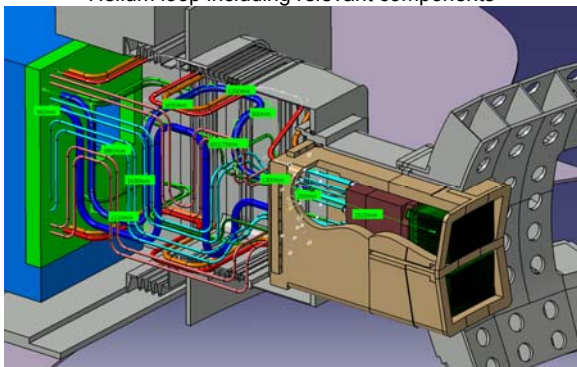
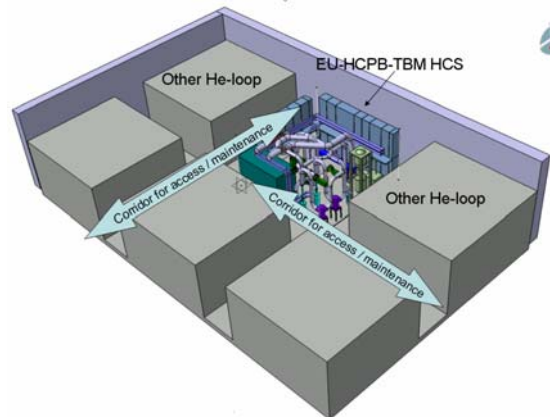
A conceptual design for the HCS based on a 8 layout (with recuperator in order to keep the compressor at low temperature, i.e.  $<150^{\circ}\text{C}$ ) has been already developed by FZK in the frame of task TW5-TTBB-001-D1c. The design has to be further developed in order to fulfil ITER requirements, especially space limitations and maintenance, piping lay-out and interface with other ITER systems (e.g. power and cooling water supply). Detailed design of the TBM cooling system turned out that the requirements for integration of the Helium cooling system in ITER have to be strongly revised with regard to the space consumption.

In the previous report on HCS integration in ITER it was pointed out that the space dedicated for the EU-Helium room in ITER is 16 m<sup>2</sup> (footprint). Detailed design turned out that the dimensions of the loop will strongly increase up to a value of 81 m<sup>2</sup> footprint (without taking into

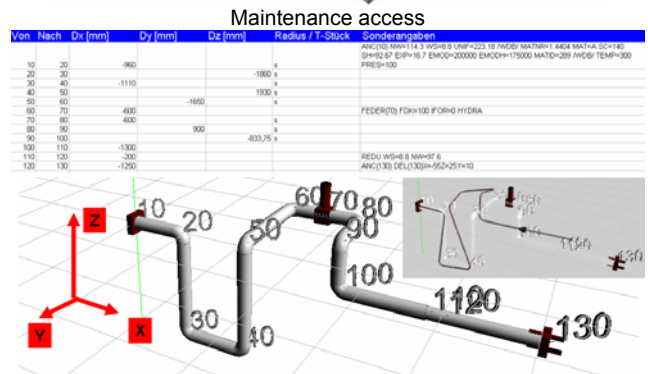
account maintenance access corridors). The following figures are taken from the draft version of the report issued in 11/2007. Additionally analysis have been performed to investigate the routing of the TBM supply pipes in the port cell inter-space (between bio-shield and port plug) with regard to flexibility for compensation of thermal expansion and expansion of the vacuum vessel during operation.



Helium loop including relevant components



Port cell inter-space (incl. port plug)



Analysis of Helium inlet pipe of upper TBM

Staff:

H. Neuberger

## TTBB-003

### Helium Cooled: Out of Pile Testing

#### TW5-TTBB-003 D 1

### Manufacturing and Testing of Mock-ups for Investigation of Coolant Flow in the Manifold System of HCPB TBM (GRICAMAN Experiments)

#### 1. Introduction

The objective of this task is to contribute to the out-of-pile testing of HCPB TBM. The activity focuses on out-of-pile testing of a look-alike mock-up of the TBM manifold system, in particular to the optimization of coolant flow.

The flow distribution in the TBM coolant system is quite complex. The coolant, helium at 8MPa and 300°C enters the manifold 1 with a mass flow rate of 1.2kg/s, from where it is distributed into coolant channels of the first wall (FW channels). The outflow from FW channels is collected in the manifold 2 where the following flow distribution should take place: 0.56 kg/s is extracted from the system via by-pass pipes, 0.38kg/s is uniformly distributed through 27 stiffening grids and 0.125kg/s flows into each cap. The mass flow rate through each cap channel is specified. The outflow from grid and cap channels is collected in manifold 3 and from there uniformly distributed among 18 breeding units. The outflow of BU's is led into the manifold 4 designed in the form of 'ships' from where it, finally, leaves TBM. In order to find out whether such a flow distribution can take place, GRICAMAN (GRIDCAPsMANifolds) experiments are proposed. The main goals of the experiments are:

1. to investigate whether the mass flow distribution in the manifold 2 among the caps and stiffening grid channels corresponds to the designed one,
2. to investigate whether individual stiffening grid and cap channels are supplied with designed portion of the coolant flow and
3. to investigate whether the mass flow distribution among breeding units is uniform.

The flow domain to be investigated in GRICAMAN experiments is defined to be the upper toroidal-poloidal half of TBM bounded at the outlets of first wall channels, at the outlets of by-pass pipes and at the inlets of breeding units, i.e. involving one half of the manifold 2, cooling channels in six horizontal and eight vertical stiffening grid plates, cooling channels within one cap and one half of the manifold 3. Significant simplifications of the experimental facility and numerical models are achieved (i) assuming that the flow is adiabatic, (ii) replacing helium at 8MPa and 643K with air pressurised at 0.3MPa and ambient temperature and (iii) representing real grid and cap channels by simplified channels that have the same flow resistance (hereafter called equivalent grid/cap channels).

#### 2. Design of GRICAMAN experimental facility

This section presents selected solutions for the construction of GRICAMAN components. It is noted that the presented issues mainly concern TBM design ref.1.1, but that the GRICAMAN facility is assembled in a way that the TBM design alt.1.0 can also be tested.

The main components of GRICAMAN facility that has to be constructed are presented in Figure 1. At the sides of the manifold 2 outlet parts of 6 **first wall (FW) channels** are connected. The cross section of these channels (rounded square 14.3x14.3mm with radius in corners of 4mm) is geometrically identical to the ones in TBM. The FW channels will be produced by milling channel halves in two steel plates. The two FW plates will be fixed with screws. For sealing O-rings will be applied. The outlets of FW channels in Mf2 will be drilled in inside plates. The length of FW channels (from inlet to the outlet in Mf2) is 454mm, i.e.

$\sim 30D_h$ . This length should be sufficient to fulfil the purpose of FW channels - establishing of velocity profiles at inlet to Mf2 that are identical to the ones in TBM.

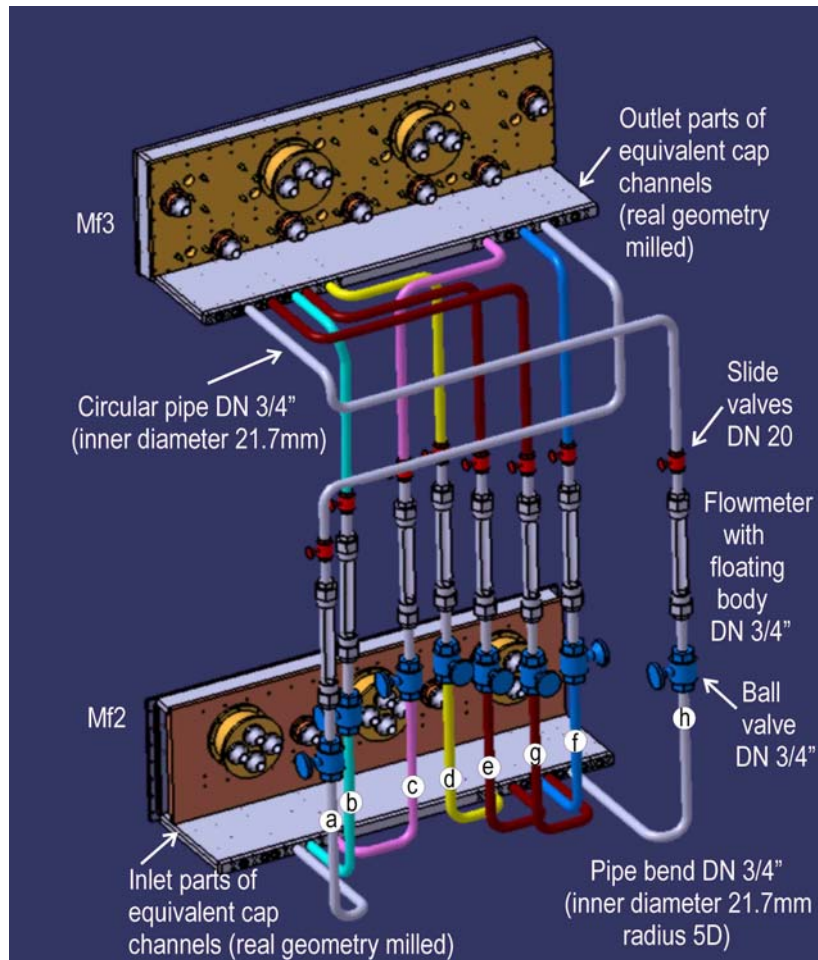


Fig. 1: Layout of GRICAMAN experimental facility. All the presented components are to be constructed and fabricated.

The connection of two manifolds with **equivalent grid channels** to be applied in GRICAMAN facility is presented in Figure 2 right up. Each equivalent grid channel consists of three main parts: (i) Inlet part with real geometry of two parallel inlet grid channels. Cross-section of the channels is rectangle 12x6mm with two round sides (half circles with radius of 3mm). The length of the channels is 0.1m. The channels will be fabricated by eroding in cylindrical steel pieces, what guarantees good sealing. At the outer side of the cylinders with inlet grid channels, a ring with 8 screw holes for fixing at the back wall of manifold 2 will be fabricated by turning (see Figure 2 right down). The sealing will be done by O-rings placed in grooves turned in the ring with screw holes. The number of inlet grid channels eroded in one cylinder depends on the pattern of grid inlets - when grid inlets form so-called crosses, 4 pairs of inlet grid channels are eroded in one cylinder, while for single grid inlets only one pair of grid channels is eroded in a "small" cylinder. On the upper side of cylinders with channels conical pieces are set in order to collect the air flow from two inlet grid channels and lead it into circular pipes. The conical pieces are screwed to cylinders with inlet grid channels and welded to circular pipes. (ii) The pipeline consists of circular tubes DN  $\frac{3}{4}$ " and circular tube bends DN  $\frac{3}{4}$ ". The isolation of individual channels is done with ball valves DN  $\frac{3}{4}$ ". The mass flow rate of air is measured by a flow meter with floating body DN  $\frac{3}{4}$ ". For adjustment of flow resistance of equivalent grid channels side valves DN 20 is applied. (iii) The outlet grid channels are to provide the most realistic conditions at grid outlets to manifold 3. The channels will be fabricated in the same way as the aforementioned inlet part of equivalent grid channels (note that the length of these channels is 0.45m, what corresponds to the length of real outlet grid channels).

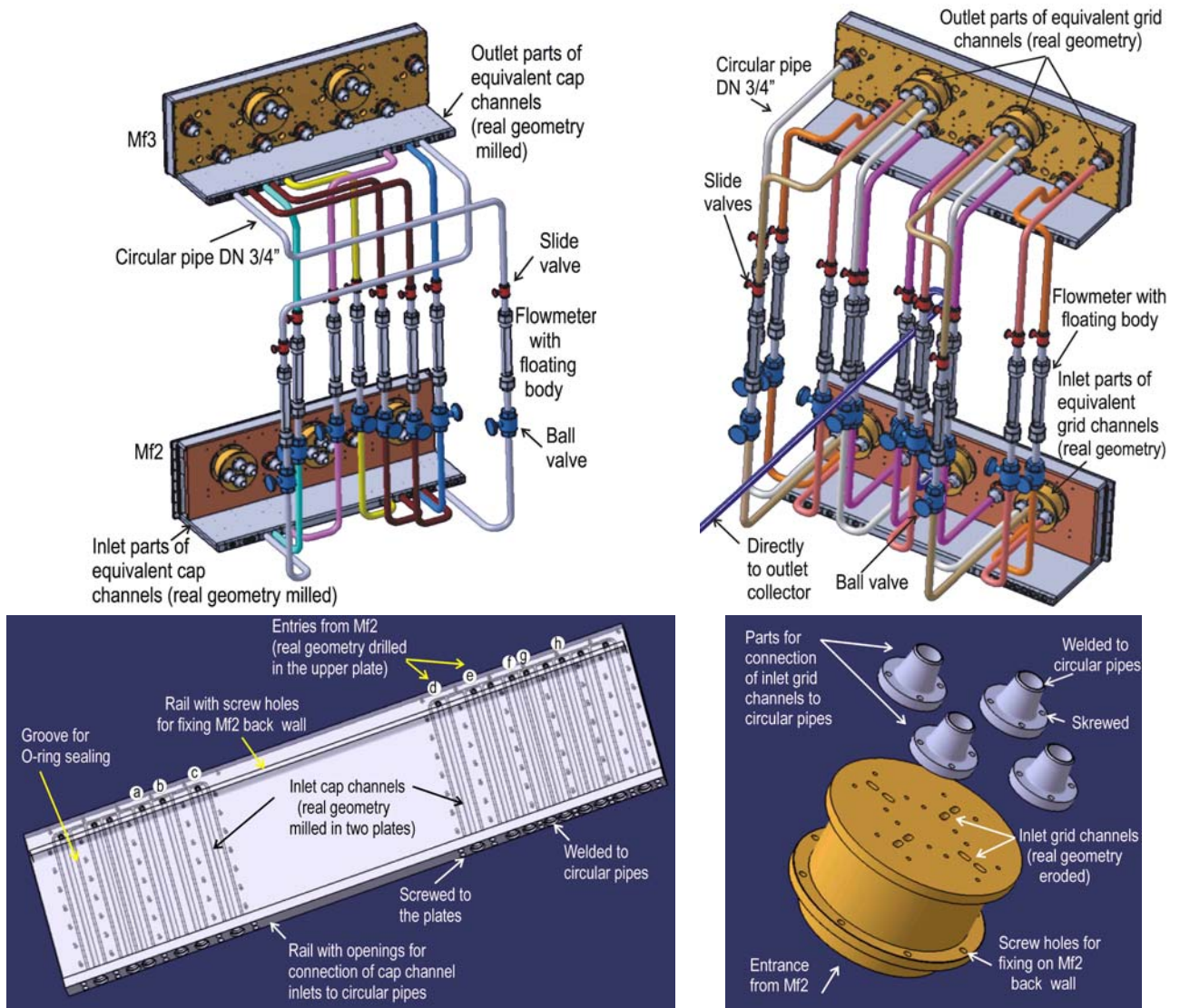


Fig. 2: Design of equivalent cap (left) and equivalent grid (right) channels. The lower figures show inlet/outlet parts of cap (left) and grid (right) channels applied in order to ensure correct inlet/outlet conditions in Mf2/Mf3 boxes.

**Equivalent cap channels** to be applied in GRICAMAN facility are designed following the same concept as in the case of the equivalent grid channels. Each equivalent cap channel consists of main three parts (see Figure 2 left up): (i) an inlet part with the real geometry of channel cross section, (ii) a circular pipeline designed in an analogous way as in the case of equivalent grid channels and (iii) an outlet part with the real geometry of the channel cross section. The inlet and outlet parts of cap channels will be fabricated in the following way: halves of the cap channel cross-section (rectangle 10x20mm with rounded corners with radius of 4mm) will be milled in two plates and the plates will be fastened to each other with screws (see Figure 2 left down). The length of inlet/outlet cap channels is 0.42m, that is  $\sim 30D_h$ . Sealing will be done with O-rings placed in grooves milled in the upper plates. It is noted that inlet/outlet cap channels in GRICAMAN facility are designed to be straight, although these parts in TBM ref.1.1 are inclined. This simplification is done for the following reason. The upper plate of the cap channels in both Mf2 and Mf3 are part of the manifold frame welded to other frame components. This solution has to be adopted in order to keep deepness of openings that connect the inlet/outlet cap channels with Mf2/Mf3 on the value of 5mm prescribed in TBM. Therefore, as the upper plate of cap channels cannot be removed, the cap channel pattern of TBM alt.1.0 design will also have to be milled for future tests of this design. As cap channels in TBM alt.1.0 design are straight, their crossing with cap channels of TBM ref.1.1 design can be avoided only when all the channels in GRICAMAN facility

are adopted to be straight. It is expected that this discrepancy will not affect flow conditions in manifolds, since the locations of the cap inlets/outlets are placed correctly.

The upper halves of manifold 2 (Mf2) and manifold 3 (Mf3) are rotated by 180° for an easier connection. The **manifold 2** (see Figure 3) will be built in the following way. First the Mf2 frame will be produced by welding the inner FW plates, the upper plate of inlet cap channels and a long narrow plate that serves as the upper Mf2 wall. For the sake of flexibility, all other components will be fixed with screws. In relation to this, front and back walls of both manifolds as well as their internal structure can be completely replaced to allow future tests of TBM alt.1.0 design. The front wall of Mf2 will be screwed along the four edges to Mf2 frame: to the Mf2 upper wall, to the outer FW plates and to the upper plate with inlet cap channels. For sealing O-rings will be placed in grooves milled at Mf2 front wall. At the outer side of Mf2 the front wall by-pass collector will be screwed. The ships will be inserted and fixed by screws at the Mf2 front wall in order to prevent its bending. To prevent air flow through possible gaps between the Mf2 wall and ship surface, O-rings will be placed in grooves milled along both sides of ship inserts. For pressure measurements capillary holes with a diameter of 0.8mm will be positioned along two parallel lines at the front wall of Mf2. Along each line 29 measuring elements are foreseen. The back wall of Mf2 will also be fixed by screws along the four edges: to the Mf2 upper wall, to the rails at the inner FW plates and to the rail at the upper plate of inlet cap channels. The sealing will be done by O-rings placed in grooves at the Mf2 back wall. The bending of the Mf2 back wall will be prevented by its screwing to ships. At this plate of Mf2 the circles of corresponding diameter will be cut out and the inlet parts of equivalent grid channels will be inserted and screwed along their perimeter. The sealing will be done by O-rings placed in grooves milled at parts with grid channels. Along a line at Mf2 back plate that lies parallel with the by-pass openings 30 elements with capillary tubes will be positioned for pressure measurements.

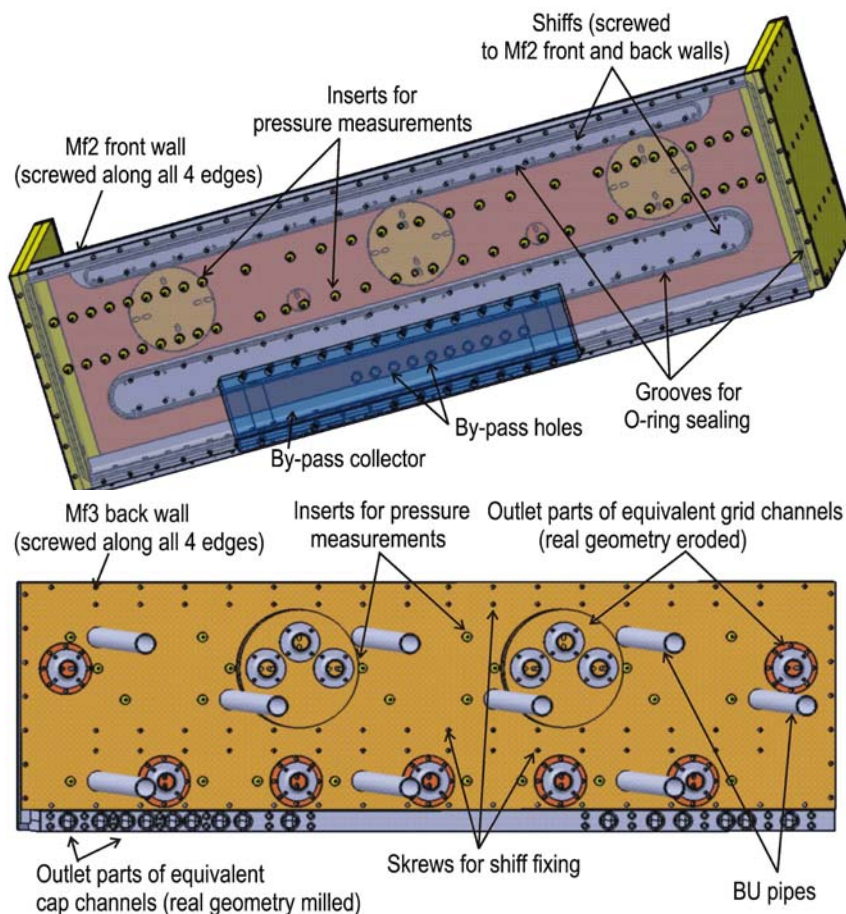


Fig. 3: Design of manifold 2 (up) and manifold 3 (down) in GRICAMAN experimental facility.

The fabrication of the frame for the **manifold 3** will be simpler than the manifold 2 since Mf3 has no connection with FW channels. The Mf3 frame will, therefore, be fabricated by welding the upper plate of cap outlets and three narrow plates representing Mf3 upper and side walls. Similar to Mf2 all other components of Mf3 box are fixed with screws. Grid legs crossing the volume of manifold 3 are represented by parallelepipeds (11x45x40mm for vertical grid and 11x55x40mm for horizontal grid) fixed by pins only to the back Mf3 wall. The outlets of equivalent grid channels are connected to Mf3 in an identical way as it is done in the case of Mf2. At the back Mf3 wall 9 holes with diameter of 30mm are drilled in which inlet parts of BU equivalent pipes are inserted and welded. Finally, at the back Mf3 wall 30 elements with capillary tubes for pressure measurements are distributed.

The GRICAMAN facility involves 9 equivalent **breeding unit (BU) pipes**. Each equivalent BU pipe consists of the following three sections: (i) circular pipe DN 30 which corresponds to the real cross-section of BU pipes in TBM. The length of this section is 1.273m i.e.  $\sim 50$  its hydraulic diameters; (ii) circular pipe DN  $\frac{1}{2}$ ". This section is necessary due to the size of calorimetric flow meters for flow rate measurements in individual BU pipes. In order to ensure necessary conditions for proper use of these devices an inlet path of 1m ( $\sim 60D_h$ ) and a path of 0.65m ( $\sim 40D_h$ ) behind the flow meter are arranged and (iii) circular pipe DN  $1\frac{1}{4}$ " at which a ball valve DN  $1\frac{1}{4}$ " for quick isolation of equivalent BU pipe and a needle valve DN  $1\frac{1}{4}$ " for adjustment of BU flow resistance are placed. The size of this section has been chosen in order to be able to apply needle valve with large flow characteristic ( $K_v=3.60$  for chosen needle valve).

### 3. Resistance calibration of equivalent grid channels

In order to ensure that the hydraulic resistance of equivalent grid channels is the same as the resistance of real grid channels the following experimental tests have been performed:

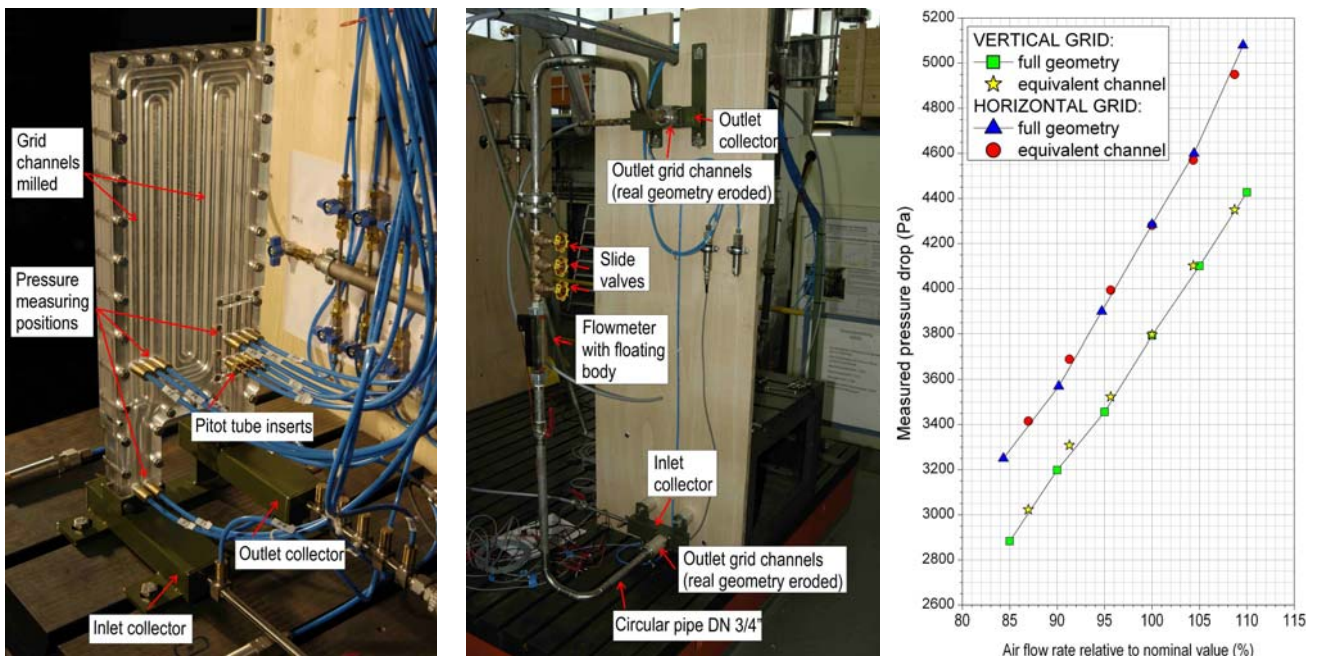


Fig. 4: Mock-up for investigation of real stiffening grid channels (left), mock-up for investigation of equivalent stiffening grid channels (middle) and comparison of measured pressure losses in real and equivalent grid channels (right).

- (i) The flow in real stiffening grid plates is investigated by building up corresponding mock-ups (in Figure 4 left mock-up for investigation of vertical grid channels is presented). By measuring pressure drops between inlet and outlet collector for different air flow rates hydraulic characteristic of cooling channels in both stiffening plates are obtained (see Figure 4 right) (ii) An individual equivalent channel (the arrangement of this channel is described in section 2) is connected to the two collectors used in tests with real stiffening grid channels

(see Figure 4 middle); (iii) At each of three applied slide valves a scale is made to denote the position of the valve stem; (iv) The nominal air flow rate is imposed and the slide valves are adjusted in a way that the pressure difference between the inlet and outlet collector corresponds to the one measured for real grid channels. The position of the valve stems found in this way is denoted as nominal (with this nominal position of the valve stem equivalent grid channels will later be inserted in GRICAMAN facility); (v) For the nominal position of the valve stem the pressure difference between the inlet and outlet collector,  $\Delta p$ , is measured for different mass flow rates,  $m$ , to obtain the dependence  $\Delta p=f(m)$ . Figure 4 right shows that in this way obtained hydraulic characteristics of equivalent grid channels fully correspond to the ones for real grid channels.

#### **4. Conclusions**

The report deals with the GRICAMAN experimental facility for investigation of flow distribution in the coolant system of HCPB TBM. The considered flow domain is the upper toroidal-poloidal half of TBM bounded at the outlets of FW channels, at the outlets of by-pass pipes and at the inlets of BU's. The facility is designed to keep the real geometry of manifold 2 and manifold 3 and to replace complicated grid and cap cooling channels with simple pipes having the same flow resistance as the real channels. The calibration of the flow resistance of equivalent grid channels is performed experimentally and presented in this report. In the next step the calibration of the cap channels will be performed. All the constructive details of the GRICAMAN assembly have been solved, the technical drawings have been made and the fabrication will start soon.

#### Staff:

O. Albrecht  
T. Ihli  
M. Ilic  
T. Kuhn

## **TTBB-005b**

### **Helium Cooled: Modelling of Swelling and Tritium Release in Beryllium under Irradiation**

#### **TW2-TTBB-005b D 1**

### **Effect of Radiation Damage and Gas Diffusion in Irradiated Beryllium: Results of High Resolution Micro-Tomography**

#### **1. Introduction**

A key issue of Helium Cooled Pebble Bed (HCPB) blankets is its behaviour under fusion neutron irradiation. In the present European HCPB blanket concept and within a 40 000 hours lifetime, an integral neutron dose of typically  $3 \times 10^{26} \text{ n m}^{-2} \text{ s}^{-1}$  ( $E_n > 1 \text{ MeV}$ ) results in the production of about 80 dpa, 25 700 appm helium, and typically 640 appm tritium in beryllium. Depending on the local neutron spectrum, the helium/tritium total yield ratio can vary between 10 and 100. According to present HCPB blanket designs an amount of about 3 100 tons metallic beryllium is foreseen as a neutron multiplier in form of layers of small pebbles. The knowledge of tritium and helium accumulation as well as the gas release kinetics from the pebbles is crucial for the reliable and safe operation of fusion DEMO reactors.

While even large amounts of about 20 000 appm helium accumulated in beryllium used as a reflector material in the mixed spectrum reactor BR2 (Mol, Belgium) do not produce bubbles visible via TEM analysis after low temperature neutron irradiation, experiments encompassing post-irradiation temperature ramps revealed pronounced  $^4\text{He}$  and  $^3\text{H}$  release peaks, accompanied by a substantial increase of swelling. Significant swelling and creep were also found by other authors after high dose neutron irradiation at high temperatures or after low temperature irradiation followed by higher temperature annealing. A combination of microstructural analysis and gas release measurements supports the evidence that at high temperatures the tritium inventory is concentrated either in helium bubbles or trapped in strain fields in the bubbles' vicinity and can be substantially released only together with helium, i.e. by the formation of open porosity networks often along grain interfaces followed by bubble venting. A holistic 3D view on bubble formation, growth, coalescence and network formation is critically important for the experimental validation of recently started multiscale modelling activities aiming to understand helium and tritium kinetics and predict tritium release characteristics at different irradiation temperatures and neutron doses.

While classical 2D microstructural analysis techniques do not actually suffice to carry out morphologic analyses of extended bubble networks and complete gas percolation paths, X-ray based tomography techniques have substantially enhanced their resolution limit to the micrometer and even sub-micrometer range during the past years. 3D computer aided microtomography (CMT) has already shown its capability in the non destructive analysis of the packing factor of beryllium beds with a spatial resolution of  $10 \mu\text{m}$ , and its potential in analysing 3D porosity networks in irradiated beryllium. In the present study, the initial results reported earlier are extended. The analysis includes now (i) the whole reconstructed volume of irradiated and unirradiated beryllium pebbles, (ii) 3D rendering of surface and porosity channels, and (iii) analysis of the open-to-total-porosity ratio.

#### **2. Experimental**

Beryllium pebbles with a diameter of 2 mm and grain sizes between 40-150  $\mu\text{m}$  were produced by Brush-Wellmann, USA, and were irradiated in the BERYLLIUM experiment at the High Flux Reactor (Petten, The Netherlands) at 770 K to a fast neutron fluence of  $1.24 \times 10^{25} \text{ n m}^{-2}$  ( $E_n > 0.1 \text{ MeV}$ ), producing 480 appm  $^4\text{He}$  and 12 appm  $^3\text{H}$ . After irradiation, the pebbles were tempered at  $\sim 1500 \text{ K}$ , just below the beryllium melting point (1556 K), since a pronounced gas release peak was found to start at about this temperature in thermal ramping

experiments. For safety reasons both the non-irradiated and the irradiated samples were embedded in a double Plexiglas cylindrical capsule of about 6 mm external diameter and glued on the very bottom of it to avoid sample jiggling during the CMT rotational scans.

The high resolution microtomography setup at the ID19 beamline of the European Synchrotron Radiation Facility, Grenoble, France, was used with a monochromatic X-ray beam of 7 keV. The entire beryllium pebbles were scanned with two different spatial resolutions: 1.4  $\mu\text{m}$  to reveal also single bubbles and 4.9  $\mu\text{m}$  to focus on bubble network formation and percolation paths. For the post-processing of the as acquired microtomography data, a filtered back projection reconstruction program written at the ESRF was deployed.

### 3. Results and discussion

The CMT analyses were performed (i) on six unirradiated Be pebbles at 4.9  $\mu\text{m}$  spatial resolution, and (ii) on two irradiated specimens at 4.9 and 1.4  $\mu\text{m}$  resolution, respectively. Fig. 1 shows a horizontal (a) and a vertical (b) cross section of an irradiated specimen, recorded at 1.4  $\mu\text{m}$  "voxel" resolution. While still a quite high fraction of smaller, partly isolated bubbles can be observed, the post-processing reveals a high density of large bubbles which are in a vast majority interconnected through percolation paths to the pebble surface. Due to insufficient contrast between grey levels, the smaller bubbles are sometimes hardly visible. The observation that even after high temperature annealing at 1500 K still closed porosities are visible supports the main outcome of the temperature ramping experiments [2], that a small fraction of helium is not released before the melting temperature is reached. Actually, a moderate gas concentration of only 480 appm helium and 12 appm tritium results after 1500 K annealing in an advanced stage of bubble coalescence and network formation with extended percolation paths. It can be expected that after high neutron dose irradiation, i.e. end-of-lifetime conditions, similar bubble coalescence and network formation kinetics might be observed not only after high temperature annealing but already at blanket relevant irradiation temperatures, assuming comparable grain sizes, impurity contents and dislocation densities.

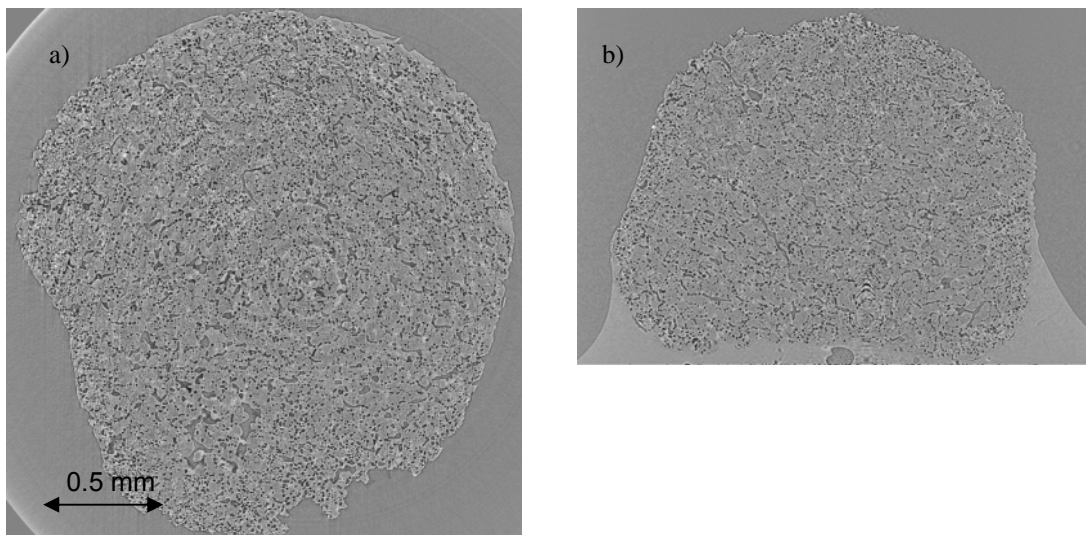


Fig. 1: Horizontal (a) and vertical (b) CMT cross sections of a Be pebble after neutron irradiation at 770 K and annealing at 1500 K. The spatial resolution is 1.4  $\mu\text{m}$ .

Fig. 2a shows a 4.9  $\mu\text{m}$  resolution horizontal cross section of a non-irradiated beryllium pebble before irradiation, revealing typical pores arising from the rapid condensation of the pebble during its fabrication process. The condensation induced voids having diameters ranging between 9-18  $\mu\text{m}$  and a total volume fraction of 0.17%. The CMT image of an irradiated and annealed beryllium pebble is shown in Fig. 2b, highlighting pronounced bubble networks with chain-like percolation paths. The typical distances between the percolation paths as well as their pattern suggest that they have been formed primarily along the grain interfaces. Accord-

ing to the CMT analysis the average diameter of the bubbles in the networks corresponds to the average width of the percolation channels, which is in the vast majority of the cases comprised in a narrow range around  $39\ \mu\text{m}$ . The mean volume fraction of the irradiation and annealing induced voids is 14.0%, and the void fraction surface within an entire pebble amounts to typically  $2.1 \times 10^{-4}\ \text{m}^{-2}$ . Thermal annealing after a relatively short neutron irradiation (480 appm helium and 12 appm tritium) causes swelling which is almost two orders of magnitude above the fabrication induced porosity. The white and bright grey areas in Fig 2a) and 2b) are the signature of impurities present in the beryllium matrix and are featuring different material densities.

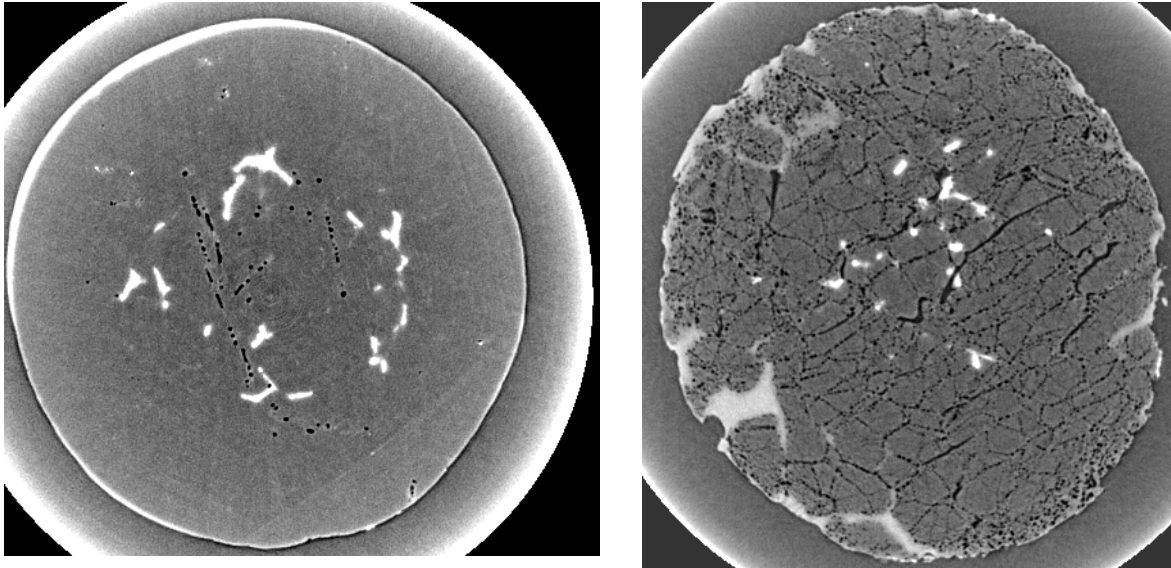


Fig. 2: Horizontal CMT cross sections of a Be pebble before (a) and after (b) neutron irradiation at 770 K and annealing at 1500 K. The spatial resolution is  $4.9\ \mu\text{m}$ , and the pebble diameter 2 mm

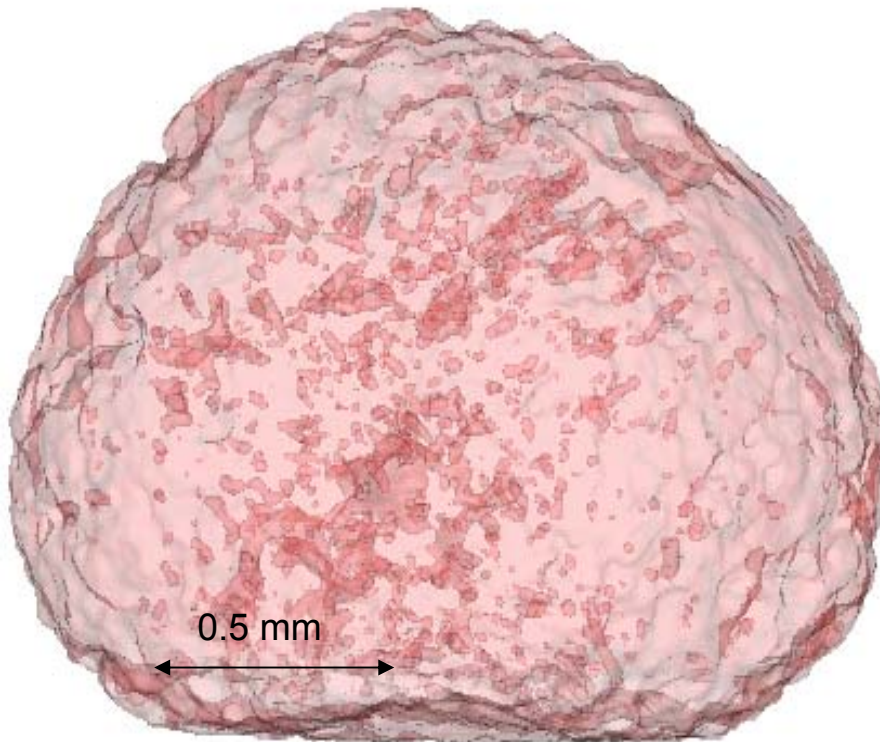


Fig. 3: Neutron irradiated (770 K, 480 appm He, 12 appm  $^3\text{H}$ ) and annealed (1500 K) Be pebble showing a superposition of the pebble surface and the volume porosity.

The 3D rendering of an entire irradiated and annealed pebble is shown in Fig. 3 as a superposition of the surface contour and the internal complex bubble network. The surface transparency was chosen to be 30%. Finally, Fig. 4 shows a sub-volume (32x32x64 voxel) extracted from the centre of an irradiated and annealed pebble to illustrate the complex, interconnected bubble network. The technique used to visualize this volume element is the "marching cube", applied directly to the binary data. The relatively high fraction of open to total porosity confirms earlier results from temperature annealing experiments. In particular, it appears that most of the helium and consequently also of the tritium content has already escaped from the beryllium after annealing around 1500 K.

#### 4. Conclusion

High resolution synchrotron radiation CMT has been applied successfully to analysing the complex mechanisms of bubble network formation and gas percolation in irradiated ( $T_{\text{irr}} = 770 \text{ K}$ , 480 appm He, 12 appm  $^3\text{H}$ ) and annealed (1500 K) beryllium pebbles. The CMT post-processing capability represents a powerful tool to analyse in a holistic manner not only the bubble sizes and densities or the channel network topology but allows also the extraction of structural parameters that are not accessible from TEM, like the 3D reconstruction of the fraction of interconnected bubbles, or the determination of the open-to-closed-porosity ratio. This non-destructive imaging technique has proven to be an essential instrument not only for the experimental validation of multiscale modelling of gas release kinetics but also for the evaluation of the structural integrity of entire pebble bed assemblies. For a given microstructure it is reasonable to expect that bubble network formation and percolation follow similar kinetics in helium cooled pebble bed blankets at higher neutron doses but lower irradiation temperatures.

#### Staff:

P. Kurinskiy  
A. Möslang  
P. Vladimirov

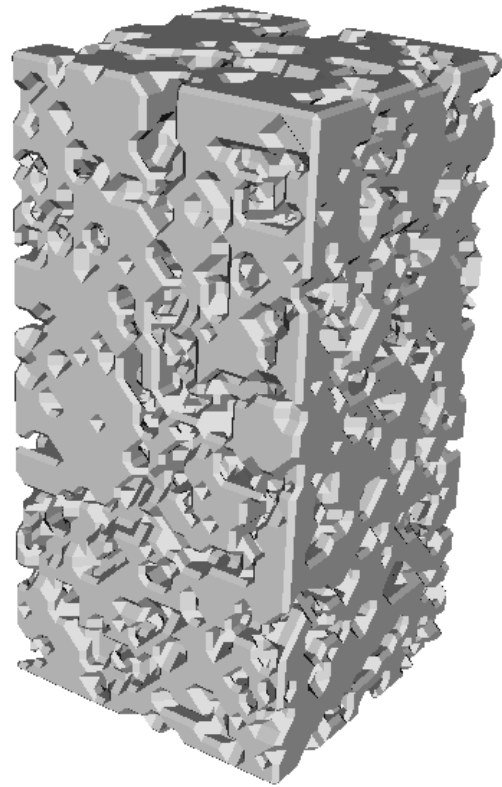


Fig. 4: A rectangular sub-volume extracted from an irradiated Be pebble showing the reconstruction of the complex bubble network (32x32x64 voxel).

## **TTBB-006**

### **Helium Cooled: Breeder and Neutron Multiplier Materials**

#### **TW6-TTBB-006 D 1**

### **Development of Beryllium and Beryllium Alloy Pebble Beds with Improved Tritium Release Characteristics**

#### **Introduction**

The most relevant properties of Be-Ti alloys besides their ability as neutron multiplier are their thermo-physical, chemical and tritium release properties. In particular, Be<sub>12</sub>Ti is considered to be one of promising materials for neutron multipliers in future fusion power plants. In order to overcome some of the disadvantages of existing Be pebbles like tritium release and He embrittlement at blanket operating temperatures, an attempt has been started to investigate relevant properties by producing own beryllium-based alloys (Be<sub>12</sub>Ti) on laboratory scale.

According to already available test results, Be<sub>12</sub>Ti shows, in comparison with metallic beryllium, faster tritium release, much smaller swelling, smaller reactivity with stainless steel, steam and water, therefore, it is becoming interesting also in view of its use in the EU-HCPB blanket. Also one should note that beryllium and its compounds are high toxic materials (especially, fine particles in air), so that special glove-boxes under controlled argon atmosphere were used to produce Be-Ti specimens. Another disadvantage is the brittleness of material what causes difficulties during mechanical treatment and decreases its potential use.

As in the previous years, the main activities were focused on fabrication and characterisation of Be-Ti specimens. Excellent results were obtained by HIP (Hot Isostatic Pressing) of Be-Ti powders at 1350 °C. Increasing of processing temperature from 1100 °C to 1300 °C led to rising of theoretical density of Be-Ti rods from 80 to 92%. TEM (Transmission Electron Microscopy) investigations reveal the presence of intermetallic phase with tetragonal structure corresponding to Be<sub>12</sub>Ti.

Also some successful attempts have been performed to fabricate a few grams of Be-Ti spheres (pebbles) by method of melting under argon-atmosphere in arc-melting facility.

Because of potential use of Be-Ti alloys in fusion reactors, a necessary assessment of some special characteristics of material relating to tritium release has been done. This experimental work has been performed and was aimed to evaluate rates of tritium release at blanket relevant temperatures (up to 850 °C).

#### **Experimental Equipment and Production of Be<sub>12</sub>Ti**

The technological equipment is placed in the area of Firma Goraieb Versuchstechnik (building 454), it was further completed during 2007 and includes meanwhile:

- a ball milling device, NETZSCH MINIZETA 03b made by company NETZSCH-Feinmahltechnik GmbH, to produce fine powder (particles 1-3 µm) of pure Be or mechanical alloying of Be-Ti powders;
- a 20-ton hydraulic press, PW 20 made by company Paul-Otto Weber GmbH, to produce tablets (diameter 15 mm), e.g. from Be and Be-Ti powders at temperatures of several hundred degrees;
- precision cutting machine (Viper-300 A2) from Firma LECO Instrumente GmbH to cut Be-based samples (Fig. 1);

- fully automatic vacuum oven for annealing tests (vacuum to  $10^{-6}$  mbar at any temperature range up to 1400 °C).



Fig. 1: Glove-box system equipped with Cutting Machine VI-PER 300 A2.

Due to a severe oxidation of beryllium and its alloys at elevated temperatures, all experiments at high temperatures have been performed in protective oxygen-free atmosphere (argon) or in vacuum. This laboratory is further equipped with necessary tools and devices for grinding, polishing and etching of specimens for further X-Ray, Scanning Electron Microscope or Transmission Electron Microscope investigations.

Fabrication of Be-Ti rods by HIP has been performed by Firma Bodycote in Munich. Mixed Be-Ti powders in proportions corresponding to chemical content of  $\text{Be}_{12}\text{Ti}$

phase (Be-30.8 wt.% Ti) were pre-compacted, outgassed and encapsulated in cylindrical capsules made out of niobium. After this operation, material was shipped to Firma Bodycote and, afterwards, delivered back to FZK for decanning and further characterisation. One should also note that Be-Ti rods produced out of coarse Be-Ti powders (Be powder – approx. 150  $\mu\text{m}$ , Ti powder ranging between 75 and 100  $\mu\text{m}$ ) have higher density as compared to rods fabricated out of Be-Ti powder mixture from the wet ball milling device. This could be explained by two factors:

- difficulties by compacting of fine particles,
- influence of residue of C14H30 (tetradecane) which prevents interaction between Be and Ti particles during processing.

One of the main goals, achieved during the reporting period, was the successful production of Be-Ti spheres (pebbles) with diameters ranging from 1 to 3 mm (Fig. 2). These geometrical values correspond to sizes of pure Be pebbles which are also supposed to be used in pebble-bed-type tritium breeding blankets. Be-Ti spheres containing, mainly,  $\text{Be}_{12}\text{Ti}$  phase were produced by melting of strips in arc-melting facility under argon atmosphere (200 mbar).

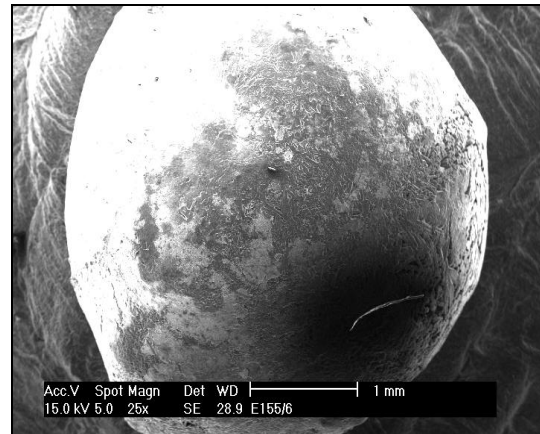


Fig. 2: SEM image of Be-Ti sphere produced by melting in argon.

During the reporting period, a new batch of  $\text{Be}_{12}\text{Ti}$  based, mostly, on powder metallurgy has been successfully fabricated. The density of Be-Ti rod was increased from 80 to 92% by a proper combination of temperature and pressure during the hot isostatic pressing. This density should be sufficient to fabricate in a second step bars from this rod that can be used for pebble production e.g. by rotating electrode method.

### Characterisation of $\text{Be}_{12}\text{Ti}$

As reported last year, a process of Hot Isostatic Pressing (HIP) has been successfully used to produce Be-Ti rods. Transmission Electron Microscope (TEM) was used for accurate determination of crystal lattice parameters of Be-Ti phases formed during the process of HIP.

The chemical composition of the produced Beryllium alloys investigated using Energy Dispersive X-Ray (EDX) analysis and Electron Energy Loss Spectroscopy (EELS). The analytical investigations were performed in Scanning TEM (STEM) regime using High Angle Annular Dark Field (HAADF) detector. A few uranium-containing precipitates have been detected in the samples. Uranium particles are visible with the brighter contrast in the image. Besides Uranium the precipitates in  $\text{Be}_{12}\text{Ti}$  contain also Fe, Co and Cu. The uranium is coming from the beryllium ore and is a natural element in Beryllium products.

Only one analysed HRTEM image can not serve as the reliable proof of the presence of  $\text{Be}_{12}\text{Ti}$  phase in the sample. There is a similarity of both tetragonal and hexagonal structures that do not appear occasionally.

The additional HRTEM investigations of grains, which are oriented with other zone axis to the electron beam, enable determination of the Be-Ti phase. The HRTEM image is presented in Fig. 3a. The Fast Fourier Transformation (FFT) image of this HRTEM micrograph presented in the Fig. 3b shows two different atomic planes with 0.516 nm distances. The angle between two these planes amount to  $90^\circ$ . This corresponds to  $[001]$  orientation of  $\text{Be}_{12}\text{Ti}$  (tetragonal structure with  $a=0.7278$  nm and  $c=0.424$  nm) perpendicular to the sample surface. The hole circles and crystallographic indexes were calculated for  $\text{Be}_{12}\text{Ti}$  tetragonal structure. As it can be seen in the FFT image (Fig. 3b), the calculated and measured structures are in the excellent correlation. The differences in calculated and experimental position of the diffraction spots were found in the range of 1-2%. The imaged structure has a good correlation (an error of about 2% was estimated) with calculated one for the  $\text{Be}_{12}\text{Ti}$  tetragonal structure. Such squared diffraction pattern can be caused only by diffraction of tetragonal phase and not on the hexagonal phase.

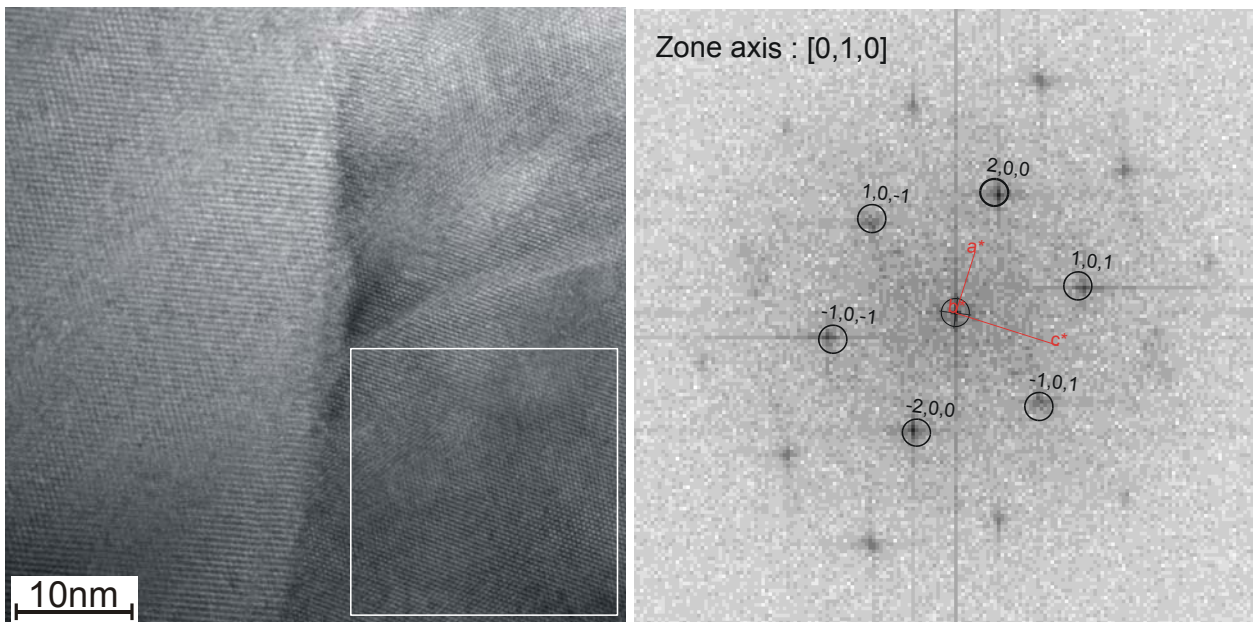


Fig. 3: HRTEM micrograph of a  $\text{Be}_{12}\text{Ti}$  grain oriented with  $[001]$  zone axis (a) and FFT image of this micrograph with calculated reciprocal lattice pattern of  $\text{Be}_{12}\text{Ti}$  tetragonal structure (b).

### Tritium Release Parameters of $\text{Be}_{12}\text{Ti}$ Samples

Under neutron irradiation, tritium production plays a much more important role than lattice damage in limiting the component lifetime. Gas atoms form bubbles and bubble growth and coalescence induce swelling. From this point of view, tritium release rate of the material of neutron multiplier is a very important specific property relating to its structural characteristics.

The activity of the released tritium has been measured using a proportional counter. The measured activity has been depicted by two different curves: one curve shows release rate in Bq/sec and another depicts integrated value (cumulative release) in Bq. Third curve reflects the changes in temperature during the experiment. Thus, each gas release experiment is represented by three curves reflecting ramping of temperature, current and integrated gas release (Fig. 4). Be<sub>12</sub>Ti samples used in this experiment have been fabricated by HIP of coarse Be-Ti powders at 1100 °C.

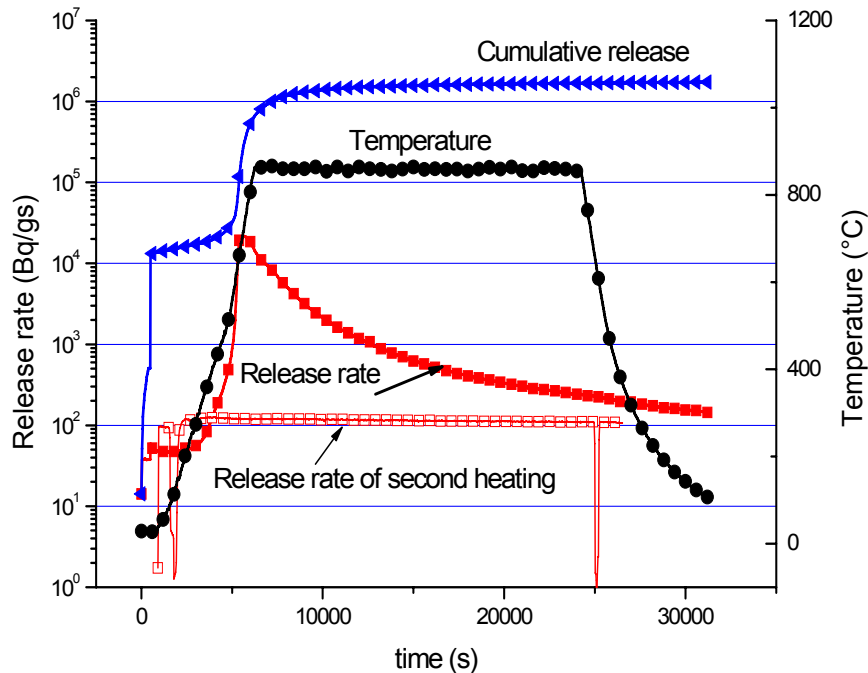


Fig. 4: Tritium release measurements of Be<sub>12</sub>Ti specimens produced by HIP.

Obtained data have been compared with already available tritium release data of 0,1-0,2 mm unirradiated Be pebbles made by NGK. The same tritium loading and gas release parameters were used in this experiment. The release rate reveals a major very encouraging result: the maximum peak of tritium release of pure Be pebbles occurs at significantly higher temperatures, at 850 °C, compared to 595 - 671 °C for Be<sub>12</sub>Ti samples.

### Conclusions and Future Prospective

Be-Ti rods with increased density (93% of theoretical density) have been successfully fabricated by HIP at 1350 °C. One should also note that these rods contain, mainly, Be<sub>12</sub>Ti phase. In parallel, the determination of tritium release parameters was done. Obtained results showed that titanium beryllides have better gas release characteristics comparing to pure Be pebbles made by Firma NGK.

The main goals of the next year are:

- further production of Be-containing samples with improved properties (esp. density);
- preparation of Be-Ti probes and their investigation by means of Transmission Electron Microscopy;
- microstructural characterisation of Be<sub>12</sub>Ti pebbles produced by wet-ball-milling, spheronising and sintering;

- review and analysis of different methods of metallic pebble fabrication from the technical literature;
- design of facility for Be<sub>12</sub>Ti pebble production in kg-scale.

Staff:

P. Kurinskiy  
A. Möslang

Literature:

- [1] P. Kurinskiy, A. Möslang, M. Klimiankou, A. Weisenburger; "Development of Beryllium and Beryllium Alloy Pebble Beds with improved Tritium Release Characteristics", Final Report on EFDA Task TW6-TTBB-006 D1
- [2] P. Kurinskiy, A. Moeslang, M. Klimiankou, A.A. Goraieb, H. Harsch, "Manufacturing methods and characterisation of titanium beryllides", Fusion Engineering and Design 82 (2007) 2353-2358
- [3] P. Kurinskiy, A. Möslang, H. Harsch, A.A. Goraieb, A. Weisenburger; "Characterisation of Titanium Beryllides" (to be published); 8th IEA Workshop on Beryllium, 4-6 December 2007, Lisbon, Portugal
- [4] E. Boller, C. Ferrero, A. Möslang, R. A. Pieritz "Gas Bubble Formation in Irradiated Beryllium Pebbles Monitored by X-Ray Micro-Tomography" (to be published); 13th International Conference on Fusion Reactor Materials (ICFRM-13), 10-14 December, 2007, Nice, France

## TW6-TTBB-006 D 2 Procurement and Quality Control of 7 kg of $\text{Li}_4\text{SiO}_4$ Pebbles for Planned Testing of Breeder Unit Mock-ups

Before installation of the HCPB TBM in ITER a number of individual components and prototypical mock-ups shall be tested out-of-pile to obtain relevant information about the components performance and the thermal-mechanical behaviour of Be and Li-ceramic pebble beds at given operational conditions. In this regard the first 7 kg of  $\text{Li}_4\text{SiO}_4$  pebbles were procured and characterised for testing of breeder unit mock-ups, where an amount of about 15 kg of lithium orthosilicate pebbles will be needed.

### Quality control of batch OSi 07/1-M

The amount of 7 kg of  $\text{Li}_4\text{SiO}_4$  pebbles in the diameter range of 250-630  $\mu\text{m}$  was delivered in 5 batches ranging from 0.62 to 1.7 kg. The batch size of this production campaign was increased in comparison to former campaigns by the use of a larger Pt-crucible. To speed up the quality control, a reduced characterisation of every batch was carried out. After satisfactory results of this pre-characterisation were obtained for all batches, the batches were mixed and a detailed quality control was carried out on representative samples of pebbles in the initial state as well as after conditioning [1].

The appearance and microstructure of the mixture (OSi 07/1-M) were examined by optical and scanning electron microscopy. Most of the pebbles are well, spherically shaped with a mean diameter of 300  $\mu\text{m}$  (Fig. 1) and exhibit the expected dendritic microstructure at the pebble surface. The cross sections reveal the usual amount of cracks and pores in the pebbles and the typical solidification microstructure of orthosilicate dendrites with small inclusions of the high-temperature phase  $\text{Li}_6\text{Si}_2\text{O}_7$  (Fig. 2).

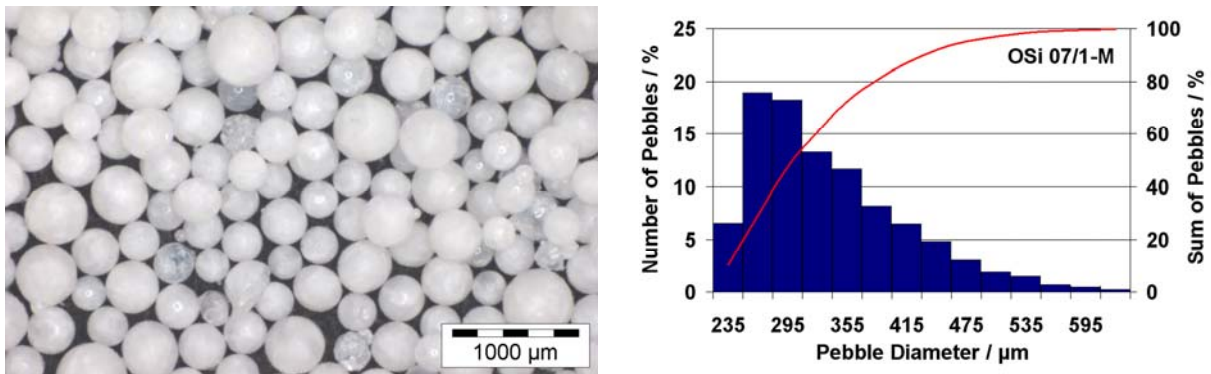


Fig. 1: Overview (OM) and size distribution of the lithium orthosilicate pebbles OSi 07/1-M.

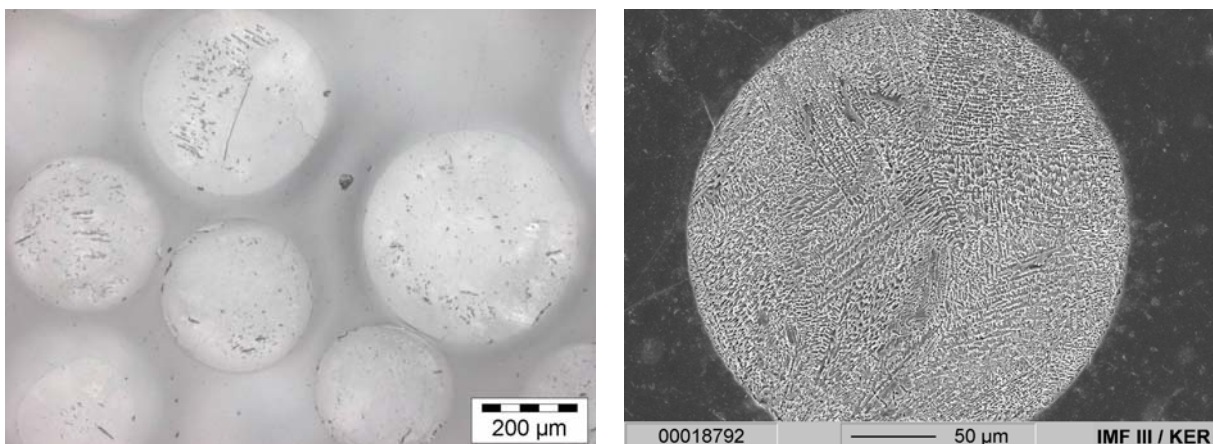


Fig. 2: Cross sections of OSi 07/1-M pebbles in the initial state (OM + SEM).

During conditioning at 970°C for 1 week, the agglomeration of small pores to larger, spherical pores and the coarsening of the microstructure take place. Due to the decomposition of the high-temperature phase, the microstructure now reveals lithium orthosilicate grains with a grain size of up to 10 µm and small inter- and intragranular grains of metasilicate ( $\text{Li}_2\text{SiO}_3$ ) (Fig. 3). Cracks and pores are mostly located at grain boundaries, only a few intragranular pores can be detected. All pebbles of the OSi 07/1-Mc batch exhibit a very similar, homogeneous microstructure after annealing.

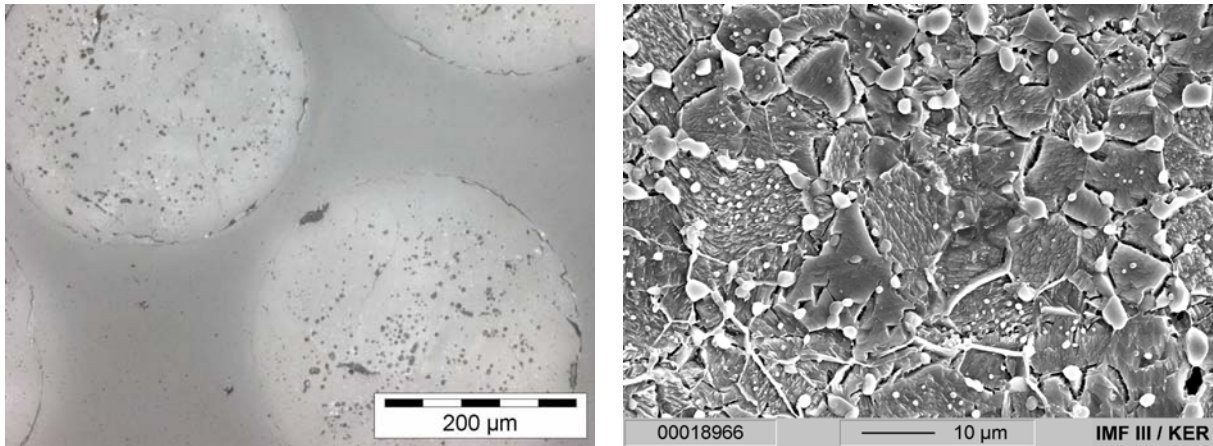


Fig. 3: Cross sections of OSi 07/1-Mc pebbles (annealed at 970°C / 1 week) (OM + SEM).

The results of the chemical analysis revealed a  $\text{SiO}_2$  excess of 3.0 wt% that is in poor agreement with the desired value of 2.5 wt% but not outside the range of formerly produced material. In general it is difficult to gain a proper composition of the pebbles due to Li-losses during fabrication. The use of a larger Pt-crucible may have additionally affected the Li-losses. The impurities of the OSi 07/1-M batch are quite low and well within the specification for the HCPB.

To determine the phases in the delivered pebbles, x-ray powder diffraction was carried out. As expected, the pebbles consist of  $\text{Li}_4\text{SiO}_4$  as the main constituent and the high-temperature phase  $\text{Li}_6\text{Si}_2\text{O}_7$  as a minor constituent. The intensity of  $\text{Li}_6\text{Si}_2\text{O}_7$  is in agreement with the relatively high  $\text{SiO}_2$  excess of the pebbles determined by chemical analysis. During annealing the high-temperature phase  $\text{Li}_6\text{Si}_2\text{O}_7$  is decomposed into the equilibrium phases, lithium orthosilicate and metasilicate. Besides  $\text{Li}_4\text{SiO}_4$  as the main constituent,  $\text{Li}_2\text{SiO}_3$  can now be observed as a second phase (Fig. 4).

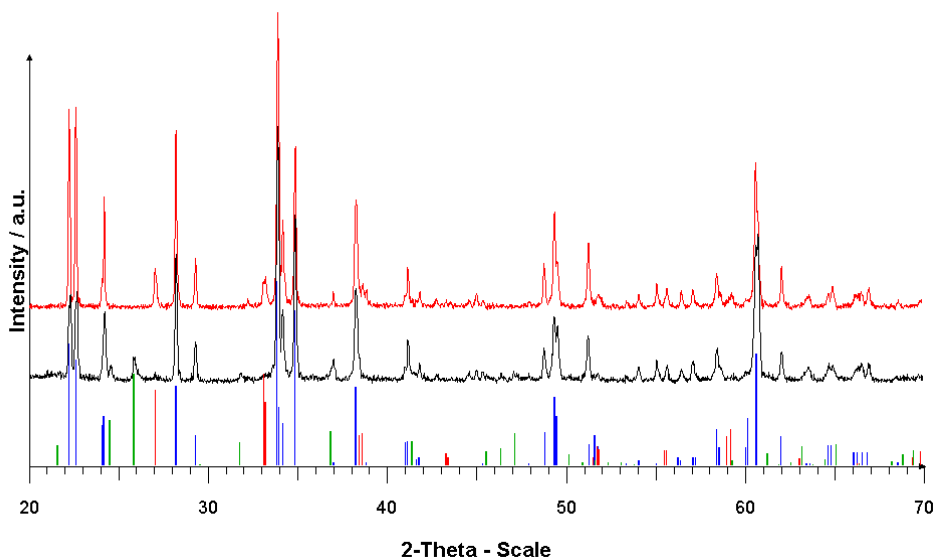


Fig. 4: X-ray diffraction pattern of OSi 07/1-M (bottom curve in black) and OSi 07/1-Mc pebbles (top curve in red) (||  $\text{Li}_4\text{SiO}_4$ , ||  $\text{Li}_6\text{Si}_2\text{O}_7$ , ||  $\text{Li}_2\text{SiO}_3$ ).

A closed porosity of less than 1 % was measured in the initial state as well as after conditioning by He-pycnometry (Table 1). By Hg-porosimetry a density of 94 % TD (TD = 2.40 g/cm<sup>3</sup>) and an open porosity of 4 % were measured. After conditioning, the density was insignificantly increased to 95 % TD by a decrease of the open porosity.

As a consequence also the tap density was slightly increased from 1.45 to 1.46 g/cm<sup>3</sup> during the heat treatment. The initial specific surface area of 0.15 m<sup>2</sup>/g was reduced to the usual 0.10 m<sup>2</sup>/g after conditioning, which is caused by the disappearance of the dendritic structure at the pebble surface. A crush load of 5-6 N with the usual large deviation of about 15 % was determined for the mixture. This value is lower than previously reported values of 8-9 N for good reference batches, but not outside the usually observed variation.

Table 1: Properties of lithium orthosilicate pebbles as received and after conditioning.

Batch	OSi 07/1-M	OSi 07/1-Mc
<b>Chemical Analysis of Principal Constituents (Schott)</b>		
Li <sub>2</sub> O / wt%	48.23	n.a.
SiO <sub>2</sub> / wt%	51.51	n.a.
excess SiO <sub>2</sub> / wt%	3.02	n.a.
<b>Size Distribution</b>		
d <sub>50</sub> / μm	300	n.a.
<b>He-Pycnometry</b>		
inner density / % TD	2.39 ± 0.00	2.39 ± 0.00
closed porosity (calc.) / %	0.4	0.5
<b>Hg-Porosimetry</b>		
density / g cm <sup>-3</sup>	2.26 ± 0.03	2.28 ± 0.05
density / % TD	94.4 ± 1.3	95.1 ± 1.9
open porosity / %	4.1 ± 0.5	2.5 ± 0.9
<b>Pebble Bed Density</b>		
tap density / g cm <sup>-3</sup>	1.45	1.46
<b>Specific Surface Area</b>		
specific surface area / m <sup>2</sup> g <sup>-1</sup>	0.15	0.10
<b>Crush Load Tests</b>		
mean crush load / N	5.9 ± 1.1	5.3 ± 0.6

The quality control assured satisfactory properties of the recently fabricated OSi pebbles. Due to limitations of furnace capacities the conditioning of the pebbles were carried out in amounts of about 500 g. The conditioned pebbles are stored under nitrogen until they will be needed for the testing of the mock-ups. The amount of 8 kg of OSi pebbles yet required for the testing should be ordered and fabricated in due time.

Staff:

- B. Löbbecke
- A. Erbe
- R. Knitter
- C. Odemer
- M. Offermann
- R. Rolli
- B. Wagner

Literature:

[1] B. Löbbecke, R. Knitter, Procurement and Quality Control of Li<sub>4</sub>SiO<sub>4</sub> Pebbles for Testing of Breeder Unit Mock-up, Final Report on the EFDA Task TW6-TTBB-006-D2, Forschungszentrum Karlsruhe, Interner Bericht, September 2007.

# **Breeding Blanket HCLL Blanket Concept**



## **TTBC-005**

### **Helium Cooled Lithium Lead: Process and Auxiliary Components**

#### **TW6-TTBC-005 D 4**

#### **Preparation of Coated Specimens for a Dedicated Pb-Li Compatibility Test: Specimen with Al Coating Produced by an Electrochemical Deposition Process**

##### **Objectives**

Low-activation-ferritic-martensitic (RAFM) steels are candidates as structural materials in HCLL blanket development for DEMO and for TBM's tested in ITER. In the last years the activities were mostly centered on the development of the improved RAFM-steels e.g. EUROFER 97 and in analyzing its corrosion behavior in bare uncoated form in flowing Pb-17Li at an exposure temperature of 480 or 550 °C. The corrosion testing performed in PICOLO loop showed for the steels OPTIFER, MANET, F82H-mod. and EUROFER 97 similar corrosion behavior with dissolution attack and linear kinetics. However, corrosion rates depend strongly on flow rate and temperature and increased dramatically by the small increase of 70 K from 480 to 550°C – the new envisaged application temperature in TBM's – by roughly a factor of 5. This dramatically increased corrosion rate illustrates clearly the risk potential by corrosion for a safe operation of blanket structures in a fusion system due to wall thinning and formation of precipitates at cooler positions with the risk of line closures.

This feature was beyond the required reduction of T-permeation in Pb-17Li blanket systems the pronounced reason to examine the effect of Al coating on EUROFER 97 on both the forming of corrosion and T-permeation barriers.

The positive effect of Al coatings was successfully demonstrated in the past, however with coating methods which were not applicable under industrial view and considering low activation requirements due the large amount of Al introduced e.g. by the earlier used Hot Dip Aluminisation (HDA) process.

Due to these facts and requirements a new Al coating process - called ECA process - based on electrochemical deposition methods was analyzed and developed and - under this task - for the first time successfully tested in coating of samples which will be exposed to Pb-17Li for compatibility testing in liquid metal environment.

Two types of sizes of specimens – flat and cylindrically shaped samples – were coated by the developed ECA (**E**lectro-**C**hemical **A**l deposition) process with two different scale thicknesses and two different surface structures (as delivered and machined). The analyzed samples are ready for delivery to the compatibility testing.

##### **Al-coating**

The liquid breeder Pb-17Li is a heavily reducing medium with high solubility limits for steel components and only a small number of metals and compounds will survive the exposure to the liquid breeder with no or very low attack. In earlier work [1, 2, 3] it was shown that reduced activation ferritic-martensitic (RAFM) steels (e.g. MANET, F82H-mod., EUROFER 97) can be coated with Al by a Hot-Dipping Process (HDA Process). To generate in surface near areas protective scales special heat treatments have to be performed to convert the deposited Al into Fe – Al phases. Hot Dipping Aluminisation and subsequently heat treatments at optimized temperatures and exposure times showed that the primarily during the dipping step formed metallic Al scale and the already formed Al-rich and brittle Fe<sub>2</sub>Al<sub>5</sub> phase can be transformed into more softer ones (e.g. α-Fe(Al) and FeAl. In compatibility tests [2] at 480°C in flowing Pb-17Li such samples showed excellent corrosion behavior without visible attack up to about 10,000 h exposure time. Fig. 1 and Fig. 2 depict the microstructure of RAFM samples coated by HDA process without and with subsequently performed heat treatment.

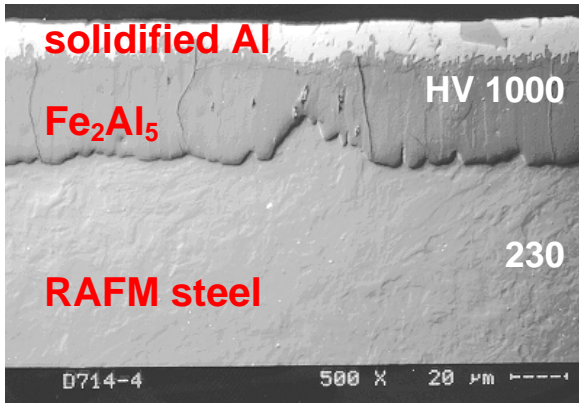


Fig. 1: Micrograph of RAFM-steel after dipping into an Al-melt at 700°C for about 30 s.

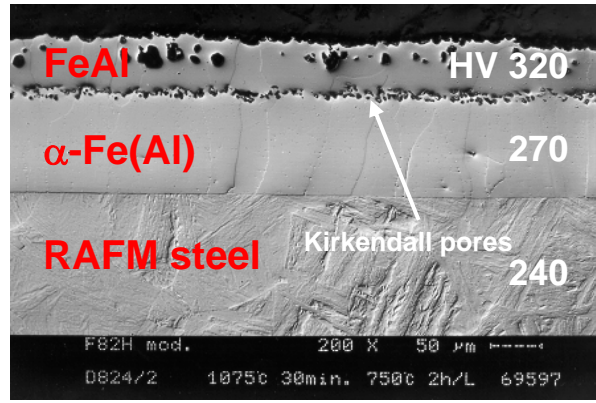


Fig. 2: Micrograph of heat treated sample at 1040°C/0.5h and 750°C/1h.

By HDA process coated EUROFER samples showed similar metallurgical behavior. However, due to other tempering conditions for optimal ferritic-martensitic structure optimized heat treatments with reduced temperature compared to the earlier tested RAFM steel (e.g. MANET) have to be analyzed and applied. Fig. 3 (right part) shows the cross section of a EUROFER sample coated by HDA and exposed to Pb-17Li in PICOLO loop (testing temperature 480°C, 0.22m/s flow velocity) after heat treatment at 980°C for 0.5 h and 760°C for 1.5 h, respectively. Fig. 3 (left part) gives the corresponding EDAX line scan together with the formed phases during the heat treatment. The cross section indicates that the desired phase formation known from the MANET steel coating was not completely reached due to not fully optimized annealing durations. However, the not optimally reacted Al scale (some amount of brittle FeAl<sub>2</sub> phase is still present) survived more than 6000 h exposure to Pb-17Li. For comparison uncoated EUROFER would show a thinning by corrosion attack of about 75 μm under the same conditions in PICOLO loop.

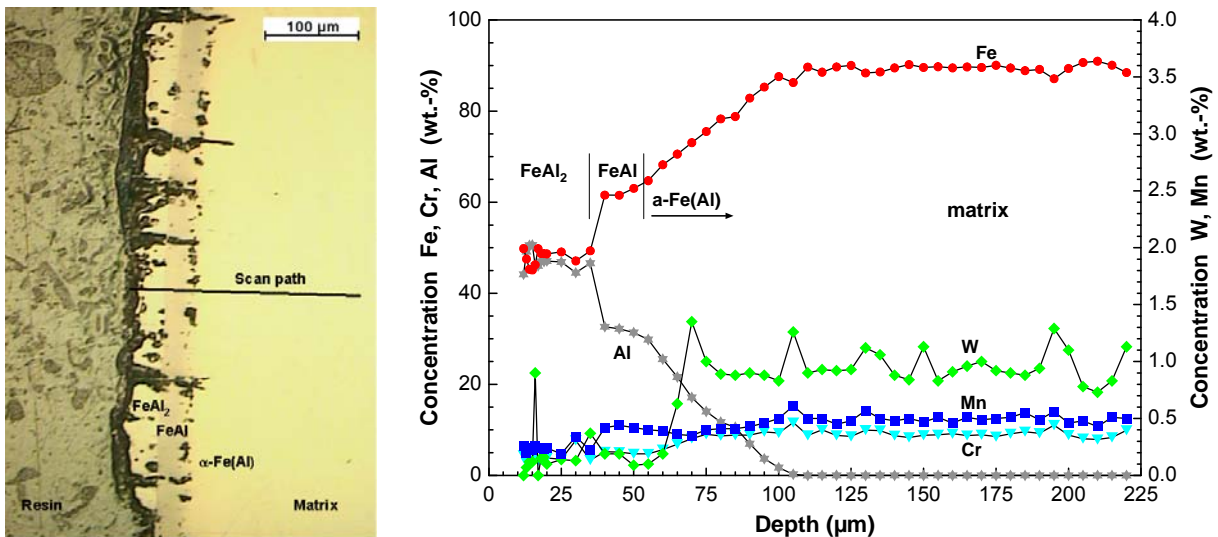


Fig. 3: Microstructure of Al coated EUROFER sample after exposure to Pb-17Li in PicoLO loop for 6292 h at 480°C with marked scan path (left) and line scan (right) for the main steel components and Al coming from coating process.

These earlier performed Al coating series indicated clearly that protective corrosion barriers can be formed on EUROFER structures and will successfully survive long term exposure to flowing Pb-17Li. However, the analyses performed showed that the Al amount deposited on top of RAFM steels by applying the HDA process is rather high and contradicts with the low activation criteria. Activation calculations indicated the demand to reduce this amount. Due to the fixed dipping temperature - by the melting point of Al - HDA can not fulfill this requirement. Another negative point of the HAD process is the fact that complex structures may be

coated only under extreme difficulties and therefore an industrial application will be strongly limited.

These positive results in testing Al based corrosion barriers triggered the search for more flexible Al coating technologies compared to the dipping process. The main requirements were a clear control of the deposited Al amount, homogeneous thin Al scale deposition and also working at complex structure with outer and inner surfaces (e.g. inside of tubes). The performed analyses of deposition methods favored electrochemically based processes to fit these requirements most closely. The result in R&D work on such innovative processes was the development of the ECA process. The abbreviation ECA is standing for **E**lectro-**C**hemical **A**luminum deposition.

### Al based barriers by ECA process

The corrosion testing in the PICOLO loop showed that at least at envisaged operation temperatures of TBM's at 550°C anti-corrosion barriers may be required to reduce corrosion attack to acceptable limits for the structure material EUROFER which is exposed to flowing Pb-17Li and bring down the risk of loop plugging due to formation of precipitates in cooler sections resulting from the high amount of dissolved steel components in the corrosion attacked areas. The previously performed examination of Al coated showed the potential of Al scales in solving / suppressing this dissolution behavior by Pb-17Li and defined the requirements for industrially applicable coating methods. Electro-chemical deposition is such a tool, however, Al cannot be deposited from aqueous systems like usual in noble metal handling caused by its high ability in formation of oxides.

Thus metallic Al deposition has to be performed in water and oxygen free environment. Organometallic complex electrolytes fulfill such requirements as nonaqueous solvents and were used for the Al deposition under inert gas atmosphere. In contrast to the dipping method HDA this electro-chemically based deposition of Al (ECA process) works at low temperatures in the range between RT and 100°C and no simultaneous reaction takes place with the steel during coating. A clearly separated Al scale is present after finishing the Al deposition. The Al scale thickness can be easily controlled and adjusted by process parameters e.g. deposition current or deposition time. The performed coating tests with pre-selected / envisaged Al scale thickness of 5 and 20 µm showed homogeneous covering of the EUROFER test pieces, good adhesion and high reproducibility as can be seen from the micrographs (Fig. 4).

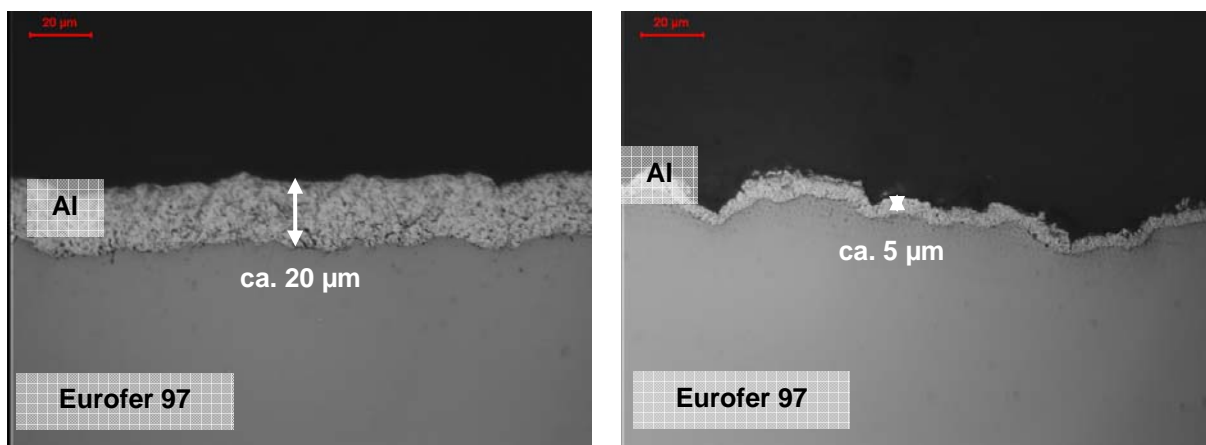


Fig. 4: Micrographs of EUROFER steel sheets (as rolled quality) coated with 5 and 20 µm homogeneously deposited Al by ECA process before heat treatment.

Similar to the formerly applied HDA process also the newly developed coating process (ECA) based on electro-chemical deposition of Al on EUROFER surfaces requires an additional second step to generate the protective Al-Fe surface scales as barriers. Optimized heat treatment parameters were evaluated by systematically performed annealing series for con-

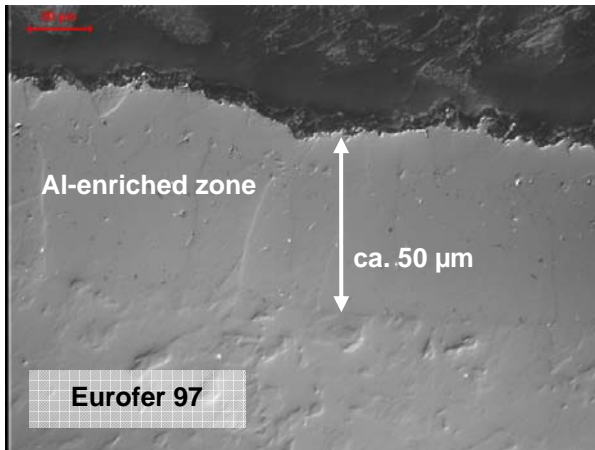


Fig. 5: Micrograph of EUROFER coated with 20 µm Al by ECA after heat treatment.

verting the deposited Al into the desired protective scales known from the HDA process. The micrograph presented in Fig. 5 shows such a structure which was formed by heat treatment at 960°C for 0.5 h and annealing at 760°C for 1.5 h. The Al enriched zone has a width of about 50 µm well below the thickness of scale sequences observed in HDA processed samples. The depicted microstructure shows additionally that the formed Al enriched zone has homogeneous thickness and follows rather exactly the rough surfaces profile of the as rolled surface quality.

### Fabrication of specimens for compatibility testing by ECA process

The above described newly developed ECA process for EUROFER coating by Al scales with protective barrier functions was applied for manufacturing of different series of test samples. Under the basic size of the TW6-TTBC-005 task 2 different thicknesses of Al coating on one shape of samples had to be fabricated for delivery of the processed specimens to a TW6-TTMS-003 task of IPP-CR. To reach higher flexibility in compatibility testing and to gain additional experience in ECA coating potential cylindrically shaped specimens and flat samples with different surface quality were additionally processed. Thus 6 different types of samples (Table 1) are now existing for compatibility testing.

Table 1: Types and numbers of coated samples.

Type \ Al thickness	5 µm Al	20 µm Al
Cylindrical Ø 8 x 200 mm	7	7
Flat as rolled 20 x 40 x 1.6 mm	19	20
Flat machined 20 x 40 x 2.0 mm	9	9

From each batch at least one reference sample was left without heat treat for analyzing the quality of coating and the deposited amount of Al by ECA. Also one reference sample without coating was manufactured for documentation of the raw material status. Fig. 6 shows the microstructure of EUROFER plates coated by 5 and 20 µm Al applying the ECA process. For both scale thicknesses an excellent and homogeneous covering of the rough surfaces inclusively the edge areas is realized. Same behavior was also found for the smooth milled plates as depicted in Fig. 7.

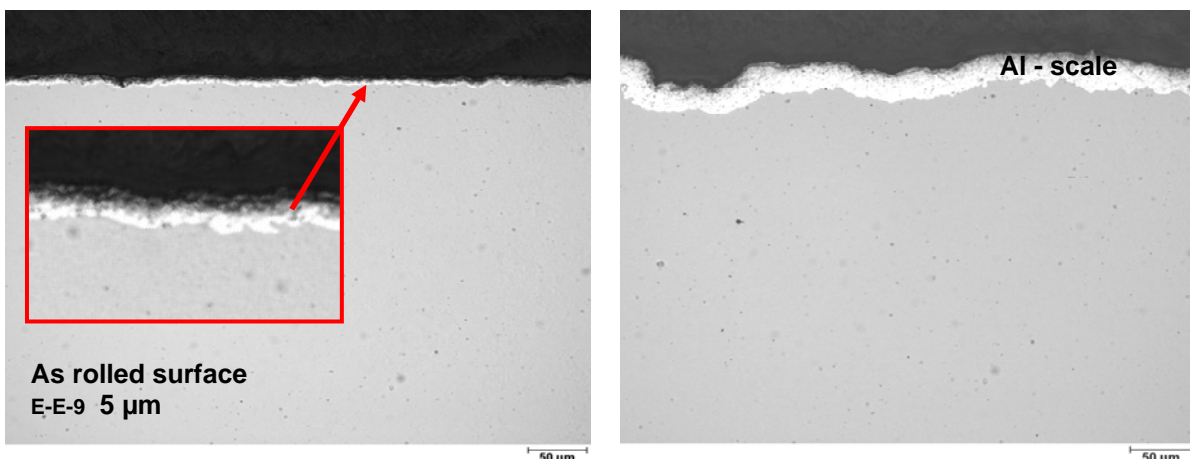


Fig. 6: Cross section of EUROFER plates (as rolled quality) after Al coating by ECA.

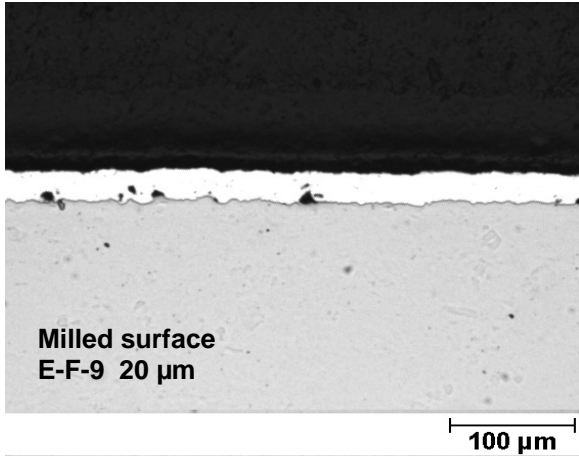


Fig. 7: Cross section of EUROFER plates (milled quality) after Al coating by ECA.

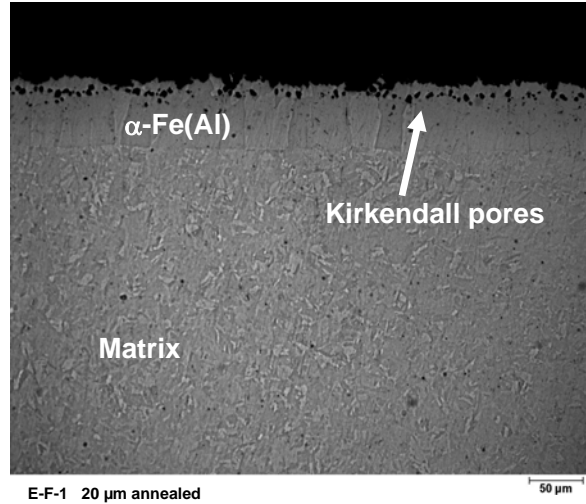


Fig. 8: Micrograph of heat treated Al coated EUROFER.

Typical Al coating data of the flat samples designed for testing under the TW6-TTMS- 003 task were:

**Typical coating data:**

- Sample size:** 20 x 40 x 1.6 or 2 mm
- Total surface:** F = ~ 18.4 cm<sup>2</sup>
- Deposited Al:** M = ~ 25.4 mg ( 5μm)
- Deposited Al:** M = ~ 101.5 mg (20μm)

All ECA coated samples were heat treated for formation of the protective Al-Fe scales at 980°C for 0.5 h and 760°C for 1.5 h, respectively. The metallographic examinations confirmed that the deposited Al scales reacted with the matrix (EUROFER steel) and formed the desired phases in the surface region. In Fig. 8 a micrograph is shown of a heat treated sample coated with an originally 20 μm thick Al scale. The Kirkendall pores visible in the surface near area are caused by difference in diffusion velocity of Fe into Al and Al into Fe during the metallurgical reaction. Clearly visible is also the solid solution of α-Fe(Al).

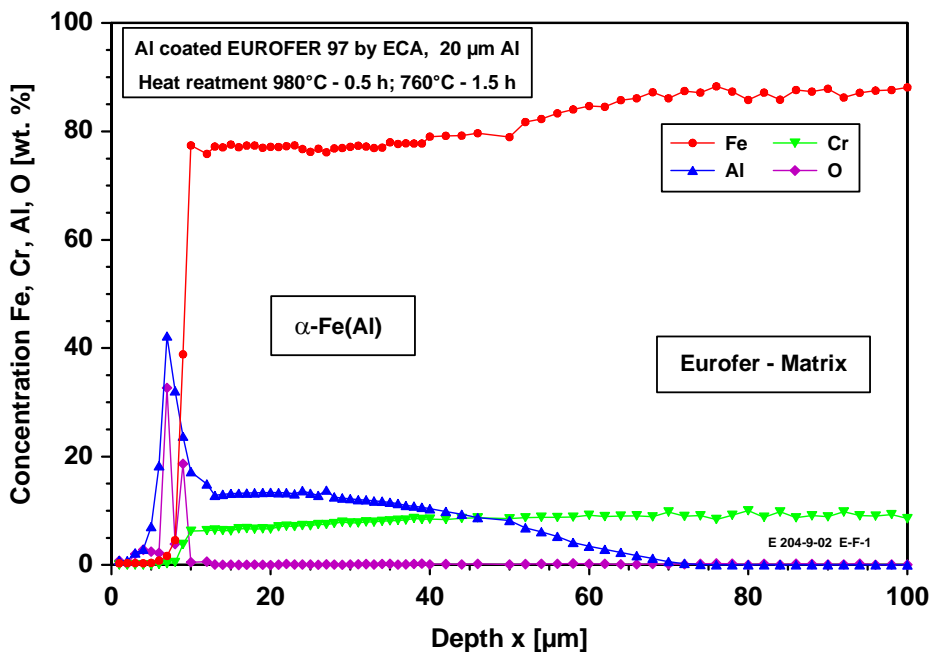


Fig. 9: Line scan of the coated sample depicted in Fig.8.

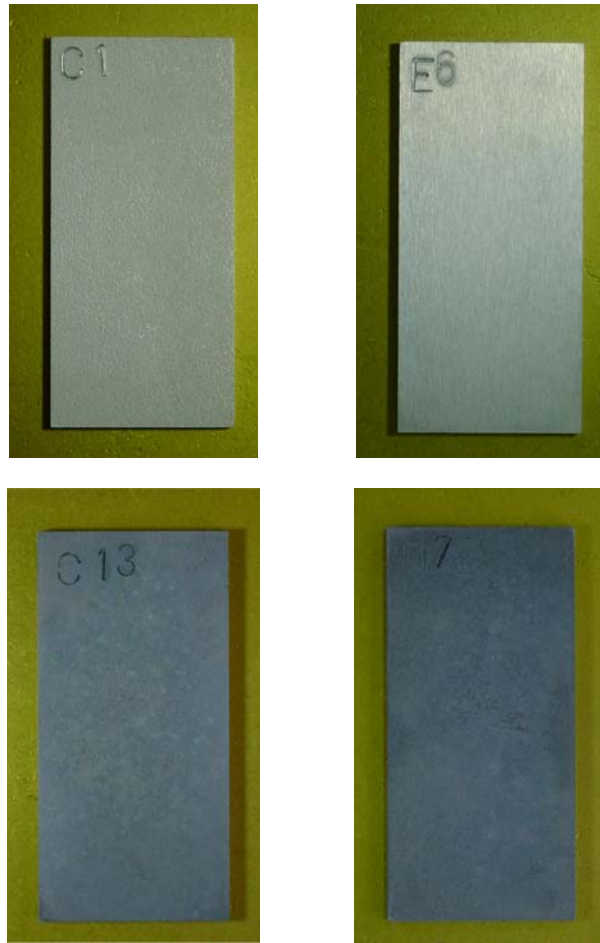


Fig. 10: ECA coated samples with rolled (C-series) and milled (E-series) surface after coating (top line) with a scale thickness of 5  $\mu\text{m}$  Al. Bottom line: Sample C 13 and D 7 represent the anneal ones with 5 and 20  $\mu\text{m}$  Al coating before heat treatment.

The changes of Al concentration in the surface near area was analyzed by performing line scans. Fig. 9 shows such a scan for a sample with milled surface after coating and heat treatment. The Al concentration decreases within the homogeneity range of the  $\alpha\text{-Fe(Al)}$  phase from about 20 (near the surface) to 0 at.% in contact with the matrix. The significant signal for Al and O near the surface may indicate the presence of an oxide surface layer.



Fig. 11: Cylindrical test samples ( $\varnothing = 8 \text{ mm}$ ) designed for corrosion testing in Pico loop.  
Top: Bare EUROFER  
Bottom: Al coated by ECA after heat treatment.

The performed quality analyses (destructive testing) were carried out on statistically selected samples of each batch and showed that Al deposition by ECA and the selected parameters for heat treatment generated the envisaged protectively acting corrosion barriers on the EUROFER samples with high quality and reproducibility. All other samples designed for the corrosion testing did not show any damages by visible checking and weight control. Fig. 10 depicts some of the fabricated flat samples for compatibility testing in flowing Pb-17Li.

For externally testing the two types of flat samples (20 x 40 mm) were fabricated as claimed in the TW6 task with Al scale thickness of 5 and 20  $\mu\text{m}$ . The first external testing series will use the samples with machined surface (Series E and F).

Fig. 11 shows cylindrical samples manufactured for testing in PICOLO loop.

## Conclusions

In total 6 series of samples with Al coating by the newly developed ECA process were successfully fabricated and analyzed. The amount of deposited Al could be significantly reduced to layers with 5 or 20  $\mu\text{m}$  scale thickness compared to the formerly used Lab process of Hot Dip Aluminisation. The performed analyses showed clearly that homogeneous Al scales could be deposited and that scale thickness can be controlled also at critical positions as edges, rear sides of samples or of cylindrical parts. The coating tests with the ECA process consisting of Al deposition and heat treatment demonstrated that an industrially relevant coating technology was developed and applied under this task to fabricate Al-based corrosion barriers. Reference samples of each batch were analyzed and will be stored for later comparison with samples exposed to Pb-17Li. The first external testing series will first use the flat samples with machined surface (Series E and F). A total number of 12 samples including the basic characterization is ready for delivery.

The performed development work in electrochemically based Al deposition showed a clear progress towards processing of barriers (corrosion and T- permeation) for TBM application also under industrially relevant conditions. The used organo-metallic complexes allowed an easy coating by Al, however, the compatibility tests are urgently needed to have a full qualification of the protective character of the formed scales and may show potential for future improvements in the fields of heat treatments, possible reduction of deposited Al amount or necessity of multi component coatings (e.g. Al plus W) which are within the potential of the improved new electrochemically salt based coating process ECX- a partner process of ECA.

### Staff:

M. Heck  
N. Holstein  
J. Konys  
W. Krauss  
J. Lorenz  
J. Novotny  
A. Skrypnik  
Z. Voss  
O. Wedemeyer

### Literature:

- [1] H.U. Borgstedt, H. Glasbrenner, Z. Peric, Corrosion of insulating layers on MANET steel in flowing Pb-17Li, J. Nucl. Mat. 212-215 (1994) 1501-1503
- [2] H. Glasbrenner, J. Konys, G. Reimann, K. Stein, O. Wedemeyer, The formation of aluminide coatings on MANET stainless steel as tritium permeation barrier by using a new test facility, Proc. 19th SOFT, Lisbon, Portugal, (1996), pp. 1423–1426.
- [3] J. Konys, W. Krauss, Z. Voss, O. Wedemeyer, Comparison of corrosion behavior of bare and hot-dip coated EUROFER steel in flowing Pb-17Li, J. Nucl. Mat. 367–370 (2007) 1144–1149.

## TTBC-006

### Helium-Cooled Lithium Lead: Magneto-Hydrodynamics and Liquid Metal Materials

#### TW5-TTBC-006 D 1

#### MHD Experiments on a 3D Relevant Mock-up of the HCLL TBM

The objective of the subtask is to investigate experimentally the magnetohydrodynamic (MHD) flow in a TBM-relevant test section for a Helium Cooled Lead Lithium (HCLL) blanket, in which a number of breeder units (BUs) arranged in columns are fed with liquid metal through poloidal manifolds. Each breeder unit contains five cooling plates that subdivide the box in slender ducts.

The liquid metal PbLi is circulated slowly through the blanket for tritium removal and purification while the heat is removed by helium. The magnetohydrodynamic interaction between the moving electrically conducting fluid and the magnetic field influences the flow distribution that has to be predicted and analyzed. Moreover, since all the walls are electrically conducting, the flow in neighboring fluid domains is electrically coupled by currents exchanging across common walls. As a result, the flow in each sub-channel is affected by the flow in all the other fluid domains and the velocity profile in adjacent ducts changes compared to that in a single channel.

Since a complete theoretical description for the HCLL blanket involving all the combined issues is very difficult, the major conclusions about 3D MHD flows in a TBM should be drawn from an experiment. This latter allows studying the 3D magnetohydrodynamic phenomena in the manifolds and the flow distribution in the breeder units for the fully coupled system.

For that reason a test section for experimental investigations of fusion relevant MHD flows in HCLL blanket modules has been inserted into the liquid metal loop in the MEKKA laboratory at the Forschungszentrum Karlsruhe. The mock-up is scaled down by a factor of two compared to the original TBM, but all the characteristic geometric elements like circular pipes, poloidal manifolds, connecting gaps at the back plate and at the first wall are considered according to the TBM design. Figure 1 highlights the complexity of the liquid metal path inside the 24 electrically coupled sub channels.

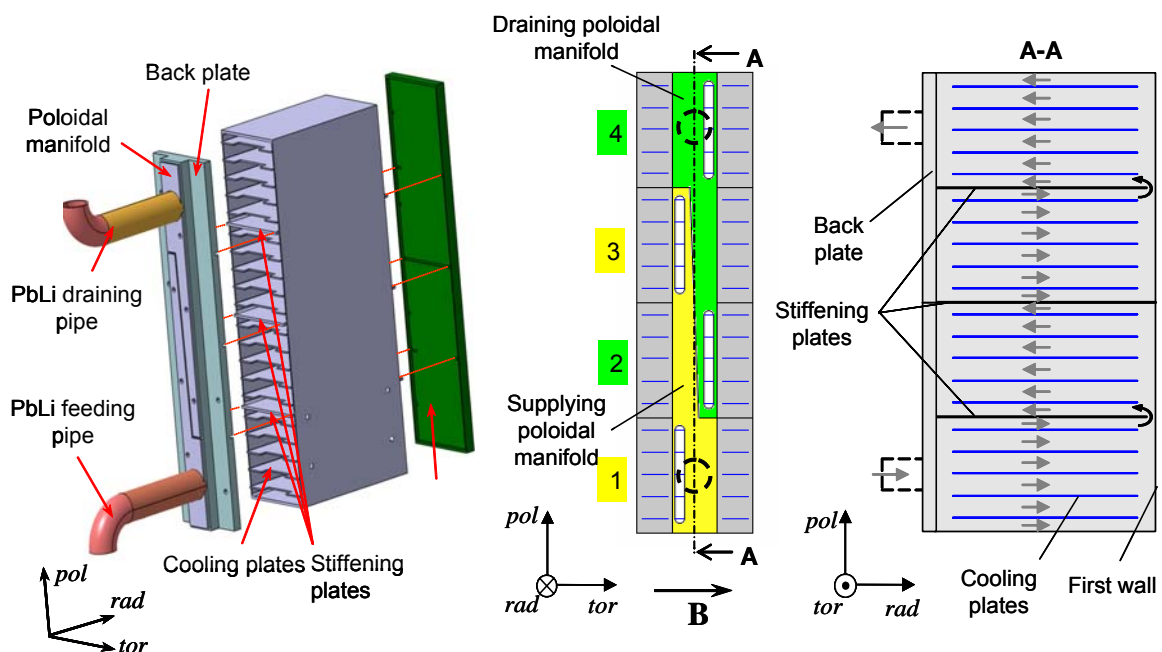


Fig. 1: Experimental test section and schematic layout of liquid metal flow in the BUs

The mock-up is installed in the liquid-metal (NaK) loop and measurements are ongoing:

- Leak tests have been performed, the liquid metal loop has been operated with electromagnetic and mechanical pumps, flow meters and pressure transducers have been calibrated.
- A wetting procedure has been carried out at 300°C for about 50 hours to remove impurities and oxides that can cover the internal surface of the test section.
- Insulating plates containing 600 electric potential sensors have been fully instrumented. The quality and the performance of the instrumentation on the plates have been checked by performing electric potential test measurements.
- The software used for controlling and recording pressure and electric potential data has been successfully tested.

First pressure measurements in the mock-up have been performed [1] showing that:

- The major part of the total pressure drop occurs in feeding and draining pipes and in poloidal manifolds.
- Additional pressure drop appears when the flow expands from the manifold into the breeder units passing through the narrow gaps at the back plate and when the fluid is collected into the draining manifold.
- Pressure drop in breeder units is small compared to that in feeding pipes and manifolds.

First experimental observations confirm qualitatively the results of asymptotic analyses [2], [3].

## **Numerical analysis**

### **HCLL blanket concept**

Fully developed MHD flows have been investigated numerically in four breeder units, each of them containing five internal plates according to the experimental mock-up [5], [6]. The numerical analysis focuses on the description of velocity and current distribution in the breeder units, for a pure toroidal magnetic field and an inclined one, namely a field with a poloidal component.

In the case of pure toroidal magnetic field, the currents induced in the cores between the cooling plates cross these internal walls and couple strongly the sub channels that form one breeder unit. As a consequence of that, in the slender ducts having same aspect ratio, a similar velocity profile is observed, which resembles the one in a channel with perfectly conducting side walls. This is characterized by uniform core flow and a slight increase at the walls parallel to the magnetic field. This strong electric coupling ensures a quite uniform flow distribution among cooling plates.

In the stiffening plates that separate adjacent breeder units and in the external side walls, the currents flow mainly in tangential direction and as a result a larger velocity appears at these side walls. No exchange of current between the breeder units is observed, corresponding to a weak electric coupling of these domains. These observations are summarized in Figure 2.

When a poloidal component of magnetic field is applied, internal layers aligned with the magnetic field  $\mathbf{B}$  develop and more complex current paths are present. This causes a stronger electric coupling of the flow across the BUs. The solutions for electric potential and velocity are inclined along the applied magnetic field and zones with locally reversed velocity compared to the main stream appear in the breeder units near the stiffening plates [5], [6].

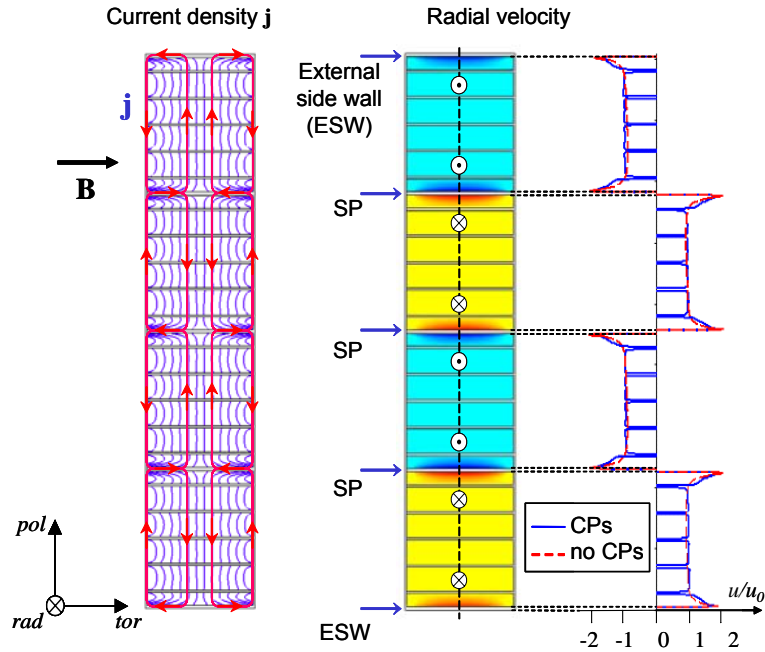


Fig. 2: Current and velocity distribution in 24 electrically coupled ducts forming 4 BUs.  $Ha=3000$ .

### DCLL blanket concept

Another liquid metal blanket concept that has been considered for testing in ITER is the Dual Coolant Lead Lithium (DCLL) blanket design. This advanced concept utilizes helium at high pressure and velocity to cool the ferritic steel structures, and slowly moving (10 cm/s or less) PbLi in the self-cooled breeder zone. In order to minimize the MHD pressure drop, in the present DCLL blanket design flow channel inserts (FCIs) made of silicon carbide composite material with low electrical conductivity are arranged inside the poloidal channels to electrically insulate the breeding zone from the walls. The inserts decouple electrically the PbLi flow from the steel walls by interrupting the current paths towards the conducting walls. Moreover, since the inserts have a low thermal conductivity, they act also as thermal insulation allowing for larger PbLi outlet temperature, i.e. higher energy conversion efficiency. The effects of electrical and thermal properties of these barriers on the velocity distribution in the blanket modules have to be carefully investigated.

Figure 3a shows a partial view of the liquid metal path inside the poloidal ducts. The liquid metal enters the blanket module through the annular region between two concentric circular pipes, flows upwards in the front parallel poloidal channels along the first wall. At the top of the breeder unit, according to a two-pass configuration, the PbLi turns by  $180^\circ$  and moves downwards near the back plate before it exits the module through the inner concentric pipe.

By cutting this assembly by means of the *rad - tor* plane marked by the dashed line and indicated as section A-A, the schematic cross-section displayed in Figure 3b is obtained. This represents the geometry used for the numerical study where six poloidal channels fully electrically coupled have been considered [7], [8]. Inside each duct a FCI is arranged. In order to reduce the primary stresses on these liners, an opening is present in one of the FCI sides, which allows equalizing the pressure in the internal and external fluid domains delimited by the insert.

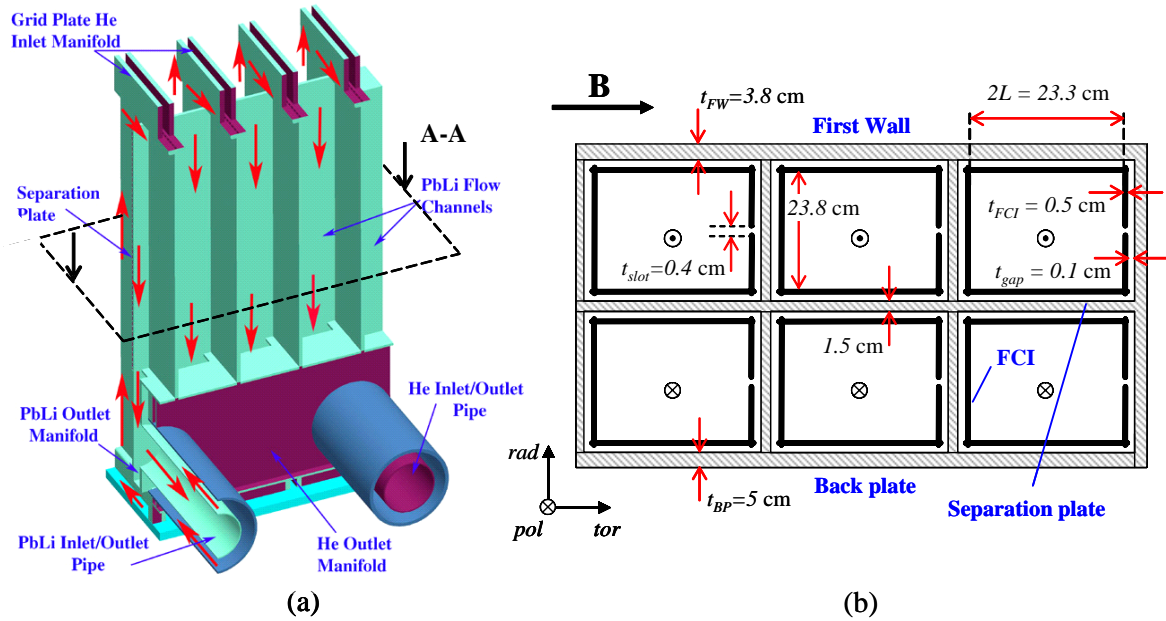


Fig. 3: (a) Partial view of PbLi flow path in the poloidal channels forming a DCLL blanket module. (b) Cross-section of the assembly showing six electrically coupled poloidal ducts as considered in the numerical analysis. The solid bold lines indicate the flow channel inserts inside each duct.

Figure 4 shows the velocity distribution when a toroidal magnetic field is applied. The velocity profile in the radial direction, shown in Figure 4b, is characterized by higher values along the FCI side walls parallel to  $\mathbf{B}$ . This rise of the velocity is due to the imperfect insulation given by the insert. Owing to a discontinuity in the electrical conductivity represented by the openings of the FCIs, internal layers develop along magnetic field lines in which the velocity is reduced. This velocity deficit may lead to a local increase of the temperature that has to be taken into account. Moreover, for sufficiently high electrical conductivity of the FCI the flow in the internal layer may even be reversed compared to the main stream. Across the side gaps between the insulating inserts and the separation plate, the velocity profile is almost parabolic (Figure 4c). Along magnetic field lines the velocity distribution, at some distance from the internal layer, resembles that of a classical Hartmann flow with uniform core velocity and thin boundary layers with strong velocity gradients.

Concerning the MHD pressure drop in the poloidal channels, it has been verified that, even in the most conservative case with relatively high electrical conductivity of the insulating barriers, the pressure losses caused by 2D currents are small and acceptable.

Staff:

- L. Bühler
- J.-J. Brinkmann
- S. Horanyi
- C. Mistrangelo
- K. Starke

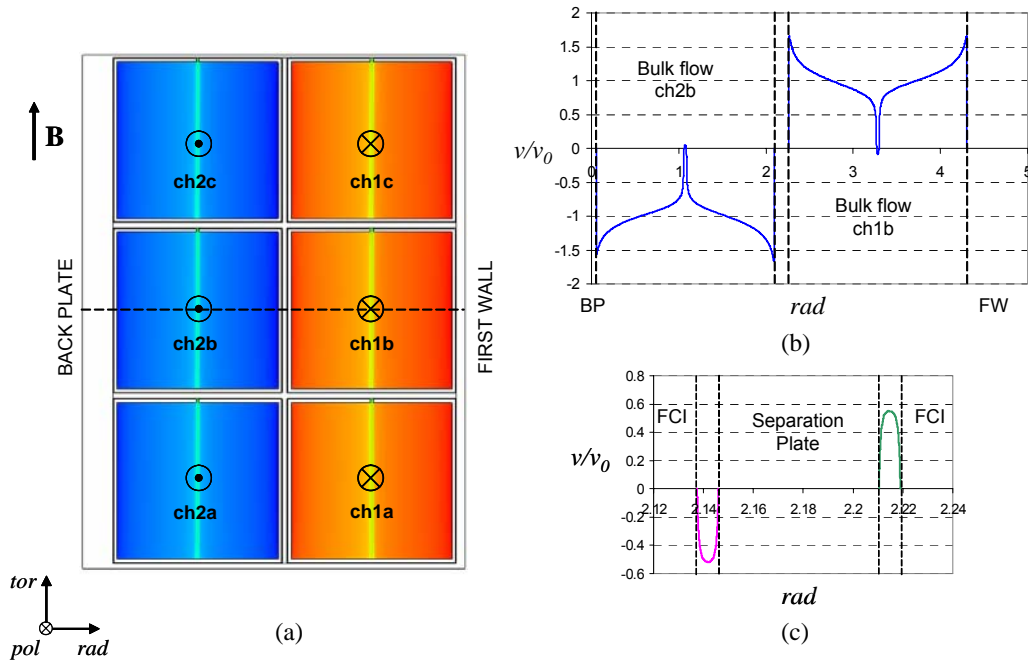


Fig. 4: (a) Contour plot of velocity in the assembly cross-section. The non-dimensional velocity is plotted along the radial direction (b) in the central internal ducts delimited by the liner, and (c) in the side gaps formed between separation plate and inserts, for  $Ha = 5000$  and  $\sigma_{FCI} = 500 \Omega^{-1}m^{-1}$ .

### Literature:

- [1] K. Starke, L. Bühler, S. Horanyi, 2007, Experimental investigations of liquid-metal MHD flows in a mock-up of a HCLL Blanket (poster), 8th International Symposium on Fusion Nuclear Technology (ISFNT-8).
- [2] L. Bühler, 2005, Magnetohydrodynamic pressure-driven flows in the HCLL blanket, *Fusion Engineering and Design, Volumes 75-79, 2005, pp. 923-926*.
- [3] L. Bühler, L. Giancarli, 2005, Magnetohydrodynamic flow in the European HCLL blanket concept, Technical report FZKA-7069, Forschungszentrum Karlsruhe.
- [4] L. Bühler, S. Horanyi, C. Mistrangelo, 2007, Interpretation of LEVI velocity signals in 3D MHD flows, 8th International Symposium on Fusion Nuclear Technology (ISFNT-8).
- [5] [5C. Mistrangelo, L. Bühler, 2007, Electric flow coupling in the HCLL blanket concept, 8th International Symposium on Fusion Nuclear Technology (ISFNT-8).
- [6] C. Mistrangelo, 2007, Magnetohydrodynamic flow in a mock up of a HCLL blanket, Technical report FZKA 7312, Forschungszentrum Karlsruhe.
- [7] C. Mistrangelo, A. R. Raffray, 2007, MHD analysis of dual coolant Pb-17Li blanket for ARIES-CS, *Fusion Science & Technology, Volume 52 (4), pp. 849-854*.
- [8] C. Mistrangelo, 2007, MHD and corrosion analysis of a Dual Coolant PbLi blanket modules for ARIES-CS, Technical report FZKA 7311, Forschungszentrum Karlsruhe.

# **Materials Development Structural Materials**



**EFDA/06-1520 (TW6-TTB-EUROFER)**

**Support and Follow-up of the EFDA/06-1903 Art. 7 Contract for Procurement of EUROFER for the TBM Fabrication Technology Trials and Mock-ups**

**Objectives**

The main objective of this task is to support the EFDA Art. 7 contract 06-1903 for the procurement of app. 11 tonnes of EUROFER 97 RAFM steel in various semi-finished product forms. This material shall be used for fabrication technology trials and to build various components and mock-ups of Test Blanket Modules (TBM). An additional goal is to check the reproducibility of properties compared to two batches of EUROFER 97 available from the previous fabrications and to assess the achievable limits of reduction of detrimental impurities like Nb, Mo, Ni, Cu, Al, Co.

In order to follow-up the EUROFER fabrication process, meetings (including kick-off and acceptance meetings) with the steel manufacturer have to be organised. If necessary, intermediate meetings to resolve questions arising during the fabrication, in particular the problems arising during rolling of thick plates (which have not been produced so far) must be organised. The outcome of the meetings has to be reported to EFDA and a final technical report describing EUROFER fabrication process details and results of the performed tests and controls has to be prepared.

**Status of work**

After a Europe-wide call for tender for the production of about 11 tonnes of EUROFER 97 RAFM steel in various product forms (see table 1) Saarschmiede was assigned for the production according to the technical specification, which is close to the specification for the recent production of EUROFER 97-2. Table 2 gives the specified chemical composition of the material to be produced. After signature of the contract by the partners, a kick-off meeting was organised to discuss the critical issues for the production.

Table 1: Dimensions and quantity of semi-finished products.

Semi-finished product	Thickness	Area	Length	Mass	Total Mass
	mm	m <sup>2</sup>	mm	kg	kg
Plates <sup>*)</sup>	1	14		109	
	8	5		312	
	10	5		390	
	12	14		1310	
	16	15		1872	
	20	4		624	
	25	10		1950	
	32	10		2496	
	35	3		819	
	48	1		374	
					10256
Forging/ billet		100 x 100 mm <sup>2</sup>	3000	234	
					234
					10490

\*) All plates 1000 x 2000 mm<sup>2</sup>

Table 2: Specified chemical composition

<b>Element</b>	<b>Min. Value (wt%)</b>	<b>Max. Value (wt%)</b>	<b>Remarks</b>
Carbon	0.090	0.120	Target 0.11
Manganese	0.20	0.60	Target 0.4
Phosphorus		0.005	
Sulphur		0.005	
Silicon		0.050	
Nickel		0.01	ALAP
Chromium	8.50	9.50	Target 9.0
Molybdenum		0.005	ALAP
Vanadium	0.15	0.25	
Tantalum	0.10	0.14	Target 0.12
Tungsten	1.0	1.2	Target 1.1
Titanium		0.02	
Copper		0.01	ALAP
Niobium		0.005	ALAP
Aluminium		0.01	ALAP
Nitrogen	0.015	0.045	Target 0.030
Boron		0.002	ALAP
Cobalt		0.01	ALAP
As+Sn+Sb+Zr		0.05	Target
Oxygen		0.01	

## Outlook

The production is according to plan. The delivery of plates ex works is scheduled for beginning of November 2008.

### Staff:

R. Lindau

**TTMS-001  
Irradiation Performance**

**TW2-TTMS-001b D 5  
Tensile, Charpy and Fatigue Specimen Testing after Neutron Irradiation up to 15 dpa in the Range of 250°C - 450°C, Completion of the Irradiation and Post-Irradiation Examination**

**Objectives**

8-10%Cr-WTaV steels are a successful material for the nuclear use in a wide temperature range. Such advanced martensitic steels are leading candidates for fusion structural components. They are interesting due to their resistance to void swelling, and good balance of different physical and mechanical properties. However, a critical effect of low temperature irradiation-induced hardening and embrittlement occurs in the range of 250 – 350 °C.

In the HFR IIb SPICE irradiation programme the emphasis is put on the investigation of irradiation induced embrittlement and hardening in the newly developed RAFM steel EUROFER 97 and a first alloy EUROFER 97-ODS-HIP. Due to the primary subjects of He formation in the RAFM steels, three heats were melted with different <sup>nat</sup>B – and <sup>10</sup>B –contents. Further alloys as e. g. the internationally investigated IEA alloy F82H mod., OPTIFER Ia and II were added to the irradiation for comparison reasons.

The objective of the results presented in this report is to characterize a series of martensitic test alloys with various <sup>10</sup>B- and <sup>nat</sup>B-contents to investigate systematically the influence of neutron irradiation generated He on tensile properties and microstructures. The irradiation was performed up to an accumulated dose of ~15 dpa in the HFR. The achieved He concentration by <sup>10</sup>B(n,α)<sup>7</sup>Li generation was <10 appm He, ~80 appm He, ~415 appm He, and ~5800 appm He, respectively. Initial results of tensile tests, SEM, and TEM are reported in this study.

**Helium effect on tensile properties and microstructure of EUROFER 97**

Three alloys on the bases of the RAFM-steel EUROFER 97 were melted in 25 kg-heats each with different <sup>10</sup>B- and <sup>nat</sup>B-contents and compared with EUROFER 97 reference heat (7 tons), table 1. The optimized heat treatment was the same in all alloys: 1040°C 30 min + 760°C 90 min.

Table 1: Chemical compositions of the test alloys.

Heat	C	Si	Mn	P	S	Cr	Mo	Ni	Al
<b>EUROFER 97</b>	0.12	0.04	0.48	0.005	0.004	8.91	<0.001	0.02	0.009
<b>806</b>	0.109	0.020	0.602	0.0035	0.0030	9.31	0.002	0.005	0.001
<b>826</b>	0.095	0.031	0.395	0.0035	0.003	8.80	0.046	0.008	0.004
<b>825</b>	0.10	0.03	0.38	0.001	0.0025	9.00	0.028	0.006	0.004

Heat	B	Nb	Ti	V	W	N	Ta	Fe
<b>EUROFER97</b>	< 0.001 <sup>nat</sup> B	0.0017	0.001	0.2	1.08	0.02	0.14	Rest
<b>806</b>	0.0082 <sup>nat</sup> B	-	-	0.190	1.27	0.021	0.055	Rest
<b>826</b>	0.0083 <sup>10</sup> B	0.005	0.001	0.193	1.125	0.028	0.088	Rest
<b>825</b>	0.1160 <sup>10</sup> B	0.002	0.001	0.197	1.06	0.0255	0.08	Rest

Circular tensile specimens were fabricated with a total length of 38 mm, and a gauge length of 18 mm and 3 mm diameter. They were taken parallel to the rolling direction. Every irradiation temperature of 250, 300, 350, 400, and 450°C was taken twice. The accumulated neutron dose was ~15 dpa, as done with the Charpy and fatigue specimens.

After the irradiation, the specimens were transported to the hot cells of the FML (Fusion Material Laboratories) Forschungszentrum Karlsruhe to perform the tensile tests. All tests were carried out with a tensile velocity of 0.1 mm/min in the temperature range 250 – 450°C. Un-irradiated specimens were tested only at 20, 300 and 450°C.

Fractures and the microstructures were investigated by light and electron microscopy at specimens of the highest ultimate strength at 250 and 300°C and the highest irradiation temperature of 450°C. TEM specimens were cut transverse from the gauge length of the tensile specimens and compared with un-deformed material of impact tests. Material segregations and inclusions of B in the un-irradiated state were controlled by Auger-analysis. Hardness was measured by Vickers HV0.1.

### Tensile Properties

After the irradiation, the tensile tests were recorded fully instrumented in stress/strain diagrams. Every material condition was irradiated and tested by two specimens. In Fig. 1-3 all the tensile results of EUROFER 97, heat 806 and 826 are shown. EUROFER 97, heat 806 and 826 had the highest strength at 250 - 300°C. At higher irradiation and test temperatures up to 450°C, the data reached the level of un-irradiated materials, but still with a reduction in elongation, due to the limitation of the thermal stability of interstitial type defects and small precipitates. The strength of heat 826 (83 ppm <sup>10</sup>B; ~415 appm He) was systematically higher than of heat 806 (82 ppm <sup>nat</sup>B; ~450 appm He). As in the <sup>10</sup>B doped alloy all B is transmuted to He after 1 dpa has been reached. The additional induced strength increase of heat 826 compared to heat

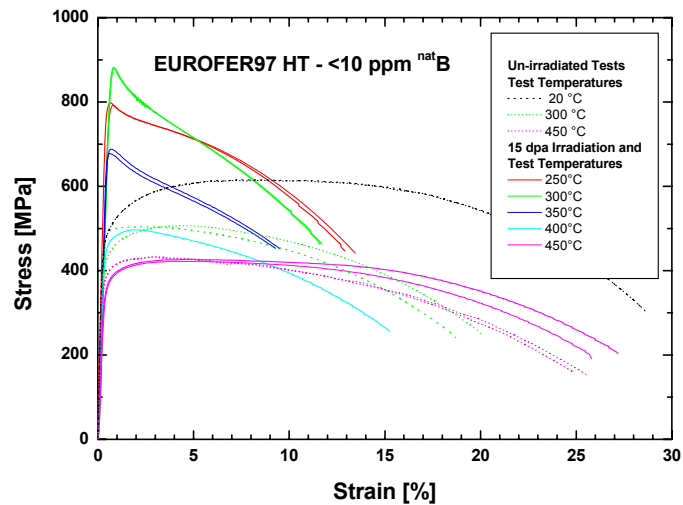


Fig. 1: Tensile properties of EUROFER 97 HT (HT = heat treated).

806 (300 – 350°C) can be interpreted as a direct proof, how He contributes to irradiation induced hardening. The absolute strength values of EUROFER97 can only be compared in a relative manner to these test heats, because it has been produced as a large batch. The third test heat 825 (1160 ppm <sup>10</sup>B; ~5800 appm He) had a similar strength behavior, but, at lower temperatures, the specimens broke brittle after having reached stress levels of 700-850 MPa.

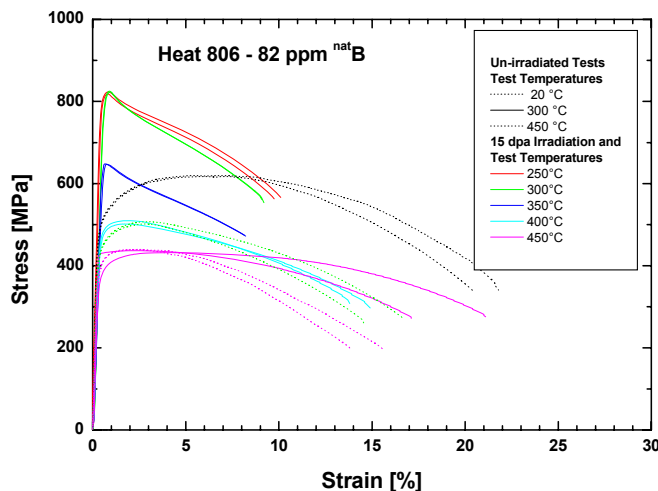


Fig. 2: Tensile properties of heat 806.

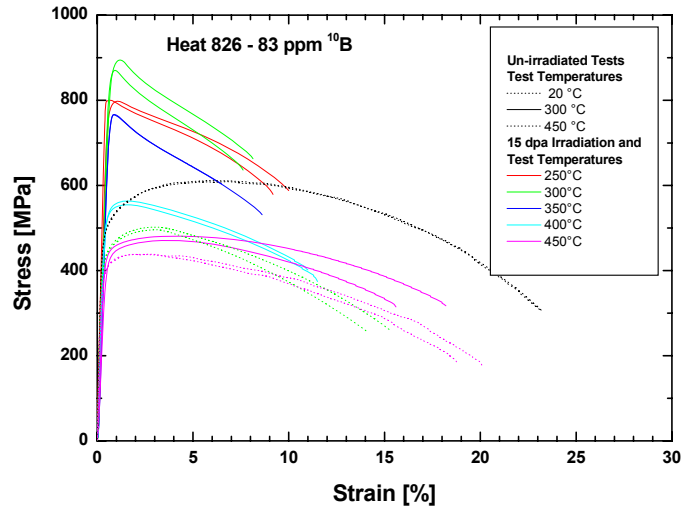


Fig. 3: Tensile properties of heat 826.

### Hardness and Fracture Behavior

Irradiation induced hardening is always a combination of He effect, interstitial loops, and small  $\alpha'$ -precipitates. But, He dependence could be seen in the comparison of heat 806 and 826. The  $^{10}\text{B}$  containing alloy 826 had higher strength than the  $^{\text{nat}}\text{B}$ -containing heat 806. This strengthening could be approved in hardness measurements, too. The higher concentration of He bubbles caused a  $\sim 10\%$  higher hardness resulting in a higher strength.

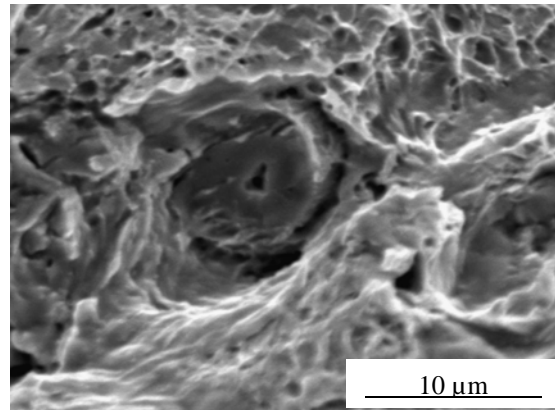


Fig. 4: Fracture area around a former B-precipitate in heat 826, irradiated and tensile tested at 300°C.

EUROFER 97, heat 806, and 826 broke always ductile with typical dimple formations in the fractures. In heat 826, small brittle areas could be found around former B-precipitates, Fig. 4. This effect is irradiation induced, and could be observed much more in heat 825. The fractures of heat 825 occurred much more brittle, mainly at grain boundaries.

### Microstructural Evolution

Before irradiation, the distribution of the alloyed boron was controlled by Auger-analysis. In heat 806 and 826 some B inclusion could be detected. Much more B inclusions and further precipitates as  $(\text{Cr,Fe})\text{B}$  and  $\text{B}(\text{C,N})$  were found in heat 825. In heat EUROFER97, just few inclusions of  $\text{MnS}$  and oxides were detected.  $\text{TaC}$  and  $\text{M}_{23}\text{C}_6$  were dominant in all heats. Prior austenitic grain sizes of ASTM 6 - 7 were determined in the metallographic cuts. Heat 826 showed a tendency to coarser grain maybe due to the lower content of the primary carbide forming element Ta.

Microstructures of the heats were investigated in TEM in the un-irradiated and irradiated state after 250, 300 and 450°C. At the lower irradiation temperatures, the microstructure was characterized by dislocation loops and  $\alpha'$ -precipitates. Only very few areas with dislocation channeling were observed at 300°C after tensile tests. Only few individual He bubbles were detected in the matrix of EUROFER 97, while in heat 806 small clusters of He bubbles have been observed. An almost homogenous distribution of He bubbles was shown up in heat 826. As expected, in all heats the He bubbles size increases with irradiation temperature.

The presented pictures are from the un-deformed materials, Fig. 5-8. The microstructure of heat 825 was especially noticeable, Fig. 7. After the irradiation at 300°C, a homogenous distribution of bubbles could be seen in the matrix, but, after 400°C irradiation, there was a bi-modal distribution of bubbles. Fig. 9 shows an example of tensile tested microstructure of EUROFER 97 at 300°C. The dislocation loops were oriented in a very pronounced manner as lines along to the gliding directions of the bcc crystal structure.

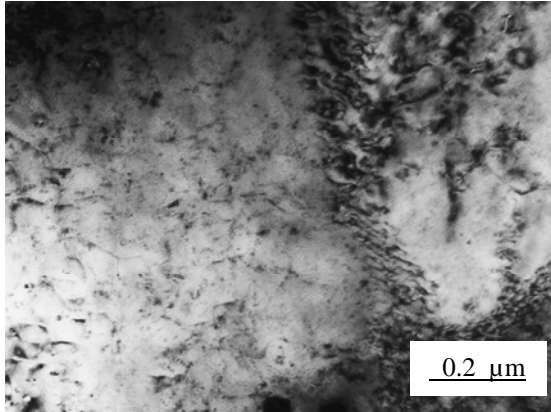


Fig. 5: Microstructure of EUROFER 97 HT (<10 appm He); irradiated at 250°C.

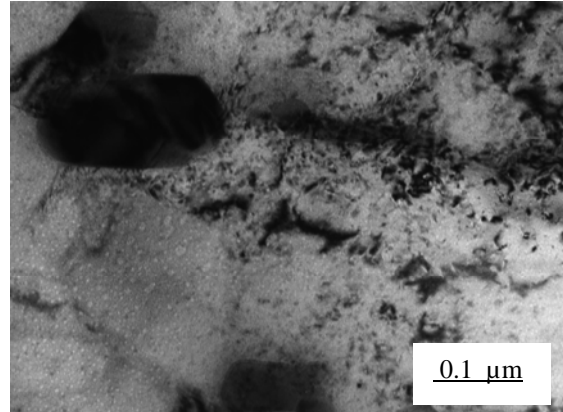


Fig. 6: Microstructure of heat 806 (~80 appm He); irradiated at 250°C.

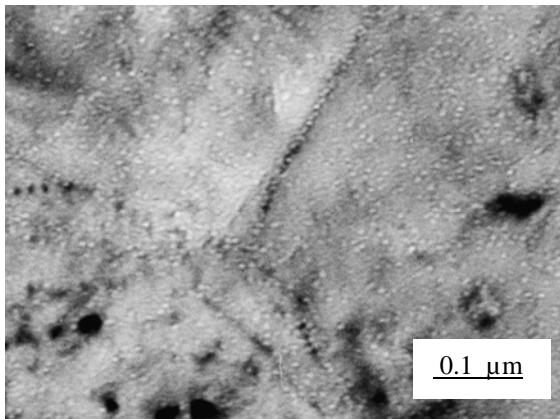


Fig. 7: Microstructure of heat 826 (~415 appm He); irradiated at 250°C.

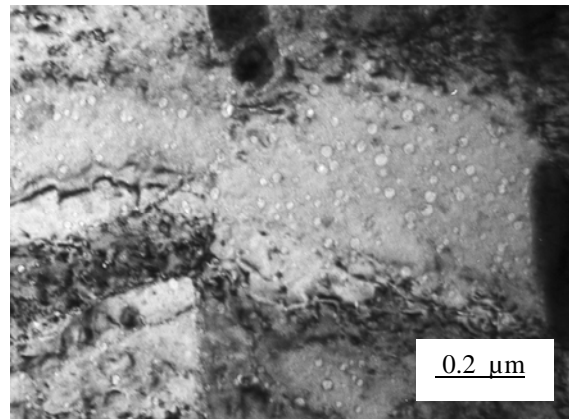


Fig. 8: Microstructure of heat 825 (~5800 appm He); irradiated at 300°C.

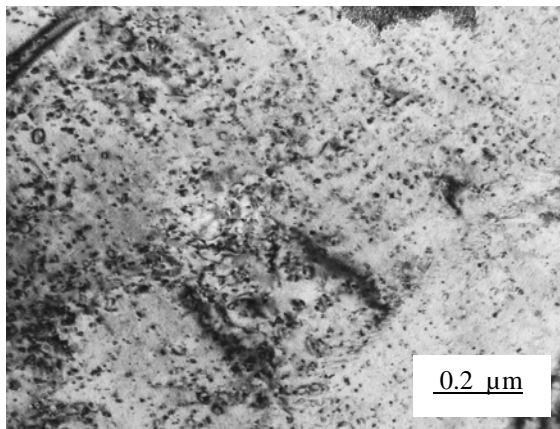


Fig. 9: Microstructure of EUROFER 97 HT (<10 appm He); irradiated and tensile tested at 300°C.

## Conclusions

- The expected strengthening at lower temperatures at 250 – 300°C irradiation and test temperature was confirmed.
- The hardening and strengthening in the test alloys were generated by dislocation loops,  $\alpha'$ -precipitates, and to a less extend be He.
- After tensile tests of 300°C, very pronounced lines of dislocation loops have been observed with a typical line distance of ~20  $\mu\text{m}$ .
- Heats with the same B contents, one with  $^{nat}\text{B}$  and the other with  $^{10}\text{B}$  alloyed, showed the clear difference irradiation induced strengthening due to the generated different He concentrations.
- The thermally induced recovery and the dissolved hardening effect of dislocation loops and  $\alpha'$ -precipitates could be observed by TEM in specimens of irradiation temperature >400°C.
- A summary of He bubble size and density has been analyzed as a function of He content and irradiation temperatures.

The investigations of the further alloys are still in work and will be published in a forthcoming report.

## Staff

J. Aktaa  
B. Dafferner  
J. Ehrmann  
E. Gaganidze  
M. Holzer  
S. Lautensack  
E. Materna-Morris  
A. Möslang  
H. Ries  
R. Rolli  
H.-C. Schneider

## Literature:

- [1] E. Gaganidze, H.-C. Schneider, B. Dafferner, J. Aktaa, J. Nucl. Mater. 355 (2006) 83.
- [2] E. Gaganidze, H.-C. Schneider, B. Dafferner, J. Aktaa, J. Nucl. Mater. 367-370 (2007) 81
- [3] E. Gaganidze, B. Dafferner and J. Aktaa, Proceedings of 2006 MRS Fall Meeting, Nov 27 Dec. 1, Boston, USA, MRS Symp. Proc.; 981E, Electronic-Only Publication.
- [4] E. Gaganidze and J. Aktaa, "The role of He on the embrittlement of RAFM Steels", Proceedings of the 8th International Symposium on Fusion Nuclear Technology, Sept. 30 – Oct. 5, 2007, Heidelberg, Germany
- [5] E. Gaganidze, C. Petersen and J. Aktaa, "Helium Embrittlement of RAFM Steels", Proceedings of the 13th International Conference on Fusion Reactor Materials, December 10-14, 2007, Nice, France
- [6] E. Materna-Morris, A. Möslang, R. Rolli, H.-C. Schneider, "Effect of Helium on Tensile Properties and Microstructure in 9%Cr-WVTa-Steel after Neutron Irradiation up to 15 dpa between 250 and 450°C", Proceedings of the 13th International Conference on Fusion Reactor Materials, December 10-14, 2007, Nice, France

## TW2-TTMS-001b D 9

### Fast Reactor Irradiation up to 30 dpa, at 340°C of Tensile, Charpy and LCF RAF/M Specimens, Completion of the PIE

#### Objectives

In an energy generating fusion reactor structural materials will be exposed to very high levels of irradiation damage of about 100 dpa. Due to the fact, that fast reactor irradiation facilities in Europe are not available anymore, a cooperation with the Russian institution SSC RF RIAR has been implemented. The irradiation project is named "ARBOR 1" (Latin for tree). Impact, tensile and low cycle fatigue specimens of Reduced Activation Ferritic/Martensitic steels, e.g. EUROFER 97, F82H mod., OPTIFER IVc, EUROFER 97 with different boron contents and ODS-EUROFER 97 have been irradiated in a fast neutron flux ( $> 0.1$  MeV) of  $1.8 \cdot 10^{19} \text{ n m}^{-2}$  at a temperature less than 340°C up to  $\sim 30$  dpa. Mechanical PIE is terminated at SSC RF RIAR.

#### Status end of 2006

The tensile-LCF-testing facility for miniaturized mini tensile specimens and the instrumented impact testing facility for KLST specimens under remote handling conditions are operating in the hot cells of SSC RF RIAR. All Impact and tensile tests have been performed.

#### PIE of ARBOR 1: Low Cycle Fatigue tests

Low activation steels reach in the lower total strain ranges,  $\Delta\epsilon_{\text{tot}} < 1\%$ , at 30 dpa irradiation damage and 330°C after LCF loading higher numbers of cycles to failure than unirradiated material. To confirm this behavior more experiments are necessary due to the high scatter of LCF data.

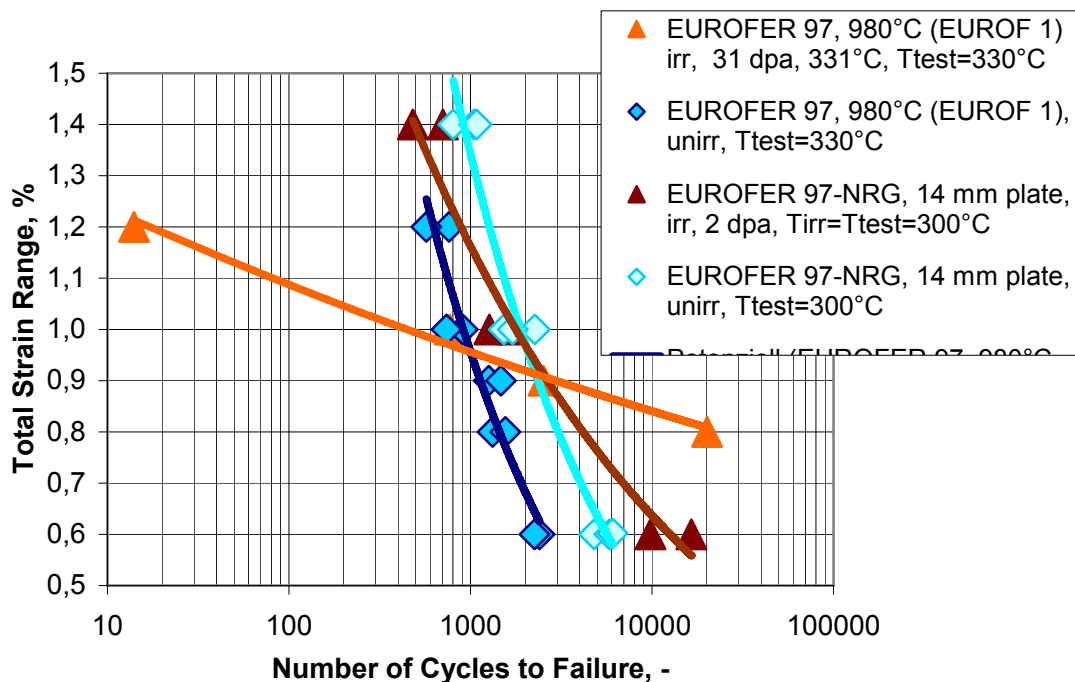


Fig. 1: Comparison of irradiation dependence on the LCF behaviour of EUROFER 97.

The ARBOR 1 LCF tests have been performed on mini-tensile-LCF specimens with a strain rate of  $3 \times 10^{-3} \text{ s}^{-1}$ . The comparison of irradiated and unirradiated cyclic loaded specimens of EUROFER 97, shown in Fig. 1, leads to an ambiguous behaviour. Even if the specimen size and raw materials for specimens preparation for the data of the laboratories taken for comparison are different, the findings are similar.

The ARBOR 1 results of the 31 dpa irradiation damage at  $331^\circ\text{C}$  and - taken for comparison - NRG results of an 2 dpa irradiation damage at  $300^\circ\text{C}$  [1] can be described by two effects. The first one occurs at high total strain ranges,  $\Delta\varepsilon_{\text{tot}} > 1\%$ , where the material is loaded remarkably over the yield stress point. Therefore in the second cycle no additional strain hardening takes place and thus the numbers of cycles to failure are smaller than under unirradiated conditions. Furthermore this effect increases with increasing irradiation damage.

The second effect occurs at low total strain ranges,  $\Delta\varepsilon_{\text{tot}} < 1\%$  where the numbers of cycles to failure of irradiated specimens are increasing. Analysing the hysteresis loops, very narrow loops are recorded with little plastic strain contribution only. This is due to the irradiation induced damage, which raised the yield stress point above the elastic strain range with increasing irradiation damage.

Also for 31 dpa irradiated F82H mod. (Fig. 2) a similar tendency was found in LCF testing, but the increase in numbers of cycles to failure for lower total strain ranges is not that high as for EUROFER 97.

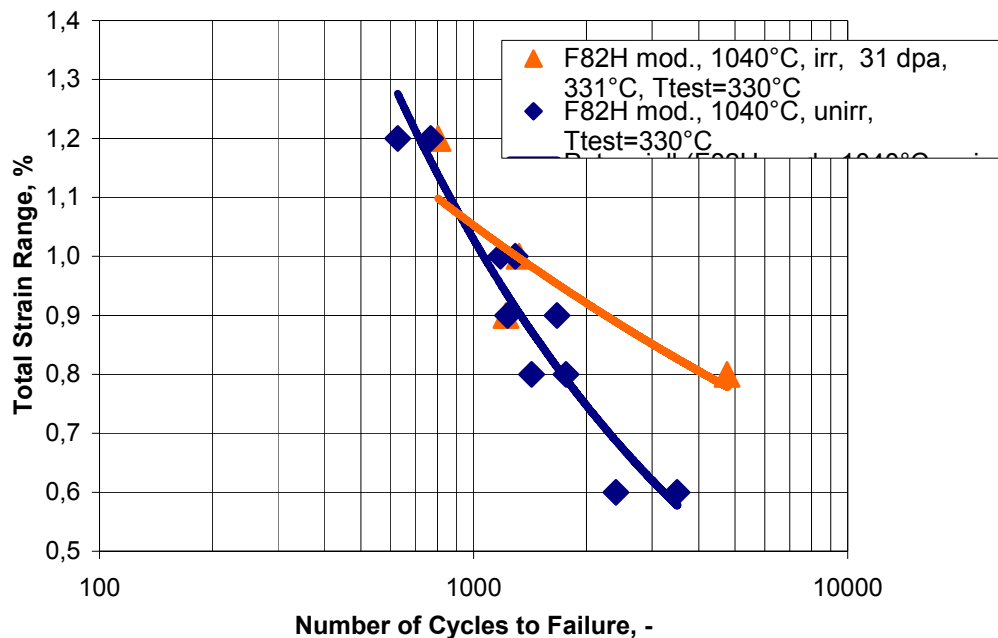


Fig. 2: Comparison of irradiation dependence on the LCF behaviour of F82H mod.

As ODS-EUROFER 97 with 0.5%  $\text{Y}_2\text{O}_3$  had also been included in the ARBOR 1 irradiation, the results of LCF testing of these specimens after the irradiation to 31 dpa damage at  $331^\circ\text{C}$  seem really encouraging. In Fig. 3 the LCF behaviour after irradiation is compared to that of unirradiated specimens. Even if the material reaches in the unirradiated state at higher total strain ranges,  $\Delta\varepsilon_{\text{tot}} > 1\%$ , the lowest numbers of cycles to failure, compared to EUROFER 97 and F82H mod., the increase of numbers of cycles to failure in the lower total strain ranges,

$\Delta\varepsilon_{\text{tot}} < 1\%$ , is remarkable. After irradiation for low total strain ranges higher number of cycles to failure could be achieved than for F82H mod.. The above mentioned tendency of the irradiation influence was found also on this material.

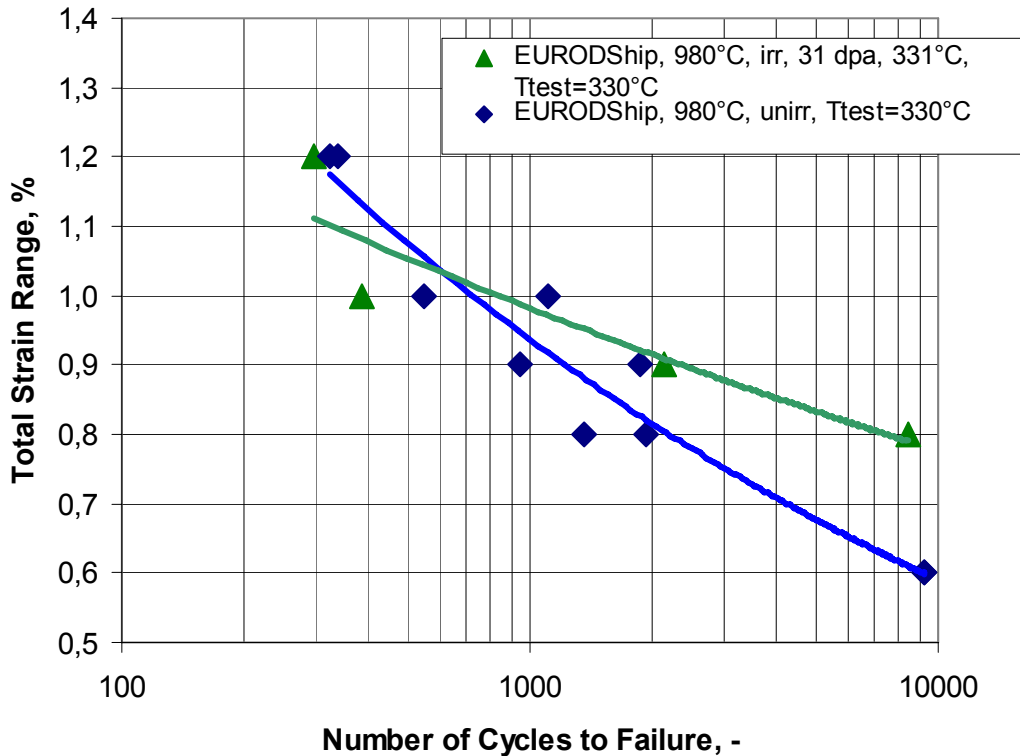


Fig. 3: Comparison of irradiation dependence on the LCF behaviour of ODS-EUROFER with 0,5 %  $Y_2O_3$ .

Low activation steels reach in the lower total strain ranges,  $\Delta\varepsilon_{\text{tot}} < 1\%$ , at 30 dpa irradiation damage and 330°C after LCF loading higher numbers of cycles to failure than unirradiated material. To confirm this behavior more experiments are necessary due to the high scatter of LCF data.

Staff:

M. Klotz  
C. Petersen  
M. Walter  
M. Lerch

Literature:

- [1] J.W. Rensman, "NRG irradiation testing: report on 300°C and 60°C irradiated RAFM steels", Final report on the EFDA Tasks TW2-TTMS-001a D 6 and TW2-TTMS-001b D 12, (2005).
- [2] C. Petersen, A. Povstyanko, V. Prokhorov, A. Fedoseev, O. Makarov and B. Dafferner: "Impact property degradation of ferritic/martensitic steels after the fast reactor irradiation 'ARBOR 1'", J. Nucl. Mater. 367-370 (2007) 544-549.
- [3] O. Yu. Makarov, A.V. Povstyanko, V.I. Prokhorov, A.E. Fedoseev, and C. Petersen: "Mechanical test methods in RIAR hot cells for subsized specimens of Fusion Reactor Materials", Proceedings of the 8. Russian Conference on Reactor Material Science on 21. -25. May 2007 at Dimitrovgrad, Russia, to be published.

- [4] C. Petersen, J. Aktaa, E. Diegele, E. Gaganidze, R. Lässer, E. Lucon, E. Materna-Morris, A. Möslang, A. Povstyanko, V. Prokhorov, J.W. Rensman, B. van der Schaaf and H.-C. Schneider: "Mechanical Properties of Reduced Activation Ferritic/Martensitic Steels after European Reactor Irradiations", IAEA- CN-149 Fusion21 proceedings, Wien, ISBN 92-0-100907-0 / ISSN 0074-1884.
- [5] C. Petersen, A. Povstyanko, V. Prokhorov, A. Fedoseev, O. Makarov and M. Walter: "Tensile and Low Cycle Fatigue Properties of different Ferritic/Martensitic Steels after the Fast Reactor Irradiation "ARBOR 1"", accepted for ICFRM-13, 9.-14.12,2007, Nice, France

## TW4-TTMS-001 D 1

## TW5-TTMS-001 D 2

# Fabrication and Irradiation of FE-54 enriched Samples to Study the Influence of He/dpa Ratio on Materials Degradation up to Medium Dose Level

### Overview

The structure components of future fusion reactors will suffer from specific irradiation damage, i.e. the ratio of helium production (in appm) to displacement rate (in dpa) varies around 10 appm He/dpa. Due to the lack of appropriate high energy neutron sources there seems to be only one promising way to generate such irradiation damages in a RAFM steel with common in-pile fission reactor irradiation experiments: If the content of natural iron would be replaced by the stable isotope Fe-54, helium production would be stimulated by the according (n, alpha) reactions. A significant advantage over the alternative boron-10 helium production technique would be a uniform helium distribution through the whole matrix.

Therefore, the goal of the task is to produce a heat similar to EUROFER using Fe-54 instead of natural iron. Then miniaturized charpy and tensile specimens with cores of Fe-54 substituted EUROFER steel have to be fabricated. Finally, an appropriate irradiation programme has to be planned and managed.

### Initial Status

During the first year the complete production processes were tested and optimized with natural iron. Then a first melt with about 200 g of the Fe-54 isotope was prepared. But unfortunately, just before casting the heat into the mold the ceramics crucible broke. Then the valuable heat flowed over graphite isolation and solidified mainly around the cooling coils of the furnace. Most of the material could be restored but the chemical composition changed significantly due to the contact with graphite: The carbon content ended at about 4 wt.%. After that accident a lot of different decarbonization treatments have been applied. In addition, more reliable crucibles have been tested and the volume of the melt has been reduced as well. Finally, with new parameters and with a BN (instead of aluminium oxide ceramics) crucible, another FE-54 EUROFER heat was produced using about 100 g of the isotope.

### Progress

First, the specimen fabrication process has been evaluated. This has been done by producing an experimental EUROFER heat with natural iron. Stripes have been cut and joined to EUROFER 97 plates by TIG and EB welding (see Fig. 1). From both weld samples charpy specimens were fabricated, tested, and compared with the results from the according base materials (Fig. 2 and 3).

While dynamic yield strength is approximately in the same range as the EUROFER 97 base material, there are differences in the charpy properties: The results of specimens from EUROER 97 and FE-54 experimental heat without joining differ in upper shelf energy (USE) by about 2 J and in ductile-to-brittle transition temperature (DBTT) by about 30 °C (Fig. 2). The charpy test results of both welds range between those of the base materials.

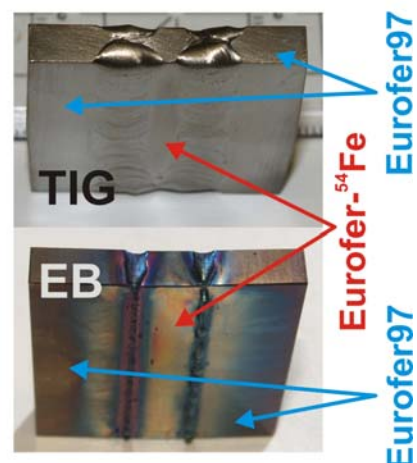


Fig. 1: Test piece of the planned Fe-54 heat specimen fabrication method. To spare the valuable Fe-54 isotope alloy, a centre stripe of the isotope alloy (red arrows) is elongated by two stripes of "normal" EUROFER 97 (blue arrows). The joints are fabricated by TIG (upper image) and by EB welding (lower image). For this study Fe-54 was replaced by natural iron.

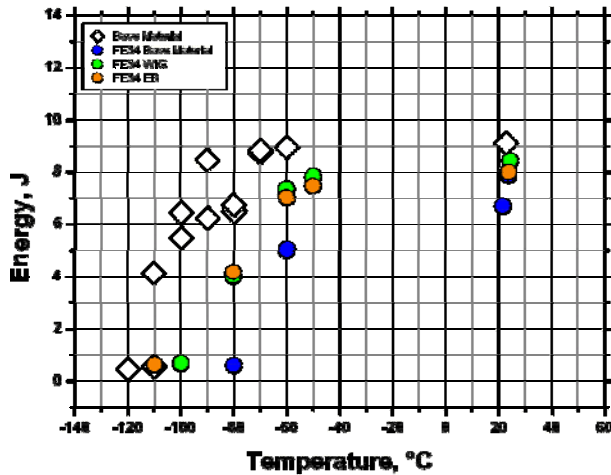


Fig. 2: Charpy test energies of EUROFER 97 base material in comparison with a test melt of EUROFER-FE-54 and the welds shown in Fig. 1.

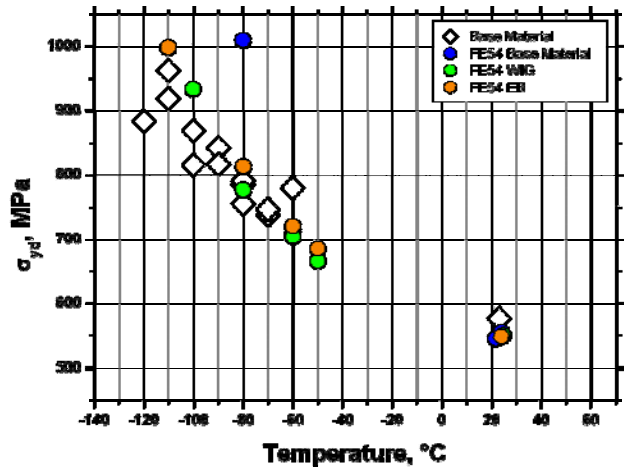


Fig. 3: Dynamic yield strength calculated from instrumented charpy tests with EUROFER 97 base material and a test melt of EUROFER-FE-54 (including welding procedures as shown in Fig. 1).

The reason for the deteriorated properties is the contamination of the FE-54 heat during melting in the ceramics crucible. In the case of aluminium oxide, the oxygen content is increased while the use of BN crucibles increases the nitrogen and boron content. A first chemical analysis has shown that the boron level was raised to about 0.3 wt%. That is, in the current condition, all FE-54 heats are useless, since they have been contaminated by boron (under neutron irradiation boron transmutes to helium).

### Conclusions and Outlook

It has been finally demonstrated that it is possible to fabricate proper FE-54 EUROFER plates in the proper dimensions by pre-melting, re-melting, casting, and joining stripes to spare isotope material. Due to the smaller heat affected zones, the most suitable fabrication method for joining would be EB welding.

Unfortunately, the use of ceramics crucibles leads to unacceptable levels of contamination. That is, contact to the ceramics crucibles has to be avoided in future melting processes. But first, the already molten isotope material has to be cleaned which delays the whole task again by about one year.

Only after a successful boron removal of the failed heats, the specimen fabrication may be completed and planning for irradiation campaigns may be started. The irradiation is foreseen to take place in the HFIR reactor of ORNL and, if possible, in the Petten HFR. A detailed irradiation programme will be elaborated after the specimen fabrication is completed.

### Staff:

- C. Adelhelm
- B. Dafferner
- A. Falkenstein
- P. Graf
- S. Heger
- U. Jäntschi
- A. Möslang
- M. Rieth
- P. Vladimirov
- H. Zimmermann

## TW5-TTMS-001 D 10

### Mechanical Post Irradiation Examinations of FZK-Specimens Irradiated in the ARBOR 2 Experiment in the BOR 60 Reactor

#### Objectives

In an energy generating fusion reactor structural materials will be exposed to very high levels of irradiation damage of about 100 dpa. Due to the fact, that fast reactor irradiation facilities in Europe are not available anymore, a cooperation with the Russian institution: SSC RF RIAR, has been implemented. ARBOR 2 is the succeeding experiment after ARBOR 1 from FZK and ALTAIR from CEA, to reach irradiation damages up to 70 till 80 dpa.

#### Status end of 2006

The negotiations of the prolonged ISTC partner contract for mechanical PIE of the FZK part of specimens from the ARBOR 2 irradiation had been signed end of 2006. To perform PIE of the FZK part of ARBOR 2 postirradiation experiments again the mechanical experiments will be performed at the hot laboratory of SSC RF RIAR under a prolonged ISTC partner contract.

#### PIE of ARBOR 2

The mechanical PIE of ARBOR 2 specimens is performed at the material science laboratory of SSC RF RIAR. Impact and tensile test results of 60 to 70 dpa irradiation damaged EUROFER 97 are available now. The impact tests are performed with an instrumented impact testing facility of Zwick 5113-HKE type, equipped with a pendulum hammer of 15 J impact energy and installed in the VK-39 hot cell of the SSC RF RIAR.

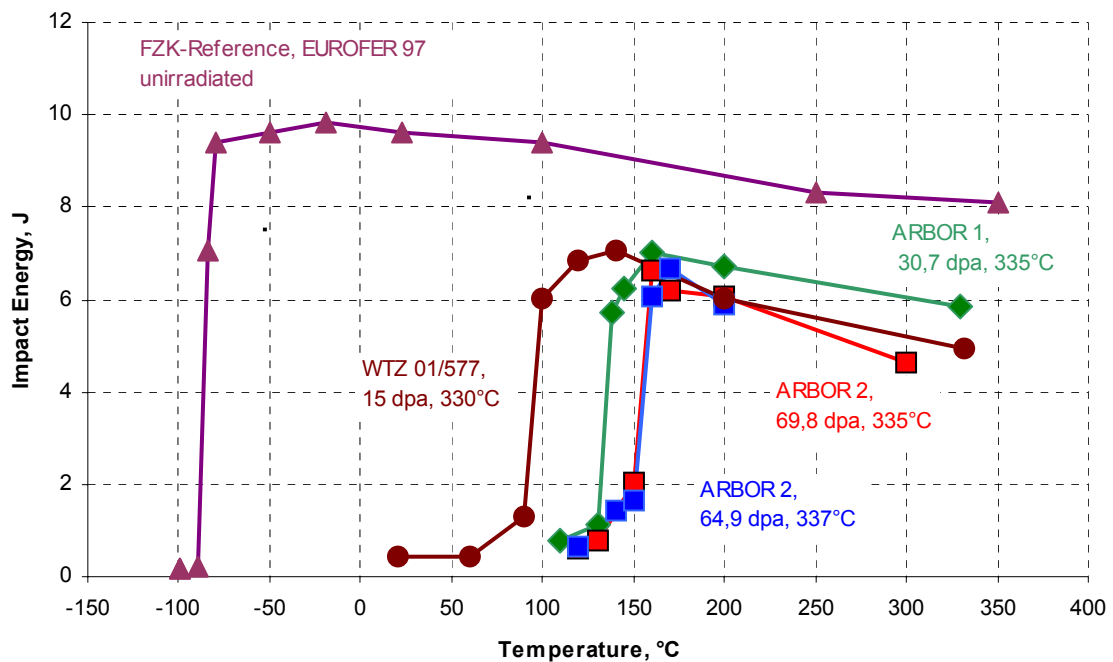


Fig. 1: KLST impact transition curves for unirradiated and irradiated EUROFER 97, the irradiation conditions are indicated in the curve colour.

The primary “force to time” curves are used to determine the impact energy for each specimen. These values are plotted vs. testing temperature (Fig. 1) and the DBTT - the characteristic value for ductile-brittle transition - is derived as the temperature at which the energy corresponds to USE/2.

To demonstrate the state of the art of the impact behaviour of RAF/M steels, in Fig. 2 the comparison of irradiation damage dependence on DBTT of EUROFER 97, F82H mod. and OPTIFER's is plotted in respect to the conventional steel MANET-I. The increase in DBTT of EUROFER 97 with increasing irradiation damage is actually 100°C lower than that of MANET-I, and the saturation state seems to be converging.

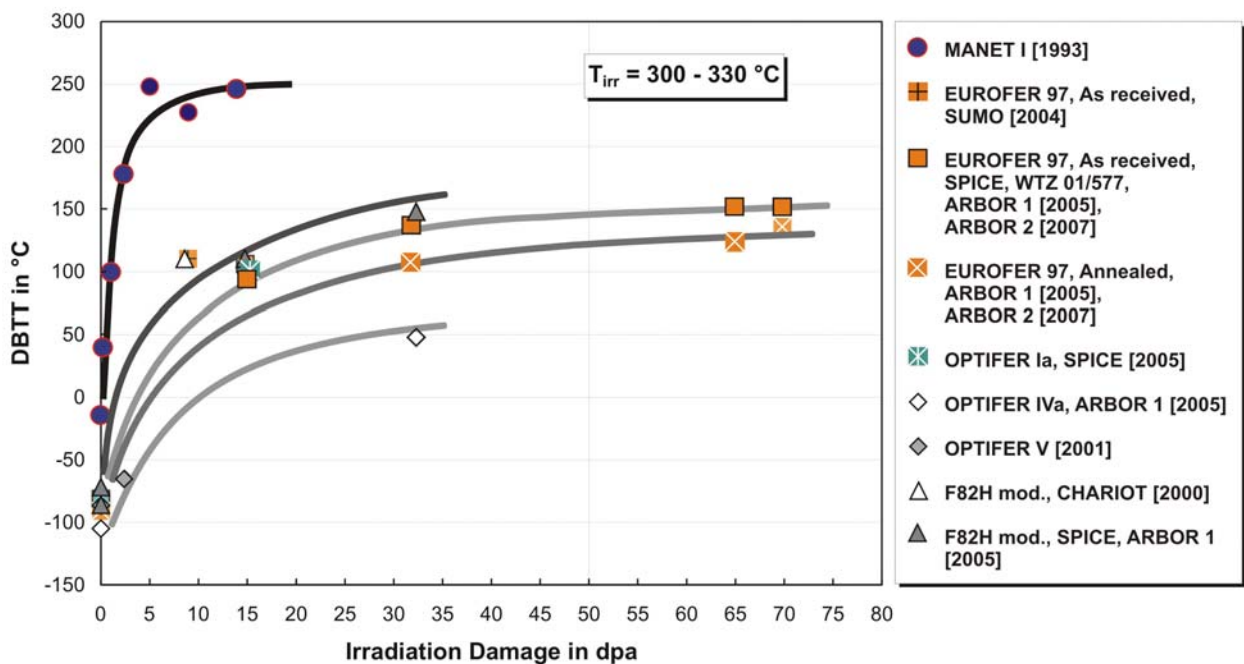


Fig. 2: Comparison of irradiation dependence on the DBTT behavior for different technically relevant RAF/M steels in respect to conventional 12%Cr steel MANET-I.

The tensile tests are performed with a tensile and LCF testing facility of INSTRON-DOLI 1362 type, equipped with a 100 KN load cell, a high temperature furnace and a strain measurement system, installed in the K-12 hot cell of the SSC RF RIAR.

For comparison results from other recently published irradiation campaigns are included. But these results were generated on different specimen shapes and under different tensile testing conditions. Tensile tests have been performed on four different kinds of specimens types utilized in the different irradiations. NRG (SIWAS-04, SUMO-02) irradiated cylindrical specimens of 20 mm gauge length and 4 mm diameter and performed the tests with a strain rate of  $5 \times 10^{-4} \text{ s}^{-1}$ [1]. In the SPICE irradiation cylindrical specimens of 18 mm gauge length and 3 mm diameter are tensile tested under vacuum with a strain rate of  $1 \times 10^{-4} \text{ s}^{-1}$  [2]. In the 15 dpa WTZ 01/577 irradiation cylindrical specimens of 15 mm gauge length and 3 mm diameter are tensile tested with a strain rate of  $3 \times 10^{-3} \text{ s}^{-1}$ [3].

Even if one takes into account the slightly different tensile testing conditions, with increasing irradiation damage a continuous increase of the yield stress increase is detectable. So the 2.5 dpa damage (SIWAS-04) has the lowest increase of around 300 MPa in yield stress and

the 42.3 dpa damage (ALTAIR) the highest increase of around 520 MPa in yield stress. The 69.1 dpa damage (ARBOR 2) results in a yield stress increase of around 500 Mpa.

In Fig. 3 the yield stress increase is plotted in dependence of the irradiation damage for irradiations performed around 300°C [4]. It follows nearly the rate proposed by Whapman and Makin [5], but do not lead to saturation yet.

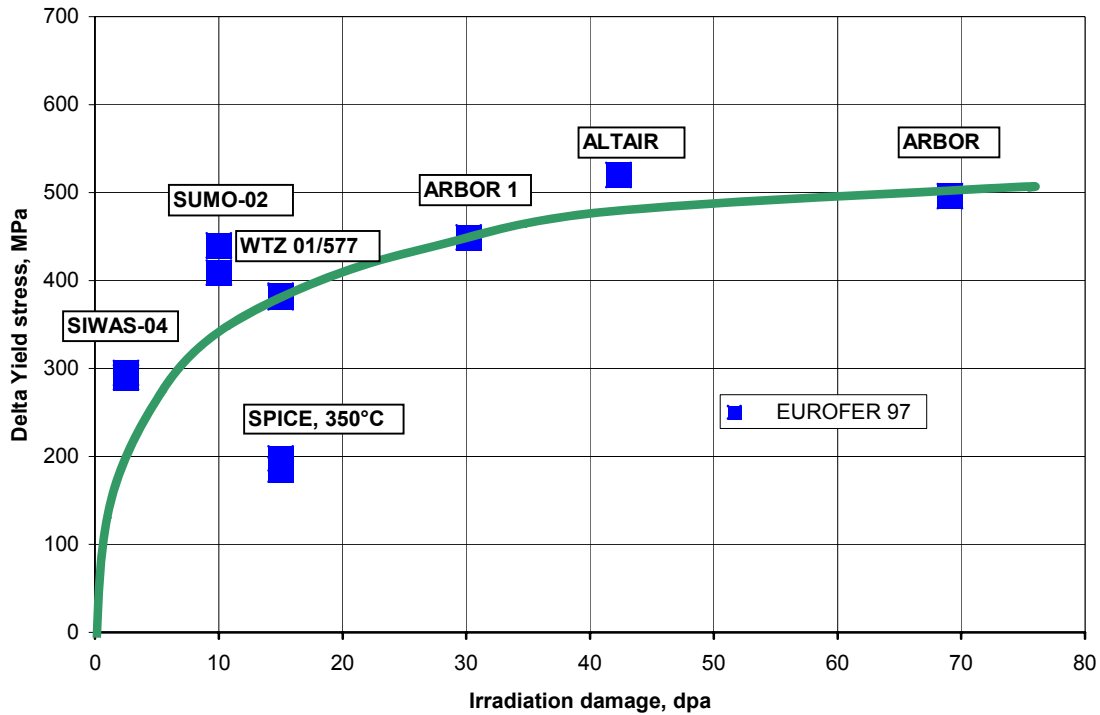


Fig. 3: Yield stress increase due to irradiation damage compared to data of the indicated irradiations (Test temperatures near to irradiation temperatures).

Only the yield stress increase of specimens irradiated at 350°C to 15 dpa damage (SPICE) are much lower and demonstrate the strong influence of irradiation temperatures in this temperature range between 300 and 350°C.

#### Staff:

B. Dafferner  
M. Klotz  
C. Petersen

#### Literature:

- [1] J.W. Rensman, "NRG irradiation testing: report on 300°C and 60°C irradiated RAFM steels", Final report on the EFDA Tasks TW2-TTMS-001a D 6 and TW2-TTMS-001b D 12, (2005).
- [2] E. Materna-Morris, personal communication.
- [3] E. Lucon and W. Vandermeulen: "Overview and critical Assessment of the Tensile properties of unirradiated and irradiated EUROFER 97", Report SCK.CEN-BLG-1042 REV.(1), Oct, 2007.

- [4] A. Alamo, P. Wident and V. Shamardin: "Post-Irradiation Examinations (PIE) of materials irradiated in BOR60 at 325°C up to 42 dpa", Internal CEA report, DMN/SRMA/2005-2767/A, March 2006.
- [5] A. D. Whapman, M.J. Makin, *Phil. Mag.* 5, 237 (1960)
- [6] C. Petersen, A. Povstyanko, V. Prokhorov, A. Fedoseev, O. Makarov and B. Dafferner: "Impact property degradation of ferritic/martensitic steels after the fast reactor irradiation 'ARBOR 1'", *J. Nucl. Mater.* 367-370 (2007) 544-549.
- [7] O. Yu. Makarov, A.V. Povstyanko, V.I. Prokhorov, A.E. Fedoseev, and C. Petersen: "Mechanical test methods in RIAR hot cells for subsized specimens of Fusion Reactor Materials", Proceedings of the 8. Russian Conference on Reactor Material Science on 21. –25. May 2007 at Dimitrovgrad, Russia, to be published.
- [8] C. Petersen, J. Aktaa, E. Diegele, E. Gaganidze, R. Lässer, E. Lucon, E. Materna-Morris, A. Möslang, A. Povstyanko, V. Prokhorov, J.W. Rensman, B. van der Schaaf and H.-C. Schneider: "Mechanical Properties of Reduced Activation Ferritic/Martensitic Steels after European Reactor Irradiations", IAEA- CN-149 Fusion 21 proceedings, Wien, ISBN 92-0-100907-0 / ISSN 0074-1884.

## TW5-TTMS-001 D 11

# Historical Development of EUROFER and a Critical Assessment of its Chemical Composition

### Overview

Since the 1970s the development of ferritic/martensitic alloys with reduced long-term activation has made significant progress and, therefore, finally led to the production of an "European Primary Candidate Alloy" for this material group: EUROFER. Up to now two heats of several tons were produced by different manufacturers and a further one is currently in production. Many data sets of countless characterization experiments on the Eurofer steel were collected during the last decade. Therefore, the time has come for a documentation of the historical developmental work that led to EUROFER and for a critical assessment of its composition.

### Progress of the Assessment Report

All relevant data for reviewing the EUROFER development has been collected and summarized within four brief chapters. Furthermore, the low-activation angle has been outlined. The main focus, however, has been laid on describing and discussing the influence of the chemical composition (including the effect of impurities) on physical metallurgy, structure and transformation, and heat treatments. Since there is a certain overlap with the EUROFER modelling review task TW6-TTMS-007, only a few topics of the final report are presented in the following.

Ideally, EUROFER should consist of the elements Fe, 8.5-9.5% Cr, and about 0.1% C, 1% W, 0.4% Mn, 0.2% V, 0.07% Ta, and 0.03% N (see also Fig. 5). Since phase diagrams of more than two elements are difficult to obtain and rather complicated, the alloying effect is easier to study by element pairs. Therefore, the basic metallurgy of EUROFER may be characterized by the iron-carbon (Fig. 1) and by the iron-chromium phase diagram (Fig. 2). For a carbon content of 0.1% there are three pure phases recognizable. At temperatures near 1400 °C there is delta-ferrite (blue area in Fig. 1). Below about 900 °C there is alpha-ferrite (red area). And in between there is the austenitic phase (gamma-ferrite). Further, there are fields of mixed phases: around 800 °C there is a mix of  $\alpha$ - and  $\gamma$ -phase, at room temperature there is a mix of  $\alpha$ -ferrite and cementite ( $\text{Fe}_3\text{C}$ ). In the iron-chromium phase diagram the  $\gamma$ -field is closed (Fig. 2). In this case the  $\delta$ - and  $\alpha$ -phase fields are connected, so that at chromium contents of more than about 12-13% phase transformations will not take place which is important for the martensite formation. The other alloying elements can then be divided into their effect on the gamma-loop: ferrite forming elements like V and W reduce the gamma-loop while austenite formers like N and Mn enlarge the gamma loop (see Fig. 3).

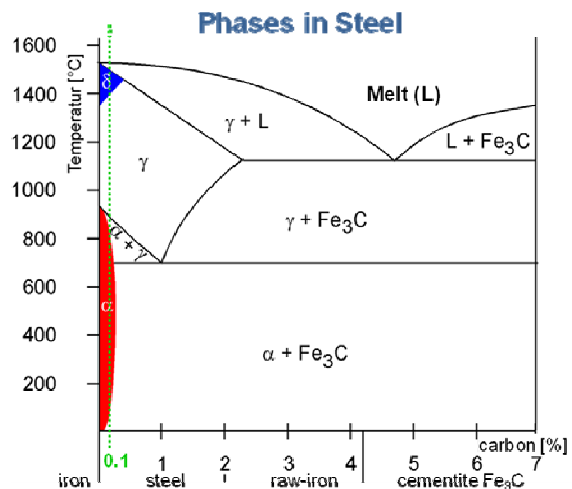


Fig. 1: Iron-carbon phase diagram. The green line indicates the carbon level of EUROFER (0.1%).

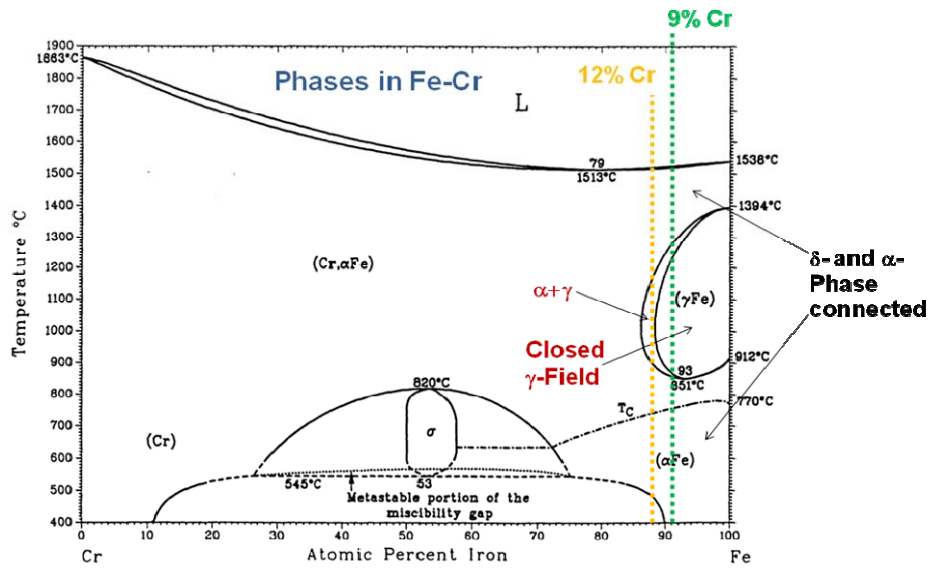


Fig. 2: Iron-chromium phase diagram. The chromium level of EUROFER is indicated by the green line (9%). A chromium content of 12% is about the maximum level for martensitic steels (yellow line).

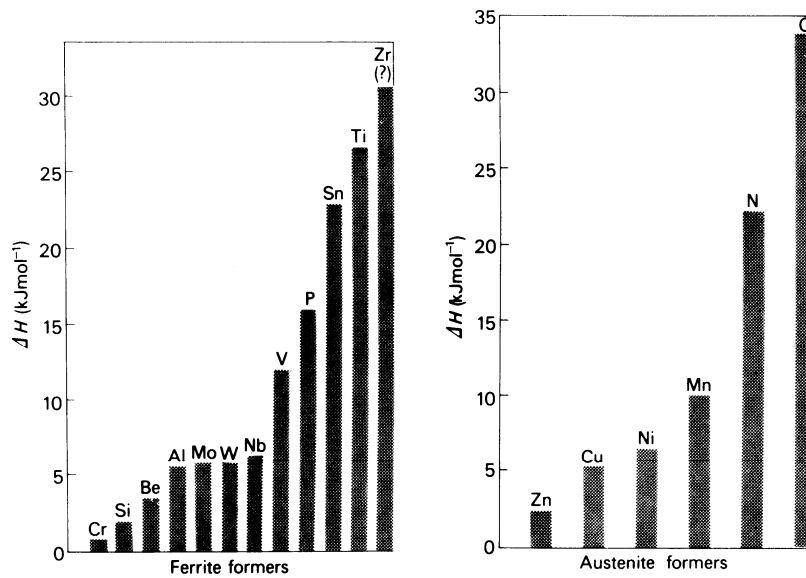


Fig. 3: Relative strength of alloying elements as ferrite and austenite formers.

One of the most convenient ways of representing the effect of various elements on the basic structure of chromium/nickel steels is the Schaeffler diagram, often used in welding. It plots the compositional limits at room temperature of austenite, ferrite and martensite, in terms of nickel and chromium equivalents (Fig. 4). At its simplest level, the diagram shows the regions of existence of the three phases for iron-chromium-nickel alloys (martensite, austenite, ferrite). However, the diagram becomes of much wider application when the equivalents of chromium and of nickel are used for the other alloying elements. The chromium equivalent has been empirically determined using the most common ferrite-forming elements:

$$\text{Cr equivalent (wt\%)} = \text{Cr} + 2 \text{ Si} + 1.5 \text{ Mo} + 5 \text{ V} + 1.75 \text{ Nb} + 0.75 \text{ W} + 1.5 \text{ Ti} + 5.5 \text{ Al} + 1.2 \text{ Ta} + 1.2 \text{ Hf} + 1 \text{ Ce} + 0.8 \text{ Zr} + 1.2 \text{ Ge}$$

**(EUROFER: 9.2 + 1 + 0.8 + 0.2 = 11.2)**

The nickel equivalent has likewise been determined with the according austenite formers:

$$\text{Ni equivalent (wt\%)} = \text{Ni} + \text{Co} + 0.5 \text{ Mn} + 0.3 \text{ Cu} + 30 \text{ C} + 25 \text{ N}$$

(EUROFER:  $0.25 + 3 + 0.5 = 3.75$ )

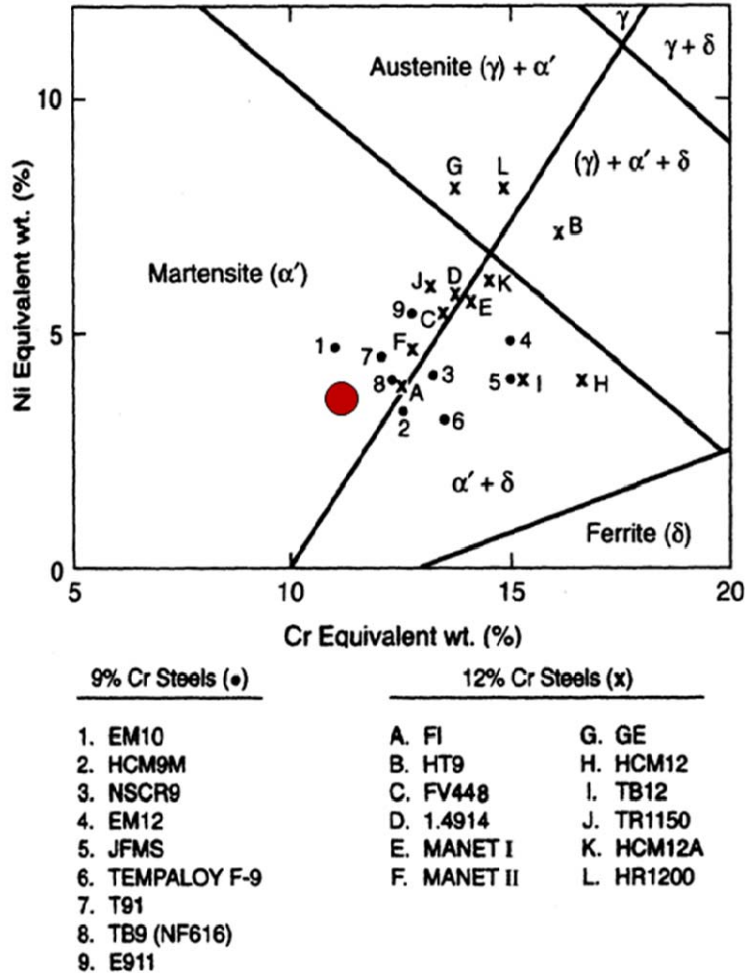


Fig. 4: The Schaeffler diagram and the equivalents for several steels. The EUROFER steel is represented by the big red dot.

With the present composition EUROFER is relatively far away from the  $\delta$ -ferrite region (red dot in Fig. 4) which is an important point for the application of certain welding processes.

Start and end of martensite formation during quenching ( $M_s$  and  $M_f$  temperatures) for the high-chromium steels usually range from 250 to 350 °C and 80 to 190 °C, respectively, but much higher  $M_s$  (< 450 °C) and  $M_f$  (< 260 °C) temperatures have been determined for some of the developmental reduced-activation steels. Such steels are air hardenable, with the martensite being formed in thick sections because the pearlite transformation is greatly retarded and bainite is not formed even within extended time periods. The martensite produced is typical low-carbon lath martensite. EUROFER also falls in this category: martensite formation starts at 385°C and ends at 215°C. With a cooling rate of only 10 °C/min 100 per cent

Table 1: Influence of alloying elements on  $\alpha$ - $\gamma$  transition temperature  $A_{c1}$ .

Effect on $A_{c1}$ Temperature (change per wt%)	
Ni	- 30
Mn	- 25
Ci	- 5
Si	+ 25
Mi	+ 25
Al	+ 30
V	+ 50

martensite formation is reached which is also a result of the alloy composition. When heating up the EUROFER steel, for example, at a slow rate of 0.4 °C per minute, the formation of austenite begins at 820 °C (temperature  $A_{c1b}$ ). At 890 °C (temperature  $A_{c1e}$ ) the EUROFER has fully transformed into austenite. The influence of certain alloying elements on the transition temperatures  $A_{c1}$  are given in Table 1. While Ni, Mn, Co lower the transition temperatures, Si, Mo, Al, and V raise  $A_{1c}$ .

## Conclusions

Basically, the EUROFER steel consists ideally of iron plus only seven alloying elements which are Cr, W, Mn, V, Ta, C, and N (Fig. 5). Cr, W, and V are important for strengthening the steel by substitutional solid solution as well as by precipitation hardening. At the same time this results also in a good thermal stability (also enhanced to some extent by manganese) which defines the maximum operation temperature of 550 °C with respect to creep and thermal aging. The effects of the different elements are compiled in Fig. 5.

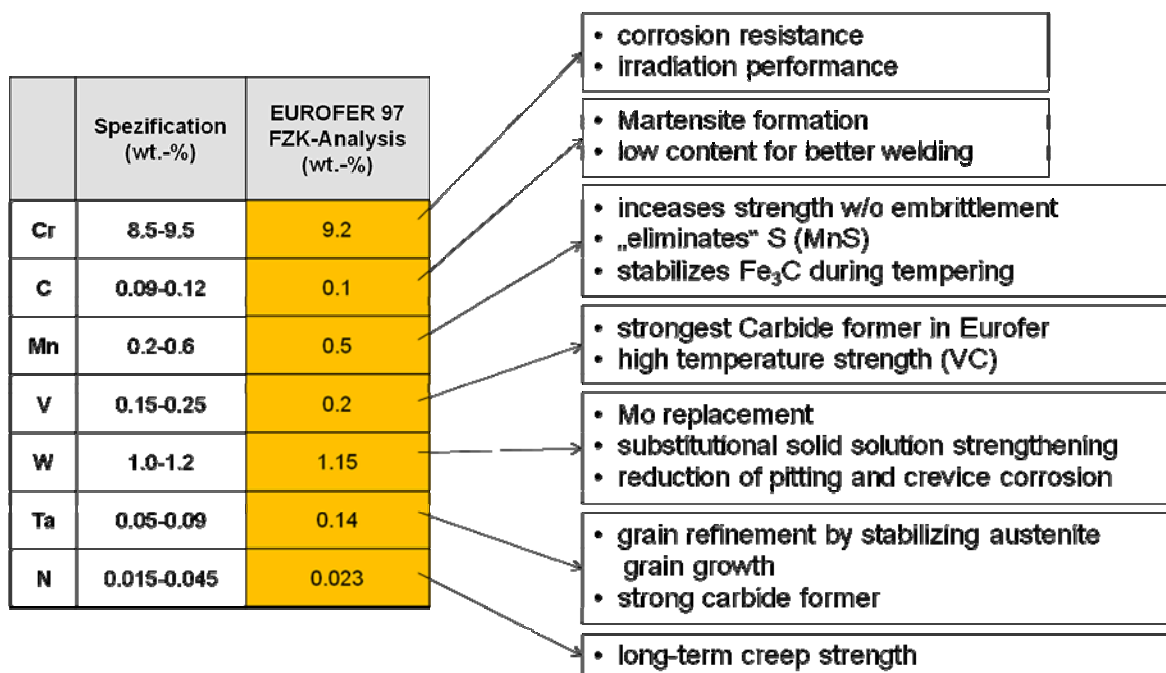


Fig. 5: Overview of the chemical composition (ideal, no impurities) and the effect of the alloying elements.

Considering all that, there is not much room for further improvement with respect to modification of the chemical composition: carbon and nitrogen are balanced, an increase of tungsten and/or vanadium and/or manganese does not further increase strength, and an increase of tantalum does not lead to even finer austenite grains. This leaves just the main alloying element: chromium. However, there is a reason why EUROFER has been specified with 9% Cr: ferritic/martensitic steels show a minimum in irradiation induced DBTT shift for chromium contents around 9%.

Since there is no material that can fulfil all requirements necessary for all fusion relevant applications, EUROFER can be considered as a standard material which might certainly cover more than 90% of all structural fusion applications. Criteria which EUROFER does not meet have to be covered by other materials which have to be tailor made for such specific cases.

In summary, a further optimization of the chemical composition of EUROFER with respect to irradiation resistance or improvement of thermo-mechanical properties seems neither possible nor necessary. Therefore, the only improvement could be a slight change of the specification:

- The chromium content should be specified to 9-9.5%.
- The tantalum content could be specified in a broader range (0.05-0.15%) since EU-ROFER already exceeded the former limit of 0.09%. However, the minimum of 0.05% Ta has to be followed in any case for grain refinement.

Staff:

B. Dafferner  
S. Heger  
U. Jäntschi  
M. Klimiankou  
A. Möslang  
M. Rieth  
H. Zimmermann

## **TW5-TTMS-001 D 11**

### **Assessment of Impact Test Experiments on Irradiated EUROFER97 and other RAFM Steels**

#### **Objectives**

Charpy impact testing on KLST type specimens is a widely used testing method for characterization of the structural material irradiation resistance. This led to a development of a large data base on the ductile-to-brittle transition temperature (DBTT). Although the reduced activation ferritic martensitic (RAFM) 7-10%CrWVTa steels (EUROFER, OPTIFER, F82H) exhibits clearly better irradiation performance compared to the modified commercial 10-11%-Cr-NiMoVNB steels, the hardening induced by neutron irradiation accompanied by the embrittlement and by reduction of toughness still remain a main concern. He and H generation is another important issue that requires careful investigation prior to structural material qualification. The assessment of impact properties of irradiated RAFM steels will support material database generation and specification of new EUROFER charge. The study of correlation of fracture mechanical and impact testing results on irradiated RAFM steels is an other important issue thoroughly discussed in [1].

#### **Data Assessment**

The assessment of available irradiated charpy impact data has been performed. The effects of irradiation temperature and dose on the embrittlement have been assessed for various RAFM steels. The DBTT of RAFM steels is influenced most at low irradiation temperatures ( $T_{irr} \leq 330$  °C). A large, non-saturating low temperature embrittlement is seen up to 32 dpa. The embrittlement rate, however, seems to be reduced at high doses. At  $T_{irr} \geq 350$  °C all investigated RAFM steels show good irradiation resistance against neutron irradiation up to 16.3 dpa.

Helium effects have been assessed by analysing the impact properties of boron doped steels irradiated in HFR IIb (SPICE) irradiation experiment. Boron doped steels show progressive embrittlement and reduction of toughness with increasing He amount up to 5580 appm. At  $T_{irr} = 250$  °C He induced embrittlement is of hardening nature for low helium contents up to 84 appm. Larger helium concentrations lead to non-hardening embrittlement mechanisms beyond to the helium induced hardening. At higher irradiation temperatures helium tends to predominantly contribute to non-hardening embrittlement mechanisms. At  $T_{irr} = 450$  °C helium effects are substantially reduced for helium concentrations up to 430 appm.

#### **Conclusion**

Assessment of the available charpy impact data on 7-10%-Cr-WVTa RAFM steels (EUROFER, F82H, OPTIFER-Ia etc.) has been finished. European reference RAFM steel EUROFER 97 and international RAFM steels show superior irradiation performance compared to the modified commercial 10-11%-Cr-NiMoVNB steels, e.g. MANET-I. Irradiation resistance of the RAFM steels for low irradiation temperatures  $T_{irr} \leq 330$  °C, however, is not satisfactory, i.e. large, non-saturating low temperature embrittlement is seen up to 32 dpa. Close correlation between irradiation induced embrittlement and hardening at  $T_{irr} \leq 350$  °C indicates the displacement damage nature of low temperature embrittlement. Irradiation performance of EUROFER 97 and international reference RAFM steels is satisfactory at  $T_{irr} \geq 350$  °C up to available damage doses (up to 16.3 dpa).

#### **Staff:**

E. Gaganidze

Literature:

- [1] E. Gaganidze, Assessment of Fracture Mechanical Experiments on Irradiated EUROFER 97 and F82H Specimens, final Report for Task TW5-TTMS 001-D14, FZKA 7310, 2007.
- [2] E. Gaganidze, Assessment of Impact Test Experiments on Irradiated EUROFER97 and other RAFM Steels, Final Report for Task TW5-TTMS 001-D11, FZKA 7327, 2007.
- [3] E. Gaganidze, H.-C. Schneider, B. Dafferner, J. Aktaa, Embrittlement behaviour of neutron irradiated RAFM steels, J. Nucl. Mater. 367–370 (2007) 81–85.
- [4] E. Gaganidze and J. Aktaa, The role of He on the embrittlement of RAFM Steels, Proceedings of the 8th International Symposium on Fusion Nuclear Technology, Sept. 30 – Oct. 5, 2007, Heidelberg, Germany.

## TTMS-003 Compatibility with Hydrogen and Liquids

### TW6-TTMS-003 D 3 Corrosion Testing of EUROFER in Liquid PbLi

#### Objectives

The aim of this task is to perform corrosion tests at 550°C extended to long term Pb-17Li exposure times in PICOLO loop with duration up to about 12,000 h to generate a realistic data base for extrapolation to TBM relevant operation times and to reduce the strong uncertainties still present after performing the TW4 task. All evaluated data should be also used for validation of the modeling tools concerning corrosion attack and also for assistance in the field of transport of corrosion products by the Pb-17Li breeder and forming of precipitates at cooler loop sections.

#### Corrosion testing

The corrosion testing of bare EUROFER 97 samples was performed in flowing Pb-17Li with a flow velocity of 0.22 m/s in the PICOLO loop. The highest temperature in the loop was present in the test section with 550°C. The coolest sections were the electromagnetic pump and magnetic trap devices with roughly 350°C. Fig. 1 shows a schematically view of the PICOLO loop with the main components. The fresh test samples had a diameter of 8.0 mm and were mounted concentrically in the test section with inner diameter of 16 mm. The flow velocity of 0.22 m/s is the calculated value for the fresh “un-corroded” configuration. The longest exposed sample was removed after nearly 12,000 h and the smallest exposure time was 500 h. Due to the high corrosion attack at 550°C a high amount of precipitates was present in the loop which caused a first plugging after about 3,000 h of operation. The blockage appeared in the mounted magnetic trap section which is installed to collect precipitates and prevent the electromagnetic pump from damages. Replaced fresh magnetic traps had in the following an average life time of around 3,000 to 4,000 h.

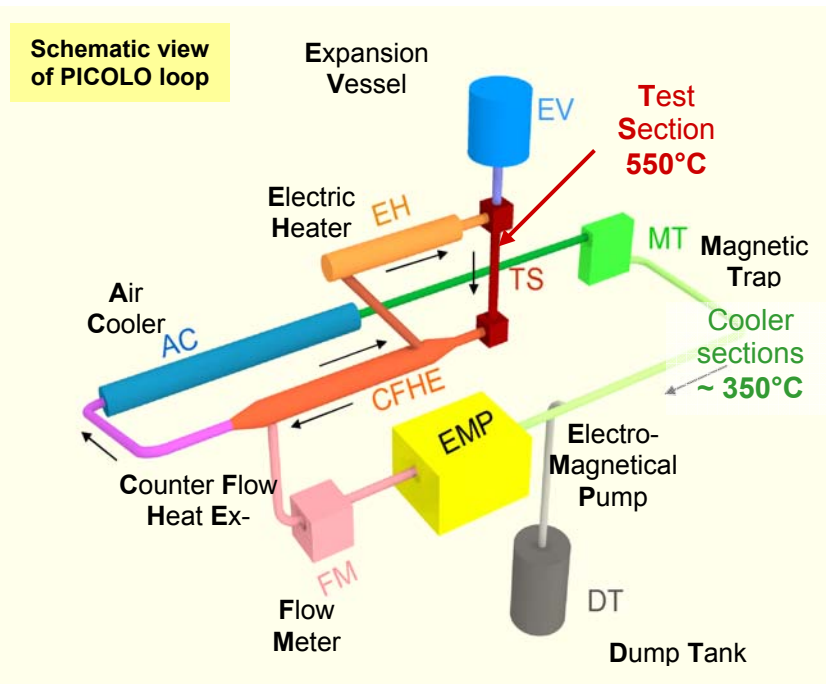


Fig. 1: Schematic view of PICOLO loop with temperature in hot test section and cooler loop parts.

### Corrosion attack

The corrosion testing of RAFM steels performed at 480°C in PICOLO loop in earlier test campaigns showed that dissolution of e.g. Fe, Cr out of the steel matrix is the acting corrosion mechanism which leads to a corrosion rate at 480°C of roughly 90 µm/year at 0.22 m/s. The new tests performed at 550°C delivered the same corrosion mechanisms and showed also a homogeneous attack of the surfaces at longer exposure times as can be seen in the micrograph depicted in Fig. 2 (left part). In contrast to 480°C testing the new corrosion testing performed under TW4 and TW6-TTMS-003 showed rather small incubation periods below 500 h. The first sample removed in this campaign after 500 exhibited only some small not attack surface fractions of about 5% as given in Fig. 2 right part. Measuring the step occurring between eroded and not attacked areas (Fig. 2 right part) gave first hints that the corrosion attack is dramatically increased and indicated possible upper margins up to 700 µm/year. The whole testing program was running up to about 12,000 h and showed always a good wetting of the surfaces and a homogeneous corrosion. Compared to 480°C only insignificant changes in the surface structure may be present. No evidence was found in metallographic analyses for leaching or cracking off of complete martensitic needles in shape of particles as can be concluded from Fig. 2 left part.

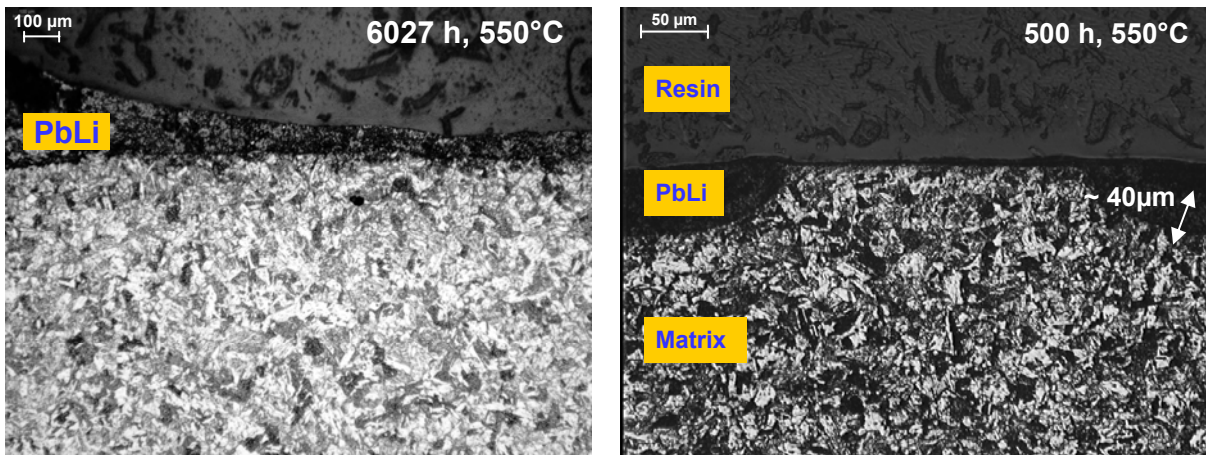


Fig. 2: The right side shows a sample exposed more than 6000 h to Pb-17Li at 550°C with an homogeneously attacked smooth surface. The picture given at the left positions shows strong attack at only 500 h exposure time and a section with delayed wetting.

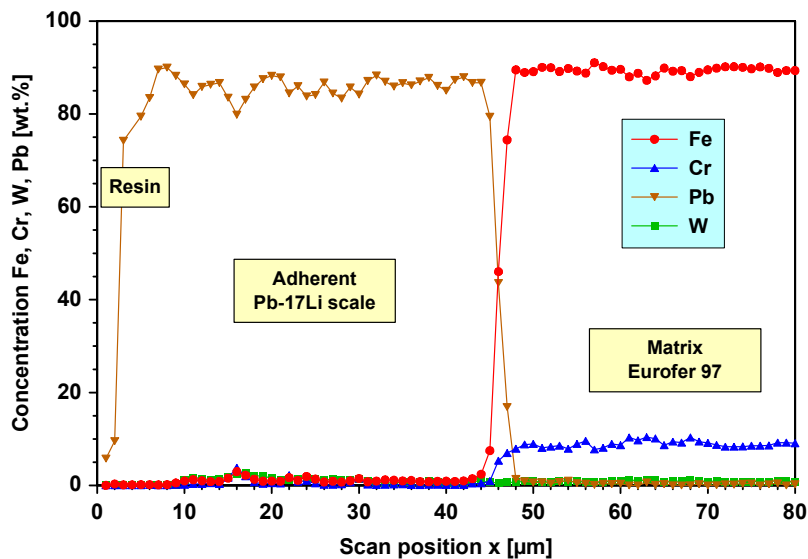


Fig. 3: EDX line scan analyses of a Eurofer sample exposed to Pb-17Li at 550°C for about 1025 h with adherent Pb-Li scale after removal from PICOLO loop.

The structural and metallographic analyses were completed by line scan analyses for evaluation of changes in surface near regions of the EUROFER samples and of the Pb-17Li melt. They showed that a sharp boundary is existing between matrix and Pb-17Li melt as can be seen in Fig. 3 by the concentration signal for e.g. Fe which drops within the resolution distance ( $\sim 3 \mu\text{m}$ ) from roughly 90 to 0%. This behaviour excludes deep grain boundary infiltration effects by Pb-17Li. The enrichment of the adherent Pb-17Li scale by e.g. Fe or W corrosion products indicate that in surface near regions a reduced mixing is present and diffusion controlled transport may be pronounced near surfaces.

### Corrosion rate

The corrosion rate = material loss of each sample was determined by measuring the diameters of each sample before and after exposure to the flowing Pb-17Li. The half difference of these diameters stands for the corrosion rate. Diameter measurements of fresh samples were done mechanically. Some specially prepared cuts of such samples were used as reference standards for calibration of the optical measurement process which is applied for determination of the diameter from the metallurgical cuts of Pb-17Li exposed samples. The cuts of all Pb-17Li exposed samples showed a symmetrical spherical attack within the resolution limits of about  $5 \mu\text{m}$  of the used measurement process.

Extrapolations done by samples removed after short times (500 to 1,500 h) deliver rather high corrosion values of about  $700 \mu\text{m}/\text{year}$ . This high rate seems to be an overestimation of the yearly loss e.g. due to high uncertainties in diameter determination and extrapolation from short exposure times to long operation times. For longer exposure times (2,500 to 12,000 h) smaller rates were evaluated. Fig. 4 depicts the measured values without and with corrections for flow velocity changes. Due to diameter changes by corrosion in the test section the flow velocity of  $v(t=0) = 0.22 \text{ m/s}$  was reduced to nearby  $0.18 \text{ m/s}$  after about 12,000 h roughly 80% of the originally selected velocity. Thus depicted measured corrosion values especially for long term exposure in Fig. 4 are too small and show a too optimistic behaviour if they are not normalized. At least the reduced flow has to be considered and a correction has to be performed for constant flow velocity  $0.22 \text{ m/s}$  to see more realistic corrosion values. Such a correction can be done e.g. by empirically deduced corrosion correlations e.g. the Sannier correlation [1]. Assuming that this correlation is valid at least for constant temperature and small changes in flow velocity a correction should be possible with high reliability. Sannier's correlation predicts material loss (ML) in the given form of dissolution depth per year by:

$$\text{ML} = 8 * 10^8 * \exp [-25690/1.98T] * v^{0.875} * d_h^{-0.125} \quad [\mu\text{m/a}]$$

Thus, the correction has to consider only the parameters  $v$  (velocity) and  $d_h$  (hydraulic diameter) to find out relative changes  $F(v*d_h)$ .

For a material loss of about  $0.48 \text{ mm}$  as determined for exposure time 12,000 h a reduced corrosion attack by about 19% is predicted if constant loop parameters would be used. Assuming that the correction factor  $F(0)/F(t)$  changes linearly all observed rates have to be increased e.g. for 12,000 h by about 9.5%. Some other parameters will also affect and reduce corrosion attack during testing. For example a reduced mass flow (90 to 100% level of nominal value due to delayed adjusting by control devices for about 10% of testing time) will cause an additional correction by 2%. This type of corrections was performed for some long term exposed samples to generate corrosion attack values at constant  $0.22 \text{ m/s}$  Pb-17Li flow velocity. These corrected values are given by separate symbols in Fig. 4. The linear interpolation of the corrected values leads to a corrosion rate of about  $400 \mu\text{m}/\text{year}$  with more emphasis to the values evaluated for the long term exposed samples.

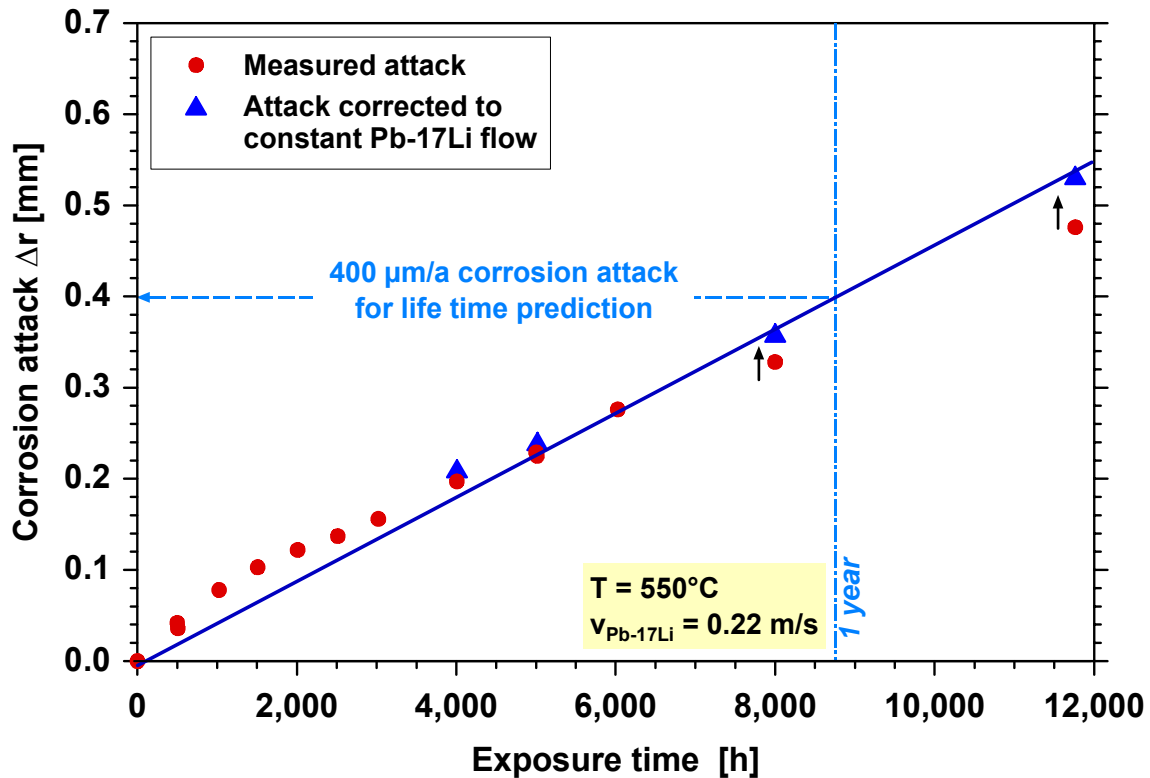


Fig. 4: Corrosion attack of EUROFER 97 at 550°C test temperature vs. exposure time.

### Precipitations

The high corrosion rate at 550°C led to an enormous amount of corrosion products dissolved in the flowing Pb-17Li which formed precipitations in cooler sections. First metallographic analyses performed at some tube segments inclusively the magnetic trap operated at 350°C revealed that no homogeneous coating takes place of the inner surfaces by deposition as opposite process of dissolution. The analyzed cuts of drained loop sections showed for example a lot of nicely grown crystals up to 100 μm in size embedded in the adherent Pb-17Li melt layer as given in Fig. 5. The dimensions of the crystals indicate that they were formed over longer time intervals, however, not necessarily at the position of detection. A higher amount of such precipitates was collected in the mounted magnetic trap device. The chemical analyses detected there a very high Fe concentration of about 4.3 wt.% in Pb-17Li. The Pb-17Li flow was heavily suppressed by these particles after an operation time of about 3,000 h at 550°C in the test section and claimed changing of the trap. This behaviour represents clearly the risk of line plugging by precipitations in a loop due to dramatically increased corrosion at hot temperature positions and the transportation/nucleation effects. The analyses of the started work on transport and precipitation effects has to be continued in future tasks to build up a reliable data base also under the view of validation modeling tools.

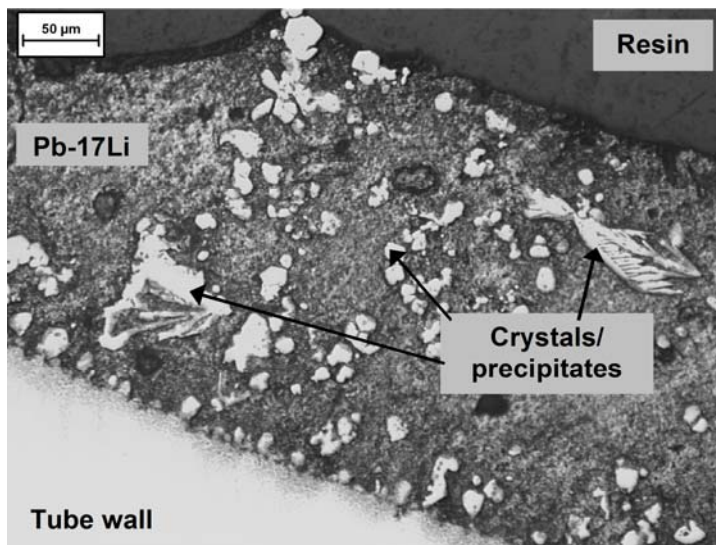


Fig. 5: The micrograph depicts precipitates embedded into Pb-17Li after draining PICOLO loop at a position near the magnetic trap device.

## Modeling

The development of modeling tools which started under TW4-TTMS-003 with the aim to assist the running corrosion testing and to increase reliability in extrapolating results to other test conditions or to predict transport / precipitation phenomena was continued with validation the modularly structured components using the evaluated data for the corrosion testing at 550°C up to about 12,000 h.

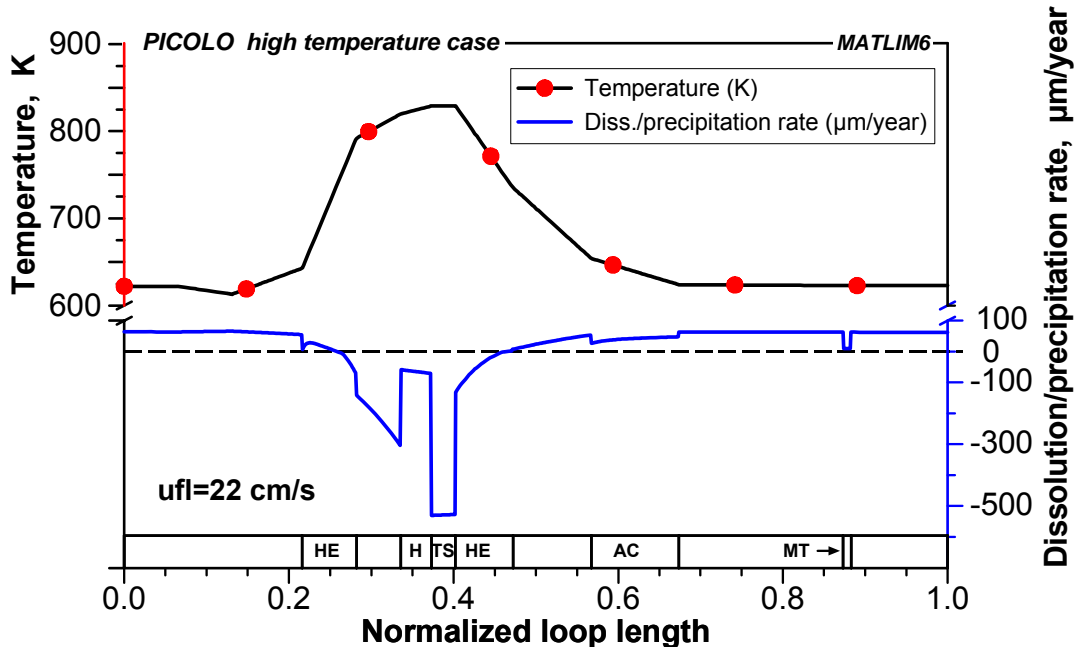


Fig. 6: Corrosion and precipitation behaviour in the whole PICOLO loop calculated by the developed MATLIM code.

The theoretical background of these tools was given in the previous TW4-report and the tools were integrated meanwhile into a computer code called MATLIM [2]. The performed calculations concerning corrosion rates and precipitations used the physical and chemical properties of the EUROFER, the Pb-17Li melt and were applying the typical features of the test loop PICOLO – therefore a parameterization of PICOLO loop (e.g. temperatures, flow velocities, diameters etc.) was performed in dependence of loop position. Fig. 6 depicts the calculated corrosion behavior at all positions within PICOLO loop. Negatively listed values indicate dissolution of the steel components and positive values are standing for formation of precipitations. The modeling shows / confirms that the highest corrosion rate is present in the test section and that all positions with temperature below roughly 400°C are predestinated in forming precipitates. The inserted abbreviations at the axis of normalize loop length are the same as given in Fig.1 and correspond to the names of main loop components.

## Conclusions

For the first time corrosion testing of EUROFER 97 was successfully performed at 550°C conditions at a flow rate of 0.22 m/s and exposure times up to about 12,000 h and by combination of experimental and modeling work a significant progress was realized especially in the change over from only mechanism-based tests to considering the whole loop behavior under corrosion, transport and precipitation view.

The corrosion testing and modeling activities showed both that a dramatically increase in corrosion rates takes place at a small increase of operation temperature from 480 to 550°C by a factor of 5. The observed dissolution/corrosion mechanisms in the testing zone are the same as detected at lower temperatures in the past and are in agreement with results reported earlier [1, 2]. The loop operation and corrosion testing pointed out the high risk of loop

blockages by forming precipitates within short operation times of roughly 3,000 h. The performed first analyses indicate that the precipitates are freely transportable in the melt and may be deposited / collected at positions with low flow velocity or special magnetic field conditions. The modeling tools developed in parallel confirm the evaluated corrosion mechanisms and rates as well as the observed precipitation behaviour. Both, experimental and analytical analyses indicate that safe operation of Pb-17Li systems without the risk of line plugging may need corrosion resistant coatings to bring down corrosion and precipitation behaviour at high operation temperatures of TBM's to a manageable level also at small flow velocities.

Staff:

M. Heck  
N. Holstein  
J. Konys  
W. Krauss  
J. Lorenz  
J. Novotny  
A. Skrypnik  
Z. Voss  
O. Wedemeyer

Literature:

- [1] J. Sannier, T. Flament, A. Terlain, Corrosion of martensitic steels in flowing Pb17Li, Proc. 16<sup>th</sup> Symp. Fusion Technology, 3-7 Sept., (1990), London, UK, 901-905.
- [2] H. Steiner, W. Krauss, J. Konys, Calculation of Dissolution/Precipitation Rates in Flowing Eutectic Pb-17Li with the MATLIM code, ICFRM-13, Nice, France, December 10-14 (2007).

## **TTMS-004 Qualification Fabrication Processes**

### **TW6-TTMS-004 D 1, D 2 and D 3 Improve Design Limits of Welded Components through Improved Post Weld Heat Treatments, Qualification and Improvement of Welded and Diffusion Bonded Joints**

#### **Overview**

According to the current design for the European Helium Cooled Pebble Bed (HCPB) ITER Test Blanket Module (TBM) there are basically six subcomponents which have to be fabricated and assembled: first wall, caps, stiffening grid, breeding units, back plates/manifolds, and attachment system. The main technologies needed for blanket fabrication are joining of parts (particularly production of plates with internal cooling channels and welding at inaccessible component areas) and applying suitable post weld heat treatments. Both steps together are the key technologies that determine the mechanical strength of the blanket, the ductile-to-brittle transition temperature (DBTT) which is important under neutron irradiation, and the potential for a compact design. While it is certain that the structural material will be EUROFER, most joining technologies and/or procedures have still to be developed, adapted, or qualified.

The designated welding techniques may be divided into two groups: diffusion or solid phase welding, and fusion welding, whereas the first is either performed in a hot isostatic press (HIP) or in a uniaxial hydraulic press, both after different specific joint preparations. Fusion welding may be performed either by electron beam (EB), laser beam, hybrid MIG/laser, or by tungsten inert gas (gas tungsten arc) welding with filler wire.

The general objective is to support the fabrication development in the blanket areas and to improve the reliability of the materials and joints according to the TBM design. The joint quality produced by a low pressure HIP diffusion bonding process has to be investigated with respect to prior surface state conditions. The quality assessment of fusion welds will be continued with special emphasis on 40 mm thick welds and their post-weld heat treatments (PWHT).

#### **Initial Status**

A comprising weld study on EUROFER plates of 5-12 mm thickness showed that under certain conditions PWHTs may be restricted to one-step tempering or can even be avoided. However, for deep welds, like those necessary to join caps to the first wall (FW), the change of microstructure is too severe to elude full two-step PWHTs. For such welds, CEA uses hybrid welding methods known from pressure vessel fabrication. But EB welding might be an alternative process which will be studied within this task.

For an efficient TBM fabrication the application of different milling processes would be unavoidable. This applies particularly to the production of cooling channels by diffusion welding, like those in the first wall or caps. Therefore, characterizing the influence of all industrial production relevant factors on the diffusion weld quality is also included in this task.

#### **Progress**

##### Deep EB Weld Development

For TBM fabrication it is necessary to develop and characterize critical joints. Joining the 40 mm thick upper and lower caps to the first wall is a typical example. Since EB welds have led to best results in our previous studies, we started with the development of an appropriate EB weld fabrication process on 40 mm thick EUROFER bars (Fig. 1). As can be seen quite

clearly in Fig. 1A, with properly adjusted parameters the EB beam produces a rather straight and equally narrow fusion zone. There is just a small heat affected zone (HAZ) and first microstructure examinations have revealed a low defect density of bubbles and micro-cracks.

Unfortunately, the fusion zone is littered with  $\delta$ -ferrite formations which reduce the strength of the joint.

Due to the chemical composition of EUROFER,  $\delta$ -ferrite transforms usually into austenite (at temperatures above 1300 °C) and then into martensite (below 385°C) during cooling. But in the case of this first EB weld, quenching was so fast that a significant amount of  $\delta$ -ferrite remained. Therefore, a second try included tempering the bars before welding to about 500 °C to prevent quenching with too high cooling rates. The result can be seen in Fig. 1C and D:  $\delta$ -ferrite formation was suppressed but many bubbles formed in the weld centre with rather large diameters in the millimetre range.

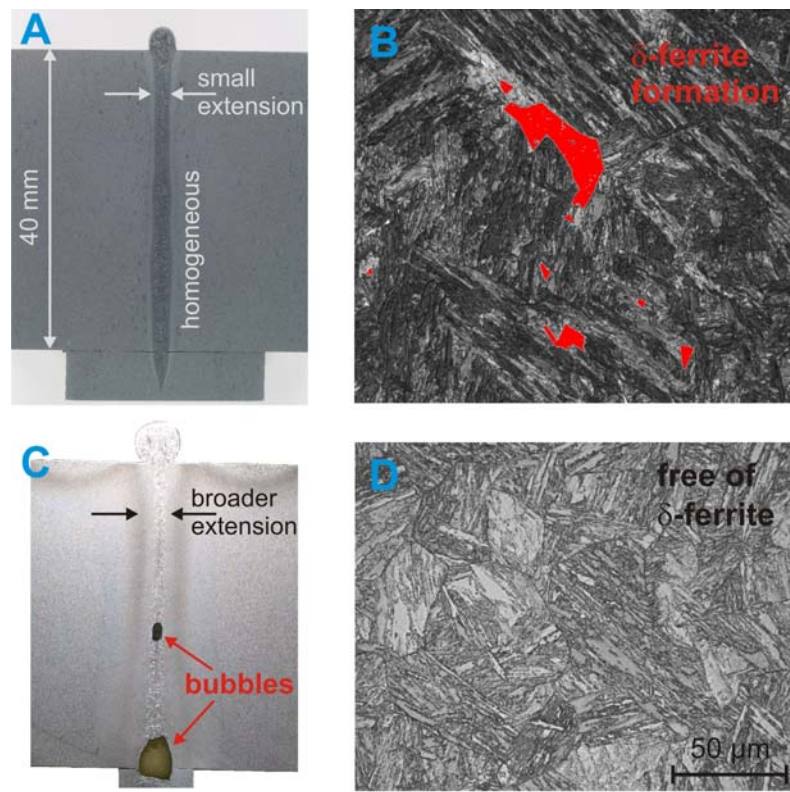


Fig. 1: Cross-sections of the first (A) and second (C) 40 mm deep EB weld. The first EB weld shows a homogeneous microstructure combined with a small lateral extension. But unfortunately, it goes along with an intense formation of  $\delta$ -ferrite (B). The second EB weld was performed after a pre-weld tempering step. With this,  $\delta$ -ferrite formation could be completely suppressed (D), but many bubbles emerged in the fusion zone of the weld (C).

### Diffusion Welding Study

For the characterization and evaluation of diffusion welding technologies for the fabrication of first wall components a large number of weld samples and some small mock-ups have been fabricated. The goal is to examine the influence of surface fabrication, contamination, cleaning, and weld processing.

The first step consisted in the production of weld surfaces by 7 different fabrication processes, that is, different milling cutters and different fabrication parameters have been used. A typical example is illustrated in Fig. 2: In spite of comparable values of surface roughness the structures reveal significant differences. Also the charpy results could be divided into two groups: 4 welds showed the same properties as the base material while the others were clearly worse (see also Fig. 4). The differences could be directly linked to the surface structures. Diffusion welds with surfaces like surface 12 in Fig. 2 resulted in low USE and high DBTT values while welds with surfaces comparable to surface 4 in Fig. 2 were as good as the base material.

The reason for this can be seen in the left image of Fig. 3. Diffusion welding of components with inner channels has to be performed at a low pressure to prevent the delicate structure from deformation. Therefore, the weld specimens were vacuum sealed and have been welded at 1050 °C under 25 MPa for 2 hours. With these conditions, small cavities and a clear weld line still remain in the welding zone. However, there is a possibility to improve such suboptimal weldings: The channels have to be opened. Then a second high pressure

welding step can be applied without deforming the channels. The result of such a second HIP step at 1050 °C under 100 MPa for 2 hours is shown in the right image of Fig. 3 and in Fig. 4. The cavities are removed and this in turn restores the charpy properties.

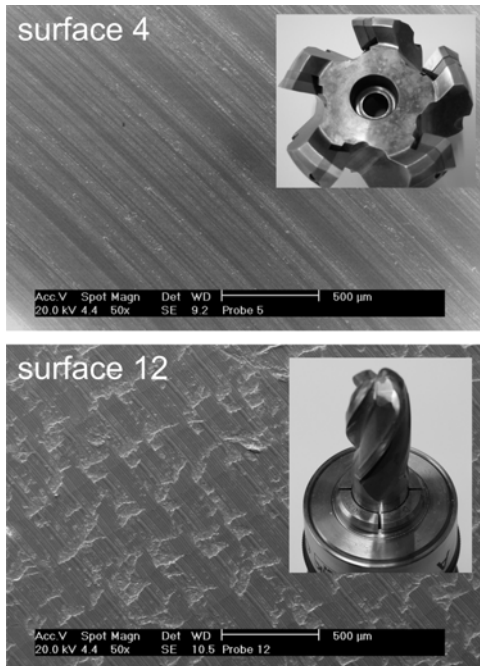


Fig. 2: Even though surface roughness is in the same range, milled surfaces are structured quite different, depending on parameters and tools. For example, surface 4 looks rather smooth with fine structured lines while surface 12 shows irregular cavities. But both surfaces have a roughness of  $\pm 0.6$  µm. Images of the according milling cutters are also shown in the figure.

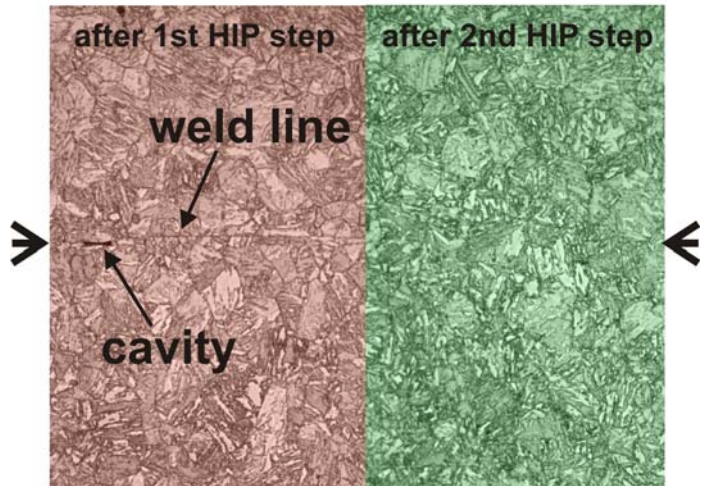


Fig. 3: After the first low pressure HIP step, the weld samples with surface 12 show still cavities (left image, red colored). A weld line between both surfaces is also recognizable. Both, weld line and cavities, vanish after the second, high pressure HIP step is applied (right image, green colored).

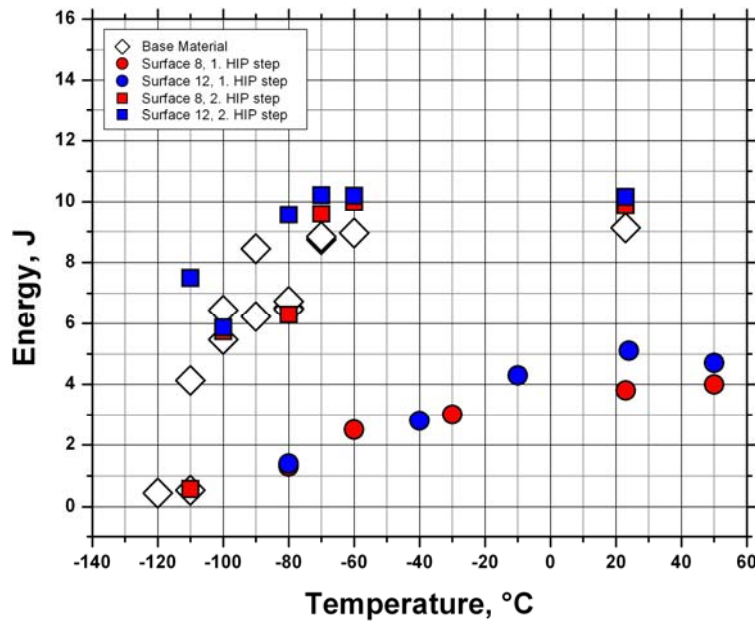


Fig. 4: Charpy test results of specimens which were diffusion welded by 2 HIP steps. Surfaces 8 and 12 have been produced by the same milling cutter (see Fig. 2) but with different parameters. Anyway, both surfaces showed about the same density of cavities. Compared to the base material (white diamonds), the charpy properties are significantly deteriorated after the first HIP step (circles). The second HIP step, however, restores DBTT as well as USE to the level of the base material. The reason for that is given in Fig. 3 and discussed in the text.

## **Conclusions and Outlook**

To utilize EB welding for joining FW and caps further optimization steps have still to be applied to prevent both, bubble as well as  $\delta$ -ferrite formation. But generally, it seems to be a promising joining alternative. The next steps in diffusion weld characterisation consist in a surface contamination study and then in the fabrication of a FW mock-up of DIN-A3 size.

### **Staff:**

A. Baumgärtner  
B. Dafferner  
S. Heger  
U. Jäntsch  
M. Klimiankou  
M. Rieth  
R. Ziegler  
H. Zimmermann

## TTMS-005 Rules for Design, Fabrication and Inspection

### TW2-TTMS-005b D 4 Creep-fatigue Lifetime Prediction Rules for Irradiated EUROFER

The objectives of this task are the modification of the lifetime prediction model developed in TW2-TTMS-005a D4 for RAFM steels under creep fatigue conditions taking into account the irradiation influence and the verification of the modified model by applying it to EUROFER 97 in the post-irradiated state.

During the reporting time period the coupled viscoplastic deformation damage model developed for EUROFER 97 in the reference un-irradiated state [1] has been modified taking into account irradiation influence by modelling the irradiation induced hardening. The modification has been done mainly by adding irradiation hardening variable with an appropriate evolution equation including irradiation dose driven terms as well as inelastic deformation and static recovery terms [2]. Thereby neutron irradiation is assumed to form in EUROFER 97 different types of obstacles, e.g. vacancy clusters, dislocation loops, displacement spikes and helium gas bubbles, which impede dislocation motion, increase strength and reduce ductility. The resulting hardening is then modelled on the base of the theory of the cutting of an obstacle by a dislocation line.

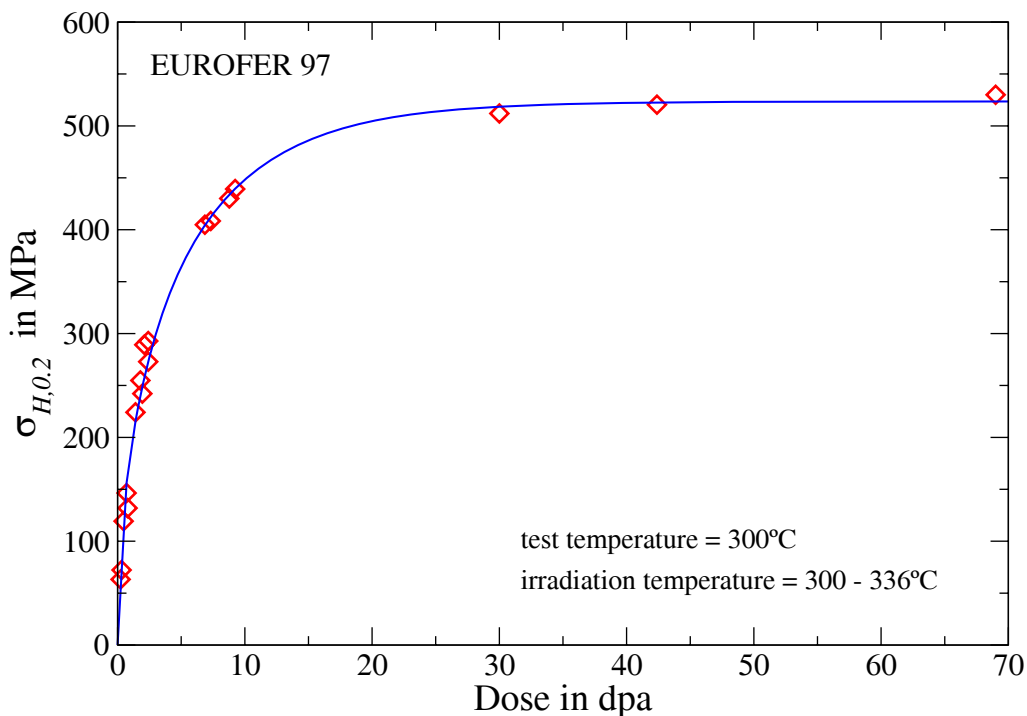


Fig. 1: Irradiation induced hardening as a function on irradiation dose, comparison between experimental data (markers) and model description (solid line).

Applying the modified model to EUROFER 97 we started using the model to describe the increase in yield stress determined after irradiation in post irradiation tensile testing. For this purpose literature data [3] as well as those determined recently within the irradiation programs SPICE and ARBOR 1 and 2 are considered. Taking into account that hardening is induced by only one type of obstacles the model yields a fairly well description of the dependence of irradiation induced hardening on the irradiation dose (see Figure 1). Moreover the model is able to describe the changes of the irradiation induced hardening within the course of inelastic deformation as it is observed in post irradiation tensile tests at 300°C (see Figure 2).

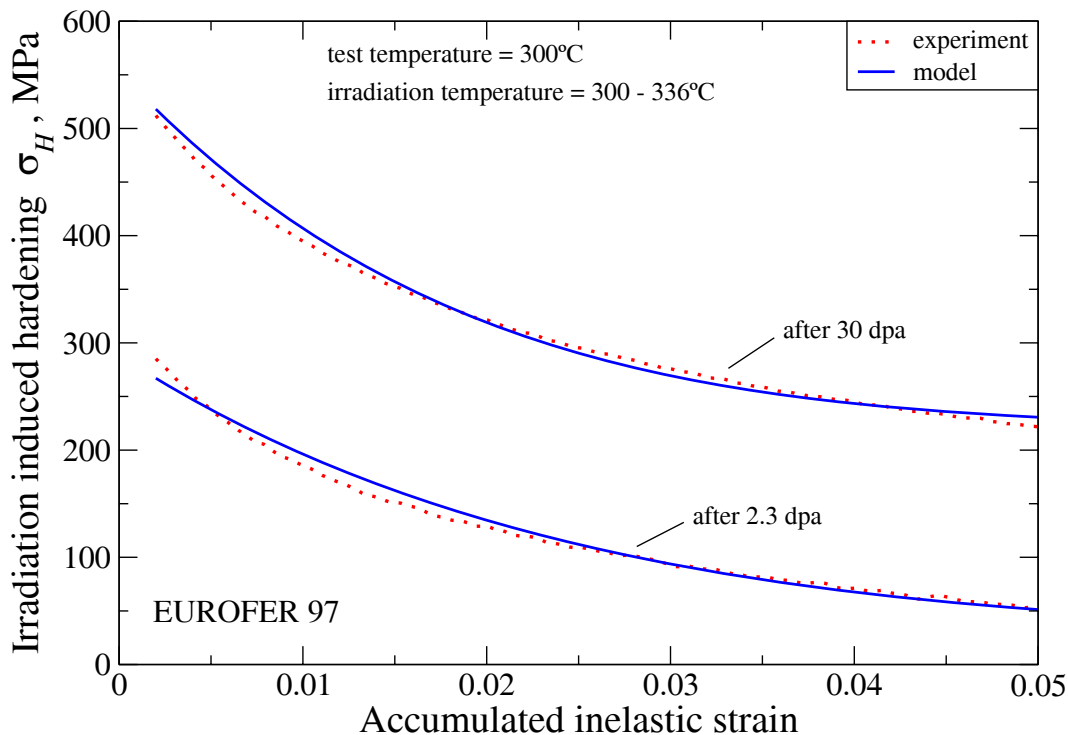


Fig. 2: Influence of inelastic deformation on irradiation induced hardening, comparison between experimental data (dotted lines) and model description (solid lines).

In conclusion the physically based model developed for the description of irradiation induced hardening allows not only the determination of hardening due to neutron irradiation but also its alteration under inelastic deformation and high temperature dwell conditions. Its coupling with the model describing the deformation and damage behavior of EUROFER<sup>97</sup> in the un-irradiated state provides a powerful tool for the prediction of the constitutive behavior of EUROFER<sup>97</sup> during and after neutron irradiation under low cycle fatigue conditions. When applying the model to the hardening behavior of EUROFER<sup>97</sup> after neutron irradiation fairly good results could be obtained determining the model parameters at 300°C. However further applications are necessary to determine the model parameters at other relevant temperatures and to verify its prediction ability.

#### Staff:

J. Aktaa

#### Literature:

- [1] J. Aktaa and R. Schmitt, Fusion Engineering and Design, 81 (2006) 2221-2231.
- [2] J. Aktaa and C. Petersen, ICFRM 13, Nice, France, Dec. 2007
- [3] E. Lucon et al., Fusion Engineering and Design, 81 (2006) 917-923.
- [4] J. Aktaa and C. Petersen, "Modeling of the Deformation and Damage Behavior of Irradiated EUROFER 97 under Low Cycle Fatigue Loading," ICFRM 13, Nice, France, Dec. 2007
- [5] J. Aktaa, M. Klotz and C. Petersen, "Deformation and damage of RAFM steels under thermo-mechanical loading: A challenge for constitutive equations," Journal of Nuclear Materials, 367-370 (2007) 550-555.
- [6] J. Aktaa, M. Weick and M. Walter, "High temperature creep-fatigue structural design criteria for fusion components built from EUROFER 97," Wissenschaftliche Berichte des Forschungszentrums Karlsruhe, FZKA-7309, August 2007.

### **TW5-TTMS-005 D 3**

#### **SSTT: Model the Ductile Region - Development of Models for Transferability of Small Size Specimens to Standard Size and FW Applications**

### **TW6-TTMS-005 D 12**

#### **SSTT: Continuation of Modelling the Ductile Region - Development of Models for Transferability of Small Size Specimens to Standard Size and FW Applications**

### **Introduction**

Due to the limited irradiation volume provided by irradiation facilities, it is necessary to develop small specimen testing technologies for fracture mechanical characterization of irradiated reduced-activation ferritic-martensitic steels (RAFM). Among others miniaturized fracture mechanical three-point bending specimens are considered with the size of Charpy-V subsize specimens (KLST), commonly used in irradiation programs. As plasticity dominates in RAFM steels the requirements for a valid standard test are not met for miniaturized specimens. The objective is to establish a method which allows transferring fracture data determined with miniaturized specimens in the ductile region for RAFM steels to standard specimens.

In this report a concept based on the cohesive zone method is presented [1]. Within the reporting period this two parameter approach has been used in finite element simulations of three-point bending tests where the effect of the specimen size and of side grooving on the crack resistance has been studied.

### **Numerical approach**

#### Phenomenological cohesive zone model

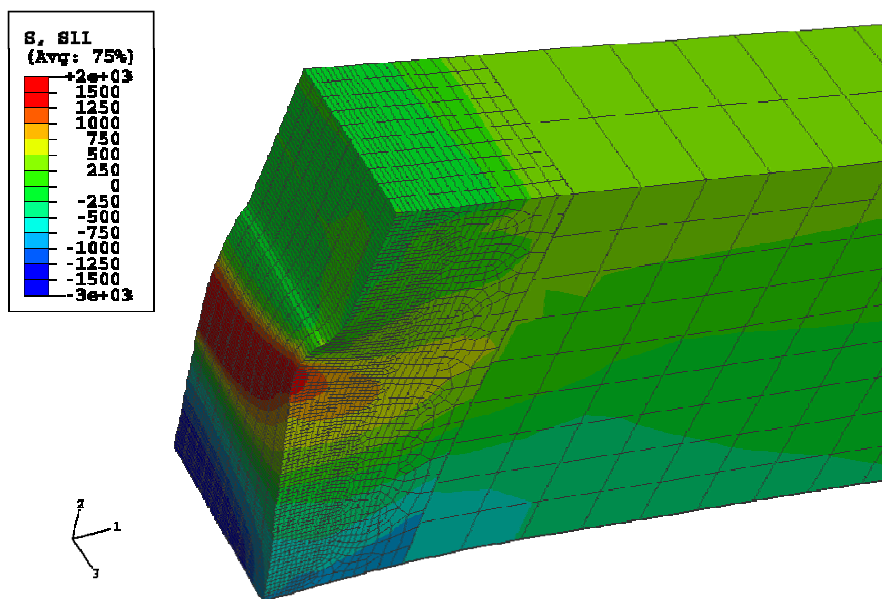
Cohesive zones are a suitable method to handle crack initiation and crack propagation with a prescribed traction separation law [1]. They have already been successfully applied to study the fracture behaviour of ductile [2] and brittle [3] materials. In case of ductile metals like RAFM steels the separation of the cohesive zone originates from the void nucleation and void growth in the process zone around the crack tip. We chose the partly constant traction-separation law (TSL) presented by Scheider and Brocks [4] for ductile behaviour. The main cohesive parameters are the cohesive strength  $\sigma_c$  and the critical separation  $\delta_c$  or alternatively the separation energy  $\Gamma_c$ . These parameters can be determined by fitting them to experimental curves such as  $J$ - $R$  curves and load-displacement curves. A good starting value for  $\Gamma_c$  can be obtained from a fracture test as the value of the J-integral at crack initiation  $J_{IC}$  and a reasonable value for the cohesive strength  $\sigma_c$  can be determined from notched tensile tests as the maximum true stress at fracture [3].

For our demonstration example we have chosen a value of 250 N/mm for  $\Gamma_c$  which is the  $J_{IC}$  value determined for EUROFER 97 [6] in the subtask D4 and a value of  $\sigma_c$  of 1500 MPa which corresponds to 3 times the initial yield stress [5] of a RAFM steel. The additional shape parameters  $\delta_1$  and  $\delta_2$  shape (for TSL) are taken to be 0.01 and 0.165 mm which results in a critical separation  $\delta_c$  of 0.173 mm.

#### Finite element modelling

Like in the experimental programme performed in D4, we chose a size of 3 x 4 x 27 mm<sup>3</sup> (BxWxL) for the miniaturized bending specimens. Due to the symmetry it is sufficient to model only one quarter by applying the appropriate symmetry boundary conditions. In accor-

dance with the three-point bending tests performed on EUROFER 97 by Gaganidze et al [6] within D4 the initial crack length of interest is  $a_0=1.4$  mm leading to an  $a/W$ -ratio of 0.35. Cohesive zone elements of the size  $0.037$  mm x  $0.15$  mm with 8 integration points are placed along the potential crack ligament ( $B \times (W - a_0)$ ) which lies at the middle plane due to pure Mode I occurring during a bending test. These cohesive zones are implemented in the commercial finite element (FE) code ABAQUS 6.6 as user defined finite elements by use of the user element subroutine UEL developed at GKSS Research Centre Geesthacht [7]. The remaining part of the small specimen is meshed with ordinary 8 noded solid brick elements. The part of the mesh along and around the crack ligament can be seen in Figure 1. The material behaviour of the continuum finite elements is modelled elasto-plastic with a Young modulus of 210 GPa, an initial yield strength of 500 MPa and strong linear hardening ( $\sigma_y=3000$  MPa at  $\varepsilon_{pl}=0.7$ ) to avoid plastic instabilities. The loading conditions are represented by displacement boundary conditions: i) support points are restricted in their vertical movement ( $v = 0$ ); ii) points in contact with the loading device are moved in vertical direction with a given cross head speed.



To study the size effect a second mesh has been created for a specimen with three times larger dimensions, namely  $9 \times 12 \times 81$  mm<sup>3</sup>. To avoid mesh dependency the size of the cohesive zone elements and of the solid finite elements around the crack tip and along the crack ligament remained unchanged.

Fig. 1: Finite element model representing one quarter of a miniaturized specimen showing the  $\sigma_{11}$  stress distribution calculated at a load-line displacement of 2 mm. The initial crack length is 1.4 mm and it has extended in average by 0.22 mm.

## Simulation results

### Influence of the specimen size

The crack growth model presented above was applied to simulate displacement controlled three-point bending tests on miniaturized KLST specimens ( $3 \times 4 \times 27$  mm<sup>3</sup>) with a distance  $S$  between the two specimen supports of 24 mm. As a result Figure 1 shows the stress distribution of  $\sigma_{11}$  (i.e. normal stress component to the crack plane) computed for a load-line displacement of 2 mm. As due to the higher triaxiality in the inner part the cohesive zones placed there experience higher tractions, consequently the cohesive strength is reached earlier and they separate to a larger extent than the ones near the surface. At the middle line the critical separation  $\delta_c$  has been already reached in 10 cohesive elements leading to a crack propagation of 0.37 mm while near the surface only 3 cohesive elements are “broken” (see Figure 1). Averaged over the whole thickness the crack length extension  $\Delta a$  is equal to 0.22 mm.

One important result of the FE calculations are load versus load-line displacement curves as they are the basis for the determination of the J-integral with the ASTM standard E 1820 [8]. As we want to compare our numerical results with the experimental crack resistance curves, we apply the same relation to calculate the plastic J-integral  $J^{pl}$  as proposed in the ASTM standard for the basic test method.

Additionally to  $J^{pl}$  the crack growth  $\Delta a$  is determined for each increment by averaging over the total area of “broken” cohesive elements divided by  $B$ . Note that in contrast to the experimental value this  $\Delta a$  does not include the crack extension due to blunting. In Figure 2  $J^{pl}$  is plotted versus the corresponding crack extension for the miniaturized specimen.

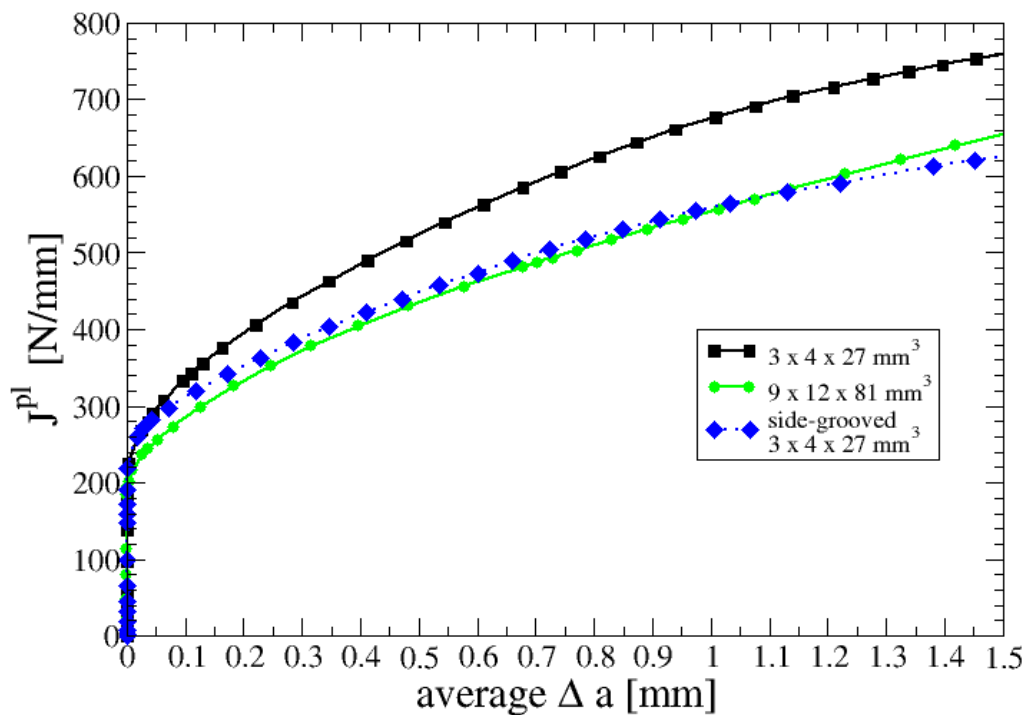


Fig. 2: Crack resistance curves computed numerically for a miniaturized unnotched specimen (marked by the square symbol), for a three times larger unnotched specimen (marked by a circle) and for a miniaturized side-grooved specimen under three-point bending.

The same procedure is repeated with the model for the three times larger specimen. Note that only the geometry is changed while material and cohesive parameters remain the same. The resulting crack resistance curve for the larger specimen is also shown in Figure 2. One can see that it lies below the corresponding curve of the miniaturized which reveals the geometry dependence of  $J(\Delta a)$  curves.

#### Influence of side grooving

To obtain a straight crack front it is common to side groove the specimens. To analyse their effect with our crack growth model, we modified the mesh of the miniaturized specimen by incorporating V-shaped 0.33 mm deep notches along the ligament. The simulations were repeated for this new geometry. The resulting  $J - \Delta a$  curve is marked in Figure 2 as dotted line. Right after the initiation it deviates from the curve of the unnotched miniaturized specimen and approaches the curve of the larger specimen.

The lower value for the J-integral can be attributed to the constraint in thickness direction occurring due to the presence of the notch which is confirmed by Figure 3. There the quarter of the side-grooved specimen is viewed along the horizontal direction looking at the crack ligament revealing the shape of the specimen and the shape of the crack front predicted for a load-line displacement of 2 mm. (see Figure 3a). One can see that only a small contraction occurs in thickness direction in the root of the side groove and that the crack front remains rather straight. For comparison reasons the same view is plotted for the unnotched specimen in Figure 3b for the same average  $\Delta a$  of 0.6 mm. Without a side groove the miniaturized specimen necks stronger resulting in a higher plastic work which is the reason for its higher value of the J-integral.

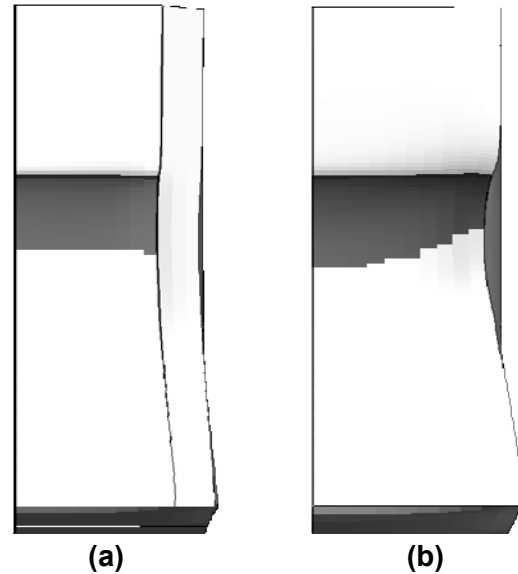


Fig. 3: View on half of the crack ligament showing the crack front for a miniaturized side-grooved specimen at a load-line displacement of 2.2 mm (a) and on the miniaturized unnotched specimen at a load-line displacement of 2.9 mm (b). In both cases the crack has extended in average by 0.6 mm. (On the left side lies the middle line and on the right side there is the free surface).

### Conclusion and outlook

It is well known that experimentally determined  $J - \Delta a$  curves depend on the geometry of the specimen. In this virtual study we could show that our crack growth model based on the cohesive element method can cope with this geometry dependence. With the two cohesive parameters cohesive strength and separation energy it is capable of predicting the different behaviour of small and large three-point bending specimen and of side-grooved specimen. The simulations confirm that side-grooving helps in obtaining a straight crack front and that miniaturized side-grooved specimens show a similar behaviour as large specimens. In the next period we will fit the cohesive parameters to the experimental curves obtained in D4 for miniaturized EUROFER 97 specimens, use the same parameters for the prediction of the crack resistance in standard specimens and verify these results

### Staff:

S.M. Weygand

### Literature:

- [1] A. Needleman, Int. J. Fract. 42 (1990) 21.
- [2] T. Siegmund, W. Brocks, Eng.. Fract. Mech. 67 (2000), 139.
- [3] R. Kabir, A. Cornec, W. Brocks, Comput. Mater. Sci 39 (2007), 75.
- [4] I. Scheider and W. Brocks, Eng.. Fract. Mech 70 (2003), 1943.
- [5] W. Brocks, SID vol.1 no.4 (2005) 233.
- [6] E. Gaganidze, B. Dafferner, J. Aktaa, Forschungszentrum Karlsruhe, FZKA 7252 (2006).
- [7] I. Scheider, GKSS Research Centre Geesthacht, GKSS/WMS/06/02 (2006).
- [8] ASTM Designation: E 1820-99a, ASTM International, 100 Barr Harbor Drive, West Conshohocken, PA 19428-2959, United States.
- [9] S. M. Weygand and J. Aktaa, "A Numerical Study of the Size Effect in Fracture Mechanical Bending Tests with the Cohesive Zone Method", ICFRM 13, Nice, France, Dec. 2007.

## **TW5-TTMS-005 D 5**

### **High Temperature Fracture Mechanical (creep-fatigue) Rules: Formulation and Implementation**

The objectives are the development of the high temperature part of a design code for fusion reactor components built from EUROFER which includes reliable fracture mechanical rules for the assessment of detected defects under creep and creep-fatigue conditions.

Therefore the high temperature fracture mechanical rules of the R5 and PD6539 (British Standards) have been adopted. For application of the rules to assess cracks detected in components built from EUROFER 97 parameters of the creep crack growth relation are required. These parameters will be determined in fracture mechanical tests performed on EUROFER under TW5-TTMS-005 D6, which are however still in progress.

Within the reporting time period the finite element simulations started to verify the validity of appropriate relations estimating crack loading parameters  $C^*$  and  $C(t)$  have been continued. Thereby, the crack loading parameters are calculated using the appropriate algorithm provided by the finite element code for one-dimensional crack in simple 3 point bending specimens and compared with the values estimated by the rules. In the simulations standard constitutive equation for creep as well as the viscoplastic deformation model developed recently to describe the viscoplastic behaviour of EUROFER 97 under low cycle fatigue loading conditions are considered. These extensive simulations and their evaluation are still in progress.

#### Staff:

J. Aktaa

#### Literature:

- [1] M. Weick and J. Aktaa, "Modeling of fatigue lifetime under non-proportional multiaxial alternating loading," *Fatigue & Fracture of Engineering Materials & Structures*, 30 (4) 311-322, 2007

## TW5-TTMS-005 D 6

### Define and Perform Accompanying Experiments to D 5 (e.g. creep crack growth at 550°C)

#### Background and Objectives

For TBM's licensing, in order to establish design rules for the materials, joints and specific sub-components, a broad set of R&D activities have been launched within the WP 2002. These activities will continue with emphasis on implementation in DSCD (Demo structural design code) and verification and validation experiments. Additional rules for HT (high temperature) fatigue-creep interaction need to be formulated, in particular for fracture mechanics.

The low ductility of EUROFER (in particular after irradiation) gives very conservative limits for design against fast fracture and local flow localization. Some experiments are required in support of special design code activities that could lower very conservative assumptions in existing frameworks. Development of small scale test techniques in fracture mechanics will continue including transferability of the small size specimens tests to the behaviour of the TBM's sub-components.

Subtask: The objective is to perform creep crack growth experiments from EUROFER to determine the  $da/dt$  (crack velocity) -  $C^*$  ( $C^*$ -integral)- behaviour at the temperatures 500 °C and 550 °C. The results are needed for to fit material parameters in HT fracture mechanical rules. Therefore long time tests must be done.

#### Status January 2007

The design and fabrication of specimens and the assembling of the experimental set-up was finished. Preliminary tests with a modified set-up for the DC potential method were done in order to determine the correct correlation between voltage and crack length at 550°C.

#### Status

Preliminary tests with the set-up for the DC potential method were done in order to determine the correct correlation between voltage and crack length at 550 °C. (Fig. 1).

Parallel to these experiments, preliminary tests to determine the suitable load cases for the long term experiments were done and new specimens had to be fabricated. Since the middle of the year the work rests, because of personnel problems.

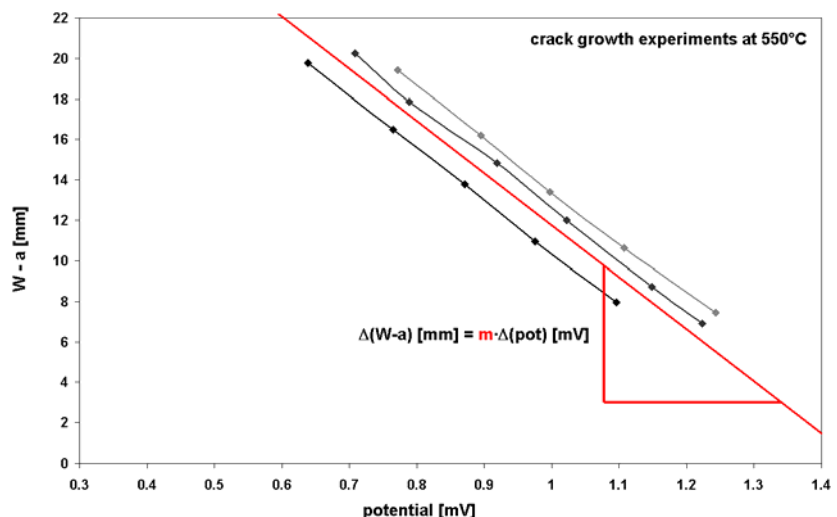


Fig. 1: Results from crack growth experiments at 550 °C to determine the crack growth-potential change-correlation.

## **Conclusion and Outlook**

The preliminary tests with the set-up for the DC potential method in order to determine the correct correlation between voltage and crack length at 500°C and 550°C have been finished and new specimens were fabricated. After the training of a new technician for the project is finished, the new specimens will be prepared (creating the incipient fatigue crack; removal of the side-notches) for the main experiments. Afterwards the preliminary tests to determine the suitable load cases for the long term experiments will be continued to start the main experiments at last.

### Staff:

M. Walter  
M. Lerch

### TW6-TTMS-005 D 3

#### Formulation and Implementation of Design Rules for Joints (TIG, EB, Laser Diffusion Welds)

The objectives are the development of the high temperature part of a design code for fusion reactor components built from EUROFER which includes reliable simplified rules for the assessment of joints under creep, fatigue and creep-fatigue interaction conditions.

Within the reporting time period the creep-fatigue evaluation rules formulated within TW5-TTMS-005 D7 for EUROFER 97 as parent material [1] have been modified for EUROFER 97 welds according to the rules of the ASME-BPV (Code Case N-47, T-1715). Thereby creep fatigue reduction factors are adopted deriving design fatigue and stress-to-rupture curves for welds. The creep-fatigue damage envelope which provides the allowable total damage values remains according to the rules the same for EUROFER 97 and its welds.

The design fatigue curves for EUROFER 97 welds were constructed taking the design fatigue curves for EUROFER 97 as parent material and reducing the values of the allowable number of design cycles by a factor of 2, i.e. the allowable number of design cycles for welds is one-half the value permitted for the parent material (see Figure 1). Assuming that for EUROFER 97 the weld metal creep rupture strength is equal to the base metal creep rupture strength – which however shall be verified by appropriate creep experiments – the stress-to-rupture curves already determined for EUROFER 97 in [2] are modified for EUROFER 97 welds by applying a reduction factor of 0.8 on the minimum stress values  $S_r$ . The resulting curves are plotted in Figure 2.

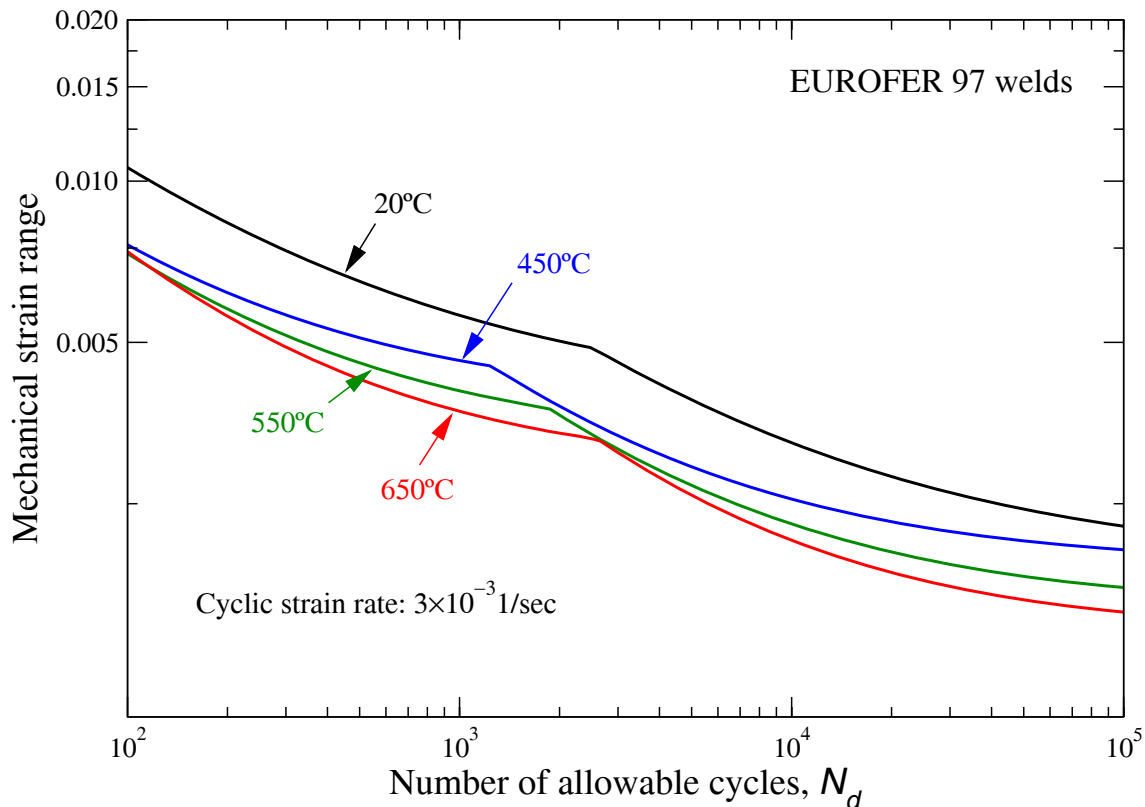


Fig. 1: Design fatigue strain range for EUROFER 97 welds.

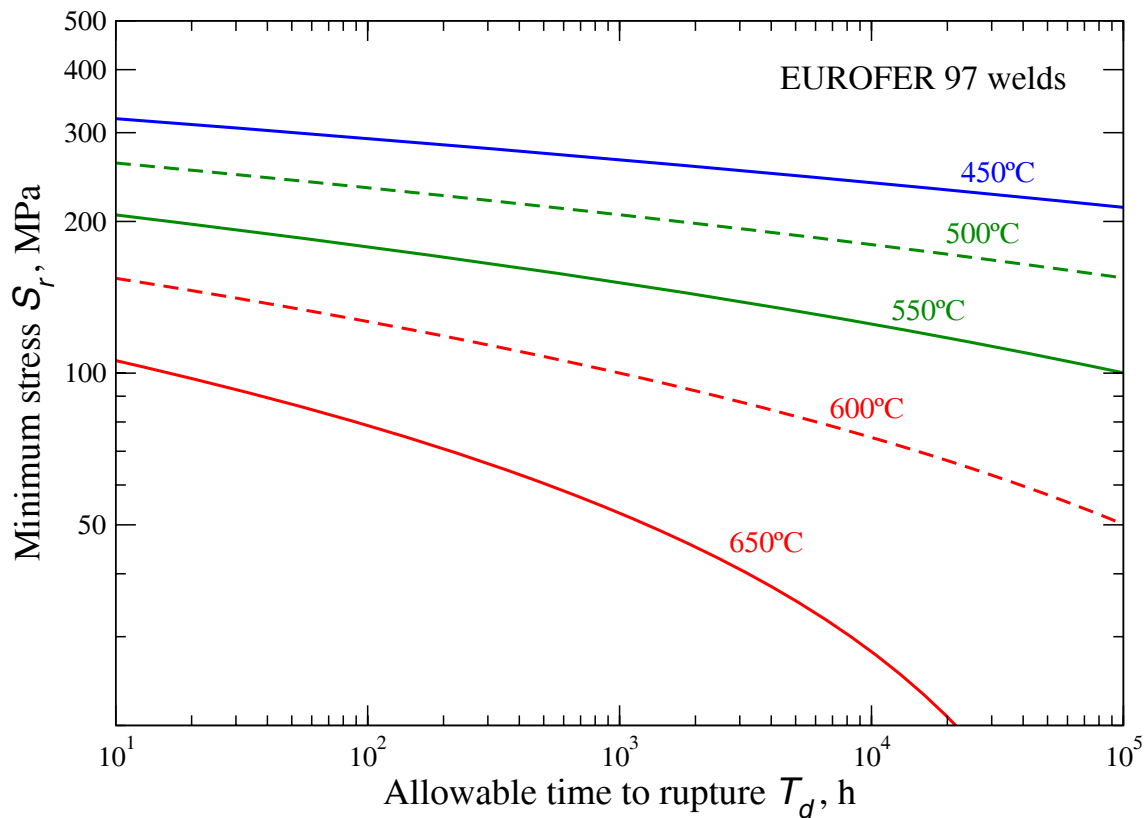


Fig. 2: Stress-to-rupture curves for EUROFER 97 welds

A final report including a draft of the formulated creep, fatigue and creep-fatigue evaluation rules for EUROFER 97 welds is now in preparation and will be shortly published.

Staff:

J. Aktaa

Literature:

- [1] J. Aktaa, M. Weick and M. Walter, "High temperature creep-fatigue structural design criteria for fusion components built from EUROFER 97," Wissenschaftliche Berichte des Forschungszentrums Karlsruhe, FZKA-7309, August 2007.
- [2] F. Tavassoli, Fusion Demo Interim Design Criteria (DISDC) / Appendix A: Material Design Limit Data / A3.S18E Eurofer Steel, DMN Technical Report, DMN/DIR/NT/2004-000/A, 2004.
- [3] J. Aktaa, M. Weick and C. Petersen, "Reduced Softening of EUROFER 97 under Thermo-mechanical and Multiaxial Fatigue Loading and Its Impact on the Design Rules," ICFRM 13, Nice, France, Dec. 2007

## **TW6-TTMS-005 D 4**

### **Experimental Verification and Validation of Newly Implemented HT Creep-fatigue Rules**

#### **Background and objectives**

For TBM's licensing, in order to establish design rules for the materials, joints and specific sub-components, a broad set of R&D activities have been launched within the FP VI. These activities will be continued with emphasis on implementation in SDC (Structural design code) and verification and validation experiments. Additional rules for HT (high temperature) fatigue-creep interaction need to be formulated, in particular for fracture mechanics and subsequently validated within experiments with increasing complexity in loading history and (mock-up) geometry.

The low ductility of EUROFER (in particular after irradiation) gives very conservative limits for design against fast fracture and local flow localization. Investigations are required to define improved fatigue rules that could lower very conservative assumptions in existing frameworks. Development and qualification of NDT (non-destructive detection techniques) should get more attention and need to be launched. In particular, NDT will provide the information needed on the minimum detectable crack-size as function of location in the TBM, which is essential for any reliable crack analysis.

Development of small scale test techniques (SSTT) in fracture mechanics will be continued including transferability of the small size specimens tests to the behaviour of the TBM's sub-components.

Subtask: The objectives are to evaluate the mechanical properties of EUROFER and EUROFER diffusion welded joints in the region of creep-fatigue performing suitable

- Uniaxial isothermal LCF-experiments with dwell time at 500/550°C on EUROFER
- Uniaxial isothermal LCF-experiments with different total strain amplitudes at 500/550°C on EUROFER diffusion welded joints
- Thermo-mechanical fatigue experiments in the temperature range 100-550°C with dwell times on EUROFER.

#### **Status**

The LCF-experiments with dwell times (1, 3 and 10 min per dwell time; dwell time under tension, under compression and under tension and compression at 500/550 °C) have been finished. In general one can observe, that dwell times under compression lead to lower lifetimes than dwell times under tension. This behaviour based on a change of the mean stress. Symmetrical dwell times are also leading to lower lifetimes than dwell times under tension. But here one can additionally see, that the lower the temperature, the lower is the decrease of the stress amplitude in comparison to corresponding tests without dwell times. This fact leads to a clearly larger decrease of the lifetime at lower temperatures. One exception was observed in tests at 500 °C with a dwell time of 10 minutes. Here, the dwell time under tension leads to the shortest lifetime. To figure out the reason for this behaviour, additional tests with longer dwell times should be done. The following Fig. 1 shows the configuration and the results of the experiments.

The fabrication of specimens for the thermo-mechanical fatigue experiments and the LCF-experiments on EUROFER diffusion welded joints has also been finished.

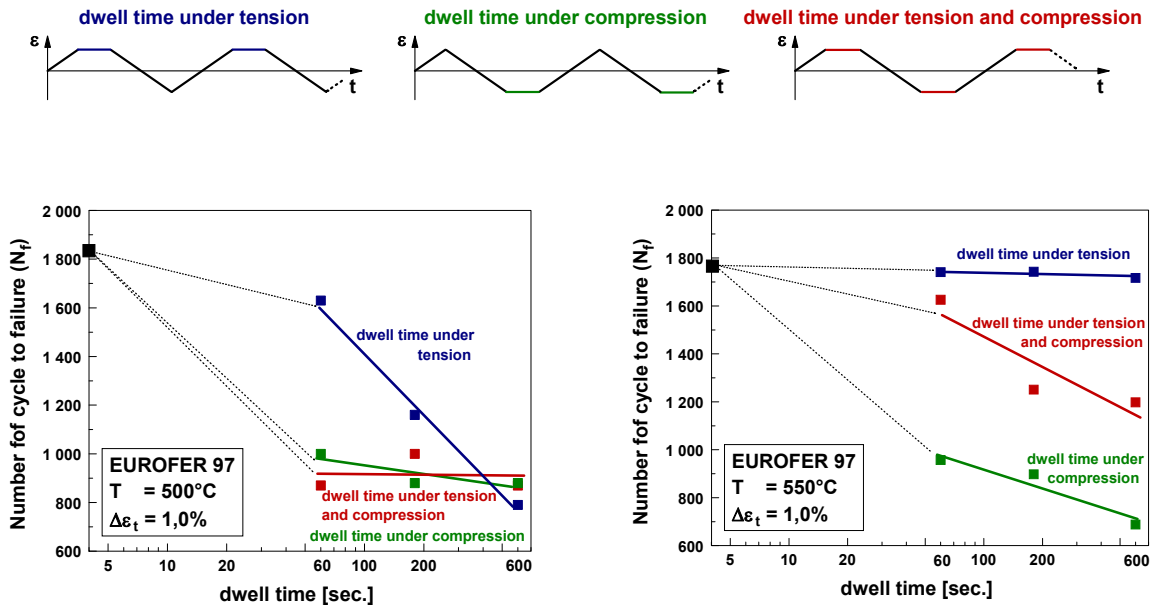


Fig. 1: Configuration and results of the dwell time tests at 500 °C and 550 °C, diagrammed in Number of cycle to failure over dwell time curves.

The LCF-tests on the specimens with diffusion welded joints are running. Experiments at RT and 550°C are nearly completed and one can see, that in general the specimens do not fail at he welded joints. Furthermore there is evidence to suggest, that the lifetimes are in the region of the lifetimes from specimens from base material without diffusion welded joints (Fig. 2).

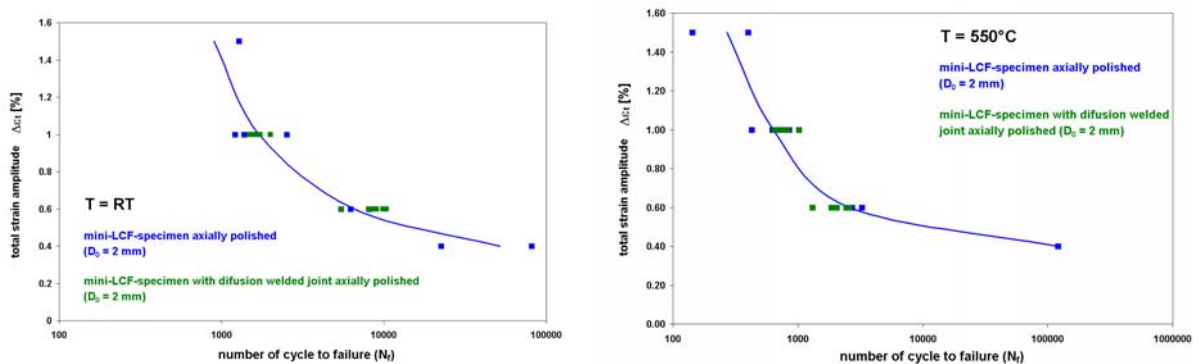


Fig. 2: Comparison of the results of LCF-tests on specimens with- and without diffusion welded joints at RT and 550 °C, respectively.

The diffusion welded material also shows the typical softening behaviour. However, it is observable that the maximum stress level is higher, whereas the single hystereses show lower plastic strain amplitudes. This could base on a marginal change of the micro structure during the welding process. For checking this assumption, additional metallographic investigations are necessary.

The thermo-mechanical fatigue tests will probably start at the end of November. Up to now two testing machines were upgraded with an additional mechanical actuator in order to do thermal- and simultaneously strain/stress controlled experiments in the future. Currently, the last investigations are carried out to test the new experimental set-up.

## **Conclusion and outlook**

The dwell time experiments have been finished, and the tests on specimens with diffusion welded joints are running. Two thermo-mechanical testing machines were upgraded with an additional mechanical actuator and investigations were carried out to test the new experimental set-up. After the completion of the investigations, the thermo-mechanical fatigue experiments will start and in parallel the tests on EUROFER diffusion welded joints will be continued.

### Staff:

M. Walter  
M. Klotz  
U. Bürkle  
M. Lerch

### Literature:

[1] Presentation of the results at EFDA design code meeting 2007 in Barcelona (November 21, 2007)

## **TW6-TTMS-005 D 5**

### **Qualification of NDT (non-destructive detection techniques) for Evaluation of Limits of Detectable Cracks**

The objectives of this task are to find out an adequate NDT (non-destructive detection techniques) for detecting cracks particularly in the welded areas of blanket components built from EUROFER 97 and to realise it with an automated NDT testing procedure.

In the EU Test Blanket Modules (TBMs) design, the low activation steel like EUROFER 97 will be used as structural material. The first wall and cooling plates with cooling channels will be HIP welded, and the stiff grids are expected to be welded by Electron beam (EB) or Tungsten Inert Gas (TIG). Welded structures can fail catastrophically if they contain cracks above a certain critical size for the load applied. Using the concepts of fracture mechanics, it is possible to determine the extent to which a pre-existing crack might propagate to an unacceptable level during service. For computation of fracture mechanics parameters like stress intensity factor, it is essential to know the exact location, configuration and the size of the cracks. Therefore, development of a non-destructive testing (NDT) method to detect the cracks in the welded area is one of the key issues in developing plasma-facing components (PFCs) for next generation fusion devices. Among the most widely used NDT techniques, Magnetic particle testing (MT), Liquid Penetrant testing (PT) and Eddy current testing (ET) can only detect the flaws on the surface of the specimen. In contrast, radiography and ultrasonic testing (UT) are the most frequently used methods of testing different test pieces for internal flaws.

Within the reporting period the ultrasonic testing has been evaluated. This method can be used to detect surface flaws such as cracks and internal flaws such as voids or inclusions of foreign material. It is also commonly used to measure wall thickness in tubes and can measure diameters of bars. In ultrasonic testing, the wavelength of the ultrasound used has a significant effect on the probability of detecting a discontinuity. A general rule of thumb is that a discontinuity must be larger than one-half the wavelength to stand a reasonable chance of being detected. As a consequence, the ultrasonic wavelength limits the minimum flaw size which can be detected. The velocities of longitudinal and transverse ultrasonic waves in steel are about 5960 and 3230 m/s, respectively. Assuming a frequency of 10 MHz used in the ultrasonic testing, a detectability of discontinuities with a size of about 0.3 mm and 0.6 mm is determined for longitudinal and transverse ultrasonic waves, respectively. A higher frequency will increase the resolution to locate smaller discontinuities; however, the maximum depth in a material that flaws can be located is reduced due to the scattering of the sound energy.

Since the non-destructive testing technique is very essential to monitor the degradation of first wall materials in the nuclear fusion reactor under neutron irradiation during their operation, the development of this technique is needed to maintain the integrity of materials used for structures and components such as first wall. The velocity and attenuation coefficient of both shear and longitudinal waves propagating in the specimens before and after subjecting to irradiation could be calculated to evaluate the embrittlement owing to irradiation.

In the next future UT experiments are planned for which specimens are fabricated with cracks of known size generated and embedded in weldments at predetermined locations, as shown in figure 1. The resolution of phased array UT on the specimens as well as the possibility of detecting cracks by phased array UT shall be determined. The artificial discontinuity with known size could be best evaluated to accurately know the "real reflector size", therefore, it is expected that ultrasonic testing can give this information. However, due to the fact that on the display only the echo can be interpreted, this means the reflected sound coming from the discontinuity, it is very often difficult, and in some cases even impossible, to reliably assert the size of the reflector. In fact, the echo height plays the decisive part when evaluating discontinuities during manual ultrasonic testing. The so called DSG scales should be obtained for the probes evaluating the EUROFER materials. DGS means that the scale is allo-

cated an echo at the Distance, with correctly set Gain and Size. In addition, a curve called Distance Amplitude Curve (DAC) can also be produced by joining the maximum echo heights on the attachment scale. When a discontinuity echo appears, an immediate assessment can be made whether or not the discontinuity echo exceeds the DAC.

After obtaining the fundamental ultrasonic parameters in EUROFER materials, the specimens will be scanned by a phased array probe (which allows an electronic scanning without moving the probe) to detect cracks. Joints between back plate and FW are performed by a UT inspection with an angle beam transducer, scanned from the surface of the back plate, as shown in figure 1. Radiographic testing method is a good alternative to inspect the welds in TMB besides UT.

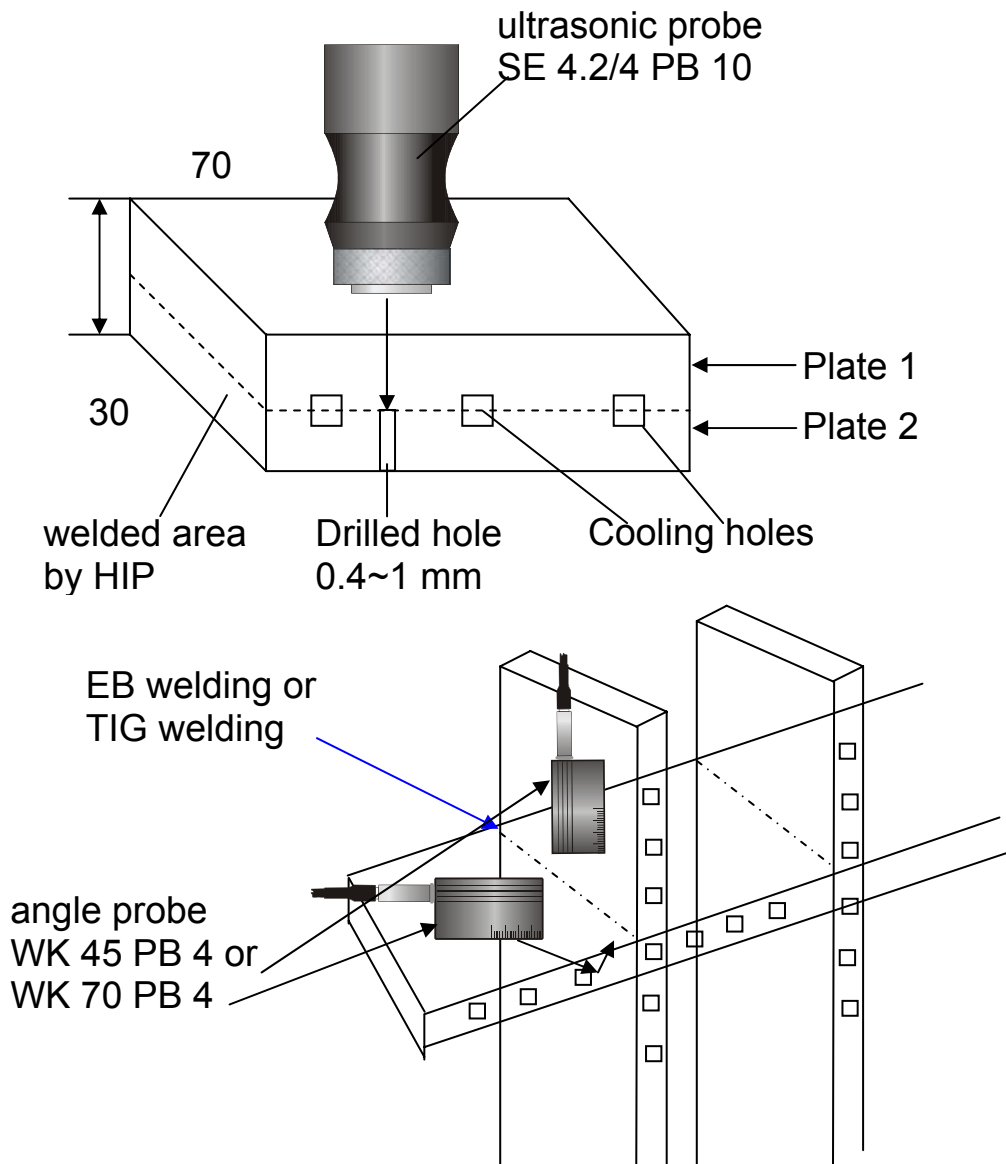


Fig. 1: Sketch of Ultrasonic testing on HIP welded and EB and TIG welded specimens.

The final objective is to build up a facility to inspect the TBM with automated ultrasonic inspection, because the ultrasonic inspection can only be fulfilled with automation owing to irradiation of neutrons in practice. The automated inspection is quite different from the manual inspection: the test traces are predefined and the subjective influence of the operator is ruled out, leading to reliable test results. Also, high quantities of specimen are more reliably

tested with an automated test procedure. Consequently, an automated ultrasonic scanning system with focused immersion transducers should be built up. The scanning system is computer based and stores the full-waveform ultrasonic A-scan (amplitude vs time), B-scan (vertical cross-section) and C-scan (plan view).

Staff:

J. Aktaa  
Y. Zhong  
S. Knaak

## **TTMS-006 High Performance Steels**

### **TW5-TTMS-006 D 5**

#### **Nano Compositing Ferritic Steels for HT Application: Identification of Promising Candidate Alloy Compositions and Respective Fabrication Routes According to the Outcome of the 2004 Study. Production of Different Laboratory Batches (14%Cr)**

The operation temperature of RAFM ODS steels like ODS-EUROFER for application as structural material in advanced blanket concepts like the Dual-Coolant Concept is limited to about 650°C. More advanced blanket concepts like the Advanced HCPB (Model C) or the use as backbone material in gas cooled divertors, require allowable operational temperatures of 700 to 750°C or even more. Reduced activation ferritic (RAF) ODS-steels could fulfil these requirements but are not commercially available at the moment and must be developed. Fe-(12-14)Cr-(2-3)W-(0.2-0.5)Ti-(0.2-0.5)Y<sub>2</sub>O<sub>3</sub> being developed in USA and Japan for fission and fusion application seem to be promising and is presently also considered to form the basis for EU efforts.

Within this task, two master alloys containing 13-14% Cr and 1.0-1.2% W and varying Ti contents were ordered and inert gas atomised. These steel powders formed the basis for the production of different ODS steels with varying Y<sub>2</sub>O<sub>3</sub> and Ti contents by mechanical alloying (MA) in a high-energy attritor mill. Hot-Isostatic-Pressing was applied to consolidate the MA powder. Powders and hiped samples of the different alloys were screened by appropriate methods like metallography, SEM, XRD, HRTEM, and chemical analyses. Tensile and Charpy tests on miniaturised specimens are used for the mechanical characterisation of these alloys. The main goal of this task is the screening of composition, production parameters and heat treatments on microstructure and mechanical properties of RAF 13-14Cr1.1W(Ti, Y<sub>2</sub>O<sub>3</sub>) ODS steels. In a further developmental step the influence of thermo-mechanical treatment and recrystallisation will be determined.

Numerous milling runs were conducted to produce the ferritic ODS-alloy. An item of major interest was the limitation of contamination effects during mechanical alloying in order to produce a final material of high purity. Chemical analyzes of the produced powders were executed to understand this phenomenon and to optimize the milling parameters in this direction.

Furthermore detailed microstructural investigations have been carried out for milling runs. Figure 1 a), b), c) contains TEM bright field images and HAADF images d),e),f) of the produced 13Cr-1W-0.3Ti-0.3Y<sub>2</sub>O<sub>3</sub> ODS-alloy for different milling times (4 h, 10 h, 28 h) but equal rotational speeds (1200/800 rpm) and HIP parameters. Those TEM images in 1a),b),c) reveal a grain structure, which can be divided into two well distinguishable areas: an area with nanometer sized grains, varying from 20 nm to 500 nm and another area with a classical ferritic grain structure from 1 µm to 8 µm. The nanometer grains are roundly shaped, while the micrometer grains have also elongated appearances. This can be interpreted as a bimodal grain size distribution: After 4 h of milling mainly nanometer-sized grains with very few embedded micrometer-sized grains are visible. Increasing the milling time to 10 h shows an enlargement of the micrometer grain areas, resulting in a mixture of both area types. A further increase to 28 h of milling leads to a tremendous reduction of the nano-structured areas. Figure 1c) shows for example, that the nano-sized areas exist only in the upper part. Furthermore the distribution and morphology of ODS-particle characteristics were analysed. In Fig. 1d),e),f) high angle annular dark field detector (HAADF) images of the same samples. ODS-particles can be identified as round spots of dark contrast. Figure 1d) contains ODS-particles with sizes of 10~50 nm located in the middle of the image.

Taking into account the bimodality in grain sizes, it can be stated, that mainly 3-4 nm ODS particles can be found in the micrometer grains, while 12-20 nm particles appear in the nanometer grains, especially on the grain boundaries (Fig. 1e). Additionally in Figure 1f) larger numbers of particles with  $d \geq 20$  nm can be seen. Near those, the 3-4 nm sized ODS-particles were completely missing. The particles were located rather at the grain boundaries than within the grains. Already 4 h milling time were sufficient to form nanometer sized ODS-particles after the HIP-process. But during the analyses several locations on the sample without any ODS-particles were found, so that a general inhomogeneous distribution is assumed. After 10 hours (Fig. 1e) the ODS-particle distribution was a lot more homogeneous, because actionally no sample areas existed, where no ODS-particles were detected. 28 hours of milling resulted also in ODS-particle formation, but the dispersion was not equally homogeneous.

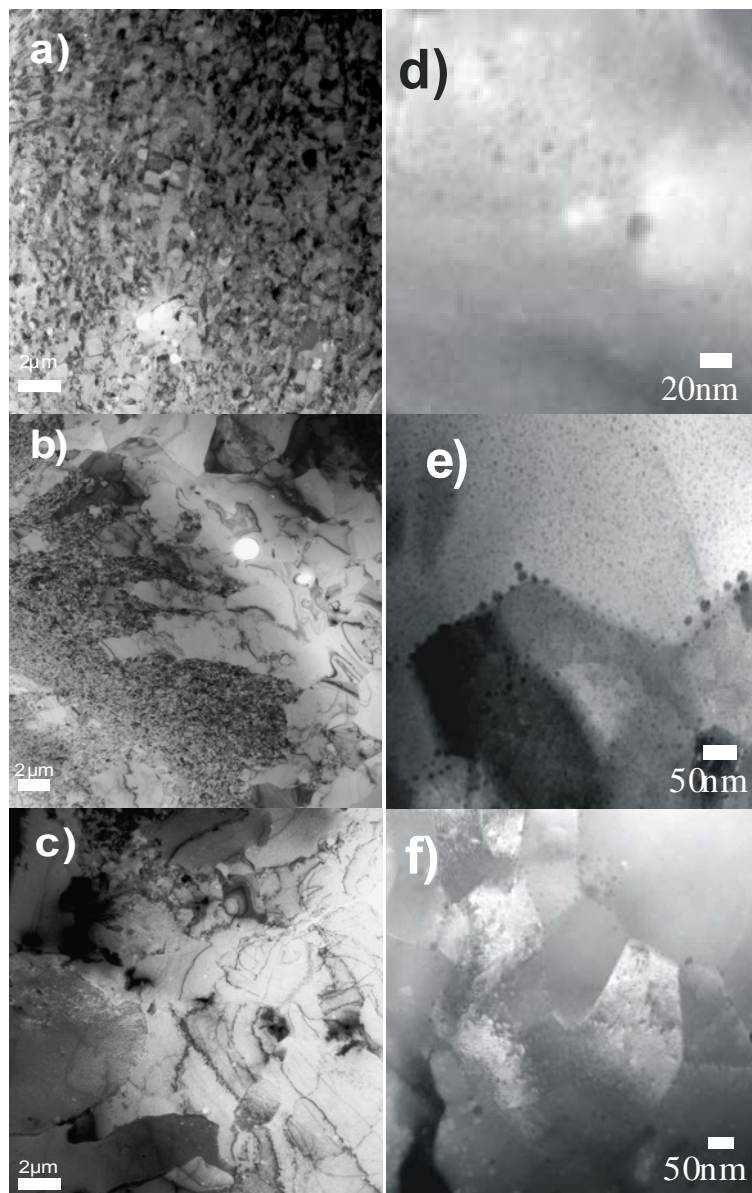


Fig. 1: BFTEM images a),b),c) and HAADF images d),f),e) of the 13Cr-1W-0.3Ti-0.3Y<sub>2</sub>O<sub>3</sub> ODS alloy; a)+d) 4h, b)+e) 10h, c)+f) 28h milling time.

In addition to TEM-analyses several mechanical tests of the produced alloys were carried out. Figure 2a) contains the ultimate tensile strengths  $R_m$  and Figure 2b) the total elongation levels of following alloys: Three types of the 13Cr-1W-0.3Ti-0.3Y<sub>2</sub>O<sub>3</sub> material are displayed, differing in the milling times and rotational frequencies: The 49 h mechanically alloyed pow-

der was milled with 500 rpm instead of 1200 rpm as the other two ferritic ODS-alloys to minimize contamination. All of them got an additional heat treatment (30'; 1050°C) after the HIP-process. FeCr13 specimen were produced from basic powders without any mechanical alloying or heat treatments and were hipped with the same parameter sets. The data of ODS-EUROFER and EUROFER 97 serve as a reference for comparison of the different ODS-alloy types. It can be seen that a significant strength increase also occurs for the three ferritic ODS alloys compared to the basic unmilled FeCr13 material, like it takes place with ODS-EUROFER and EUROFER 97. This increase is even stronger for the ferritic ODS-alloys.

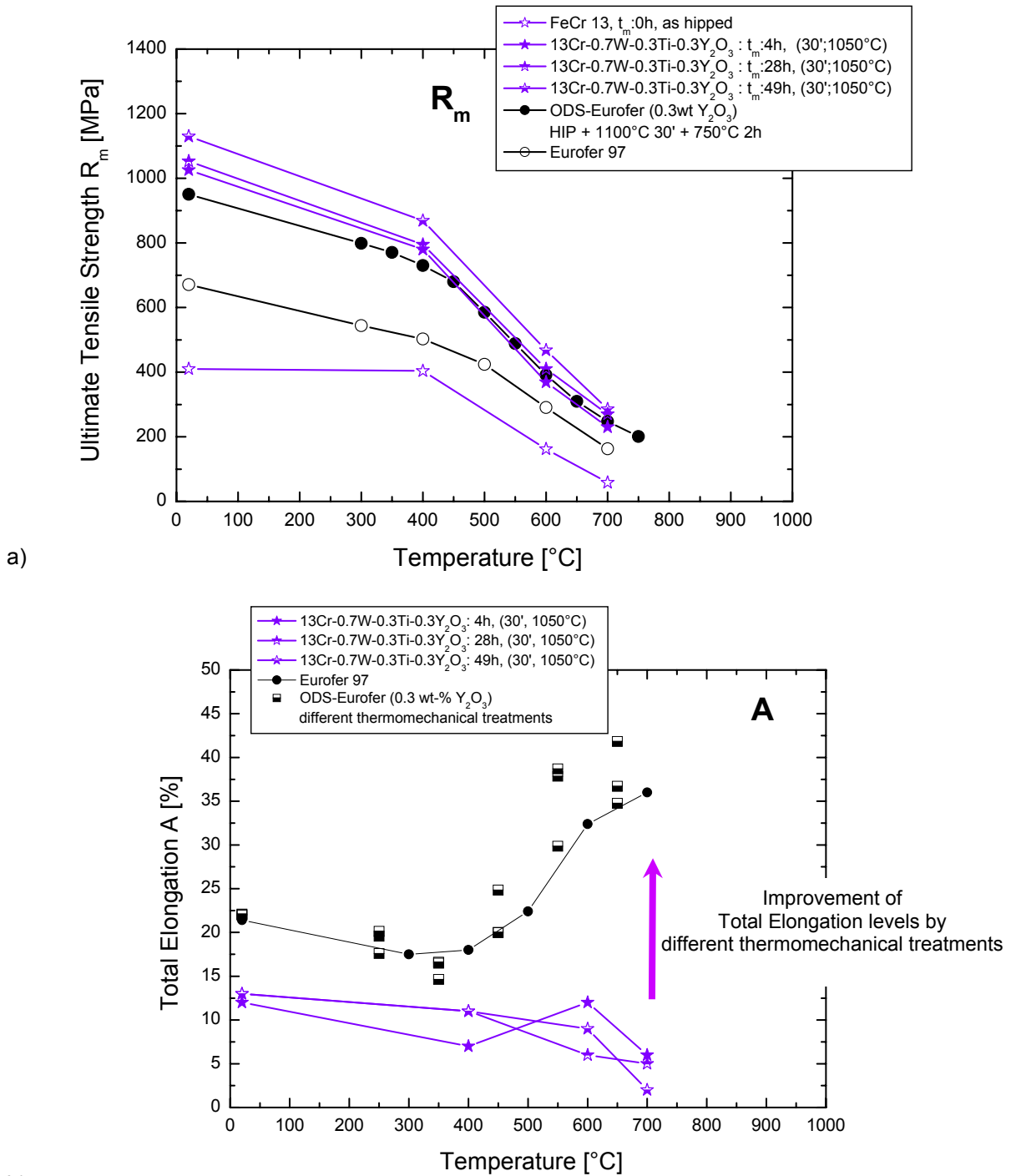


Fig. 2a): Ultimate tensile strengths and 2b) Total elongation of 13Cr-1W-0.3Ti-0.3Y<sub>2</sub>O<sub>3</sub>, manufactured with alternating milling times and following HIP-parameters:  $p_{HIP} = 1000$  bar,  $T_{HIP} = 1150^\circ\text{C}$ ,  $t_{HIP} = 2$  h; comparison with EUROFER 97 and ODS-EUROFER as reference alloys.

At the investigated temperatures, the manufactured ferritic ODS-alloys behave similarly to ODS-EUROFER, with only slightly different  $R_m$  values. The total elongation A of the ferritic ODS-alloys in the conducted mechanical tests is smaller than that of ODS-EUROFER (Fig. 2b).

Furthermore Charpy impact tests for the specimen produced with the same parameter sets have been executed. Hereby the ferritic ODS-alloys have a low ductility at the investigated temperatures. Generally the results of the mechanical tests of the ferritic ODS alloys are very promising, but high temperature ductility and impact behaviour are not yet satisfactory. It is expected, that thermo-mechanical treatments such as rolling or extrusion, which are under execution, shall improve the impact energy levels.

#### Staff:

C. Adelhelm  
S. Baumgärtner  
C. Eiselt  
P. Graf  
M. Klimenkov  
T. Kaiser  
R. Lindau  
A. Möslang  
U. Jäntschi  
R. Ziegler  
H. Zimmermann

#### Literature:

- [1] Ch. Ch. Eiselt, R. Lindau, A. Möslang; First results and prospects on the characterization of the 13Cr-1W-0,3Ti-0,3Y2O3 RAF-ODS-Steel; Poster EUROMAT, Nürnberg, September 10th – September 14th, 2007
- [2] Ch. Ch. Eiselt, M. Klimenkov, R. Lindau, A. Möslang; Characteristic results and prospects of the 13Cr1W0.3Ti0.3Y2O3 ODS-Steel; J. of Nucl. Mat. (2007), Nice, December 10th – 14th, 2007
- [3] Ch. Ch. Eiselt, M. Klimenkov, R. Lindau, A. Möslang; Characteristic results and prospects of the 13Cr1W0.3Ti0.3Y2O3 ODS-Steel; Poster ICFRM 13, Nice, December 10th – 14th, 2007

## TW6-TTMS-006 D 6 Investigate Joining Technologies for ODS/ODS and ODS/conventional EUROFER

### Background and objectives

The use of Oxide Dispersion Strengthened (ODS) steels instead of presently considered conventional RAFM steels would enhance the efficiency of future fusion power plants by increasing the operating temperature by about 100K to 650°C. Advanced blanket concepts like the Dual-Coolant Pb-Li/He Blanket consist of a EUROFER structure with SiC<sub>f</sub>/SiC channel inserts and an ODS-plated First Wall to withstand the higher thermal and mechanical loads. The proof of reliable joining techniques of ODS and RAFM steels is essential to demonstrate the feasibility of such a blanket concept. Diffusion welding is regarded to be one of the most promising methods to produce the necessary ODS-plated structures. It has been successfully demonstrated that diffusion bonding can be applied to produce reliable dissimilar joints of hipped ODS-EUROFER and EUROFER material with good tensile and Charpy impact properties.

Advanced He-cooled modular divertor-designs contain ODS steels as backbone material. The design requires the necessity to join ODS/ODS and ODS/EUROFER. Besides diffusion welding other joining technologies shall be examined. First trials show, that Electron Beam welding could be applied in principle although no experience exists on the mechanical and microstructural properties of such a joint.

Since the first wall of a Dual-Coolant Pb-Li/He Blanket will consist of a layer of rolled ODS-EUROFER plate material, the experiments will be performed on plate material of the new improved 50 kg EU-ODS-EUROFER batch and conventional EUROFER plate material. The welding parameters will be adapted to the material combination as well as to the joining method. Different post-weld-heat treatments PWHT will be examined. Tensile and impact properties will be examined using qualified miniaturised specimens (Ø2x27 mm tensile, KLST). Microstructural investigations by means of OM, SEM, and TEM will be performed to understand the underlying mechanisms.

### Status of work

Basing on the experience with earlier diffusion welding experiments of EUROFER and ODS- EUROFER of the first generation, blocks of 60x60x20 mm of these materials have been produced to perform the diffusion welding experiments. The diffusion weld (DW) surfaces were dry milled to a surface roughness of  $R_t \leq 2 \mu\text{m}$ . Degreasing was performed in an ultrasonic bath in acetone. Immediately after cleaning the specimen halves were seal welded at the edges of the parting line by electron beam welding. The sample preparation is accomplished.

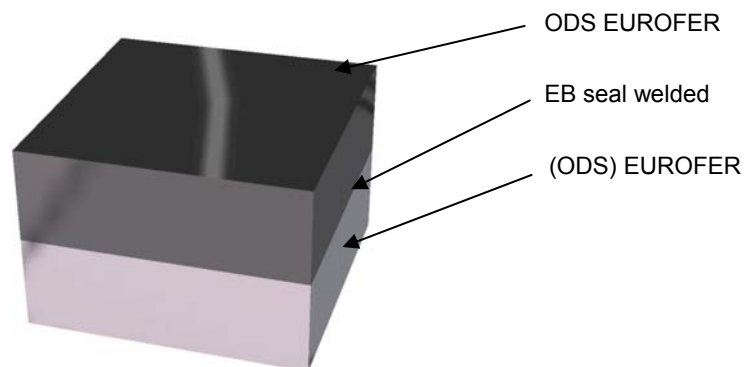


Fig. 1: Sample layout for diffusion welding of ODS-EUROFER/ODS-EUROFER and ODS-EUROFER and EUROFER.

## Outlook

In the next step the HIP diffusion welding will be performed in each case at temperatures between 980 and 1100°C and a pressure of 100 MPa followed by a post weld heat treatment (PWHT). The PWHT conditions will be varied with respect to the austenitising temperature as well as to the tempering treatment to study their influence on the mechanical and microstructural behaviour. The specimen sampling can be seen from Fig. 2.

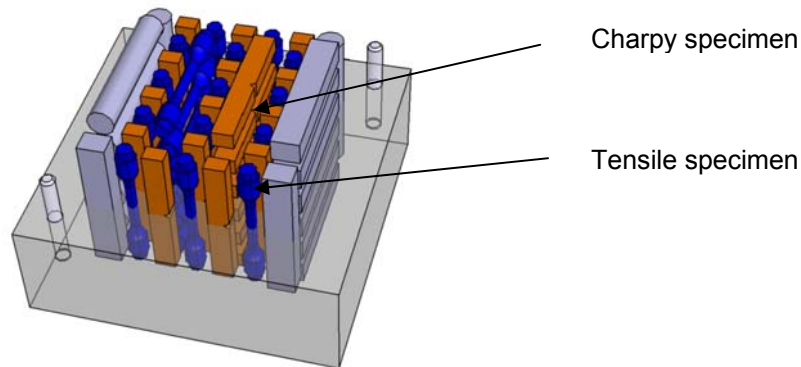


Fig. 2: Example of the specimen sampling from the diffusion welded blocks.

## Staff:

U. Jäntsch  
Dr. M. Klimenkov  
R. Lindau  
R. Ziegler  
H. Zimmermann

## Literature:

- [1] "Nuclear Fusion Programme Annual Report of the Association Forschungszentrum Karlsruhe/Euratom October 2002 – September 2003", FZKA Report 6966, 2004, p 156.

## TW5-TTMS-006 D 10

### Characterisation of Reference EU-ODS-EUROFER Batch: Optimisation of Heat Treatment, Ageing Behaviour and Microstructural Characterisation

The efficiency of future fusion reactors will strongly depend on the operating temperature allowed by selected structural materials. With this respect, ODS steels are attractive candidates since they would allow to increase the operating temperature by approximately 100°C. The reduced activation martensitic steel EUROFER-97 (8.9Cr, 1.1W, 0.2 Ta, 0.42 Mn 0.11 C wt%), which is currently considered as a European reference for structural application, has been selected as a base material. Based on the experience with a precursor a 50 kg EU-ODS-EUROFER batch has been specified and produced (TW3-TTMS-006 D1a). Within this task an optimum heat treatment should be determined. The influence of different heat treatments on microstructure was also investigated.

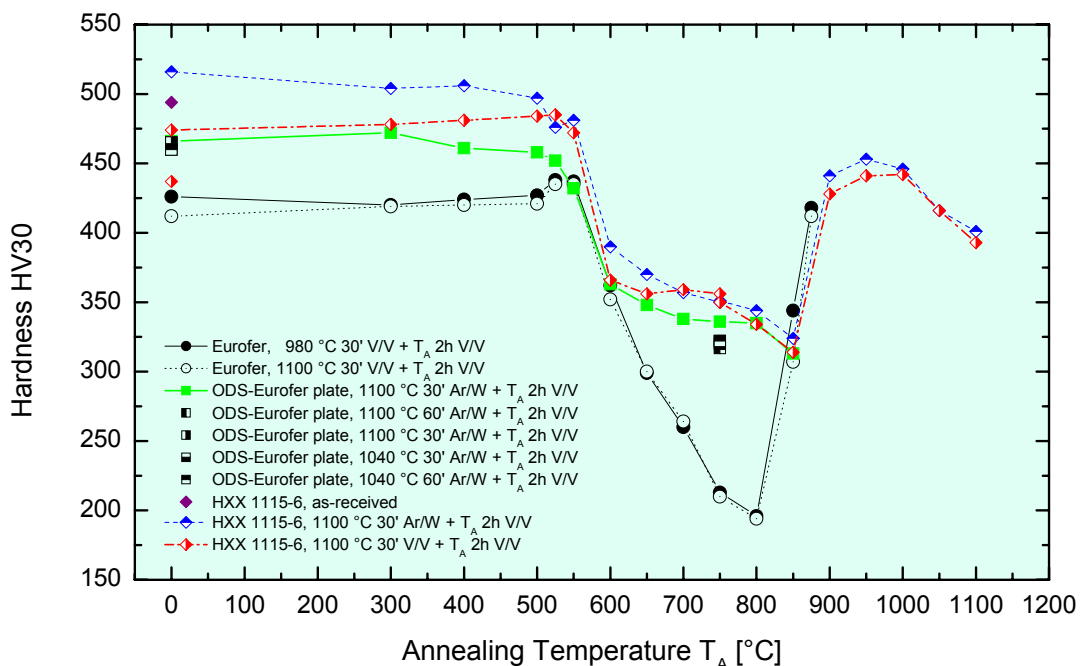


Fig. 1: Vickers hardness HV30 in dependence of the annealing temperature.

First heat treatment trials on the EU-ODS-EUROFER material were performed. The samples were normalized at 1100°C for 30 min following a tempering treatment at temperatures between 300 and 850°C for 2 hours. The cooling to room temperature after austenitisation was performed either by air- or water- quenching. Fig. 1 gives the development of hardness HV30 in dependence of the annealing temperature. The tempering treatment was performed in a tubular 3-zone furnace. The cooling was performed by withdrawal of the furnace from the vacuum quartz recipient. Due to the small specimen size the cooling rate is equivalent to air-cooling. The tempering behaviour of the EU-batch (HXX 1115-6, blue and red diamonds) is compared to the precursor alloy (green and black squares) and standard non-ODS EUROFER steel (full and open black circles). The Vickers hardness of all ODS alloys in the interesting temperature range between 550 and 850°C is very similar. According to the good mechanical behaviour of the precursor ODS-EUROFER steel, 1100°C 30 min air-/ water-quenching + 750°C 2 h air-cooling was chosen as reference heat treatment. Due to a higher C-content (0.13 wt.-%) of the EU-batch compared to the pre-cursor alloys, the material was air-hardening.

The microstructural examinations included OM, SEM, and TEM methods.

The optical micrograph of the HXX 115-6 (Fig. 2) shows a very homogeneous grain structure with grain sizes of about 1  $\mu\text{m}$ . Fig. 3 presents two SEM images that show very similar precipitate distribution in the air-hardened and water-quenched samples.

STEM investigations using a HAADF detector show the presence of well visible with a darker contrast precipitates (Fig. 4). The precipitates show a round shape and their size varies from 30 nm to 300 nm. Statistical evaluations show that their

spatial density amounts to  $(3\pm 2) \cdot 10^{13} \text{ cm}^{-3}$ . In most cases the precipitates are statistically embedded in the matrix, however areas where they are ordered along lines have also been observed (Fig. 4). These lines often extend to a length of more than 10  $\mu\text{m}$  – the entire TEM transparent area on the specimen edge. These lines are apparently not coincident with the prior austenitic grains.

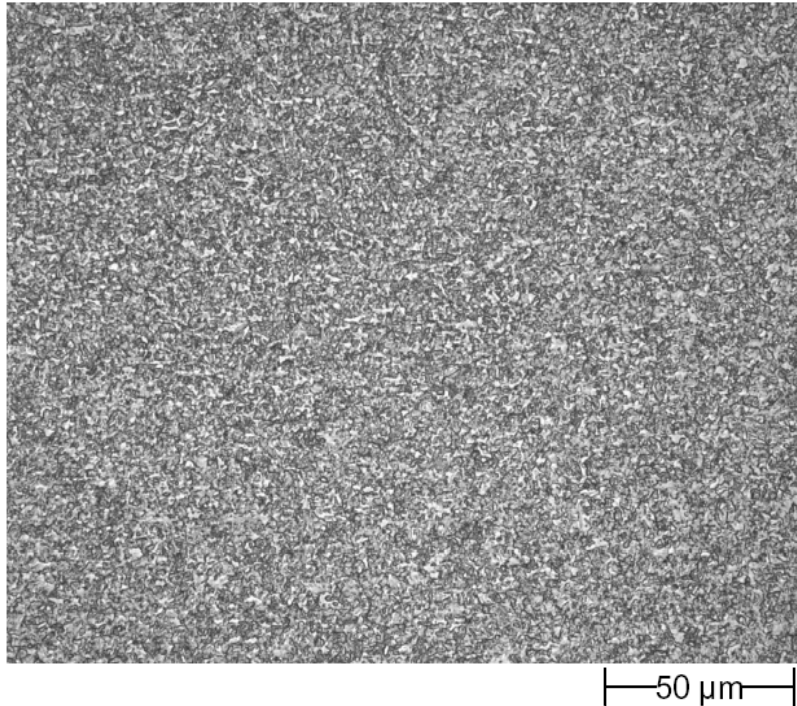


Fig. 2: Grain structure of EU-ODS-EUROFER

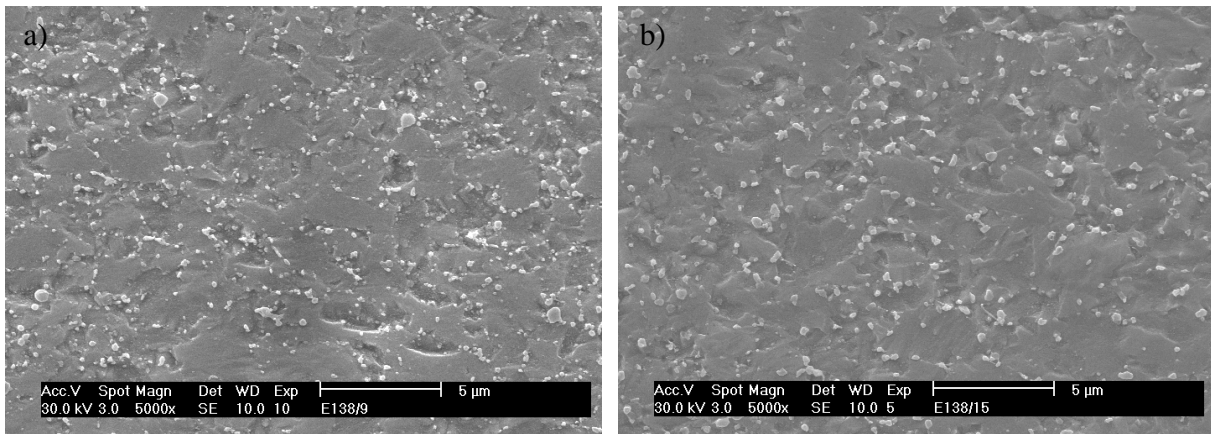


Fig. 3: SEM images taken from air-hardened (a) and water-quenched (b) samples.

Fig. 5 shows the impact energy of this EU-batch in comparison to the former FZK ODS-EUROFER heat and EUROFER base steel. The results clearly show a higher Ductile to Brittle Transition Temperature (DBTT) and lower Upper Shelf Energy (USE) compared to the precursor FZK ODS-EUROFER heat, independently from the applied heat treatment. It is assumed, that the occurrence of the above mentioned aligned precipitates are the reason for the deterioration of the impact properties.

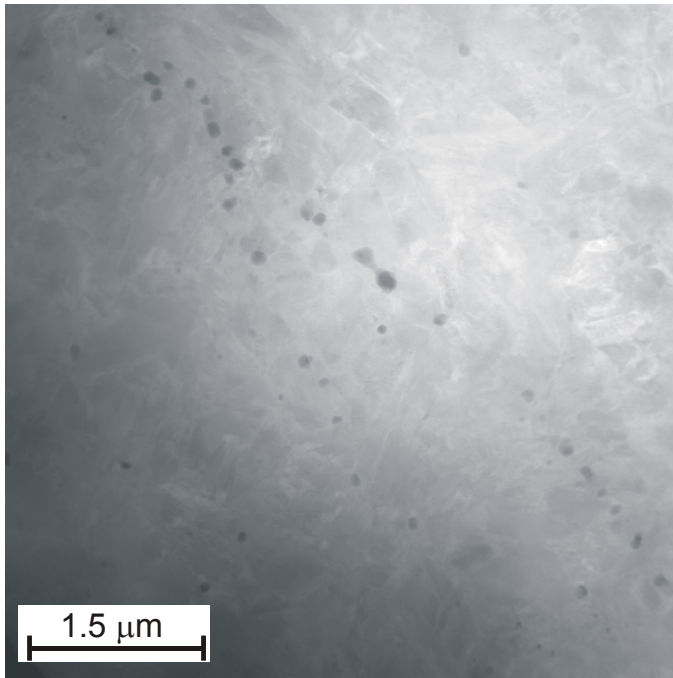


Fig. 4: The HAADF image of area with ordered precipitates.

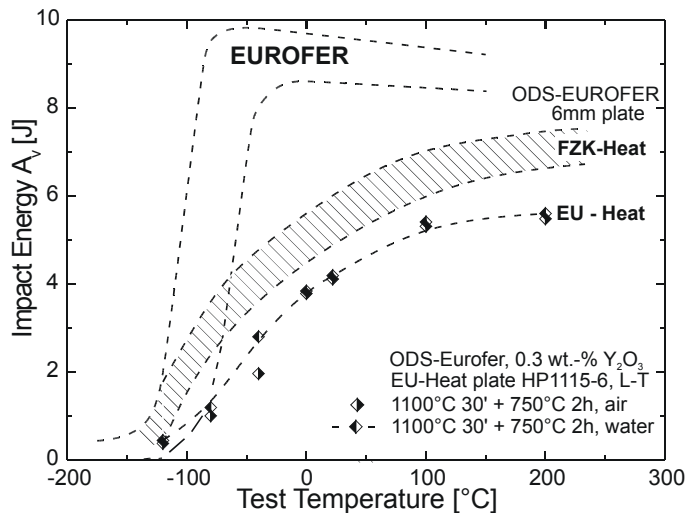


Fig. 5: Test temperature dependence of total absorbed energy of ODS-EUROFER (FZK-Heat, EU-Heat) compared with RAFM steel EUROFER 97.

nm interplanar distance with an  $85^\circ$  angle between them. The pattern was compared with several simulated diffraction patterns of known Cr-Mn(V) oxides. This pattern corresponds to the [521] orientation of a spinel structure with 0.845 nm lattice constant. The theoretical calculations show that the atomic planes of {311} type in this structure have a distance of  $d_{311}=0.255$  nm with an angle of  $84.6^\circ$  between them. Taking into account the measured chemical composition, it can be suggested that the oxide precipitates consist of manganese chromium oxide with  $(\text{Mn,Fe})(\text{Cr,V})_2\text{O}_4$  composition. This phase is more suitable concerning chemical composition among the other manganese chromium oxide phases with the same crystalline structure.

Analytical investigations of the precipitates were performed using EDX and EELS methods. A typical EDX spectrum obtained from such a precipitate shows the presence of V, Cr, Mn and Fe inside (Fig. 6a). The precipitates were also investigated using EELS analysis (Fig. 6b). The background in the spectrum was corrected using power law. The spectrum clearly shows that additionally to V, Cr and Mn, detected by EDX, this precipitate contains also oxygen. The EELS measurements, in contrast to the EDX analysis, clearly show the absence of Fe inside the precipitates. It is well known that the EELS method shows more reliably the presence or missing of Fe inside a precipitate, because the lines in EDX spectra could be influenced by several scattering effects, which may contribute to the error of 3-4%. The EELS investigations have also shown that N or C are not present in the precipitates. Both analytical methods clearly show that the type of the observed precipitate is V-Mn-Cr-oxide. The performed EDX mapping of  $25 \mu\text{m}^2$  areas prove that all visible precipitates show the same composition. In this way such precipitates can be clear distinguished from the carbide precipitates, which appear in the samples after thermal treatments experiments.

The phase identification of the oxide precipitates was performed using HRTEM. The image of a precipitate and its fast Fourier transformation (FFT) image are shown in Fig. 7. The two imaged atomic planes have 0.25

The spatially resolved analytical investigations show that the discussed oxide precipitates are in most cases not single-phased. Fig. 8 shows that the oxide inclusion has two smaller (Y,O)-rich particles, which are located on its surface. The precipitate was scanned with the electron beam in the STEM regime simultaneously acquiring EELS and EDX spectra in each point. Such investigations allow the imaging of the spatial distribution of both, 3-d metals and light (C,N,O) elements. The HAADF image of the precipitate is presented in Fig. 8a. In Figs. 8b, c, d and e the spatial distribution of Fe, Cr, Mn and Y is presented, respectively. As can be seen the Fe concentration reduces to zero in the particle (Fig. 8b). The Cr and Mn elemental maps clearly show increasing concentration inside the precipitate (Fig. 8c,d). At the lower edge of the particle two 40 nm areas, depleted of Fe, Cr, V and Mn are clearly visible. These areas exhibit a bright contrast in the Y and O map (Fig. 8e,g). The particles consist of  $Y_2O_3$  phase – the typical compound of ODS particles. The V-L<sub>2,3</sub> signal increases as expected in the particle. Additionally the V-map clearly shows the formation of a V rich layer around the precipitate. Its thickness was measured to vary from 7 nm on the left side of the to 3 nm on the right side. The layer does not completely surround the precipitate. It is missing on several surface regions. The O-K elemental map (Fig. 8g) shows that the spatial distribution of oxygen also correlates with the precipitate, the two  $Y_2O_3$  particles, as well as the V-rich layer. The direct identification of the phase of the layer is not possible using HRTEM or diffraction methods due to the small thickness.

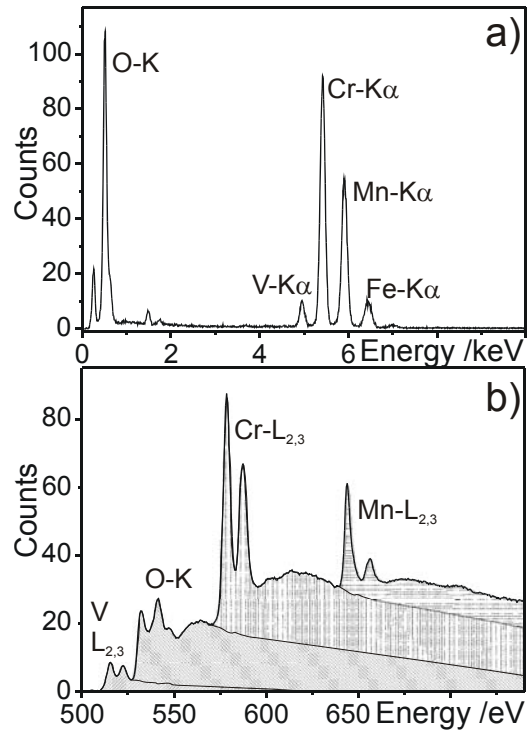


Fig. 6: The EDX (a) and EEL spectrum (b) of an precipitate.

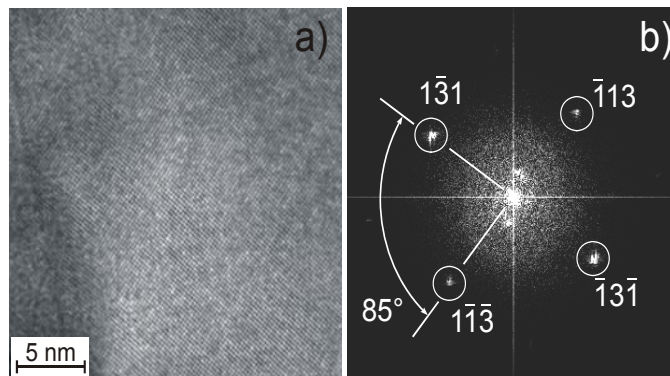


Fig. 7: HRTEM image of an precipitate (a) and corresponding Fast Fourier transformation image.

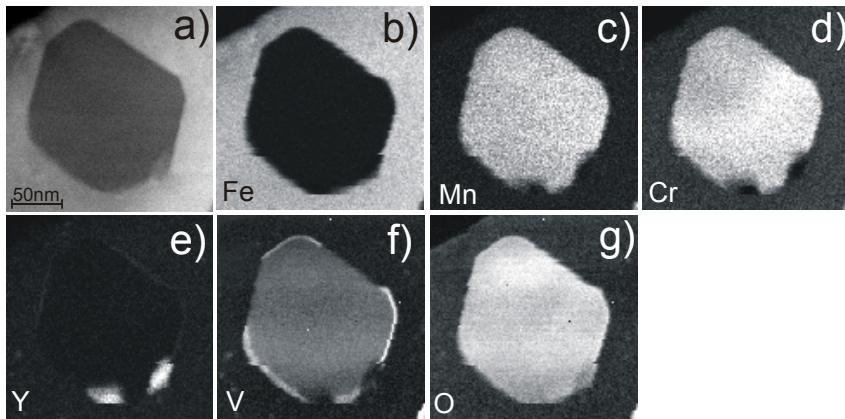


Fig. 8: The HAADF image of an precipitate (a) and Fe, Mn, Cr, Y, V and O elemental maps are presented in parts (b)....(g) respectively.

Staff:

H. Zimmermann  
P. Graf  
U. Jäntschi  
M. Klimenkov  
R. Lindau

Literature:

- [1] M. Klimenkov, R. Lindau, A. Möslang "TEM study of internal oxidation in ODS-Eurofer alloy and its possible influence on mechanical properties", Poster at International Conference on Fusion Reactor Materials (ICFRM-13) December 10-14, 2007
- [2] M. Klimenkov, R. Lindau, A. Möslang "TEM study of internal oxidation in ODS-Eurofer alloy and its possible influence on mechanical properties", Journal of Nuclear Materials, *submitted*

**TTMS-007**  
**Modelisation of Irradiation Effects**

**TW5-TTMS-007 D 5**  
**TW5-TTMS-007 D 10**  
**Defect Microstructure Evolution**

To improve modelling of irradiation effects in FeCr steels there are still answers needed to a lot of open questions, e.g. the interaction of Cr with dislocation loops, the chemical composition at the border of loops and the morphology of the loops formed after ion irradiation. The Fe and Fe-15Cr single crystal specimens were purchased from the Firma MaTeck - Material-Technologie & Kristalle GmbH, Im Langenbroich 20, D-52428 Juelich. The specimens were preliminary cut as discs of 3 mm diameter and 0.1 mm thickness. The crystallographic orientation discs surface was [100].

The discs were implanted in the Center for Ion-Beam-Techniques at Hahn-Meitner Institute Berlin with Au<sup>+</sup> ions. The implantation energy was 350 MeV. The implanted area of 2 mm diameter was located in the middle of the disc (Fig. 1). Totally 4 specimens have been prepared: two Fe-15Cr specimens and two Fe single crystals. The used irradiation conditions are listed in Tab.1.

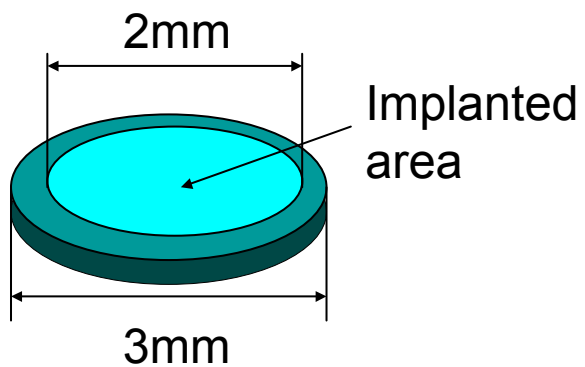


Fig. 1: The schematic image of single crystal specimen with marked irradiated area.

The concentration of implanted ions and radiation induced damages of material were calculated using SRIM program, which is a free available software. The example of these calculations for the Fe-15Cr specimen is presented in Fig. 2. The damage value of the material shows a maximum at 11.7 μm under surface. The maximum of the concentration of implanted ions is located at 12 μm. The implantation of pure Fe specimens shows nearly the same damage distribution.

Table 1: Ion implantation conditions.

No.	Au <sup>+</sup> /cm <sup>-2</sup>	Damage(peak) dpa	Material
1.	5*10 <sup>14</sup>	2.1	Fe-15Cr
2.	3*10 <sup>15</sup>	12.6	
3.	5*10 <sup>14</sup>	2.1	Fe single crystal
4.	3*10 <sup>15</sup>	12.6	

The FIB preparation technique was applied for cross-sectional preparation of TEM lamellas. This method enables imaging in TEM of area that located 8-13 μm under surface (the area with maximal damage).

The TEM investigations were performed using a FEI Tecnai 20 F microscope equipped with EDX System of EDAX Company, Gatan Image Filter (GIF) for EELS measurements as well as with an HAADF detector for scanning TEM. The microscope was operated at 200 kV accelerating voltage with a field emission gun. The EELS experiments were performed in the STEM regime using the HAADF detector with a camera length of 200 mm for imaging. This large value of camera length allows for the STEM imaging of defects of crystalline structure, which can be imaged in conventional TEM using different electron diffraction conditions. For EELS measurements an energy resolution of 1.1 eV and dispersion of 0.1 eV/channel was employed. Experimental conditions were chosen such that the collection semi-angle was 13 mrad.

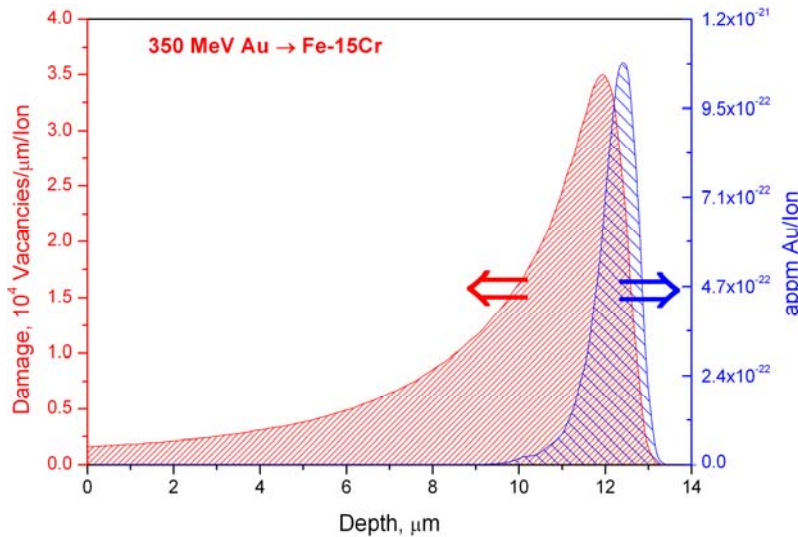


Fig. 2: Depth distribution of implanted Au atoms and damage of the target.

In order to insure substantial TEM characterization of implanted specimens, several lamellas from the different parts of the specimen were prepared. The lamellas after their preparation in FIB show usually the TEM-transparent area till the depth of 18  $\mu\text{m}$ . The STEM and TEM micrographs of such lamella obtained at low magnification are shown in the Fig. 3. The micrographs show clearly that prepared lamella has a low deformation. The bending lines

parallel to the specimen surface are visible in the image. The area of higher damage which is located 9-12  $\mu\text{m}$  under surface is well visible in the scanning mode using dark field detector (Fig. 3a). The material located at the depth of 1-2  $\mu\text{m}$  from the surface is polycrystalline (Fig. 3b). This should be caused by mechanical polishing procedure of the specimen, that has been performed before irradiation.

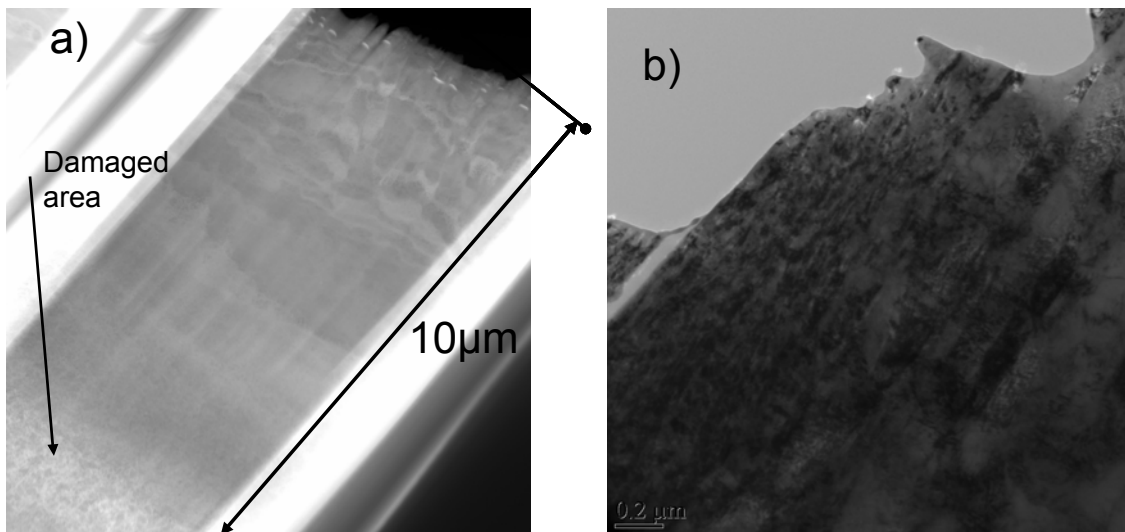


Fig. 3: DF images of the prepared lamella (a), and the bright field image of polycrystalline surface (b).

This lamella with homogeneous thickness appear to be too thick for the imaging of single loops. In the area of maximum damage the thickness has been estimated to be more than 100 nm. The numerous defects, which are also presented in non irradiated area, overlap due to the high thickness and produce unclear TEM images. The imaging of the single loops, the necessarily condition for its detailed analysing, was possible only after further thinning of the lamella. This additional sputtering of the lamella leads to the formation of the small holes around which the lamella thickness allows imaging of single dislocation loops. The lamellas with such holes are presented in Fig. 4.

TEM investigations of the area with maximum damage show the presence of dislocation loops, line dislocations and other small defects (Fig. 5). The lamella has been oriented with [011] zone axis to the electron beam. The beam conditions used for the imaging of disloca-

tion loops are  $g=[002]$  and  $g=[0-11]$ . The typical micrographs with  $g=[0-11]$  are presented in Fig. 5.

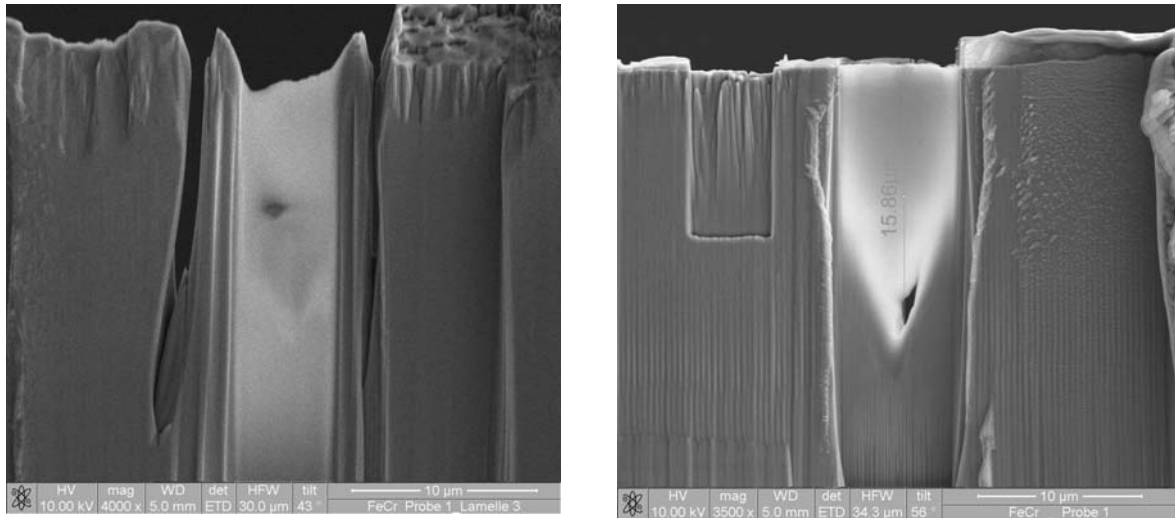


Fig. 4: SEM images of lamellas with formed holes in 9-14 μm depth.

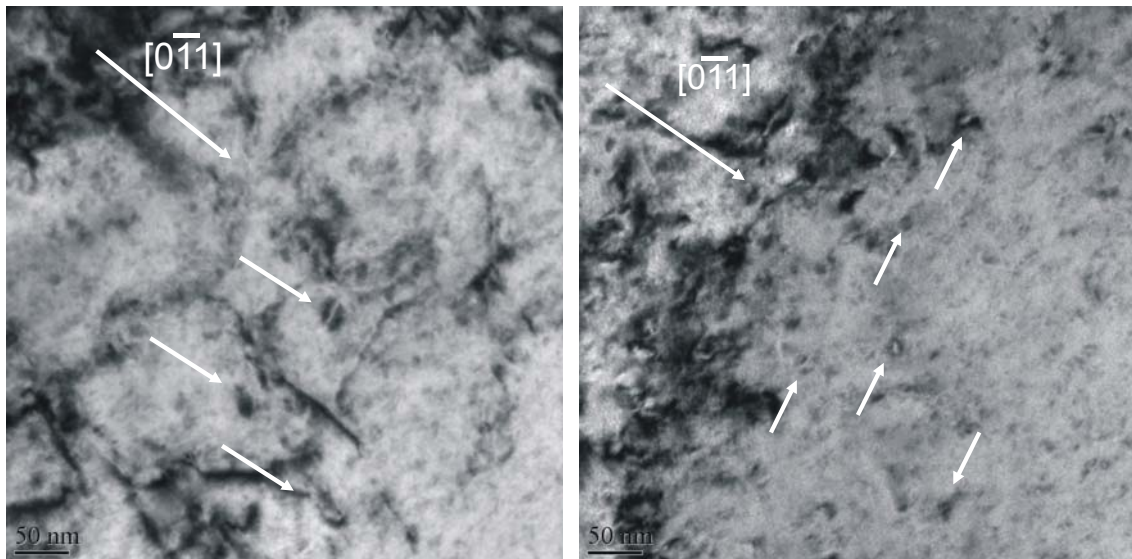


Fig. 5: TEM images of the dislocation loops in Fe-15Cr material (2.1 dpa), marked with arrows.

The dislocation loops are visible as the small rings with the sizes 8-15 nm. The imaging of the loops over the large areas in lamella is difficult due to the slight deformation of the lamella. This deformation results in the changing of specimen orientation by simple specimen shift (bended lamella). The definite orientation conditions, and herewith the imaging conditions, are fulfilled only for the small region in the lamella. For the reliable statistic of dislocation loops the lamella has been several times tilted after specimen moving.

The imaging of the same specimen using  $g=[002]$  shows the invisibility of dislocation loops (Fig. 6). Only few of them could be observed under these conditions. This observation suggest that this dislocation loops have a Burger vector of  $\langle 100 \rangle$  type rather than  $\frac{1}{2}\langle 111 \rangle$  type which should be visible at this imaging conditions. The density of dislocation loops has been estimated to  $(3 \pm 2) \cdot 10^{16} \text{cm}^{-3}$ . The determination of vacancy/interstitial nature of the loops and investigations of their type have not been performed because of the mechanical deformation of the lamella. Such investigations required flat clean specimens and precise crystallographic

orientation to the electron beam. The slight deformation of lamella makes fulfilling of the second condition almost impossible.

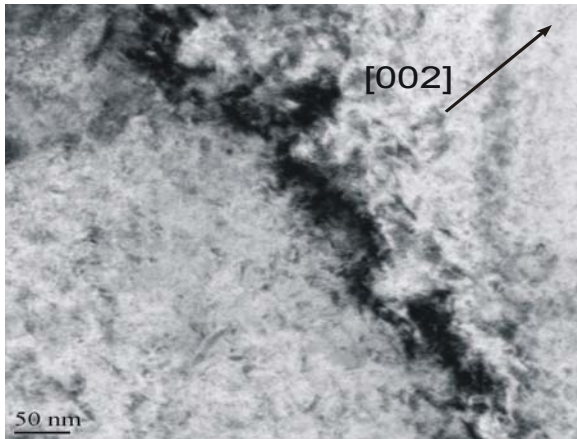


Fig. 6: TEM micrograph of the area imaged with  $g=[002]$ .

The investigation of the lamella areas beyond the implantation (depth  $>13 \mu\text{m}$ ) is necessary for the comparison with the defect structure of irradiated area. This comparison allows clear distinguishing the effects of ion irradiation from material properties and possibly damages during FIB preparation. In the Fig. 7 is presented the DF (HAADF) image of material that has been taken in the area ranging from  $14 \mu\text{m}$  to  $15.5 \mu\text{m}$  depth. The image show the small defects and several line dislocations. The dislocation loops have not been detected even using  $g=[0-11]$  (Fig. 7). This orientation has been successfully used for imaging of dislocation loops in presented specimen.

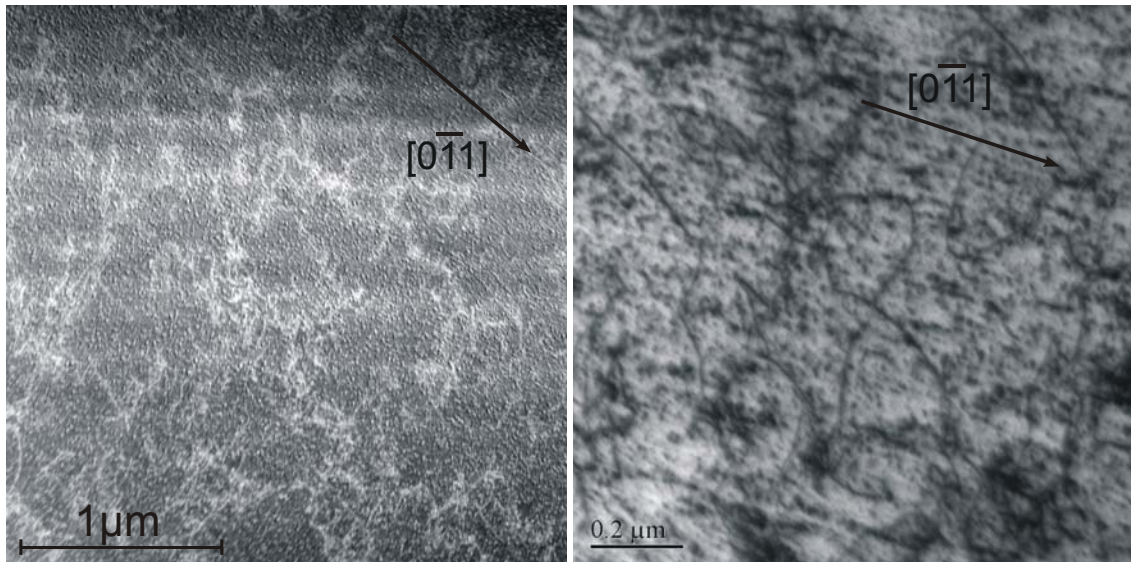


Fig. 7: DF(HAADF) and BF TEM images ( $g=[0-11]$ ) undamaged area (depth  $> 13 \mu\text{m}$ ) in Fe-15Cr material.

EDX and EELS analysis in the scanning regime. The specimen has been oriented in the investigated area with  $g=[0-11]$ . Application of 200 mm camera length allows using HAADS detectors as DF detector and image dislocation loops in the sufficient contrast. This enables the imaging of the dislocation loops with the sufficient contrast. The scan of the electron beam through the well visible dislocation loop and recording of EDX and EELS signals allows the measurement of spatial differences in the Cr or Fe signals and herewith the differences in their concentration. The example of such a line-scan measurement with calculated EDX Cr- $K\alpha$  liner and EELS Cr- $L_{2,3}$  edge profiles is presented in Fig. 8. The electron beam scans through the line marked in the image. The intensity profiles of the EDX Cr- $K\alpha$  and EELS Cr- $L_{2,3}$  signals are shown in the corresponding diagrams. It is clearly visible that both signals increase in the same scanning points. The intensity of the EDX line increases by a factor of 1.2. This corresponds to the increasing of the local Cr concentration to 19-21%. Taking into account a statistical error of 10% (at 1 s acquisition time) which has been estimated by scanning of the area without loops it can be claimed that around the dislocation loop an area with 10-15% increased Cr concentration exists. The intensity of Cr-EELS edges increases also by the factor of approximately 1.25. However the usual statistical error caused by the background correction is also about 10-15% that shows an of about 10% increased Cr concentra-

tion. The detected increasing of both signals is a good confirmation of formation of Cr rich areas near the dislocation loop.

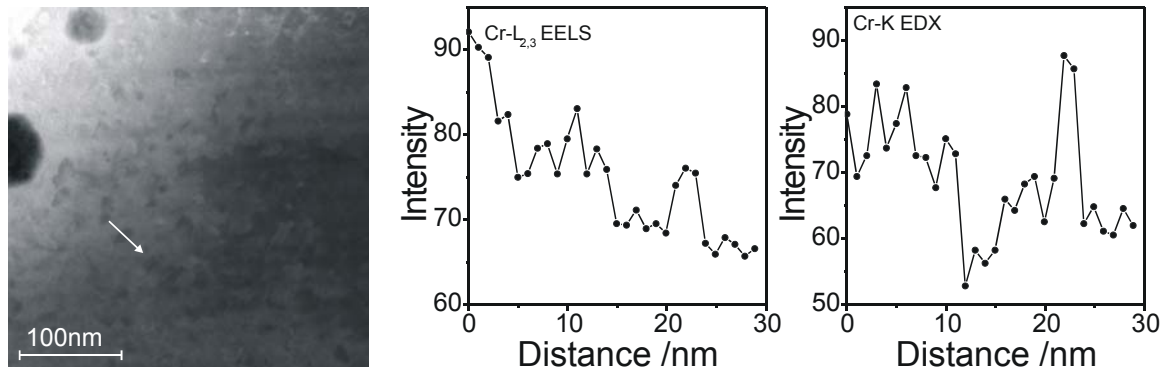


Fig. 8: Analysis of Cr concentration in the area around dislocation loop using line scan method. Both diagrams show the distribution of measured signals along the scanning line.

Within the scope of TW5-TTMS-007 D10 sub-task neutron irradiation of FeCr and Fe single crystals was performed. The first specimens were investigated by TEM at SCK.CEN after irradiation of 0.25 dpa. The investigation reveals that the density of created defects is insufficient for the reliable TEM analysis of irradiation effects. The next irradiation dose we will be targeted over 1 dpa. The comparison of formation of irradiation induced defects in FeCr and Fe single crystal samples will be performed.

Staff:

- U. Jäntschi
- M. Klimenkov
- A. Möslang
- M. Rieth
- P. Vladimirov
- H. Hofmann (HMI)

**TW5-TTMS-007 D 7**  
**TW6-TTMS-007 D 10**

**Production and Characterization of Single Fe-Cr Crystals and Elaboration of a Critical Review of the Physical Metallurgy of EUROFER Alloying Elements and Impurities, Heat-treatment/Phases/Microstructure, Phase Stability, and Segregation**

**Overview**

Until today there is still a lack of physical and mechanical data for Fe-Cr single crystals (SC) with a low Cr content. But it would be important for the development of Fe-Cr potentials to know the real elastic constants and thermal expansion coefficients. Furthermore, the goal of the modelling efforts within the fusion program is the numerical simulation of a real material like the EUROFER steel. Therefore, a critical review of all relevant modelling aspects would be a helpful source for the definition of future development trends.

**Initial Situation**

Specimens of Fe-15%Cr SC have been produced, prepared and used for nano-indentation tests. With the results it is now possible to calculate the elastic constants and use these values for a fine adjustment of the interaction potentials which are needed for atomistic simulation methods such as molecular dynamics. Unfortunately, the SC are too small for an accurate determination of thermal expansion coefficients. Therefore, the SC task has been finished at that stage.

**Progress of the Critical Review**

All relevant data for compiling the review has been collected. There is a significant overlap to the EUROFER assessment task TW5-TTMS-001 with respect to effects of chemical composition and to metallurgy. Therefore, the focus is laid on microscopic properties which might be modelled directly by atomistic methods. In the following a few examples are given.

Martensite is a supersaturated solid solution of carbon in iron which has a body-centred tetragonal (bct) structure, a distorted form of bcc iron. The tetragonality measured by the ratio between the axes,  $c/a$ , increases with carbon content:  $c/a = 1 + 0.045 \text{ wt}\%C$ , implying that at zero carbon content the structure would be bcc, free of distortion. It is interesting to note that carbon in interstitial solid solution expands the fcc iron lattice uniformly, but with bcc iron the expansion is non-symmetrical giving rise to tetragonal distortion. To understand this important difference in behaviour, it is necessary to compare the interstitial sites for carbon in the two lattices. In each case, carbon atoms oc-

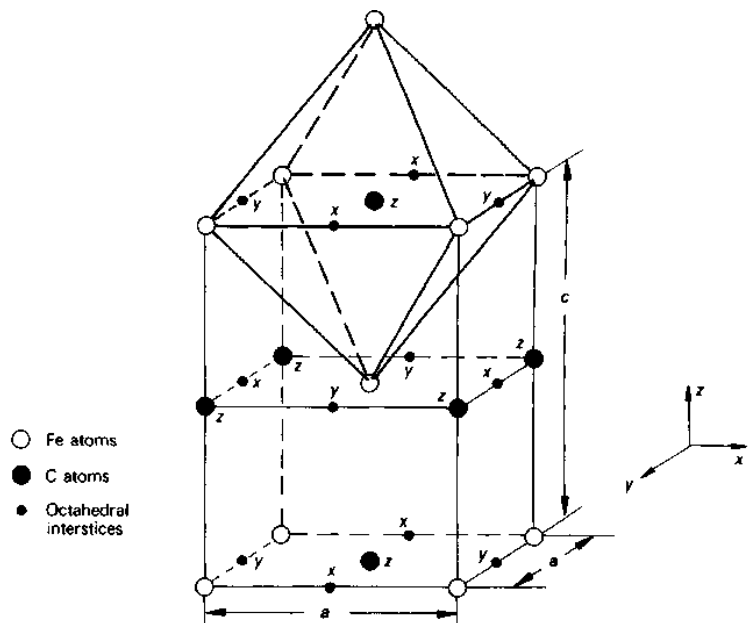


Fig. 1: Martensite body-centred tetragonal lattice illustrating the three sets of octahedral interstices. The z-set is fully occupied by carbon atoms.

copy octahedral sites, indicated for martensite in black in Fig. 1, and have six near-neighbour iron atoms. In the fcc lattice the six iron atoms around each interstitial carbon atoms form a regular octahedron, whereas in the bcc case the corresponding octahedra are not regular, being shortened along the z-axis. These compressed octahedra only have four-fold symmetry along the shortened axis in each case, in contrast to the fcc structure in which the regular octahedra have three four-fold axes of symmetry.

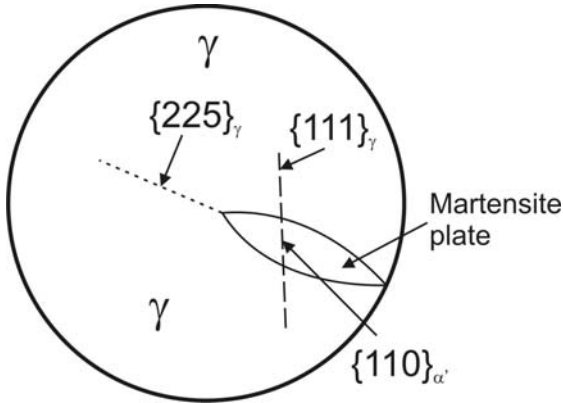


Fig. 2: Typical crystallography of a martensitic plate (schematic diagram).

The martensite reaction is readily recognized by its appearance in the optical microscope. Each grain of austenite transforms by the sudden formation of thin plates or laths. The laths have a well-defined habit plane (Fig. 2) and they normally occur on several variants of this plane within each grain. The habit plane is not constant but changes as the carbon content is increased. For example, in lower carbon steels the habit plane is usually  $\{111\}_\gamma$ , while for 0.5 to 1.4% carbon, the usual plane observed is  $\{225\}_\gamma$  and at very high carbon levels (above 1.4%) the plane changes to  $\{259\}_\gamma$ .

In principle, for EUROFER all heat treatments at temperatures above 890 °C ( $A_{c1e}$ ) lead to a complete formation of austenite. Since solubility of interstitial solute elements like carbon and nitrogen is rather high in austenite (see Table 1) one can assume that all prior precipitations (carbides and nitrides) are fully solved in the austenite phase, which is the reason for the name “solution annealing”. Obviously, at the stage of solution annealing – or austenitization – all prior material properties which are connected to the microstructure are restored, that is, by solution annealing the thermo-mechanical history (aging, hot-, cold-work, welding, etc.) of the material is reset. The hardness of the resulting martensite after annealing does not depend on the annealing temperature. It is practically at the same level for all annealing temperatures which exceed  $A_{c1e}$ . However, the effect on the austenite grain size is different. Here, with rising annealing temperatures the grain size raises, too. That is, with help of the annealing heat treatment the austenite grain size can be controlled. Indirectly, the austenite grain size influences also the form and distribution of the martensite laths which in turn affect the mechanical properties.

Table 1: Differences between austenite and ferrite with respect to interstitial solubility.

Solubility of C and N in wt%		
C in $\gamma$ -iron	1150°C	2.04
	723°C	0.80
C in $\alpha$ -iron	723°C	0.02
	20°C	$<5 \times 10^{-5}$
N in $\gamma$ -iron	650°C	2.8
	590°C	2.35
N in $\alpha$ -iron	590°C	0.10
	20°C	$<10^{-4}$

## Conclusions

Of course, the characteristics of the EUROFER steel mainly originate in its martensitic nature. Therefore, the martensite transformation has to be described sooner or later by modern simulation methods. However, at the present stage of materials modelling, there is no method available which could predict even one of the properties outlined above (martensitic lattice, martensite microstructure,  $\alpha$ - $\gamma$  transformation). Since there are much more typical EUROFER properties (metallurgical, physical, chemical, thermo-mechanical) it is easy to imagine that materials modelling still needs decades of developmental work until a steel like EUROFER could really be simulated.

Staff:

B. Dafferner  
S. Heger  
U. Jäntsch  
M. Klimiankou  
A. Möslang  
M. Rieth  
H. Zimmermann

## **EFDA/06-1469 (TW6-TTMS-MODUNI2)**

### **Parameterization of Dislocation Dynamics Code for Non-irradiated and Irradiated Fe**

#### **Background**

The plasticity of materials is controlled by the behaviour of linear defects called dislocations. Plasticity phenomena are multi-scale in nature. The following scales have to be understood and modelled:

- The mobility of a single dislocation in a perfect single crystal is governed by energetic parameters describing the core structure and the glide mechanisms. These energetic characteristics are obtained via ab initio computation and Molecular Dynamics simulation based on empirical potentials.
- The glide of a single dislocation in a radiation-modified microstructure requires obstacle forces to overcome the obstacles, which can be obtained via ab initio computation for small obstacles or computed via Molecular Dynamics simulation for the large ones.
- Finally the long range elastic stress field interaction between dislocations, has to be taken into account in the Discrete Dislocation Dynamics (DDD) codes, into which the mobility laws and obstacle forces have to be introduced to describe the collective behaviour of dislocations at the meso-scale of an irradiated single crystal of a few  $\mu\text{m}^3$ .

#### **Objectives**

The parameterization of the DDD code consists in designing glide mechanisms, mobility law, and rules describing the interaction of dislocations with obstacles at the atomic scale using existing or improved versions of inter-atomic potentials. Based on the existing knowledge from ab initio and empirical potentials, the main objectives will be:

- (i) To provide this parameterization for the bcc Fe,
- (ii) to simulate the plastic behaviour of non irradiated and irradiated bcc Fe, using the meso-scale Discrete Dislocation Dynamics based on this parameterization,
- (iii) to design critical experiments that can be used to validate of the proposed tools and models.

The Institut für Zuverlässigkeit von Bauteilen and Systemen (IZBS) at the University of Karlsruhe will (i) compare the core structure, glide mechanisms and energetics of screw dislocations as they can be calculated via Molecular Dynamics using the most advanced potentials, (ii) compare the interaction occurring within isolated dislocation junctions via Molecular Dynamics, (iii) implement these laws in a bcc DDD code under development and initiate the study of the collective behaviour of dislocations in non-irradiated bcc Fe at various temperatures.

#### **State of the Art at the beginning of the project**

##### *Molecular Dynamic modelling*

The description of the atomic interactions will be based on the semi-empirical many-body potentials recently developed by Mendeleev et al. [1] and by Dudarev and Derlet [2]. Both potentials represent currently the best state-of-the-art for large-scale atomistic simulations in bcc iron. The potential of Mendeleev et al. has been very recently applied in studies of screw dislocation behaviour with encouraging results [3]. A few of the calculations specified below will be reruns of these results for comparison. Mostly the programme will be focussed however on the comparison to the novel potential of Dudarev and Derlet which implicitly contains physically-motivated magnetic interactions, which are crucial for a correct description of the structural stability of iron phases as well as the behaviour of extended defects.

### Three dimensional discrete dislocation modelling

The current version of the DDD code [4] is adapted to the fcc crystallography. It will be extended to the bcc crystallography. The major challenge in the DDD simulation is the flexible handling of all possible dislocation reactions respecting both the topology and the resulting physical properties (e.g. sessile or glissile) products. The nodal code of IZBS (Karlsruhe) handles all fcc pair reactions between dislocations.

### Progress report

Deliverable 01: Report on: Selection of the most appropriate Fe atomic potentials to reproduce (i) the core structure and glide mechanisms of screw dislocations versus temperature and (ii) the point defects.

A summary of dislocation properties predicted by the three interatomic potentials together with results of ab initio calculations are listed in table 1.

Table 1: Properties relevant to dislocation behaviour predicted by different methods (Courtesy of L. Ventelon) [5].

Model	$\gamma$ -surface	Core structure	Peierls barrier
DFT		Non-degenerate	Single hump
Dudarev-Derlet		Degenerate	–
Ackland	✓	Degenerate	–
Mendelev	✓	Non-degenerate	Double-hump

Since the correct description of dislocation behaviour and the core structure is one of the primary requirements for a successful completion of this project the deficiencies of the existing interatomic potentials, summarized in table 1, present a significant obstacle to further progress. Only when the potentials are sufficiently reliable and transferable the results of atomistic simulations can be utilized for the parameterization of dislocation properties in discrete dislocation modelling codes.

Even though new developments and improvements of the existing models are on the way they are not likely to become available before the planned completion of this project. In order to attempt to carry out the proposed tasks we therefore decided to construct and test a novel semi-empirical potential for iron in collaboration with Dr. D. Nguyen-Manh from UKAEA Culham and Prof. D. Petti for from Oxford University. This so-called Bond-order potential (BOP) is based on the tight-binding (TB) approximation and the Stoner model of itinerant magnetism and contains therefore implicitly information from the electron structure theory. Details of the underlying TB theory and parameterization has been published recently [6]. The tight-binding method within the two-centre approximation provides a natural framework for bridging between the first-principles DFT calculations and the semi-empirical interatomic potentials for non-magnetic materials. By coarse graining the TB electronic structure in terms of atom-centred moments and bond-centred interference paths interatomic bond-order potentials may be derived that correctly predict (rather than fit) the observed structural trends across the periodic table of elements. For the d-valent transition metals and intermetallics, BOPs have been used to model dislocation behaviour [7], [8]. The Stoner model of band magnetism allows then the TB approximation to be generalized to magnetic materials.

It should be noted that the presented model is not yet in its final form. The parameterization was taken from the original TB model and has not been optimized. Our primary goal was to validate the BOP model for iron and to test whether and how well it is able to describe prop-

erties of dislocations. We expect that the potential may need to be still modified in order to reach the best performance.

### Dislocation core structure from BOP

Using the constructed BOP we computed the core structure of the  $\frac{1}{2}\langle 111 \rangle$  screw dislocation and compared it to the result of DFT calculations. This comparison is shown in figure 1. The obtained core structures are visualized using the usual differential displacements maps, in which the arrows correspond to relative displacements of neighbouring atoms. Atoms shown in different colours belong to three different  $\{111\}$  planes before the dislocation is introduced into the lattice.

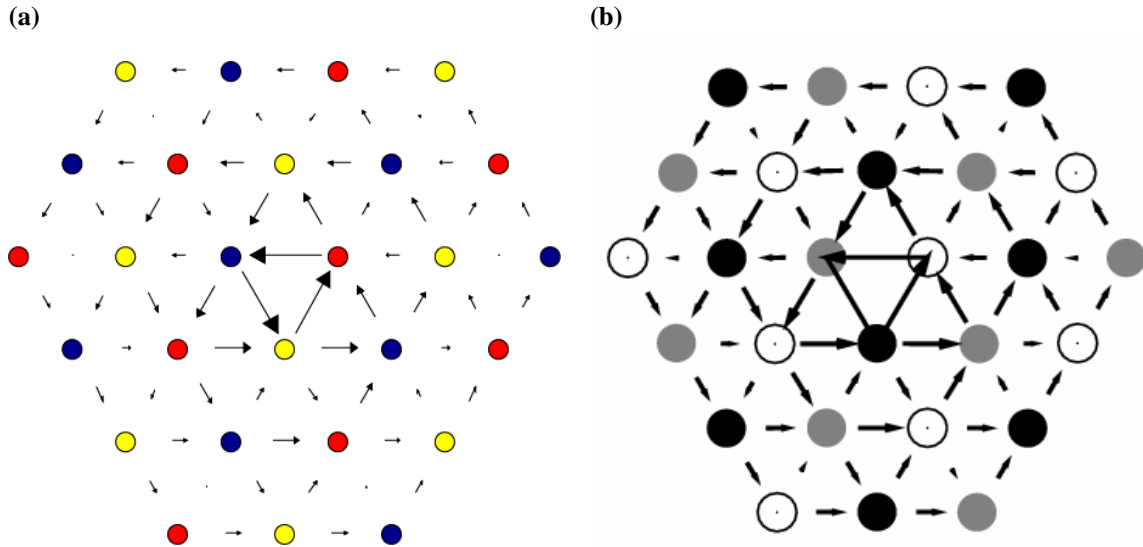


Fig. 1: Core structure of the  $\frac{1}{2}\langle 111 \rangle$  screw dislocation calculated by (a) BOP and (b) DFT [9].

The relaxed core structure obtained using BOP is very close to that predicted by DFT. Both cores are non-degenerate and not too dissimilar to the elastic solution. This is in contrast to the degenerate cores obtained with FS and DD (Dudarev, Derlet) potentials. In addition, we computed the energy difference between the easy and hard core configurations, which are characterized by opposite Burgers vectors for a given dislocation position. A configuration similar to the hard core may be encountered as the dislocation moves between two equilibrium easy positions and this information can be therefore related to the Peierls stress. Again in agreement with DFT results, BOP gives the easy core as the more stable one with the energy difference between the hard and easy configurations  $\Delta E=0.07$  eV/b (compared to 0.05 eV/b from DFT calculations). This suggests that BOP is likely to provide also reliable values of Peierls stress unlike the ME potential.

### Summary Deliverable 01

The development of the BOP model, triggered by the mentioned deficiencies of the existing potentials for Fe, goes beyond the initial proposal. The deliverable D-01 has been reached.

In summary, we found that the BOP model for iron that combines a basic electronic structure with the Stoner model of itinerant ferromagnetism is able to capture the essential physics governing the cohesion in iron. Unlike the available many-body interatomic potentials it predicts correctly stabilities of magnetic and ferromagnetic iron phases as well as the core structure of the screw dislocation. In the next period, we will focus on additional properties of dislocations as well as further validation of the BOP model and attempt to link the results of atomistic simulations with the discrete dislocation dynamics calculations.

## Progress DDD:

The bcc crystallography has been implemented into the DDD code. As the  $1/2\langle 111 \rangle$  Burgers vectors are shared by three  $\{110\}$  planes, so called multi-reactions between dislocation may occur. The figure 2 shows the intersection of three dislocation, all on different glide planes, which intersect along a common line.

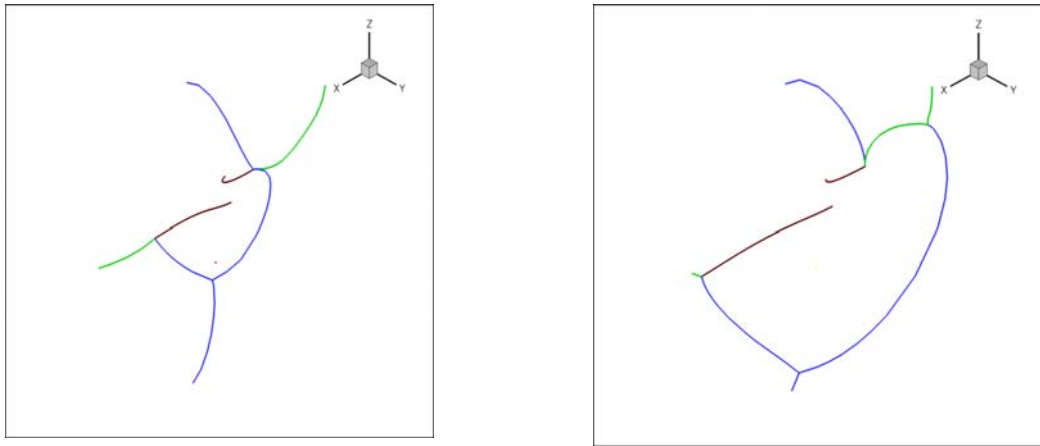


Fig. 2: bcc reaction between three dislocations, leading to glissile reactions along intersection line of the glide planes (a) or within the glide plane (b).

These reactions involve the formation of junction with a  $[100]$  Burgers vector. The properties of dislocations of this type are not well known, but must be included in the DDD code. Therefore reactions of this type will be calculated by MD, in order to derive appropriate mobility rules.

## Conclusion

It is concluded that the existing potentials will not give reliable results for dislocation properties. The development of a new BOP model for Fe, originally not planned within this project, has been started and gave promising first results. The computational costs for this new potential are extremely high, and relatively small systems can be calculated. It is planned to include this potential into a parallel MD code used at IZBS.

The bcc crystallography is richer in reactions as initially estimated, especially of the  $\langle 100 \rangle$  type. The properties of these dislocations will be explored by MD and continuum descriptions.

## Staff:

D. Weygand  
M. Mrovec  
A. Spielmannova  
Z. Chen  
A. Haug

## Literature:

- [1] Mendeleev et al., Philos. Mag. A 83:3977 (2003).
- [2] Dudarev S.L. and Derlet P., J. Phys. Cond. Mat. 17:7097 (2005).
- [3] Chaussidon J., Fivel M. and Rodney D., Acta Mater. 54:3407 (2006).

- [4] Weygand D., Friedman L.H., Van der Giessen E., Needleman A., *Modelling Simul. Mater. Sci. Eng.* 10 (2002) 437.
- [5] Ackland G.J. et al., *Philos. Mag. A* 75:713 (1997).
- [6] Liu G. et al., *Phys. Rev. B* 71:174115 (2005).
- [7] Mrovec M., *Phys. Rev. B* 69:94115 (2004).
- [8] Mrovec M., *Phys. Rev. B* 75:104119 (2007).
- [9] Ventelon L. And Willaime F., TWS-TTMS-007 meeting, Lausanne, December 2006, unpublished.



# **Materials Development Advanced Materials**



**TTMA-002  
Divertor and Plasma Facing Materials**

**TW3-TTMA-002 D 3  
Mechanical Testing of Improved W Alloys: Tensile and Fracture Toughness Testing**

**Objectives**

A structural component like the divertor is subjected during service to very high heat loads and also to alternating thermal and mechanical stresses as a consequence of the pulsed reactor operation. Even for helium cooled ITER divertor concepts the operating temperatures override the recrystallization of pure tungsten or tungsten alloys. Due to the cyclic operation under service conditions, the knowledge of the reasons of fatigue endurance of these materials becomes more important.

**Status end of 2006**

After performing Low Cycle Fatigue (LCF) tests on both reference materials, which was pure tungsten and  $WLa_2O_3$ , at the high temperature of 800°C the numbers of cycles to failure,  $N_f$ , of both materials are ranging in a broad scatter band from 3220 to 11480 cycles.

**Tensile testing of single crystals of tungsten and tungsten-Tantalum**

The Russian Institute of Solid State Physics, Chernogolovka, Moscow region, delivered the crystals, listed in table 1 of the dimensions 6 x 30 mm (diameter x length) of pure tungsten in the orientations (100) and (111) as well as of tungsten-tantalum in the same orientations. The orientations had been controlled at IMF I. So finally the tungsten crystals with (100) orientation were “polycrystalline” (red) and two tungsten tantalum crystals with (100) orientation contained two or more grains (yellow). The crystals indicated in green were real single crystals. Three crystals had been destroyed on the way to the finally successful production route for tensile specimens fabrication.

Table 1: Characteristics of the delivered tungsten and tungsten-tantalum crystals.

Batch/No.	Sample	Material	Orientation	X-Rays	Tested at
0/1	W-0-a1	W	100	Polycr.	destroyed at production
0/2	W-0-a2	W	100	Polycr.	destroyed at production
0/3	W-0-a3	W	100	Polycr.	1000°C
0/4	W-1-a1	W	111	OK	destroyed at production
0/5	W-1-a2	W	111	OK	1000°C
0/6	W-1-a3	W	111	OK	600°C
1/5	WT-1-a1	WTa	111	OK	600°C
1/6	WT-1-a2	WTa	111	OK	1000°C
1/7	WT-1-a3	WTa	111	OK	1500°C
2/4	WT-0-a1	WTa	100	OK	1000°C
2/5	WT-0-a2	WTa	100	5-7 grains	600°C
2/6	WT-0-a3	WTa	100	2 grains	1500°C

From the single crystals (Fig. 1a) of tungsten and tungsten-tantalum had been machined by electro erosion high temperature testing specimens (Fig. 1b) with 8 mm gauge length and 2 mm diameter and these specimens were tested at the temperatures 600°C, 1000°C and

1500°C in a high temperature tensile testing facility with a strain rate of  $9,21 \times 10^{-4}$  1/sec (Fig. 1c).

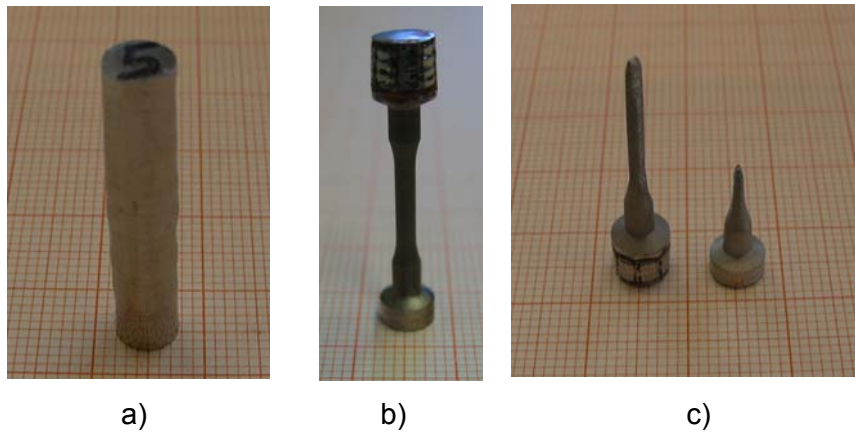


Fig. 1: a) single crystal, b) specimen, c) deformed specimen.

For comparison also polycrystalline specimens of tungsten had been tested in the same temperature range.

Both stresses, i.e. Yield Stress,  $R_{p0,2}$ , and Ultimate Tensile Stress,  $R_m$ , decrease on all materials with temperature (Fig. 2). This effect is much more dramatically for polycrystalline tungsten than for the crystal materials. Tungsten and tungsten-tantalum crystals with the (111) orientation show the highest values in both quantities, whereas  $R_{p0,2}$  seems nearly independent of temperature for all crystalline materials. The hardening capacity, that is the stress increase from Yield Stress,  $R_{p0,2}$ , to Ultimate Tensile Stress,  $R_m$ , is very pronounced for all crystal materials and for polycrystalline tungsten at 1500°C.

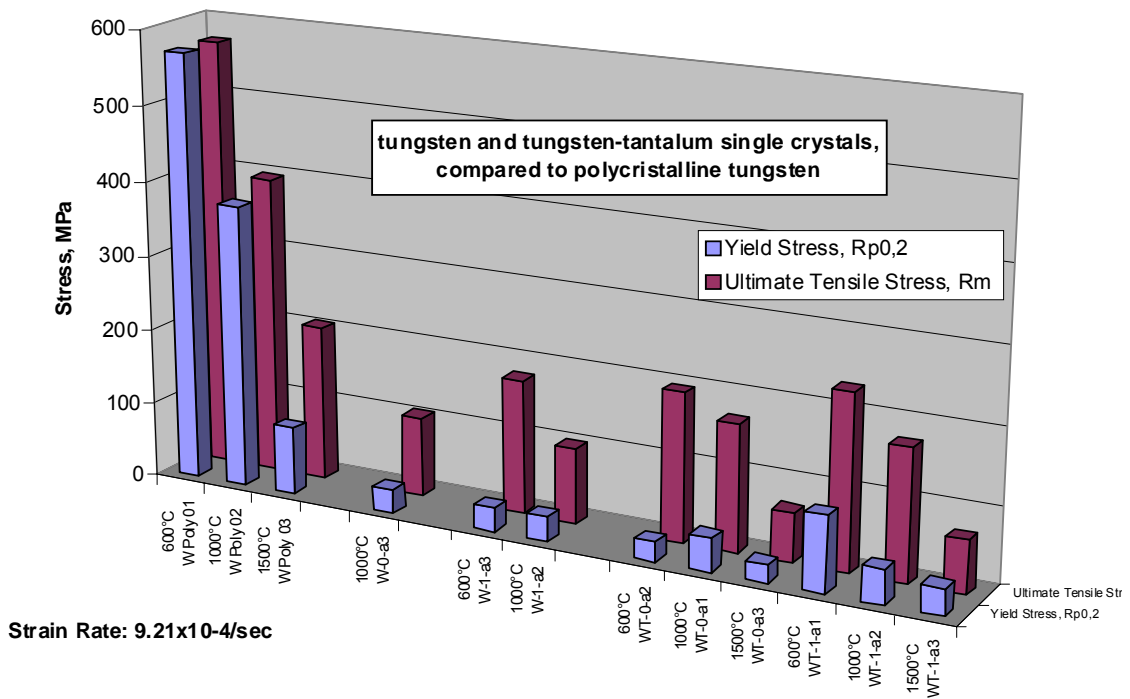


Fig. 2: Overview over the stress dependence of different materials with temperature.

Both strains, i.e. Uniform Strain,  $A_g$ , and Total Strain,  $A$ , override a maximum on tungsten-tantalum crystalline materials with temperature (Fig. 3). The temperature influence on polycrystalline tungsten is nearly negligible. The crystalline materials reach very high strains so in case of the “polycrystalline” crystal of tungsten with the (100) orientation maximum values of  $A_g = 105\%$  and  $A = 159\%$ . But also tungsten-tantalum crystals with the (111) orientation show higher values in both quantities.

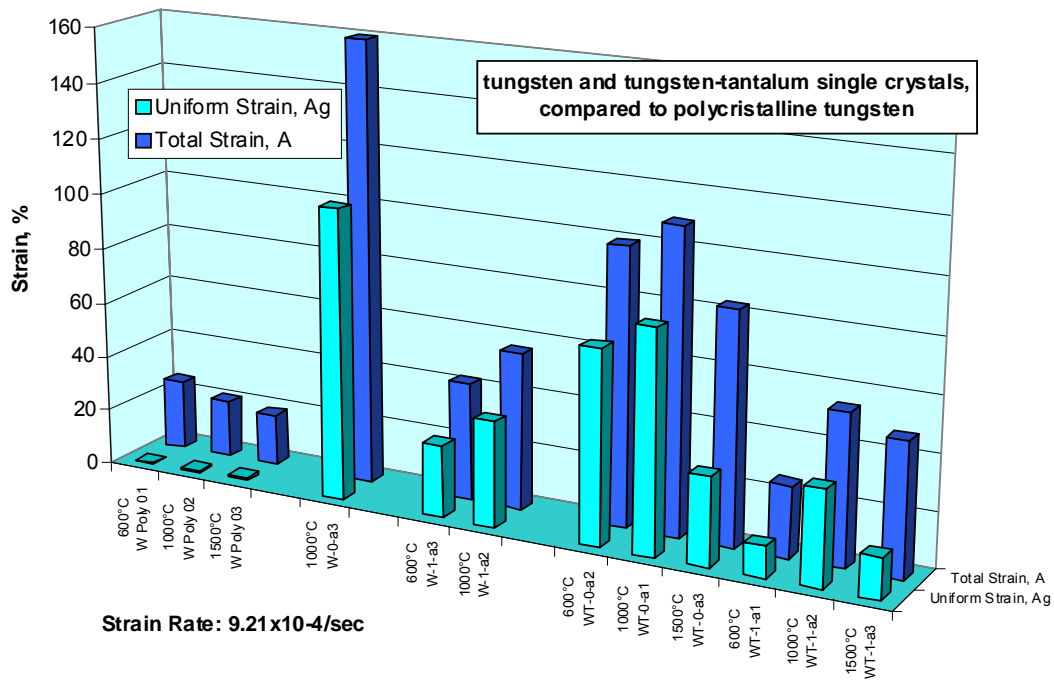


Fig. 3: Overview over the strain dependence of different materials with temperature.

As conclusion can be drawn that even not pure single crystals of tungsten and tungsten-tantalum are qualified for applications where at lower stress level high straining capacities are necessary.

Staff:

- U. Bürkle
- M. Klotz
- C. Petersen

## TW3-TTMA-002 D 7 TW6-TTMA-002 D 6 Fundamental Studies on Mechanical Properties of W-alloys

### Overview

Tungsten or tungsten materials are considered to be the primary candidates for armour and structure of DEMO divertor designs. Present design outlines are based on a structural material with temperatures up to about 1300 °C. The most critical issues are ductile-to-brittle transition and recrystallization. The first defines the lower, the second the upper operation temperature limit. Another problem consists in the fact that the microstructure of these refractory alloys depends strongly on the manufacturing history. Since mechanical properties are defined by the underlying microstructure, refractory alloys can behave quite different, even if their chemical composition is the same.

Therefore, the goal of this task is a systematic screening of mechanical properties of standard tungsten materials to determine the influence of microstructure characteristics like grain size, anisotropy, texture, or chemical composition.

### Initial Situation

In the previous years, creep tests of pure tungsten and W-1%La<sub>2</sub>O<sub>3</sub> rods (Ø8 mm) from Plansee were performed. Both materials were tested at 1100 °C and 1300 °C for up to 5000 hours. The results allowed for accurate extrapolations to operation times of about 20,000 hours. Present divertor designs are based on a structure material with creep strength of more than 55 MPa for a time-to-rupture of 20,000 hours at 1200 °C. According to our tests, WL10 just fulfils this design criterion while pure tungsten is too soft.

However, a far more difficult criterion of the divertor design is the ductile-to-brittle transition temperature (DBTT) of about 300 °C in the unirradiated condition. First preliminary measurements (with gas burners and a standard charpy facility) have given DBTT values of 800 °C for W and 950 °C for WL10 which would be far too high for the application.

It has been shown that ductility is the most problematic criterion for a divertor structural material. Therefore, it has been decided to concentrate on charpy testing during the further screening phase. Also, for a more reliable and reproducible method to perform charpy tests at high temperatures in vacuum, a recently developed test equipment was modified (Fig. 1).

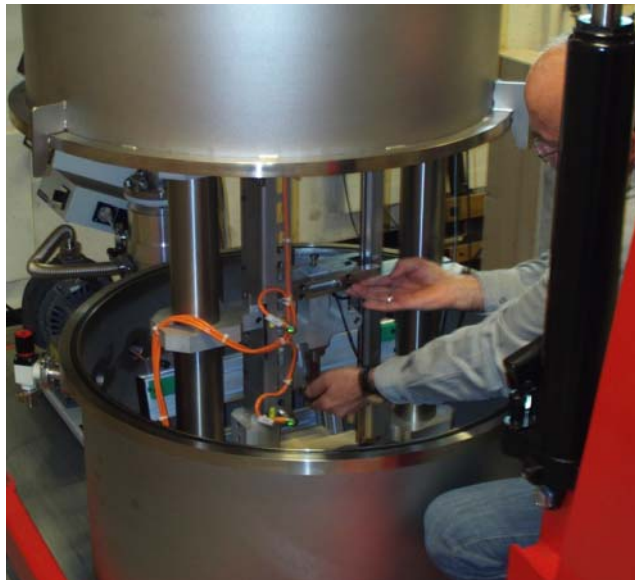


Fig. 1: Instrumented charpy tests on refractory alloys are performed in-situ. Therefore, a vacuum vessel contains the drop weight testing machine with a furnace for testing temperatures of more than 1000 °C.

### Progress of the Screening Phase

Plansee provided five different tungsten rod materials (W, WL10 standard and optimised, WVM, WL10 with 1% Re). Tungsten, WL10 and the bulb wire material WVM (tungsten doped with potassium) was also delivered in form of plates. Standard specimen (KLST type) were fabricated and tested.

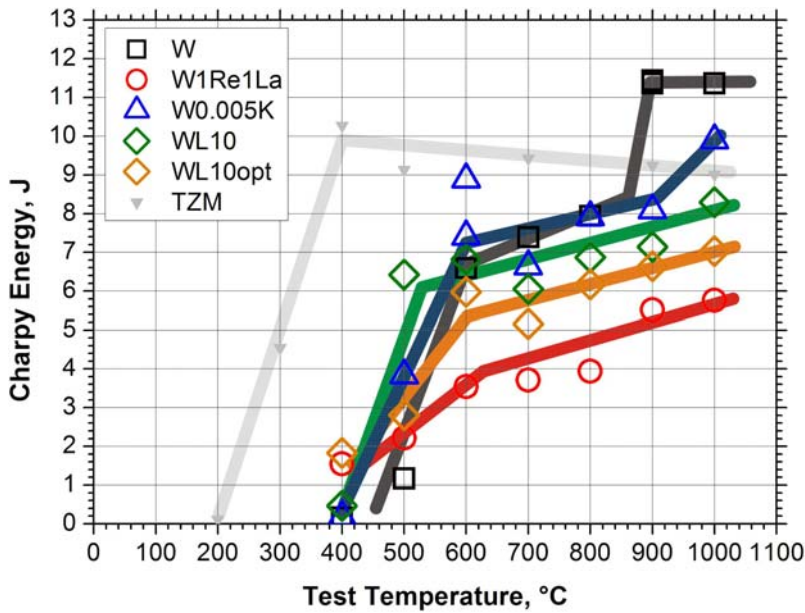


Fig. 2: Charpy test results of different refractory rod materials. The specimens were fabricated parallel to the rod axis, that is, the notches are perpendicular to the rod axis. Only TZM (molybdenum material) shows a distinct ductile fracture regime. Tungsten, pure (W) and potassium doped (WVM), are only ductile at temperatures at or above 900 °C. All other materials show cleavage fractures (see Fig. 3) in the whole test temperature range, that is, they show no upper shelf regime. The “classical” transition to brittle fracture is around 500 °C for all tungsten materials.

But all other rod materials don't show ductile fracture within the whole test temperature range. However, all tested materials tend to brittle fracture at temperatures below 500 °C. But above that temperature, the specimens show cleavage fractures which propagate along the former rod axis, that is, parallel to the specimen's long side and perpendicular to the notch (see Fig. 3).

In summary, there are three types of fractures (brittle, cleavage, ductile) which are linked by a brittle-to-cleavage transition and a cleavage-to-ductile transition. The brittle-to-cleavage transition temperature (defined in analogy to the DBTT) varies around 500 °C for all tungsten materials while the cleavage-to-ductile transition temperature is about 900 °C for tungsten and about 1000 °C for the potassium doped tungsten (see Fig. 2). For the other materials (WL10 and W1Re1La) the transition to ductile fracture starts probably at even higher temperatures.

Charpy tests with the specimens of the plates have just been started but, compared to the according rod materials, two trends are already recognizable at this early stage: (1) the energies are lower by more than 50%, and (2) there is a smaller but still significant difference in the specimen's orientation (parallel or perpendicular to rolling direction). However, the later result is not surprising since rolling direction was not changed frequently during production. Therefore, a distinct anisotropy of the microstructure can be expected. A reasonable explanation for the severe reduction of charpy energy might also be found in the specific plate microstructure and, as a result, a specific fracture type which is called delamination (for details see Fig. 4).

The results of the rod materials are shown in Fig. 2 together with the results from specimen of a TZM (molybdenum, stabilized by Ti and Zr) rod. It can be clearly seen that only TZM shows the classical embrittlement behaviour which is typical for most body-centred cubic structured metals: (1) there is a clear transition from brittle (at lower temperatures) to ductile (at higher temperatures) fracture (DBTT), and (2) there is an extended regime of ductile fracture (area of almost constant energy → upper shelf).

Compared to TZM, the results of the tungsten materials look quite different. Only specimens of pure tungsten show an upper shelf starting at 900 °C. Potassium doped tungsten seems just to reach the upper shelf at 900 °C. But all other rod materials don't show ductile fracture within the whole test temperature range.

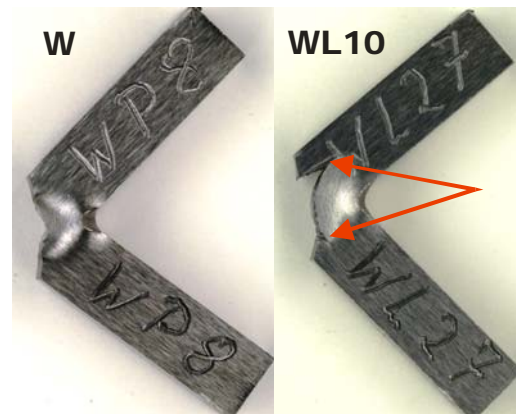


Fig. 3: Charpy specimen fracture of pure tungsten and WL10 at 1000°C. The tungsten specimen fractured ductile while the WL10 specimen shows cleavage fractures parallel to the former rod axis (indicated by red arrows).

## Fracture Surfaces

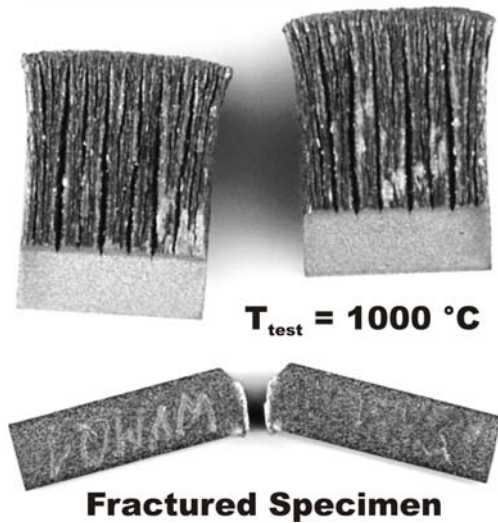


Fig. 4: Due to the rolling processes during production, plates of refractory material show a distinct two-dimensional texture. This, however, leads to a weakening of intergranular cohesion. That is, during charpy tests, the specimens break along the texture overlaps even at temperatures as high as 1000 °C. The effect can be seen quite clearly by the fracture surfaces which are oriented perpendicular to the rolling plane. A look on the fractured charpy specimen shows that there was almost no ductile deformation. Such kind of fracture is called delamination.

## Conclusions and Outlook

For a given temperature, WL10 compared to pure tungsten may be stressed slightly more and still reaches the same life-time. So WL10 meets just the current diver-tor creep design criterion while pure tungsten does not. With that, the benefit of lanthanum-oxide in tungsten is an improvement of the processability, the suppression of recrystallization, and a slight strengthening effect. But at the same time, the already high ductile transition temperature of pure tungsten is still increased by the addition of lanthanum oxide.

The reason for the high ductile transition temperature is not brittle fracture but cleavage fracture. First examinations have shown that EDM fabrication produces microcracks at surfaces perpendicular to the rod axis (see Fig. 5). If such cracks can be avoided (by other fabrication methods) or sealed (by brazing, for example), DBTT might be improved significantly.

The next steps, however, will be the completion of charpy tests with the plate materials and a detailed SEM study of the fracture surfaces. Finally, chemical analysis of the interstitial impurities and some TEM examinations will be performed. The goal is to determine the lowest possible ductile transition temperature of tungsten materials.

### Staff:

S. Baumgärtner  
B. Dafferner  
S. Heger

U. Jäntschi  
M. Klimenkov  
A. Möslang

M. Rieth  
R. Ziegler  
H. Zimmermann

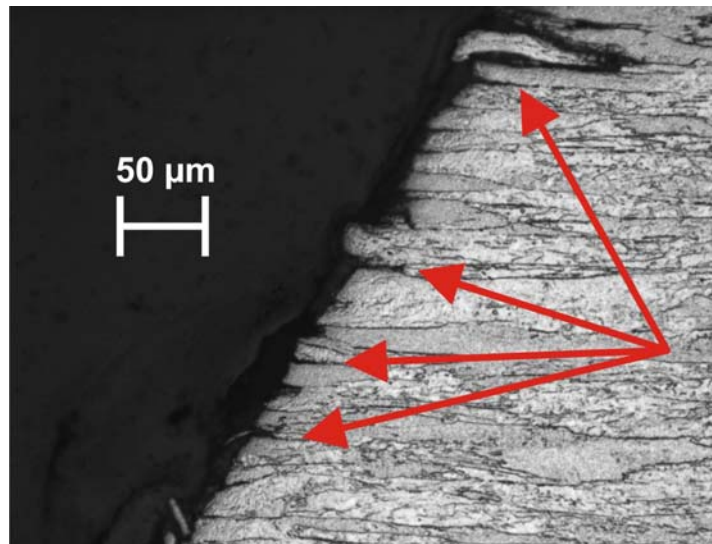


Fig. 5: The V-shaped notches of the charpy specimens are fabricated by wire eroding (EDM). This causes small cracks of about 20-50 μm length in the tungsten rod materials. Unfortunately, the cracks are preferably located at grain boundaries (indicated by red arrows) which certainly promotes the initiation of cleavage fracture (see Fig. 3).

## **TW6-TTMA-002 D 8**

### **Production of Small Laboratory Scale Batches of Improved Materials for Characterization**

#### **Objectives of the task**

As already known, commercially available refractory alloys show a rather high DBTT and would never meet the current design criteria for a He-cooled divertor. Therefore, ductility is still the most critical property that has to be improved and investigated if tungsten alloys should be used as structural material. In FZK a new PIM (Powder Injection Molding) process for refractory alloys has been developed and can be used for fabrication of all geometries of divertor components. PIM of steels is well-known in industrial manufacturing as it exhibits large economic potential for production of tungsten divertor components in case of large scale series. The W-PIM approach directly yields tungsten products or components without any finishing work being required. But this new technology still has to prove its suitability in terms of material properties like ductility and tensile strength.

#### **State of the art when R+D work commenced**

The specimens studied were sintered at the company of Plansee-Metall in Reute. Notch impact specimens of tungsten were tested without any finishing. Notch impact testing at 880 °C revealed an impact energy of about 0 J, which corresponds to an absolutely brittle material behaviour. At this point, the question occurred if the PIM samples would achieve better values at higher test temperatures and/or under decreased deformation velocities. For this purpose six tensile specimens were delivered by Plansee. They exhibited noticeable distortion, such that it was assumed first that they could not be tested at all. To test them nevertheless, the specimens had to be straightened before testing. These tests are the subject of the present report.

#### **Results**

##### Straightening process

All tests were carried out with a pre-load of 70 N. This value had been obtained by estimating the force required for four-point bending with the tensile strength of polycrystalline tungsten at about 1100 °C. The temperature of 1100 °C had been chosen in order to be able to straighten the specimens with a minimum force (decreasing bending force), small damage, and minimum grain growth.

As straightening with the help of the originally round lens-shaped specimen heads was considered to be hardly promising, the specimen heads were cut off by spark erosion and deburred later by careful grinding.

##### Execution of the tensile tests

The heads of the straightened specimens were not parallel. This gave rise to dangerous line loads and an asymmetrical load distribution in the specimen holders of the facility. To reduce the associated risk of damaging the facility or the specimen holders, the straightened specimens were subjected to tension with a low speed of 1 µm/s in order to give the specimen heads time to fit into the specimen holders. To study comparability with a conventional tensile test, the following experiments were carried out in advance: As a reference, a WL10 specimen and a tungsten specimen made of pultruded material were subject to tension at about 800 °C and 1000 °C according to the DIN standards 50145 and 50146, the traverse speed being 50 µm/s. In addition, a tungsten specimen of pultruded material was tested at 1 µm and 800 °C.

Maximum stress was reduced slightly from 530 MPa to 460 MPa. Strain to rupture showed a negligible difference of 1%. Hence, the results are comparable in spite of the deviating tension rate.

The first test of injection-molded specimens (specimen 4) revealed a very strongly reduced strain to rupture and a reduced maximum stress. The specimen did not break in the range of the test section like all the others, but near the head, which implies a negative effect on the test result. This problem was solved by detaching the straightening unit of the facility.

Results of the Tensile Tests

Injection-molded tungsten shows a ductile material behaviour at 800 °C. The specimens exhibit a strain to rupture ranging from 35 to 45%. According to the material behaviour of metals, this increase in the strain to rupture is accompanied by a reduction of maximum tensile strength  $R_m$ . The results are summarized in Table 1.

Table 1: Results of the tensile tests.

Straightening Test	Chemical Composition	Test Temp. [°C]	Rm [MPa]	A [%]	Remarks
1	WL10				Specimen broke when installed into the diffusion welding facility already
2	WL10	1000	240	33	Specimen breaks in the center
3	WL10	800	260	44	Specimen breaks in the center
4	WL10	1000	220	8	Specimen breaks in the head
5	W	800°C	300	35	Specimen breaks in the center
6	W	-	-	-	Specimen breaks in the center when applying the pre-load, reason not yet clear

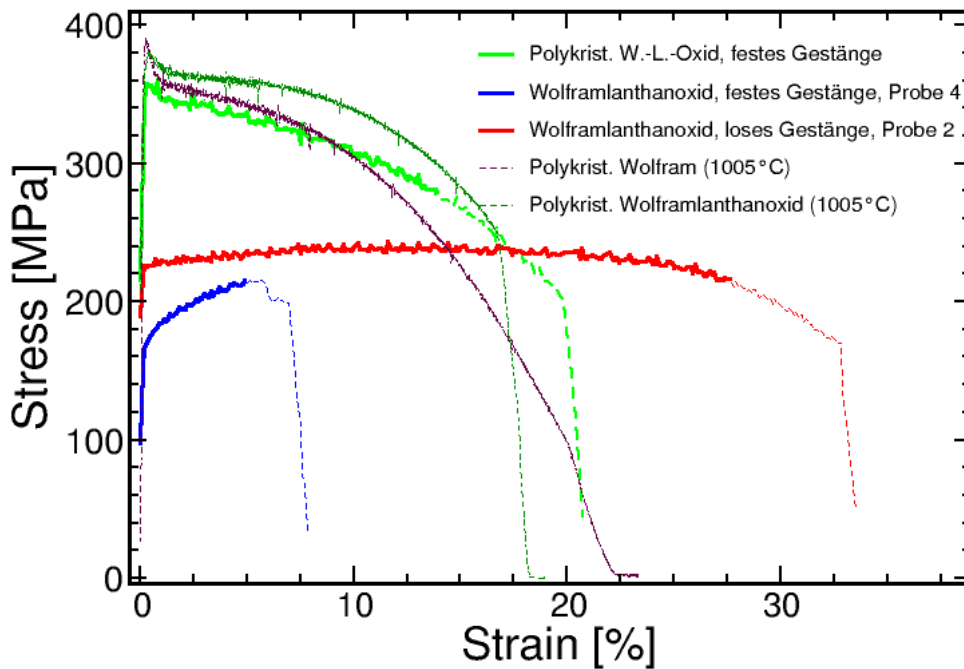


Fig. 1: Tensile tests of various tungsten specimens at 1000 °C. All specimens designated polycrystalline tungsten were tested at 50 µm/s traverse speed. In contrast to this, the injection-molded specimens 2 and 4 were tested at 1 µm/s; (green curve: polycrystalline tungsten-lanthanum oxide, fixed rods; blue curve: tungsten lanthanum oxide, fixed rods; red curve: tungsten lanthanum oxide, loose rods; violet curve: polycrystalline tungsten; dark green curve: polycrystalline tungsten).

## Conclusions and outlook

It may only be speculated about the question of what is the cause of the difference between the notch impact test results and the tensile test results published here. It might be explained by various sintering conditions at Plansee, which could possibly be due to thermal gradients in their sintering furnace. But this seems to be improbable in view of the competence of the Plansee company. However, the IMF-III had no possibility to control this hypothesis.

Another possible explanation of the difference between the tensile and notch impact test results is thermal treatment during straightening. But tungsten specimen No. 5 was straightened at 900 °C and tested at 800 °C. The test temperature of the notch impact test facility amounted to 880 °C, which nearly corresponds to the temperature of straightening. Is the difference caused by the duration of the thermal treatments? It is highly improbable that a thermal treatment at 900 °C (homolog temperature  $T/T_{\text{melt}} = 0.32$ ) has any effect. These questions might be answered in the future.

The results of the straightening and tensile experiments demonstrate that injection-molded material is highly promising for use in fusion technology. As ductile deformation of straightening starts at relatively low temperatures between 500 °C and 750 °C and a low pre-load of 70 N already, this indicates a low DBTT of about 650 °C. This is in agreement with the statements made by the company PLM-Mechanik for pultruded tungsten [Mr. Ramsperger, private communication].

### Staff:

U. Bürkle

V. Piotter

M. Rieth

Mr. Santa Cruz (ITU - Institute for Transuranium Elements)

A. von der Weth

R. Vouriot

B. Zeep (former FZK/IMF III, now Philips Lighting)



**Materials Development  
IFMIF**



## **TTMI-003 IFMIF – Test Facility**

### **TW6-TTMI-003 D 1 Manufacturing and Procurement of a Complete HFTM Compartment Including the Whole Set of Test Samples and the Qualification of Brazing Procedure for the Heating Systems**

#### **1. Background and Objectives**

For the generation of a materials database, definition of engineering rules and verification of materials performance in future fusion power reactors the IFMIF d-Li neutron source is accepted as the most promising irradiation facility. With IFMIF a fusion relevant radiation environment with accelerated testing could be provided.

The design of the test facilities has been advanced significantly, comprising neutronics, thermal and mechanical analyses.

The objective of the subtask was to complete the manufacturing of a High Flux Test Module compartment with three fully equipped and instrumented irradiation rigs. The brazing technology of heater wires to the capsule shall be qualified to complete the fabrication route of the HFTM rigs. In addition, the NaK filling of narrow channels has to be demonstrated.

#### **2. Status 2006**

The manufacturing of three irradiation rigs has reached the state where some additional exercises on brazing and sodium filling techniques have to be performed. The full set of miniaturized samples has been fabricated.

#### **3. Recent Design Changes and Analyses**

Although a quasi reference design of the High-Flux-Test-Module (HFTM) for the International Fusion Material Irradiation Facility (IFMIF) has been elaborated a continuous effort is devoted to optimization and refinement of the design. Those originate from the concurrent performance analyses conducted in support of the design work.

Several changes have been introduced in the last year. A serious issue has been raised when examining the layout for the 650 °C samples. Hot spots in the compartment stiffening wall caused by the continuously heated helium gas occurred which in turn caused non-acceptable thermal stresses. It could be concluded, that the channel width has to be increased from 0.5 mm to 0.6 mm. An additional safety margin is provided also since the cooling gas mass flow could be increased accordingly.

Whereas the general stress situation of the container structure has reached a very satisfactory status, still high peak concentrations are observed at the spaceholder top and bottom edges. On the bottom side a modest weakening of the structure allowed for stress relaxation below the yield strength. Ongoing work is devoted to the upper end. A new concept of cut-free lateral reflectors has been launched to remedy several interconnected problems when combining a weak structure (test section area) with massive elements (reflectors).

#### **4. Manufacturing tests: Brazing and liquid metal filling**

The major challenge for the brazing procedure of the ohmic heater wires on the capsule surface is to fill very small gaps and grooves. Previous tests have been refined; in particular the homogeneity of the temperature field inside the vacuum oven has been adjusted.

Sample mock-ups, resembling the groove structure of the original capsule, have been brazed. The groove depth was 0.2 mm, which was chosen to be representative of the gap formed when a cylindrical wire is pressed into a rectangular groove (groove width in both cases: 1.0 mm). After cleaning the samples by Acetone and drying, the braze procedure using Microbraze proceeds as follows:

- 4 h: 20°C  $\Rightarrow$  850 °C
- 3 h: arrest temperature at 850 °C with gas release
- 45 min: 850 °C  $\Rightarrow$  990 °C
- 25 min: arrest temperature
- Cooling down under vacuum

A vertical cut through the brazed grooves (Fig. 1) reveals the excellent result of this optimized procedure. To avoid a brazing of the cold end wires to the structure a braze stop paste has been used which successfully kept the braze material for sufficient time within the narrow gap. Since several samples have been brazed successfully in a reproducible manner it was decided to apply the above mentioned procedure to the HFTM capsule manufacturing.



Fig. 1: Vertical cut of a braze sample showing a complete homogeneous filling at the bottom.

A liquid metal filling of the irradiation volume is foreseen to guarantee the heat transfer in the volume and to the capsule wall. To check this proposed method a filling test has been prepared using Na as liquid metal. The apparatus designed for this purpose is shown in Fig. 2. It will be located in a glove box under inert atmosphere (Ar). Remaining oxygen will be trapped by the open Na surface where the oxide layer could be removed easily. The liquid metal container will be heated well above the melting temperature of Na and pressurized by an Ar gas bottle. The capsule will be filled until Na is spilled out from the top reservoir tube. The filling tube will be cut and closed by welding followed by heating up the capsule and blowing out of the balancing volume at the top of the capsule.

The capsule used for this test has been manufactured previously as a HFTM capsule prototype. The ohmic heater winding in this case is vertically. The capsule has been modified to allow for filling from the bottom, and a Na balancing volume has been welded to the top.

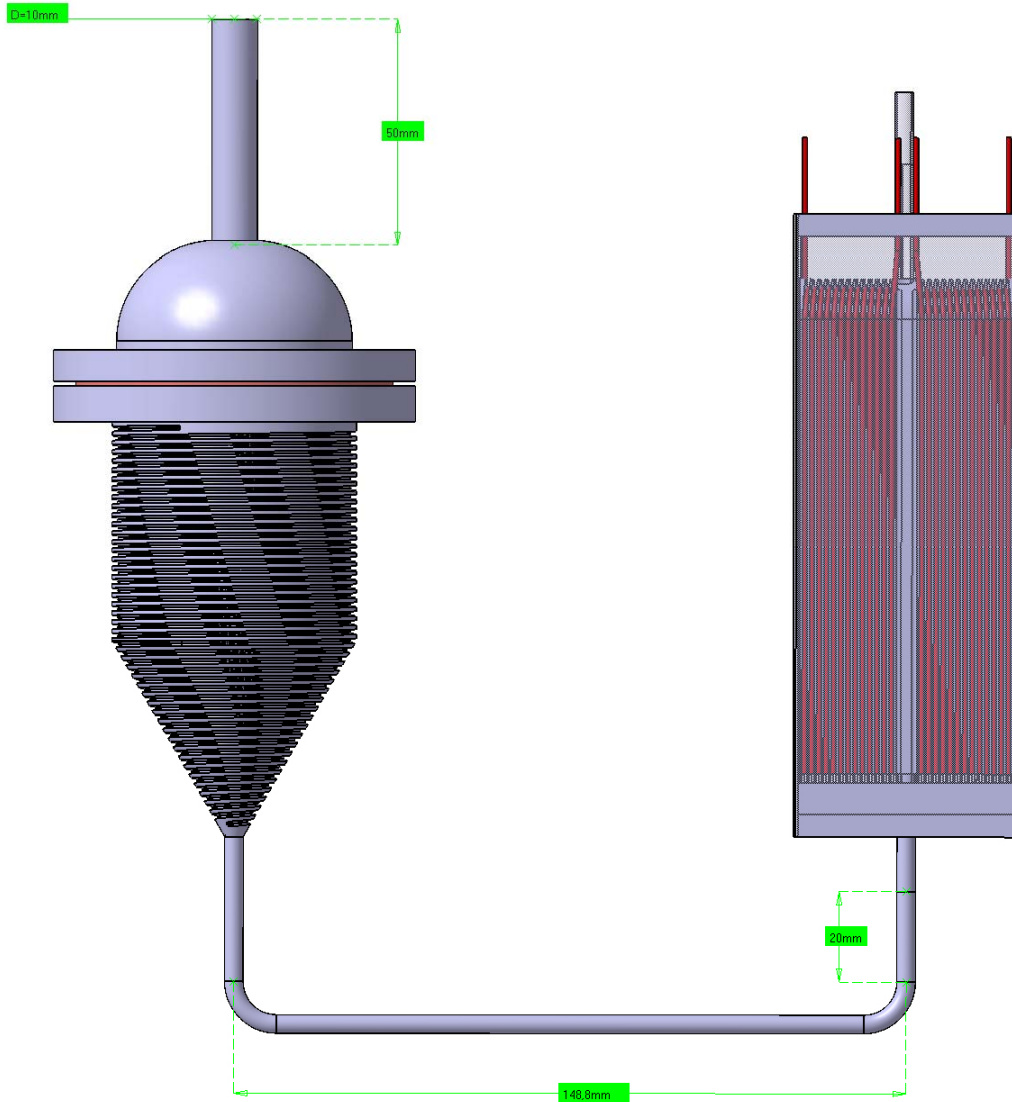


Fig. 2: Design of a liquid metal filling apparatus showing heated Na container (left) and capsule (right, old design). The filling tube (bottom) will be heated, too (not shown).

## 5. Manufacturing of a full compartment

Three rig casings, two of them made of AISI 316 (DIN 1.4301) and one of Eurofer steel, resp., have been produced already. They were manufactured by milling, stress-free annealing and spark erosion of the interior. The outside was directly spark eroded to form the rib structure on the surface. The manufacturing of the capsules started with the coarse and fine milling of the outside of the capsule casing from a massive slug. It followed the milling of the grooves by a 5-axes milling machine. For the embedding of the heater wires into the grooves a special clamping device was required to fix mechanically the wires at the long sides of the capsules. The wires were brazed to the capsule wall with help of a dedicated braze guidance box described above. The outer surface was ablated down to the original capsule surface by spark erosion. Finally the interior was spark eroded to obtain the specimen volume.

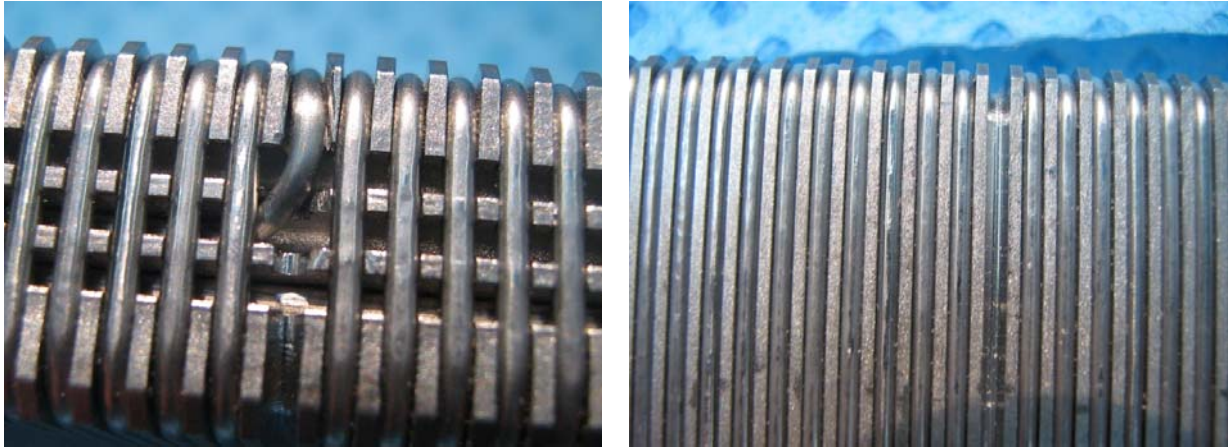


Fig. 3: Heater wire windings of the HFTM capsule: small side (left), long side (right).

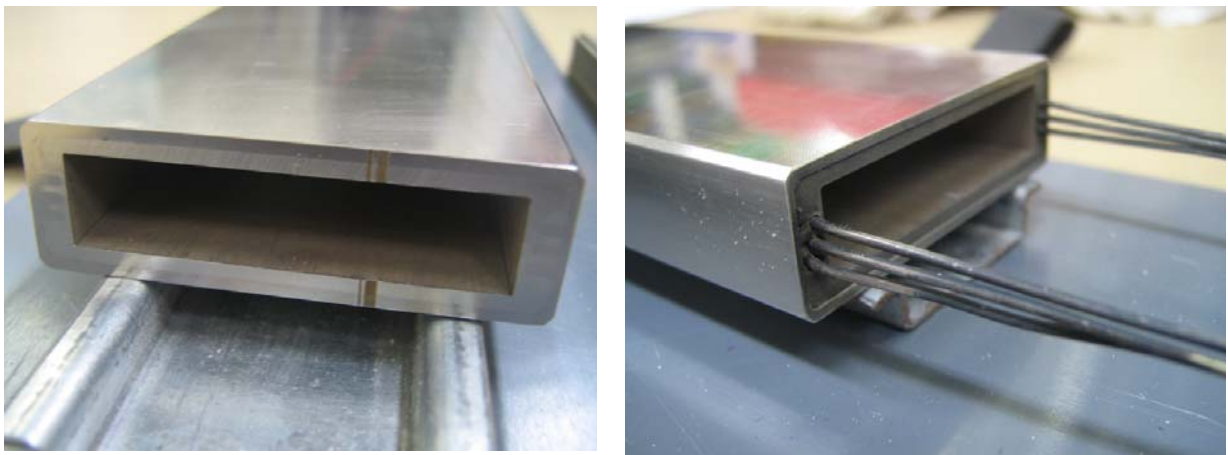


Fig. 4: Close-up view of the capsule after brazing of heater wires and machining of interior and outer surface.

## Conclusion and outlook

The final procurement of the full compartment consisting of three fully equipped HFTM rigs is expected to take place soon after the first successful Na-filling test described above. All necessary pieces have been fabricated. A thermographical investigation of the capsule wall has been already performed indicating now extended failures. The rigs will be analyzed further by X-ray tomography for a detailed microscopic inspection of the brazed layer and of the liquid metal filled specimen stack.

### Staff:

O. Albrecht  
F. Arbeiter  
V. Heinkel  
T. Ihli  
K.H. Lang  
D. Leichtle  
E. Stratmanns  
J. Konrad

Literature:

- [1] V. Heinzl et al., IFMIF high flux test module and test cell – Design and design validation, Fus. Eng. Des. 82(2007) 2444-2450
- [2] B. Dolensky, V. Heinzl, D. Leichtle et al., Engineering design and performance analyses of the High Flux Test Module of IFMIF, Proceedings Jahrestagung Kerntechnik 22-24.5.2007, Karlsruhe, Germany
- [3] D. Leichtle et al., IFMIF High Flux Test Module – Recent progress in design and manufacturing, to appear in Fus. Eng. Des.

## TW6-TTMI-003 D 5 Structural Materials Selection Guideline for In-Test-Cell Components

### Introduction

This task is aimed at providing designers as soon as possible with basic Materials Selection Guidelines (MSG) and recommendations for material selection using existing experimental data published in the literature. The MSG should bridge the time gap before the IFMIF material properties handbook (MPH) and dedicated structural design criteria (SDC) are not yet available.

After a compilation of all loading parameters and operation conditions for the major test cell components, an evaluation of the relative importance of these parameters was made for each component and screening of potential suitable materials was performed. Based on the evaluation of already available materials properties it was decided what structural material should be used for

- Li target
- HFTM (canister, rigs, capsules)
- MFTMs

In addition, listings of urgent data on materials irradiated under specified conditions were prepared.

### Results

Operation conditions for construction materials used at various parts of IFMIF were collected from the IFMIF Comprehensive Design Report as well as from various presentations given at IFMIF meetings (see Table 1).

Table 1: Operation Conditions at IFMIF Target, Test Cell Components and Surroundings

Component	T, °C	Displ. damage, dpa/fpy	He, appm/fpy	Max Stress, MPa	Environment	Lifetime
<b>Li target</b>						
back plate	270-360	60	600	260 / 60	liquid Li	<11 months
nozzle	250	< 10	< 60			
coolant tubes	250-350					
<b>HFTM</b>		<b>20÷55</b>	<b>250÷600</b>			
container	50-150	55				~ 1 year
rigs	250-650			263 (T91) 294 (316L)	helium	~ 1 year
capsules	250-650					~ 1 year
neutron reflector						> 1 year
<b>MFTMs</b>		<b>7÷13</b>	<b>70÷120</b>			
specimen clamping	250-550	6.7÷8.5	60÷80			
puling rods	< 100	2.8÷6.5	20÷60			
frames	< 100	0.01÷0.9	< 8			
<b>Test cell liner</b>	< 60	< 0.1		0.1	argon	

After a compilation of all loading parameters for the major test cell components, an evaluation of the relative importance of these parameters is giving rise to a Materials Selection Guideline for each component. We performed initial screening among possible candidate

materials such as austenitic stainless steel (316LN), reduced activation ferritic-martensitic (RAFM) steel (Eurofer 97, F82H) as well as reduced activation oxide dispersion strengthened ferritic-martensitic steel (Eurofer ODS), which is currently under developing for fusion applications.

As the test module temperature is typically below 100°C, and the ductility of 316L(N) is sufficient at irradiation temperatures below ~200 °C, the austenitic steel 316L(N) is presently considered as the most favorable startup material. This steel is also a reference material in other large scale nuclear facilities like ITER and SNS, where it is suggested for similar irradiation temperatures but smaller displacement damage doses.

Irradiation rigs and capsules, which should operate at higher temperature (250-650°C), could be made of reduced activation ferritic-martensitic steel (e.g., Eurofer-97).

Critical is the situation for the target back-plate that operates between 270 and 350°C, just in the temperature regime where the irradiation induced ductility reduction for 316L(N) is most pronounced. Based on the analysis of the irradiation resistance of 316L(N) one can conclude that the austenitic steels of this type are hardly suitable for the back plate due to the drastic reduction of ductility after irradiation at about 330°C. The results of thermo-mechanical analysis of the bayonet type back-plate performed at ENEA, Italy have shown that AISI 316L steel is not suitable as a black-plate material: the stress induced in the plate, in every configuration of constraints and back-plate geometry, exceed those admissible by the ASME standard. Conversely, ferritic-martensitic steels (e. g., F82H and the T91) satisfy ASME requirements. Therefore, Eurofer 97 is suggested as a candidate material for the IFMIF target back plate.

## Conclusions

Suggested IFMIF structural materials for various IFMIF components are listed in Table 2:

Table 2: Proposed structural materials for various IFMIF components.

Component	Temperature, °C	Damage, dpa	Helium, appm/fpy	Candidate material
<b>Target</b>				
Back plate	270-380	60	600	RAFM (Eurofer/ Eurofer ODS)
<b>HFTM</b>		20÷55	250÷600	
Container	50-150			316LN
Rigs	250-650			RAFM
Capsules	250-650			RAFM

During the work some urgent data needs were identified. Data on irradiated RAFM/RAFM ODS steels in the range of irradiation temperatures 50-150°C and on 316L(N) austenitic steel in 270-330°C with irradiation dose more than 30 dpa are required to evaluate suitability of these materials for the back-plate and HFTM container respectively.

### Staff:

A. Möslang  
P. Vladimirov

## Literature:

- [1] Fischer U., Chen Y., Simakov S.P., Wilson P.P.H., Vladimirov P., Wasastjerna F., *Overview of recent progress in IFMIF neutronics*, Fusion Engineering and Design, **81** (2006) 1195-1202
- [2] Heinzl V., Arbeiter F., Dolensky B., Fischer U., Gordeev S., Lang K.H., Leichtle D., Möslang A., Simakov St., Stratmanns E., Slobodtchouk S., Vladimirov P., *IFMIF high flux test module and test cell—Design and design validation*, 24<sup>th</sup> Symp. on Fusion Technology (SOFT 2006), Warszawa, Poland, September 11-15, 2006 (to be published in Fusion Engineering and Design)
- [3] Heinzl V.; Leichtle D.; Arbeiter F.; Dolensky B.; Fischer U.; Gordeev S., Möslang A.; Lang K.H.; Simakov S.P.; Stratmanns E.; Slobodchuk V.; Tsige-Tamirat H.; Vladimirov P., *IFMIF target and test cell - towards design integration*, 21<sup>st</sup> IAEA Fusion Energy Conf., Chengdu, China, October 16-21, 2006, Proc. publ.in the web, Wien : IAEA, 2006 Paper FT/P5-36, (Proceedings Series),ISBN 92-0-100907-0, [http://www-naweb.iaea.org/naweb/physics/FEC/FEC2006/papers/ft\\_p5-36.pdf](http://www-naweb.iaea.org/naweb/physics/FEC/FEC2006/papers/ft_p5-36.pdf)
- [4] P. Vladimirov, A. Möslang, U. Fischer, S. Simakov, *Material Irradiation Conditions for the IFMIF medium Flux Test Module*, J. Nucl. Mater. **367-370** (2007) 1574
- [5] P. V. Vladimirov, A. Möslang, P. Marmy, *Material Responses in IFMIF Creep-fatigue Testing Machine*, 8<sup>th</sup> International Symposium on Fusion Nuclear Technology, September 30-October 5, 2007, Heidelberg, Germany (poster presentation, paper submitted to Fusion Engineering and Design)
- [6] U. Fischer, P. Pereslavitsev, S. Simakov, A. Möslang, M. Rieth, P. Vladimirov, *Transmutation and Activation Analysis for Divertor Materials in a Fusion Power Reactor*, 13<sup>th</sup> International Conference on Fusion Reactor Materials, December 10-14, 2007, Nice, France (poster presentation)
- [7] U. Fischer, P. Pereslavitsev, S. Simakov, A. Möslang, M. Rieth, P. Vladimirov, *Transmutation and Activation Analysis for Divertor Materials in a Fusion Power Reactor*, 13<sup>th</sup> International Conference on Fusion Reactor Materials, December 10-14, 2007, Nice, France (poster presentation)
- [8] P. Vladimirov, S. Bouffard, *Displacement damage and transmutations in metals under neutron and proton irradiation*, (book contribution) Fusion and Generation IV Fission Power Reactors: Behaviour of Materials Subjected to Fast Neutron Irradiation, Eds. J. L. Boutard (EFDA), S. Dudarev (UKAEA) and G. Martin (CEA), (submitted to les Comptes Rendus Physique de l'Academie des Sciences)

# **EFDA/05-1291 (TW6-TTMI-003a)**

## **Preliminary Design Description Document for the IFMIF Test Facility**

### **1. Background and Objectives**

During the last few years a sound design for the different facilities of IFMIF has been developed, with special European responsibility for the Test Facility. The scope of this work is to publish a preliminary Design Description Document (DDD) for the IFMIF Test Facility based on the design work already done so far for the IFMIF systems. This report will document and summarize the work already done in relation with the Test Facility and shall identify future R&D activities, if needed.

### **2. Status 2006**

After the second monitoring meeting held at FZK on 11.12.2006 the DDD has been elaborated for the major parts of the chapters 3 and 4 (Engineering design and Performance Analyses). Several missing parts have been identified and also corrections and amendments to the provided chapters.

### **3. Final preparation of the Design Description Document**

The missing parts of the main chapters 3 and 4 have been collected, adapted to recent changes and fitted to the structure of the document. A chapter on manufacturing focused on the High Flux Test Module has been provided. UKAEA delivered a subchapter of chapter 2 (Design requirements) and the full contribution for chapter 7 (Safety requirements and waste management). Chapter 6 (Remote handling procedures) will be a summary of the corresponding part in the Preliminary Remote Handling Handbook prepared in parallel by the Italian and French associations. The editors of the DDD contributed with the Introduction chapter and Design requirements.

The DDD has been prepared as a Word-Document containing 164 pages in 7 chapters (1 to be extracted from the Remote Handling Handbook). About 100 figures, 14 tables and 130 selected references are given. The table of content is listed here:

1. Introduction and general description	7
2. Design requirements	11
2.1 User requirements	11
2.2 Operational requirements	12
2.3 Test facilities design requirements	13
2.4 Remote handling requirements	15
2.5 Safety and waste requirements	15
3. Engineering design	19
3.1 Overall system description	19
3.2 Lithium target system	23
3.3 Test modules	30
3.4 TTC vessel and removable cover	57
3.5 Instrumentation	62
4. Performance analysis	67
4.1 Nuclear responses	67
4.2 Thermohydraulic layout	87
4.3 Structural/mechanical analyses	120

5. Manufacturing / assembly	129
5.1 HFTM	129
6. Remote handling procedures	139
7. Safety requirements and waste management	141
7.1 Introduction	141
7.2 Safety approach	141
7.3 Hazards and source terms	147
7.4 Design quality assurance	151
7.5 Safety systems	152
7.6 Environmental protection provisions	158
7.7 Waste management overview	161
7.8 Waste management requirements	161
7.9 Initial waste characterisation	163

The DDD has been completed in November 2007.

Staff:

F. Arbeiter  
B. Dolensky  
U. Fischer  
S. Gordeev  
V. Heinzel  
T. Ihli  
D. Leichtle  
A. Möslang  
S. Simakov  
V. Slobodtchouk  
E. Stratmanns  
P. Vladimirov

## **Fuel Cycle Vacuum Pumping**



## TW5-TTFF-VP 51

### Mechanical Tests and Post-operational Examination of TIMO

#### Background

Following more than five years of successful performance testing of the (50% scale) ITER model torus exhaust cryopump in TIMO, in 2006 the TIMO facility was opened and the model pump dismantled from the test vessel. All parts of the pump were examined in detail. In 2007, three remaining issues were analysed: Firstly, the investigation of degradation effects of the sorption properties of the charcoal material; secondly, the analysis of the Belleville washers, which are regarded as the source for some valve problems, and, thirdly, the determination of the origin of the coloured material identified on the bottom of the test vessel.

#### Final analyses and examinations with the ITER model pump

To reveal any performance degradation which might have happened during the lifetime of the pump, two samples of the activated charcoal particles from the model pump were subjected to sorption isotherm measurements for different gases and temperature levels in the facility COOLSORP [1]. The first sample was taken from the small amount of loose material collected from the bottom of the pump (careful separation was performed to separate

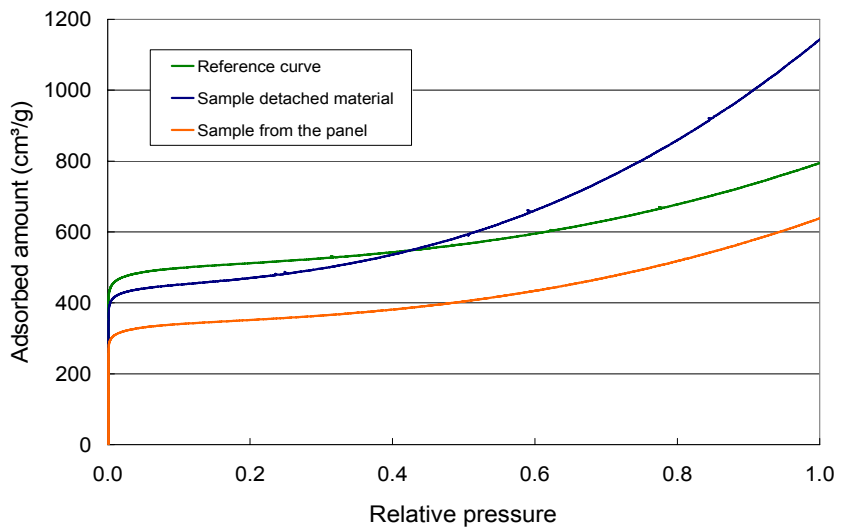


Fig. 1: Comparison of the sorbed amounts (helium at 4 K) for fresh and used charcoal samples.

the charcoal particles from other materials such as dust or black coating), the second was directly scraped off the cryopanel. Both samples (similar weight of ~ 1 g) were regenerated in an oven prior to the sorption measurements to provide comparable initial conditions. Fig. 1 compares the results for the sorbed amounts of helium at 4.0 K. In general, the sorbed amounts of the used charcoal is somewhat less than that measured for the fresh charcoal. This decrease is more pronounced for the panel charcoal than for the detached charcoal sample, which is attributed to the strong interaction with the higher hydrocarbons during the final test campaigns in TIMO.

In the 2006 analyses, the Belleville washers used for mounting the valve plate were identified to be the origin of the failures in that area. They were found to be plastically deformed and this was assumed to be due to a wrong material choice by the model pump main assembly manufacturer (see Fig. 2). To clarify this, the material composition was examined by a steel analysis institute. The result of the analysis showed that the chemical composition of the washers corresponds with stainless steel grade 1.4307, which is normally not used as washer material due to its non-elastic behaviour. This was re-confirmed with company SCHNORR which is one of the leading companies in that area. Consequently, this failure can easily be excluded in the future by proper material choice and effective QA.

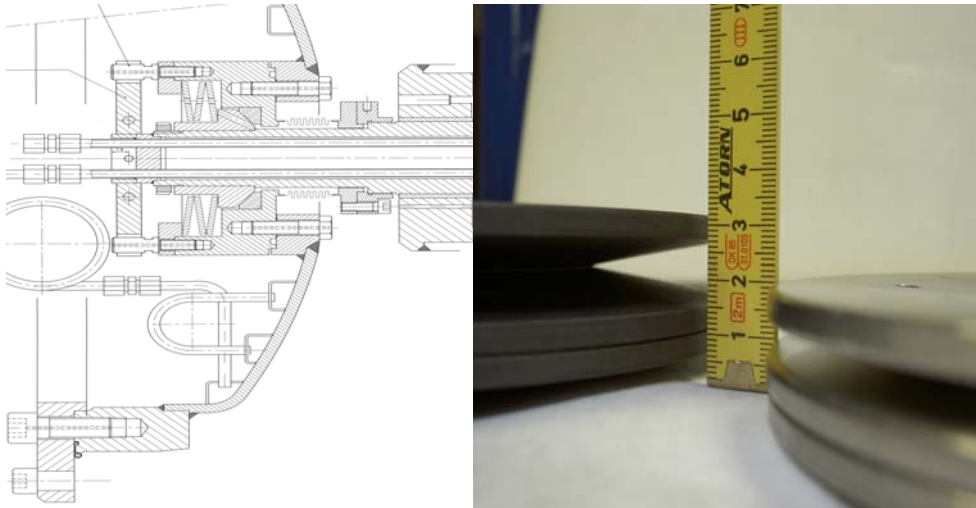


Fig. 2: *Left:* Drawing of the inlet valve with the construction details concerning the Belleville washers. *Right:* Photo showing the spring arrangements with the old Belleville washer set (right side) and the new one (left side), highlighting the reduced height of the old package due to plastic deformation.

After opening of the TIMO vessel, brown coloured deposits were found at the bottom of the test vessel, see Fig. 3. Because of the performed tests with different liquid impurities in the end of the model pump test phase and the leak in the inlet valve cooling loop at some unknown time during the tests, it could not be immediately clarified where these deposits arose from. Therefore, a chemical elementary analysis was performed which showed that the principal composition of the deposits corresponds to that of glycol. With this result the water/glycol mixture used for the pump inlet valve cooling loop can be determined as the source of the deposits inside the TIMO test vessel. This is a positive result, as it can now be confirmed that the charcoal stayed inert against the hydrocarbons used in the final model pump campaigns.



Fig. 3: View into the TIMO test vessel and the deposits at the bottom of the vessel.

Meanwhile the test vessel was cleaned and is ready for the installation of the prototype torus cryopump [2].

Staff:

Chr. Day  
H. Haas  
V. Hauer  
Th. Johann  
H. Jensen  
J. Weinhold  
D. Zimmerlin

Literature:

- [1] Chr. Day, V. Hauer, Adsorption on activated carbons at cryogenic temperatures, 9th Internat. Conf. on Fundamentals of Adsorption, Giardini Naxos, I, May 2007.
- [2] H. Haas, Status of TIMO-2 preparation, 14<sup>th</sup> ITER-EFDA-FZK Interface meeting, July 2007, ITER IDM ITER\_D\_27LAVZ.

## **TW5-TTFF-VP 58 Upgrade of TIMO**

Following the dismantling of the TIMO facility and examination of the ITER model pump (under EFDA task TW5-TTFF-VP51) the activities towards the TIMO upgrade, TIMO-2, for the new test campaigns with the ITER prototype torus cryopump (PTC) started.

### **Revision activities at the TIMO-2 control cryostat**

The 4.5 K TIMO-2 control cryostat was opened and completely refurbished. Especially, seven of the originally eleven installed temperature sensors (Si diode type) had to be replaced. During that exercise, it was found that in all cases, the reason for the malfunction was wrong installation handling going back to the cryostat manufacturing. To complete the instrumentation for the next test campaigns, additional redundant temperature sensors were installed at essential positions like the cryogenic inlet and the transfer connection to the valve box. In total, nine new temperature sensors were installed (see Fig. 1).



Fig. 1: Revision activities at the 5 K control cryostat of TIMO-2.

### **Operational tests at cryostat temperatures below 4.5 K**

ITER is considering to use an additional cold blower in the cryogenic valve boxes which supply the torus cryostat cryopumps. This gives the possibility to supply the pumps with SCHe at 4.3 K instead of 4.5 K. Keeping the maximum outlet temperature at the same value of 4.7 K, this would double the allowed  $\Delta T$  across the cryopump and therefore give way to reduce the flowrate accordingly. In view of this discussion, the feasibility of a new operation mode for TIMO-2 with operation temperatures  $< 4.5$  K was checked. One option to achieve this condition is to reduce the operation pressure of the control cryostat from the normal value 1.3 bar (corresponding to 4.5 K for boiling liquid helium) to close to atmosphere (corresponding to 4.2 K). The available infrastructure at the Institute does allow for such an operation by tuning of the inlet of the gas compressor stations. A series of tests were carried out manually under provisional conditions as the instrumentation of the data acquisition as well as the PLC was not completely available [1].

Due to the constructive conditions of the TIMO-2 control cryostat a continuous operation at a pressure  $< 1000$  mbar is not permitted. The pressure range for the operation was therefore

fixed between  $1000 < P \text{ [mbar]} < 1400$ . With the performed tests it could be shown that the operation with reduced pressure inside the TIMO control cryostat is feasible, see Fig. 2.

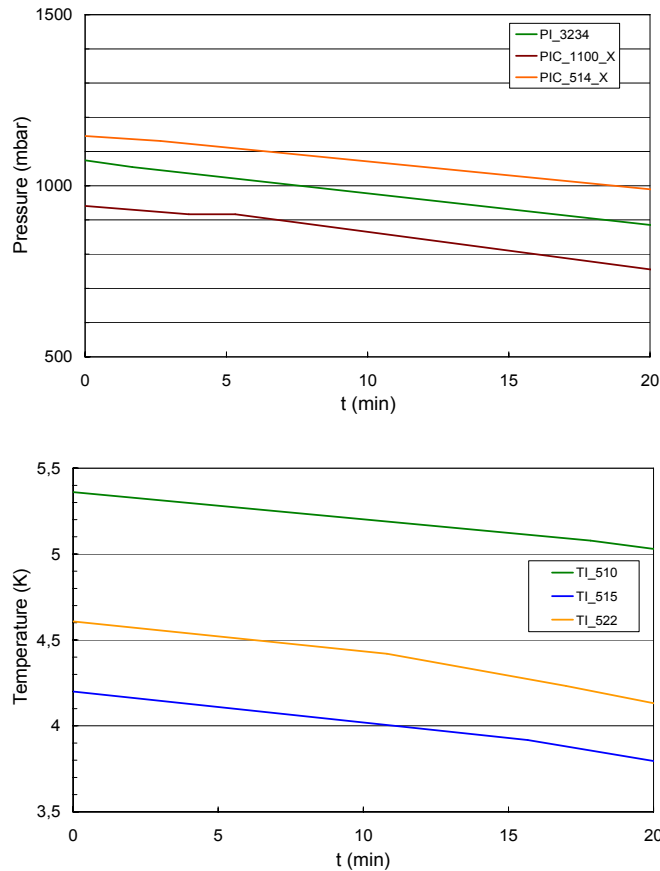


Fig. 2: Operational tests at reduced pressures in the control cryostat. The top figure shows the pressures in the cryostat (orange) and in the compressor arrangement (green and brown); the bottom figure shows the corresponding temperatures at different positions inside the control cryostat installations.

### Adaptor flange preparation for TIMO-2

An adaptor flange is necessary for the installation of the PTC into the TIMO-2 test vessel due to different flange dimensions (the test vessel was re-used from the former TIMO set-up with the smaller model pump). To identify the geometric interface between the existing vessel opening and the new adaptor flange most accurately, a point-to-point tactile measurement was employed to determine the roundness, see Fig. 3. This work included the over all flange dimensions as well as the area of the seal and the 72 screw holes. On the basis of the measured results the exact adaptor flange design and the specification was prepared. The manufacturing is under way.



Fig. 3: Roundness measurement activities at the TIMO-2 test vessel flange.

### New cryotransfer line for TIMO-2

In the existing TIMO configuration a fixed transfer line was used between the valve box and the pump flange of the test vessel (see Fig. 4, left). As it is planned to use TIMO-2 for testing

the PTC and for a limited number of the serial ITER torus cryopumps and the ITER cryostat cryopumps as well, this existing concept must be modified towards a more versatile solution. This is also a pre-requisite to reduce the assembly turnover time associated with each cryopump change. It was therefore decided to procure a new, flexible corrugated cryotransfer line. An additional issue for the new transfer line concept was the compatibility with the ITER "cryo-jumper". With these cryo-jumpers all cryopumps in the ITER pump system will be connected with the valve boxes of the cryodistribution system for both the 4.5 K and the 80 K circuits.



Fig. 4: Configuration of the old (left) and the new (right) cryo transfer line between the TIMO-2 valve box and test vessel flange.

The new transfer line will consist of several parts as shown in Figure 4. It will be connected with a fixed part at the valve box, which is not ITER-relevant but provides for essential TIMO-2 instrumentation. For the connection to the pump flange of the test vessel two flexible line sections and the allocated Johnston couplings will complete the new transfer line. At TIMO-2 the cryogenic supply includes forced flow gaseous Helium (GHe) at different temperature levels as for example 4.5 K and 80 K for nominal operation and 20 K, 100 K, 300 K and 475 K for various cryopump regeneration procedures.

To be able to qualify and test the cryoline without installed cryopump, a bypass line for closed loop operation will also be integrated.

The design of this ITER-relevant cryoline was completed, and the order was finally placed at a German supplier; the delivery is expected for early 2008.

## Outlook

The TIMO upgrade has progressed according to plan and will be ready in due time before the PTC will be delivered to FZK (end of 2008) for acceptance testing.

## Staff:

H. Haas  
Th. Johann  
H. Jensen  
K. Müller  
P. Pfeil  
H. Strobel  
H. Stump  
J. Weinhold  
D. Zimmerlin

## Literature:

- [1] H. Haas, Status of TIMO-2 preparation, 14<sup>th</sup> ITER-EFDA-FZK Interface meeting, July 2007, ITER IDM ITER\_D\_27LAVZ.

## EFDA/06-1468 (TW6-TTFF-VP 54)

### Support to EFDA CSU Garching in Monitoring of Contract for ITER 1:1 Prototype Torus Exhaust Cryopump (PTC) Fabrication and Associated Fatigue Test (under task TW6-TTFF-VP 55)

#### Background and objectives

The ITER exhaust gas pumping will be utilised by installing 8 cryopumps situated at the lower part of the ITER machine, the cryopumps will be connected to the torus via ducts branched from torus divertor region. The main exhaust species resulting from the fusion process consist mainly of helium and hydrogen molecules, which will be pumped by cryosorption panels situated in an array inside the cryopumps [1]. The 8 cryopumps will be operated in a staggered mode and thus providing continuous pumping. The PTC design has been based on the  $\frac{1}{2}$  scale ITER model cryopump, which was successfully tested in the TIMO facility at FZK (2000-2005), see Fig. 1. The design phase of the PTC and the procurement specification was completed by FZK in 2006 under the task TW4-TTFF-VP41 [2].

The aim of this task is to ensure the requirements specified in the PTC technical specification are adhered to in all aspects. FZK will act as Technical Liaison Organisation (TLO) on behalf of EFDA. The task includes monitoring of the main contractor and all subcontractors which are manufacturing parts for the PTC including the manufacture of hardware, verifying all thermo hydraulic- and heat loss calculations, inspection of quality assurance documentation, physical monitoring during pressure- and vacuum leak testing, etc. Calculations for optimised PTC pumping speed are being performed at FZK using MOVAK software. In addition, the charcoal coating of the cryosorption panels will also be provided under this present task to the PTC manufacturer.

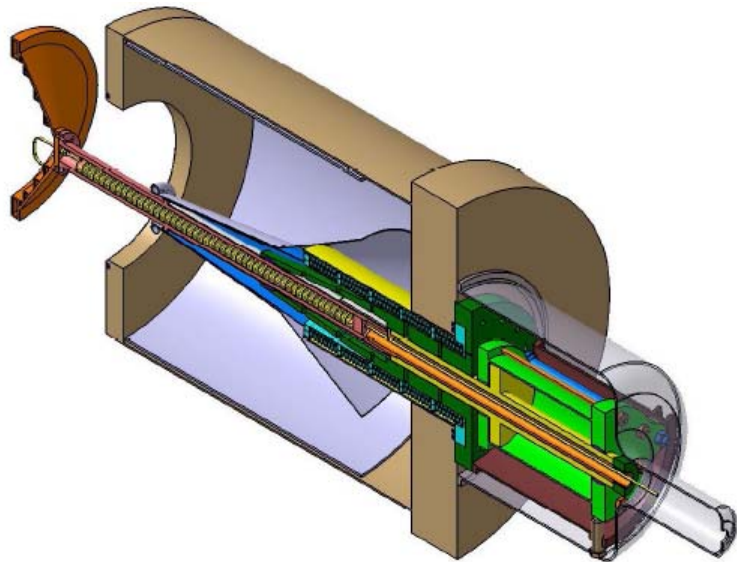


Fig. 1: Schematic of the ITER torus exhaust primary pump.

#### PTC manufacturing progress

**Contract start:** The PTC contract was signed by the European Commission January 2007 and the contract kick-off meeting took place 13.02.2007 [3, 4] at DeMaCo in Holland, who was awarded the PTC contract. At this point the FZK manufacturing drawings were handed to this main manufacturer, including technical details of wiring, temperature monitoring, pneumatic actuation etc.

**Design issue:** The FZK technical specification identifies the envelope of the PTC but the manufacturer has the option of improving the mechanical design, especially with regard to the actuating system of the integral inlet valve which must withstand minimum 30,000 cycles. Also the 80 K circuits are up to the manufacturer to complete, as the thermo hydraulic requirements have to be checked with the chosen 80 K panel manufacturer. All PTC drawings have been drawn in CATIAv5 format which is the prescribed ITER standard. The manufacturer has decided to sub-contract the major design issues to Dutch Space, Holland. All components have been scrutinised for improvements and subsequently verified by calculations which are approved by TLO and EFDA. In particular, the challenge of a high load bearing in

cryogenic environment and the pneumatic actuation, which will be tested up to 80,000 cycles in a dedicated fatigue test stand, has received special attention during the process of completing the design stage.

Pilot production of 4.5K panels: A Dutch company (Omega) will be manufacturing the 4.5 K (1000 mm long x 200 mm wide) and 80 K panels, which will all be produced in quilted design. During an initial pilot production exercise 5 of 4.5 K panels were manufactured.



Fig. 2: 4.5 K hydroformed stainless steel panels - pilot production by Omega.

The internal flow characteristics of all different panel types are optimised and verified to ensure minimum pressure loss between the inlet and the outlet tubes, also the temperature gradient along the surfaces must be homogeneous.

Quality assurance: The PTC will be certified to EN13445 which entails comprehensive quality assurance requirements that must be in place from the start. The main manufacturer and the present subcontractors have been examined in view of quality assurance. Extensive and very detailed procedures have been completed for the PTC manufacture; this will ensure a very high standard of manufacture for all components. The written procedures will also guarantee reproducibility of the quality when the manufacture of the series pumps will be carried out.

Clean condition: The manufacturer of the hydroformed panels has been audited and a part of the factory floor has been allocated for clean manufacture. All stages of the manufacturing process are monitored and optimised for clean conditions. This includes all handling procedures starting from the raw stainless steel supplied by the manufacturer and completed at the final product when pressure- and vacuum leak tested.

Raw material: The delivery time for cross forged grade material is long and the manufacturer has ensured the supply by an order for 5 heavy duty stainless steel flanges. The total weight of the PTC will be in excess of 8 tons, mainly stainless steel.

## Outlook

The drawing package will be completed by DS January 2008 and the manufacturing will start immediately afterwards [5]. The 4.5 K panels will be coated with activated charcoal at FZK in a special coating facility. The dedicated fatigue test stand will start operation March 2008 and possible problems identified during this test will be rectified, re-tested and implemented in the final PTC, which will be completed September 2008. After acceptance testing at FZK, the PTC, which is a prototype, will be validated in the TIMO-2 facility at FZK starting end of 2008.

Staff:

Chr. Day  
M. Dremel  
H. Haas  
V. Hauer  
H. Jensen  
R. Simon  
H. Strobel

Literature:

- [1] D. Murdoch et al., Vacuum technology for ITER, 17<sup>th</sup> Int. Vacuum Congress, Stockholm, S, July 2007.
- [2] V. Hauer et al., Design of the ITER torus prototype cryopump, Fusion Engineering and Design 82 (2007) 2113-2119.
- [3] EFDA Newsletter 1/2007, Fusion News March 2007.
- [4] ITER Newslines, Issue 8, March 2007, <http://www.iter.org/newsline/issues/8/ITERnewsline.htm>
- [5] G. Piazza, The ITER PTC design update, 1<sup>st</sup> ITER Vacuum Interface Workshop, Dec. 2007, Aix, France, ITER IDM ITER\_D\_29PGL4

**EFDA/07-1704-1566 (TW6-TTFF-VP 78)**  
**ITER Torus Cryopump Mechanical and Thermal EM Load Study**

**Background and objectives**

The eight torus cryopumps for ITER are connected to the torus lower ports within the port cells. The pumps will be subject to electromagnetic loads (EM) due to their close proximity to the torus. The mechanical (forces, torques) and thermal effects (heat loads) of the EM loads need to be analysed in order to confirm the design and to ensure sufficient margin on the cryopumps and cryogen supplies, and mechanical loading on the cryo-array supports.

The torus cryopump geometry is shown in Fig. 1. Agreed input conditions for the calculations are summarized in Table 1.

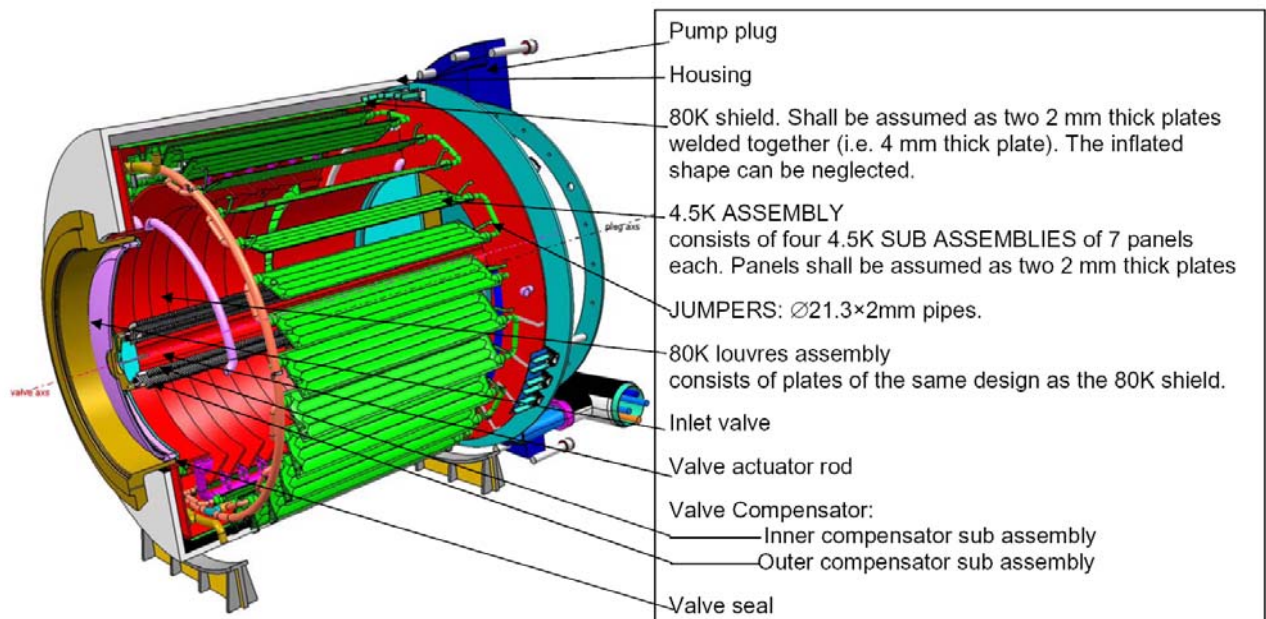


Fig. 1: Torus cryopump structure, as input for EM calculations.

Table 1: Operating conditions of the torus cryopump.

Cryogenic media:	Supercritical helium at 4.5 K and 0.4 MPa Gaseous helium at 80 K and 1.8 MPa
Regeneration cool down time (100 K → 4.5 K) or warm up time (4.5 K → 100 K)	150 s
Number of thermal life cycles:	
fast regeneration 100 → 4.5 → 100 K	≥ 30000
daily regeneration 300 → 4.5 → 300 K	≥ 7500
high temperature regeneration 475 → 300 → 475 K	≥ 1000
Pneumatic valve actuation media	helium gas (during manufacture N <sub>2</sub> )
Valve opening/closing time (100%)	10 seconds

**Results of earlier analysis**

The first EM assessment of the torus cryopump has been performed in 2001, based on which the support scheme of the cryopump had to be modified.

The most dangerous load case was revealed to be: deadweight + thermal fields at operating temperature + dynamic accelerations and local EM loads at fast downwards vertical displacement event. Displacements of the cryopump structure for all design load cases were calculated and it was shown to not exceed 4.3 mm in the region of the 4.5 K quilted cryopanel. The analysis of natural frequency of the cryopump supporting structure showed that the natural frequency in the range 16...25 Hz reflects the movement of the 4.5 K quilted cryopanel as a whole (this range of natural frequencies coincides with the typical range of seismic excitation). Results of the EM analysis have confirmed that the values of the integral loads on the cryopump supporting structure (quilted cryopanel, inner and outer chevron) are less than 10% of the loads coming from the total weight of the cryopump, and are therefore uncritical.

However, as the cryopump design has progressed since 2001 (now frozen with the design of the prototype torus cryopump) and the ITER load cases have been revised [1], the analysis needs to be repeated, now based on a less simplified cryopump model.

### **Definition of load cases**

The EM calculations under the current task are provided by experts from the D.V. Efremov Scientific Research Institute in St. Petersburg, Russia, who have already been in charge for the 2001 calculations. The calculations are using the 3D code TYPHOON. For the current task, the load cases have been revised with the goal to identify the worst cases of analyses to be performed in detail and to only roughly evaluate the cases, which produce significantly smaller loads than the others.

In accordance with [1], disruptions are classified into three types called I, II and III. Each disruption is characterized by two phases at least: thermal and current quenches. During the thermal quench, the full plasma current grows from the normal value 15 MA up to 16.5 MA approximately. The thermal quench time is 3 ms, 1.5 ms and 1 ms for disruption types I, II, and III, respectively. During the current quench, the full plasma current drops to zero. For each type of disruption there are two possible current quench laws: linear and exponential.

As specified in [1], vertical displacement events (VDE) are classified into two types called VDE III (or "Extreme" VDEs) and VDE II. In contrast to disruption, each VDE is characterized by three phases: start of plasma vertical movement, thermal and current quenches. During the first phase, which lasts between 100 ms and 1 s, the plasma current position drifts vertically and the current value keeps practically constant. Depending on the direction of the plasma current movement, upward and downward VDEs are distinguished. In terms of the current quench time, each VDE type is specified as fast or slow.

At fast discharges, the currents in the PF and TF coils decay from their initial values down to zero nearly exponentially. The time constant for the fast discharge is typically a few seconds.

As noted above, eddy currents induced in the cryopump steel depend on the rate of field variations near the cryopump and the period when the field varies monotonously. At plasma disruptions, the time derivative of the plasma-generated field surrounding the cryopump is a function of the rate of plasma current variations and the distance between the plasma and the cryopump.

After classification of all principle cases, the following conclusions were made:

1. Among all studied events (Disruption I,II,III and VDE II,III), the fast downward VDE III with linear current quench will produce the most loaded conditions for the cryopump.
2. The maximum cyclic loads take place at the fast downward VDE II with linear current quench.

3. Under fast discharge, the most loaded conditions are associated with the TF coils and PF4 and PF5 coils.

The next step is the detailed calculation of these three loads, starting with fine meshing of the cryopump as input to the TYPHOON model.

Staff:

A. Antipenkov

A. Belov (STC, Efremov Institute)

Chr. Day

S. Sychevsky (STC, Efremov Institute)

Literature:

- [1] G. Sannazzaro, ITER Load Specifications and combinations for in-vessel components, ITER Project Office, Sept. 2007.

## TW5-TTFF-VP 57 ITERVAC Validation Test

### Background and Objectives

The ITERVAC code is being used for the optimisation of the ITER vacuum pumping systems which are at most locations characterised by very high throughputs and therefore being operated in transitional flow regime (cf the parallel task TW6-TTFF-VP68 for assessment of the divertor system). Thus, the standard vacuum formulae for molecular or laminar flow and Monte Carlo codes are not applicable [1].

Because of the importance which is given to the calculation results of ITERVAC, the code must be extensively benchmarked. A theoretical benchmarking was done in the field of laminar and purely molecular flow, however, it has been found that literature data for (intermediate) transitional flow range, which is of major importance for the ITER conditions, are scarce and even not existing for geometries as complex as for the ITER vacuum pumping ducts. In order to validate proposed design modifications, such as to increase the conductance of the path from the divertor to the torus exhaust cryopumps, which have to be made while respecting other functions of the design (e. g. shielding, structural strength of the cassette), an experimental confirmation of the modelling results is required. The TRANSFLOW facility was built up and is now under routine operation to provide a broad and relevant range of well defined experimental data which can be used to benchmark the code.

### Experimental results for the long circular channel

The basic idea of the new TRANSFLOW test rig (Transitional Flow Experiments) is the measurement of the conductance of different channels in the transitional flow regime. The philosophy of this approach is not in first line to investigate directly a 1:1 model of the ITER duct, as this would necessitate a huge facility with expensive instrumentation. It is rather foreseen to use different interchangeable test pieces which would be modelled by ITERVAC and the measured results compared against predictions from the ITERVAC modelling calculations.

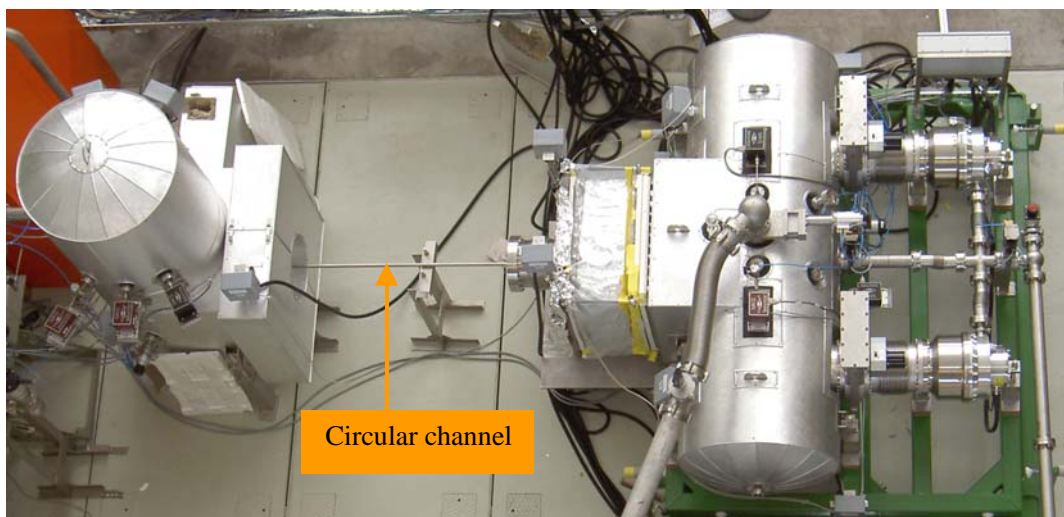


Fig. 2: Circular test channel installed in TRANSFLOW [2].

For the start, a long cylindrical duct was used, which is the only cross-section for which there existed solutions for the whole range of rarefied gas flows. The first channel had an inner diameter of 16 mm, a length of 1280 mm (length to diameter ratio of 80), and a wall thickness of 2 mm. The inner surface of the channel had no special treatment; it is foreseen to com-

pare with internally electropolished tubes in future experiments. Fig. 1 shows the test channel installed in the TRANSFLOW test rig.

The experiments started with higher mass flows to have measurement results for the laminar flow. The lowest flow reached with the mass flow controllers was 1 sccm because of stability limitations in the lower end of the mass flow controllers. The full range of intermediate and the range of molecular flow could not be reached with the foreseen flow controllers. A new flow controller with a flow rate range between 0.02 sccm and 1 sccm was therefore installed additionally. New measurements including other duct cross-sections showed that a recalibration of the mass flow controller was needed; moreover, the inlet conditions need to be carefully maintained during flow operation. The latter necessitated to install an additional buffer vessel so as to keep the inlet pressure practically constant during the tests. A small rig for calibration of the mass flow controller via p-v-T measurements was built up next to the TRANSFLOW facility, see Fig. 2. The recalibration was done on a regular basis and the new results were used for calculating the mass flows in the transitional flow regime.



Fig. 2: Calibration set-up for the low flow mass flow controller.

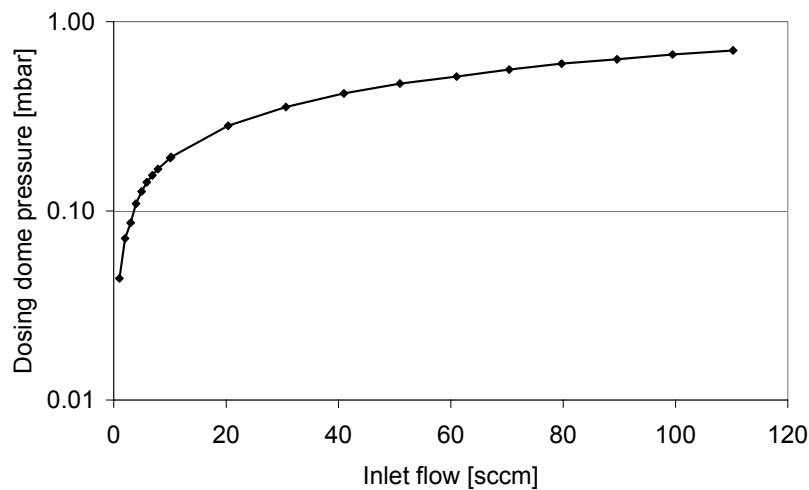


Fig. 3: Pressure in the dosing dome vs. the inlet flow for the long circular channel.

In Fig. 3 and Fig. 4 the measured and corrected pressures in the dosing and pump dome as a function of the mass flow are shown, respectively. The conductances shown in Fig. 5 were calculated from the pressures inside the dosing and the pump dome, and corrected so as to extract the conductance of only the test channel itself. Fig. 5 also compares with theoretical solutions for such a channel [3] and with predictions based on an ITERVAC model [4].

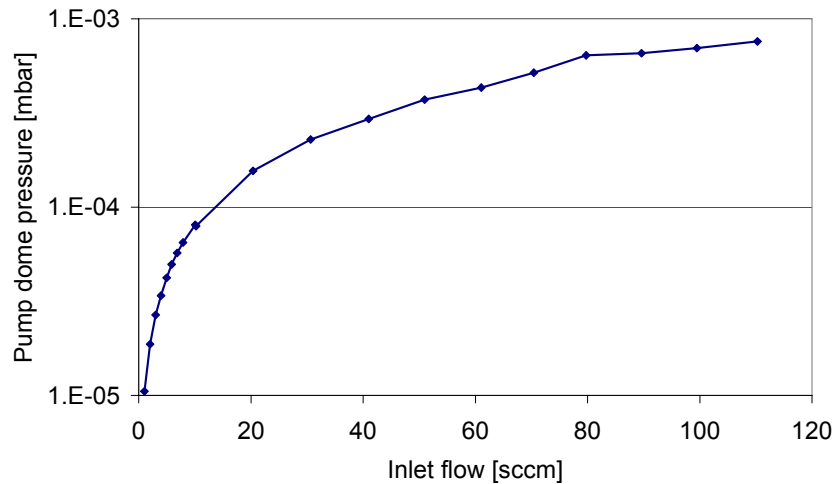


Fig. 4: Pressure in the pump dome vs. the inlet flow for the long circular channel.

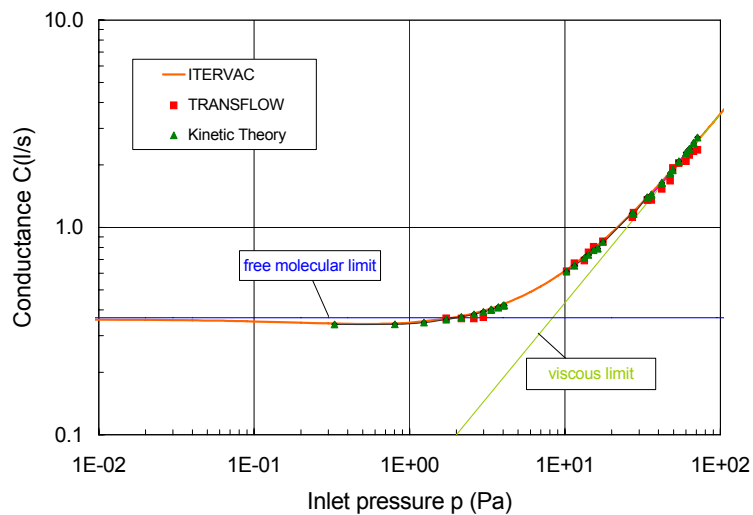


Fig. 5: Calculated conductance of the long tube including adapter flanges.

## Outlook

A completion of the measurements campaign with the four long test channels (circular, square shaped, triangular, trapezoidal cross section) and one short channel with a trapezoidal cross section is planned in the first quarter of 2008 [5]. A detailed comparison of the TRANSFLOW results with the simulation results of ITERVAC will follow in mid 2008 and close this task. The collaboration with the EURATOM/Hellenic Republic Association in University of Volos on calculations of vacuum flows through non-circular cross-sections based on solutions of the Boltzmann kinetic equations will also be continued.

## Staff:

Chr. Day  
V. Hauer  
H. Jensen  
P. Pfeil  
H. Stump  
St. Varoutis (Guest scientist, University Thessaly, Volos, Greece)  
J. Weinhold  
D. Zimmerlin

Literature:

- [1] Chr. Day, The need to model the ITER high vacuum systems in transitional flow regime – an engineering perspective, 51st IUVSTA Workshop on Modern Problems and Capability of Vacuum Gas Dynamics, Värmdö, S, July 2007.
- [2] Chr. Day, V. Hauer, TRANSFLOW – Building of the test rig (Report of EFDA Task TW4-TTFF-VP47 Deliverable 2), Internal report FE.5130.1023.0014/B, Forschungszentrum Karlsruhe, January 2007.
- [3] S. Varoutis, D. Valougeorgis, Chr. Day, Computational and experimental investigation of flows in long channels of various cross sections under low, medium and high vacuum conditions. 17th Internat. Vacuum Congress, Stockholm, S, July 2007.
- [4] V. Hauer, Chr. Day, ITERVAC - a semi-empirical code for calculations in the transitional flow regime. 51st IUVSTA Workshop on Modern Problems and Capability of Vacuum Gas Dynamics, Värmdö, S, July 2007.
- [5] Chr. Day, V. Hauer, TRANSFLOW - a test rig to measure conductances in the transitional flow regime, 17th Internat. Vacuum Congress, Stockholm, S, July 2007.

## EFDA/06-1498 (TW6-TTFF-VP 68) Conductance Modelling of ITER Divertor and Torus Pumping Duct

### Background and objectives

The simulation of the ITER torus vacuum system was started in 2004/2005 under the EFDA Task TW4-TTFF-VP47. The results revealed a strong conductance limitation of the reference pumping duct. The calculated pressure profile of the duct identified the divertor pumping slots as the bottlenecks.

The scope of this present task is to estimate the conductance of the redesigned ITER divertor and torus pumping ducts. The aim is to give a hint to the improvements which can be expected from a more open divertor design as well as to give a more detailed picture of the flow distribution inside the ITER torus vacuum system. This shall be achieved by intense use of the ITERVAC code [1]. Fig. 1 illustrates the modelling situation. The work in 2007 was limited to the set-up of a first, preliminary model, which will be extended in 2008.

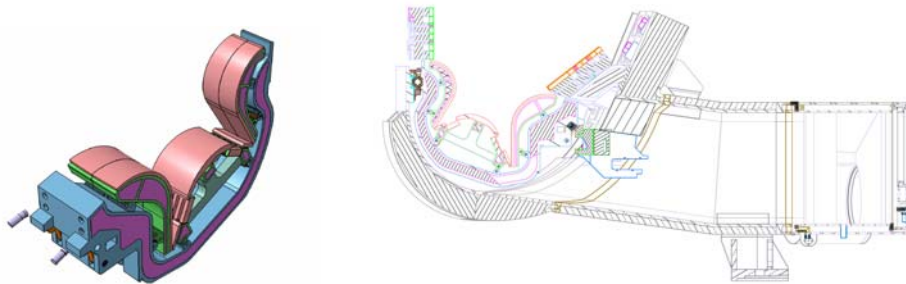


Fig. 1: View of the divertor and the pumping duct.

### ITERVAC model and input data

A modified model of the full ITER ring was developed in the simulations starting from the half ring model used in the previous task, see Fig. 2. The three divertor pumping duct connections to the divertor (the fingers) were taken out and the duct following the fingers in direction to the pumps was elongated to maintain the same length of the complete duct as before. Moreover, the toroidal and radial conductances of the open duct connection were appropriately considered. By that, the integral effective cross-sections became larger; however, the effect was found to be not very pronounced, as the major bottleneck is still the element in direction of the pumping duct.

Since the development of the old model, the philosophy of how to connect to the pump was also revised. The old calculations were done at varied pumping speeds of the torus cryopumps in order to get a feeling of the pumping speed that is needed to meet the ITER requirements (focussed on burn conditions). From these calculations, we fixed to come up with a target pumping speed of  $\sim 80 \text{ m}^3/\text{s}$  per torus cryopump. In the following detailed design process of the prototype torus cryopump (PTC), Monte Carlo calculations were necessary which included the double bellows upstream the torus cryopump. The pumping speed data given for the final design of the PTC do therefore refer to the combination of (cryopump + bellows). To reflect this approach in the new calculations presented here, the element that modelled the bellows in the old model was taken out and the pumping speed to use in the future is the one of the (cryopump + bellows) combination.

In ITERVAC there is no possibility to simulate gas mixtures. Only the maximum throughput for one gas species at isothermal conditions can be calculated. The divertor pressure was chosen to  $10^{-4} \text{ Pa}$  (at 420 K) for calculations of the effective pumping speed in the molecular flow regime. It must be noted that the absolute pressure value is only relevant in terms of the throughput; the derived conductance is independent of the chosen divertor pressure as long

as the system stays in molecular flow. The pumping speeds were chosen from the original FZK PTC design to 51.6, 55 and 49.4 m<sup>3</sup>/s for the gases helium, deuterium and DT, respectively, and corrected for the higher gas temperature of 420 K for the throughput calculations.

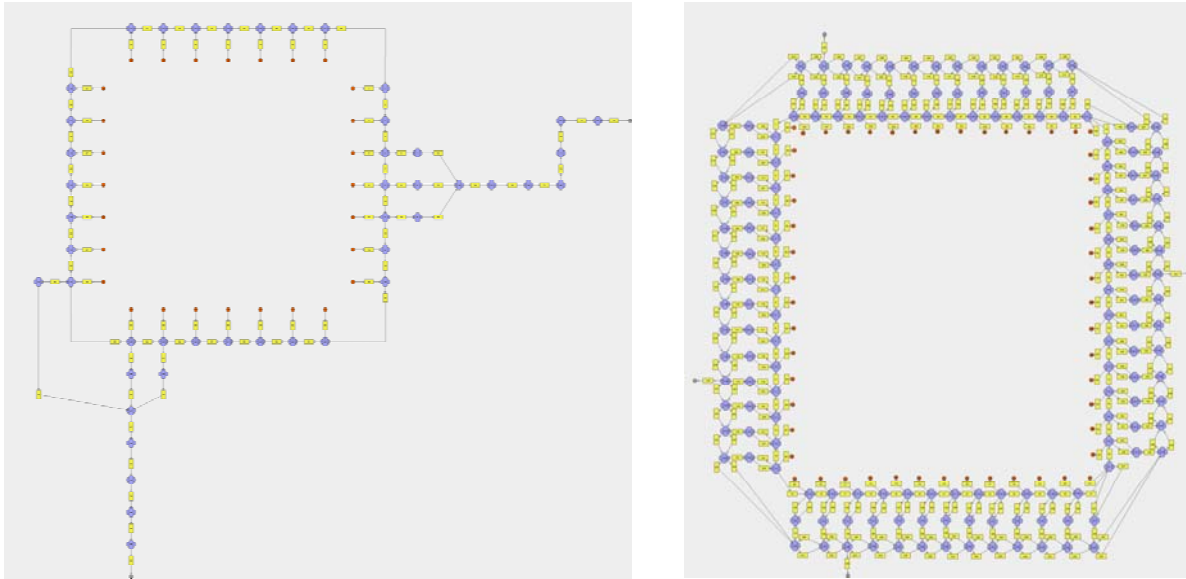


Fig. 2: ITERVAC models (left: half ITER torus vacuum system with the three fingers, 2004, right: new full ITER torus vacuum system, 2007). The fingers were taken out and the toroidal and radial conductances were introduced.

### Simulation results

The ITERVAC results for the conductances, calculated separately for the branched and the direct duct within the half ITER model are given in Table 1. Under the approximation that the parallel flows of lined and branched duct are independent, one can apply the addition theorem to each individual duct to determine the duct effective pumping speed and add these four to obtain the total effective pumping speed for complete ITER. The resulting values are also given in Table 1.

Table 1: Calculated individual conductances for the two types of torus exhaust ducts and derived total conductances and effective pumping speeds for the complete ITER torus vacuum system.

	Molecular flow conductance (duct in line) [m <sup>3</sup> /s]	Molecular flow conductance (branched duct) [m <sup>3</sup> /s]	Molecular flow conductance (complete ITER) [m <sup>3</sup> /s]	Effective pumping speed (complete ITER) [m <sup>3</sup> /s]
Helium	12.9	11.5	48.8	39.4
Deuterium	12.9	11.6	49.0	40.1
DT	11.6	10.4	43.9	35.9

The obtained molecular flow pumping speeds are clearly higher (around 40%) than the ones calculated previously for the three-fingered model [2].

### Staff:

Chr. Day  
V. Hauer

Literature:

- [1] Chr. Day, The need to model the ITER high vacuum systems in transitional flow regime – an engineering perspective, Workshop on modern problems and capability of vacuum gas dynamics, Varmdö, S, July 2007.
- [2] V. Hauer, Chr. Day, R. Pearce, Assessment of the gas flow paths of the ITER divertor cassettes, 8<sup>th</sup> Int. Symp. on Fusion Nuclear Technology, Heidelberg, Sept. 2007.

## TW6-TTFF-VP 53 Tritium Test of Ferrofluidic Cartridge Seals for Roots Roughing Pump

### Background and objectives

In accordance with the ITER vacuum requirements [1] and the results achieved in the previous tasks, the ITER forevacuum pumping system shall provide a unit pumping speed at its inlet of at least  $1 \text{ m}^3/\text{s}$ . The best pump type to meet this goal is a roots pump. A tailor-made tritium compatible pump of  $250 \text{ m}^3/\text{h}$  was tested at FZK on helium in the frame of the previous R&D Task TW3-TTF/VP12.

To make a catalogue pump tritium compatible the following main modifications are needed: a stainless steel housing, metal stationary seals, and tight rotary shaft seals between the process and the lubricant chambers, namely ferrofluidic rotary feedthroughs (see [2]). The testing of one of such seals made as a replaceable cartridge is now going on with tritium.

### Test programme and facility

The tritium test of a ferrofluidic rotary feedthrough completes the investigation programme of this seal [3] in order to allow the start of its industrial application. The test unit consists of two compartments, separated by the ferrofluidic test cartridge. The tritium leak through the cartridge is continuously monitored by an ionisation chamber under rotation of the shaft at 1500 rpm and at pressure differences of 500 mbar. The continuous test is planned for about 2000 hours, assuming the leak rate will not significantly exceed the expected maximum level of  $\sim 10^{-6} \text{ mbar l/s}$ . The test will be completed by investigation of the seal degradation after a long term exposure to the tritium and the measurement of the tritium intake by the ferrofluid.

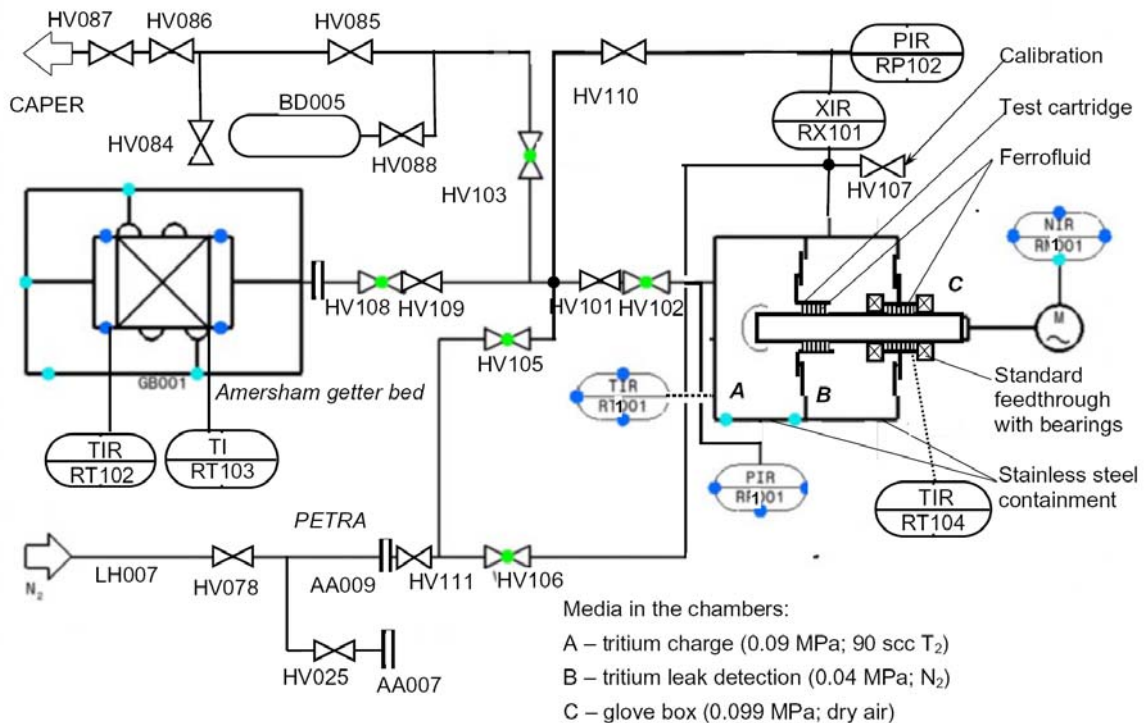


Fig. 1: FACT flow diagramme.

The tests will be performed in the test facility FACT (Ferrofluidic Advanced Cartridge Tritium Experiment) which is located in an existing glove box in the Tritium Laboratory Karlsruhe. The flow diagram of FACT is shown in Fig. 1.

The chamber A is filled with tritium (~90%) at 0.9 bar pressure. The chamber B is filled with nitrogen at 0.4 bar and connected to an ionisation chamber. The pressure in both chambers is measured by precise diaphragm gauges (type BARATRON 690A) and continuously recorded together with the signal from the ionisation chamber, which has been calibrated prior to the test campaign (1 Ci/m<sup>3</sup> corresponds to 195 pA electric current). The data acquisition system also continuously records the temperatures of the housing (which is the temperature of the tritium charge and of the ferrofluidic test cartridge) and of the bearings. The rotation speed is controlled by a frequency inverter. The FACT set-up inside the glove box is shown in Fig. 2. The tritium has been provided using a uranium getter bed, which was filled with 1.2 std. l and heated to ~ 470°C; 870 mbar filling pressure was reached in about 80 min.

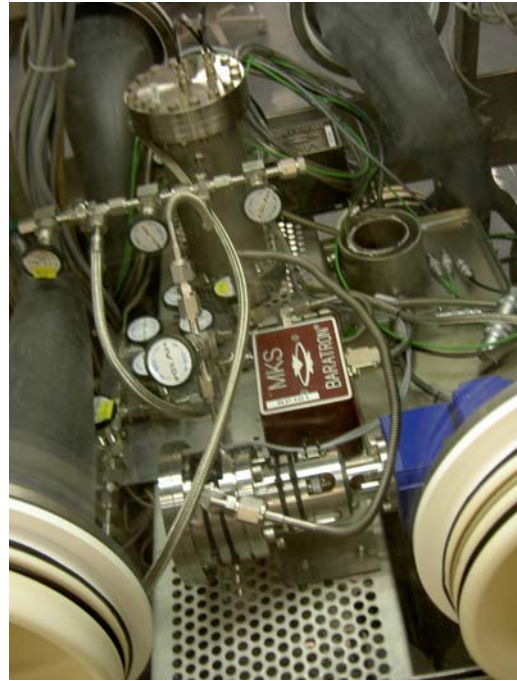


Fig. 2: FACT set-up inside the glove box.

### First results

During the measurements, the temperatures of the bearings and the tritium were found to be stable at 36/37°C and 42/43°C, correspondingly (depending on the glove box temperature fluctuation). The pressures in the tritium compartment and the ionisation chamber were stable at 882/890 mbar and 396/398 mbar, correspondingly (depending on the temperature). The tritium concentration evolution in the ionisation chamber compared with a pre-assessed theoretical tritium rise curve for a constant leak rate is presented in Fig. 3.

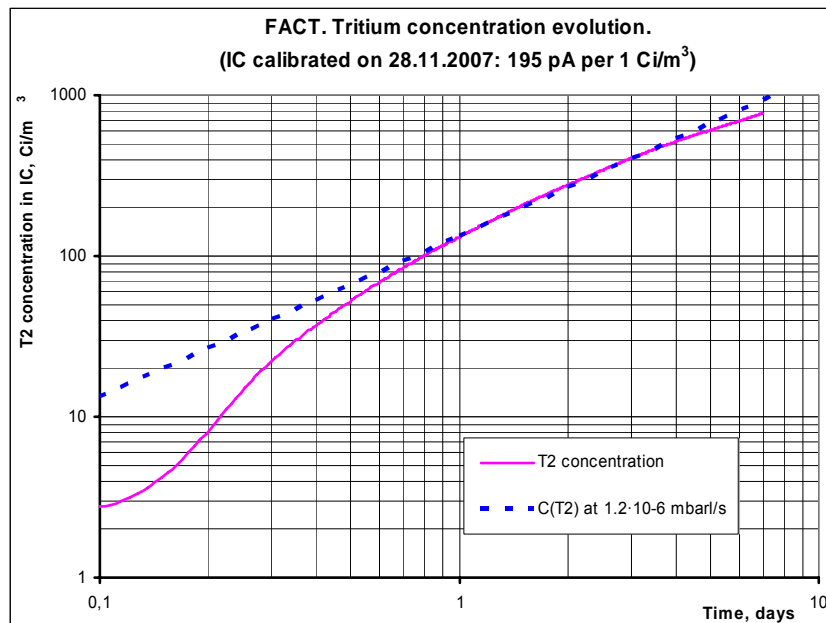


Fig. 3: Tritium concentration evolution in the monitored volume.

The measured leak rate of  $\sim 1.2 \cdot 10^{-6}$  mbarl/s is on the acceptable level. The non-linear curve on the graph reflects the fact, that the gas penetrating through the cartridge into the compartment B (30 cm<sup>3</sup>) is diffusing to the ionisation chamber (2300 cm<sup>3</sup>) via a straight (D = 4 mm L = 300 mm) pipe, which causes a response delay time of a few hours.

## **Conclusion**

The cartridge type of a ferrofluidic rotary seal is recommended for ITER. The catalogue cartridge shall be modified with metal C-rings inside the cartridge and to the pump housing. The FACT facility operation is still ongoing and expected to be continued until March 2008. It is aimed to demonstrate the radiation stability of a ferroseal under long term exposure to tritium in order to qualify it for use in the ITER roughing systems and for future thermonuclear reactors.

### Staff:

A. Antipenkov  
Chr. Day  
L. Dörr  
Chr. Caldwell-Nichols  
U. Besserer  
H.-D. Adami

### Literature:

- [1] A. Antipenkov, Chr. Day, T.D. Le, D. Müller, O. Stahlschmidt, Hydrogen operation of fusion specific forevacuum pumps, 17<sup>th</sup> Int. Vacuum Congress, Stockholm, S, July 2007.
- [2] A. Antipenkov, Chr. Day, R. Lässer, A. Mack, Tritium pumps for ITER roughing system, Fusion Science and Technology 48 (2005), pp. 47-50.
- [3] A. Antipenkov, Chr. Day, H.D. Adami, Tritium test of a ferrofluidic rotary seal, 8<sup>th</sup> Int. Conf. On Tritium Science and Technology, Rochester, NY, US, Sept. 2007.

# **Fuel Cycle Tritium Plant**



**TW1-TTF-TR 31**  
**Improvements to the Mechanical Design of PERMCAT Reactors**

**TW4-TTFD-TR 41**  
**Experimental Investigation of Undesired Side-reactions in PERMCAT**

**TW4-TTFD-TR 43**  
**Comparison of Batch and Continuous Operation Modes for the Impurity Processing Stage of the Tokamak Exhaust Processing System**

**Introduction**

The Tokamak Exhaust Processing (TEP) system is one of the key systems of the inner-fuel cycle of fusion machines like ITER. It allows recovering of almost all the tritium coming from the torus, which is then sent to the Isotope Separation System (ISS); the detritiated gas fraction is routed to the Normal Vent Detritiation System (N-VDS) for a latter treatment prior to the final release into the environment. The high requirements in term of decontamination factor (DF of  $10^8$  for tritium flow rates,  $10^6$  for tritium concentration) ask for a multi-step TEP process.

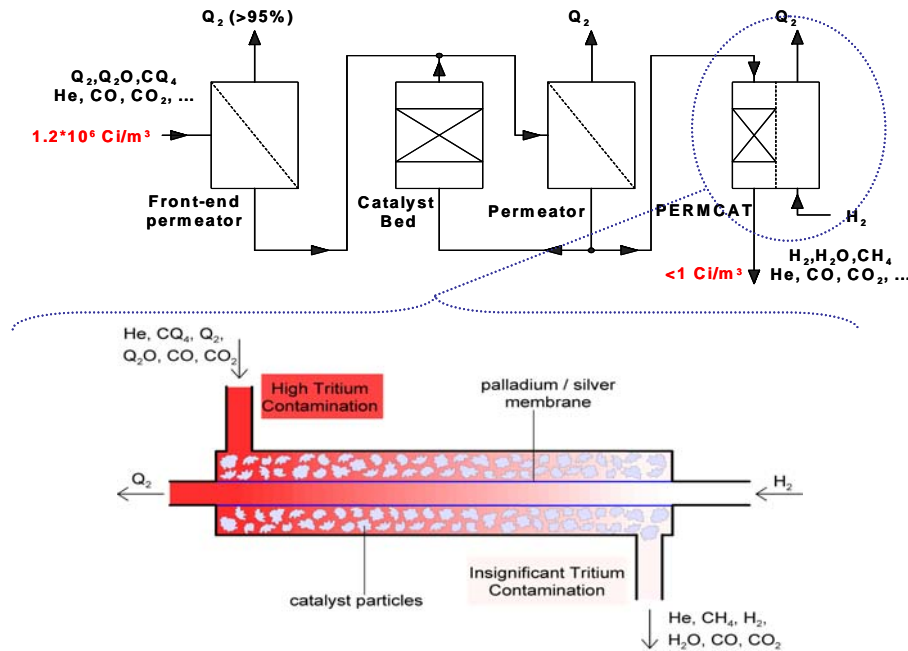


Fig. 1: Principle of the 3 steps of TEP system for ITER based on the CAPER process (up) with emphasis on the final clean-up step using the PERMCAT process (bottom).

The CAPER facility operated at the Tritium Laboratory Karlsruhe (TLK) for more than one decade is the unique experimental facility that integrally covers all the 3 stages of TEP as proposed for ITER (Fig. 1). The first stage uses a permeator using Pd/Ag membranes (exclusively permeable to molecular hydrogen isotopes) to recover the major part of the tritium in the molecular form. The second stage comprises a catalytic reactor that splits tritiated molecules (mainly hydrocarbons) to produce molecular tritium which is removed using a second Pd/Ag permeator. The third (last) stage is based on the PERMCAT process that allows removing almost all of the residual tritium.

A PERMCAT reactor is a direct combination of a catalyst bed and a Pd/Ag permeator operated in the so-called counter current isotopic swamping mode. The catalyst bed promotes isotope exchange reactions between tritium bound in molecules (hydrocarbons, water vapour) and pure hydrogen fed as a purge gas. The tritium liberated in the molecular form is

removed by permeation through the Pd/Ag membrane. The purge gas is fed in counter current so that the outlet of the impurity side can be maintained at a very low tritium level.

The CAPER facility is also an essential and central system within the closed tritium cycle of the TLK. All primary gaseous wastes arising from experiments at TLK are detritiated using CAPER. Thus, the integral CAPER operation can be considered as representative for the duty of the TEP system of ITER, since numerous systems within the tritium plant will produce tritiated effluents that need to be processed.

The main objective for CAPER is to demonstrate the overall process in an integral manner, and by the way providing a comprehensive database in order to scale up the processes and components to the desired ITER throughputs.

This report presents and discusses the main achievements for 2007 related to the EU-EFDA tasks on the TEP system, essentially focussing on the validation of upgraded PERMCAT mechanical design throughout an experimental test campaign with tritium in the CAPER facility. The use of PERMCAT reactor to process highly tritiated water is also briefly discussed.

### **Tritium test campaign for the validation of upgraded PERMCAT mechanical design**

#### Background

The design of PERMCAT reactors has to provide technical solutions to avoid or compensate mechanical constraints. Two different sources for stresses are considered for the Pd/Ag membrane: thermal expansion and lattice parameter increase due to hydrogen absorption. Since the membrane elongates (more or less) during operation, it cannot be simply fixed at both ends as shown in Fig. 1.

The first generation of PERMCAT mechanical design integrates "finger-type" Pd/Ag membranes (i.e. fixed at one end and closed at the other end) traditionally used for technical permeators at TLK. However, this option presents some drawbacks and limitations:

- an additional inner capillary tube is needed to allow a proper flow of the non-permeating fraction, leading to a rather complex design with a 3 coaxial tubes pattern,
- it cannot withstand off-normal events, as unfortunately learned from the failure of the first technical PERMCAT reactor installed in the CAPER facility.

Two different options have been proposed to improve the PERMCAT mechanical design: either using a straight tubular Pd/Ag membrane coupled with an edge welding bellow or a special corrugated Pd/Ag membrane acting itself like a bellow. Both options not only improve the robustness of the component but also simplify the design (2 coaxial tubes) for an easier manufacture process. According to preliminary tests on prototypes, the reactor involving a corrugated membrane has shown higher processing capability for H<sub>2</sub>O / D<sub>2</sub> isotope exchange reactions. Therefore this corrugated design has been retained for further tests with tritium.

#### Upgraded PERMCAT reactor

An upgraded tritium compatible PERMCAT reactor has been produced in collaboration with the main workshop of FZK. The production of the special corrugated Pd/Ag membranes has been realised in collaboration with the company BEST-Swagelock. Details for this particular reactor are shown on Fig. 2. The rather short length of such a PERMCAT is compensated using 2 single-tube units operated in line. It allows integrating in between a monitoring system (ionisation chamber, not shown on the picture), which is of advantage not only for the control but also for the comprehension of the PERMCAT process.



This upgraded reactor has been submitted to a gas processing tests campaign using relevant tritiated gaseous mixtures over a wide range of gas composition and activity, as expected in ITER. The preparation of such mixtures is realised within CAPER using different combinations of reactors, and their characterisation including gas composition and specific activity is achieved using the CAPER gas chromatograph. The experimental campaign has covered the process of helium including the following species as "impurities": water vapour (up to 2%), hydrocarbons (up to 9%), and carbon dioxide (up to 2%). For example, a parametric study on tritiated methane processing has been carried out over 4 runs. Activity and gas composition of these mixtures are given in Table 1.

Table 1: Composition and activity (both  $\pm 10\%$  relative) measured with the CAPER gas chromatograph for different gas mixtures containing tritiated methane

Permcatal Run	A	B	C	D
CQ <sub>4</sub> [%]	1.2	3.2	8.7	8.6
CQ <sub>4</sub> [kCi/m <sup>3</sup> <sub>STP</sub> ]	12	32	69	69
QT [%]	0.3	0.2	0.7	0.3
QT [kCi/m <sup>3</sup> <sub>STP</sub> ]	5	4.5	10	5

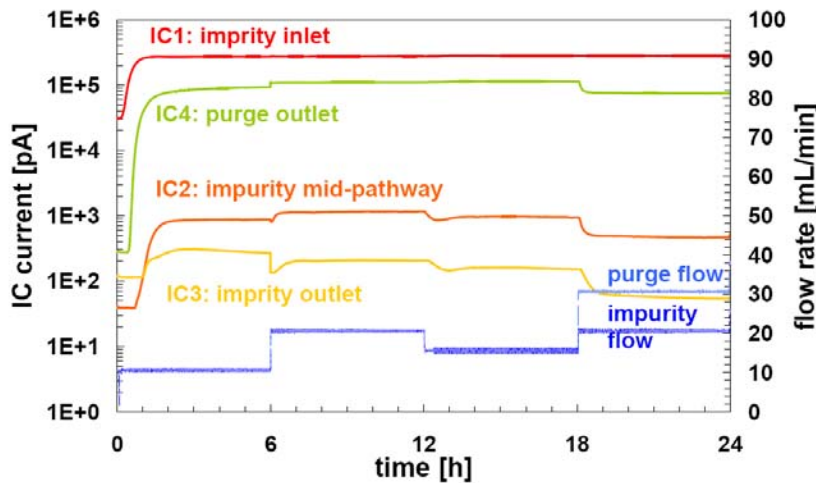


Fig. 4: Evolution with time for both flow rates (impurity and purge) and the resulting signals of the 4 ionisation chambers along the PERMCAT process during run D (see Table 1).

As an example of the processing test, Fig. 4 displays the evolution with time of the 4 ionisation chambers during the PERMCAT Run D. It shows 4 successive parts corresponding to different flow rates. Given the high amount and activity of tritiated methane, the impurity / purge flow rate ratio is firstly set at 1 / 1 (both blue curves are superimposed), in order to keep the PERMCAT impurity outlet at a reasonably low contamination level around 1 Ci/m<sup>3</sup>.

For the last part of the run, the impurity / purge ratio has been increased up to 1 / 1.5. It appears that after about 20 min of gas processing, the IC2 signal (impurity mid-pathway) starts to increase and the same behaviour is observed for IC3 (impurity outlet) 20 min later. It is clear that IC2 and IC3 exhibit the same tendency (parallel evolution) with a 20 min time interval. The activity measured at the impurity outlet (using a dedicated off-line analytical method) is 0.6 and 0.4 Ci/m<sup>3</sup> at 18 and 24 hours respectively. This corresponds to DF of  $1.2 \times 10^5$  and  $1.9 \times 10^5$  respectively.

A direct and quantitative comparison between this reactor and the first one is not straightforward. One needs to consider the difference in size (capacity) of these reactors: the new PERMCAT is a "single-tube" reactor, while the first reactor included 6 tubes in parallel. The difference in length of about 20% (2 x 225 and 530 mm) could firstly be neglected. However, the upgraded reactor is 2 or 3 times smaller than the first one if the amount of catalyst or the permeation area is considered, respectively. Under conditions similar to run D for methane concentration and activity, the first technical unit led to 0.3 Ci/m<sup>3</sup> at the impurity outlet for an inlet flow rate of 30 ml/min. So, it can be agreed that the performances of the new reactor are more or less comparable to the one obtained with the first technical reactor. In other words, the performances are not suffering from the design simplification.

The use of at least 2 PERMCAT units operated in line is of advantage. It allows including a dedicated ionisation chamber to monitor in real-time the impurity flow activity at the mid-pathway. Then, it is possible to see any variation of the activity level at this location, for instance after a change of the gas composition of the flow rate, enabling to predict the evolution of the activity at the outlet of the process. This additional monitoring system could then be used as a control loop for the flow rates so as to optimise in real-time the throughput.

All types of gas mixtures produced throughout this campaign have been successfully processed, i.e. detritiated below the level of  $1 \text{ Ci/m}^3$ . This can be achieved provided adapted parameters, primarily by adjusting the impurity / purge flow rate ratio. It should be noted that the majority of these gas mixtures are (far) above the specifications for the nominal operation of PERMCAT, which was originally designed to process in total 0.1 - 1% of tritium with impurities (hydrocarbon and/or water) up to 0.5%.

In total, 13 PERMCAT runs have been performed with this reactor. About 2.6 g of tritium has been recovered without any problems from 1080 l gas within 330 h of processing time. According to this campaign, one can admit that the upgraded PERMCAT design has successfully passed the endurance test phase, which was in fact to the last step of the study concerning the improvement of the PERMCAT mechanical design.

#### Design and production of an upgraded technical (multi-tube) PERMCAT reactor

The design and production of new PERMCAT reactors is going on. The process of larger throughputs asks for a technical (i.e. multi-tube) PERMCAT reactor. The production of the next reactor involving a battery of 13 Pd/Ag membranes inserted in a single common catalyst bed is nearly completed. Even if it uses finger-type membranes (together with capillary tubes), it is considered as an upgraded design. The first technical PERMCAT reactor was a straightforward parallel arrangement of finger-type single-tube units. In this case, the failure of one tube might spoil the overall detritiation efficiency of the entire reactor. In contrast, for the next reactor, if one membrane fails, one can rely on the others to keep the efficiency of the reactor at a reasonable level.

This next multi-tube reactor has been designed to enable the exchange of the capillary tube set in order to study the influence of the capillary tube diameter. In fact, it has been observed on prototypes that this parameter could have a crucial impact on the performances. As soon as an optimal configuration will be experimentally pointed out, this optimised configuration will be duplicated in order to operate 2 PERMCAT reactors (hosted in a single common outer jacket) in line.

Processing experiments to point out the optimal configuration could be first carried out throughout cold tests (without tritium) using isotope exchange reactions between  $\text{H}_2\text{O}$  and  $\text{D}_2$ . Afterwards this optimised configuration could be further characterised with tritium using the CAPER facility. These experimental tests should be completed in 2008.

### **Highly tritiated water processing with PERMCAT**

#### Background

The large variety in streams to be processed is an essential feature for the TEP system. Numerous operations within ITER, in particular wall conditioning and in-situ tritium recovery from Plasma Facing Components (PFC), will produce tritiated effluents with composition and flow rate that will largely differ from the nominal burn and dwell scenarios. These particular operations will be likely the design limiting cases, especially for the 2<sup>nd</sup> and 3<sup>rd</sup> stages of TEP.

Tritium recovery from PFC is a key issue for ITER operation. In addition to the techniques already considered for the in-situ tritium recovery from PFC (mainly He and  $\text{H}_2/\text{D}_2$  glow discharges), oxidative treatments are now under discussion. In fact, it has been experimentally demonstrated that thermo-oxidation (bake-out in presence of oxygen) is the most effective

and straightforward solution to recover tritium trapped in the machine. However, the main drawback is the final production of significant amounts of Very High Level (VHL) tritiated water.

Based on the current ITER design, tritium recovery from this VHL tritiated water remains an open issue. In fact, this point was not identified up to now, but according to the most recent estimation, up to 2 kg DTO at 1.4 MCi/kg could be weekly produced.

On the one hand the amount is too excessive to process it as water vapour with TEP since it would require a huge dilution with a carrier gas to avoid condensation along the process lines. Therefore the direct condensation of this water downstream the cryo-pumping system is now envisaged. However, the detritiation of such "stoichiometric" liquid DTO ( $1.4 \times 10^6$  Ci/kg) remains an issue since the tritium level is about 5000 times higher than the maximum specific activity (300 Ci/kg) to be accepted and processed within the Water Detritiation System (WDS) according to the present design.

#### Principle of water processing with PERMCAT

The alternative to process this VHL water using a special and dedicated PERMCAT reactor has been recently proposed. This could be performed either within TEP or WDS. The principle of water processing using PERMCAT has been highlighted throughout "cold" experiments (without tritium) primarily carried out to validate upgraded PERMCAT mechanical design. A parametric study on key parameters has revealed that the optimal processing efficiency is obtained:

- when the concentration of water in the impurity flow is around 50% (i.e. there is no need for a significant dilution with a carrier gas),
- for a PERMCAT reactor (design) that contains relative to the permeation area high amount of catalyst (an enlarged the cross section for the impurity side increases the residence time, leading to a more efficient conversion).

So, the ability for PERMCAT to deal with high partial pressure of water vapour has been demonstrated. In addition, very high decontamination factors have been measured on tritiated gaseous mixtures within CAPER. Combining these both considerations, the potential for PERMCAT to process VHL water should be investigated.

#### Preliminary study for VHL tritiated water processing with PERMCAT in CAPER

The CAPER facility design needs to be revisited to allow performing tests to validate and demonstrate the capability to process VHL tritiated water with PERMCAT. The main changes concern the water vapour feed into the PERMCAT unit and the processed water recovery downstream the unit. The following options have been retained for CAPER:

- water production and feed using an oxidative catalytic reactor that converts a tritiated hydrogen mixture into water vapour (this option allows producing water vapour with activity up to the MCi/kg level without handling problems),
- processed water recovery onto a molecular sieve bed (small size to allow tritium measurement with high sensible calorimeter).

The water recovery onto a molecular sieve bed is rather trivial and does not require any special investigation. However the production of water using an oxidation reactor has to be studied in details to define the type and amount of catalyst as well as the experimental conditions that are needed for the later tritium experiments within CAPER. Preliminary tests on prototypes are going on to validate and scale these options.

### Experimental validation for VHL tritiated water processing with PERMCAT in CAPER

The experimental plan for VHL tritiated water processing in CAPER will be carried out in a staged approach. The first part will be performed at rather low tritium concentration to demonstrate the ability to process tritiated water. Then, a parametric study will be carried out at the intermediate activity level so as to optimise the process. During the latter part, the activity shall be progressively increased so as to end up with the process of "stoichiometric" DTO. The experimental campaign should start in 2008.

If these investigations are successful, the ability for PERMCAT to process not only tritiated gaseous mixtures but also highly tritiated water would be demonstrated. Then, the high versatility of the PERMCAT would be of great advantage for accommodating to any possible in-situ detritiation techniques of future DT fusion machines like ITER.

### **Conclusion**

The Tokamak Exhaust Processing systems of fusion machines like ITER have been studied at the TLK for more than one decade using the CAPER facility. Both the first and second steps are now well characterised, providing a comprehensive database to scale up these processes at the ITER throughputs. The study and optimisation of the last stage is still going on given the complexity and the high potentials of the PERMCAT process.

An upgraded PERMCAT reactor has been submitted to a tritium test campaign. This reactor offers several advantages from the technical point of view: simplified design which makes the manufacture easier and better control of the process using an additional monitoring system at the mid-pathway of the process. Very high detritiation efficiencies have been obtained with this reactor, even on gas mixtures above the specifications, confirming that PERMCAT can easily cope with activities and impurity concentrations far above the design values.

In parallel, an important effort has been done to evaluate a significant amount of experimental data related to recent experimental studies on:

- the comparison between different operational modes for the 2<sup>nd</sup> loop of CAPER,
- the influence of side reactions for PERMCAT due to carbon oxides.

According to the last review on the TEP related studies at TLK, all the 4 EFDA tasks ongoing at the beginning of 2007 should be completed before the end of the first trimester of 2008. TEP related R&D activities will focus next year on PERMCAT technology, focussing on:

- Experimental validation of highly tritiated water using the current PERMCAT reactor installed in CAPER.
- Experimental campaign on processing performances with the next upgraded multi-tube PERMCAT reactor.
- Validation of the recently upgraded PERMCAT numerical simulation in collaboration with Kyushu University (Japan) and wide use of this tool to support the R&D on PERMCAT design and process.

### Staff:

D. Demange  
B. Bornschein  
M. Glugla  
K. Guenther  
T.L. Le

P. Schuster  
F. Scheel  
K.H. Simon  
S. Welte  
R. Wagner

Literature:

- [1] M. Glugla et al. "The ITER tritium systems" *Fus. Eng. Des.* **82** (2007) 472.
- [2] B. Bornschein et al. "Experimental validation of a method for performance monitoring of the impurity processing stage in the TEP system of ITER" *Fus. Eng. Des.* **82** (2007) 2133.
- [3] D. Demange, S. Welte and M. Glugla "Experimental validation of upgraded designs for PERMCAT reactors considering mechanical behaviour of Pd/Ag membranes under H<sub>2</sub> atmosphere" *Fus. Eng. Des.* **82** (2007) 2383.

## **TW1-TTF/TEP 13A**

### **Self-Assay, Fast Delivery Tritium Storage Bed Development**

## **TW3-TTFD-TR 33**

### **Determination of Isotopic Effect during Rapid Delivery from Storage Beds**

For the safe storage and handling of the D/T mixtures in ITER the SDS system is provided with the major duties as 1) supply of the required D/T mixtures to the fueling systems (DT flow rate  $<120 \text{ Pa m}^3\text{s}^{-1}$ ), 2) storage and accountancy of the D/T mixtures delivered by ISS in the reservoirs and metal-hydride getter beds, 3) storage of up to 1 kg tritium recovered from the plasma facing components in the LTS, 4) accountancy of the tritium shipped to and from the Tritium Plant in the transport shipping containers, 5) supply of the non active pure gases (He, Ar, Ne, N<sub>2</sub>, H<sub>2</sub>, D<sub>2</sub>, He+O<sub>2</sub>) for the torus operation.

Hydrogen isotopes are stored in the batteries of the metal hydride beds: D product battery (0.6% of T in D), D/T product battery for 50/50 mixture and T product battery for 90%T/10%D mixture. Each getter bed has to have a physically limited capacity of 70 g of tritium. Metal hydride beds of SDS system will be equipped with in-built gas flow calorimetry for the tritium accountancy.

A prototype storage bed of a full scale has been designed and manufactured in the Forschungszentrum Karlsruhe with a capacity of 100 g tritium and a target supply rate of up to  $200 \text{ Pa m}^3\text{s}^{-1}$ . The bed was filled with ZrCo powder and intensively tested in the test rig (see [1]) in the Tritium Laboratory. The test rig is equipped with a PVT vessel with a volume of  $0.5 \text{ m}^3$ , a compressor for the hydrogen transfer of PBT 105-C18 (Thales Engineering&Consulting S.A.) type, pressurized air supply for the active cooling loop operations, two vacuum trains and sampling manifold for the measurements of the isotope composition of the supply stream. The design of the getter bed allows for the in-bed tritium inventory accountancy by flowing gas calorimetry. A helium stream with flows of up to 40 l/s is circulated through the "U" shaped tube installed inside the ZrCo container. Helium circulation is provided by two compressors of MB 158E (Metal Bellows) type and is controlled by flow and pressure controllers. The temperature of the inlet and outlet helium is measured with Pt100 thermometers.

Performance parameters listed for the tritium storage beds foreseen for ITER were studied including loading/deloading operation and performance of the calorimetric loop. The results of the tests with hydrogen/deuterium mixtures in respect of the isotope effect during rapid delivery have been presented in [1].

The basic pressure-composition-temperature properties of the hydrogen-metal hydride system is a key parameter for the application of the hydride storage beds. Therefore the pressure-composition isotherms for the ZrCo/H and ZrCo/D systems have been measured using the full scale getter bed. Fig. 1 shows the absorption and desorption isotherms. Desorption isotherms were obtained by desorbing deuterium from the bed into the PVT vessel with the help of the hydrogen compressor at constant temperature. The pressure-composition isotherms at temperatures below 400 °C exhibit slope and hysteresis.

At the temperature of 300 °C a plateau region is found from 0.2 to 1.5 with an equilibrium dissociation pressure of about 6 kPa. In practice pressures close to 100 kPa are desired in order to supply hydrogen isotopes with the required rate. Based on the pressure composition data of the ZrCo/D system and on the experience of operation of the ZrCo bed we suggest the following operation cycle as illustrated in the lower part of Fig. 1. For the deloading operation the hydride temperature is set to a rather high value of 350 °C in order to facilitate rapid supply. Further increase of the temperature is not recommended due to the occurrence of the disproportionation reaction. The operation pressure of the bed is limited to 100 kPa. To avoid over pressurizing during hydrogen desorption, the allowable ZrCo/hydrogen ratio shall

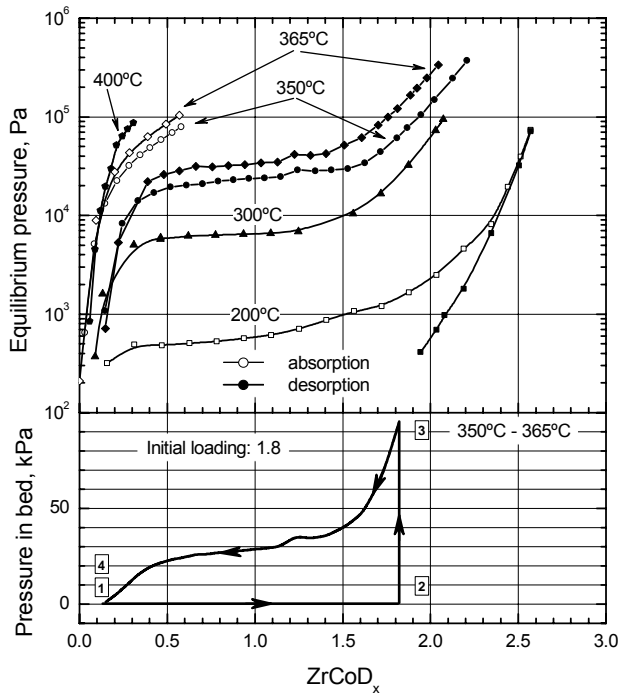


Fig. 1: Upper: pressure-composition isotherms of the ZrCo/Deuterium system; open symbols – absorption isotherm, close symbols- desorption isotherm (log. scale) Lower: operating lines of the ZrCo getter bed (lin. Scale).

be limited to 1.8. This value is taken from the isotherm data for 365 °C giving a margin for the temperature distribution in the getter bed. As shown in Fig. 1 the bed is loaded at room temperature to the Q/ZrCo ratio of 1.8 (line “1”-“2”), the bed is heated to the temperature of 350-365°C (line “2”-“3”) to provide the required hydrogen pressure. At the beginning of the supply the pressure in the bed is slightly lower than 100 kPa and gradually decreases (line “3”-“4”) following the slope of the pressure-composition isotherm. At a ratio  $x$  below 1.2 the pressure in the bed will be about 30 kPa. Hydrogen stored at a ratio  $x$  below 0.5 is not available at reasonable flow rates. In order to supply hydrogen isotopes with the required rate and pressure, a hydrogen compressor shall be used. Once the ZrCo getter bed is heated to the supply temperature it is desirable to empty the bed completely in order to avoid disproportionation from the one hand and to prepare for the loading on the other hand. Loading is preferable to be performed only with an empty bed to make

sure that the requirement to limit the Q/ZrCo ratio to  $x=1.8$  is met. After deloading the bed is cooled to room temperature (“4”-“1”) in order to allow for the next loading/deloading operation.

### Hydrogen supply performance

The high rate of the hydrogen isotopes supply is one of the requirements for the getter beds of the SDS. Intensive parametric testing of the supply and loading parameters has been carried out with the prototype ZrCo bed. An example of the supply run carried out with deuterium under the “reference” temperature and initial loading conditions is shown in Fig. 2.

The loaded bed was heated up with a controlled heating rate of 60 °/min until the temperature of the getter bed reached the set point of 350 °C. Deuterium was transferred from the ZrCo bed into the PVT vessel by the compressor PBT 105-C18. The pressure increase in the PVT vessel was recorded and used for the evaluation of the deuterium supply rate. The supply rate curve shows a rather sharp peak with the peak value of 30 Pa m<sup>3</sup>s<sup>-1</sup>.

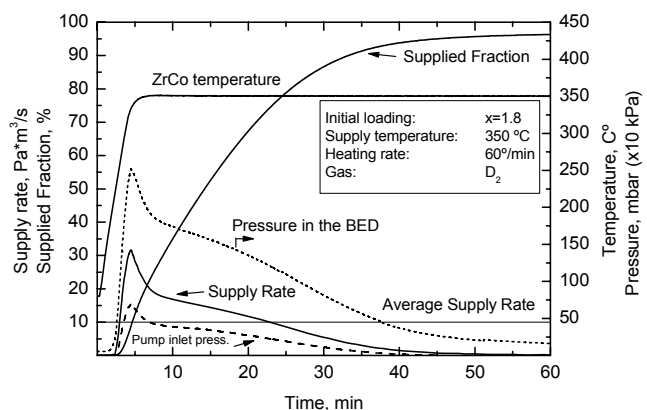


Fig. 2: Deuterium supply under “reference” conditions.

The average supply rate during the run is 10 Pa m<sup>3</sup>s<sup>-1</sup> which is very low in comparison with the target design value of 200 Pa m<sup>3</sup>s<sup>-1</sup>. As can be seen in Fig. 1 and Fig. 2 the pressure inside the getter bed during deloading is almost equal to the equilibrium dissociation pressure at a given D/ZrCo ratio. However, the pressure at the pump inlet is much lower (dashed curve in Fig. 2). This indi-

icates that in the presented run the supply rate limiting step is a flow resistance of the getter bed outlet filter. In general, reactions of the hydriding and dehydriding are very fast and supply/uptake rates of hydrogen are limited by the heat and mass transfer in the hydride powder and by gas conductancy of filters and the design of the primary container [2].

For the required rate of supply the SDS will require an arrangement to supply hydrogen isotopes from more than one bed of the particularly battery at the same time. Due to the initially low dissociation pressure above ZrCo hydride and thermo-hydraulic characteristics of the getter bed a high pumping speed shall be provided which may require additional pumps to be installed.

Within the reasonable deloading time at 350 °C the ZrCo bed cannot be deloaded to 100% due to the very low dissociation pressure and the possible disproportionation. Thus after the run the ZrCo powder temperature is raised to 400 °C in order to completely empty the bed.

### Hydrogen uptake rate

The absorption rate of the ZrCo getter was obtained in the series of the tests shown in Fig 3. Hydrogen was introduced from the PVT vessel into the initially empty getter bed through the 15 µm filter at the inlet of the ZrCo container. The bed was loaded to the Q/ZrCo ratio of 1.8 corresponding to the pressure change in the PVT vessel from 100 kPa to 40 kPa. The pressure decrease in the PVT vessel was recorded and used for the evaluation of the uptake rate. The first test was performed without active cooling and with the insulation jacket being under vacuum (Fig. 3, solid lines). During the second test (Fig. 3, dashed lines) active cooling of the bed was applied by passing pressurized air through the cooling loop. In addition the insulation jacket was padded with helium in order to allow improved heat transfer. The absorption time for both tests was about 360 s; the uptake rate shows almost no difference. Because of the exothermic reaction the temperature of the powder has raised to about 160 °C.

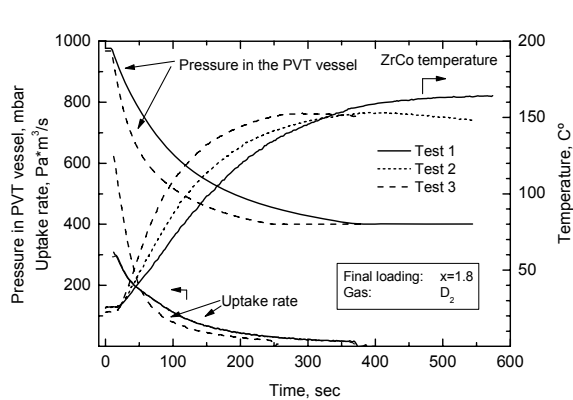


Fig. 3: Comparison of the deuterium uptake rate under different cooling options.

In the third test (Fig. 3, short-dashed lines) deuterium was introduced to the ZrCo container through both inlet and outlet filters in order to investigate the influence of the filter conductance on the uptake rate. The same cooling as in the second test was applied. A much faster uptake rate was obtained with absorption time of 240 s indicating that the gas conductance of the filters has a great influence on the uptake rate of the getter bed.

### Conclusions

We suggest to change the configuration of the SDS in order to meet the systems requirements with the present ZrCo getter bed design. It is proposed to have two additional manifolds, one - for supply, another - for loading, buffer vessel for supplied gas, calibrated PVT vessel. These changes will allow the operation of two beds for supply and two beds for loading at the same time.

Due to the safety requirements the sorption capacity of the bed shall be limited to a value equivalent to 70 g T2. However due to the limit on ratio Q/ZrCo of 1.8 the real usable capac-

ity of bed will be equivalent to 45 g T<sub>2</sub>, which is considerably smaller than the maximum thermodynamic sorption capacity.

It is strongly recommended to reconsider the reference getter material for the ITER SDS system.

Staff:

S. Beloglazov  
E. Fanghänel  
R. Wagner

Literature:

- [1] S. Beloglazov, M. Glugla, R. Wagner, E. Fanghänel, S. Grünhagen "Investigation of isotope effects in the gas streams supplied by a 1:1 ITER storage bed using a micro gas chromatography", Fusion Sci. and Tech., 48 (2005) 67-70
- [2] S. Beloglazov<sup>1</sup>, M. Glugla<sup>1</sup>, E. Fanghänel<sup>1</sup>, A. Perevezentsev<sup>2</sup>, R. Wagner<sup>1</sup> "Performance of a full-scale ITER metal hydride storage bed in comparison with requirements", to be published in proceeding of Tritium 2007 conference

## **TW4-TTFD-TR 44**

### **Inactive Tests of Selected SDS Control Loop Performance under Typical ITER Operating Conditions**

One of the original tasks of the Storage and Delivery System (SDS) of the ITER Tritium Plant was to deliver to the fuelling systems of ITER deuterium/tritium gas mixtures of various compositions produced from the 3 gas streams from the Isotope Separation System (ISS), namely deuterium, 50/50 % deuterium-tritium and 10/90 % deuterium-tritium. This involved several pumps, flow controllers and a control system in a control loop. ITER later decided that the final gas mixtures would be controlled at Gas Valve Boxes closer to the ITER vacuum vessel and only the raw gas streams were required from SDS and hence the control loop in SDS was no longer required. A proposal to redefine the task to analyse the performance of comparable gas composition control on the CAPER facility which uses gas flow controllers has been assessed. However, potential changes to other ISS operational parameters, notably to remove the requirement for the 50/50 % deuterium-tritium mixture, has led to the agreement with EFDA that this task will be suspended with the possibility that the resources may be used for tasks resulting from design changes in the ITER Tritium Plant.

#### Staff:

C.J. Caldwell-Nichols

## TW4-TTFD-TR 47

### Upgrading of LPCE (Liquid Phase Catalytic Exchange) Column for Trade-off Studies between WDS and ISS

The Combined Electrolysis Catalytic Exchange (CECE) process, based on the Liquid Phase Catalytic Exchange (LPCE) column, developed in the TRENDA facility consists of two main units:

- A preparatory unit for the tritiated water to be fed in the electrolyzers and the LPCE column. This unit should receive the tritiated water from the TLK infrastructure and from the LPCE column and prepare the required composition of tritiated-deuterated water for different operation conditions. It consists of several vessels, pumps and pipework.
- A tritium water processing unit, which basically consists of the LPCE column and the two enhanced electrolyzers for operation with tritium.

From the preparatory unit, the tritiated water can be sent both to the electrolyzers and to the LPCE column. The feeding location into the LPCE column depends on tritium and deuterium content of feed water to be established for each campaign of experiments. The deuterium content in the processed water will be in the range of  $10^{-3}$  up to  $10^{-4}$  deuterium atomic ratio and the tritium content in the range of  $5 \times 10^8 \text{ Bqkg}^{-1}$  up to  $5 \times 10^{10} \text{ Bqkg}^{-1}$ . The LPCE column is filled with a mixture of catalyst/packing developed by TLK and ICIT Romania. The length of the LPCE column is 8 m and it is provided with feeding and sampling points at each 2 m. At the top of the LPCE column, demineralised water is supplied at different flow-rates in order to achieve inside the LPCE column specific ratios between gas and liquid. The vapours carried by the hydrogen stream at the top of the LPCE column are condensed and returned into the LPCE column. From the top of the LPCE column, the decontaminated hydrogen is released to the TLK stack via a flame arrester and a water seal pool.



Fig. 1. The LPCE column and sampling manifold of the CECE process.

The tritiated and deuterated hydrogen to be fed into the bottom of the LPCE column is provided by two solid polymer electrolyzers (SPM) enhanced for tritium operation. The content of deuterium and tritium in the water fed into the electrolyzers should be kept as constant as possible during one campaign of experiments. Therefore, a special procedure for water preparation is implemented. The oxygen stream produced by water electrolysis is sent for decontamination to the oxygen stripping column. In the stripping column, the tritium and deuterium contained in

the vapours carried by the oxygen stream are transferred into demineralised water fed in at the top of the column. At the bottom of the stripping column, a catalyst bed is provided with the aim to convert to water the hydrogen that may be contained in the oxygen stream. From the bottom of the stripping column, the tritiated and deuterated water is sent into the preparatory unit for further processing.

The installation and commissioning of all components of the CECE process have been completed. The middle part of the LPCE column is shown in Figure 1, and the preliminary results are shown in Figure 2.

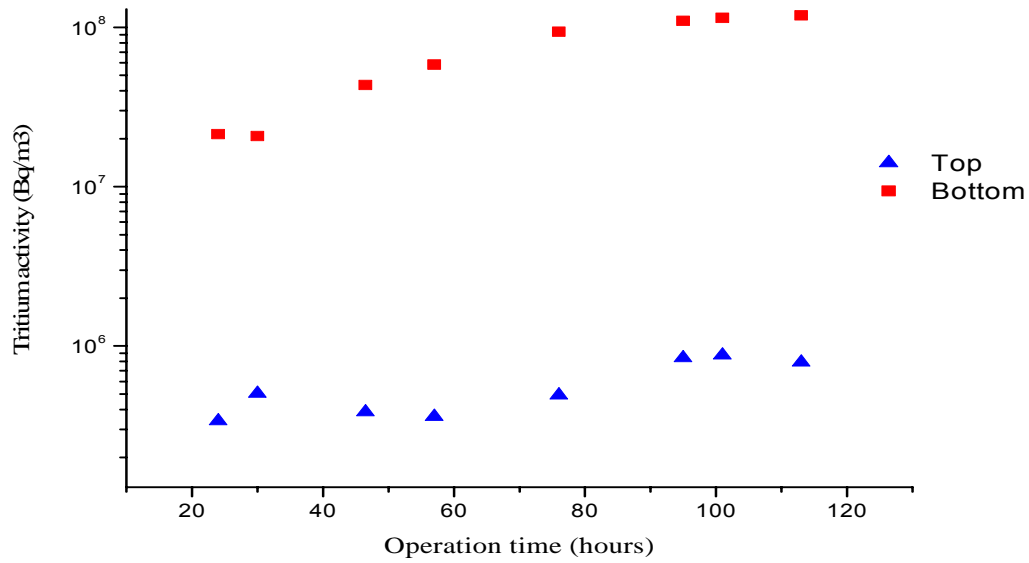


Fig. 2: Time evolution of tritium activity in hydrogen stream at the bottom and top of the LPCE column.

Staff:

- I. Cristescu
- I. R. Cristescu
- L. Dörr
- G. Hellriegel
- R. Michling
- P. Schäfer
- S. Welte
- W. Wurster

## TW6-TTFD-TR 64 Endurance Tests of Water Detritiation System

The Water Detritiation System (WDS) and the Vent Detritiation Systems (VDS) are the only systems in ITER which have a direct interface with the environment after processing tritiated streams. Moreover the WDS is in direct combination with the ITER Isotope Separation System (ISS) which should process tritiated streams in a fluctuation mode in view of flow rates and composition. An evaluation of the time behavior of the critical components, such as the catalyst/packing mixture of the LPCE columns and the SPM electrolyte of the electrolysis unit is compulsory in order to implement an appropriate management and maintenance scheme in the ITER WDS.

The so-called TRENTA facility for water detritiation which consists of a Combined Electrolysis Catalytic Exchange (CECE) process employing a LPCE column has been commissioned with tritium at the Tritium Laboratory Karlsruhe (TLK). The TRENTA CECE is in operation on a long term basis for process performance studies and endurance tests of critical components needed for the design of ITER WDS. The maximum tritium activity in the tritiated water that should be processed within the TRENTA facility at TLK is 10 Ci/kg. In order to extend the endurance tests in similar conditions as envisaged in ITER, an experimental rig is in operation at ICIT Rm. Valcea with tritiated water of 100 Ci/kg, shown in Figure 1.



Fig. 1: The experimental rig for endurance tests with 100 Ci kg<sup>-1</sup> tritium activity in water.

The experimental programme on both experimental rigs is carried out in cooperation. The experimental rig at ICIT Rm. Valcea consists of a small LPCE column of 200 mm length, 30 mm in diameter and will be equipped with the same type of catalyst as used in the TLK TRENTA facility. In the TLK LPCE column catalyst of stick shape is used in combination with a structured Sulzer packing. In addition to the TLK catalyst shape, a catalyst with a round plate shape will be introduced in the ICIT LPCE column. Tritiated water of 100 Ci kg<sup>-1</sup> should be processed in closed loop over the catalyst. The temperature of the LPCE column should

be maintained constant at 70<sup>0</sup>C during the endurance test period. For this purpose the LPCE column has a double wall and water at 70<sup>0</sup>C should continuously circulated in the jacket.

Staff:

I. Cristescu  
I.-R. Cristescu  
L. Dörr  
G. Hellriegel  
R. Michling  
P. Schäfer  
S. Welte  
W. Wurster

## TW6-TTFD-TR 56 Isotope Separation Tests for Evaluation of Column Packing Options

The tritium inventories in the Fuel Cycle of ITER and the amount of tritium released into the environment have a significant impact on the ITER licensing. According to the actual configuration of the fuel cycle and the experimental data available, the inventory in the Isotope Separation System (ISS) of ITER based on cryogenic distillation (CD) process is the largest inventory in the fuel cycle. The ISS consists of four cryogenic distillation columns and the top product of final stage column for tritium and deuterium recovery is routed to the Water De-tritiation System (WDS).

The main objective of the task is to realize a comparison of three types of packings, namely Helipack-C, SULZER EX and SULZER CY with respect to the liquid hold-up and separation performances. This comparison allows to establish the type(s) of packing to be used within each CD column with the aim to minimize the tritium inventory and the capacity of the entire CD system.

The experiments have been divided into two major campaigns:

1. Experiments to define the types of packing for each ITER CD column. The following experiments will be carried out:
  - A. Measure the hold-up and separation performances of Helipack-C for hydrogen and a mixture hydrogen-deuterium (containing ~ 10% deuterium)
  - B. Measure the hold-up and separation performances of Sulzer EX and Sulzer CY using a mixture hydrogen-deuterium with ~ 10% deuterium.
2. Experiments to investigate the influence of gas composition on the liquid hold-up within a CD column.

The investigation will be carried out onto the packing type assigned for the ITER CD column 4. The estimation of tritium inventory within this column will be done by extrapolating the experimental results on the liquid hold-up of various mixture hydrogen-deuterium with deuterium content increased in steps from 10% up to 90%. The characterization of the Helipack-C packing has been completed and in Figure 1 is shown the typical behaviour when the flooding occurs. The activity for the others two packings is ongoing.

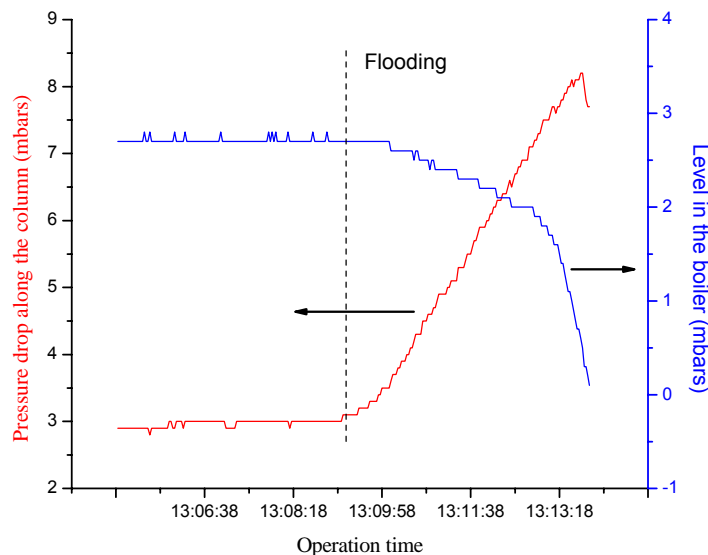


Fig. 1: Behaviour of the liquid level in the CD boiler and pressure drop along the CD column at flooding.

### Staff:

I. Cristescu  
R. Michling  
S. Welte  
W. Wurster

## **TW6-TTFD-TR 63**

### **Testing of Isotope Separation System (ISS) with the WDS**

In order to mitigate the concern over tritium release into the environment during pulsed operation of the Torus, the Water Detritiation System (WDS) and Isotope Separation System (ISS), based on cryogenic distillation (CD), will operate in such way that WDS will be a final barrier for the processed protium waste gas stream discharged from ISS. To investigate the capability of the WDS to achieve this goal, the influence of the additional basically hydrogen stream from ISS and its feeding location into the WDS, the separation performances of Liquid Phase Catalytic Exchange process has to be investigated and accurately mathematically modeled.

The main issue of the experimental programme on the TRENDA facility at TLK is to investigate the combination WDS-ISS processes during isotopic and thermal transitory regimes. Therefore, a detailed investigation of the control system and separation performances of the CECE process when working as a final barrier of the top product of the CD column to be discharged into the environment is under investigation.

The cryogenic distillation column consists of a separation section of 2.7 m and has the boiler and condenser incorporated. The separation section is connected to the boiler and condenser by flanges in order to allow installation of several separation section filled with different packings to be tested.

In order to develop the experimental data base needed for design of the ITER WDS and ISS, the following modes of operation have been considered during the design of the combination WDS-ISS:

- Operation of the LPCE column with composition fluctuation in the stream returned from the CD column
- Operating of the CD column with composition and flow rate fluctuations in the feeding stream
- Operation in different dynamic modes in order to validate and bench mark the TRIMO code.

In order to support the above activities the following issues have been completed in 2007:

- the P&ID and devices specifications of the combination WDS-CD
- the design of the heat exchangers to be installed within the cold-box, for processing the gas provided by WDS and the gas returned to the LPCE column
- the detailed design of the valve box, in between the CD and WDS systems
- the 3-D of the glove box which accommodate the components for operation of the combination WDS-CD, shown in Figure 1.

#### Staff:

I. Cristescu  
I.-R. Cristescu  
L. Dörr  
G. Hellriegel  
R. Michling  
P. Schäfer  
S. Welte  
W. Wurster

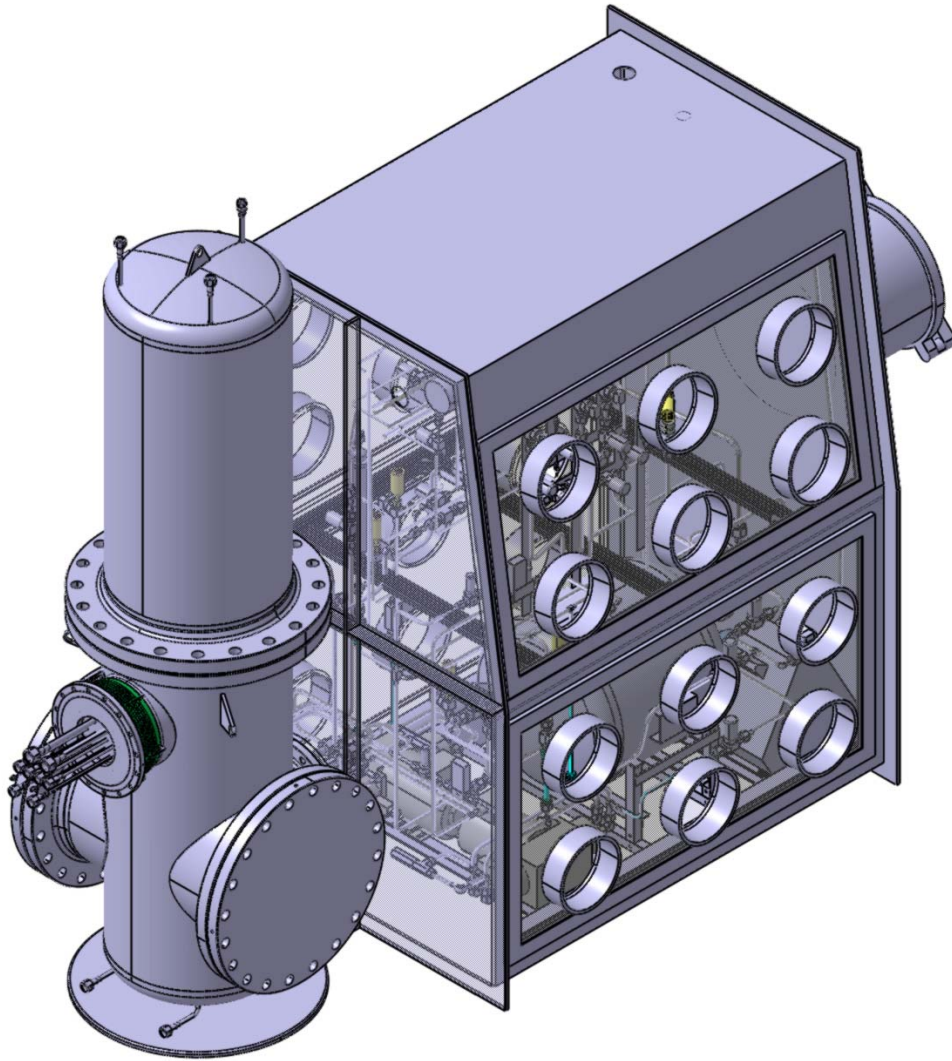


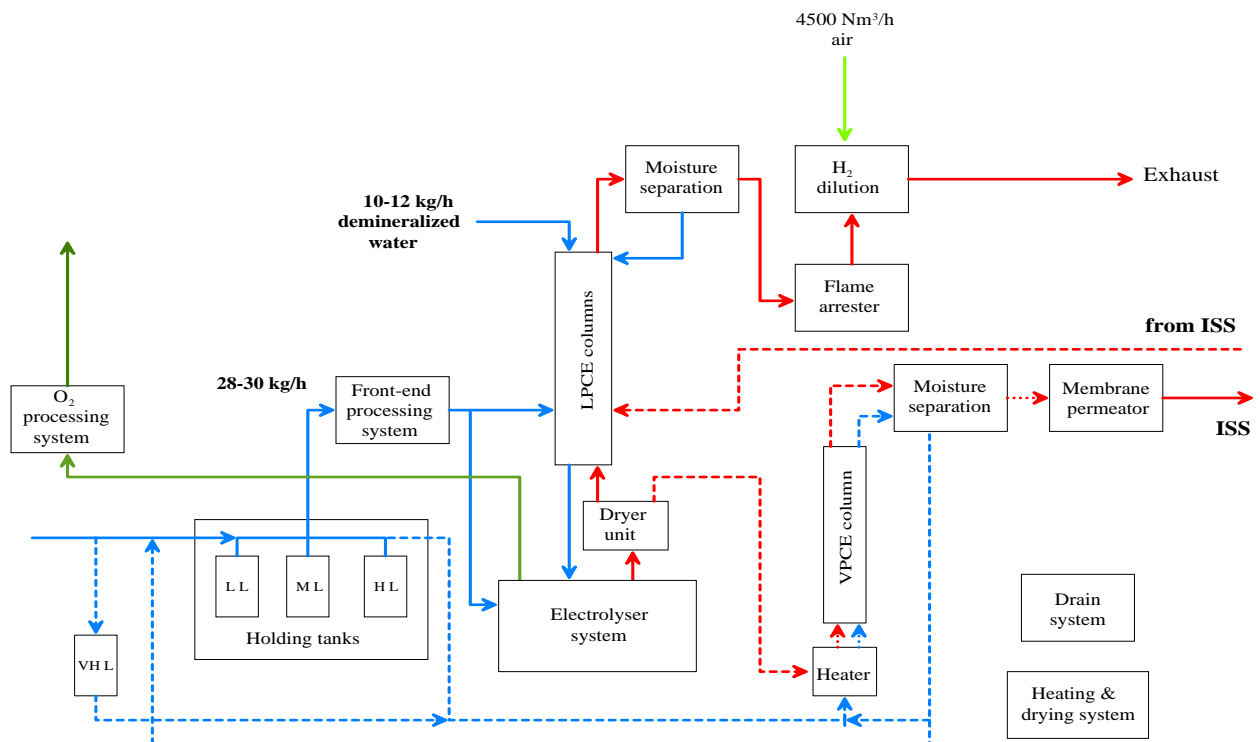
Fig. 1: 3-D layout of the glove box in between the WDS and CD.

**EFDA/06-1510 (TW6-TTFD-TPI 55)  
Update of ITER ISS-WDS Process Design -1**

The objective of this task is to update the designs of the ITER ISS and WDS as documented in the 2001 FDR (Final Design Report). The carried out activities have been focussed on establishing the input parameters for the ISS and WDS for the main ITER operating modes, as the basis of the design. The following operating modes have been considered for investigation:

- Plasma operation (helium, protium, deuterium and DT) taking into account fluctuations between burn and dwell phases and due to cryopump partial regeneration schedules;
- Overnight shifts when full regeneration of cryopumps is carried out;
- Tritium recovery from PFC's and vessel wall conditioning;
- Long term maintenance outages when the WDS will remain in operation but no "high tritium" streams to the ISS are present;
- Special operations such as tritium inventory determinations.

The update of ITER ISS-WDS design is developed on the basis that the ISS and the WDS will be integrated by routing the top product stream from the WDS to a feed point near the bottom end of the WDS Liquid Phase Catalytic Exchange (LPCE) column. In this respect the evaluation of the optimum position of the feed points, hydrogen stream from ISS and the combined "low tritium" feed stream which includes the WDS electrolyser Q<sub>2</sub> stream and the NBI regeneration gas and (possibly) pellet injector propellant, is on going.



The main achievements are:

3. Development of the WDS-ISS configuration which allow reduction of the tritium activity in water to be fed in the CECE process. The new configuration, see figure, allows also to process the highly tritiated water which was identified during the development of TW5-

TTFD-TPI 53 task – Definition of the interfaces between the Tritium Plant and the Torus Pumping, Neutral Beam Injection Pumping and Fuelling Systems.

4. Substantiation of removing the 50 % D-50% T from the ISS production streams, which will lower the overall tritium inventory in the fuel cycle and simplify the design and operation.
5. Space allocation and preliminary 3-D layout of the WDS-ISS

Staff:

I. Cristescu

I. R. Cristescu

A. Lazar (ICSI-Rm. Valcea – Romania)

## **EFDA/06-1451 (TW6-TTFD-TPI 57) Dynamic Modelling of ITER Tritium Inventories (TRIMO)**

Development of the TRIMO code provides a valuable analysis tool for ITER for dynamic modelling of tritium inventories in the Fuel Cycle systems and Vacuum Vessel. Upgrading of certain features of the code have been carried out to maximize the applicability to ITER and ensure consistency of the code modules with the evolving ITER design. Several topics have been addressed in the present task, detailed below.

- Review and incorporation into TRIMO of data from task TW5-TTFD-TPI-53 (Definition of the interfaces between the Tritium Plant and the Torus Pumping, Neutral Beam Injector Pumping, and Fuelling Systems). Typical fuelling cases, as shown in the PID (or additional operational scenarios) have been investigated with TRIMO and the behaviour of the sub-systems has been analysed. A more detailed model for the pellet injector has been introduced to take into account the influence of the ablated gas from the pellet injector to the TEP/ISS functioning and tritium inventories in the fuelling systems, TEP and ISS.
- As it is envisaged that the top extraction stream from CD1 ISS to be returned in the WDS, this link has been made active in TRIMO. A dynamic model for a WDS system based on a Combined electrolysis catalytic exchange process considering both deuterium and tritium transfer has been implemented. The behaviour (i.e. concentration profile) of the LPCE columns in a ISS – WDS linked configuration for short and long pulses has been investigated; however accurate values are dependant on the measurements on mass transfer coefficients at simultaneous tritium and deuterium transfer. This part of the task is an input for the task TW6-TTFD-TPI-55 for the integration of the ISS and WDS process design. The results of this development will be experimentally validated in the task TW6-TTFD-TR63.
- An assessment of the possible tritium fluxes associated with standard divertor cassette refurbishments from Hot Cells is on-going in the ITER IO. As presently it is not well decided how these fluxes can be processed in Tritium Plant, for full flexibility feed streams were introduced in CD1 and CD2.
- The graphical user interface has been updated with the necessary plots for the new developed/improved modules from the code.
- During 2006-2007 TRIMO was intensively tested for various fuelling scenarios for short and long pulses. The tests mainly regarded the ISS system where verifications for different design parameters have been done. As a result of this activity several extensions of the graphical interfaces have been identified and implemented. Additionally due to the on-going ISS-WDS design activities at TLK in the frame of the task TW6-TTFD-TPI55 some hard-wired values in TRIMO are now user-defined and can be changed as desired.
- Implementation in TRIMO the changes as result of ITER licensing (status July 2007); a study of reducing the allowable inventory in a fire zone from 100 g to 70 g tritium impact to the fuel cycle functioning has been accomplished in addition to an analyze of the tritium needed for non-interrupted burn/pulse and the ability of the present configuration of the fuel cycle to cope with the requirements of fast tritium processing have been performed using TRIMO.
- The second version of the TRIMO documentation has been issued; the operational philosophy of the Fuel Cycle, the physical assumptions used to model the subsystems and the employed numerical methods is described.

### Staff:

I.-R. Cristescu

## **EFDA/05-1251 (TW5-TTFD-TPI 54) Development of a Tritium Manual for ITER**

A Tritium Manual is required for use by ITER designers and operators as the prime source of relevant information on tritium properties, tritium processes in ITER, tritium compatible components, tritium safety, QA procedures and design guidelines for ITER systems that handle tritium. It will be mandatory to use components and devices for ITER tritium systems recommended in the manual and to follow procedures laid down in the manual. Two volumes were initially anticipated, one covering tritium properties and interactions of tritium with materials and the second defining codes and standards. A third volume is in preparation by external contractors under a separate contract covering safety standards and safety issues.

Preliminary versions of Volume 1 and Volume 2 have been posted in ITER IDM. The ITER Participating Teams have been invited to review these documents as they have to agree and approve the contents before the provisions come into force. The manual will be updated as a result of comments received, updating of the manual is expected to continue throughout the lifetime of ITER as components, concepts etc. develop. Certain topics, such as water detritiation, have not been addressed as these systems are under preliminary design and hence design standards have not been developed. These will be added when the development of the design allows.

### Staff:

C. J. Caldwell-Nichols  
R.-D. Penzhorn

## **Safety Analysis and Environmental Impact**



## TW6-TSS-SEA 2.1 Occupational Radiation Exposure – ALARA in ITER: Further Refinement

The objective of the two deliverables was to evaluate the time evolution of airborne tritium concentration and the surface contamination after a tritium release within the NBI cell. The estimation of the amount of tritium that may be released during the maintenance activities within the NBI box, namely the replacement of the NBI box bellows and the rupture discs of the Vacuum Vessel Pressure suppression System (VVPSS), has been done based on experimental data related to the tritium adsorption on the ITER cryopanel mock-ups and on the amount of tritium out-gassed during JET torus venting. Within very conservative assumptions the amount of tritium that may be released during 100 hours maintenance in the NBI box should be below 1 gram of tritium.

The calculations of tritium airborne concentration, as HT and HTO forms, and the surface contamination with HTO, after a tritium spill event within the NBI box has been performed considering both theoretical investigations and experimental data on:

- Tritium dispersion and contamination time evolution within a confined volume
- Conversion of tritium gas to tritiated water
- Sorption and desorption of tritiated water on different materials

The reference scenarios considered for the parametric studies in view of evaluation of the NBI cell contamination during and after a tritium spill event are: 0.01, 0.1 or 1 gram of tritium released in 1, 10 or 100 hours, the throughput of the Stand by Vent Detritiation System (S-ADS) is  $4500 \text{ m}^3\text{h}^{-1}$ , the decontamination factor of S-ADS is 100 and the conversion rate of HT to HTO is 1% per day. For all investigated cases it was considered that the S-VDS is in operation from the beginning of tritium release, no delay in the tritium release detection.

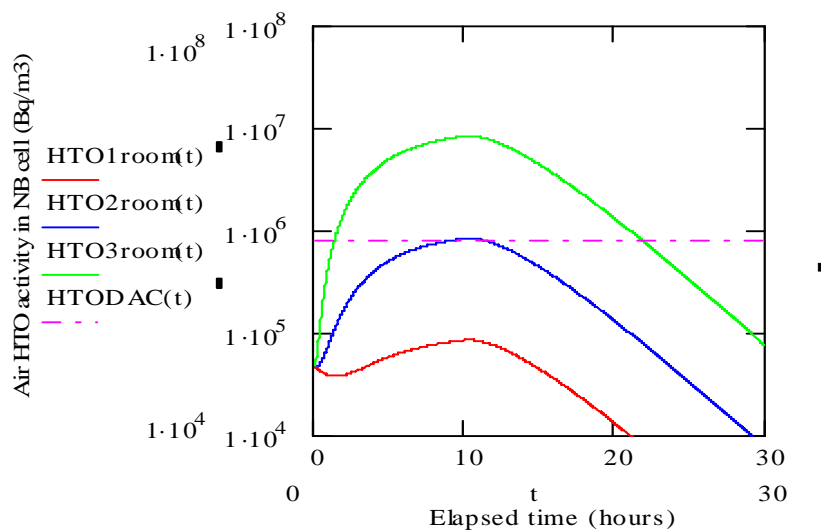


Fig. 1: Time evolution of HTO activity in the case of 10 hours tritium release  
— 0.01 g T; — 0.1 g T; — 1 g T

Within these assumptions the results of evaluations are:

1. The NBI cell atmosphere contamination with HT and HTO is lower when the same amount of tritium is released within a longer period of time;
2. The contamination with HTO exceeds 1 DAC (max. ~ 10 DAC) if 1 gram of tritium is released within the NBI cell and the release time is between 1 hour and 10 hours.

3. The throughput of the S-ADS has the major influence in the time evolution of the contamination within the NBI cell;
4. The additional surface contamination of the NBI cell walls is below 1 Bq·cm<sup>-2</sup> for all cases investigated.

Staff:

I. Cristescu  
I.-R. Cristescu

## **TW5-TSS-SEA 3.5C**

### **In-vessel Safety: Small and Medium Scale Experiments on Combined Hydrogen/Dust Explosions and Mitigation for Model Development**

#### **Objectives**

Risk studies for ITER have shown possibilities for the generation of reactive hydrogen-dust-air mixtures, which after ignition could result in potential pressure loads to the vacuum vessel and to mobilization of tritium. The work aims at fundamental understanding and numerical modelling of hydrogen and dust explosions for ITER-typical gas and dust mixtures. The results will be used to derive effective mitigation measures against hydrogen/dust reactions in ITER.

To evaluate the dust explosion hazard in ITER, it is proposed to develop a semi-phenomenological code able to model the combustion/explosion process under ITER typical conditions for the whole variety of the accident scenarios. The main objective of this work is to complete the experimental data on ITER-relevant dusts to support the code development/validation. The effective dust burning rates necessary for the code combustion module are to be measured depending on the dust particle size, dust concentration, and turbulence level using the method of open-end combustion tubes. Another activity on this way is to support mitigation methods of the dust/hydrogen explosion hazard. With this aim the Limiting Oxygen Concentrations of explosion atmospheres preventing the dust/H<sub>2</sub> explosions are to be measured.

#### **Status**

The investigations of the explosion behaviour of some ITER-relevant dusts have been performed in 2002-2006 using a standard method of 20-l sphere (DUSTEX facility) and a combustion tube technique (PROFLAM I and II facilities). The main conclusions drawn from the obtained results can be formulated as follows:

- Fine graphite and tungsten dusts of micron particle size can explode in a wide concentration range generating explosion overpressures about 5-7 bar.
- The ignition energy required to explode the dusts is rather high, about several kJ. Furthermore, some screening tests in a big combustion tube (PROFLAM II) with 4-micron graphite dust performed last year demonstrated no flame propagation even with higher energy of the igniters.
- Measurements of Limiting Oxygen Concentration of the dusts even under over-conservative conditions have shown that a weak dilution of the pre-explosion atmosphere can drastically decrease the explosion overpressures.
- The tests performed in DUSTEX with hybrid dust/hydrogen/air mixtures ignited by a weak electric spark demonstrated the possibility of inducing ITER-relevant dusts to explode in hydrogen-containing atmospheres by a weak ignition source. The resulting combined explosions can be even more severe than those of pure hydrogen or the dusts alone.

Taking these into account, it has been decided to focus main efforts on studying the explosion properties of the hybrid dust/hydrogen/air mixtures. The tasks 2007 are:

- Measurements of the efficient flame propagation velocities in graphite dust/H<sub>2</sub>/air by the method of open-end combustion tube (PROFLAM I facility);
- Measurements of the Limiting Oxygen Concentrations of graphite dust/H<sub>2</sub>/air mixtures by the method of 20-l sphere (DUSTEX facility);

- Flame propagation tests with 1-micron tungsten dust in the larger combustion chamber (PROFLAM II facility, closed geometry).

## Results

The efficient velocities of flame propagation in graphite dust/hydrogen/air mixtures were measured using the open-end combustion tube method in the PROFLAM I facility (15 cm inner diameter, 3 m length). To create mixtures to test, a dust layer pre-deposited on the combustion tube bottom was dispersed by a row of air jets from a dispersion pipe directed on the layer. The dispersion was performed in 0.6 bar air atmosphere containing hydrogen. The hydrogen content varied from 9 to 17 vol. % (at the moment of ignition); the dust concentration ranged from 100 to 700 g/m<sup>3</sup>. Four-micron graphite dust was used in the tests. The mixtures were ignited by a weak electric spark generated between a pair of electrodes mounted at the open end of the tube. The process of flame propagation was recorded by an array of thermocouples and photodiodes. The thermocouples of 0.1 mm wire diameter were installed at 5 different distances from the open end. The times of the flame front arrival at the sensor positions were recorded; the flame velocity was calculated as the distance divided by the travelling time.

Generally, addition of the graphite dust to the hydrogen/air mixtures lowered the efficient flame propagation velocity. However, at each tested hydrogen concentration but for 9 % there is a specific dust concentration at which the flame propagation velocity is higher than that in the pure hydrogen/air mixture (see Fig. 1 for [H<sub>2</sub>]=17 vol. % and Fig. 2 presenting the 'optimal' velocity versus dust concentration).

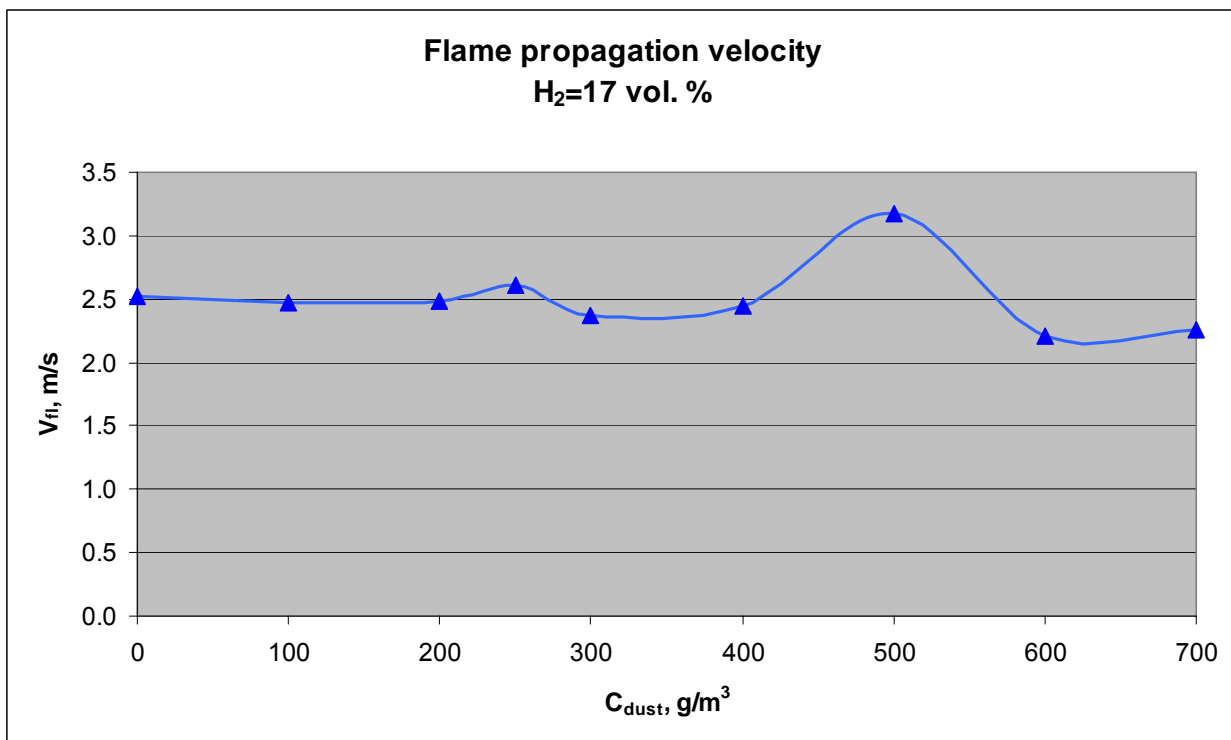


Fig. 1: Averaged flame propagation velocity in PROFLAM I facility (open end) in hybrid graphite dust/hydrogen/air mixtures at [H<sub>2</sub>]=17 vol. % versus dust concentration.

The obtained data on flame propagation in hybrid hydrogen/graphite dust air mixtures will be used to validate a 3D CFD code developed to model explosion scenarios of severe accidents in ITER.

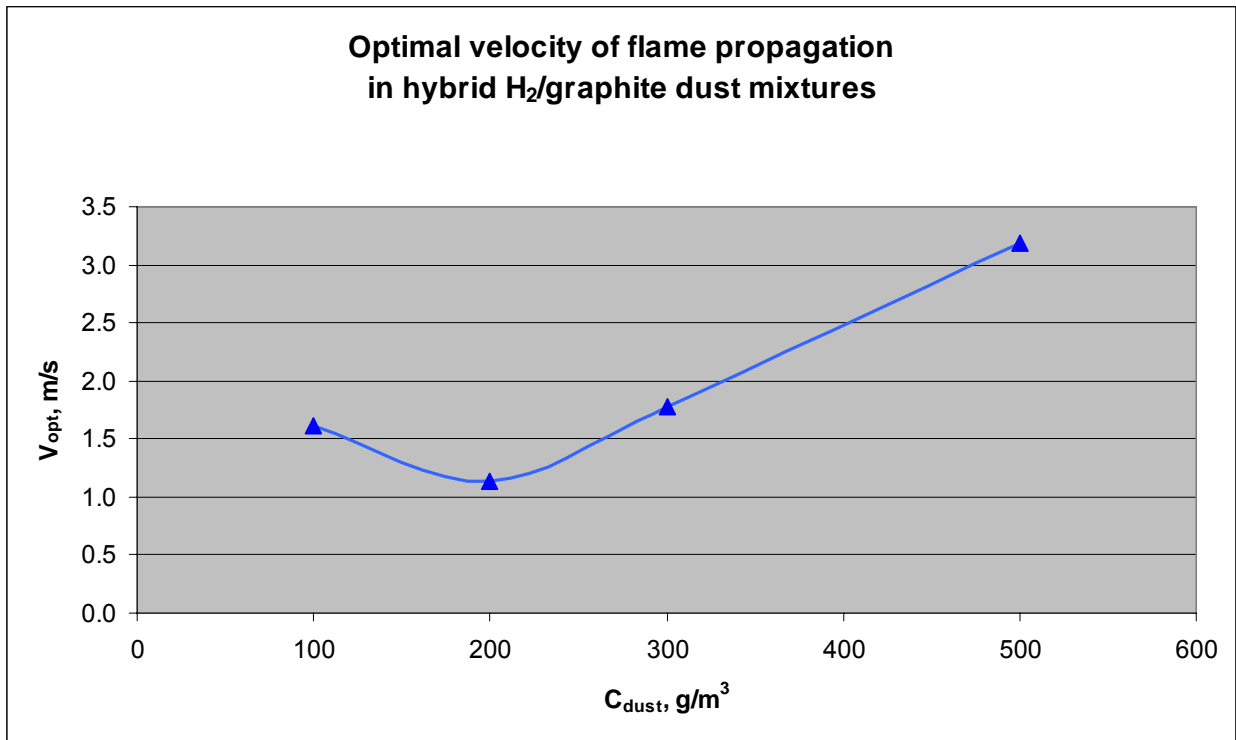


Fig. 2: Optimal velocity of flame propagation in PROFLAM I facility (open end) in hybrid graphite dust/hydrogen/air mixtures versus dust concentration.

The tests to check the possibility of flame propagation in 1-micron tungsten dust/air mixtures in large volumes are prepared to be performed in PROFLAM II facility (about 300 l volume). The dust dispersion tests were done to choose the dispersion system parameters. The tests showed an acceptable quality of the dust clouds formation. The ignition tests are under run.

The tests to measure Limiting Oxygen Concentration in graphite dust/hydrogen/air mixtures are in progress.

## Outlook

Measurements of LOC of tungsten/hydrogen/air mixtures in the DUSTEX facility.

Measurements of efficient flame propagation velocities in tungsten dust/hydrogen/air mixtures in the PROFLAM I facility

## Staff:

S. Baur  
W. Breitung  
A. Denkevits  
B. Kaup  
F. Prestel  
A. Friedrich, ProScience  
K. Sempert, ProScience  
G. Stern, ProScience

## Literature:

- [1] A. Denkevits. Explosibility of hydrogen-graphite dust hybrid mixtures. *Journal of Loss Prevention in the Process Industries* 20 (2007) 698–707.

## EFDA/06-1517 (TW6-TSS-SEA 4.5) Feasibility Study of Possible Prevention of Hydrogen and Dust Explosion in ITER by Injection of Neutral Gas

### Objectives

During ITER operation, plasma-wall interaction is expected to generate hundreds of kilograms of beryllium, carbon and tungsten dusts which are loose particles with very high specific surface and high chemical reactivity. In the “wet bypass” scenario with in-vessel coolant leakage accompanied by a failure of windows in the vacuum vessel (VV) and cryostat penetration, the interaction of hot dust with water and steam would produce hydrogen, and air ingress may lead to hydrogen and dust explosions.

The objective is to study the feasibility of a Nitrogen injection system to prevent hydrogen combustion and explosion in ITER. The current ITER strategy to cope with the risk of hydrogen combustion and explosion is based on the inertion of gas mixtures by injecting Nitrogen from the bottom of the vacuum vessel. GASFLOW is being used to investigate the distribution of hydrogen-oxygen-nitrogen-steam mixtures and evaluate the risks of flame acceleration (FA) and deflagration to detonation transition (DDT).

### Status

A GASFLOW 3-D geometry model for ITER has been developed. GASFLOW II has been extended to model the specific conditions for the ITER scenario analysis. Several models were developed: an isentropic expansion model to introduce super-heated water vapor and air into the plasma chamber; a hydrogen production - steam destruction model to simulate the  $\text{Be} + \text{H}_2\text{O} > \text{BeO} + \text{H}_2$  chemical reaction in fluid cells adjacent to the hot beryllium surfaces; and a water vapor destruction and energy destruction model to simulate the effects of the pressure suppression tank.

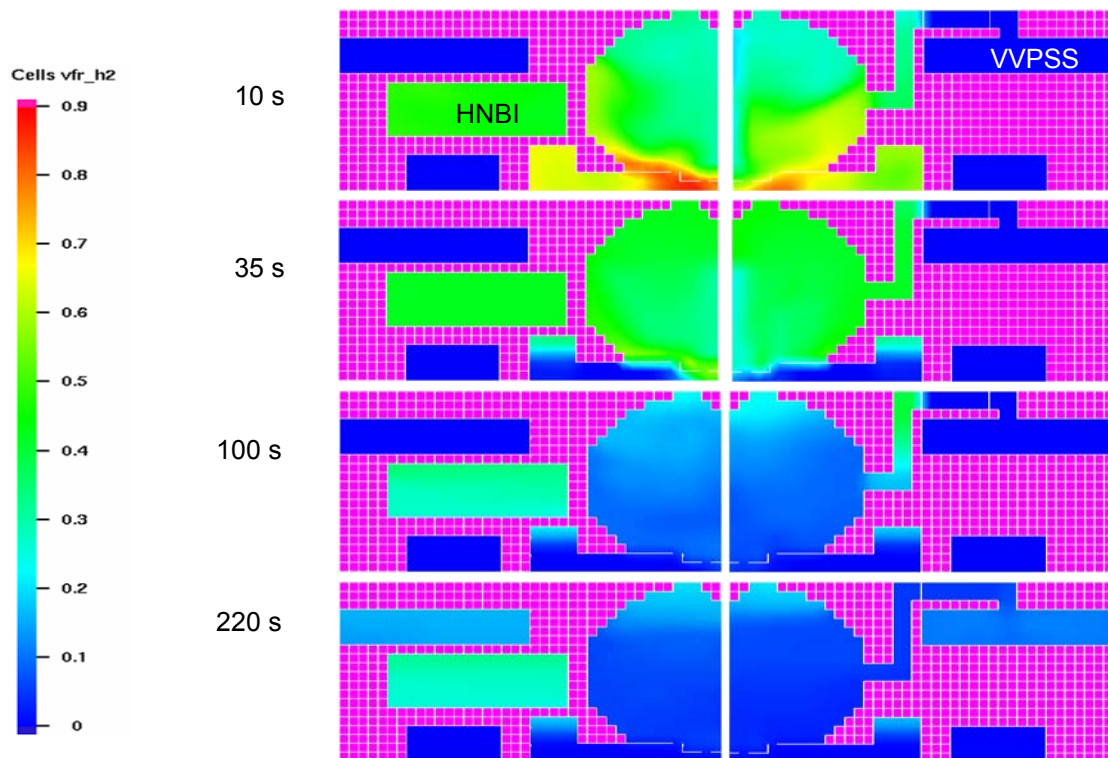


Fig. 1: GASFLOW simulation of hydrogen concentration in the ITER wet bypass scenario.

GASFLOW parameter studies have been implemented. Parameters, including nitrogen injection time and location, air ingress area, hydrogen mass generated by the dust-steam interaction, pressure differences when bypass valve fails, initial pressures in the pressure suppression tank, etc, are varied to evaluate the hydrogen risk and the feasibility of a nitrogen injection system.

The proposed nitrogen injection system will generally decrease flame velocities. DDT can be excluded with delayed N<sub>2</sub> injection (40 s) in the plasma chamber (PC), pressure suppression tank (ST) and neutral beam injector (NBI). A potential for FA remains for a restricted space and time region in the subvolumes, and a potential for slow deflagration remains in the PC for the cases calculated.

The study indicates that the nitrogen dilution approach has principle weaknesses. Instead of being removed from the system, the burnable substances are diluted by nitrogen and remain in the system which seems to be a potential threat. To meet the requirement of hydrogen safety in ITER and to achieve full inertization, more inert gas is needed which will pressurize the PC, vent to the vault, and possibly create other problems. Therefore, a significant reduction or removal of the oxygen source seems to be an effective way to eliminate the remaining risks of slow combustions in ITER.

### **Further work**

The GASFLOW code will be used to study the removal of slow combustion regimes in ITER scenarios. Currently there are two potential ways: using a more effective flame suppressant than N<sub>2</sub>, i.e., a chemically active radical scavenger or removing H<sub>2</sub> and O<sub>2</sub> by early deliberate ignition in local burns, for instance the spark igniter which is simple, cheap, and a countermeasure to air ingress by pressure build-up in the vacuum vessel.

### Staff:

W. Breitung  
J. Travis  
T. Jordan  
J. Xiao

### Literature:

- [1] J. R. Travis, J. W. Spore, P. Royl, K. L. Lam, T. L. Wilson, C. Müller, G. A. Necker, B. D. Nichols, and R. Redlinger. GASFLOW: A Computational Fluid Dynamics Code for Gases, Aerosols and Combustion. Volume 1: theory and computational model. FZK and LANL, 2001
- [2] J. R. Travis, J. W. Spore, P. Royl, K. L. Lam, T. L. Wilson, C. Müller, G. A. Necker, B. D. Nichols, and R. Redlinger. GASFLOW: A Computational Fluid Dynamics Code for Gases, Aerosols and Combustion. Volume 2: user manual. FZK and LANL, 2001

## **TW6-TSS-SEP 1**

### **Uncertainty Assessment and Analysis of ITER In-VV Tritium Inventory Determination**

Tracking of tritium inventories on ITER will be essential to ensure that the safety limits established for the mobilizable tritium inventory in the vacuum vessel are not violated.

Even starting with the tritium import the value of tritium inventory at ITER site will be known with a certain error that will then propagate in time. The most important aspect on error propagation for tritium inventory at ITER site was found to be the error in the tritium burnt; the quantity of tritium burnt in JET or TFTR was very modest in comparison with the amount of tritium planned to be burnt at ITER and somehow the importance of these measurements have been overlooked. If systematic errors will not be avoided in the determination of tritium burnt, according to the present tritium delivery and plasma operation schedules, the value of the absolute error of the tritium inventory will raise to a maximum of 420 g at approximately 8 years after the first tritium delivery. If systematic errors in tritium burnt can be avoided (however at a same value of 10% error in the tritium burnt) the absolute error of the tritium inventory will be only 61 g. In the case of random error in the diagnostics, the error in the tritium inventory at ITER site is mainly governed by the error in the tritium imported measured by calorimetry and this error is also systematic however at a much lower value of 0.5%.

During plasma operation, continuous monitoring of the tritium delivered to the torus and recovered will allow to compute at the end of the day of experiments the tritium amount trapped in the torus. Due to error propagation this value will also bear errors. Independent of the measurement techniques or monitored streams, this type of accountancy carries significant errors. An alternative method is to measure overnight the inventory in the storage and delivery system. While the errors associated with this method are lower than the ones obtained by tritium monitoring on a shot-by-shot basis, within time these errors would also accumulate at high values. Therefore a dedicated procedure for global tritium inventory has to be employed at certain established time intervals.

The method of global tritium inventory, consists in a first step of transferring all the mobilizable tritium from the plant and measurement of this inventory in the self-assay beds from the storage and delivery system. In parallel, assessment of the ex-vessel portion of the total trapped tritium inventory has to be carried out and eventually the in-vessel portion is calculated by difference. For this procedure, error propagation come from the error of the total tritium inventory on ITER site and associated errors with the tritium inventory measurement procedures. The highest uncertainty is linked to the error for the tritium trapped ex-vessel (flakes, dust and tiles existing in the Hot Cell at the moment of the tritium inventory procedure). A parametric study considering values from 1 to 40 g for the absolute error for the tritium trapped ex-vessel was therefore performed and its influence upon the tritium trapped in-vessel after the cleaning procedure has been quantified.

Possible ways of reducing the uncertainties in the in-VV tritium inventory determination has been outlined and the necessary R&D main lines of investigation have been identified.

#### Staff:

I.-R. Cristescu

## **EFDA/06-1489 (TW6-TSS-SEP 2)**

### **Doses to the Public due to ITER Accidental Releases**

#### **Objectives**

The objective was to perform site-specific assessments for accidental releases of tritium and activation products for the ITER site in Cadarache. This included the investigation whether protective actions such as evacuation, sheltering or banning of food products are necessary.

#### **Work performed**

Calculations were performed with UFOTRI and COSYMA to support licensing of the ITER plant at the Cadarache site. In particular, doses and activity concentrations in food products at various distances from the ITER site at Cadarache were estimated. Source terms for ITER, defined for activated dust (AP), activated corrosion products (ACP) and tritium in form of tritium gas (HT) and tritiated water (HTO) were used as basis for the calculations. Three different weather conditions were selected for the calculations. Sequence one is characterised by poor diffusion condition and a wind speed of 2 m/s and no rain. Sequence two and three contained normal diffusion conditions with a wind speed of 5 m/s differing only in precipitation with either none or 10 mm/h, respectively. A release from a 60 m high stack (with building wake effects) and from a 10 m release point (without building wake effects) were assumed. Special dispersion parameters for France, the so-called Doury parameterisation scheme, were applied. Calculations were carried out for three age groups (adult, 10 year old child and one year old infant) for tritium and for two age groups (adults and one year old infant) for activation products.

Having released only one gram of the material, doses are in general low and do not reach any of the dose criteria. Maximum doses in the near range do not exceed two mSv for the release of one gram of tritium or activation products. Adults are in most cases the critical group, however children might be of higher importance in case of a different diet. In our calculations, children consumed no milk products produced in the region around Cadarache. Activity levels in food products are much closer to potential intervention levels than doses from ingestion which are far below 10 mSv, a dose used to derive action levels for food products.

#### **Further work**

The task is completed.

#### Staff:

F. Fischer  
I. Hasemann  
W. Raskob

#### Literature:

- [1] L. Di Pace, E. Letellier, H. Maubert, B. Patel, W. Raskob; Biological hazard issues from potential releases of tritiated dust from ITER; At: 8th International Symposium on Fusion Nuclear Technology, Heidelberg, 30.9.2007 – 5.10.2007
- [2] D. Galeriu, P. Davis, W. Raskob, A. Melintescu; TRITIUM RADIOECOLOGY AND DOSIMETRY-TODAY AND TOMORROW; At: 8th International Conference on Tritium Science and Technology, September 16-21, 2007 Rochester, New York
- [3] S. Ring Peterson and Wolfgang Raskob; HISTORICAL DOSES TO THE PUBLIC FROM ROUTINE AND ACCIDENTAL RELEASES OF TRITIUM – LAWRENCE LIVERMORE NATIONAL LABORATORY, 1953 – 2005; At: 8th International Conference on Tritium Science and Technology, September 16-21, 2007 Rochester, New York

**EFDA/06-1415 (TW6-TSL-002)**  
**Safety Assessment for EU-Test Blanket Modules to support ITER Licensing Process – 4**

**Subtitle: Deterministic Safety Analysis for HCPB TBM System**

**Objectives and the description of the selected accident case**

The objective of the present task is the deterministic analysis of the most severe accident sequences for one of the two EU TBM concepts (HCPB). From FMEA a particular sequence, namely a LOCA in ex-vessel with failure of the plasma shutdown system, has been selected for the deterministic safety analysis. As Postulated Initiation Event (PIE), it is assumed that during the plasma burn a failure of the He coolant confinement located in the tokamak cooling water system (TCWS) vault takes place, which means a double-ended pipe break in a large diameter pipe. The evolution of the accident is divided in three phases shown in Fig. 1: phase 1 He blow-down; phase 2 delayed plasma shutdown and phase 3 long term behavior. Based on the preliminary study of accidental sequences in [1] following parameters have to be estimated for the 3 phases using qualified codes:

- Phase 1: (a) time constant for the loss of TBM cooling; (b) pressurization of the TCWS vault; (c) release of T transported by the coolant He into the vault.
- Phase 2: (d) Maximum temperatures in the TBM during the plasma burn; (e) Evaluation of damage of the TBM box structure as consequence of thermal load and plasma disruption.
- Phase 3: (f) Temperature transient in the long term regarding the decay heat and the chemical energy due to the Be reaction with air/steam; (g) The H<sub>2</sub> production caused by Be-steam reaction; (h) The T, dust and ACP transport.

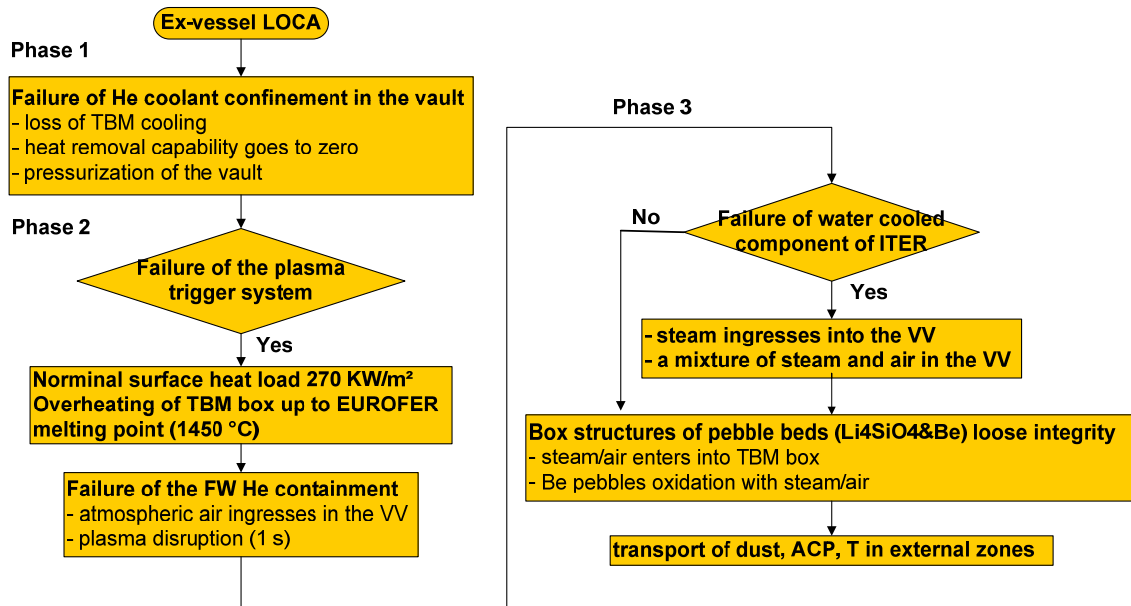


Fig. 1: Schema of the accident evolution for ex-vessel LOCA.

**Study and results of the accident case**

Phase 1 is studied using the thermo-hydraulic system code RELAP5/MOD3.2 modeling HCPB TBM and HCS (Fig. 2). The blow-down begins during the normal operation at steady state (8 MPa and 300 °C at TBM coolant inlet, plasma burn at the nominal surface heat load

270 KW/m<sup>2</sup>). The calculated time constant is 1.05 s, when e. g. 63% of the pressure drop at the TBM inlet is reached (point (a)). The pressurization of the vault is estimated by ~977 Pa, which is irrelevant compared with the design limit for over-pressurisation in the vault (200 KPa). The primary coolant contains at maximum 1 mg of T at the design partial pressure of HT of 0.3 Pa. This small amount released in the vault is negligible compared to the T limit as HT (50 g) (point (c)).

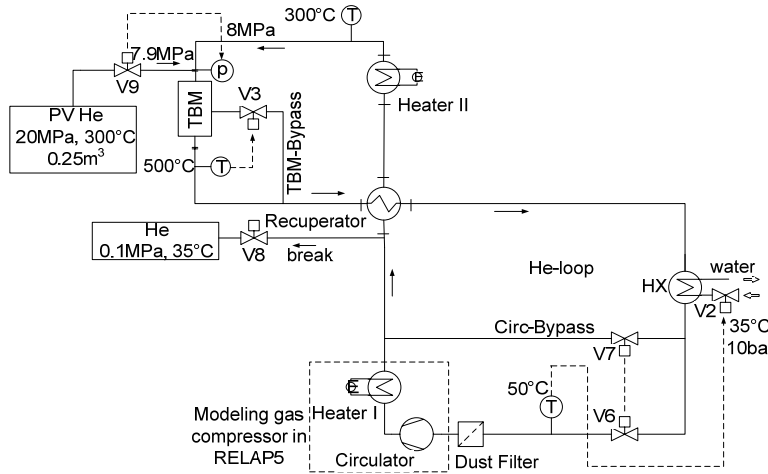


Fig. 2: Scheme of RELAP5 modeling for the HCS.

In phase 2 the thermal analysis is performed using a 3D-ANSYS-model of a radial cell cut out of the HCPB TBM (Fig. 3). ANSYS calculation is started with steady state regarding the plasma burn; nuclear power density; temperature and heat transfer coefficients (HTC) of He coolant and material properties. The followed transient calculation simulates heating-up. HTC are ramped down within 3 s based on the time constant obtained in phase 1. Heat is transported from the FW to TBM back plate

by heat conduction and radiations on the breeding unit (BU) back plate and TBM back plate.

ANSYS calculation shows that after 258 s from the PIE the FW surface facing the plasma reaches the EUROFER melting point at 1450 °C (point (d)). At this point the FW channels are going to fail surely and the air enters the VV through the FW break causing abrupt plasma shut-down. The present calculation cannot account for the delay effect because of energy absorption in the melting process of the Be-cover. For the 3.4 Kg Be-cover this delay can be estimated of ~17 s that have to be added to the calculated shutdown time. Following points are resulted at the end of phase 2: 1) Status of the Be-cover: because of Be melting point at 1283 °C, the whole Be layer is melted and can be considered removed from the modeling. 2) Status of the FW structure: all temperatures in the FW structures are higher than 900 °C. The structural integrity of the FW cannot be assured against the box internal pressure of 100 KPa and possible damage caused by the disruption loads. The box fails and the exposition of the internal beds to the VV atmosphere cannot be avoided (point (e)). 3) Status of the internal beds: the maximal temperature in the Be pebble reaches 915 °C and 1015 °C in the breeding ceramic; the temperature in the hot spots are high but still under the respective melting points.

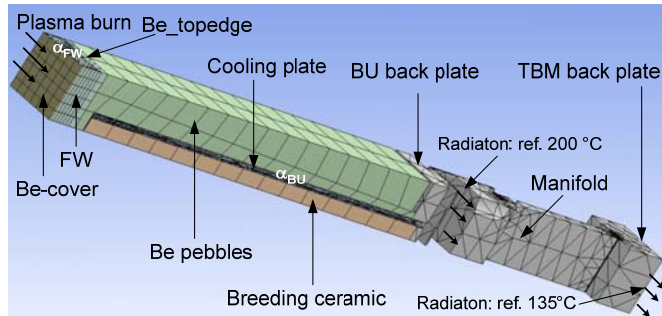


Fig. 3: ANSYS-model for the thermal analysis in phase 2.

Phase 3 is studied regarding the decay heat and the chemical energy from possible Be oxidation with air/steam. Be reaction rates is temperature and pressure dependent and taken from [2]. As at moment the requirements for FPSS intervention have not be defined and this affects the classification of the accident as DBA (Design Base Accident) and BDBA (Beyond Design Base Accident), both calculation cases have been done with MELCOR 1.8.2 version [3]. Table 1 shows the calculation cases with respect to different failures. Code A denotes ANSYS and M means MELCOR. MELCOR code is considered as the main code available

for safety analyses. Its main limitation is the relatively poor modeling of the heat structures (only a 1D-modeling with rough meshing), that arises some questions on the possibility to see local discontinuity effects. Therefore additional thermal calculations have been done for almost all the analyzed cases using the same 3D-ANSYS-model in phase 2. This model has been completed implementing a chemical heat source for the Be oxidation with air/steam. As this additional model cannot take into account for time dependent VV temperature, pressure of consumed O<sub>2</sub>/steam in Be pebbles etc., these quantities have been taken from the corresponding MELCOR calculation and used as input for the ANSYS calculation.

Table 1: Calculation cases regarding assumptions for phase 3.

Case Nr.	Failures				MELCOR DBA or BDBA	Safety factor		Code			
	FW	TBM box	water confinement			decay heat	Be reaction				
	Air ingress		steam ingress								
	VV	TBM box	VV	TBM box							
1/2		no	yes	no	DBA	1.2	no	M/A			
3a/4a		yes	no	no	BDBA	1.0	1.0	M/A			
3b/4b	DBA				1.2				5.0		
5/6	yes	yes	yes	yes	BDBA	1.0	1.0	M/A			
5*								M			
7					no	no	no	DBA T/ dust	1.2	no	M
8					no	yes	no				

\* Refinement for modeling Be pebble beds.

MELCOR results for the representative calculation case Nr. 3a and 5 are shown in Fig. 4 (a) and (b) respectively. The first pressure drop in the VV denotes working of the VVPSS, if the VV pressure reaches 90 KPa. For case Nr. 3a, due to O<sub>2</sub> consumption by the Be-air reaction, pressure increase of remained O<sub>2</sub> in Be pebbles is delayed compared to the one in the VV. For case Nr. 5, steam ingress is dominant against air ingress; that means that steam builds up pressure very quickly hindering the air ingress. Indeed, the pressure level of O<sub>2</sub> in the VV and Be pebbles remains lower than 2800 Pa, while the maximal steam pressure can exceed the atmospheric pressure. The building of a H<sub>2</sub> pressure in the Be beds denotes the reacted steam. Limited H<sub>2</sub> is produced by the Be-steam reaction (point (g)).

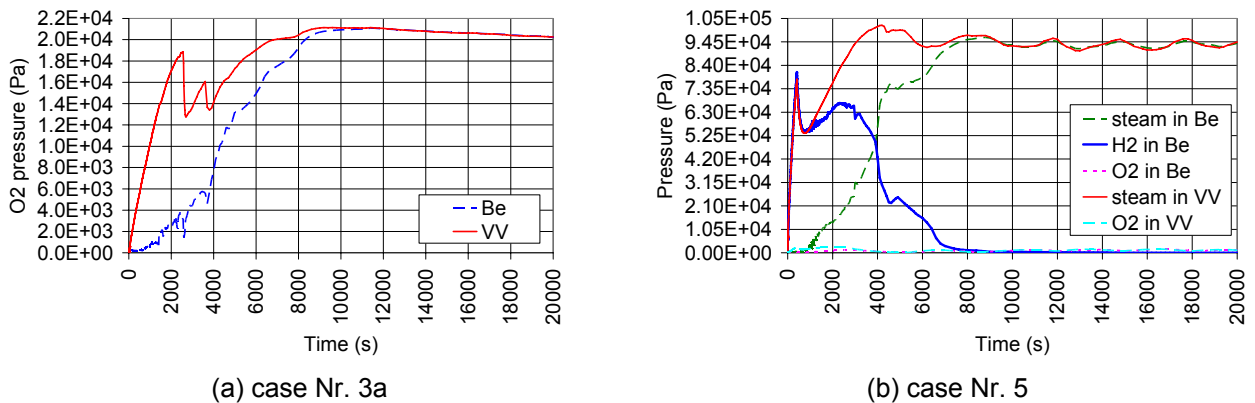


Fig. 4: MELCOR results for case Nr. 3a and 5.

The followed ANSYS calculations as case Nr. 4a and 6 show temperature results in Fig. 5 (a) and (b) respectively (point (f)). FW2 to FW5 indicate FW structures from the side of the FW surface to the boundary of Be pebbles (Be\_topedge). The first 260 s refer to phase 2. The FW is cooled down firstly after the plasma shutdown, later the reaction energy increases temperature near the FW up to divergence. Case Nr. 6 shows that its discontinuity effect begins ~558 s earlier than it for case Nr. 4a.

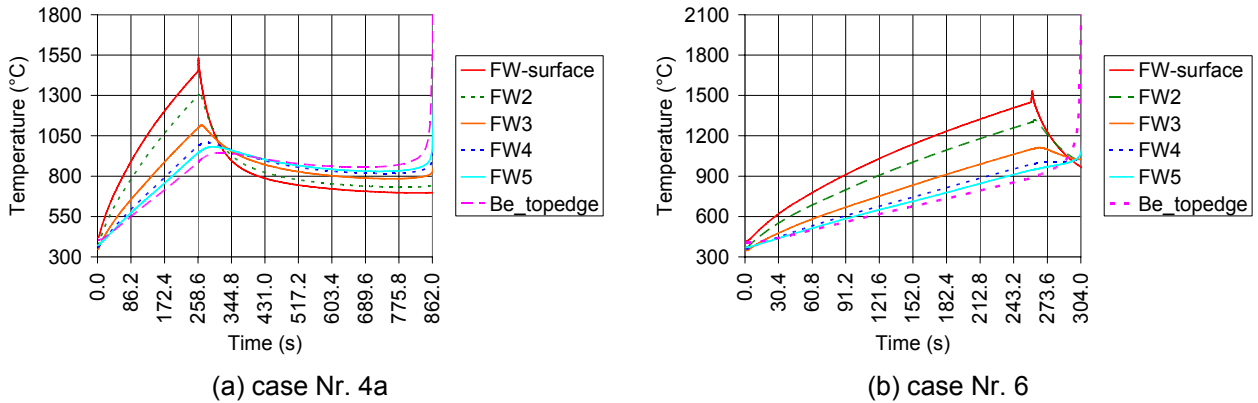


Fig. 5: Temperature results of the ANSYS calculation for case Nr. 4a and 6.

In case of the steam ingress, T, dust and ACP can be transported to the TCWS vault (case Nr. 8), while this does not happen if air ingresses only (case Nr. 7). The amount of these products has been quantified, which is lower than the limitation of the ITER safety (point (h)).

### Conclusions and outlook

The selected accident case has been examined in detail during three different, successive stages. The blow-down phase, studied by RELAP5, is very fast resulting in a quasi immediate loss of the TBM coolant capability. Direct effects like over-pressurization of the TCWS vault or T contamination are negligible for the overall ITER safety.

With ANSYS calculation in phase 2, after 275 s (including Be melting time) the EUROFER melting point is reached on the FW and the subsequent ultimate failure of the FW channels determinates the plasma shutdown followed by a major disruption. At this point the Be-cover is already melted; high FW temperature in the overall wall thickness makes the failure of the TBM box with exposition of the beds to the VV atmosphere very probable.

In phase 3 the consequences in the long term have been examined by means of MELCOR and ANSYS calculation. Main differences of these two codes are summarized in Table 2, which cause different results. The ANSYS calculations are coupled to the MELCOR calculation that offers input parameters; the back coupling with high local temperature from the ANSYS calculation to the Be reaction in MELCOR is up to now missing.

Table 2: Comparison between MELCOR and ANSYS.

Item	MELCOR	ANSYS
geometry	Whole TBM in 4 CVs	A radial cell cut out of TBM in meshes (26182 nodes)
Heat transfer	1D	3D
HS for pebbles	Single pebble surface	block
Radiation between pebbles	modeled	cannot be modeled
Gas mixture behavior	accounted	cannot be accounted
Melting process	not required	cannot be modeled

Without the failure of the TBM box, the FW and TBM box can be well cooled down according to both MELCOR and ANSYS calculation. With the probable failure of TBM box, the MELCOR calculations show in every case that the long term cooling of the TBM can be assured without reaching melting in the pebble beds. On the contrary, the corresponding ANSYS calculations show undesirable local discontinuity effects that suggest the possibility of local melting of Be in the hot spots. To continue the investigation, refining control volume meshes

and its heat structures in MELCOR or developing an advanced coupling strategy among MELCOR and ANSYS should be taken into account.

T, dust and ACP that can be transported to the TCWS vault have been quantified and the low amount in the vault cannot affect the ITER safety.

The open issues in the definition of DBA and BDBA cases depending on the assumptions regarding the FPSS will be clarified in the future work.

The final report on this task has been finalized in November 2007.

Staff:

L. V. Boccaccini

X. Jin

Literature:

- [1] X. Jin, L.V. Boccaccini, R. Meyder, Preliminary study of accidental sequences following an ex-vessel LOCA for the HCPB TBM system safety assessment, internal report, FZK April 2007.
- [2] H.W. Bartels et al.: Safety Analysis Data List (SADL), Version 5.1.1, 2006.
- [3] ITER, pedigreed MELCOR182 for DBA and BDBA, June 2007.
- [4] X. Jin, L.V. Boccaccini, R. Meyder, Deterministic safety analysis of the reference accidental sequence for the European HCPB TBM system, ISFNT-8, Heidelberg, 2007.

## **DEMO Conceptual Studies**



**TRP-001  
PPCS He-cooled Divertor Concepts**

**TW6-TRP-001 D 1 + D 2  
He-cooled Divertor Development: Conceptual Design, Analysis, and Tests**

**1. Introduction**

Work carried out in 2007 (TW6-TRP-001) under cooperation with Efremov focused on the HHF He-loop experiments for 1-finger divertor mock-ups which are based on the reference design HEMJ [1] with jet impinging cooling (Fig. 1). It is based on the use of small hexagonal W tiles (18 mm width over flat) as a thermal shield and a sacrificial layer (5 mm thickness). They are brazed to a thimble ( $\varnothing 15$ , 1 mm wall thickness) made of WL10, thus forming a cooling finger, which is connected to the supporting structure made of Oxide Dispersion Strengthened (ODS) steel. To compensate the large mismatch in the thermal expansion coefficients of W and steel a transition piece is needed. The current transition piece design uses Cu casting with conical interlock (optionally, Co brazing). For HEMJ, a steel cartridge carrying the jet holes is placed concentrically inside the thimble. The number, size, and arrangement of the jet holes, as well as the jet-to-wall distance are important parameters. With the support of the Computational Fluid Dynamic (CFD) analyses [2] the following geometry was found suitable: 24 holes  $\varnothing 0.6$  mm and 1 center hole  $\varnothing 1$  mm, jet-to-wall spacing 0.9 mm resulting in maximum tile and thimble temperatures of about  $1700^{\circ}\text{C}$  and  $1170^{\circ}\text{C}$ , respectively, and a pressure loss ( $\Delta p$ ) of 0.13 MPa, under nominal design conditions (10 MW/m<sup>2</sup>, 6.8 g/s mfr).

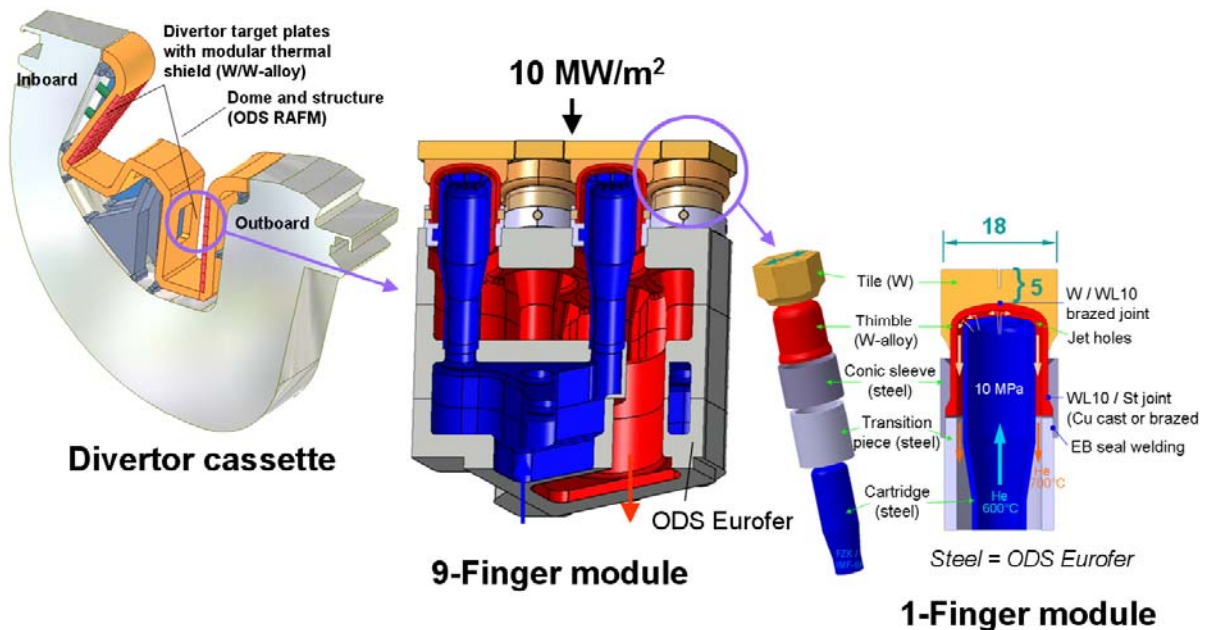


Fig. 1: He-cooled modular divertor designs HEMJ.

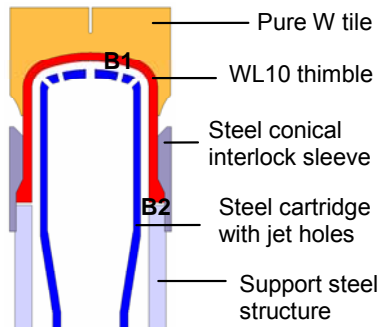
Further, HEBLO experiments for validation of computational fluid dynamics (CFD) codes; work on the Test Divertor Module (TDM) and on the manufacturing of a cooling finger (qualification and quality management) will be discussed in this report.

**2. Tungsten module design, fabrication and high heat flux tests**

The design principle [1] is the use of small hexagonal W tiles as a thermal shield and a sacrificial layer. They are brazed to a thimble made of W-1%La<sub>2</sub>O<sub>3</sub> (WL10) alloy, thus forming a cooling finger. The W cooling finger unit is fixed to the front plate of a supporting structure

made of oxide dispersion-strengthened (ODS) steel. To compensate thermal expansion coefficients mismatch between W and steel, a transition piece is necessary. The current transition piece is based on copper casting (alternative, cobalt brazing) with a conical interlock. The W finger module is cooled with helium at 10 MPa and 600°C/700°C (inlet/outlet temperatures). Based on the knowledge gained from previous technological investigations [3, 4], materials and joining methods for W modules manufacturing were defined in Table 1. Tile and thimble parts are produced from semi-finished rod material using regular machining procedures, e.g. turning, milling, grinding, and polishing. Nearly all geometry and materials of the components are conforming to the DEMO design, except the steel structure of the mock-up which is made of EUROFER instead of the designated ODS EUROFER material. For the joining of W tile and thimble, STEMET brazing material is used with a brazing temperature of 1050°C. For the joining of WL10 thimble with EUROFER, two solutions have been considered, the Cu cast and (optional) Co brazing in the conical interlock. The W and EUROFER mock-up parts were manufactured from full rod material by means of regular machining processes. Special cutting tools for turning the W tile and thimble are used.

Table 1: Definition of the tungsten modules fabrication for HHF tests.



Materials	
W tile	<ul style="list-style-type: none"> <li>Plansee W grade (modules #1, #7-20)</li> <li>Russian W grade (modules #2-6)</li> </ul>
W thimble	Plansee WL10 (W-1%La <sub>2</sub> O <sub>3</sub> )
Support structure	EUROFER
Joining methods	
W/W (B1)	Brazing with nickel-based filler metal STEMET <sup>®</sup> 1311, T <sub>br</sub> = 1050°C
W/Steel (B2)	Conical lock filled with cast copper Alternative: brazing with cobalt-based filler metal 71KHCP; T <sub>br</sub> = 1100°C

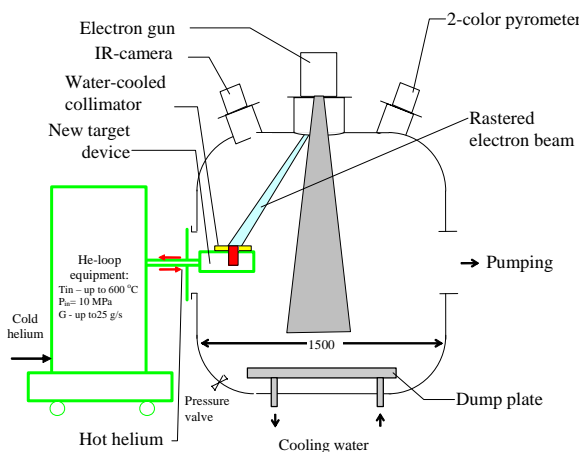


Fig. 2: The combined He loop and TSEFEY testing facility at Efremov.

The modules were tested in the TSEFEY facility combined with a helium loop (Fig. 2). It enables testing at a nominal helium inlet temperature ( $T_{He, in}$ ) of 600°C, an internal pressure of 10 MPa, and a pressure loss in the module of up to 0.5 MPa. In the first stage of the helium loop a stationary helium mass flow rate of 24 g/s was achieved by means of an oil-free membrane compressor. The target device with mock-up is moved to the right position in the

EB facility, schematically shown on the left). The EB is inclined at an angle, the power is pre adjusted by a water cooled calorimeter. The absorbed power is determined by the temperature rise of the helium. The temperature cycles were realized by switching beam on and off, default value is 30s and 30s.

### 3. HHF experimental results

The first experiment series performed in 2006 (Table 2) covered six mock-ups (five of HEMJ and one of HEMS types). The mock-ups were tested within an HHF range of 5–13 MW/m<sup>2</sup>. The heat flux is determined via the heat power absorbed in the He loop. The He cooling parameters are 10 MPa inlet pressure, ~ 500–600°C inlet temperature, and a varying mass flow rate in the range of ~ 5–15 g/s. The thermocyclic loading was simulated by means of switching the beam on and off (30s/ 60s as default cycle). The experimental results of this first testing campaign are reported in detail in [4, 5]. Altogether, it can be said that the performance of the He-cooled divertor concepts (HEMJ and HEMS) of 10 MW/m<sup>2</sup> was already demonstrated by the first experiment series. The results of destructive post-examinations revealed that W parts of these mock-ups and the thimble contain pre-existing defects, presumably by micro cracks initiated during the fabrication processes. Nevertheless, sudden destruction and/or completely broken mock-ups, i.e. brittle failure were not observed. No recrystallisation of W thimble was observed in any mock-up. The measured pressure losses were regarded optimistic compared to the calculated value (~50% overestimation). Four additional HEMJ mock-ups were fabricated; however, cracking occurred in the tiles of all four mock-ups during the brazing of the W tiles (W rod material from Plansee) with the thimbles. Therefore, these mock-ups were not brought to HHF tests.

Table 2: Results of the HHF campaign for 1 finger modules #1-5 (HEMJ) and #6 (HEMS) (1st test series, 2006).

Mock-up #	Cycle number @ heat flux (MW/m <sup>2</sup> ) / ((beam on/off cycles: default 30s/60s)	mfr (g/s)	T <sub>He</sub> In/Out (°C)	Δp (MPa) @ mfr
1 (C)	10 @ each 4.8, 6.2, 7.9; 2 @ 9.7 (→ cracks in tile & thimble, He leakage)	9.0	600 / 650	0.17
2 (A)	10 @ each 6, 10, 11.5, 12.5; 35 @ 9 (→ cracks in tile & thimble, He leakage)	13.5	520-580 / 540-630	0.38
3 (A)	10 @ 5.2; 10 @ 6.5; 5 @ 9; (→ cracks in tile & thimble, He leakage)	7.0	570-580 / 610-640	0.10
4 (A)	10 @ each 4, 6, 10, 11; 6 @ 13 (→ tile detached, no leakage)	13.5	520-570 / 550-600	0.32
5 (B)	10 @ each 3.8, 6, 7.3, 9, (i); 100 @ 9 / (15/15), (i); 24 @ 9 / (15/15), (ii); (→ cracks in tile & thimble, He leakage)	i) 13.5, ii) 7.0	580-605 / 600-635	i) 0.29, ii) 0.08
6 (D)	10 @ each 4.5, 5.7, 7.8, 9.5; 100 @ 9 / (30/30), iii); 100 @ 9 / (30/30), iv) (→ no damage, no He leakage)	iii) 10.0, iv) 7.5	600 / 650	iii) 0.50, iv) 0.3

	W tile	WL10 thimble	W-WL10 joint	WL10-EUROFER joint
A	non-castellated	Plansee grade	STEMET <sup>®</sup> 1311 brazing	Cu casting in conical lock
B	non-castellated	Plansee grade	STEMET <sup>®</sup> 1311 brazing	Co brazed conical lock
C	castellated	Plansee grade	STEMET <sup>®</sup> 1311 brazing	Cu casting in conical lock
D	castellated	Plansee grade	STEMET <sup>®</sup> 1311 brazing	Co brazed conical lock

For the following test series in 2007 [6, 7] technological/technical improvements have been made: a) the mock-up geometry was optimised to reduce the thermal stresses by means of finite element analyses FEM (Figs. 3, 4, mock-ups #17&18), b) new target device for 1-finger mock-ups was designed and manufactured which allows for changing the mock-ups without cutting and rewelding, and c) additional grinding process was applied after turning the W mock-up parts. In Fig. 4 ten HEMJ mock-ups (#11-20) manufactured for the second test series in 2007 are illustrated. The mock-ups #11 and 16 were used for the metallographic analysis without HHF tests. The results of the 2007 HHF tests are summarized in Table 3. Test conditions are: 10 MPa He, at 550°C inlet temperature, mfr = 9-13 g/s, thermal screening (thermal response) in the range of 6-10 MW/m<sup>2</sup> (few cycles per step), thermal cyclic tests at 10 MW/m<sup>2</sup> till damaging or for n ≤ 100 cycles without damages. A beam on/off sharp ramp of 30/30s was applied to all mock-ups for simulating the thermal cyclic loading, with the exception of the last test with mock-up#18, performed with a soft ramp (20s–up, 20s–hold, 20s–down, 20s–pause).

Table 3: Results of the HHF campaign for modules #11-20 (2nd test series, 2007).

Mock-up #	Cycle number @ heat flux (MW/m <sup>2</sup> )/(beam on/off cycles: default 30s/30s, soft ramp: 20s up, 20s hold, 20s down, 20s pause)	mfr (g/s)	T <sub>He</sub> In/Out (°C)	Δp (MPa) @ mfr
#11 (b)	Not tested			
#12 (b)	18 @ 10; gas leak at the central upper area of the tile, no significant visible damage	9-10	560-610	0.2 @ 9-10
#13 (c)	70 @ 9; gas leak at the central upper area of the tile, slight cracking of the tile top surface	9	570-620	0.19 @ 9
#14 (c)	90 @ 9; surface temperature increasing during cycling, tile detaching and melting, no gas leak	9	560-610	0.17 @ 9
15 (c)	Gas leak appeared between tile and conic sleeve during screening tests, no visible damages	9	550 / 590	0.17 @ 9
#16 (c)	Not tested			
#17 (b, d)	89 @ 10; experiment terminated after detection of tile temperature increase, no gas leak, no damage	9	570-620	0.18 @ 9
#18 (b, d)	102 @ 9.5; excellent performance, no damage, no leak, stable surface temperature from cycle to cycle	12.5	550-590	0.33 @ 12.5
19 (b)	Gas leak between tile and conic sleeve during first heating at 450°C and 8 MPa, cracks inside the thimble (vertical visible) and in thimble/conic sleeve brazing zone.			
20 (b)	Gas leak appeared between tile and conic sleeve during screening tests, no visible damages	9	550 / 590	0.17 @ 9

	W tile	WL10 thimble	W-WL10 joint	WL10-EUROFER joint
a	Russian W, non-castellated	Plansee grade	STEMET <sup>®</sup> 1311 brazing	Co brazed conical lock
b	Plansee W, castellated	Plansee grade	STEMET <sup>®</sup> 1311 brazing	Co brazed conical lock
c	Plansee W, castellated	Plansee grade	STEMET <sup>®</sup> 1311 brazing	Cu casting in conical lock
d	FEM optimized tile geometry			

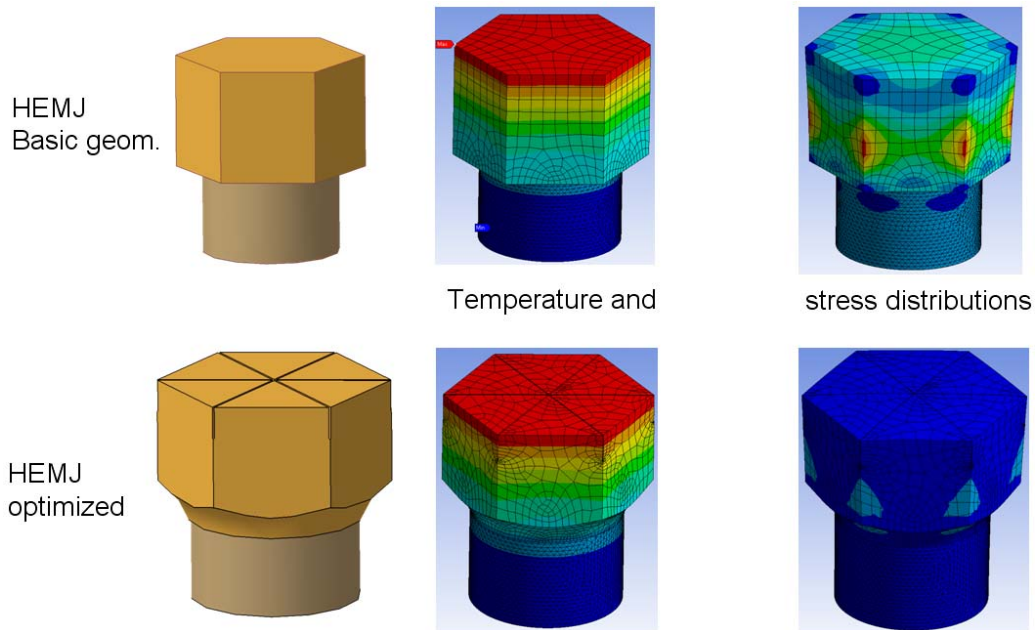


Fig. 3: Optimised 1-finger HEMJ mock-up in 2007.

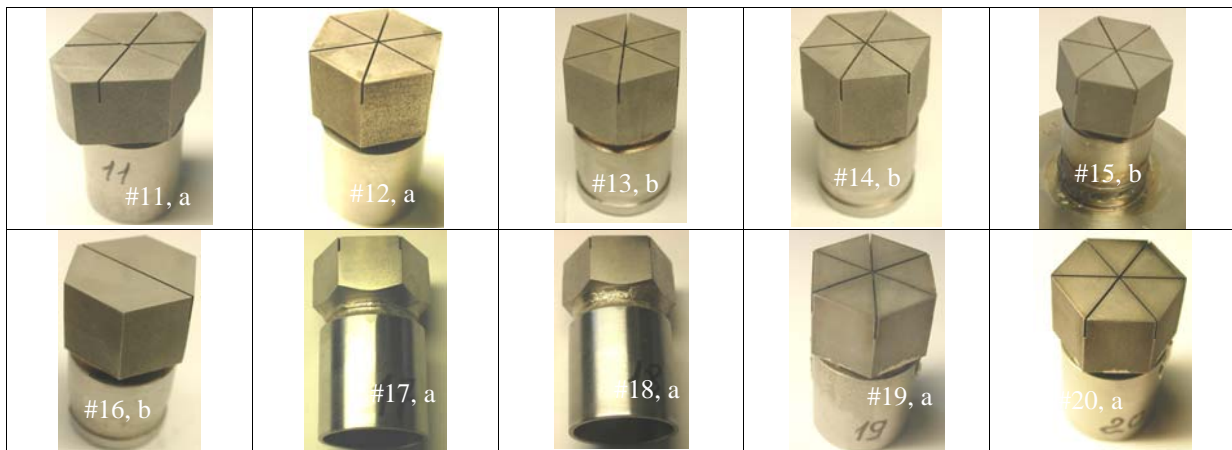
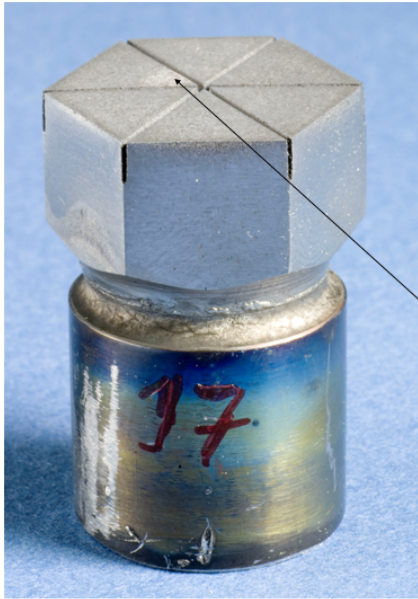


Fig. 4: 1-finger HEMJ mock-ups for 2007 HHF tests. Tile material: rod (Plansee, vertical grain orientation), regular machining of tile and thimble (turning and grinding). Thimble/conic sleeve joining: a) Co brazing (71KHCP, 1050°C), b) Cu cast (1100°C).

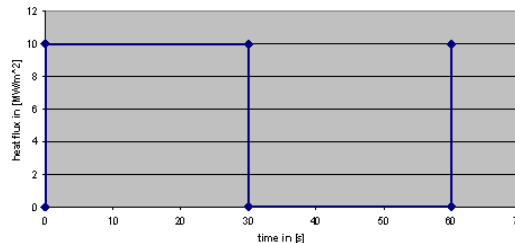
The 2007 experiments started with the mock-up #12 with a castellated W tile. Heat flux loading was applied to the mock-up surface at a constant mfr of  $\sim 9\text{-}10$  g/s. The mock-up survived 18 cycles at  $10\text{ MW/m}^2$ . Gas leak appeared at the central area of the loaded tile surface. No remarkable visible damages were detected. The following mock-up #13 with a castellated W tile survived up to 70 cycles at  $9\text{ MW/m}^2$  at mfr  $\sim 9$  g/s,  $T_{\text{He, in}} \sim 570^\circ\text{C}$ . Slight cracking of the tile top surface with gas leak were detected. Mock-up #14 (castellated) withstood 90 cycles at  $9\text{ MW/m}^2$ . Surface temperature increased during cycling. Finally the W tile detached from the thimble, which caused further overheating and melting of the W tile. The mock-ups #15, 16, and 19 were defective at the beginning during the screening tests (gas leak failure). The mock-up #17 with the optimised tile geometry was successfully tested at 89 cycles under  $10\text{ MW/m}^2$  (Fig. 5). The experiment was terminated after detecting tile temperature increase, no gas leakage, no damages. The measured pressure losses at 9 g/s mfr stayed in a range of about 0.16-0.18 MPa which agreed well with the values obtained from the first test series. The tile surface temperatures of these mock-ups during the tests interpreted from infrared pictures reached at a range between 1600 and  $1700^\circ\text{C}$ . The following mock-up #18 with the same geometry was subjected to the same heat load of  $10\text{ MW/m}^2$  but at an increased mfr of 12.5 g/s in order not to exceed the remelting temperature of the W-W

joint. In addition, a soft ramp which was regarded more realistic to the DEMO condition was applied in this test at the same time. This mock-up outstandingly withstood 102 thermal cycles without any damages.



Test conditions:

- 10 MW/m<sup>2</sup>
- 30s / 30s sharp power ramp



$T_{\text{He,in}}$  550°C, 10 MPa, mfr 7 g/s

- Tile temperature rise after 89 cycles\*  
--> tile probably partially detached.
- He Loop and thimble still intact.
- Post examination underway

\*n required ~ 100 - 1000

Fig. 5: Mock-up #17 (FZK optimised geometry) withstood 89 thermal cycles at 10 MW/m<sup>2</sup> without damage.

#### 4. Post examination

Post examination was performed at FZJ under cooperation with FZK. 9 1-finger mock-ups (#5, #11-17, and #20) were delivered by the FZK for post-examination at the FZJ. Results of this work will be presented in detail in [8].

All tile/thimble parts of the mock-ups were made of Plansee tungsten/WL10 with the exception of the mock-up #5 (1<sup>st</sup> series, 2006), its tile being made of a Russian tungsten grade. Except for the untested mock-up #11, all other mock-ups had been subjected to the maximum HHF between 7 – 11 MW/m<sup>2</sup>. Summarising the results, it can be noted that:

- The Russian tungsten grade (tile material) exhibits a better quality and performance than the Plansee grade in terms of pre-existing defects, less heat-affected microstructures after HHF tests, less developed surface cracks after HHF tests. It is recommended to qualify proper W grades for the use.
- Cracks exist on the tungsten surface after the final manufacturing step already (e.g. cutting by EDM). This was clearly seen on the top surface of the tile (Fig. 6) and of the castellated slots as well as at the ground of the castellation grooves. Hence, a careful W surface finishing (e.g. surface grinding, polishing by ECM) is strongly recommended.
- A thin layer of STEMET 1311 filler metal components was detected on the top tile surface of the HHF-tested mock-ups. This indicates that due to overheating in the W-W joint, the re-molten filler metal was transported capillarily through the cracks. In some cases, e.g. mock-up #5, holes/channels were created by erosion of W by molten braze filler metal. The loss of braze filler metal at the joint caused a detachment of tile/thimble and led to a further overheating of the tile. To prevent overheating of this joint region, use of another filler metal with a significantly higher brazing temperature than that of the STEMET 1311 is urgently recommended, preferably  $\geq 1300^\circ\text{C}$ . It is recommended to use softer and less reactive braze filler metal in the joint.

- The vertical grain orientation of thimble material WL10 could be a risk to cause gas leak easily.
- Cracks were always observed in the W-steel joint region of all mock-ups. Chamfering the upper shoulder of the conical sleeve could help reduce the thermal stresses in the same manner as applied to the rounded shoulder of the tungsten tile of the optimised mock-up #17.
- A thin oxide layer also was detected on the inner surface of the thimble. This was probably due to the contaminated He gas circulating in the loop.

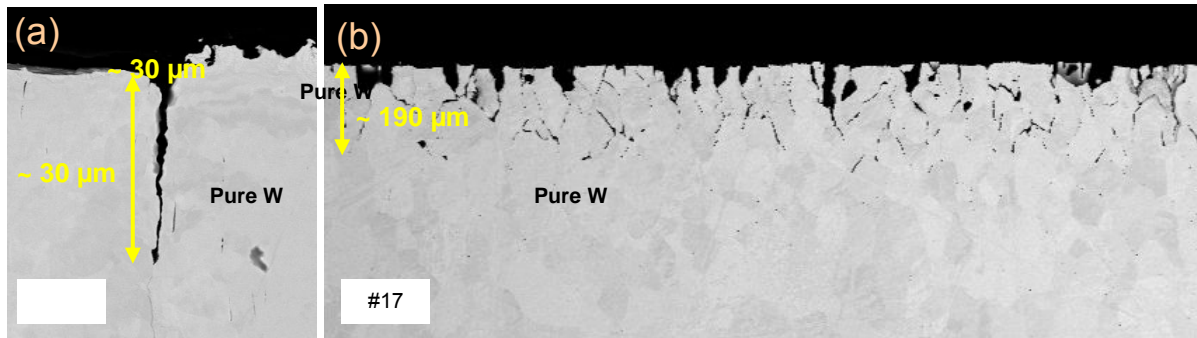


Fig. 6: Cracks on tile top surface after manufacturing, (a) #11, non-tested; (b) #17 after HHF testing [8].

## 5. HEBLO experiments for validation of computational fluid dynamics (CFD) codes

In 2006/07, a new 1:1 mock-up of the reference HEMJ concept was designed, manufactured and successfully tested in an air loop at the Georgia Institute of Technology, Atlanta [9]. The geometry nearly matches the original HEMJ geometry. The thimble (Fig. 7) was fabricated from free-machining brass; the tile was replaced by a copper part which contained a heater to simulate heat loads of up to 2 MW/m<sup>2</sup>.

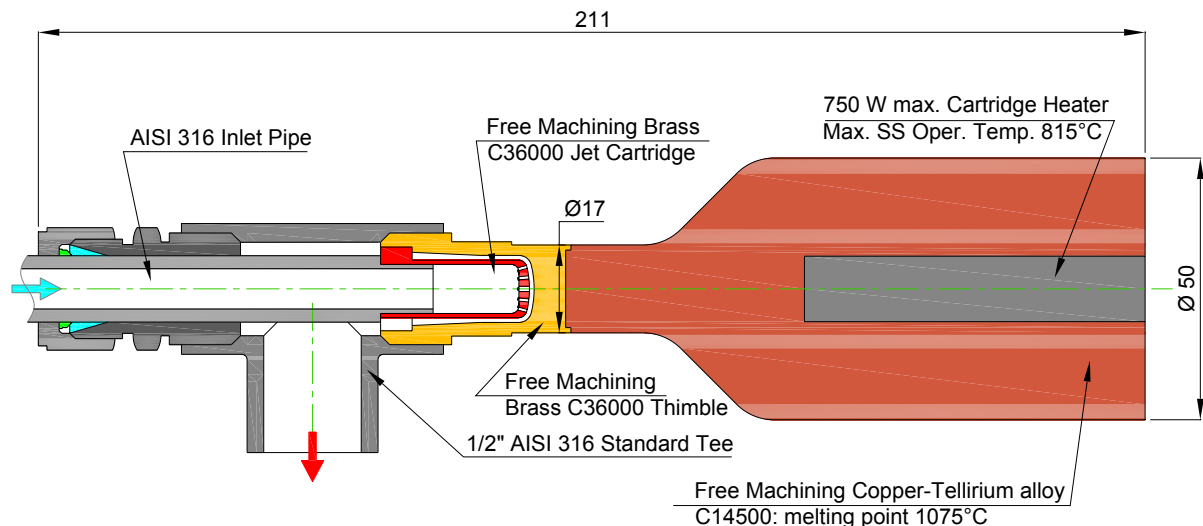


Fig. 7: The HEMJ divertor test section for code validation in HEBLO.

The mock-up was integrated into the helium loop HEBLO at FZK. The thermohydraulic conditions were adapted to come as close as possible to the real DEMO operation conditions. The objective of these experiments is to compare the experimental results for the temperatures and pressure loss with the simulated ones from a commercial CFD program (ANSYS CFX).

The agreement is excellent. The thermohydraulic code provides reliable results on the temperature distribution; the measured and simulated temperatures in the thimble differ by less than 1 K (Fig. 8). The pressure loss is about 30% overestimated by the CFD codes, which

fits the results obtained during the HHF tests at EFREMOV. Scaled to the real operating conditions of a divertor in a fusion power plant, a pressure loss of 1.0 bar per cooling finger would be obtained. Detailed results will be given in [10].

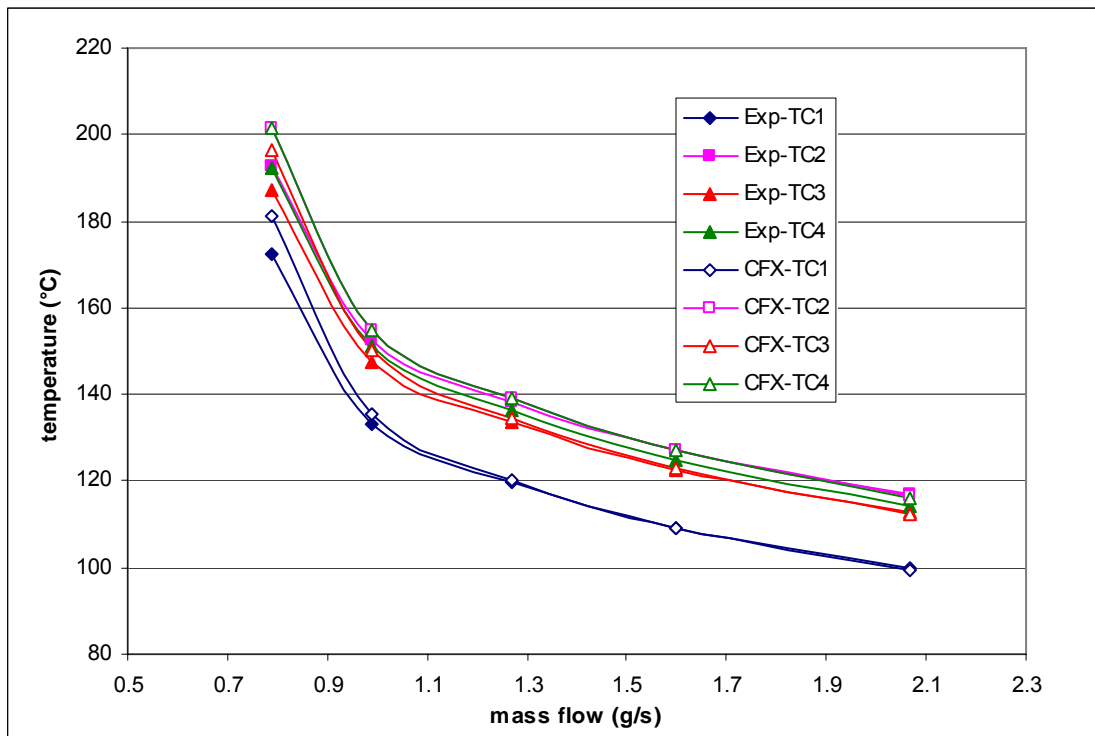


Fig. 8: Comparison of measured and simulated temperatures in the brass thimble of the mock-up for the case of a heat load of 1 MW/m<sup>2</sup>. Exp = experimental value, CFX = simulated value, TC1 = thermocouple 1, etc.

The outcomes of this investigation provide confidence in the results of the numerical model and its applicability to the design of the HEMJ divertor, as well as other gas-cooled high heat flux components at fusion reactor operating conditions.

## 6. Test Divertor Module (TDM)

First assessment of the TDM [11] was based on information obtained from the ITER water-cooled divertor, which was taken as a basis of the TDM helium-cooled cassette. A design adaptation was performed i.e. the outer vertical target (OVT) geometry and the change of fixed support. The first assessment includes also the dimensioning of the He tubes with material choice and the localization of the port, where the TDM will be tested.

As a continuation, the design of the target plate was investigated. The collectors for helium and the integration of the cooling system (header and manifold) in the outboard were carried out. Figure 9 shows the first assessment steps on the upper part and on the lower part, the new design from the outboard cladding over the detailed inner assembly up to the He flow path within the target plate [12]. Another new development is the optimization of the 1-finger-module [13], which withstood well 89 High-Heat-Flux cycles at 10 MW/m<sup>2</sup> (see above).

An examination and design of a coolant piping route, including the route from the OVT to the helium loop as well as the connection points in the biological shield, and a detailed layout and dimensioning of the He loop and controlling components is still in progress.

## TDM detailed integration

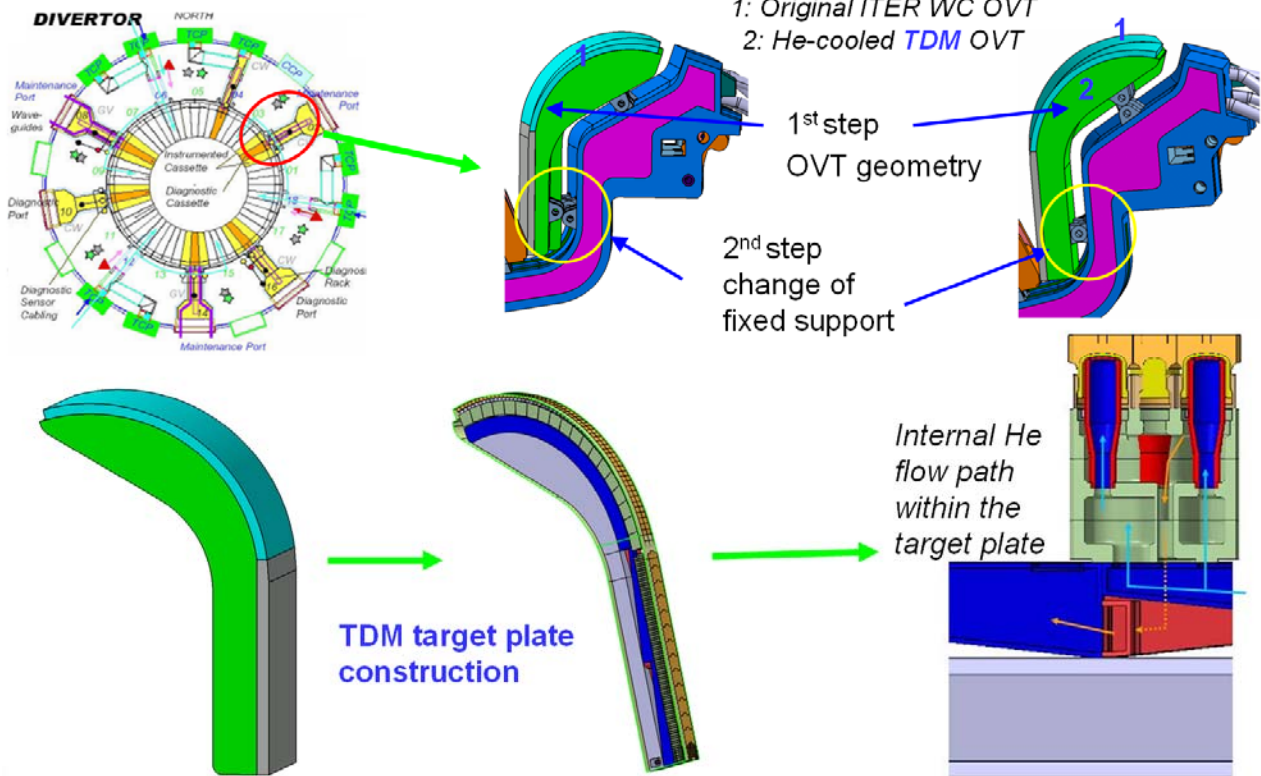


Fig. 9: Upper part: design adaptation of the He-cooled OVT for TDM, lower part: development of the detailed inner assembly of the target plate with He flow path within the target plate.

## 7. Manufacturing of a cooling finger: Qualification and Quality Management

In 2007 a quality management for the cooling finger has been launched at FZK. It includes the non-destructive testing (NDT) of the raw material and the brazed parts, the manufacturing of the tungsten parts, and the brazing of the finish sized parts. It is aimed to perform all manufacturing steps at FZK. For the NDT a cooperation with the University of Stuttgart for a feasibility study has been arranged.

This chapter will focus on the manufacturing of such a cooling finger unit at FZK. It will cover the machining of the tungsten tile as well as of the thimble, and the brazing of the parts. The major aim of this activity is, on the one hand, to obtain functioning mock-ups with high quality and high reliability, in particular in terms of minimising the surface roughness, cracks, and micro-cracks. On the other hand, effort should also be laid on realising the mass production from economic point of view.

### 7.1 Challenge: Machining of the Tungsten Parts (Turning, Milling, EDM, ECM at FZK)

The machining of tungsten requires experience because of the material's hardness and brittleness (460 [HV30] source Plansee).

The first priority of tungsten machining is the quality in terms of minimising micro-cracks or cracks and surface roughness. The second priority is the possibility of mass production, i.e. time and cost reduction.

The tungsten parts (tile and thimble) are made of a rod of 25 mm in diameter. The rod is fixed in a machining center, where turning and milling can be performed without any repositioning being required (see Fig. 10). The first inserts for turning were cut with cooling and cold machining in cooperation with Co. Sandvik Coromant. Parameters, such as the cutting

speed  $v_c$ , the feed  $f$ , the depth of the cut  $a_p$ , and the kind of cutting inserts (positive vs. negative, coated vs. uncoated, sintered vs. ground), were tested for rough machining and finishing. The investigation of the milling parameters covered cutting speed  $v_c$ , the feed  $f$ , the depth of the cut  $a_p$ , the use of cutting inserts, and the kind of milling (front vs. peripheral milling) for rough machining and finishing.



Fig. 10: Left: Different machining types to make the tile. Middle: Machining center. Right: First results.

The tile castellation (2.7 mm depth) was accomplished by EDM (electrical discharge machining) with a wire thickness of 0.25 mm. Unfortunately, EDM induces micro-cracks between 30  $\mu\text{m}$  and 150  $\mu\text{m}$  in wire cutting direction [14], which could be removed by ECM (electrochemical machining) [15].

It can be concluded that turning and milling may be used in mass production in contrast to die sinking (EDM). The castellation of the tile should not be done by EDM due to the micro-cracks formed. Other machining options are the cutting with a diamond wire or the use of ECM with a form cathode.

### 7.2 Brazing: Choice of the Filler Metal, Wetting Tests, Tensile Test Samples, Shear Test Samples and Die Set

The machined parts have to be brazed together. There are two brazing joints. The first joint is the brazing between tungsten and tungsten exposed to an operation temperature of 1200°C at the maximum and the second brazing joint is the brazing between tungsten and steel subject to an operating temperature of 700°C (see Fig. 1). Table 4 gives an overview over the possible filler materials. In the first step wetting tests have been performed with several filler metals in an induction furnace under vacuum (see Fig. 11). All filler metals used show good results.

Table 4: Filler metals tested for tungsten/tungsten and tungsten/steel brazing.

Filler metal				
<b>W-W</b>	PdNi ( $T_{br} = 1250^\circ\text{C}$ )	CuNi44 ( $T_{br} = 1300^\circ\text{C}$ )	NiTi10 ( $T_{br} = 1310^\circ\text{C}$ )	Ni ( $T_{br} = 1430^\circ\text{C}$ )
<b>W-St</b>	Cu ( $T_{br} = 1085$ )	Cu-based	STEMET1309 ( $T_{br} = 1150^\circ\text{C}$ )	Ni-based

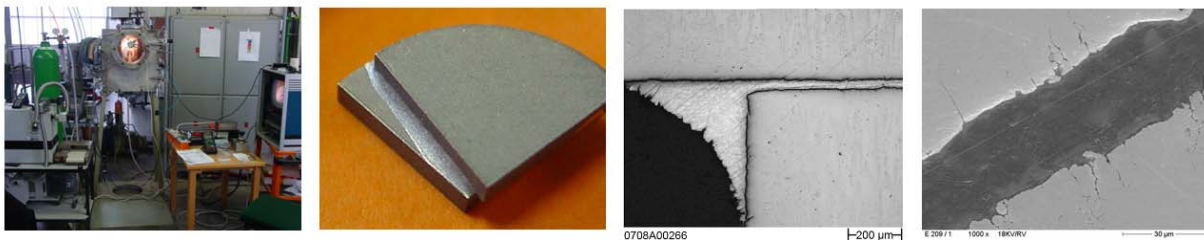


Fig. 11: Left: Induction furnace. Left middle: Wetting test with W-PdNi-W. Right middle: Metallography. Right: SEM.

After successful completion of the wetting tests, samples were brazed for tensile and shear tests (see Figs. 12 and 13). The tensile test samples are made of two finish-sized tungsten parts which are fixed in a ceramic holder ( $\text{Al}_2\text{O}_3$ ) during brazing. In order to guarantee reproducible brazing gaps of  $30\ \mu\text{m}$ , a tungsten wire of  $30\ \mu\text{m}$  is placed in-between. First tensile tests at RT showed a max. strength of  $500\ \text{N}/\text{mm}^2$ .

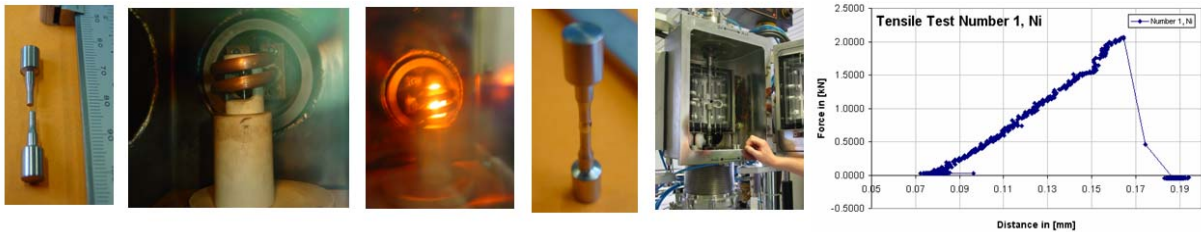


Fig. 12: Tensile test samples. Before, during, and after brazing. On the right side, the tensile test facility together with the data of a tensile test are displayed.

The shear test samples were made according to DIN 12797. The steel with a thread is pressed into a tungsten ring. At the top, a gap of  $300\ \mu\text{m}$  is left for the filler metal. After brazing, the press fit of the sample is cut by EDM and put into a holder made of TZM<sup>®</sup> (titanium, zirconium, and molybdenum). First shear tests at RT showed a max. strength of  $120\ \text{N}/\text{mm}^2$ .

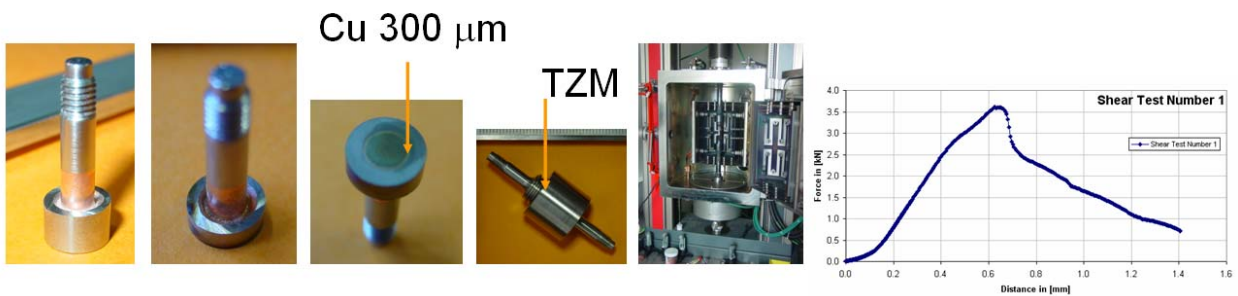


Fig. 13: Shear test sample and sample holder (DIN 12797). On the right, the test facility as well as the data of a shear test are shown.

Nevertheless the joining technology between tungsten and steel is a big challenge. That is why an assessment for a brazed joint between tungsten and steel was performed. A conical transition joint was investigated using the commercial software ANSYS<sup>®</sup> Classic by varying the cone angle. The evaluation criteria were on the one hand the shear stress in the brazing gas as well as the maximum plastic strain under thermocyclic loading (ratcheting or shake-down). The results show that a butt joint ( $90^\circ$ ) shows the best results in terms of both evaluation criteria [16].

## 8. Conclusions and outlook

The current step of work is aimed at the high heat flux tests of divertor mock-ups to demonstrate their fabricability and their performances. In cooperation with the Efremov Institute, a combined electron beam and He loop facility was built. Comprehensive technological studies were performed on W/W and W/steel joining of the divertor parts. First mock-up series were successfully fabricated and HHF tested in 2006. The 2006 results already confirmed performance of the divertor module under  $10\ \text{MW}/\text{m}^2$ . For the second test series in 2007 the mock-ups were further improved in view of thermal stress reduction as well as the manufacturing quality of the parts. This brought to a noticeable improvement in performance and resistance against thermal cyclic loadings. The last successfully tested mock-ups survived outstandingly more than 100 cycles under  $10\ \text{MW}/\text{m}^2$  without any damages.

Nevertheless, it became clear that the major reasons for the high failure rate of mock-ups generally lie in: a) base material quality, b) manufacturing quality (W turning, jet holes drilling,

EDM of W surfaces, etc.), c) overheating of the tile/thimble brazed joint leading to detachment, and d) induced high thermal stresses. Non-destructive testing is regarded indispensable measures for the verification/qualification of a) and b). A filler metal with a higher brazing temperature than that of STEMET® 1311 (e.g. CuNi 44,  $T_{br} = 1300^{\circ}\text{C}$ ) will be used [14] in further tests as a measure against c). Further design optimization is also required in particular for the W-steel joint region with a large mismatch, where cracks were always observed in all tested mock-ups. Work on qualification of W mock-ups exposed to high heat fluxes has been launched. The evaluation results of 1 finger mock-up tests will be used as a basis for completion of the 9-finger mock-ups and their following HHF tests.

A new 1:1 mock-up was tested in an air loop and in the helium loop HEBLO. The geometry was nearly the same as for the HEMJ design, the operation conditions were set as close as possible to DEMO operation conditions. The agreement of the experimental results for the temperatures and the ones simulated with a commercial CFD program was excellent. The code overestimated the pressure loss by 30%, which matches the results during the HHF tests. These results provide confidence in the application of simulation tools for the development of helium-cooled parts of fusion reactors.

After the first assessment of the TDM, including i.e. the design adaption of the OVT, the choice of the port or the dimensioning of the He tubes, the detailed design of the inner assembly of the target plate was investigated. The collectors for the helium and the manifolds were integrated into the target plate. Also the 1-finger-module was optimized by FEM calculations. Future work will be an examination of the cooling piping route as well as the dimensioning of the He loop for the TDM.

Furthermore a quality management for the cooling finger has been launched at FZK. This quality management includes the non-destructive testing (NDT) of the raw material and the brazed parts, the manufacturing of the tungsten parts, as well as the brazing of the finish sized parts. It is aimed to perform all manufacturing steps at FZK. For the NDT a cooperation with the University of Stuttgart for a feasibility study has been arranged. The assessment of tungsten machining using a machining centre in the main factory of the FZK has been started and the first results are promising. The wetting tests for tungsten/tungsten brazing and tungsten steel brazing have been successfully, and even the brazing of tensile and shear tests samples was a mentionable achievement. For 2008 two important goals are the brazing of complete cooling finger using a die set as well as the construction of a thermo cyclic experimental set-up working between RT and  $600^{\circ}\text{C}$ .

#### Staff:

L. Anselment  
N. Holstein  
W. Krauss  
R. Kruessmann  
G. Messemer  
V. Piotter  
J. Reiser  
P. Norajitra  
J. Reiser  
M. Rieth  
H.-J. Ritzhaupt-Kleissl  
R. Ruprecht  
V. Widak  
B. Zeep  
K. Zinn

## Literature:

- [1] P. Norajitra, R. Giniyatulin, T. Ihli, G. Janeschitz, P. Karditsas, W. Krauss, R. Kruessmann, V. Kuznetsov, D. Maisonnier, I. Mazul, C. Nardi, I. Ovchinnikov, S. Papastergiou, A. Pizzuto, P. Sardain, European Development of He-cooled Divertors for Fusion Power Plants, *Nucl. Fusion* 45 (2005) 1271-1276.
- [2] R. Krüßmann, Parametric study to evaluate the design options of the HEMJ divertor cooling concept by CFD simulations (Task TW4-TRP-001), Internal Report Forschungszentrum Karlsruhe/Fusion (2006), unpublished.
- [3] R. Giniyatulin, A. Gervash, W. Krauss, A. Makhankov, I. Mazul, P. Norajitra, Study of technological and material aspects of He-cooled divertor for DEMO reactor, 23rd SOFT, Venice, Italy, 20.–24.9.2004.
- [4] P. Norajitra, A. Gervash, R. Giniyatulin, T. Ihli, G. Janeschitz, W. Krauss, V. Kuznetsov, A. Makhankov, I. Mazul, I. Ovchinnikov, He-cooled divertor development: Technological studies and HHF experiments for design verification, Proceedings of the 21st IAEA Fusion Energy Conference, Chengdu, 16-21 October 2006, ISBN 92-0-100907-0 / ISSN 0074-1884.
- [5] P. Norajitra, W. Krauss, R. Kruessmann, V. Widak, A. Gervash, R. Giniyatulin, A. Kokoulin, A. Komarov, V. Kuznetsov, A. Makhankov, I. Mazul, I. Ovchinnikov, V. Smirnov, N. Yablokov, He-cooled Divertor Development: The Reference Design and High-Heat-Flux Tests of 1-finger Mock-ups (TW5-TRP-001), Internal Report Forschungszentrum Karlsruhe/Fusion (2006), unpublished.
- [6] P. Norajitra, A. Gervash, R. Giniyatulin, T. Hirai, G. Janeschitz, W. Krauss, V. Kuznetsov, A. Makhankov, I. Mazul, I. Ovchinnikov, J. Reiser, V. Widak, Helium-cooled divertor for DEMO: Manufacture and high heat flux tests of tungsten-based mock-ups, proceedings of the ICFRM-13, Nice, France, 10 –14.12.2007.
- [7] Compiled and edited by R. Giniyatulin, He-cooled target module mock-ups development for DEMO fusion reactor divertor (Contract No. DE/08626377/02/25 between Forschungszentrum Karlsruhe and EFREMOV Institute STC Sintez, St. Petersburg), interim report, November 2006, unpublished.
- [8] G. Ritz, T. Hirai, J. Linke, P. Norajitra, R. Giniyatulin, Post-Examination of Helium Cooled Tungsten Modules Exposed to Cyclic Thermal Loads, Proceedings of Jahrestagung der Kerntechnischen Gesellschaft Deutschland, Hamburg, Germany, May 2008, submitted.
- [9] J. B. Weathers, R. Kruessmann, S. I. Abdel-Khalik, L. Crosatti, D. L. Sadowski, Development of Modular Helium-cooled Divertor for DEMO Based on the Multi-Jet Impingement (HEMJ) Concept: Experimental Validation of Thermal Performance. Proceedings of the ISFNT-08, Heidelberg, Germany, Oct. 2007, submitted.
- [10] R. Kruessmann, G. Messemer, K. Zinn, New 1:1 mock-up for HEBLO: Design, layout, thermohydraulic simulation, and experimental validation of the mock-up built by Georgia Institute of Technology. Internal Report Forschungszentrum Karlsruhe/Fusion (2008), in preparation.
- [11] V. Widak, P. Norajitra, Assessment of the He-cooled Test Divertor Module (TDM) for ITER, Internal Report Forschungszentrum Karlsruhe/Fusion (2006).
- [12] V. Widak, P. Norajitra, L.V. Boccaccini, G. Janeschitz, Assessment of the He-cooled Test Divertor Module for ITER, proceedings of the ISFNT-8, Heidelberg, Germany, 01. –05.10.2007
- [13] V. Widak, P. Norajitra, He-cooled divertor: Optimisation of HEMJ finger geometry, Internal Report Forschungszentrum Karlsruhe/Fusion (2007), in progress.
- [14] J. Reiser, P. Norajitra, V. Widak, W. Krauss, He-cooled Divertor for Demo: Fabrication Technology for Tungsten Cooling Fingers, Proceedings of Jahrestagung der Kerntechnischen Gesellschaft Deutschland, Hamburg, Germany, May 2008, submitted.
- [15] W. Krauss et al., Strategies in electro-chemical machining of tungsten for divertor application, *Fusion Eng. Design* (2007), 1799-1805, article in press, doi: 10.1016/j.fusengdes.2007.06.029.
- [16] J. Reiser, P. Norajitra, R. Ruprecht, Numerical Investigation of a Brazed Joint between W-1%La<sub>2</sub>O<sub>3</sub> and EUROFER components, Paper at the ISFNT, Heidelberg, Germany, 2007

## **TRP-002 DEMO Physics Studies**

### **TW6-TRP-002 D 3 Development of an Improved Treatment of Plasma Radiation for Medium- and High-Z Impurities**

#### **Introduction**

The aim of this task is to extend the assessment of operation of a DEMO-sized tokamak at high core radiation using the current integrated 2D edge and 1.5 D core plasma model developed in EFDA Task TW5-TRP-002 [1] to include the effect of seed impurities on the SOL/divertor region and assess the additional coupling between core and edge thus introduced, as well as toward longer pulse operation. The task uses a 2D plasma edge code (B2-EIRENE) and a 1.5D core transport code (ICPS), which allows the radiation fraction in tokamak reactor scenarios to be analyzed and characterized in terms of edge and core plasma parameters, in particular to quantify the core impurity contamination associated with a given level of radiation. The task is carried out with the integrated modelling as described in more detail in [2], in the previous Annual report [3], and in [4].

#### **2. Core Plasma Modelling**

In the previous work on this task, the implications of impurity-seeding on long-pulse operation of DEMO were investigated using the reference model of [1], i.e. with neoclassical transport of particles in the absence of an anomalous pinch. Four different impurities were modelled ranging from medium-low to medium-high Z (neon to xenon). The additional heating power, which could also be used to drive current, was held fixed at 50 MW, while the fuelling was adjusted so as to obtain a fusion power of 3 GW, resulting in an essentially ignited plasma ( $Q=60$ ). Power deposition profiles were either peaked near the mid-radius (at 0.4 minor radius) or far off-axis (at 0.7 minor radius). The effect of a modest decrease of plasma current from the nominal 21 MA to 18 MA was also investigated.

The gas puffing and impurity seeding were adjusted so as to operate at 70% of the edge-based pressure limit at a peak power load of 5 MW/m<sup>2</sup>.

For the same fusion power, the normalized beta increases from 2.6 to a moderately optimistic value of 3.1. Whereas the ratio of density to Greenwald limit increases from 1.1 to 1.3, the density remains at 0.7 of the edge-based density limit.

The burn duration, assuming 100 Vs available for burn at 21 MA, is approximately 3000s in the absence of impurity seeding and current drive, and is reduced to 1800 s by neon seeding (the decrease is less for higher Z impurities). Reduction of the plasma current to 18 MA extends the burn duration with neon seeding to 4000s in the absence of current drive, 10000 s with near-axis current drive, and 25000 s with off-axis current drive. Increase of the Z of the seed impurity to xenon then yields a burn duration of ~50000 s at these conditions.

In the previous Annual Report, the requirements for further work were identified. The inclusion of the effect of the seed impurity on the SOL/divertor region was considered especially important because of the resulting strong coupling between core plasma and divertor operation. This has been confirmed by the results of ongoing ITER simulations. Further work on this task for DEMO has been suspended until these ITER simulations are further advanced (see next section).

### 3. Divertor Plasma Modelling

As reported SOL/divertor simulations require the complete nonlinear neutral model with heavier impurities, for which convergence is very slow even for the ITER conditions for which the model is presently being developed. Further work on this task also requires implementation of parallel processing of EIRENE since the convergence under DEMO conditions is otherwise too slow. Both developments are being actively pursued.

### 4. Perspectives

The task has followed up on Task TW5-TRP-002.D2. The present task has been ongoing since September 2006. Further work is indicated in the two sections above.

#### Staff:

H. D. Pacher (INRS-EMT, Varennes, Québec, Canada)  
G. W. Pacher (Hydro-Québec, Varennes, Québec, Canada)  
A. S. Kukushkin (ITER Organization)  
G. Janeschitz  
I. Landman  
S. Pestchanyi - with the collaboration of G. Pereverzev (IPP Garching)

#### Literature:

- [1] Pacher H.D., Pacher G.W., "Task TW5-TRP-002.D2 DEMO Physics Studies, D2 Analysis of total radiation in tokamak reactor scenarios", this Annual Report (Systems Studies Section)
- [2] Pacher H.D., Pacher G.W., in collaboration with ITER IT Garching, FZ Karlsruhe, Max-Planck-Institut für Plasmaphysik Garching, EFDA CSU Garching, "Divertor and core plasma modelling for ITER - Final Report June 2006", INRS Energie, Mat. et Télécom. Report, INRS-EMT-029-0606, June, 2006
- [3] Pacher H.D., Pacher G.W., "Divertor and Core Plasma Modelling for ITER", FZK Annual Report 2006 (Physics Section)
- [4] Pacher H.D., Pacher G.W., in collaboration with ITER IT Garching, FZ Karlsruhe, Max-Planck-Institut für Plasmaphysik Garching, EFDA CSU Garching, "Divertor and core plasma modelling for ITER - Final Report June 2007", INRS Energie, Mat. et Télécom. Report, INRS-EMT-038-0607, June, 2007

## TRP-005 Neutronic Analysis

### TW6-TRP-005 D 1 TBR and Shielding Analyses for the HCPB DEMO Reactor

The objectives of Task TW6-TTRP-005, Deliverable 2, were (i) to proof the ability of the HCPB blanket concept developed for DEMO to achieve tritium self-sufficiency, (ii) to proof the capability of the internal components and the vacuum vessel to provide sufficient shielding, and (iii) to provide the nuclear power generation data required for the thermo-hydraulic layout of the DEMO reactor(s).

Assessments of the shielding requirements were performed with the objective to minimize the radial dimension of the shield system and verify the specified reactor parameters. The related shielding analyses were conducted on the basis of 3D shielding calculations with the MCNP code employing a modified version of the PPCS reactor model AB (HCLL reactor). A minimum radial thickness of 65 cm was recommended for the inboard shield system of the HCLL DEMO reactor consisting of an efficient radiation shield including tungsten carbide, water and steel, and the vacuum vessel. The required total thickness of the inboard system is at 115 cm assuming 50 cm for the HCLL blanket and 30 cm for the manifold system. It was also shown that an integrated inboard shield system consisting of a 50 cm thick vacuum vessel (providing major shielding functions) and a thin 15 cm thin radiation shield is sufficient to protect the superconducting TF-coil. The re-weldability of in-vessel components is, however, crucial and limits the lifetime of the vacuum vessel to 10 full power years assuming a total helium production of 1 appm.

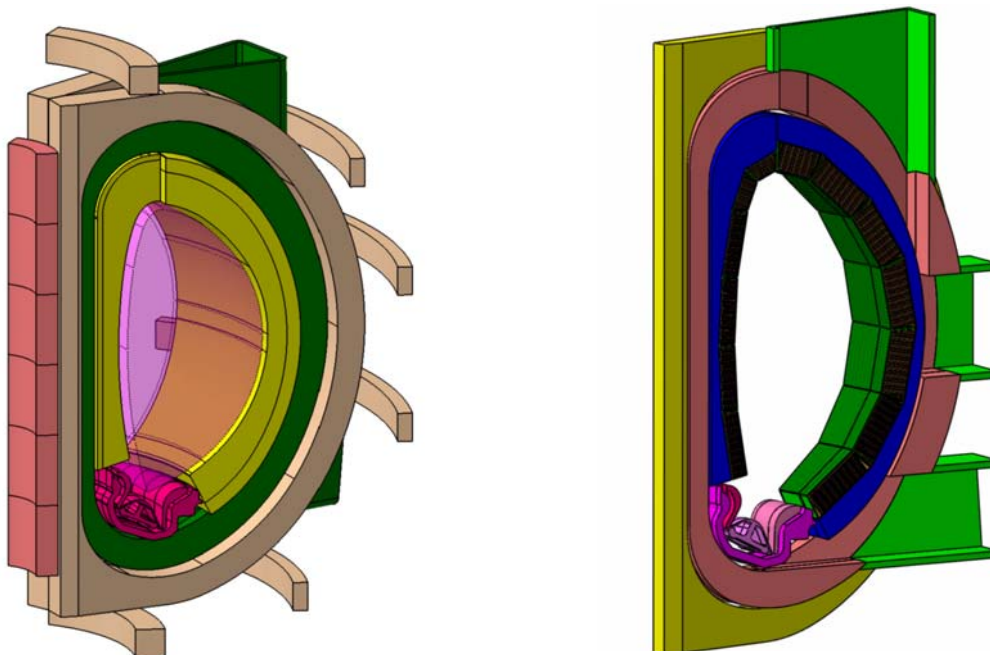


Fig. 1: DEMO reactor models: CAD model provided by EFDA (left) and MCNP torus sector model (11.25°) with integrated HCLL blanket modules (right).

Based on these results a generic set of reactor parameters was defined by EFDA to provide the basis for a DEMO reactor model with HCLL, or, alternatively, HCPB blanket modules. By making use of the interface programme McCAD of FZK, an MCNP torus sector model was generated from the underlying CAD model provided by EFDA. HCLL blanket modules were integrated to this model on the basis of an engineering design model of the HCLL blanket provided by CEA Saclay, see Fig. 1 for the CAD and MCNP models. According to the agreed approach for the neutronic analyses, this model will be also adapted by FZK for the HCPB

blanket concept and provided to ENEA Frascati for the adaptation and analyses of the DCLL and WCLL blanket concepts. The neutronics analyses for the HCLL and HCPB will be again conducted by FZK.

Staff:

U. Fischer  
P. Pereslavitsev  
S. Stickel  
H. Tsigé-Tamirat

## EFDA/06-1454 (TW6-TRP-007) DEMO Conceptual Design – FZK Contribution

### Objectives

The main lines in the European breeder blanket development are the ceramic breeder and the liquid metal breeder blanket. In both cases the breeder blankets are cooled by helium gas whilst the different breeder materials result in different Tritium extraction and circulation systems (purge gas for ceramic breeder and liquid metal for the liquid metal blanket).

The Forschungszentrum Karlsruhe (FZK) breeder blanket development is predominantly focussed on the ceramic breeder blanket, namely the HCPB (helium-cooled pebble bed) concept, but nevertheless also studies for the HCLL (helium-cooled lithium lead) concept were carried out. In addition in continuation of the long experience in the area of dual coolant blanket concept, which was developed at the FZK in the 1990th a new version of the concept has been investigated with special regard to the Multi-Module-Segment (MMS) integration concept.

The engineering activities in the view of DEMO are substantially broadened towards overall reactor integration including the development of radial build and shielding concepts, mechanical layout and attachment systems, maintenance schemes, piping concepts and the development of the according remote handling systems as well as considerations on electrical power generation.

The MMS concept consisting of a “banana” back-plate supporting a number of smaller modules is the most promising integration concept for DEMO reactor and has been analysed.

### HCPB Blanket Concept: Attachment of Multi Module Segment (MMS) to Hot Ring Shield (HRS)

An analysis of the integration of the HCPB blanket into a DEMO device with the MMS concept has been done. The conceptual design developed by FZK considering the possibility of a HRS directly connected to the MMS is shown in Figure 1. The strong manifold constitutes the supporting structure carrying blanket modules. The stiffness of the manifold that is realized by introducing a strong manifold box and back plate is a key element of this concept (Figure 2). The Helium pipes are vertical through the upper part of the manifold since the pipes are lead through the upper ports of the reactor (Figure 3 and 4). It is a conceptual advantage that the permanent self-supported shield structure can be operated at the same temperature as the MMS structure. Thus relative thermal expansions are of minor importance and a design of an attachment relying on shear keys with low clearances and bolts is possible. The attachment comprises upper, middle and lower shear keys.

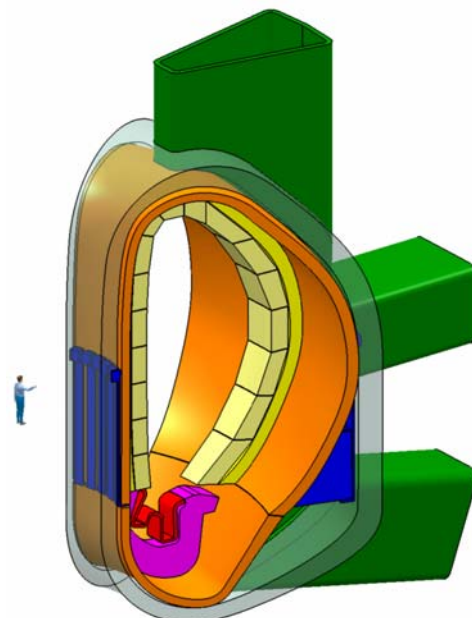


Fig. 1: Layout of the DEMO FZK concept with hot ring shield, manifold and blanket modules.

The MMS have to be inserted under restricted geometric conditions due to limited in-vessel design space by vertical and rotational movements (see Figure 5).

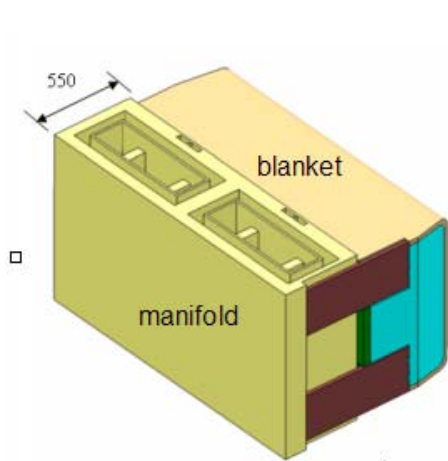


Fig. 2: Manifold layout.

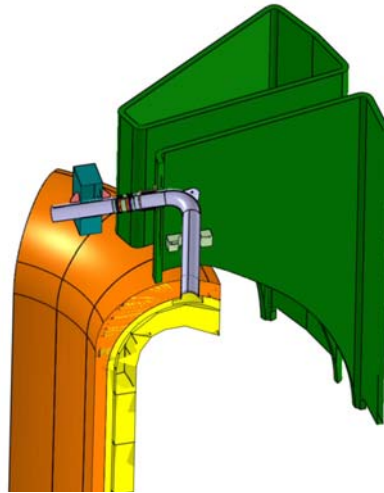


Fig. 3: Layout of the upper ports.

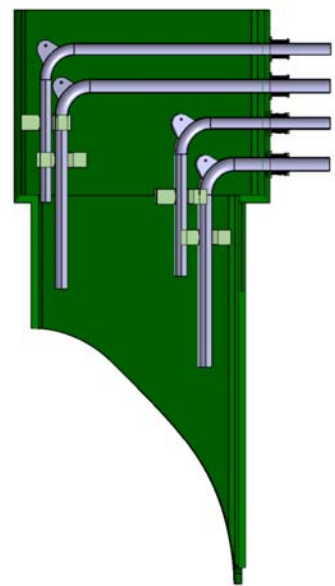


Fig. 4: Layout of the upper ports.

After the insertion, the attachment is locked by bolts at the lower end of the MMS where the access is possible as the divertor is disassembled during this procedure. A sketch to illustrate the principle with shear keys and tensioning by bolts is given in figure 6 and 7. This principle of attaching the MMS to the HRS is a result of investigating different possible solutions and judging their advantages and disadvantages. The attachment of the MMS to the HRS has to reliably support the gravity loads and the more severe dynamic electro-magnetic (EM) loads during disruptions. The basic dimensioning of the joining elements, assuming different normal (gravity loads) as well as off-normal load cases (EM loads), determine the design.

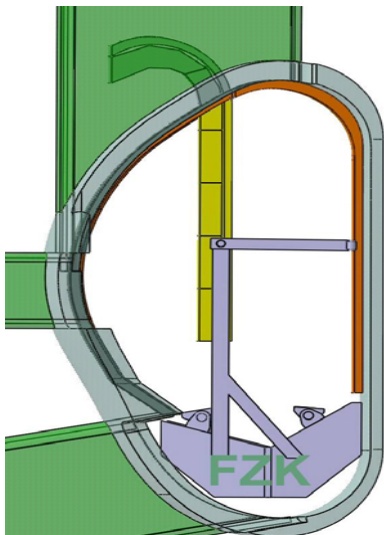


Fig. 5: MMS insertion through the upper port.

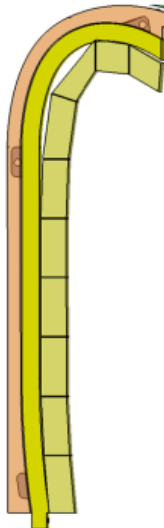


Fig. 6: MMS with 3 keys attached to the hot ring shield.

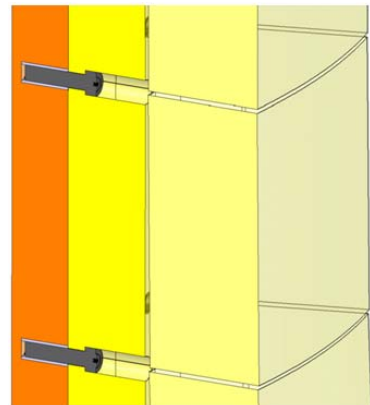


Fig. 7: MMS attached.

### DCLL Blanket Concept using the Segmentation Concept

A new design approach for a DEMO relevant MMS Dual Coolant Lithium Lead (DCLL) blanket was studied (Figure 8). The concept seems to have the potential to fulfil the requirements in term of mechanical strength and a promising hydraulic lay-out could be derived. Open issues remain especially in the following areas:

- Behaviour of the flow channel inserts under operational conditions.
- Tritium extraction from the hot breeder stream.
- Tritium permeation into the Helium stream.
- Detailed Magneto-Hydro-Dynamic (MHD) pressure loss in 3D geometries to be determined and adjusted.
- Integration of the MMS-DCLL blanket into the reactor, especially providing a suitable attachment system.

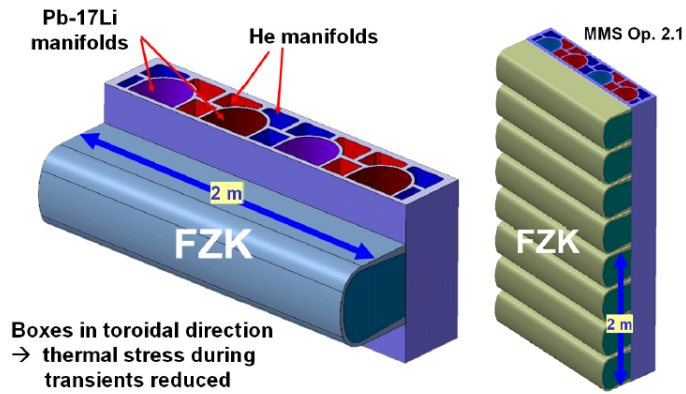


Fig. 8: DCLL blanket layout.

- Need of advanced power conversion cycle (better than Helium Brayton Cycle) to offer significant improvements over the HCPB equipped plant. While a number of promising new approaches and proposals for the DCLL blanket were presented, it is evident that further work will be necessary to develop more detailed design solutions and allow for final judgments on feasibility and performance. From the results available and under the precondition that reliable high temperature high efficiency power conversion cycles won't be developed in time for DEMO, it seems not reasonable to expect improvements in regard on the DEMO efficiency, if a DCLL blanket is used instead of HCPB blanket, while still a DCLL based DEMO could offer a better plant efficiency than the HCLL equipped version.

### In-vessel Integration of the HCPB Blanket Concept

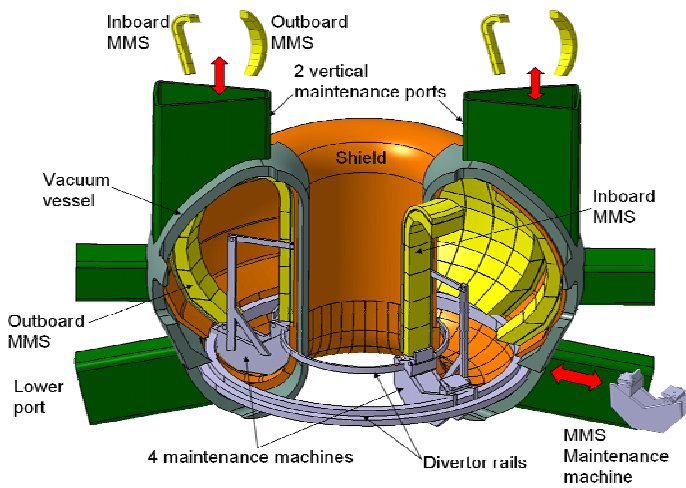


Fig. 9: In-bore tools

A blanket maintenance concept for DEMO was developed considering a multi-module segment (MMS) blanket and vertical ports for inserting and removing the MMS. Each MMS consists of a number of blanket modules, which are connected to a strong vertical manifold structure by use of a flexible attachment system and concentric hydraulic connections in the zero point of the relative motion between blanket module and manifold. The MMS are transported toroidally in the

vacuum vessel by a remote handling transport machine located in the divertor region (Figure 9). The transport machine is equipped with sliding carriage systems for the movement of the inboard and outboard MMS in transverse radial/poloidal direction. In the final position the MMS are bolted onto a permanent self-supporting shield structure, which is operated at nearly the same temperature as the MMS manifold structure. The shield structure is toroidally closed and can expand fairly unconstrained during heat up within the vacuum vessel. The maintenance time can be strongly reduced in comparison to a separate module maintenance scheme, the flexible attachments and hydraulic connections between the blanket modules and the manifolds could be done outside the reactor, large flexible attachment sys-

tems between vertical segments and cold components are not needed, a small number of ports have to be opened for maintenance, only relatively simple and low accuracy remote handling steps are necessary for the large components and a small number of independent units have to be handled. A drawback of the MMS system is the increased waste volume (manifolds behind the blanket modules are likely not re-weldable due to He production in the steel). The thermal compensation system needed for Helium pipes to cope with the differential expansions of pipes and surrounding low temperature structure was investigated in detail and a high pressure multi-layer compensator system was proposed to be applied.

Thermo-mechanical analyses of the MMS and shield components have been performed by Finite Element Modeling (FEM) and some results are shown in Figure 10.

Advantages of this maintenance concept are:

- The maintenance time can be strongly reduced in comparison to a separate module maintenance scheme.

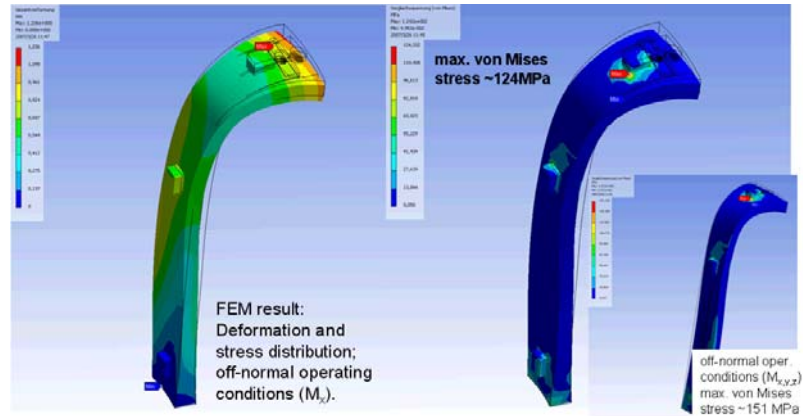


Fig. 10: FEM analyses of the MMS.

- The flexible attachments and hydraulic connections between the blanket modules and the manifolds could be done outside the reactor
- Large flexible attachment systems between the vertical segments and the cold components are not needed.
- Only a small (two/four) number of ports have to be opened for maintenance.
- Only relatively simple and low accuracy remote handling steps are necessary for the large components.
- A small number of independent units have to be handled.

Staff:

- L. Bühler
- D. Filsinger
- U. Fischer
- T. Ihli
- C. Köhly
- E. Magnani
- J. Rey
- P. Pereslavitsev
- C. Polixa
- D. Nagy (Visiting scholar at FZK from HAS, KFKI-Research Institute, Budapest, Hungary)

## **TRP-012**

### **Optimisation of a Fusion Power Plant for the Production of Hydrogen**

#### **TW6-TRP-012 D 1b**

### **Optimisation of a 'Start-up' Scenario where the Power is less than 100 MW**

#### **1. Introduction**

The aim of this task is to optimise the "start-up" of a DEMO-sized tokamak including the L- to H-mode transition with auxiliary power below 100 MW. The task is carried out with the integrated modelling based on a 2D plasma edge code (B2-EIRENE) and a 1.5D core transport code (ICPS), as described in more detail in [1] and [2]. The present task has been active since the autumn of 2006.

#### **2. Initial Plasma Modelling**

The geometric parameters chosen for the DEMO modelling task are similar to those of ITER as developed in the Conceptual Design Activity (1991) ( $B=5.7T$ ,  $R=8.1m$ ,  $a=2.8m$ ,  $\kappa=1.7$ ,  $\delta=0.36$ ). (see Figure in [4]).

The ICPS model for core plasma transport in the connected work described in [3], [4] is a time-dependent model. For the work described in the previous annual report, accelerator algorithms had been introduced to obtain more rapid convergence to quasi-steady-state conditions. Removal of these algorithms, as required for the present task, has commenced.

Work on this task had to be suspended, initially to pursue the investigation of ITER operating windows in the framework of the ITER design review, but particularly to improve the edge model in the presence of heavier impurities. This improved model is being developed first for ITER conditions. This task also requires implementation of parallel processing of EIRENE since the convergence under DEMO conditions is otherwise too slow. Both developments are being actively pursued.

#### **3. Perspectives**

When the improved SOL/divertor impurity model is available, the ramp-up of plasma current from ~5 MA onwards and the concurrent rampup of density and auxiliary power will be optimised using the ICPS model in ASTRA so as to obtain an L- to H-mode transition with an auxiliary power below 100 MW. Simplified boundary conditions will be used while the plasma is in the limiter configuration and the full integrated model for core and edge will be used after transition to the diverted geometry.

#### Staff:

H. D. Pacher (INRS-EMT, Varennes, Québec, Canada)

G. W. Pacher (Hydro-Québec, Varennes, Québec, Canada)

A. S. Kukushkin (ITER Organization)

G. Janeschitz

I. Landman

S. Pestchanyi - with the collaboration of G. Pereverzev (IPP Garching).

#### Literature:

- [1] Pacher H.D., Pacher G.W., in collaboration with ITER IT Garching, FZ Karlsruhe, Max-Planck-Institut für Plasmaphysik Garching, EFDA CSU Garching, "Divertor and core plasma modelling for ITER - Final Report June 2006", INRS Energie, Mat. et Télécom. Report, INRS-EMT-029-0606, June, 2006

- [2] Pacher H.D., Pacher G.W., in collaboration with ITER IT Garching, FZ Karlsruhe, Max-Planck-Institut für Plasmaphysik Garching, EFDA CSU Garching, "Divertor and core plasma modelling for ITER - Final Report June 2007", INRS Energie, Mat. et Télécom. Report, INRS-EMT-038-0607, June, 2007
- [3] Pacher H.D., Pacher G.W., "Divertor and Core Plasma Modelling for ITER", this Annual Report (Physics Section)
- [4] Pacher H.D., Pacher G.W., "Task TW5-TRP-002.D2 DEMO Physics Studies, D2 Analysis of total radiation in tokamak reactor scenarios", 2006 Annual Report (Systems Studies Section)

## TW6-TRP-012 D 2

# Assessment of the Impact of a Fusion Power Plant for H<sub>2</sub> Production on Internal Components

## Objectives

Studies carried out in the EU on fusion power plants have focused so far on electricity production. Another important alternative is the production of hydrogen in view of a hydrogen economy (e.g. heating and transportation). The objectives of the present study are the optimization of the design of a fusion plant for the production of hydrogen rather than electricity – a Hydrogen Production Fusion Power Plant (HPFPP).

The scope of the work performed under this DEMO technology subtask comprises the following more or less independent aspects: 1) The impact on the design of internal components of an HPFPP, including possible alternative blanket layouts. 2) Cooling fluid(s), in particular the possible use of CO<sub>2</sub> rather than He. 3) The impact of pulsed operation on the design of the mechanical structures.

## 1) Design of Internal Components

Breeding blankets are key components of fusion power plants and determine to a large degree their attractiveness. Regardless of other aspects, the key parameter to judge the attractiveness of a blanket concept is the prognoses of the achievable outlet temperature. The outlet temperature determines the choice of the most appropriate cycle for energy production and its efficiency. Therefore it also determines the most decisive value of a power plant, namely the cost of electricity. The blanket outlet temperature determines the possible processes for hydrogen production from fusion power and it also determines the thermal-to-hydrogen conversion efficiency to be expected. The blanket outlet temperature is an indicator to assess the impact of a HPFPP on the design of internal components.

An overview of applicable hydrogen production processes is given and their requirements on process temperature are specified. The presented processes were selected considering conceivable technical feasibility and sufficient efficiency. Thermo-chemical water splitting is the conversion of water into hydrogen and oxygen by a series of thermally driven chemical reactions (Figure 1). Currently the leading alternatives for thermo-chemical hydrogen production are the Westinghouse Hybrid Sulphur Process (WSP) and the Sulphur-Iodine Process (SI).

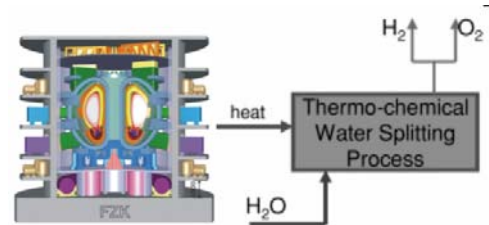


Fig. 1: Schematic of thermo-chemical water-splitting process for hydrogen production coupled with a fusion reactor.

Of particular interest for the presented study is the process in which High Temperature Steam Electrolysis (HTSE) is coupled with an Advanced Gas cooled fission Reactor (AGR). The HTSE average process temperature is 900°C, whereas the reactor exit temperature and the SCO<sub>2</sub> cycle turbine inlet temperature are: 550°C to 700°C. The 900°C at the HTSE unit, which is higher than the reactor exit temperature, is achieved with recuperative and electrical heating. With direct coupling between the power conversion cycle (supercritical CO<sub>2</sub> recompression Brayton cycle) and the reactor it should be possible to achieve 39% to 48% of net hydrogen production energy efficiency in the temperature range between 500 and 600°C.

Therefore can be stated that the HTSE process seems to be the best solution for a typical fusion reactor where the exit temperature is limited due to technological requirements or limitations (Figure 2 and 3).

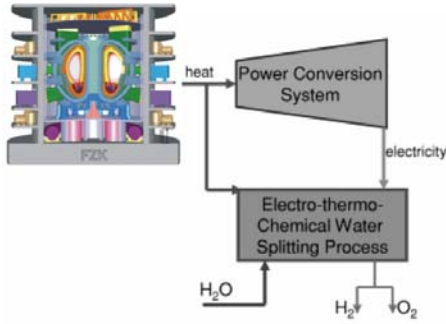


Fig. 2: Schematic of High Temperature Steam Electrolysis (HTSE) process for hydrogen production coupled with a fusion reactor.

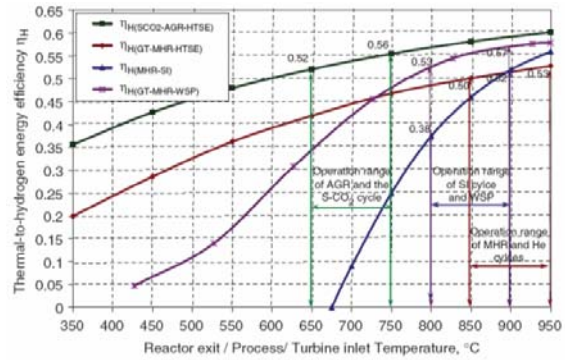


Fig. 3: Thermal-to-Hydrogen production efficiency vs. reactor exit temperature.

## 2) Cooling Fluids: CO<sub>2</sub> – Helium Comparison

Helium is the current choice of coolant for DEMO. The decision to use it in large power plants will probably rest not only on thermodynamic considerations; for instance, a satisfactory solution of the practical problem of sealing the system at the high pressures is required. Experience with sealing high-pressure carbon dioxide in gas-cooled reactors has shown that leakage is substantial, and helium, being a lighter gas, will be even more difficult to contain.

Moreover, the required pumping power for the coolant is of high relevance since it directly reduces the achievable output power.

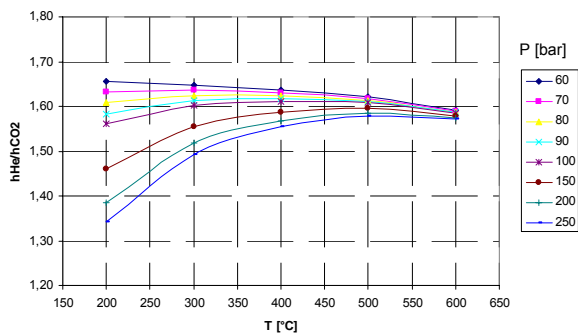


Fig. 4: Heat transfer coefficient ratio for helium and CO<sub>2</sub>.

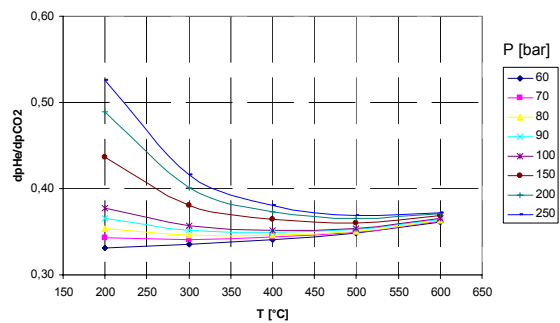


Fig. 5: Pressure losses ratio for helium and CO<sub>2</sub>.

In Figure 4 it can be seen that the ratio  $h_{He}/h_{CO_2}$  is always above unity, meaning that the heat transfer coefficient for He assuming the same thermodynamic conditions ( $p, T$ ) and the same pressure loss is higher than the one for CO<sub>2</sub>. For lower pressure this effect is pronounced. At about 80 bar the influence of the temperature nearly diminishes. The influence of the pressure decreases with higher temperature.

In Figure 5 all values of the  $dp$ -ratio are below unity, meaning that the pressure loss for He is lower than the one for CO<sub>2</sub>. The effect is pronounced for low pressures. Again, as could be expected at about 80 bar, the influence of the temperature is low. For higher temperatures a nearly constant value for all pressures of about 37% is determined.

Figure 6 shows the maximal value of 190% for high pressure and low temperature. Meaning that under this conditions the pumping power for He is higher than the one for CO<sub>2</sub>. At 300°C and 60 bar (the lowest investigated pressure) the pumping power for He is only 80% of the pumping power required for CO<sub>2</sub>. For DEMO the pressure of the cooling fluid is set to 80 bar.

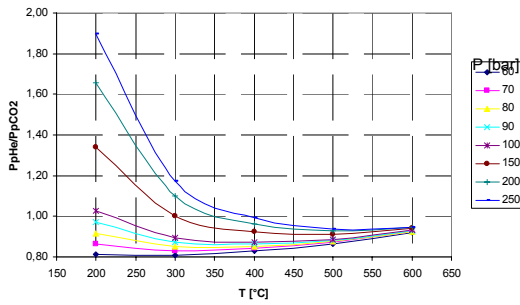


Fig. 6: Pumping power ratio for helium and CO<sub>2</sub>.

For this pressure of the medium the ratio  $P_{pHe}/P_{pCO_2}$  is below unity for the investigated temperature range. This means that in terms of pumping power the use of He is advantageous! The investigation exhibits lower pumping power for CO<sub>2</sub> only for higher pressures and lower temperatures. In addition to this it must also be observed that CO<sub>2</sub> is affected by neutron activation instead of helium that is not sensitive to neutron irradiation. All this leads to the conclusion that for current blanket designs operating in the temperature range between 300°C and 500°C at 80

bar substitution of He by CO<sub>2</sub> does not seem to be advantageous. The only advantage of CO<sub>2</sub> can be seen in Figure 3, namely the higher efficiency reached by a HTSE coupled with a CO<sub>2</sub> AGR. The option of an indirect coupling He-CO<sub>2</sub>-HTSE could be analyzed.

### 3) Impact of Pulsed Operations on the Design of the Mechanical Structure

Steady-state electricity production is an essential requirement of a fusion reactor and it has generally been assumed that the most cost-effective approach to this goal involves steady-state plasma operations. The cost disadvantage associated with pulsed plasma operations may be acceptable if certain physics challenges involved in achieving steady-state is proved to be more difficult or more expensive to resolve than assumed. Therefore, more detailed comparisons between steady-state and pulsed Tokamak operations, including physics as well as technological aspects, have to deliver essential input for future DEMO studies.

Regarding technology aspects these comparisons need to include the transient operations of the internal components. As a first step the agreement about a representative pulsed scenario is necessary. Only limited information is available but former work in the scope of the DEMO studies and also the US PULSAR study can serve as starting point.

An estimation of cyclic temperatures and cyclic mechanical loads faced by the most relevant reactor components needs to be provided. Appropriate stress (strength) estimations need to be performed. Prospective life time analyses are required considering the expected number of cycles. Pulse length is more or less determined by the burn time; depending on radiation damage due to swelling and transmutation the minimum number of cycles to be tolerated can be determined.

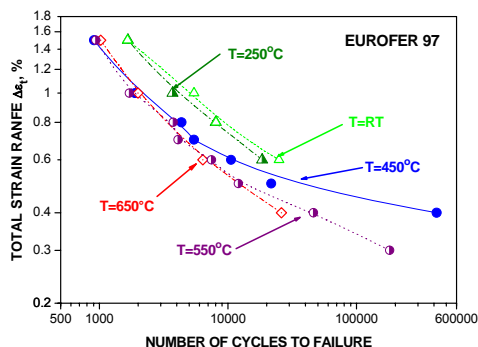


Fig. 7: Total strain vs. number of cycles to failure for un-irradiated EUROFER97 at different temperatures.

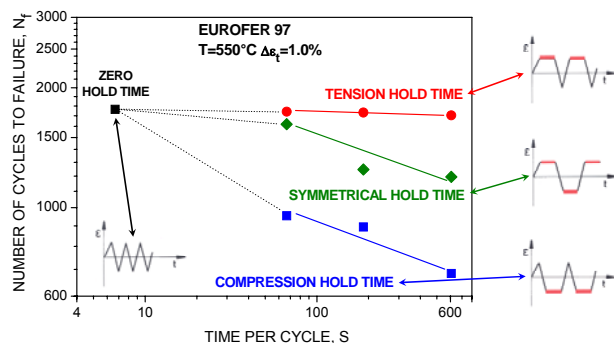


Fig. 8: Number of cycles to failure for un-irradiated EUROFER97 vs. time per cycle for different hold time modes.

The curves stress amplitude versus cycles to failure have to be provided for the selected structural materials for thermal and mechanical fatigue at the operating temperatures of the

different blanket concepts and under neutron irradiation. EUROFER, ODS-EUROFER, Tungsten Alloys, Vanadium Alloys, Silicon Carbide are the reference structural materials for the DEMO concepts. EUROFER is the most advanced and some relevant data exist. The other structural materials are under development and very few data exist. Stress-strain estimations on the most loaded components must be provided; this will impose a limit on the number of cycles that the component can face; vice versa the restriction imposed on the permissible stress by a fixed number of cycles can affect the design of the components (Figure 7). During pulsed operations mainly, but also in steady state operations, the reactor components will suffer the hold time effect (Figure 8). This effect has to be seriously taken into account.

Further on it is not clear today if the cyclic thermal loads have to be taken into account in the same manner as mechanical loads. Both mechanical and thermal cyclic fatigue are affected by neutron irradiation. In general the effects in Low Cycle Fatigue (LCF) of 300 °C irradiation are significant. 300 °C irradiation causes severe hardening in EUROFER97 (Figure 9). This induces two effects in LCF loading situations.

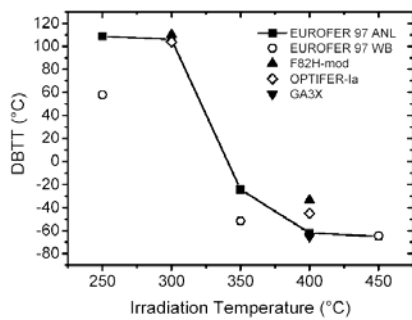


Fig. 9: Ductile to brittle transition temperature vs. irradiation temperature at 15 dpa.

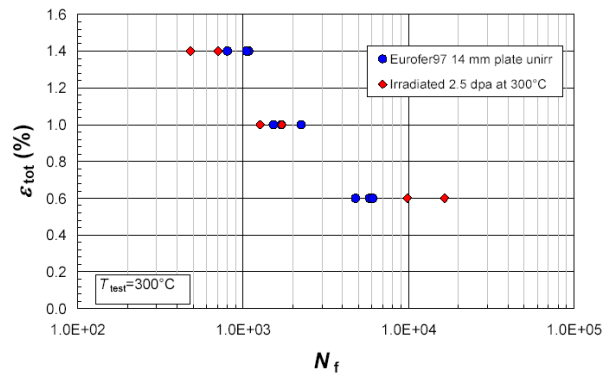


Fig. 10: Total strain vs. number of cycles to failure for irradiated and un-irradiated EUROFER97 at 300°C.

These effects are illustrated in Figure 10 using irradiated and un-irradiated EUROFER97 plate specimens, but they hold for other product forms as well. The first effect occurs at high strain ranges where the fatigue life is shortened. The second effect occurs at low total strain ranges where the fatigue life is extended. Nowadays data at DEMO doses (70-80 dpa) are not available and data for thermal fatigue are very few and collected for specific cases so that general assumptions cannot be done.

The necessary materials data have to be collected as far as the current state of material development allows. If the relevant data are not available, meaningful assumptions have to be established for an estimation of the feasibility of the different DEMO concepts.

Staff:

- D. Filsinger
- T. Ihli
- E. Magnani



## **Design Support and Procurement**



## **EFDA/05-1331 (TW4-TDS-CLDES) Final Design of HTS Current Leads for ITER**

### **Introduction**

In line with ITA-11-62-EU the objective of this task is to perform a final design of ITER high temperature superconducting (HTS) current leads (CL), quantifying the issues associated with the lead cooling conditions. The results include confirmation of the lead size and orientation and the preferred cooling requirements.

The work will be done in collaboration with the Centre de Recherches en Physique des Plasmas (CRPP), Villigen, Switzerland (EFDA contract 05-1332). The Forschungszentrum Karlsruhe will focus on the steady state 70 kA HTS CL for the Toroidal Field Coils and CRPP on the pulsed 45 kA HTS CL for the Central Solenoid and Poloidal Field Coils.

### **Background**

High temperature superconductors have successfully demonstrated their considerable advantages over conventional materials and entered the market. Therefore, an R&D program was launched in Japan and EU in order to design and construct HTS components for ITER. The EU 70 kA ITER prototype current lead using HTS was assembled in 2003 and tested in 2004 in nominal conditions. Afterwards, the 70 kA HTS current lead was successfully operated at a He inlet temperature of 80 K and retested using LN<sub>2</sub> as requested by the International Team.

As a consequence, the International Team in agreement with the Participant Teams has decided to introduce HTS CL in ITER. Since several years, the Forschungszentrum Karlsruhe and CRPP Villigen have been involved in the development and construction of high amperage current leads including the European 70 kA HTS current lead for ITER.

### **Results of the Work**

The programme conducted by the Forschungszentrum Karlsruhe within the framework of deliverables 4.2 and 4.3 was to perform a conceptual design of a steady state 70 kA CL. Factors to be considered in the design were:

- Advantages/necessity of inclining the lead or orientating it vertically
- Critical technologies to be developed (typically joints to the HTS conductor) and target parameters to be achieved (like joint resistance)
- Design optimization to reduce HTS requirements (for example, graded HTS stacks)
- Warm and cold end heat loads
- Control of current distribution in the lead (tolerable contact resistances to HTS stacks)
- High voltage features (ground voltage requirements are in ITER DDD)
- Flow arrangement and temperature control. The preliminary requirements for the lead cooling are the following:
  - With gas cooling, a tolerance to a loss of cooling flow event of >3mins is required.
  - With LN<sub>2</sub> cooling a LN<sub>2</sub> reservoir and an ability to operate without external LN<sub>2</sub> supply for >30mins should be considered as an option.

Final schematic drawings of the lead layout are provided to allow the Coil Terminal Boxes (CTB) to be defined around it.

*A) Advantages/necessity of inclining the lead or orientating it vertically*

The present design of the CTB is based on the operation of the current lead in horizontal position. This was the reason why the 70 kA HTS current lead developed by the Forschungszentrum Karlsruhe and CRPP was designed and operated horizontally. No performance degradation with respect to expectations was observed during all the runs. So it can be concluded that the current lead operated with the FZK-type heat exchanger is able to operate horizontally with the same operation parameters as in vertical or inclined orientation. No change of the ITER design is necessary.

*B) Critical technologies to be developed and target parameters to be achieved*

Here we concentrated on the HTS module. Table 1 show the main target parameters which should be achieved.

Table 1: Main target parameters for the HTS module to be achieved.

Parameter	Target value
Maximum operation temperature	65 K
He inlet temperature	50 K
Current sharing temperature at warm end	> 77 K
Cold end joint resistance of HTS-Cu transition	< 1 nΩ
Warm end joint resistance of HTS-Cu transition	3 nΩ
Joint resistance distribution	< 20%
Warm end joint resistance of HTS module and HEX	5 nΩ
Electrical quench detection system	
Offset voltage due to end cap resistances	0.27 mV
Detection level and integration time	10 mV / 1 s
Sensitivity	10 μV
Temperature quench detection system (warm end of HTS module)	
Detection level	90 K
Sensitivity	0.1 K

The room temperature end of the HTS current lead has to stay above the dew point of the air around it. This can be achieved by installing heaters which will be controlled by temperature sensors installed in the warm end head of the lead. In normal conditions, the heaters will only be switched on at zero or low currents. For high currents, active water cooling of the warm end head would have advantages because it is able to fix the temperature in a wide current range. Both options were realized in the 70 kA HTS current lead and worked very reliable.

The reliable operation of the current lead over 20 years of ITER life time requires reliable sensors operating on HV-potential. Both sensor types are indispensable for a quench detection of the HTS part.

*C) Design optimisation to reduce HTS requirements*

In the past, people had the idea to use graded stacks, i.e., to use less tapes in the low temperature region of the HTS module than in the warm temperature region. This idea looks clever because at lower temperatures the HTS tapes have higher current capacity than at higher temperatures. The disadvantage is that there will be resistive joints within the HTS module which will occur at higher currents (for low currents this will not be the case because not all tapes are needed to carry the current). These resistive joints can not be controlled during fabrication of the stacks.

Nowadays no high current capacity HTS current lead uses graded stacks.

#### D) High voltage features

The 70 kA HTS current lead developed by the Forschungszentrum Karlsruhe and CRPP did not have a Paschen-tight HV-insulation. Due to the very high heat load of the 80 kA conventional current lead developed and manufactured for the TFMC experiment in both the standby and current operation, it was decided to avoid stagnant Helium outside the heat exchanger but operate the lead in vacuum.

The consequence is that the HV insulation has to be performed directly on the Helium tight container of the current lead heat exchanger which has to be extended to the HTS module region. Moreover, a Paschen-tight solution has to be found for the cold end contact area. A consequence of this is the installation of the support flange which connects the current lead to the CTB has to be connected on top of the HV insulation. This connection has to withstand all forces which act on the lead itself.

#### E) Dimensions

The present design of the CTB is based on the operation of the current lead in horizontal position. The 70 kA HTS current lead developed by FZK and CRPP in the frame of the European Fusion Development Programme was consequently designed such to meet this requirements. Although the outer dimensions (overall length: 2284 mm, maximum outer diameter: 236 mm) were chosen such to fit the current lead in the TOSKA test facility, it would also fit in the ITER coil terminal box CTB. Figure 1 shows the Overview drawing of a typical 68 kA HTS current lead for ITER to allow the CTB to be defined around it.

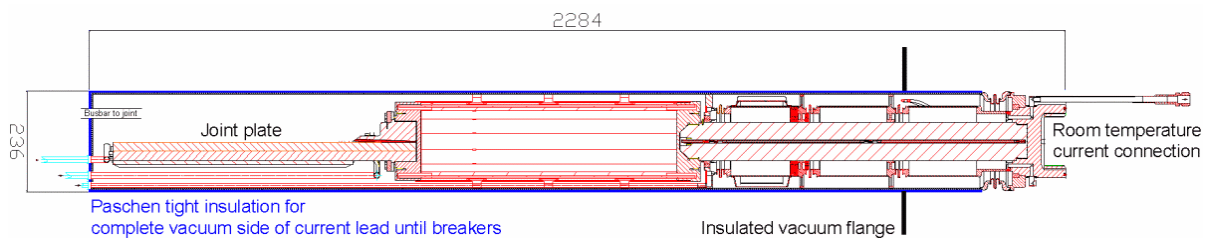


Fig. 1: Overview drawing of a typical 68 kA HTS current lead for ITER to allow the Coil Terminal Boxes (CTB) to be defined around it.

#### Staff:

R. Heller



## **JET Technology**



## JW2-FT-2.4

### Tritium Inventories of Spent Cryopanel and Waste Conditioning

#### Background and objectives

An ITER-relevant cryosorption pump (PCP) has been manufactured, installed and operated at the Active Gas Handling System (AGHS) of JET. Under the previous task JW1-FT-6.1, the pump has been fully characterized, firstly for direct operation of the tokamak, secondly in parametric test campaigns. This present task aims to assess the tritium retained on the ITER cryopanel after operating under these representative conditions. It will provide data for the composition of gas evolved following regeneration over a range of temperatures and determine the amount of tritium retained on the cryopanel [1]. The efficacy of one or more methods of detritiating the cryopanel will also be measured.

#### Current status

In preparation of the gas processing, the analytical system and the impurity processing system in AGHS had to be refurbished, see Fig. 1. The valve connecting to the sample manifold of the analytical system was not operating correctly, and had to be exchanged with the windows removed from the glovebox to provide ready access. Repairs and enhancements were carried out to one of the palladium permeator in the impurity processing system. Failed heater units have been removed and replacement units have been given an electroless nickel coating to improve heat transfer between the elements and heater shell. The heater control and protection have been improved and new controllers, drives and trip amplifiers have been bench tested and installed. Thermocouple sensors have been brazed to feedthroughs.

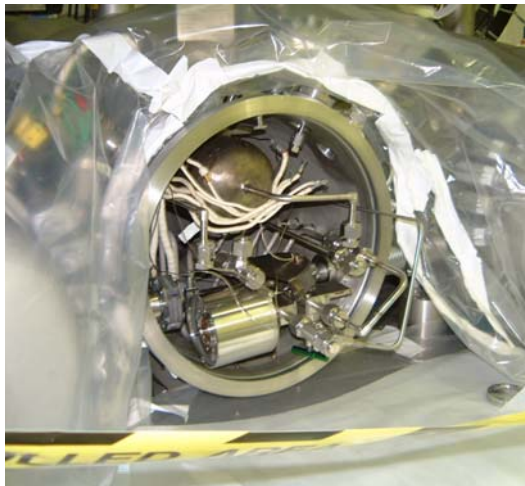


Fig. 1: Photographs of the preparation work. Left: The permeator awaiting installation of the replacement heaters. Right: Opened analytical glovebox.

The PCP has been regenerated to 300 K following completion of the work in Task JW1-FT-6.1, and the gas been collected and processed. According expectation, a significant part of tritium retained on the pump has been released. It was processed in the Ni catalyst bed and the permeator of the AGHS impurity processing system. Preliminary integral results are that there was 3.2 bar-l of gas containing 30 TBq of  $T_2$ .

However, as the bound tritium is anticipated to be incorporated into tritiated hydrocarbons, which were the pumped gas species of the final test campaigns, the predominant fraction is still sorbed. A preliminary balance of the tritium fractions pumped out and seen by the PCP

and released during the various regenerations performed in the past yields a residual overall tritium inventory of the PCP of about 1 g. Based on that value, the 300 K regeneration achieved a release of ~ 15%.

The next step is to repeat this exercise after regeneration at 475 K, which is planned for early 2008. Following this step, a series of gas purges will be carried out periodically to further reduce the tritium retained in the PCP and to see if the off-gassing trends observed are slowing down or not. The quantitative composition analysis of the released gas will finalize this task.

Staff:

Chr. Day

S. Grünhagen (delegated to JET)

P. Camp (UKAEA)

S. Knipe (UKAEA)

Literature:

- [1] Chr. Day, H. Haas, Experimental confirmation of the ITER cryopump high temperature regeneration scheme, ISFNT-8, Heidelberg, Sept. 2007.

## **JW4-FT-3.18**

### **Assessment of in-situ Detritiation in JET**

#### **Introduction**

In the ITER fusion machine, carbon-based target materials are foreseen to be used in the divertor area. However, using carbon tiles there is likely to be a major problem in terms of tritium retention in re-deposited carbon films. It is estimated that at least 2g tritium per pulse (400 s) will be deposited to the first wall [1], [2] and therefore, detritiation of Plasma Facing Components (PFC's) of such tritium installations will play an increasingly important role in the future development of fusion. In this respect, it is important to develop a technology for the *in-situ* detritiation of the carbon tiles to meet the safety criteria for ITER which allow a total tritium amount into the vacuum vessel of 350 g. Fast and efficient tritium removal is therefore needed, for future DT machines having carbon tiles as plasma facing components. Among the various methods tested so far, photon cleaning has been proposed as a potential *in-situ* detritiation method which can be applied to remove co-deposited layers. The method has been tested treating samples retrieved from some smaller tokamaks, such as the TEXTOR (Jülich, Germany) and Tore Supra (Cadarache, France). However, it was not yet tested *in-situ*.

Testing the applicability of the technique to the next step devices, an engineering scale demonstration of the technique was needed to be performed *in-situ*. With this aim, during the JET 2004 shutdown, several tiles of the Outer Poloidal Limiter (OPL) and the divertor region of the JET machine (Culham, UK), were treated *in-situ* or, in the Beryllium handling facility (BeHF) at JET, by photon-cleaning. In order to assess the efficiency of the H-removal process, 2 adjacent divertor tiles (one treated and one untreated) were shipped to the Tritium Laboratory Karlsruhe (TLK) to evaluate and finally compare their total tritium content and their tritium depth profile, using calorimetry and full combustion respectively. Similar tiles were also analysed for their relative deuterium contents by Ion Beam Analysis (IBA) methods [3]. The IBA was carried out by UKAEA using the special glove-box facilities at Sussex University in Sussex, UK.

The flash lamp delivered to the divertor tile G4A up to 350 J in  $\sim 140 \mu\text{s}$  with a repetition rate of  $\sim 1\text{Hz}$  and up to 500 J with a repetition rate of 5 Hz for tile G4B. Each treated position had about 12 mm wide and 125 mm discharge length (treated area  $\sim 15 \text{cm}^2$ ). From these series of experiments it appeared that at the highest energies the co-deposited material is partly ablated from the surface of the divertor tiles. The poloidal limiter tiles were treated at lower energies (250-350 J), which was expected to only desorb hydrogen isotopes from the surface films.

The calorimetric and combustion measurements for the treated 3BWG4A and partly untreated 3BWG4B divertor tile are presented hereafter.

#### **Experimental**

##### ***Calorimetric measurements***

Calorimetric measurements for the untreated divertor tile 3BWG4B gave an average total tritium activity of about  $1.619 \pm 0.080 \text{ Ci}$  or 59.9 GBq, while the calorimetric measurement for the 3BW4GA treated tile estimated a total tritium content averaging  $1.089 \pm 0.041 \text{ Ci}$  or, 40.3 GBq. Assuming that both tiles had initially a similar activity, these measurements indicate that after the photon cleaning approximately 33% of the tritium activity has been released when treating the tile with energies up to 350 J. Speaking in terms of thickness of the co-deposited material, we can estimate that from the  $\sim 100\mu\text{m}$  co-deposited layer measured before irradiation approximately 30  $\mu\text{m}$  have been removed.

### Full combustion measurements

#### G4A treated tile

In order to evaluate the efficacy of the Flash-lamp photon-cleaning detritiation technique, 8 cylindrical cores, having a diameter of 7.8 mm, have been removed from various positions from the tile's surface. Each cylinder was sectioned into two discs; the plasma facing disc having a thickness of 1mm and the rest cylinder. Both specimens have been ultimately combusted and their tritium content determined by scintillation analysis. The coring of the cylindrical specimens has been performed by the



Fig. 1: Drawing (a) and picture (b) of the G4A after coring.

Hot-Cells department at the Forschungszentrum Karlsruhe. The position of the various cylinders is illustrated in Fig. 1, while the combustion results obtained for tile G4A are reported in Fig. 2. As it is illustrated in Fig. 2, the higher tritium release has been observed for cylinders 1 to 3. Cylinders 1 and 2 are corresponding to photon-cleaned positions whereas cylinder 3, 6, 7 and 8 are belonging to untreated zones of the tile. Among them only cylinder 3 is located in the shadowed area of the tile and therefore its tritium concentration on the very surface is the highest measured for this tile. On the other hand, despite the fact that cylinder 6, 7 and 8 are belonging to a non treated area of the tile, their tritium concentration is much lower compared to the treated part of the tile (cylinder 1, 2). This is related to the fact that cylinders 6 to 8 are located in an erosion area (private area for cyl-8) where there is only little or, no co-deposition at all.

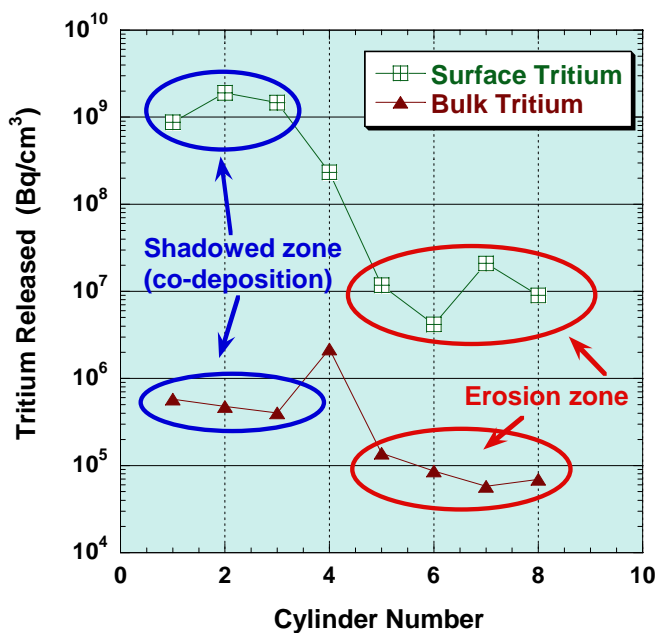


Fig. 2: Combustion results for samples retrieved from the G4A treated tile.

If we compare the tritium surface activities for the positions 1 to 3, we realise that even after the tile was "flashed" with 80-100 pulses at 250 J (cylinders 1 and 2) the average tritium activity remaining on the surface is  $\sim 1.39 \pm 0.7 \cdot 10^9$  Bq/cm<sup>3</sup> which is very similar to the  $1.47 \cdot 10^9$  Bq/cm<sup>3</sup> measured for the cylinder 3 which was untreated. Of course, the initial tritium activity deposited on the surface of the tile at these three positions may vary, and looking into the corresponding bulk tritium concentrations (tritium released for the rest cylinders) we may notice that the bulk concentration for cylinder 3 is even lower than the corresponding bulk concentration for cyl-1 and cyl-2. As the bulk concentration is a function of the tritium amount present at the surface,[4] this

indicates that initially the tritium surface concentration for cylinders 1 and 2 was initially higher for these cylinders than for cyl-3 and after the tile has been flashed at these positions with 80-100 pulses, a substantial amount of tritium has been removed. However, compared to the total tritium content of the samples, the tritium release is not substantial and we can therefore, draw the conclusion that the photon-cleaning process using pulses at the maximum energy of 350 J is not efficient. In a previous attempt performed with the poloidal limiter tiles and using flash-lamp with a maximum energy of 100 J, it was showed that only a small fraction of tritium was desorbed demonstrating that such a treatment at so low energies is meaningless. This time, the combustion results presented above for tile G4A have shown that using the flash-lamp at the energies ranging from 250-350 J, the photon-cleaning process is able to ablate some of the co-deposited layer but only partly (~30%), even though the tile was submitted to many pulses, sometimes up to 100. In a final attempt, aiming to increase the efficiency of the photon-cleaning treatment, the flash-lamp has been used once more but at its maximum available energy i.e. 500 J per pulse.

For this purpose, the untreated tile (G4B) was sent back to JET for further treatment, cleaning only part of the tile (~2/3), across the poloidal direction, while the rest of the tile (1/3) remained untreated.

#### *G4B partially treated tile*

Three zones on Tile 4 were treated; zone 1 was at the edge of the tile, zone 2 was in the centre of the shadowed area, whereas zone 3 was at the beginning of the sloping part of the tile (Fig. 3). A mask was placed at the right end of the tile to prevent removal of tritium and thus provide a reference between treated and untreated regions. Each zone was subject to a series of pulses from the flash-lamp. The total number of pulses for zones 1 and 2 and 3 were 2460, 2785 and 1838 respectively. The photon-cleaning treatment for this tile was investigated and reported in details by Widdowson et al. [5]. The combustion results are also illustrated in Fig. 4. From that figure we can clearly see that the photon-cleaning was inefficient even though the maximum energy of 500 J has been used. Combustion measurements show that for the masked zone (cyl-11, 14 and 15), the average tritium concentration on the surface of the tile was  $9.34 \pm 2.78 \cdot 10^8 \text{ Bq/cm}^3$ , while for the photon-cleaned part of the tile, the surface tritium concentration is about 4 times lower, giving an average value of  $2.45 \pm 0.68 \cdot 10^8 \text{ Bq/cm}^3$ . Of course this represents ~26% of the initial tritium concentration and this means that 74% of the surface tritium has been released during the treatment. The corresponding Decontamination Factor (DF) is only 4 and which is not sufficient to qualify the treated tile as Low Level Waste material which in the UK has an upper limit of 12 MBq/kg.

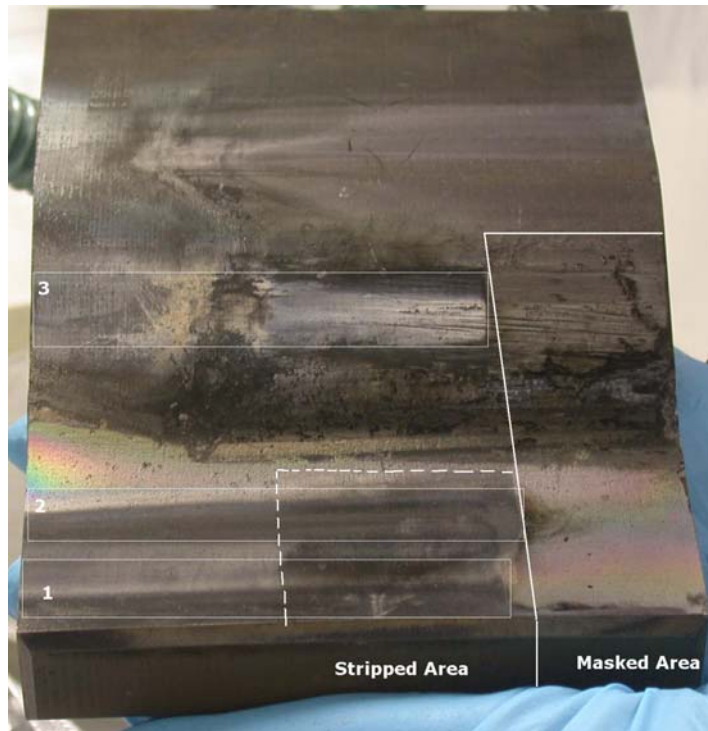


Fig. 3: Picture of the G4B after photon cleaning. The positions of treatment and masked area are indicated.

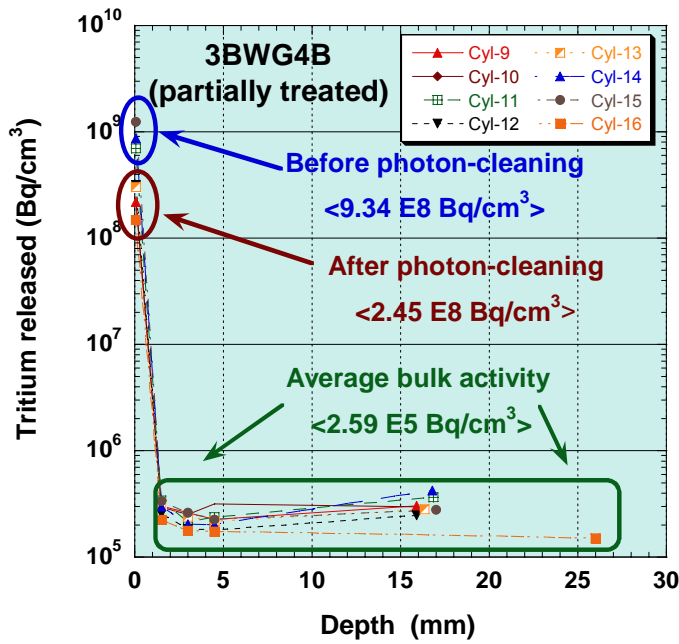


Fig. 4: Comparison of tritium depth profiles for tile G4B before and after photon cleaning.

A remarkable point concern the tritium activities measured for the bulk of the tile. Combustion shows that, no matter the type of samples, photon-cleaned or not, the tritium concentration into the bulk remains constant averaging the  $2.59 \pm 0.62 \cdot 10^5 \text{ Bq/cm}^3$ , which is three orders of magnitude lower than the tritium activity measured for the surface samples. This is consistent with previous observations showing that only a very small fraction of the surface tritium diffuses into the bulk of the sample, the driving force for such a diffusion been the temperature and the tritium surface concentration [6, 7]. Moreover, as it was already pointed out [8, 9], we may also notice here too, that during the treatment there is no tritium diffusing inside the tile. Indeed, in such a case the tritium bulk concentration

for the treated samples would have been higher than the untreated samples, but this has not been observed.

### Conclusions

Flash lamp photonic cleaning has been tested in-situ and at the Beryllium Handling Facility (BeHF) at JET. Two adjacent number 4 divertor tiles (G4A and G4B) from the MKII-GB configuration, have been exposed to numerous pulses up to the nominal energy of 500 J. Starting with tile G4A the photon-cleaning process using energies ranging between 250 and 350 J did not appeared to be efficient. Indeed the average tritium activity remaining on the surface of the tile after treatment was very similar to the tritium concentration measured for the untreated samples. Increasing the energy density delivered by the lamp did not improve spectacularly the results. Indeed, using higher energy densities of  $0.06 \text{ MJ/m}^2$  with a peak power density of  $375 \text{ MW/m}^2$ , only "part" of the deposited film ( $\sim 100 \mu\text{m}$  thick), has been removed. Combustion measurements showed that even at 500 J, the photon-cleaning process was still inefficient as the "part" of the tritium released is about 74% of the initial tritium concentration. This indicates that 26% of the surface tritium remains on the surface of the tile giving an average tritium concentration on the surface of the tile after treatment about 4 times lower than the initial activity. However, it is remarkable to notice that the bulk activity of the tiles did not change. Combustion measurements show that, no matter the type of samples, photon-cleaned or not, the tritium concentration into the bulk of the tile remains remarkably constant which is three orders of magnitude lower than the tritium activity measured for the surface samples.

### Staff:

- N. Bekris
- B. Kloppe
- C.J. Caldwell-Nichols
- A. Erbe
- J. Ehrmann

Literature:

- [1] G. Federici, H. Wuerz, G. Janeschitz, R. Tivey. Erosion of plasma-facing components in ITER. Fusion Engineering and Design 61-62 (2002) 81-94.
- [2] G. Federici, P. Andrew, P. Barabaschi, J. Brooks, R. Doerner, A. Geier, A. Herrmann, G. Janeschitz, K. Krieger, A. Kukushkin, A. Loarte, R. Neu, G. Saibene, M. Shimada, G. Strohmayer, M. Sugihara. Key ITER plasma edge and plasma-material interaction issues. J. Nucl. Mater. 313-316 (2003) 11-22.
- [3] J.P. Coad, M. Rubel, N. Bekris, D. Hole, J. Likonen, E. Vainonen-Ahlgren and EFDA-JET Contributors. Distribution of hydrogen isotopes, carbon and beryllium on in-vessel surfaces in the various JET divertors. Fusion Science and Technology 48, (2005), 551 and J.P. Coad. EFDA-JET report JW4-FT-3.18. del.1-3.
- [4] A. Widdowson, J.-P. Coad, N. Bekris, G. Counsell, M. J. Forrest, K.J. Gibson, D. Hole, J. Likonen, W. Parsons, T. Renvall, M. Rubel. Efficacy of photon cleaning of JET divertor tiles. J. Nucl. Mater. 363-365, (2007), 341-345.
- [5] N. Bekris, C.H. Skinner, U. Berndt et al. Tritium depth profiles in 2D and 4D CFC tiles from JET and TFTR. J. Nucl. Mat. 313-316 (2003) 504-509.
- [6] N. Bekris, C.H. Skinner, U. Berndt, C.A. Gentile, M. Glugla, A. Erbe, W. Pilz. Assessment of the heating technique as a possible ex situ detritiation method for carbon wall materials from fusion machines. J. Nucl. Mater. 329-333 (2004) 814-819.
- [7] N. Bekris, C.H. Skinner, U. Berndt, C.A. Gentile, M. Glugla, B. Schweigel. Tritium depth profiles in 2D and 4D CFC tiles from JET and TFTR. J. Nucl. Mater. 313-316 (2003) 504-509.
- [8] N. Bekris, U. Berndt, L. Doerr, A. Erbe, B. Kloppe, K. Sugiyama. Tritium Removal from JET Tiles. EFDA-JET Report JW2-FT-2.9, Oct-2005.
- [9] N. Bekris, J.P. Coad, K. Sugiyama, C. Caldwell-Nichols, T. Tanabe, B. Kloppe, R. Rolli. Ex-situ Tritium removal from JET tiles using RF inductive heating. Proceedings ISFNT-8, September 30-October 5, 2007, Heidelberg, FRG.

## JW5-FT-5.20 Shutdown Dose Rate at JET Tokamak – Code Benchmark

The objective of Task JW5-FT-5.20 was to validate the computational methods for shutdown dose rate calculations through the comparison with dose rates measured in dedicated benchmark experiments on JET. The experiments have been delayed several times resulting in a revised task schedule. In 2007, measurement campaigns have been performed by the experimental team of ENEA Frascati. The task of FZK was to analyse the experiments by means of the rigorous 2-step (R2S) approach, developed at FZK for the Monte Carlo based calculation of shut-down dose rates in 3D geometry [1].

The related task deliverables were on the adaptation of the JET MCNP model to the R2S requirements and pre-analysis, on the R2S calculations for the benchmark experiments, and on the data analysis and comparison of D1S/R2S experimental results. ENEA Frascati provided the MCNP model of JET octant 1 including descriptions of the two measurement positions and surroundings in the upper irradiation end (IE) and outside the vessel. The dose measurements were performed with a Thermo Luminescence Detector (TLD) in the upper IE and a Geiger-Mueller (GM) detector outside the vessel. The model was adapted at FZK to comply with the requirements of the R2S computational approach, see Fig. 1.

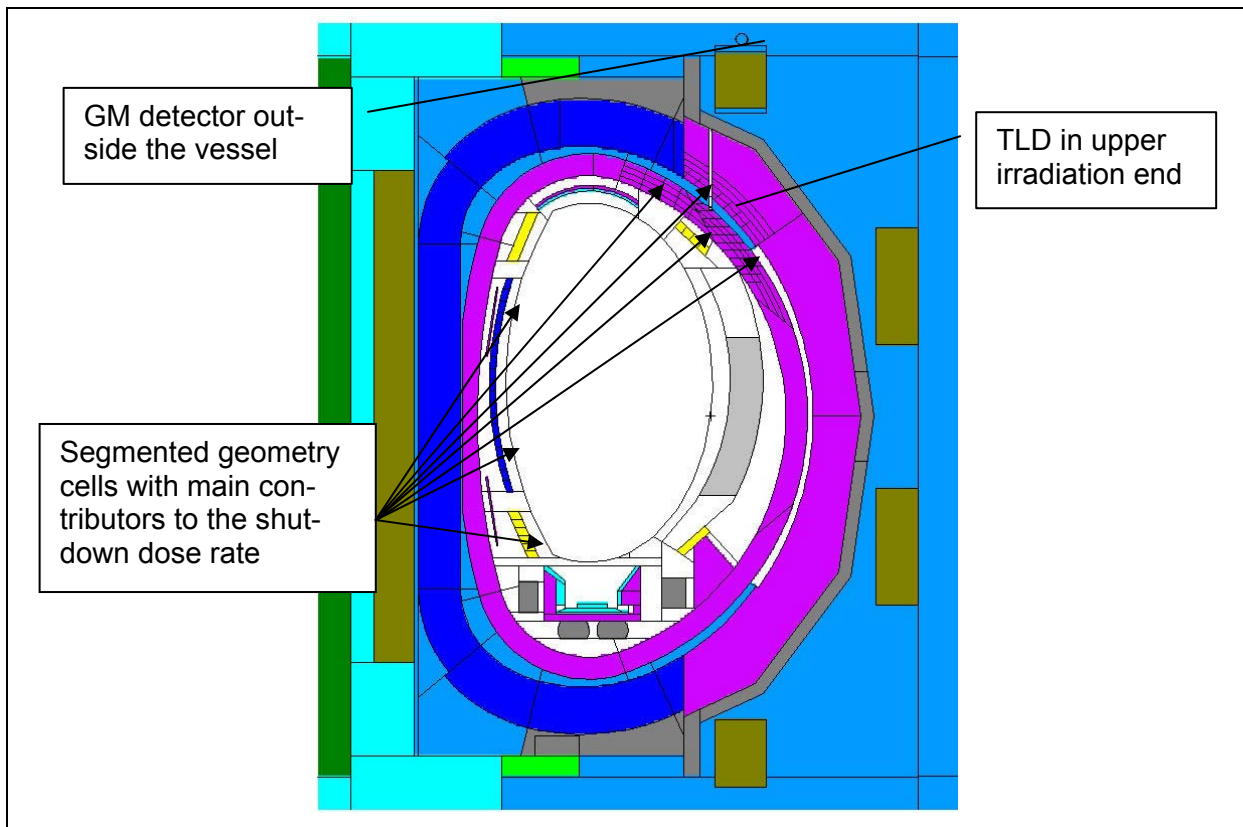


Fig. 1: MCNP model of JET octant 1 (vertical cut) adapted for R2S dose rate calculations showing the detector locations inside and outside the vessel.

This included a R2S pre-analysis on the basis of the original JET MCNP model to identify the decay gamma source cells contributing significantly to the shut-down doses at the specified detector positions inside and outside the vessel. These were shown to be in-vessel components such as the inner walls, limiters and the saddle coil. Accordingly, a fine spatial segmentation was applied to these geometry cells. This is required with the R2S-approach to achieve a sufficiently high accuracy when calculating the neutron flux and decay gamma source distribution.

R2S shutdown dose rate calculations employing the refined MCNP model were finally performed for the two measurement positions accounting for the full irradiation history including the relevant DD and DT operations. According to the measurement campaigns, three different decay times after shutdown were considered for each of the detectors. The related irradiation history data and measurement results were provided by ENEA Frascati [2].

The analyses showed satisfactory agreement of the R2S calculations and the TLD dose measurements for the upper IE inside the vessel. Qualitatively the same results were obtained by ENEA Frascati employing the D1S approach for the shutdown dose rate calculations. The D1S results were, however, systematically higher than the measurements while the R2S results were slightly lower. The GM measurements in the ex-vessel position were underestimated significantly by both the R2S and D1S approach with C/E (calculation/experiment) ratios varying between 0.3 and 0.5, see Table 1. This is presumably due to a still insufficient description of the very complex surrounding of the detector location with regard to the geometrical configuration and the material description.

Table 1: Measured and calculated shut-down dose rates for for three different decay times at the two detector positions inside and outside the JET vessel.

Experiment/detector measurement date	Measured dose rate ( $\mu\text{Gy h}^{-1}$ )	Calculated dose rate ( $\mu\text{Gy h}^{-1}$ )			Calculation/Experiment (C/E)
		Due to DD neutrons	Due to DT neutrons	Total	
Upper IE (TLD)					
29.09.05	$51.1 \pm 9.6$	14.0	27.5	$41.5 \pm 4.1$	0.81
20.12.06	$134.9 \pm 22.3$	82.8	24.8	$107.6 \pm 10.7$	0.80
03.01.07	$117.3 \pm 20.6$	69.0	24.2	$93.2 \pm 9.2$	0.79
Ex-vessel (GM)					
22.12.06	$2.59 \pm 0.28$	0.58	0.19	$0.77 \pm 0.08$	0.30
03.01.07	$1.64 \pm 0.18$	0.56	0.24	$0.80 \pm 0.08$	0.49
14.05.07	$1.88 \pm 0.21$	0.45	0.22	$0.67 \pm 0.07$	0.36

Staff:

U. Fischer  
P. Pereslvtsev

Literature:

- [1] Y. Chen, U. Fischer, "Rigorous MCNP based shutdown dose rate calculations: Computational scheme, verification calculations and applications to ITER", Fus. Eng. Des. 63-64 (2002), 107-114.
- [2] R. Villari, M. Angelone, P. Batistoni, U. Fischer, P. Pereslvtsev, L. Petrizzi, S. Popovichev et al, Validation of shutdown dose rate Monte Carlo calculations through a benchmark experiment at JET, paper contribution to International Symposium on Fusion Nuclear Technology, Heidelberg, Germany, September 30 – October 5, 2007.



# **Heating Systems Technology Project**



## **Coaxial Cavity Gyrotron and Test Facility**

### **TW6-THHE-CCGDS4 D 1b**

#### **Design, Support to the Industrial Development and Preparation of Technical Specifications**

### **TW6-THHE-CCGT1 D 1**

#### **Scientific Execution and Co-ordination of the Tests**

In cooperation with European research institutions (CRPP, Lausanne, TEKES, Helsinki) and European tube industry (Thales Electron Devices (TED), France), the development of a 2 MW, CW, 170 GHz coaxial cavity gyrotron for ITER is going on. In summer 2004, EFDA has placed a contract at TED for the fabrication of a first industrial prototype of a 2 MW, CW, 170 GHz coaxial cavity gyrotron. Within the cooperation, the physical specifications and the design of the gyrotron components have been developed by the research institutions, and TED has manufactured the first prototype. The fabrication of the prototype gyrotron has been finished at the end of 2006. In the meantime, a usable SC magnet has been delivered. Thus, experiments with the prototype tube will start next. Before a series production can start, in total 3 prototypes are foreseen.

Because of the long delay mainly due to problems in fabrication of the SC magnet, time for development has been lost. Thus, in order to be able to provide the microwave sources for ITER in time, a 1 MW, 170 GHz conventional gyrotron with a cylindrical cavity is under design. This conventional tube is considered as a fall back solution in case of further delays in the development of the coaxial gyrotron.

In parallel to the industrial activities, an experimental short pulse coaxial gyrotron (pre-prototype) is in operation to verify the design of the prototype and to identify unexpected problems as early as possible.

#### **2 MW, CW 170 GHz prototype of a coaxial cavity gyrotron for ITER**

The fabrication of the first industrial prototype of the 2 MW, CW 170 GHz coaxial cavity gyrotron has been finished and the gyrotron has been delivered to CRPP Lausanne in December 2006, where a suitable gyrotron test facility has been constructed. With a strong delay, the SC magnet has finally been delivered in November 2007 to CRPP Lausanne, and the acceptance tests have been performed. Though the magnet does not fulfil all specifications (e.g. the He losses are very high,  $\sim 5$  l He/h), gyrotron tests are deemed to be possible. Therefore, very recently the gyrotron has been installed into the magnet as shown in Fig. 1. The operation of the gyrotron has started at the beginning of December 2007.

In case of unexpected problems with the SC magnet, the possibility of testing the coaxial gyrotron at FZK has been considered. The upgraded HV power supply allows tests of the tube at nominal parameters (90 kV/75 A) up to 10 sec. The SC magnet existing at FZK has a large bore hole with a diameter of 275 mm. Thus the required magnetic field of 6.86 T can be obtained by inserting a normal conducting solenoid coil into the bore hole. The design of such a coil has been done. Further modifications on the test facility at FZK, necessary for performing the tests with the coaxial gyrotron, have been studied in detail. According to this, about three months are needed to carry out the required adaptations before a testing of the tube with the equipment at FZK could start.

The design of a 1 MW, CW, 170 GHz conventional gyrotrons with a cylindrical cavity started in July 2007 in a European cooperation under the coordination of FZK. Detailed results as needed for starting an industrial design will be available end of 2008. This 1 MW conventional gyrotron is considered as a fall back option in case of major difficulties in the develop-



Fig. 1: Photography of the first industrial prototype of the 2 MW, CW, 170 GHz coaxial cavity gyrotron (fabricated by Thales ED) installed in the SC magnet at CRPP Lausanne.

ment of the 2 MW coaxial cavity gyrotron. If due to serious problems, keeping the time schedule in the development of the coaxial gyrotrons should become uncertain, a decision for developing of a conventional 1 MW gyrotrons has to be taken in 2009, in order to be still in time for fulfilling the commitment for ITER taken by the EU.

### **170 GHz experimental pre-prototype coaxial cavity gyrotron**

In parallel to the work on the industrial prototype, experimental investigations with the pre-prototype 170 GHz coaxial cavity gyrotron have been continued at FZK. Recently, in particular the following aspects have been studied:

- mechanism of excitation of the parasitic low frequency (LF) oscillations
- influence of the level of internal stray radiation on RF generation
- improvement of the q.o. RF output system.

#### • *Parasitic low frequency oscillations:*

Based on theoretical modeling with the code "CST Microwave Studio", a mechanism for the occurrence of the parasitic LF oscillations around 260 MHz and 330 MHz has been proposed. According to this hypothesis, the excitation of the LF oscillations is related to the presence of the coaxial insert. The velocity of the emitted electron beam is modulated by the electric field component of the LF oscillations around the cathode (Fig.2, upper part). The velocity modulation results in a density modulation (bunching) of the beam. The bunched beam is interacting with an axial component of the LF field near an aperture on the cathode side of the cavity. This axial component is strongly enhanced by the radial steps of the insert (indicated in Fig. 2). In order to reduce the interaction between the bunched beam and the LF field, the radial steps have been removed as shown in Fig. 2. Due to this, a significant reduction of the level of the LF oscillations has been found in measurements. In particular, the corresponding starting currents  $I_{startLF}$  increased by a factor of about 3 to a value above 40 A. Recently, measurements have been performed with the electron gun previously used in the coaxial gyrotron at 165 GHz. The anode has been modified for operation at 170 GHz in the TE<sub>34,19</sub> mode. In the operation with this gun, no LF oscillations have been observed at all, thus confirming the observations of the 165 GHz gyrotron.

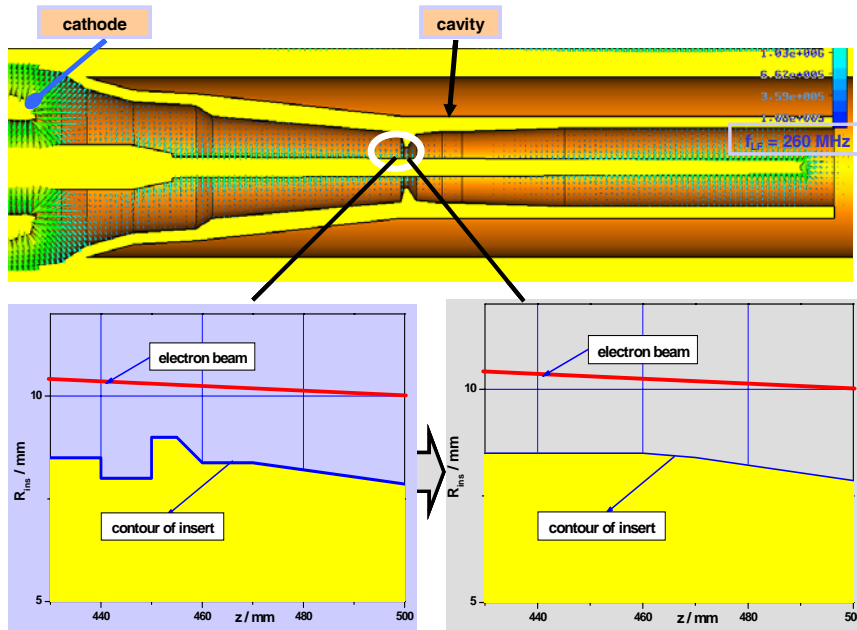


Fig. 2: Distribution of the LF field at the 260 MHz resonance (upper figure). Lower figures show the zoomed out part of the insert in front of the cavity. Left side: old geometry:  $I_{startLF} \sim 12 - 15$  A; right side: modified geometry  $I_{startLF} \sim 40$  A. The position of the electron beam is indicated.

- *RF generation:*

It has been observed experimentally that an increase of the level of microwave stray radiation in the gyrotron resulted in a decrease of both the single mode operating range and the efficiency. To investigate whether, particularly, the level of stray radiation in the competing modes has an influence on the gyrotron operation, a Brewster window has been installed. No significant influence on gyrotron behaviour has been observed due to the reduced window reflection.

In the experiments recently performed, it has been observed that over a wide parameter range in addition to the nominal mode at 170 GHz, a parasitic oscillation around 160 GHz is excited simultaneously with very low power. There are some indications that the parasitic oscillations could be generated inside the beam tunnel on the cathode side of the cavity. To study the effect, the beam tunnel has been replaced by a tunnel with a conical shape. Experimental measurements are in progress.

- *Improvement of the quasi-optical (q.o.) RF output system:*

The performance of the q.o. RF output system which is installed in the first industrial prototype gyrotron has to be improved, especially because the Gaussian content of the microwave output beam is too low. In addition, the amount of stray losses has been measured to be as high as 8% of the output power. As a first step for improvement, a q.o. RF output system with a modified launcher (with only  $\Delta m=3$  azimuthal corrugation) has been designed and fabricated. According to calculations, a Gaussian content of the RF output beam of  $\sim 87\%$  is expected, as well as some reduction of the amount of the internal microwave stray losses. The performance of the modified q.o. RF output system has been measured both in the pre-prototype gyrotron and "cold" at low power. The experimental data are only partly in agreement with results of simulations. The measured microwave power distribution is in good agreement, including the Gaussian content, up to the position of the 2<sup>nd</sup> mirror. The performance of the RF beam at the plane of the RF output window is not as expected from simulation. In particular, the Gaussian content is only about 77 % and not 87 % as calculated. There are indications that the 3<sup>rd</sup> mirror which is a phase correcting mirror with a complicated surface contour is not working as expected. The reason is under investigation. For further improvement of the q.o. RF output system, the development of a new code for optimization

of the launcher is in progress with the goal to obtain an RF output beam with a Gaussian content  $\geq 95\%$  and to reduce the stray losses below 5% of  $P_{\text{out}}$ .

## Summary and outlook

The first industrial prototype of the 170 GHz, 2 MW, CW, coaxial cavity gyrotron has been delivered to CRPP Lausanne for testing. The SC magnet has been delivered recently after a long delay. Even if the specifications are not fully reached, the performance of the magnet allows testing of the gyrotron. The prototype gyrotron has been installed in the SC magnet and the operation has started beginning of December 2007.

The excitation mechanism of the LF oscillations has been recognized and experimentally verified. Corresponding modifications for reduction of the level of the parasitic oscillations have been performed in the industrial prototype. In experiments employing the pre-prototype with a Brewster window, no significant effects on gyrotron operation as a consequence of reduced microwave stray losses in the neighbouring, competing modes have been observed. A crucial component which requires further improvement is the q.o. RF output system. Work for improvement mainly of the launcher design is going on.

## Staff:

A. Arnold  
G. Dammertz  
J. Flamm (Uni Karlsruhe)  
G. Gantenbein  
S. Illy  
J. Jin  
S. Kern  
R. Lang  
W. Leonhardt  
D. Mellein  
B. Piosczyk  
O. Prinz  
T. Rzesnicki  
M. Schmid  
W. Spieß  
J. Szczesny  
M. Thumm

## Literature:

- [1] Piosczyk, B.; Albajar, F.; Alberti, S.; Benin, P.; Bin, W.; Bonicelli, T.; Cirant, S. et. al.; STATUS OF THE 2 MW, 170 GHZ COAXIAL CAVITY GYROTRON FOR ITER. 4th IAEA Technical Meeting on ECRH Physics and Technology for ITER, Wien, A, June 6-8, 2007; CD-ROM
- [2] Rzesnicki, T.; ANALYSE EINES NEUARTIGEN 1.5 MW, 170 GHZ PROTOTYP-GYROTRONS MIT KOAXIALEM RESONATOR. Wissenschaftliche Berichte, FZKA-7299 (Juni 2007); Dissertation, Universität Karlsruhe 2007
- [3] Henderson, M.A.; Alberti, S.; Benin, P.; Bonicelli, T.; Chavan, R.; Campbell, D.; Cirant, S.; Dammertz, G.; Dormicchi, O.; Dumbrajs, O.; Fasel, D.; Goodman, T.P.; Heidinger, R.; Hogge, J.P.; Kasperek, W.; Lievin, C.; Piosczyk, B.; Poli, E.; Ramponi, G.; Saibene, G.; Sauter, O.; Serikov, A.; Taddia, G.; Thumm, M.; Tran, M.Q.; Verhoeven, A.G.A.; Zohm, H.; EU DEVELOPMENTS OF THE ITER ECRH SYSTEM. Fusion Engineering and Design, 82(2007) S.454-62
- [4] Bonicelli, T.; Alberti, S.; Cirant, S.; Dormicchi, O.; Fasel, D.; Hogge, J.P.; Illy, S.; Jin, J.; Lievin, C.; Mondino, P.L.; Piosczyk, B.; Rzesnicki, T.; et al.; EC POWER SOURCES: EUROPEAN TECHNOLOGICAL DEVELOPMENTS TOWARDS ITER. Fusion Engineering and Design, 82(2007) S.619-26
- [5] Louksha, O.I.; Piosczyk, B.; Sominski, G.G.; Thumm, M.; Samsonov, D.B.; SUPPRESSION OF PARASITIC SPACE-CHARGE OSCILLATIONS IN A GYROTRON. Radiophysics and Quantum Electronics, 49(2006) S.793-98

- [6] Rzesnicki, T.; Piosczyk, B.; Dammertz, G.; Gantenbein, G.; Thumm, M.; Michel, G.; 170 GHZ, 2 MW COAXIAL CAVITY GYROTRON - INVESTIGATION OF THE PARASITIC OSCILLATIONS AND EFFICIENCY OF THE RF-OUTPUT SYSTEM. 8th IEEE Internat. Vacuum Electronics Conf. (IVEC 2007), Kitakyushu, J, May 15-17, 2007; Proc.S.45-46; ISBN 1-4244-0633-1
- [7] Jin, J.; Thumm, M.; Piosczyk, B.; Flamm, J.; Rzesnicki, T.; IMPROVEMENT OF QUASI-OPTICAL MODE CONVERTER FOR 170 GHZ COAXIAL CAVITY GYROTRON AT FZK. Griffin, M.J. [Hrsg.] Joint 32nd Internat. Conf. on Infrared and Millimetre Waves, and 15th Internat. Conf. on TeraHertz Electronics, Cardiff, GB, September 2-7, 2007; Conf. Digest Vol. I S.440-41; ISBN 1-4244-1438-5
- [8] Hogge, J.P.; Albajar, F.; Alberti, S.; Benin, P.; Bonicelli, T.; Cirant, S.; Fasel, D.; et al.; THE EUROPEAN 2MW, 170GHZ COAXIAL CAVITY GYROTRON FOR ITER. Griffin, M.J. [Hrsg.]; Joint 32nd Internat. Conf. on Infrared and Millimetre Waves, and 15<sup>th</sup> Internat. Conf. on TeraHertz Electronics, Cardiff, GB, September 2-7, 2007; Conf. Digest Vol. I S.38-40; ISBN 1-4244-1438-5
- [9] Piosczyk, B.; Rzesnicki, T.; Dammertz, G.; Dumbrajs, O.; Flamm, J.; Gantenbein, G. et al.; INVESTIGATIONS ON AN EXPERIMENTAL 170 GHZ COAXIAL CAVITY GYROTRON. Griffin, M.J. [Hrsg.]; Joint 32nd Internat. Conf. on Infrared and Millimetre Waves, and 15<sup>th</sup> Internat. Conf. on TeraHertz Electronics, Cardiff, GB, September 2-7, 2007 Conf. Digest Vol. I S.96-97; ISBN 1-4244-1438-5
- [10] Dumbrajs, O.; Avramides, K.A.; Piosczyk, B.; MODE COMPETITION IN THE 170 GHZ COAXIAL GYROTRON CAVITY FOR ITER. Joint 32nd Internat. Conf. on Infrared and Millimetre Waves, and 15th Internat. Conf. on TeraHertz Electronics, Cardiff, GB, September 2-7, 2007; Conf. Digest Vol. I; ISBN 1-4244-1438-5
- [11] Illy, S.; Piosczyk, B.; SIMULATION OF HIGH POWER CW GYROTRON COLLECTORS INCLUDING THE EFFECT OF SECONDARY EMISSION. Joint 32nd Internat. Conf. on Infrared and Millimetre Waves, and 15th Internat. Conf. on TeraHertz Electronics, Cardiff, GB, September 2-7, 2007; Conf. Digest Vol. I; ISBN 1-4244-1438-5

## **EFDA/05-1352 (TW5-THHN-MONRF)**

### **Monitoring the EU/RF Collaborative Tasks on the First ITER NB Injector and the ITER NB Test Facility**

#### **Background and objectives**

The central work of this task is related to gas flow and density calculations for the Neutral Beam Test Facility (NBTF) and the ITER Neutral Beam Injector (NBI). The Kurchatov Institute of the Russian Federation (KIAE) is performing calculations using the three codes: PDP (Power Deposition Profiles), MC-GF (Monte Carlo - Gas Flow) and BTR (Beam Transport and Re-ionisation), developed in KIAE for ITER NBI and similar tasks. These codes describe different substantial features of the NB systems and also serve for different kinds of studies on the proposed or chosen set of injector parameters. The present task with FZK has defined the input parameters from the cryopump point of view, which acts as the dominant gas sink, having a strong influence on the gas profile along the entire beam line and, thus, on the re-ionisation processes and the efficiency of the machine.

The aim of the task is to set up a user-friendly interface for the input data of these codes and to adapt them to the present design of the ITER NB and NBTF as well as to carry out computations of power deposition, power balance, gas flow and density profiles in the NB line components.

#### **Used beam line geometry**

Within the parallel EFDA-Task TW6-THHN-NBD1 [1] the design of the beam line vessel for the ITER HNB has been re-developed so as to cover the consequences introduced by the new top access requirements for the HNB cell and the changes made to the beam line components. It was also decided to use an accelerator which can be re-assembled from MAMUG to SINGAP configuration. In this design work, it turned out that the extraction and acceleration of the needed ITER-relevant ion current from the beam source will lead to a very high heat load by positive ions to the accelerator. This heat load is sensitive on the gas pressure between the accelerator and the neutralizer. Hence, the focus of the work being performed in 2007 under the present task was given to minimization of the pressure in this region of the beam line.

#### **Detailed design investigations of cryopumps with the RF MC-GF code**

FZK has proposed a new draft cryopump design with a 50% increased gas capture coefficient and adopted it to the actual vessel geometry. It is based on two rectangularly shaped cryopumps which are placed to the left and the right of the beam line components and can be assembled and disassembled through the top flange.

The design of the cryopumps was driven by maximisation of pumping speed combined with a quantitative assessment of the pumping capacity. As an ongoing enterprise, the present input parameters for the gas throughputs were re-calculated with the Russian Monte Carlo-Gas Flow code and its user interface, with all the different versions being released by KIAE. A gas throughput of 320 (mbar-l)/s was given for protium, and a value of 240 (mbar-l)/s for deuterium, both of which could be confirmed by the FZK vacuum codes ITERVAC and ProVac3D as well.

#### **New MC code development at FZK: ProVac3D**

Under this task, many re-iterations between FZK and KIAE became necessary and several weaknesses of the MC-GF code could be identified. In order to have a well defined benchmark process, FZK decided to develop its own code, based on the same underlying model idea as the MC-GF code, but with a view on maximum versatility for broader application to

arbitrarily complex vacuum systems in general. This new Monte Carlo code, called ProVac3D (Pressure Profiles in Vacuum Systems) covers complex vacuum systems with several gas sources and gas sinks (pumps). In addition the energy transfer of gas particles between surfaces of different temperatures can be described, which provides essential input information for heat load assessments. The code results in a detailed 3-dimensional gas distribution of the entire vacuum system including densities, velocities and temperatures of the gas particles. The used geometrical models have been taken from the detailed and actual CATIAv5 drawings of the ITER database [2]. A drawing is shown in Fig. 1 and the resulting (axial) gas density distribution along the NB vessel in Fig. 2.

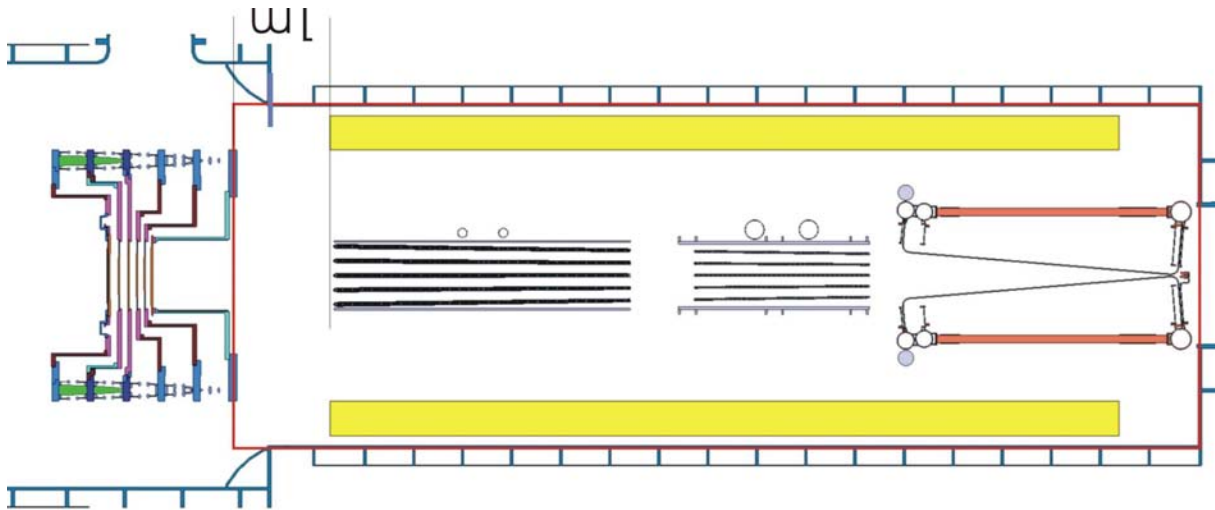


Fig. 1: Sectional cut through the ITER HNB as used for the MC models. In yellow the cryopumps. The blue circles show the main gas sources, one in the Ion source (on the left) and one in the Neutralizer (on the right).

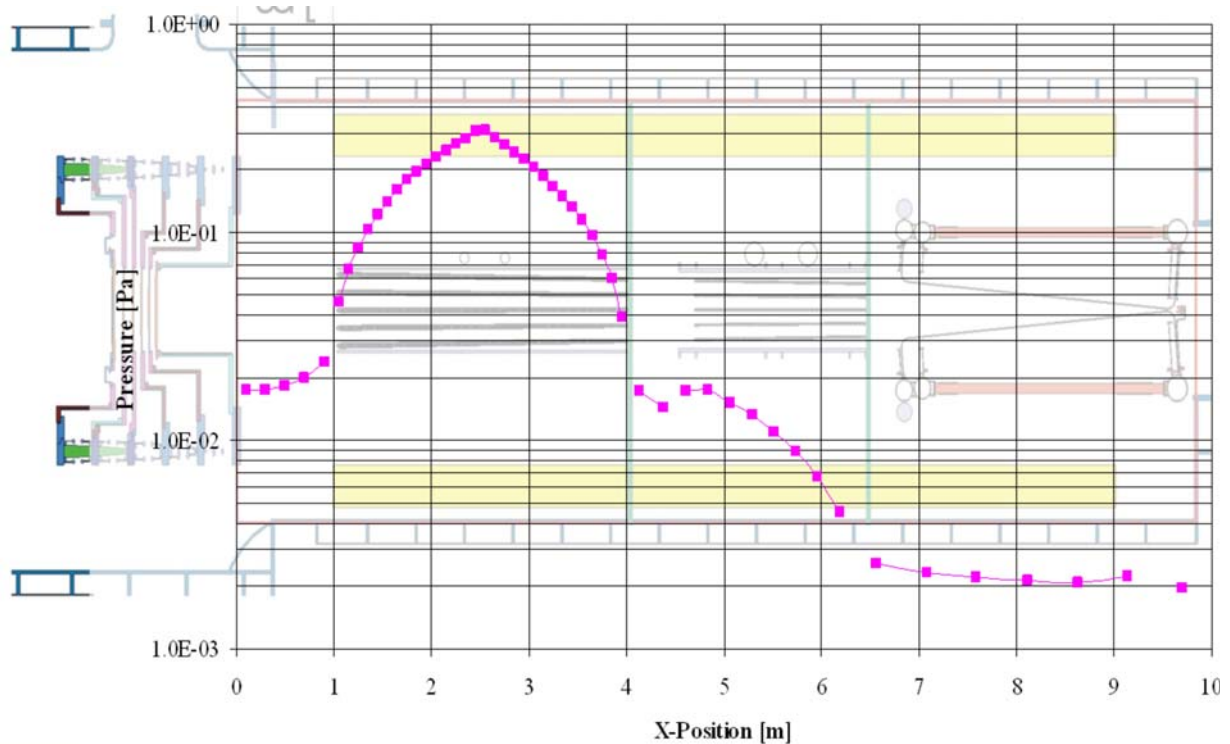


Fig. 2: Resulting gas distribution in the beam line vessel of the ITER HNB.

### Benchmarking of the different codes

The Russian MC-GF code includes the interaction of the gas molecules with the surfaces of the beam line components and needs a proper description of the surface temperatures and the expected accommodation coefficients. These values are subject to change during the design evolution. Therefore, the idea for refining the existing code was to list the input parameters in a separate file to be as flexible as possible. The development of an interface for how to handle that file has been achieved in 2007.

The results of the Russian calculations have always been cross-checked with the results from the FZK codes ITERVAC and ProVac3D. Within these investigations FZK could develop the use of ITERVAC not only for single duct systems but also for a complex network of ducts [3]. Compared to a Monte Carlo code (such as MC-GF or ProVac3D), ITERVAC is finally limited in the flexibility of the geometry of the vacuum system but it has the advantage to cover the entire pressure range, from molecular flow to viscous flow conditions, whereas the Monte Carlo code is limited to the free molecular UHV regime. In the relevant ranges the comparison of the ITERVAC results with the results from MC codes show a very good agreement and the use of ITERVAC was very successful as shown in Fig. 3.

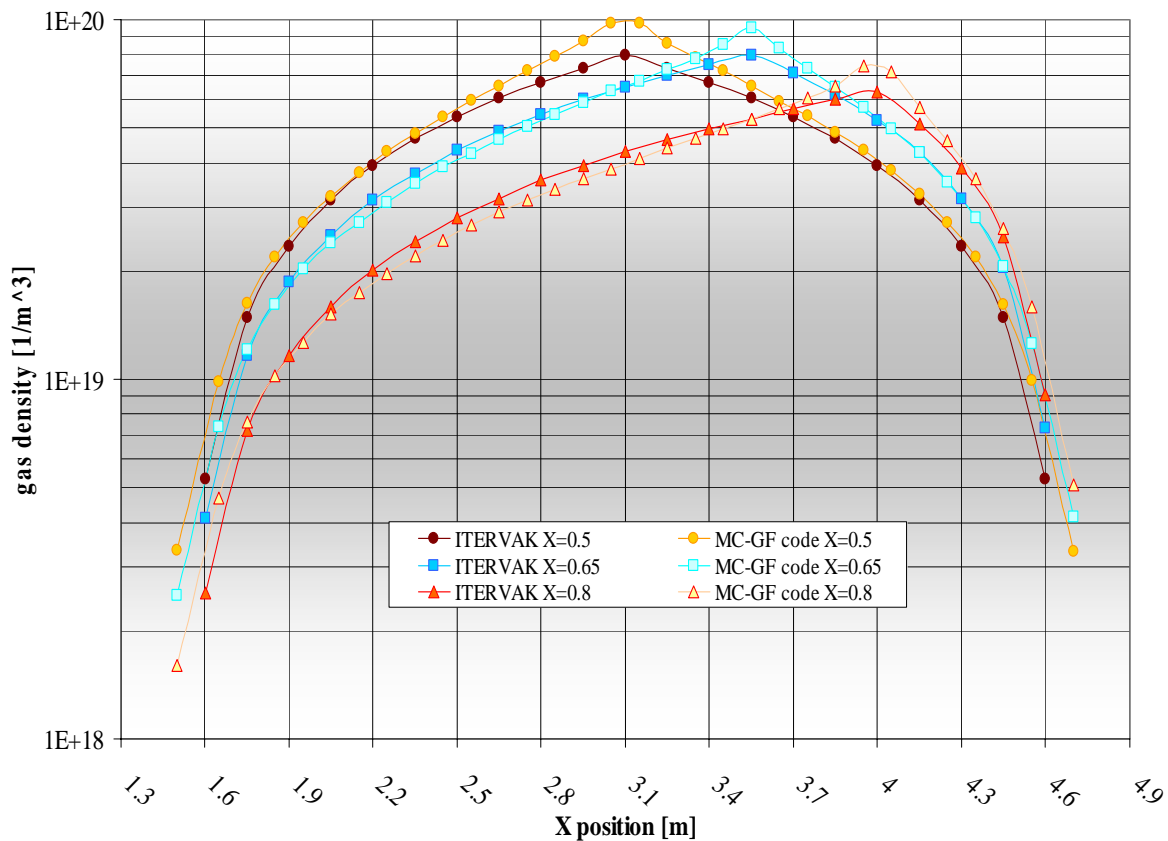


Fig. 3: Comparison of the gas distribution calculation between the Russian MC-GF code and ITERVAC, calculated for the neutraliser with varied inlet position.

Based on this code, the final cryopump geometry for the HNB with the needed gas baffles along the HNB vessel has been calculated. The cross check of both codes was successful. The task will be continued until February 2008 and be finalized with a final cross-check.

Staff:

M. Dremel  
V. Hauer  
X. Luo

Literature:

- [1] M. Dremel, Gas density profiles for the H-NBI, 14th ITER-EFDA-FZK Interface meeting, July 2007, ITER IDM ITER\_D\_27LBHX
- [2] X. Luo, Calculation and modelling comparison of density profiles of the heating NBI, 1<sup>st</sup> ITER Vacuum Interface Workshop, Dec. 2007, Aix, France.
- [3] M. Dremel, Status of the H-NBI cryopump design, 14th ITER-EFDA-FZK Interface meeting, July 2007, ITER IDM ITER\_D\_27LATY

## EFDA/06-1502 (TW6-THHN-NBD1) Design Activities for the First ITER HNB Injector

### Summary of the design work in 2007

The change in 2006 from a circular to a rectangular shaped beam line vessel led to a total change of the available base geometry of the ITER HNB cryopumps. An additional consequence was that the pumping surface had to be reduced by 20% due to space limitations. Moreover, the new vessel geometry leads to a less uniform distribution of the cryopump pumping speed of the beam line, which makes the cryopump design more difficult. Finally, new experimental investigations have shown that the needed gas density between the accelerator and the neutralizer must be further decreased, at least below 0.02 Pa.

The main result of all these constraints is that a cryopump in the classical design as used for the torus cryopumps, i.e. using a chevron baffle as radiation shield and including hydroformed cryopanel for the 4.5 K circuit, is not anymore capable to fulfil these new and challenging set of requirements. Consequently, detailed investigations on the development of a new cryopump design were made. Various designs have been elaborated and their properties (pumping speed, heat loads, etc.) have been compared to find the best solution. After a final review discussion held with ITER IO and EFDA, the agreed result was a cryopump model with a gas capture coefficient of 0.34, see Fig. 1, which is an increase of 50% in pumping speed [1], compared to the classical cryopump design.

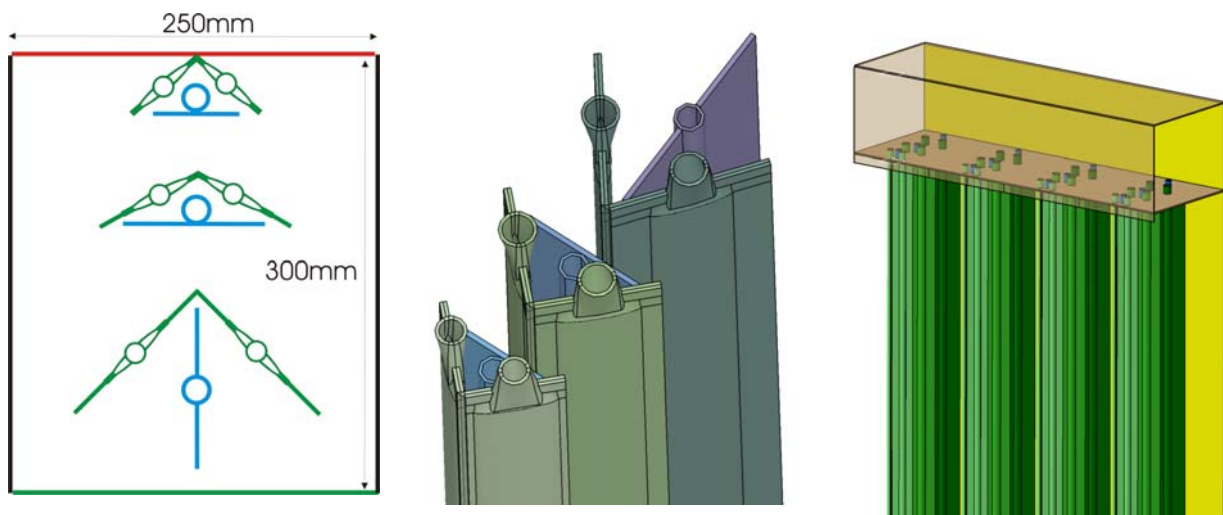


Fig. 1: Illustration of the new cryopump conceptual design for the HNB. The left part shows the top view and the middle part a 3D view of one cryopump section. The right part shows one cryopump module with 4 of these sections. The entire cryopump will consist of 8 modules, each 1m in width and 2.6 m in height.

To investigate the pumping properties of such a new cryopump and to come to an optimised detailed design, a full 3-dimensional model of the ITER HNB has been set up in a new Monte Carlo code (ProVac3D) developed in the vacuum group of FZK under the parallel task TW5-THHN-MONRF [2]. The improvements by the higher pumping speed have been worked out in detail. The resulting pressure in the critical region between accelerator and neutralizer was decreased to about 0.015 Pa, which meets the ITER requirements. Within the modelling work with ProVac3D, the installation of additional gas baffles along the beam line has been proposed to ITER to improve the operation conditions of the Neutral Beam, see Fig. 2.

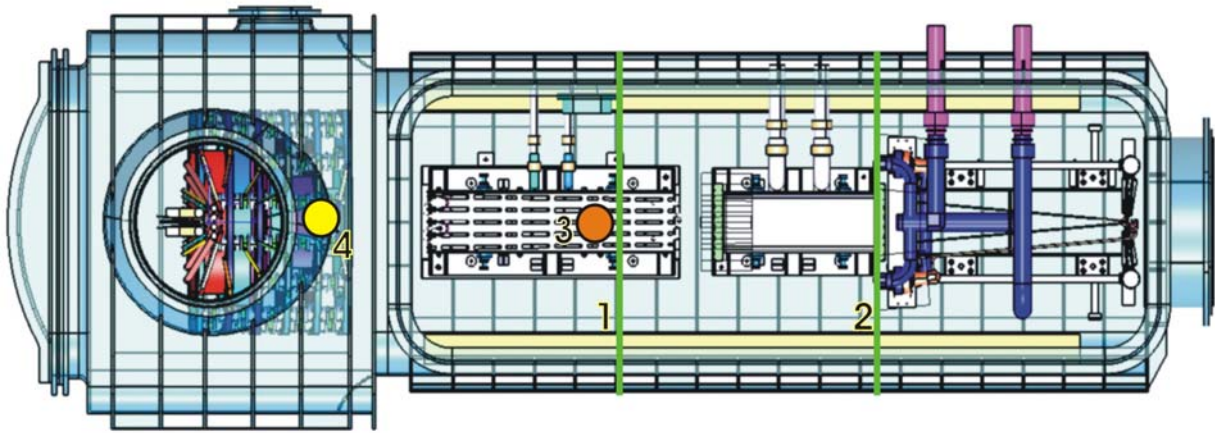


Fig. 2: Sketch of the actual beam line design of NBTF distributed by RFX/EFDA in April/May 2007. The gap between the accelerator and the neutralizer was reduced to 1.0 m. This sketch was used as basis for the Monte Carlo modelling. '1' and '2' indicate the proposed baffles along the beam line. The red circle with number '3' is the gas inlet in the neutralizer as the main gas source and '4' is the position of the gas source in the ion beam source.

An additional 3-dimensional Monte Carlo model (in MOVAK3D) of the cryopump was further used for the determination of the heat loads to the 80 K shielding and the 4.5 K circuits. The use of a Monte Carlo model allows to determine very accurately the viewing factors, which allows to assess and intercompare different surface treatments of the 80 K shields and thus to optimize the cryopump with regard to heat loads. In Table 1 the heat loads for different operation scenarios are listed. For the stand-by operation of the beam line, only radiation and solid heat conduction are contributing. For the pulsed operation, additional heat loads by the pumped gas must be taken into account [3, 4]. The Neutral Beam Test Facility might have a different cryogenic cooling loop than the ITER cryoplant, therefore the values have been calculated for both conditions.

Table 1: Heat loads for the proposed NB cryopump design.

	80 K cooling conditions	Heat loads		
			80 K	4.5 K
ITER	$T_{in} = 80\text{ K}$ $T_{out} = 90\text{ K}$	Stand by	8.6 kW	221 W
		Pulse op.	9.1 kW	375 W
NBTF	$T_{in} = 80\text{ K}$ $T_{out} = 105\text{ K}$	Stand by	8.6 kW	285 W
		Pulse op.	9.1 kW	440 W

## Outlook

Based on the agreement on the proposed conceptual design, the detailed engineering design work on the HNB cryopump system has started and will lead to a full design package in CATIAv5 until June 2008, which is in line with the planning schedule. A final report including manufacturing issues and a procurement plan will be delivered to EFDA.

Staff:

Chr. Day  
M. Dremel  
St. Hanke  
V. Hauer  
X. Luo  
R. Simon  
H. Strobel

Literature:

- [1] M. Dremel, Status of the H-NBI cryopump design, 14th ITER-EFDA-FZK Interface meeting, July 2007, ITER IDM ITER\_D\_27LATY
- [2] X. Luo, Calculation and modelling comparison of density profiles of the heating NBI, 1<sup>st</sup> ITER Vacuum Interface Workshop, Dec. 2007, Aix, France.
- [3] M. Dremel, The heating NBI cryopump design progress, 1<sup>st</sup> ITER Vacuum Interface Workshop, Dec. 2007, Aix, France.

# Physics



## ECR Heating and Current Drive – Step-Tunable Gyrotron Development

### Introduction

In recent years, electron cyclotron resonance heating and current drive (ECRH and ECCD) has been established as a successful instrument in magnetically confined fusion plasmas. Gyrotrons are the unique devices which meet the extraordinary requirements of those applications: output power in the MW range, 100 – 200 GHz output frequency, pulse length of several seconds up to continuous wave. Due to its excellent coupling to the plasma and the very good localisation of the absorbed RF power, ECRH is applied in present day machines and is also foreseen in large forthcoming fusion projects: it will be the main heating system for the stellarator W7-X which is currently under construction, and it will play a major role in the ITER tokamak. In particular, advanced tokamaks are operated in a plasma regime where MHD instabilities which may limit the performance are present. To a large extent the stability in a tokamak is influenced by the distribution of the internal plasma currents which can be manipulated by the injection of RF waves. The location of the absorption of RF-waves with the angular frequency  $\omega$  is dependent on the resonance condition  $\omega - k_z v_z = \omega_c$ . Thus, by changing the wave frequency  $\omega$  the absorption can be moved to any radial position where the local cyclotron frequency of the electrons  $\omega_c$  holds for the expression above ( $k_z$ ,  $v_z$ : longitudinal wave number and velocity of electrons, respectively).

Industrial gyrotrons in the relevant frequency range with an output power of about 1 MW are usually designed for a fixed frequency. However, frequency tunable gyrotrons are not a standard product since these broadband tubes require additional optimisation of major components of the gyrotron like the electron beam forming optics, cavity, quasi-optical mode converter and output window.

For experiments on plasma stabilization at ASDEX Upgrade (IPP Garching) with advanced ECRH and ECCD, multi-frequency tunable (105 – 140 GHz) 1-MW long-pulse gyrotrons are highly needed.

### Quasi-optical mode converter

The quasi-optical mode converter transfers the cavity mode into a Gaussian beam which fits through the window aperture. It consists of a dimpled-wall antenna, the so-called launcher, and a set of three beam-forming mirrors. For the multi-mode gyrotron the mode converter has to be optimized to convert all the nine modes between  $TE_{17,6}$  and  $TE_{23,8}$  with different properties to a Gaussian beam which does not change its properties from mode to mode. The optimization to achieve this properties can be splitted in two tasks. First, the launcher's inner waveguide wall is optimized to a Gaussian output pattern and a minimum of stray radiation. Second the mirrors are designed to a maximum power transmission through the window aperture by optimizing the diameter and position of the waist of the Gaussian beam for all modes.

In the past year a second and a third generation mode converter were designed. The theoretical and modelling results are presented below.

The optimization of the launcher, which is used in the second and third generation, led to a complex Gaussian content of more than 90 % for all nine modes. The output beam is well focussed and stray radiation is low. The detailed values shown in Table 1 were determined in a plane behind the quasi-elliptical mirror because the beam is paraxial there.

As the spread angles of the nine modes deviate, the output pattern of the launcher and the direction of radiation changes from mode to mode. This has the effect that each mirror is hit at a different position depending on the operating mode. If a focussing mirror is not hit in the center, the beam will be reflected to a direction deviating from central reflection. A smaller curvature radius has a larger effect. Thus, this effect will add an extra shift of the beam in the window plane. It can be reduced if the mirrors are less focusing. For the Brewster angle window described in the next paragraph, a very small window aperture of 50 mm must be the optimization criteria. By optimizing the curvature radii of the toroidal mirrors a transmission through the window of more than 95 % for all modes has been achieved, for most of the modes even more than 97 %. The numbers are given in Table 1.

Table 1: Gaussian content and transmission through the output window.

Mode	Frequency [GHz]	Complex Gaussian content [%]	Transmission [%]
TE <sub>17,6</sub>	104,9	95,2	96,9
TE <sub>18,6</sub>	108,2	92,9	96,2
TE <sub>19,6</sub>	111,5	90,4	95,4
TE <sub>19,7</sub>	120,8	94,8	97,5
TE <sub>20,7</sub>	124,1	93,4	97,3
TE <sub>21,7</sub>	127,4	91,7	97,1
TE <sub>21,8</sub>	136,7	93,0	97,8
TE <sub>22,8</sub>	140,0	93,3	97,9
TE <sub>23,8</sub>	143,3	91,5	97,4

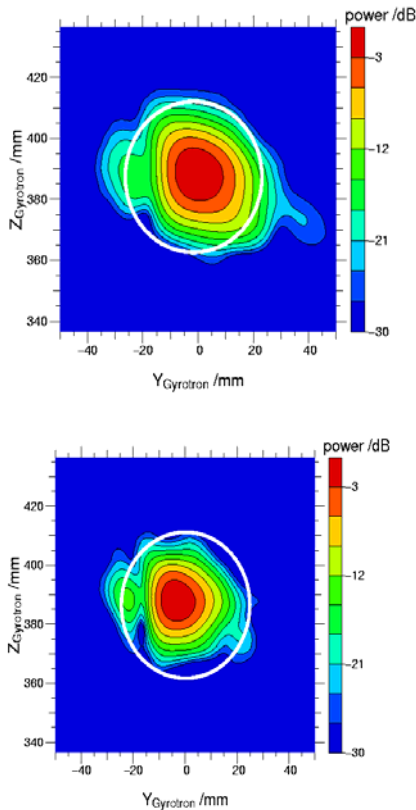


Fig. 1: Field pattern at the window for the modes TE<sub>17,6</sub> (top) and TE<sub>22,8</sub> (bottom).

The radiation pattern at the window position for the modes TE<sub>17,6</sub> and TE<sub>22,8</sub> of the second generation mode converter are plotted in Fig. 1. The white circle in the figure shows the window aperture. For all modes, the beam is nicely focussed with a side lobe which has its origin in the radiation of the launcher.

In the cross section of the mode converter, which is shown in Fig. 2, the focussing properties of the mode converter are demonstrated for the TE<sub>17,6</sub> mode.

A further optimization of this mode converter was performed with the use of mirrors with a non quadratic phase correcting surface contour function which led to the third generation mode converter. These mirrors are based on the toroidal mirrors of the second generation, with an additional phase correction on the smooth mirror surface. By a multi-frequency optimization of the phase correction, a significantly higher Gaussian mode content could be realized, which is shown in Table 2. With a Gaussian mode content of more than 93 %, an increase of 2 % in average was achieved. Also, the transmission through the window was enhanced by the phase correction as shown in Table 2. The enhancement can also be verified at the mode pattern in the window plane for the third generation mode converter shown in Fig 3. When comparing these patterns with the ones from Fig. 1, a reduction of the side lobes is visible.

It is planned to confirm these theoretical results by low power measurements of the quasi-optical mode converter using a D-band vector network analyzer with high dynamic range.

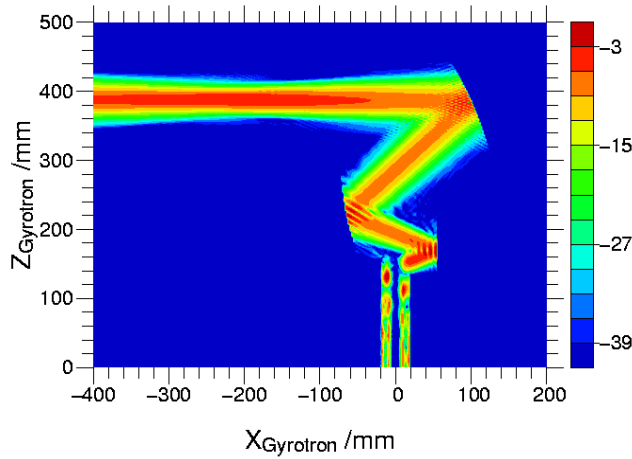


Fig. 2: Cross section of the second generation mode converter for  $TE_{17,6}$ .

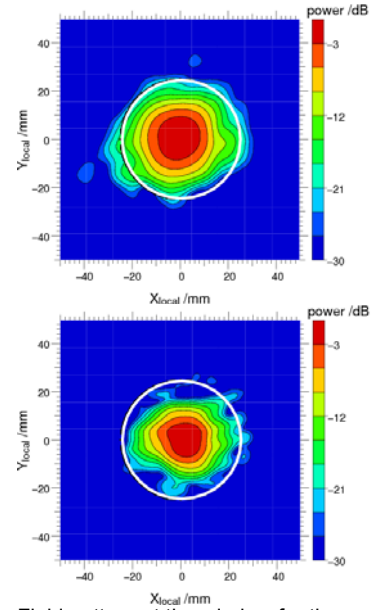


Fig. 3: Field pattern at the window for the modes  $TE_{17,6}$  (top) and  $TE_{22,8}$  (bottom) for the third generation of mode converter.

Table 2: Gaussian content and transmission through the output window for the third generation mode converter.

Mode	Frequency [GHz]	Complex Gaussian content [%]	Transmission [%]
$TE_{17,6}$	104,9	97,7	97,3
$TE_{18,6}$	108,2	97,1	97,5
$TE_{19,6}$	111,5	95,0	97,1
$TE_{19,7}$	120,8	96,7	97,7
$TE_{20,7}$	124,1	96,0	97,3
$TE_{21,7}$	127,4	94,5	96,9
$TE_{21,8}$	136,7	93,3	97,9
$TE_{22,8}$	140,0	95,1	98,0
$TE_{23,8}$	143,3	94,2	97,7

### CVD-diamond Brewster window

Efficient operation for the large number of operating modes at different frequencies is only possible by using a broadband diamond Brewster window fabricated by chemical vapor deposition (CVD). Due to the large Brewster angle, the diameter of the disk has to be rather large in order to have a sufficiently large aperture for the RF beam. One disk with a thickness of 1.7 mm and a diameter of 140 mm was developed by Element Six and already delivered. This disk can be used for the elliptic shape of a Brewster window with an effective aperture of 50 mm.

Because of the ellipticity, the stresses during the brazing procedure are different from circular disks. These stresses were calculated to be increased by a factor of 1.3. To investigate whether a diamond disk will sustain these stresses, brazing tests are being performed at Thales Electron Devices with a quartz disk, a ceramic disk and a small diamond disk, for

which the stresses are increased compared to the circular one. In case of successful brazing, the 140 mm diamond disk will be brazed with copper cuffs, so that it will be possible to cool the disk at the edge.

However, the first brazing of a ceramic disk failed and a small leak occurred. Refined FEM calculations of the brazing tool and the small diamond disk have been performed. They show that the stresses in the diamond disk are far below the usual conservative critical stress levels. These results suggest that there is a good chance for a successful brazing of the diamond disk provided that the brazing quality is good.

## **Auxiliaries**

### **1. Step-tunable Magnet**

In 2007 the order of an industrial fast step tunable magnet has been placed. The design of the magnet has been checked thoroughly with the manufacturer and a common design has been agreed. This magnet is specified for a fast change of the field in the range of 4.15 – 5.67 T, thus allowing to change the gyrotron frequency from 105 GHz to 143 GHz in steps of approximately 3 GHz within 0.5 s every 10 s. The maximum field will be 7.2 T which makes it suitable also to operate a 170 GHz gyrotron, corresponding to the design frequency of the ITER ECRH system.

### **2. Spare Electron Gun**

A spare electron gun has been ordered at Gycom Ltd.. It was delivered in 2007, acceptance tests of the electron gun together with the gyrotron were passed successfully.

### **Staff:**

A. Arnold  
G. Dammertz  
J. Flamm (Uni Karlsruhe)  
G. Gantenbein  
R. Heidinger  
S. Illy  
S. Kern  
W. Leonhardt  
D. Mellein  
B. Piosczyk  
O. Prinz  
M. Schmid  
W. Spieß  
D. Strauss  
J. Szczesny  
M. Thumm

### **Literature:**

- [1] Arnold, A., O. Prinz, D. Wagner, M. Thumm: Operation of a quasi-optical multi-mode generator for 105-150 GHz, Conf. Digest Joint 32<sup>nd</sup> Int. Conf. on Infrared and Millimetre Waves and 15<sup>th</sup> Int. Conf. on Terahertz Electronics, Cardiff, UK, 2007, pp. 434-435.
- [2] Prinz, H.O.; Gantenbein, G.; Thumm, M.. Matching the output beam of a multi-frequency gyrotron to a Brewster window with small aperture. 8th IEEE Internat.Vacuum Electronics Conf. (IVEC 2007), Kitakyushu, J, May 15-17, 2007 Proc.S.49-50
- [3] Prinz, O.; Arnold, A.; Dammertz, G.; Flamm, J.; Gantenbein, G.; Jin, J.; Piosczyk, B.; Rzesnicki, T.; Thumm, M., Quasi-optical mode converter for a multi-frequency D-band gyrotron. Joint 32nd Internat.Conf.on Infrared and Millimetre Waves, and 15<sup>th</sup> Internat.Conf.on TeraHertz Electronics, Cardiff, GB, September 2-7, 2007

- [4] Wagner, D., Leuterer, F., Manini, A., Monaco, F., Münich, M., Ryter, F., Schütz, H., Stober, J., Zohm, H., Franke, T., Danilov, I., Heidinger, R., Thumm, M., Gantenbein, G., Kasperek, W., Lechte, C., Litvak, A., Denisov, G., Tai, E., Popov, L., Nichiporenko, V., Myasnikov, V., Solyanova, E., Malygin, S., Meo, F., Woskov, P., The new multifrequency electron cyclotron resonance heating system for ASDEX upgrade. *Fusion Science and Technology*, 52(2007) S.313-20
- [5] Wagner, D., Leuterer, F., Stober, J., Manini, A., Monaco, F., Münich, M., Schütz, H., Zohm, H., Franke, T., Thumm, M., Heidinger, R., Danilov, I., Gantenbein, G., Flamm, J., Litvak, A.G., Popov, L.G., Nichiporenko, V.O., Myasnikov, V.E., Denisov, G.G., Tai, E.M., Solyanova, E.A., Malygin, S.A., Present status of the new multi-frequency ECRH system for ASDEX Upgrade. *Pulsed Power and Plasma Science Conf.*, Albuquerque, N.M., June 17-22, 2007, Book of Abstracts S.554

## Microwave Heating for Wendelstein 7-X

### Introduction

In the recent years electron cyclotron resonance systems have been established as a standard method for localised heating (ECRH) or current drive (ECCD) in fusion relevant plasmas. Thus ECRH will be the basic day-one heating system for the stellarator W7-X which is currently under construction at IPP Greifswald. In the first stage W7-X will be equipped with a 10 MW ECRH system operating at 140 GHz in continuous wave (CW). The complete ECRH system will be provided by FZK, which in 1998 established, together with EU partners, the 'Projekt Mikrowellenheizung für W7-X' (PMW). The responsibility covers the design, development, construction, installation and integrated testing of all components required for stationary plasma heating on site at IPP Greifswald. PMW also coordinates the contributions from Institut für Plasmaforschung (IPF) of the University Stuttgart, which is responsible for the microwave transmission system and part of the HV-system, and from the team at IPP Greifswald, which is responsible for the in-vessel components and for the in-house auxiliary systems. PMW benefits from the collaboration with Centre de Recherche de Physique des Plasmas (CRPP) Lausanne, Commissariat à l'Energie Atomique (CEA) in Cadarache and Thales Electron Devices (TED) in Vélizy. A contract between CRPP, FZK and TED had been settled to develop and build the continuously operating series gyrotrons. The first step of this collaboration was the development of a prototype gyrotron for W7-X with an output power of 1 MW for CW operation at 140 GHz. This step has been completed successfully.

At the industrial company TED, 7 series gyrotrons have been ordered. First operation and long pulse conditioning of these gyrotrons will take place at the teststand at FZK, where pulses up to 180 s at full power are possible (FAT); 30 minutes shots at full power are possible at IPP (SAT). Including the pre-prototype tube, the prototype tube and the 140 GHz CPI-tube, ten gyrotrons will be available for W7-X. To operate these gyrotrons, eight superconducting magnetic systems have been ordered at Cryomagnetics Inc., Oak Ridge, USA.

### Series Gyrotrons

In 2007, the series gyrotron #4 was taken into operation and tested at FZK with short and long pulses. The gyrotron was optimized in short pulse operation and the dependence of the output power and stable oscillating region of the design mode (TE<sub>28,8</sub>) on different parameters was investigated. The total RF output power is measured by a short pulse calorimetric load which is mounted close to the output window of the gyrotron. In the experiments shown in Fig. 2, the beam radius has been varied from 10.278 mm to 10.392 mm. In short pulses (2.8 ms) it shows a stable output power of up to 1 MW for the design values.

For medium pulse length (~ 1 s) and long pulses (several seconds up to 30 minutes) a CW load with massive water cooling is used in combination with an optical mirror system including two matching mirrors, two polarisers and a focusing mirror which transmits the beam from the output window to the entrance of the load. All RF radiation appearing outside the gyrotron during transmission is monitored calorimetrically, allowing a precise determination of the different



Fig. 1: The 4<sup>th</sup> series tube at the test facility of FZK.

loss channels. About 3 % of the total power measured outside the gyrotron window is lost as spurious radiation. At pulses longer than  $\sim 1$  s, the gyrotron is usually operated with depressed collector, which increases the efficiency and reduces the thermal loading of the collector. Since some physical parameters have time constants which are in the order of several hundreds of ms or even several seconds (e.g. cooling of cathode by extraction of electrons, thermal expansion of cavity, space charge neutralisation), operating conditions have to be modified. In general, this behaviour requires operating parameters which result in a loss of performance.

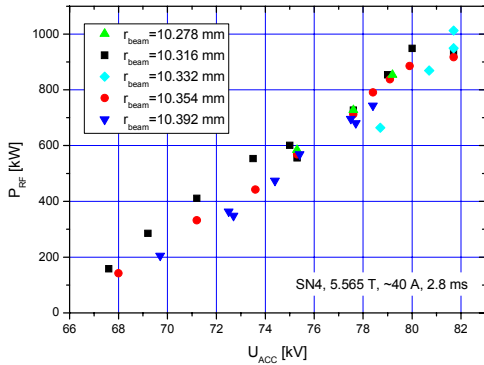


Fig. 2: RF power measured by the short pulse calorimetric load for different beam radii in the cavity.

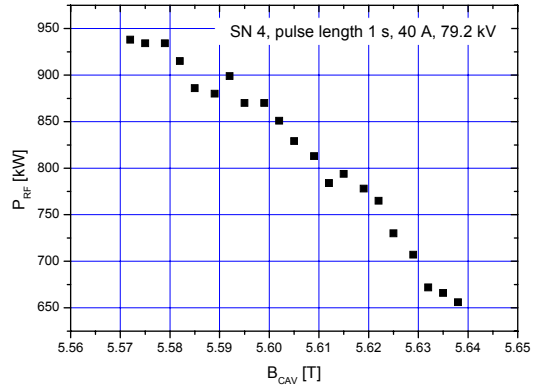


Fig. 3: Output power versus main magnetic field.

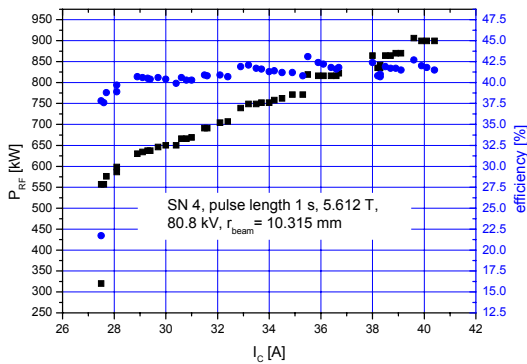


Fig. 4: Output power and efficiency versus beam current.

range 27 A up to 44 A with a depression voltage of up to 28 kV.

CW pulses have been performed up to 30 minutes, however with a reduced beam current ( $< 30$  A) due to a limitation in the power supply at FZK. The output power thus obtained was about 500 kW.

At maximum RF-power (910 kW), repetitive operation of the gyrotron was possible with a pulse length of 3 minutes.

In order to avoid additional losses during transmission, an excellent matching of the gyrotron output beam to the fundamental Gaussian beam of the transmission system is very important. The output beam of each gyrotron is measured carefully with an infrared system, detecting the thermal image of a short gyrotron pulse (few ms) on an appropriate target. Several images will be analysed to calculate the beam parameters and optimise the surface of two external matching mirrors. It was found that the beam parameters of SN4 are within the usual range and that the Gaussian content of the output beam is 97 %. Fig. 5 illustrates the thermal image of the output beam.

The dependance of the output power on the magnetic field in the cavity is shown in Fig. 3 for 1 s pulses. To obtain a stable operation at this pulse length, the magnetic field in the cavity has to be increased compared to pulses in the ms region. For  $B_{CAV} < 5.57$  T, spurious oscillations in competing modes occurred. The efficiency of the gyrotron was above 40 % for beam currents from 28 A up to 40 A with a maximum of 42.5 % (see Fig. 4). This indicates a good performance of the electron gun and a good electron beam quality. Safe operation of the gyrotron under CW conditions was possible in the current

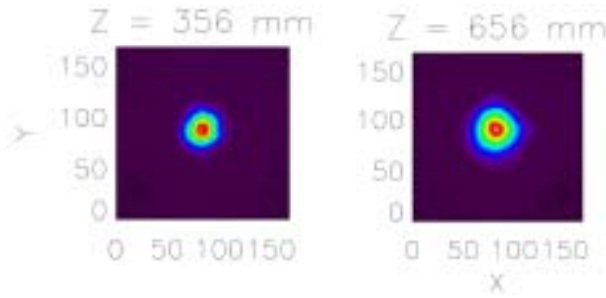


Fig. 5: Thermographic images of the output beam of SN 4 recorded on a PVC target at 356 mm and 656 mm from the window.

On the basis of these results, the gyrotron was accepted and shipped to IPP Greifswald in order to pass the site acceptance tests at full power and full pulse length. The tube was tested with pulses up to app. 8 minutes and an output power of 820 kW. Unfortunately, there was a water cooling failure during operation of the gyrotron. A first analysis showed that parts of the internal optical system are damaged due to thermal overloading. This tube was sent back to the manufacturer for repair.

The series gyrotron #2 and #3 (SN2 and SN3), which failed the acceptance test at FZK and IPP in 2006 and which were sent back to the manufacturer, were opened and carefully examined. All parts were in excellent conditions but the beam tunnel region showed severe damages. That region is equipped with several rings of ceramics and copper stacked together. The main purpose of this design is to suppress and prevent the excitation of parasitic oscillations which would deteriorate the electron beam parameters in front of the cavity and may lead to a high heat load to the structural material. It was found that brazed joints were molten and ceramic rings had cracks. These results indicate an excessive heat development with insufficient cooling of the structure. According to the technical experts, these damages were caused by bad brazings. The beam tunnel region of both tubes were remachined and the brazing process was improved.

The repaired series gyrotron SN2a was delivered to FZK for acceptance tests. At optimised parameters the gyrotron delivered 1210 kW at 50 A beam current and about 950 kW at the design parameters (see Fig. 6). The Gaussian content of the output beam is 95 %. No limitation of the pulse length is observed with that version of SN2a, pulses up to 30 minutes at 550 kW and 180 s at 850 kW were possible. However, for this gyrotron parasitic oscillations were detected at a frequency of 122 GHz, which limited the pulse length due to an excessive increase of the body current and the vacuum pressure. Currently, investigations are underway to clarify whether this undesired oscillation may be excited by a cyclotron resonance mechanism in the beam tunnel area.

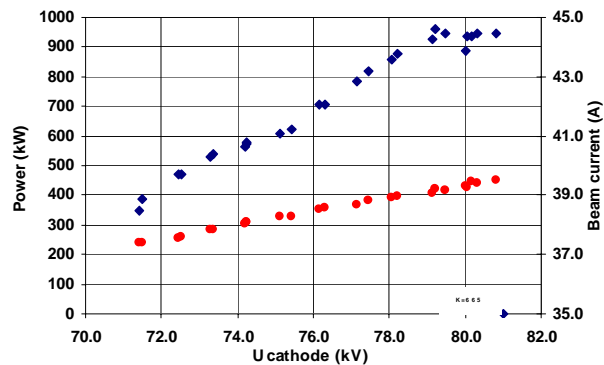


Fig. 6: Output power versus accelerating voltage and corresponding beam current for SN2 (short pulse operation).

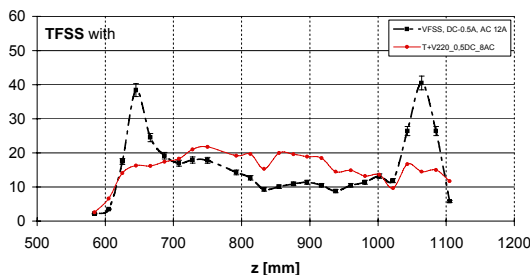


Fig. 7: Temperature increase at the collector for conventional sweeping (black line) and combined sweeping (red line).

The conditioning of that gyrotron has been stopped due to the occurrence of a water leakage in the absorber load; the acceptance tests of SN2a will be continued at IPP in Greifswald.

The collector is a component which must be designed very carefully since it has to withstand high thermomechanical stress. All gyrotrons are equipped with a solenoid coil at the collector which sweeps the strike points of the electron beam up and down with a low frequency ( $< 10$  Hz). Thus the specific heat dissipation on the collector surface is kept within

technically acceptable limits of about  $500 \text{ W/cm}^2$ . In addition to that, a six-coil 50 Hz transverse field sweep system (TFSS) has been realised and tested. Due to the increased sweep frequency of the TFSS, the maximum temperature at the inner collector surface should be reduced considerably, in combination with the standard sweep system a reduction of a factor of  $\approx 2$  has been achieved (see Fig. 7).

### Transmission Line

The transmission line consists of single-beam waveguide (SBWG) and multi-beam waveguide (MBWG) elements. For each gyrotron, a beam conditioning assembly of five single-beam mirrors is used. Two of these mirrors match the gyrotron output to a Gaussian beam with the correct beam parameters, two others are used to set the appropriate polarization needed for optimum absorption of the radiation in the plasma. A fifth mirror directs the beam to a plane mirror array, the beam combining optics, which is situated at the input plane of a multi-beam wave guide. This MBWG is designed to transmit up to seven beams (five 140 GHz beams, one 70 GHz beam plus an additional spare channel) from the gyrotron area (entrance plane) to the stellarator hall (exit plane). At the output plane of the MBWG, a mirror array re-separates the beams and distributes them via CVD-diamond vacuum barrier windows to individually movable antennas (launchers) in the torus. To transmit the power of all gyrotrons, two symmetrically arranged MBWGs are used.

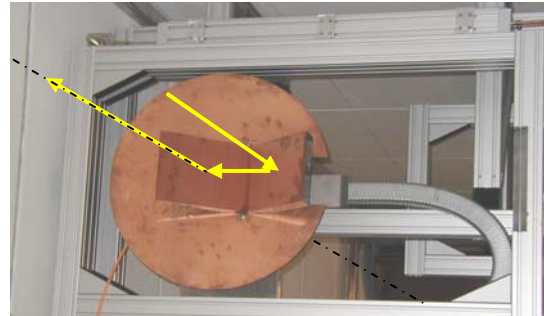


Fig. 8: Retro-reflector mounted in the beam duct. The forward input beam and the output beam as well as the axis of symmetry (dashed) of mirror rotation are indicated.

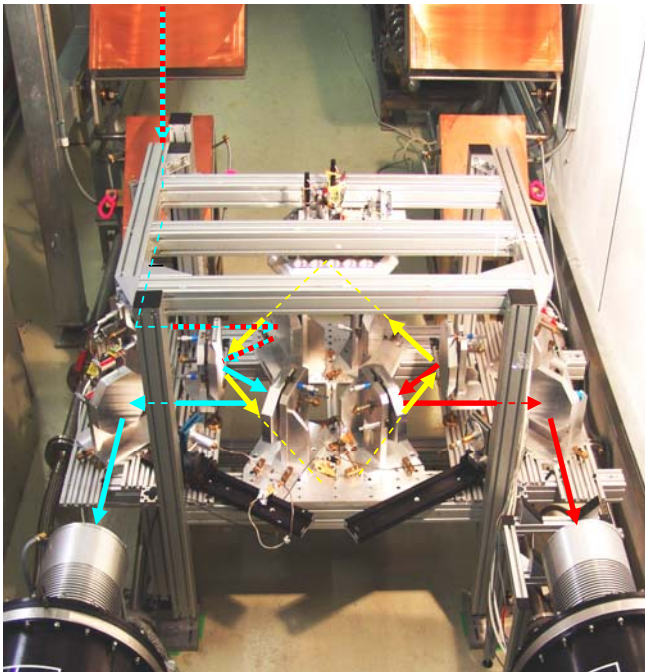


Fig. 9: Photograph of the FADIS installed in the beam duct of the ECRH system on W7-X. The input beam from the prototype gyrotron is coupled from the rear to the resonator, the output beams are focussed to absorbing loads in the foreground left (output 1) and right (output 2).

In 2007, a major work package was the manufacturing of the transmission system near the torus. This comprises the reflectors type M13 and M14, which will be installed in two "towers" in front of the stellarator W7-X. The fabrication of these towers is completed, and installation of control systems for reflectors and launchers, support structures, and granite absorbing plates is being performed. Finally, the retro-reflectors for testing the MBWGs will be installed in the towers as well. In the time before the towers will be installed at their final position, the retro-reflectors are mounted in the beam-duct in the image plane in the middle of the MBWG (Fig. 8). First measurements of the two-pass transmission efficiency of the first part of the MBWG were performed, yielding a loss of about 3 % for 10 reflections on the  $2 \times 3$  MBWG and the 4 additional guiding mirrors, which is in good agreement with calculations.

For the gyrotrons installed in 2007, matching mirrors were designed and

fabricated on the basis of thermographically recorded beam profiles and subsequent phase retrieval. A new setup for power monitoring on the first matching mirror was manufactured and cold-tested; it will be put into operation with the next gyrotron in Greifswald.

As in the past years, the ECRH system could be used for testing special components. Among others, a test campaign was dedicated to the investigation of a high-power diplexer, which is developed for use as a combiner for the power of two gyrotrons and as a fast directional switch (FADIS) between two outputs. The switching is performed (without moving parts) by a tiny frequency-shift keying initiated by modulation of the acceleration voltage of the gyrotron. For the test, a quasi-optical prototype FADIS, which had been developed in collaboration with colleagues from IAP Nizhny Novgorod, was installed into the transmission duct and connected to the prototype gyrotron (Fig. 9). Switching experiments with frequencies in the range of 1 - 20 kHz have been performed. At 5 kHz and a modulation voltage of 4 kV, a switching contrast of more than 90 % was reached. The tests show good agreement with theory and confirm the possibility of fast switching of high-power millimetre wave beams. An experiment for combination of two gyrotrons is in preparation.

## HV-Systems

For the operation of gyrotrons with depressed collector, a precisely controlled beam acceleration voltage is necessary, which is supplied by the body voltage modulator. The beam current of the gyrotrons is controlled by the cathode heater supply, which is on cathode potential (about -55 kV). In case of arcing inside the gyrotron, a thyatron crowbar protects the tubes from being damaged.

The fabrication of the body voltage modulators and the heating and tube protection units by IPF Stuttgart has been completed. All ten HV-control systems have been delivered to IPP Greifswald and were put into operation. An additional protection unit was developed to allow the exact location of the source of a fault in case of malfunction of the gyrotron. The prototype modulator is being upgraded to meet the same specifications as the series systems. During operation of the modulators together with several gyrotrons, the HV-systems did demonstrate their performance. Especially during the fast voltage modulation during the FADIS tests, the modulation slew rate of  $600 \text{ V}/\mu\text{s}$  could be confirmed. Fig. 10 shows a HV modulator as well as the typical output signal of the HV modulator at a modulation frequency of 10 kHz with a voltage swing of 15 kV.

## In-vessel Components

The design of the ECRH-antenna, which is shown in Fig. 11, was completed. Most of the antenna components are already manufactured now and the assembly has started.

The operation range of the ECRH heating system can strongly be increased, when heating scenarios with the second harmonic ordinary mode (O2) and the third harmonic extraordinary mode (X3) can be applied. The first allows high plasma density, which is necessary for efficient divertor operation. The second allows operation at a lower magnetic field.

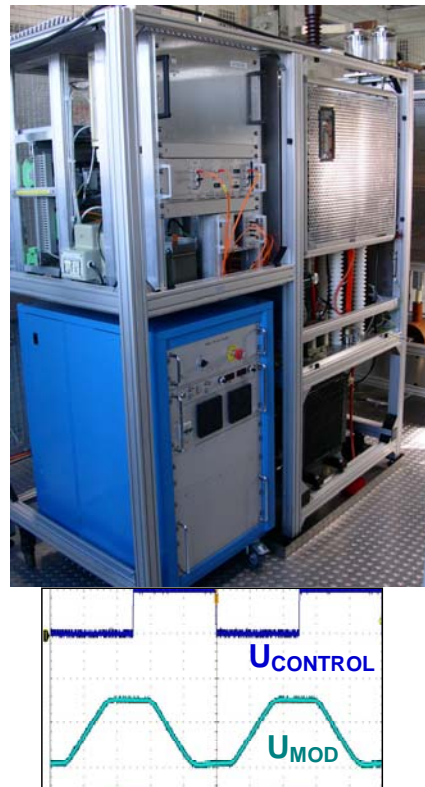


Fig. 10: High-voltage modulator and the measured output voltage for a voltage swing of 15 kV at a modulation frequency of 10 kHz, confirming the specification of the slew rate of  $600 \text{ V}/\mu\text{s}$ .

The expected single pass absorption is between 40 % and 80 %. To avoid thermal overloading by the non-absorbed beam power at the plasma vessel wall, specially shaped reflectors made from TZM (titanium, zirconium, molybdenum alloy) will be used. After first, preliminary high power test in 2006, the tile was re-designed and the tile surface was polished. The reflector tile was tested again in the ECRH-installation at Greifswald with the same power-load as expected in W7-X. The calorimetrically measured absorption at high power reached 0.3 % and was consistent with the theoretical value deduced from the material properties, and with low power tests.

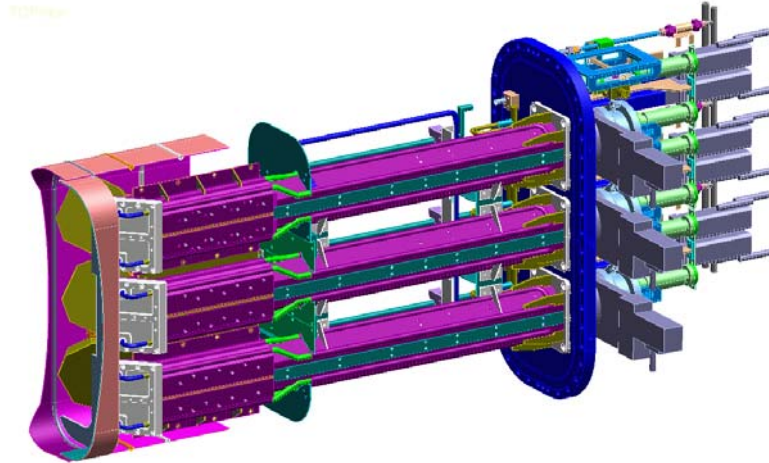


Fig. 11: CAD drawing of the W7-X front steering launcher.

The determination of the beam position and power load at the reflector tiles is essential for reliable X3- and O2-operation. For this purpose, small pick-up holes will be integrated into the tiles. The microwave signal will be transferred by 4 mm copper tubes over a distance of about 2 m towards the B-type port in the W7-X vacuum vessel. The positions of the 100 pick-up horns and the line routing was defined in close co-operation with the W7-X KIP group (Komponenten im Plasmagefäß).

Staff:

IHM / FZK

A. Arnold  
K. Baumann  
G. Dammertz  
G. Gantenbein  
R. Heidinger (IMF I)  
S. Illy  
S. Kern  
M. Kupper  
W. Leonhardt  
R. Lang  
D. Mellein  
B. Piosczyk  
H. O. Prinz  
U. Saller  
M. Schmid  
W. Spiess  
J. Szczesny  
M. Thumm  
J. Weggen  
C. Zöller

IPF  
(University of Stuttgart)

P. Brand  
C. Lechte  
M. Grünert  
W. Kasperek  
H. Kumric  
M. Krämer  
R. Munk  
F. Müller  
B. Plaum  
S. Prets  
P. Salzmann  
K.H. Schlüter  
D. Wimmer

IPP  
(Greifswald/Garching)

B. Berndt  
H. Braune  
V. Erckmann (PMW)  
F. Hollmann  
L. Jonitz  
H. Laqua  
G. Michel  
M. Nitz (Diplomand)  
F. Noke  
F. Purps  
T. Schulz  
P. Uhren  
M. Weißgerber

## Literature:

- [1] V. Erckmann, P. Brand, H. Braune, G. Dammertz, G. Gantenbein, W. Kasperek, H.P. Laqua, H. Maassberg, N.B. Marushchenko, G. Michel, M. Thumm, Y. Turkin, M. Weissgerber, A. Weller: W7-X ECRH Teams at FZK Karlsruhe and IPF Stuttgart. *Electron Cyclotron Heating for W7-X: Physics and Technology. Fusion Sci. Technol.* 52 (2007), 291 – 312.
- [2] M. Thumm, S. Alberti, A. Arnold, P. Brand, H. Braune, G. Dammertz, V. Erckmann, G. Gantenbein, E. Giguet, R. Heidinger, J.P. Hogge, S. Illy, W. Kasperek, H.P. Laqua, F. Legrand, W. Leonhardt, C. Lievin, G. Michel, G. Neffe, B. Piosczyk, M. Schmid, K. Schwörer, M.Q. Tran: EU Megawatt-Class 140-GHz CW gyrotron. *IEEE Trans. Plasma Science*, PS-35 (2007), 143 – 153.
- [3] W. Kasperek, M.I. Petelin, V. Erckmann, D.Yu. Shchegol'kov, A. Bruschi, S. Cirant, M. Thumm, B. Plaum, M. Grünert, M. Malthaner: Fast switching and power combination of high-power electron cyclotron wave beams: principles, numerical results and experiments. *Fusion Sci. Technol.* 52 (2007), 281 – 290.
- [4] W. Kasperek, P. Brand, H. Braune, G. Dammertz, V. Erckmann, G. Gantenbein, F. Hollmann, L. Jonitz, H. Kumrić, H.P. Laqua, C. Lechte, W. Leonhardt, G. Michel, F. Noke, B. Plaum, F. Purps, M. Schmid, T. Schulz, M. Thumm, Fellow, IEEE, P. Uhren, M. Weißgerber, and the W7-X ECRH teams at IPP Greifswald, FZK Karlsruhe and IPF Stuttgart: The Electron Cyclotron Heating System for the Stellarator W7-X: Status and Recent Achievements *Proc. of 2007 Joint 32nd International Conference on Infrared Millimeter Waves and 15th International Conference on Terahertz Electronics*, Sept. 3 – Sept. 7, 2007, Cardiff, Wales, UK, IEEE Catalog number: 07EX1863, ISBN: 1-4244-1438-5, Vol. 2, 939 – 940 (2007).
- [5] W. Kasperek, M. Petelin, D. Shchegolkov, V. Erckmann, B. Plaum, A. Bruschi, ECRH groups at IPP Greifswald, FZK Karlsruhe, and IPF Stuttgart: FaDiS, a Fast Switch and Combiner for High-power Millimetre Wave Beams. *Proc. of 2007 Joint 32nd International Conference on Infrared Millimeter Waves and 15th International Conference on Terahertz Electronics*, Sept.3 – Sept.7, 2007, Cardiff, Wales, UK, IEEE Catalog number: 07EX1863, ISBN: 1-4244-1438-5, Vol.1, 389 – 390 (2007).
- [6] G. Gantenbein, H. Braune, G. Dammertz, S. Alberti, V. Erckmann, J.P. Hogge, S. Illy, W. Kasperek, H.P. Laqua, F. Legrand, W. Leonhardt, C. Lievin, G. Michel, G. Neffe, F. Noke, B. Piosczyk, F. Purps, M. Schmid, M. Thumm, M.Q. Tran: High-power experiments with 140 GHz series gyrotrons for W7-X. *8th IEEE Internat. Vacuum Electronics Conf. (IVEC 2007)*, Kitakyushu, Japan, May 15-17, 2007, Proc. S.41-42, Piscataway, N.J. : IEEE Operations Center, 2007, ISBN 1-4244-0633-1
- [7] G. Gantenbein, G. Dammertz, V. Erckmann, S. Illy, W. Kasperek, C. Lechte, F. Legrand, G. Lietaer, C. Lievin, B. Piosczyk, M. Schmid, M. Thumm: Experimental results on high-power gyrotrons for the stellarator W7-X. Griffin, M.J. [Hrsg.] *Joint 32nd Internat. Conf. on Infrared and Millimetre Waves, and 15th Internat. Conf. on TeraHertz Electronics*, Cardiff, GB, September 2-7, 2007 *Conf. Digest Vol. I S.102-03* Piscataway, N.J. : IEEE, 2007 ISBN 1-4244-1438-5
- [8] W. Kasperek, P. Brand, H. Braune, G. Dammertz, V. Erckmann, G. Gantenbein, F. Hollmann, L. Jonitz, H. Kumric, H.P. Laqua, C. Lechte, W. Leonhardt, G. Michel, F. Noke, B. Plaum, F. Purps, M. Schmid, T. Schulz, M. Thumm, P. Uhren, M. Weißgerber, W7-X ECRH Teams at IPP, FZK and IPF: The electron cyclotron heating system for the stellarator W7-X: status and recent achievements. Griffin, M.J. [Hrsg.] *Joint 32nd Internat. Conf. on Infrared and Millimetre Waves, and 15th Internat. Conf. on TeraHertz Electronics*, Cardiff, GB, September 2-7, 2007 *Conf. Digest Vol. II S.939-40*, Piscataway, N.J. : IEEE, 2007, ISBN 1-4244-1438-5
- [9] H. Braune, P. Brand, G. Dammertz, V. Erckmann, G. Gantenbein, W. Kasperek, H.P. Laqua, C. Lechte, W. Leonhardt, D. Mellein, G. Michel, F. Noke, F. Purps, K.H. Schlüter, M. Schmid, M. Thumm, W7-X ECRH Teams at IPP, IPF and FZK: Extended operation of the 1 MW, CW gyrotrons for W7-X. Griffin, M.J. [Hrsg.] *Joint 32nd Internat. Conf. on Infrared and Millimetre Waves, and 15th Internat. Conf. on TeraHertz Electronics*, Cardiff, GB, September 2-7, 2007, *Conf. Digest Vol. I S.104-05* Piscataway, N.J. : IEEE, 2007
- [10] M. Thumm, S. Alberti, A. Arnold, P. Brand, H. Braune, G. Dammertz, V. Erckmann, G. Gantenbein, E. Giguet, R. Heidinger, J.P. Hogge, S. Illy, W. Kasperek, H.P. Laqua, F. Legrand, W. Leonhardt, C. Lievin, G. Michel, G. Neffe, B. Piosczyk, M. Schmid, K. Schwörer, M.Q. Tran: EU megawatt-class 140-GHz CW gyrotron. *IEEE Transactions on Plasma Science*, 35(2007) S.143-53 DOI:10.1109/TPS.2007.892144
- [11] M. Thumm, G. Dammertz, G. Gantenbein, S. Illy, W. Leonhardt, G. Neffe, B. Piosczyk, M. Schmid, H. Braune, V. Erckmann, H.P. Laqua, G. Michel, M. Weissgerber, P. Brand, W. Kasperek, C. Lechte: 10 MW, 140 GHz, CW millimeter wave system for nuclear fusion plasma heating, *Proc. 41st IMPI Annual Microwave Symp.*, Vancouver, CDN, 2007, p. 2 (invited).

- [12] G. Gantenbein, A. Arnold, G. Dammertz, J. Flamm, R. Heidinger, S. Illy, J. Jin, W. Leonhardt, G. Neffe, B. Piosczyk, O. Prinz, Th. Rzesnicki, M. Schmid, M. Thumm, X. Yang: Gyrotron development for electron-cyclotron-resonance heating systems in fusion devices at FZK. Jahrestagung Kerntechnik 2007, Karlsruhe, 22.-24.Mai 2007, Berlin : INFORUM GmbH, 2007 S.624-28, CD-ROM
- [13] B. Piosczyk, G. Dammertz, A. Arnold, G. Gantenbein, S. Illy, J. Jin, O. Prinz, J. Flamm, T. Rzesnicki, M. Thumm, S. Alberti, T. Goodman, J.P. Hogge, M.Q. Tran, V. Erckmann, H. Laqua, G. Michel, O. Dumbraijs, P. Benin, E. Giguët, C. Lievin: Development of high power gyrotrons for fusion applications at FZK Karlsruhe. Pulsed Power and Plasma Science Conf., Albuquerque, N.M., June 17-22, 2007
- [14] G. Gantenbein, H. Braune, G. Dammertz, V. Erckmann, S. Illy, W. Kasperek, H.P. Laqua, C. Lechte, F. Legend, C. Lievin, W. Leonhardt, G. Michel, F. Noke, B. Piosczyk, F. Purps, M. Schmid, M. Thumm: 1 MW, 140 GHz, CW gyrotron for W7-X. Status report on series gyrotrons. 19th Joint Russian-German STC Workshop on ECRH and Gyrotrons, Karlsruhe/Stuttgart/Garching, July 18-24, 2007
- [15] G. Gantenbein, G. Dammertz, V. Erckmann, S. Illy, W. Kasperek, C. Lechte, C. Lievin, B. Piosczyk, M. Schmid, M. Thumm: Status report on series gyrotrons for the 10 MW, 140 GHz, CW ECRH system of the stellarator W7-X. Workshop on RF Heating Technology of Fusion Plasmas, Heidelberg, September 10-12, 2007, Book of Abstracts
- [16] V. Erckmann, P. Brand, H. Braune, G. Dammertz, G. Gantenbein, W. Kasperek, H.P. Laqua, H. Maassberg, N.B. Marushchenko, G. Michel, M. Thumm, Y. Turkin, M. Weissgerber, A. Weller, W7-X ECRH Teams at IPP, IPF and FZK: Electron cyclotron heating for W7-X: physics and technology. Fusion Science and Technology, 52(2007) S.291-312
- [17] M. Thumm, G. Dammertz, G. Gantenbein, S. Illy, W. Leonhardt, G. Neffe, B. Piosczyk, M. Schmid, H. Braune, V. Erckmann, H.P. Laqua, G. Michel, M. Weissgerber, P. Brand, W. Kasperek, C. Lechte: 10 MW, 140 GHz, CW gyrotron and optical transmission system for millimeter wave heating of plasmas in the stellarator W7-X. 1st Shenzhen Internat.Conf.on Advanced Science and Technology – THz, Radiation Science and Technology, Shenzhen, China, November 18-23, 2007
- [18] M. Thumm, G. Dammertz, G. Gantenbein, S. Illy, W. Leonhardt, G. Neffe, B. Piosczyk, M. Schmid, H. Braune, V. Erckmann, H.P. Laqua, G. Michel, M. Weissgerber, P. Brand, W. Kasperek, C. Lechte: Progress on the 10 MW GHz ECH system for the stellarator W7-X. Pulsed Power and Plasma Science Conf., Albuquerque, N.M., June 17-22, 2007, Book of Abstracts S.236
- [19] H. Braune, P. Brand, V. Erckmann, L. Jonitz, W. Leonhardt, D. Mellein, G. Michel, G. Müller, F. Purps, K.-H. Schlüter, M. Winkler, The W7-X ECRH Teams at IPP, IPF and FZK: Architecture of central control system for the 10 MW ECRH-plant at W7-X, Fusion Engineering and Design, 82, 677-685 (2007).
- [20] M. Schmid, S. Illy, G. Dammertz, V. Erckmann, M. Thumm: Transverse field collector sweep system for high power CW gyrotrons, Fusion Engineering and Design, 82, 744-750 (2007).



## **Underlying Technology**



## Underlying Technology

### Operation of the Fusion Materials Laboratory (FML)

The Fusion Materials Laboratory provides the infrastructure for the performance of tasks defined in the EFDA workprogramme related to the characterisation and testing of irradiated and non-irradiated materials. Methods such as optical and electron microscopy, tritium adsorption and desorption, He pycnometry and Hg porosimetry, crush load, micro hardness, creep, Charpy impact, tensile, LCF and instrumented indentation tests as well as long-time annealing tests are applied. The work includes Post Irradiation Examinations (PIE) of Reduced Activation Ferritic Martensitic (RAFM) steels (reference material for DEMO and ITER-TBMs), investigations on materials relevant for the HCPB blanket (ceramic breeder materials, beryllium) and Plasma Facing Materials (tiles) from tokamaks (JET, TFTR).

PIE on selected samples from the HFR IB and HFR IIB experiments were performed. For this purpose tensile tests were performed and tested specimens' small cuts for light optical, scanning and transmission electron microscopy were prepared and examined. LCF tests were started. Broken halves of Charpy specimens were prepared for instrumented indentation and served for identifying material parameters and Vickers hardness. The aim of the investigations was to study the irradiation effects on the mechanical and structural properties of these materials.

The investigation of blanket materials was continued with the characterisation of materials. Lithium orthosilicate pebbles were investigated by light optical microscopy and their porosity and deformation hardness were determined. Different batches of materials were characterised with respect to the influence of parameters of the fabrication process on the mechanical and structural properties. Tritium adsorption/desorption tests were done on grain size fixed lithium orthosilicate pebbles.

Adsorption and desorption experiments were also done with unirradiated beryllium titanium pebbles. Furthermore different beryllium titanium alloys were characterized by light optical microscopy and porosity measurements.

The characterization of pebbles from a uniaxially compressed metallic pebble bed for the determination of the mechanical parameters and the thermal conductivity of the metallic pebble bed was finished.

Further samples from ASDEX, JET and TFTR carbon tiles were prepared for the investigation of tritium retention in these materials. In the TLK these samples were analysed.

Detailed results and consecutive analysis of the measurements are reported in the respective chapters of this Annual Report.

For the PIE the following equipment was used:

- Charpy impact and tensile testing devices
- Indentation device for instrumented ball-indentation and Vickers hardness-test
- Light optical, scanning electron and transmission electron microscopes
- Desorption device with high temperature furnace for tritium and helium release measurements
- He-pycnometer and Hg-porosimeter
- Sphere crush and creep testing apparatus.

In the frame of the upgrading programme, a new 200 kV transmission electron microscope for investigation of radioactive material was specified and tendered. The specified new remotely operated light optical microscope was ordered and is under construction at the contractor.

### **Future activities**

Continuation of measurements as referred to above:

- PIE of the HFR II B irradiation phase: some 160 samples of steel, 15 dpa
- PIE of the BOR 60 irradiation campaign: some 100 samples of steel, 15 – 30 dpa
- Development of a device for instrumented indentation at elevated temperatures
- Characterization of new batches of ceramic breeder materials and beryllium
- Installation of a gamma-ray spectrometer to study the activation of RAFM steels

### Staff:

P. Barié  
J. Ehrmann  
A. Erbe  
M. Gilpert  
M. Holzer  
H. Jackisch  
S. Lautensack  
P. Lauterbach  
G. Mangei  
W. Nägele  
H. Ries  
R. Rolli  
G. Rösch  
I. Sacksteder  
Schmidt  
H.-C. Schneider  
H. Steinle

### Literature:

- [1] N. Bekris, J.P. Coad, K. Sugiyama, C. Caldwell-Nichols, T. Tanabe, B. Kloppe, R. Rolli and JET-EFDA Contributors, "Ex-situ Tritium removal from JET tiles using RF inductive heating", ISFNT 8, paper PS2 – 3002, October 2007
- [2] J. Reimann, R.A. Pieritz, C. Ferrero, M. di Michiel, R. Rolli, "X-ray tomography investigations on pebble bed structures", ISFNT 8, paper PS3 – 3024, October 2007
- [3] Schneider, H.-C., Aktaa, J. and Rolli, R.: "Small fracture toughness specimen for post-irradiation experiments", Journal of Nuclear Materials, 367-370 (2007), pages 599-602
- [4] Gaganidze, E.; Schneider, H.C.; Dafferner, B.; Aktaa, J.: "Embrittlement behaviour of neutron irradiated RAFM steels", Journal of Nuclear Materials, 367-370 (2007), pages 81-85

## Appendix I: FZK Departments Contributing to the Fusion Programme

<b>FZK Department</b>	<b>FZK Institut/Abteilung</b>	<b>Director</b>	<b>Ext.</b>
Institute for Materials Research	Institut für Materialforschung (IMF)	I. Prof. Dr. K.-H. Zum Gahr	3897
		II. Prof. Dr. O. Kraft	4815
		III. Prof. Dr. H. Haußelt	2518
Institute for Pulsed Power and Microwave Technology	Institut für Hochleistungsimpuls- und Mikrowellentechnik (IHM)	Prof. Dr. M. Thumm	2440
Institute for Nuclear and Energy Technology	Institut für Kern- und Energietechnik (IKET)	Prof. Dr. T. Schulenberg	3450
Institute for Reactor Safety	Institut für Reaktorsicherheit (IRS)	Dr. J. Knebel (Acting Head)	2550/ 5510
Institute for Technical Physics	Institut für Technische Physik (ITP)	Prof. Dr. M. Noe	3500
- Tritium Laboratory Karlsruhe	- Tritiumlabor Karlsruhe (TLK)	Dr. L. Dörr	4546
Institute for Data Processing and Electronics	Institut für Prozessdatenverarbeitung und Elektronik (IPE)	Prof. Dr. H. Gemmeke	5635



## Appendix II: Fusion Programme Management Staff

<b>Head of the Research Unit</b>	Dr. G. Janeschitz	ext. 5460 e-mail: guenter.janeschitz@fusion.fzk.de
Assistant:	Mrs. M. Winkelmann	ext. 5461 e-mail: miriam.winkelmann@fusion.fzk.de
Secretariat:	Mrs. M. Lettow-Rattu	ext. 2435 e-mail: mira.lettow-rattu@fusion.fzk.de
<b>Program Budget, Administration, Reports, EU-Affairs</b>	BW. M. Henn	ext. 5547 e-mail: michael.henn@fusion.fzk.de
	Mrs. V. Lallemand	ext. 6461 e-mail: vera.lallemand@fusion.fzk.de
	Mrs. I. Pleli	ext. 8292 e-mail: ingrid.pleli@fusion.fzk.de
<b>Blanket and Divertor Development, HELOKA, IFMIF, Public Relations</b>	DI. W. Bahm	ext. 5465 e-mail: werner.bahm@fusion.fzk.de
	Dr. D. Radloff	ext. 8750 e-mail: dirk.radloff@fusion.fzk.de
<b>Fuel Cycle, Structural Materials, Superconducting Magnets, CAD-Office</b>	DI. S. Gross	ext. 5468 e-mail: sigurd.gross@fusion.fzk.de
<b>Plasma Heating Technology, Safety Studies, Neutronics, Physics</b>	Dr. K. Hesch	ext. 5462 e-mail: klaus.hesch@fusion.fzk.de
<b>Quality Management</b>	DI. P. Freiner	ext. 4194 e-mail: peter.freiner@fusion.fzk.de
<b>Resource Loaded Planning, Document Management</b>	Mrs. C. Hermsmeyer	Ext. 5466 e-mail: carmen.hermsmeyer@fusion.fzk.de

**Address:**

**Forschungszentrum Karlsruhe GmbH  
Nuclear Fusion Programme Management  
Post Office Box 3640, D - 76021 Karlsruhe / Germany**

**Telephone No:**

**07247-82- Extensions .....**

**Telefax No:**

**07247-82-5467**

**world wide web:**

**<http://www.fzk.de/fusion>**



### Appendix III: Glossary

3D	Three-dimensional
A	Total Strain
AC	Alternating Current
$A_{c1b}$	Temperature at which the transformation from ferrite to austenite begins (during heating)
$A_{c1e}$	Temperature at which the transformation from ferrite to austenite is complete (during heating)
ACP	Activated Corrosion Products
ADS	Atomosphere Detritiation System
$A_g$	Uniform Strain
AGHS	Active Gas Handling System
AGR	Advance Gas Cooled Fission Reactor
ALTAIR	Fast Reactor Irradiation from CEA in BOR 60
AP	Activated Dust
Appm	Atomic parts per million
ARBOR-1	Fast Reactor Irradiation from FZK in BOR 60
ARBOR-2	Fast Reactor Irradiation from FZK and CEA in BOR 60
ASDEX	Axial-Symmetrisches Divertor-EXperiment
ASTM	American Society for Testing and Materials
BD	Brittle Destruction
BFTEM	Bright Field Transmission Electron Microscope
BIXS	Beda-Induced X-ray Spectrometry
BN	Boron Nutride
BOP	Bond Order Potential
BOR 60	Fast Reactor at SSC RF RIAR
BSM	Blanket Shield Module
BU	Breeding Unit
CAD	Computer Aided Design
CD	Cryogenic Distillation
CEA	Commissariat à l'Energy Atomique
CECE	Combined Electrolysis Catalytic Exchange
CFC	Carbon Fiber Composite
CFD	Computational Fluid Dynamic
CICC	Cable in Conduit Conductor
CL	Current Lead
Co	Cobalt
COSYMA	<u>C</u> ode <u>S</u> ystem <u>M</u> aria

CPI	Communication and Power Industries
CRPP	Centre de Recherches en Physique des Plasmas
CS	Central Solenoïd
CTB	Coil Terminal Box
Cu	Copper
CW	Continuous Wave
D1S	Direct one-step method for shut-down dose rate calculations
DACS	Data Acquisition and Control System
DBTT	Ductile-to-Brittle Transition Temperature
DCLL	Dual Coolant Lithium Lead
DD	Deuterium Deuterium Fusion Process
DD	Dudarev Derlet Potential
DDD	Design Description Document
DDD	Discrete Dislocation Dynamics
DEMO	Demonstration Power Station
DFT	Density Functional Theory
DOURY	French Dispersion Parametrisation
dpa	Displacement per atom
DSCD	Demo Structural Design Code
DT	Deuterium Tritium Fusion Process
EB	Electron Beam
ECA	Electro-Chemical Aluminium Deposition
ECCD	Electron Cyclotron Current Drive
ECH&CD	Electron Cyclotron Heating and Current Drive
ECRH	Electron Cyclotron Resonance Heating
EDM	Electron Discharge Method
EDX	Energy Dispersive X-ray Analysis
EELS	Electron Energy Loss Spectroscopy
EFDA	European Fusion Development Agreement
ELM	Edge Localized Mode
EM	Electro Magnetic
ENEA	Ente per le Nuove Tecnologie, l'Energia e l'Ambiente, Italy
EUROFER 97	European RAF/M Steel
F82H mod.	Japanese RAF/M Steel
FCI	Flow Channel Insert
Fe <sub>3</sub> C	Cementite

FEM	Finite Element Method
FFT	Fast Fourier Transformation
FIB	Focussed Ion Beam
FMEA	Failure Mode and Effect Analysis
FML	Fusion Materials Laboratory
FOM	FOM-Institute for Plasma Physics Rijnhuizen
FPD	Full Power Days
FPSS	Fusion Power Shutdown System
FS	Finnis Sinclair
FW	First Wall
FZJ	Forschungszentrum Jülich
FZK	Forschungszentrum Karlsruhe
HAADF	High Angle Annular Dark Field Detector
HAZ	Heat Affected Zone
HCLL	Helium Cooled Lithium Lead
HCPB	Helium Cooled Pebble Bed
HCS	Helium Cooling System
HDA	Hot Dip Aluminisation
HELICA	Helium-Fus3 Lithium Cassette
HELOKA	Helium Loop Karlsruhe
HEMJ	Helium-cooled Divertor Concept with Multiple JET Cooling
HEMS	Helium-cooled Modular Divertor Concept with Integrated Slot Array
HETRA	HEat TRAnSfer Experiment
HEXCALIBER	Helium-Fus3 Experimental Cassette of Lithium, Beryllium Pebble Beds
HFIR	High Flux Isotope Reactor
HFR	High Flux Reactor
HFTM	High Flux Test Module
HHF	High Heat Flux
HIP	Hot Isostatic Press
HKE	Manufacturer of Instrumented Impact Testing Facilities
HMI	Hahn-Meitner-Institut
HNB	Heating Neutral Beam
HP	High Pressure
HPFPP	Hydrogen Production Fusion Power Plant
HRS	Hot Ring Shield
HRTEM	High Resolution Transmission Electron Microscope

HT	High Temperature
HTC	Heat Transfer Coefficient
HTO	Tritiated Water Vapour
HTS	High Temperature Superconducting
HTSE	High Temperature Steam Electrolysis
IAEA	International Atomic Energy Agency
IFMIF	International Fusion Materials Irradiation Facility
IPF	Max-Planck Institute for Plasma Physics, Garching
IPP	Institut für Plasmaforschung, Universität Stuttgart
IR	Infrared
ISO	International Organization for Standardization
ISS	Isotope Separation System
ISTC	International Science and Technology Center
ITER	International Thermonuclear Experimental Reactor
ITERVAC	Code for Vacuum Gas Flows
JET	Joint European Torus
JETT	J-Evaluation on Tensile Test
KLST	Kleinlast Impact Specimen
KN	Kilo Newton
LCF	Low Cycle Fatigue
LF	Low Frequency
LHT	Launcher Handling Test Facility
LOCA	Loss of Coolant Accident
LPCE	Liquid Phase Catalytic Exchange
LTS	Low Temperature Superconducting
MANET-I	European 12 % Cr Steel
MBWG	Multi-beam Waveguide
MC	Monte Carlo
McCad	Interface programme for the conversion of CAD to MCNP geometry data
MCNP	Monte Carlo Neutron Photo (code for particle transport simulations)
MD	Molecular Dynamics
MEKKA	Magneto-Hydrodynamic Experiments in NaK Karlsruhe
$M_f$	Temperature at which martensite formation is complete (during quenching)
MFTM	Medium Flux Test Module
MHD	Magneto Hydrodynamic
MK-200UG	The Name of a Plasma Gun in TRINTI, Troitsk, Russia

MMS	Mechanical Monitoring System
MMS	Multi-Module-Segment
MPa	Mega Pascal
$M_s$	Temperature at which martensite formation starts (during quenching)
MS	Monitoring System
NB	Neutral Beam
NBI	Neutral Beam Injector
NBTF	Neutral Beam Test Facility
NDT	Non-destructive Detection Techniques
$N_f$	Number of Cycles to failure
NRG	Nuclear Research and Consultancy Group, National Nuclear Research Institute of the Netherlands, located in Petten
N-VDS	Normal Vent Detritiation System
OBT	Organically Bound Tritium
ODS	Oxide Dispersed Strengthened (steel)
OM	Optical Microscopy
OPL	Outer Poloidal Limiter
OPTIFER IVc	German RAF/M Steel
ORNL	Oak Ridge National Laboratory
OSi	Lithium Orthosilicate
OST	Oxford Superconducting Technology
PCP	Prototype Cryosorption Pump
PF	Poloidal Field
PFC	Plasma Facing Components
PICOLO	Pb-Li Corrosion Loop
PIE	Post Irradiation Examination
PIM	Powder Injection Molding
PLC	Programmable Logic Control
PMW	Projekt Mikrowellenheizung for W7X
PPCS	Power Plant Conceptual Study
PTC	Prototype Torus Cryopump
PWHT	Post Weld Heat Treatment
QSPA	The Name of a Plasma Gun in TRINTI, Troitsk, Russia
R2S	Rigorous two-step method for shut-down dose rate calculations
RAF	Reduced Activation Ferritic (steel)
RAFM	Reduced Activation Ferritic Martensitic
REM	Raster Electron Microscope

RF	Radio Frequency
RF	Russian Federation
RGA	Residual Gas Analyser
RH	Remote Handling
R <sub>m</sub>	Ultimate Tensile Stress
R <sub>p0.2</sub>	Yield Stress
RT	Room Temperature
SBWG	Single-beam Waveguide
SC	Single Crystal
sccm	Cubic centimetre per minute at standard conditions (0°C, 101325 Pa)
SCHe	Supercritical Helium
SDC	Structural Design Code
SDS	Storage and Delivery System
SEM	Scanning Electron Microscopy
SI	Sulphur-Iodine Process
SiC <sub>f</sub>	Silicon Carbide (f = fibre)
SIWAS	Reactor Irradiation from NRG
SOL	Scrape-off Layer
SPICE	Sample Holder for Irradiation of Miniaturised Steel Specimens Simultaneously at Different Temperatures
SPM	Solid Polymer Electrolyser
SSC RF RIAR	State Scientific Centre of Russian Federation Research Institute of Atomic Reactors
SSTT	Small Scale Test Techniques
SUMO	Reactor Irradiation from NRG
TB	Tight Binding
TBM	Test Blanket Module
TD	Theoretical Density
TED	Thales Electron Devices, Vélizy
TEKES	National Technology Agency (TEKES), Helsinki, Finland
TEM	Transmission Electron Microscope
TEP	Tokamak Exhaust Processing
TF	Toroïdal Field
TFSS	Transverse Field Sweep System
TFTR	Tokamak Fusion Test Reactor (Princeton)
TIG	Tungsten Inert Gas
TIMO	Test Facility for ITER Model Pump
TLD	Thermo Luminescence Detector

TLK	Tritium Laboratory Karlsruhe
TLO	Technical Liaison Organisation
TRIMO	Tritium Inventory Modelling
TSEFEY	Electron-beam Testing Facility
UFOTRI	<u>U</u> nfall <u>f</u> olgenmodel <u>T</u> ritium
UHV	Ultrahigh Vacuum
UKAEA	United Kingdom Atomic Energy Authority
USE	Upper Shelf Energy
VAMAS	The Versailles Project on Advanced Materials and Standards
VDE	Vertical Displacement Event
VDS	Vent Detritiation System
VHL	Very High Level
VV	Vacuum Vessel
VPSS	Vacuum Vessel Pressure Suppression System
W	Tungsten
WCLL	Water Cooled Lithium Lead
WDS	Water Detritiation System
WL10	Tungsten, Dispersion Strengthened with 1 wt.% La <sub>2</sub> O <sub>3</sub> Particles
WLa <sub>2</sub> O <sub>3</sub>	Tungsten Lanthanum Oxide Alloy
WSP	Westinghouse Hybrid Sulphur Process
XRD	X-ray Diffraction
YBCO	YBa <sub>2</sub> Cu <sub>3</sub> O <sub>x</sub>